Spectroscopic Analysis of the $^3\mathrm{He}$ Anomaly in B-Type Stars

Masterarbeit aus der Physik

Vorgelegt von
David Schneider

Bamberg, 6. Februar 2017

Dr. Karl Remeis Sternwarte Bamberg
Astronomisches Institut der
Friedrich-Alexander-Universität Erlangen-Nürnberg

ERLANGEN CENTRE
FOR ASTROPARTICLE
PHYSICS

Betreuer:
Prof. Dr. Ulrich Heber
Dr. Andreas Irrgang

Zusammenfassung

In der jüngeren Vergangenheit wurden heliumreiche Hauptreihensterne (14 000 K $\lesssim T_{\mathrm{eff}} \lesssim$ 21 000 K) und heiße Unterzwerge mit 27 000 K $\lesssim T_{\mathrm{eff}} \lesssim$ 31 000 K der Spektralklasse B (auch unterleuchtkräftige B-Sterne oder kurz sdBs genannt) sowie blaue Horizontalaststerne mit einem erhöhten Anteil des $^{3}\mathrm{He}$ Isotops entdeckt. Es steht außer Frage, dass Diffusionsvorgänge auf atomarer Ebene in der Atmosphäre dieser Sterne zu den beobachteten Häufigkeitsanomalien führen. Jedoch brauchen gewöhnliche gravitationsbedingte Diffusionsvorgänge verglichen mit der Lebenszeit des jeweiligen Sterns zu lange, um die meisten dieser Anomalien erklären zu können. Andere theoretische Modelle wie das Zusammenspiel zwischen stellaren Winden und Diffusionsvorgängen in der Atmosphäre von Hauptreihensternen oder der sogenannte „Light induced drift“ (LID) verschaffen hier Abhilfe. Eine detaillierte quantitative Spektralanalyse mit Hilfe von hochauflösenden Spektren zur Bestimmung des atmosphärischen Heliumisotopieverhältnisses in bekannten $^{3}\mathrm{He}$-Sternen der Spektralklasse B wurde bis jetzt aber noch nicht durchgeführt.

Folglich besteht das Hauptziel der vorliegenden Arbeit darin, zwischen den beiden Isotopen $^{3}\mathrm{He}$ und $^{4}\mathrm{He}$ zu unterscheiden und ihre jeweiligen Elementhäufigkeiten in der Atmosphäre von 17 ausgewählten Sternen der Spektralklasse B zu bestimmen, um die $^{3}\mathrm{He}$-Anomalie untersuchen und Häufigkeitsverhältnisse ableiten zu können. Die Stichprobe beinhaltet zwei blaue Horizontalaststerne mit $^{3}\mathrm{He}$ sowie 15 heiße Unterzwerge der Spektralklasse B (13 mit $^{3}\mathrm{He}$ und zwei ohne, die als Vergleichssterne dienen sollen). Ebenso sollen die Metallhäufigkeiten von C, N, O, Ne, Mg, Al, Si, S, Ar und Fe für die betreffenden Sterne bestimmt werden. Die quantitative Spektralanalyse wird anhand von hochauflösenden Spektren durchgeführt, die mit Hilfe von fünf unterschiedlichen Echelle Spektrographen, darunter CASPEC (ehemals verwendet am ESO 3.6 m Teleskop), FEROS (am ESO 2.2 m Teleskop), FOCES (am Calar Alto 2.2 m bzw. 3.5 m Teleskop), HRS (am Hobby-Eberly Teleskop) und UVES (am ESO VLT), aufgenommen wurden.

Zur quantitativen Spektralanalyse wird die Temperatur- und Dichteschichtung im lokalen thermodynamischen Gleichgewicht (LTE) mit Hilfe des Programms ATLAS12 modelliert. Die erzeugten Modellatmosphären basieren dabei auf mittlerer Metallizität für heiße Unterzwerge der Spektralklasse B. Abweichungen vom LTE werden mit dem Programm DETAIL bei der Bestimmung der atomaren Besetzungszahlen im statistischen Gleichgewicht berücksichtigt. Zuletzt werden die optischen Spektren im Detail mit Hilfe des Programms SURFACE synthetisiert, wobei alle Modellatome, darunter auch ein erst kürzlich entwickeltes für $^{3}\mathrm{He}$, verwendet werden.

Die meisten der analysierten heißen Unterzwerge mit $^{3}\mathrm{He}$ häufen sich in einem engen Temperaturbereich zwischen $\sim$ 26 000 K und 30 000 K. Neben den bereits bekannten heißen Unterzwergen der Spektralklasse B mit $^{3}\mathrm{He}$ wurde zudem noch ein Sample von insgesamt 76 zusätzlichen sdBs aus dem „ESO Supernova Ia Progenitor Survey“ im für $^3\mathrm{He}$ sdBs relevanten Temperaturbereich untersucht, von denen vier Sterne ebenfalls als sogenannte $^3\mathrm{He}$ sdBs klassifiziert werden konnten. Alle untersuchten $^3\mathrm{He}$-Sterne weisen Häufigkeitsverhältnisse von $^4\mathrm{He}/^3\mathrm{He} \sim$ 0-7 auf, die die beobachteten Isotopieverschiebungen mehr oder weniger reproduzieren. Die Profile der untersuchten Heliumlinien einiger Sterne, darunter diejenigen der beiden analysierten blauen Horizontalaststerne sowie diejenigen von drei heißen Unterzwergen, können jedoch nicht korrekt reproduziert werden. Diese Sterne zeigen Hinweise auf vertikale Heliumschichtung in ihren Atmosphären, was bis jetzt nur bei einigen wenigen Hauptreihen- und blauen Horizontalaststernen nachgewiesen wurde. Zu guter Letzt weisen die Metallhäufigkeitsmuster der $^3\mathrm{He}$-Sterne keine Abweichungen gegenüber denen normaler unterleuchtkräftiger B-Sterne auf. Jedoch gehören die unterleuchtkräftigen $^3\mathrm{He}$-Sterne der Spektralklasse B zur Gruppe der kohlenstoff-, silizium-, schwefel- und argonreichen heißen Unterzwerge.

Abstract

In the recent past, $^3\mathrm{He}$ isotope enrichment in helium-weak B-type main-sequence (14 000 K $\lesssim T_{\mathsf{eff}} \lesssim$ 21 000 K) as well as in blue horizontal branch (BHB) and hot subdwarf B stars (short sdBs, but also known as hot subluminous B stars) with 27 000 K $\lesssim T_{\mathsf{eff}} \lesssim$ 31 000 K has been discovered. It is out of question that atomic diffusion processes occurring in the atmosphere of these stars lead to the observed abundance anomalies. However, normal diffusion processes driven by gravitational settling take too long compared to the particular stellar lifetime and, therefore, are inadequate to explain most of these anomalies. Here, other diffusion models like the diffusion mass-loss model for main-sequence stars and the light induced drift (LID) provide remedies. A detailed quantitative spectral analysis of high-resolution spectra in order to derive photospheric isotopic helium abundance ratios for known $^3\mathrm{He}$ B-type stars has not been performed yet, though.

In consequence, this thesis' main goal is the distinction between $^3\mathrm{He}$ and $^4\mathrm{He}$ and the determination of their individual elemental abundances in the atmospheres of a sample of 17 B-type stars which consists of two $^3\mathrm{He}$ BHB, and 15 sdB stars (13 $^3\mathrm{He}$ sdBs and two He-normal sdBs) in order to spectroscopically study the $^3\mathrm{He}$ anomaly and to derive abundance ratios. Also, metal abundances for C, N, O, Ne, Mg, Al, Si, S, Ar, and Fe are derived for the relevant stars. The quantitative spectroscopic analysis is performed by means of high-resolution spectra obtained by five different Echelle spectrographs, including CASPEC (used at ESO 3.6 m telescope in the past), FEROS (at ESO 2.2 m telescope), FOCES (at Calar Alto 2.2 m and 3.5 m telescope, respectively), HRS (at Hobby-Eberly telescope), and UVES (at ESO VLT).

For the quantitative spectral analysis the temperature and density stratification is modeled in local thermodynamic equilibrium (LTE) by means of the program ATLAS12. Computed model atmospheres are based on the mean metallicity for sdB stars. Deviations from LTE are taken into account as occupation number densities are calculated in statistical equilibrium by means of the program DETAIL. Finally, the optical spectra are synthesized in detail by means of the program SURFACE, whereby all model atoms, including a lately developed $^3\mathrm{He}$ one, are used.

Most of the analyzed $^3\mathrm{He}$ sdBs cluster in a narrow temperature strip between $\sim$ 26 000 K and 30 000 K. Besides the already known $^3\mathrm{He}$ sdBs, a sample of 76 additional sdBs in total from the hot subdwarf list of the ESO Supernova Ia Progenitor Survey has been re-investigated in the relevant $^3\mathrm{He}$ sdB temperature regime, whereby four of these stars could be identified as $^3\mathrm{He}$ enriched sdBs as well. All analyzed $^3\mathrm{He}$ stars exhibit abundance ratios of $^4\mathrm{He}/^3\mathrm{He} \sim$ 0-7, more or less reproducing the observed isotopic line shifts. For some stars, including both analyzed BHB stars and three sdBs, the investigated helium line profiles cannot be properly reproduced, though. These stars show evidence for vertical helium stratification what has only been reported for a few main-sequence and BHB stars before. Concerning metal abundance

patterns, the $^{3}\mathrm{He}$ sdBs finally show no peculiarities with respect to their He-normal siblings. However, they belong to the group of carbon-, silicon-, sulfur-, and argon-rich sdBs.

Contents

1. Introduction

Astronomy and astrophysics aim to develop a comprehensive understanding of what we call the Universe, putting mankind and the evolution of our home planet Earth into context. It is generally known that our host galaxy is the Milky Way, being only one out of an endless number of galaxies populating the entire Universe. Each of the individual galaxies itself is populated by a countless number of (gravitationally bound) constituents, i.e., by a large number of visible stars, potentially hosting planets like it is the case in our solar system. The scientific topics of present-day research in both fields are numerous. For instance, the search for a second Earth, i.e., for new extrasolar planets in so-called habitable zones of their own solar systems, understanding the fact that only around 5% of the entire Universe consists of "normal matter" and the question of what the remaining 95%, i.e., dark matter and dark energy, actually are, the recent discovery of gravitational waves and the sophisticated knowledge behind their origin, just to mention a few of them. However, the most intuitive and yet simplest access to other galaxies is and remains the investigation of the shining objects - the stars.
Since the beginning of the 20th century, several milestones for the detailed understanding of the nature of stars have been set in astronomy and astrophysics. Amongst others, the development of the so-called Hertzsprung-Russell diagram in order to understand the evolution process of stars and the Harvard spectral classification system for grouping stars into different spectral types according to their individual spectral characteristics. Beyond spectral classification the physical modeling of the stellar atmosphere remains. An extremely fascinating but at the same time challenging task is the detailed understanding of the origin of spectral emission and absorption lines in the stellar atmosphere, in particular the optical part of a stellar spectrum originating in the so-called photosphere. While it is generally accepted that the behavior of the atmosphere is mainly controlled by the density of the gases in it and the interaction of radiation with the stellar plasma, the dependencies of the latter two on chemical composition is not fully understood, though. Specifically, atomic diffusion as a fundamental physical process in stellar atmospheres is out of question, but often ignored because of its complexity. However, it is known today, after several decades of studies, that atomic diffusion can significantly affect the superficial elemental abundances of stars and even their evolution. Abundance anomalies are observed throughout the Hertzsprung-Russell diagram (see Fig. 1.0.1) even though, in first approximation, a large fraction of stars have a chemical composition similar to that of the Sun. Whereas in giants or supergiants with luminosities $L \geq 10^4 L_\odot$, the anomalies appear to be caused by nuclear reactions within the star itself, in most other types of stars, they are mainly the result of atomic transport, i.e., diffusion processes. For instance, some 30% of the warmer main-sequence B, A and F stars with effective temperatures between around 7000 K and 21 000 K display abundance anomalies (Michaud et al., 2015). But anomalies are also present in evolved stars, most notably on the (extreme) horizontal branch in blue

horizontal branch (BHB) and hot subdwarf O and B-type (sdO and sdB) stars. Furthermore, the surface abundances of all white dwarfs are caused mainly by atomic transport processes. Even a closer look at the Sun often reveals the presence of small anomalies caused by diffusion (Michaud et al., 2015).
In a simplistic atmospheric diffusion theory model the particular elemental abundances are set

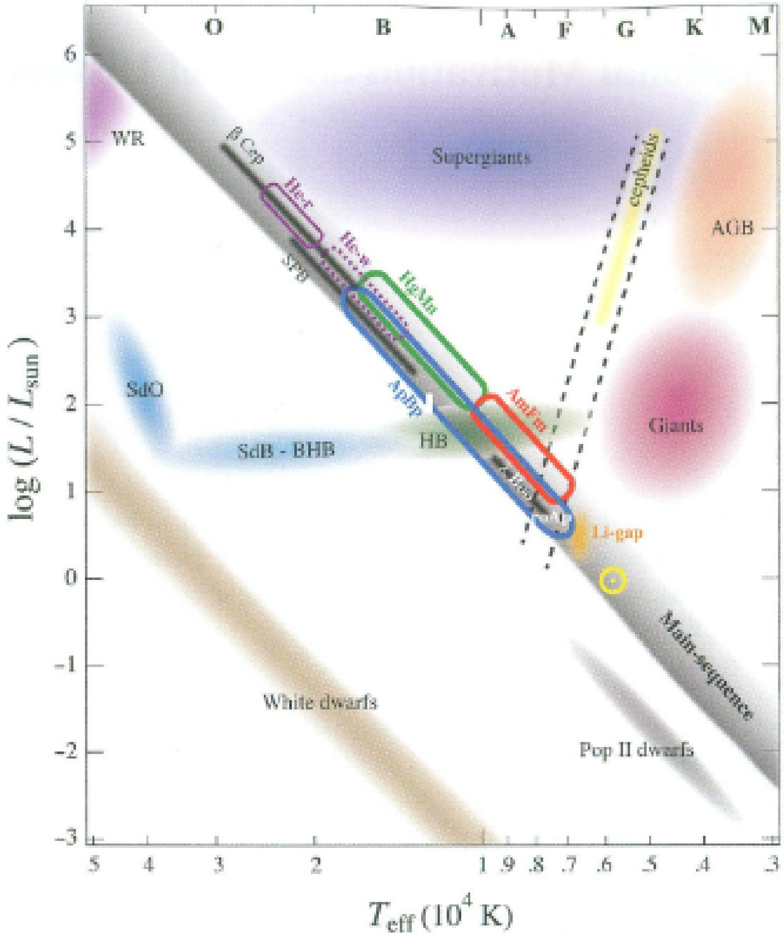

Figure 1.0.1.: Groups of stars showing abundance anomalies in the Hertzsprung-Russell diagram. On the main sequence, anomalies are nearly all believed to be mainly caused by atomic diffusion processes with each group being identified using a heavy colored frame. Abundance anomalies among hot subdwarf O and B-type (sdO and sdB) stars as well as among blue horizontal branch (BHB) stars and white dwarfs are also due to atomic diffusion. Only anomalies in giants and stars with luminosities $L \geq 10^4 L_\odot$ are attributed to nuclear reactions. Adopted from Michaud et al. (2015).

by a balance between gravitational settling caused by gravity and radiative levitation caused by the radiation pressure, since the latter depends on the elemental abundance. Interestingly, if simple atomic diffusion is taken into account, it turns out that all B-type main-sequence and (extreme) horizontal branch chemically peculiar stars have to be helium deficient in their upper layers with the element being depleted on time scales much shorter than the evolutionary one. At such low abundances no helium spectral lines should be observable at all in optical spectra of these stars, being at odds with observations (Heber, 2016; Michaud et al., 2015).

Moreover, the discovery of helium-rich B-type main-sequence stars with effective temperatures, $T_{\rm eff}$, between around 20 000 K and 25 000 K, but also up to $\sim$ 32 000 K (see the solid purple colored frame in Fig. 1.0.1), at the beginning of the 1970s and the existence of $^3\mathrm{He}$ isotope enhancement in helium-weak B-type main-sequence with 14 000 K $\lesssim T_{\rm eff} \lesssim$ 21 000 K (see the dotted purple colored frame in Fig. 1.0.1) as well as in BHB and sdB stars were difficult to reconcile with the general weakness of the radiative acceleration of helium. In principle, the smaller atomic mass of $^3\mathrm{He}$ leads to a slower gravitational settling for it than for $^4\mathrm{He}$, thus increasing the $^3\mathrm{He}/^4\mathrm{He}$ abundance ratio with time. Unfortunately, the time needed to obtain the observed $^3\mathrm{He}$ overabundances is too long compared to the stellar lifetime in order to explain $^3\mathrm{He}$ stars, when applying the simplistic diffusion theory model. That is why other diffusion theory models had to be developed (Michaud et al., 2015).

Of course, knowledge of the possible diffusion processes occurring in the stellar atmosphere of $^3\mathrm{He}$ B-type stars is indispensable for the detailed understanding of their evolution. Empirical information on the photospheric $^3\mathrm{He}/^4\mathrm{He}$ abundance ratios are required to constrain theoretical concepts, though. Therefore, detailed quantitative spectral analyses of high-resolution spectra have to be conducted. The identification of $^3\mathrm{He}$ is made by accurately measuring the small isotopic shifts of the He I absorption lines in the optical part of the spectrum. The isotopic shifts with respect to the $^4\mathrm{He}$ isotope vary from line to line. Whereas some lines like $^3\mathrm{He}$ I, 5875 Å are shifted only slightly (0.04 Å) towards redder wavelengths, the shifts of $^3\mathrm{He}$ I, 4922 Å and $^3\mathrm{He}$ I, 6678 Å are considerably larger, reading 0.33 Å and 0.50 Å, respectively (Fred et al., 1951).

With the above mentioned aspects in mind, this thesis' scientific goal is the distinction between $^3\mathrm{He}$ and $^4\mathrm{He}$ and the determination of their individual elemental abundances in the stellar atmosphere of 17 analyzed B-type stars, including two $^3\mathrm{He}$ BHB, and 15 sdB stars (13 $^3\mathrm{He}$ sdBs and two He-normal sdBs). In order to guarantee a sophisticated quantitative spectral analysis, synthetic model spectra are calculated by means of use of a detailed $^3\mathrm{He}$ model atom and a hybrid local thermodynamic/non-local thermodynamic equilibrium approach. In addition, metal abundances, i.e., chemical abundances of elements exhibiting a higher atomic mass than hydrogen and helium, are derived. Last but not least, atmospheric parameters (effective temperature, $T_{\rm eff}$, and surface gravity, $\log{(g)}$) as well as radial and projected rotation velocities are determined for all analyzed stars, too.

Chapter 2 summarizes the basic principles of astronomical instruments needed to obtain a stellar spectrum, i.e., spectrographs. The different Echelle spectrographs used to obtain the analyzed spectra are briefly introduced. In chapter 3 the basic concepts of modeling synthetic spectra are presented. Chapter 4 is then a general review about quantitative spectral analysis and its importance in stellar astronomy. While chapter 5 gives a general overview of the properties, the chemical composition and the formation of hot subdwarf stars as well as of atomic diffusion processes, in particular taking place in hot subdwarf stars of spectral type B, both, chapter 6 and chapter 7, deal with the $^3\mathrm{He}$ anomaly in B-type stars. Chapter 8 briefly introduces the analysis programs used for the local thermodynamic equilibrium (LTE) analysis of chapter 10 and for the hybrid LTE/non-LTE analysis of chapter 11. The results derived from the hybrid LTE/non-LTE analysis are presented in chapter 12.

2. Study of Stellar Spectra with Optical Instruments

Spectroscopy provides astronomers access to plenty of parameters describing the physical state and behavior of stars by obtaining and studying the distribution of electromagnetic radiation as a function of wavelength. Hence, it is one of the most powerful tools in astronomy. Analyzing spectra of excellent quality with very high precision requires the development of larger telescopes but also high-resolution spectrographs.

The following chapters 2.1 and 2.2 deal with the basic properties of a grating spectrograph as well as of an Echelle spectrograph and, in principle, are an English version of both chapters 2.1 and 2.2 of the thesis *"Eine Radialgeschwindigkeitsstudie des Röntgen-Doppelsterns BD +37 ° 442"* by D. Schneider from 2014 (Schneider, 2014).
Chapter 2.3 then gives a short overview of all the Echelle spectrographs used to obtain the spectra analyzed in chapters 10 and 11.

2.1. Grating Spectrograph

All analyzed spectra in this thesis were obtained by so-called Echelle spectrographs. In order to understand their functionality, the "normal" (long-slit) grating spectrograph has to be explained at first.
A spectrograph is used for the dispersion of starlight into its components. As Fig. 2.1.1 shows, it consists of several components which are briefly presented below (Drechsel et al., 2015).

- By means of the **telescope**, the starlight is collected and focused in the focal plane afterwards.
- The **slit** serves for shielding of undesirable scattered light. The slit width b has strong influence on the resolution of the obtained spectrum.
- A **collimator** is installed between slit and dispersion element so that the starlight falls in parallel onto the dispersion element.
- The **dispersion element** is responsible for the separation of light into its constituent wavelengths. Here, it is either dealt with a tilted reflection grating (so-called blaze grating) or a prism.

- The **camera lens** images the resulting spectrum created by the dispersion element onto a CCD detector.
- Eventually, the digital image of the obtained spectrum is created in the **CCD detector**.

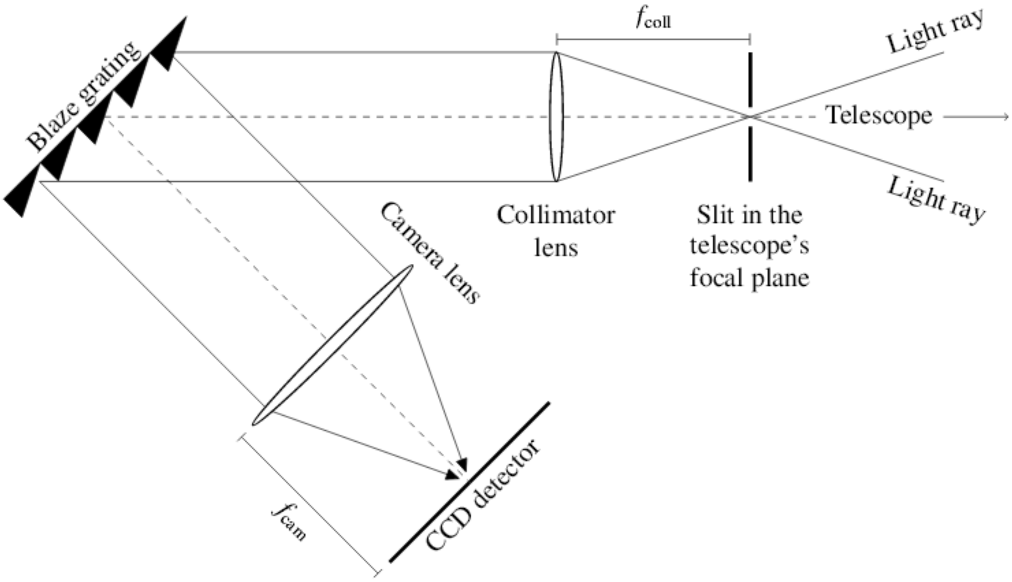

Figure 2.1.1.: Schematic setup and light path in a grating spectrograph. While the telescope focuses the light beam at the slit with slit width b, the collimator lens with focal length f_{coll} is for parallelization. After the light has been dispersed by the blaze grating, the resulting spectrum is imaged onto a CCD detector. This is done by a camera lens with focal length f_{cam}. Adopted from Irrgang (2014).

The spectral resolving power R_{Slit}, defined as the ratio of wavelength λ to its corresponding minimal resolvable wavelength difference $\Delta\lambda$, reads for a spectrograph with a blaze grating:

$$R_{\text{Slit}} = \frac{\lambda}{\Delta\lambda} = \frac{n \cdot f_{\text{coll}}}{d \cdot b \cos\alpha} \cdot \lambda \ \sim \lambda \ . \tag{2.1}$$

Here, n is the diffraction order number, f_{coll} marks the collimator focal length, d is the distance between two blaze grating's grooves which are tilted by the so-called blaze angle Θ relative to the surface normal, b is the slit width and α is the angle of incident radiation relative to the grating's surface normal. From equation (2.1), two simple possibilities for increasing the resolving power and thus the quality of the spectrum can be derived. On the one hand the slit width b should be chosen preferably small and on the other hand it is recommended to observe in high order numbers n. Due to the local *seeing*, i.e., atmospheric disturbances (turbulences within different atmospheric layers, variably strong scattering of starlight off atoms and molecules of Earth's atmosphere etc.), observed objects appear to be larger in the focal plane of the telescope. If the slit width is therefore chosen to be smaller than the so-called seeing disk, this would result in unnecessary light loss. Thus, in order to reach a high spectral resolving power, a good location with preferably good seeing is necessary (Drechsel et al., 2015).

2.2. Echelle Spectrograph

The problem accompanying high diffraction order numbers n is the overlapping of the individual orders. In this case, light of different orders and wavelengths is diffracted under the same emergent angle β at the blaze grating. That is why the so-called *Echelle spectrograph* (*Echelle* $=$ French word for *stair* or *ladder*) is applied. Compared to the constituents of the grating spectrograph already mentioned above, it consists of an additional grating or prism which is placed between camera lens and blaze grating perpendicularly to the initial dispersion. This so-called *cross dispersion element* ensures that the individual overlapping diffraction orders are separated afterwards. In this way, a striped Echelle spectrum is created whose individual orders do not image the whole spectrum as usual for a transmission grating, but each of these orders covers only a small section of the spectrum (see Fig. 2.2.1). This can be accomplished by a convenient choice of all the involved parameters n, α, β and d. The whole continuous spectrum is then created by merging the individual orders. Thus, a relatively small and rectangular CCD detector is sufficient to cover the whole spectral range (Drechsel et al., 2015).
The individual orders are influenced by the so-called blaze wavelength λ_{n}^{0} which leads to the

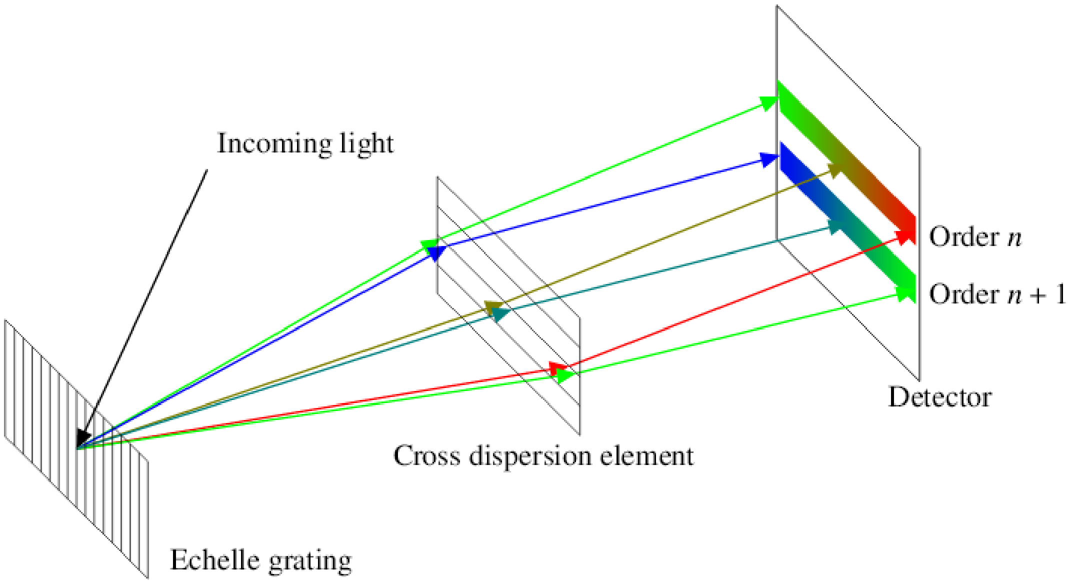

Figure 2.2.1.: Schematic setup and light path in an Echelle spectrograph. The overlapping higher diffraction order numbers are separated by the additional cross dispersion element before reaching the CCD detector. In addition, each of the orders only covers a section of the whole spectrum. For simplicity, slit, camera lens and collimator lens are not displayed here. Adopted from Irrgang (2014).

effect that only the spectral range around λ_{n}^{0} is covered in each of the orders. More precisely, the intensity profile is given by the blaze function which has a maximum at λ_{n}^{0} and falls steeply at the sides (Drechsel et al., 2015).
By using the blaze wavelength λ_{n}^{0}, the spectral resolving power R_{Echelle} of an Echelle spectrograph is approximately given by:

$$R_{\mathrm{Echelle}} = \frac{\lambda_{\mathrm{n}}^{0}}{\Delta\lambda_{\mathrm{n}}^{0}} \approx \mathrm{K} = \mathrm{const.}\ . \tag{2.2}$$

Here, K describes a device-specific constant which can be derived from the different parameters of the Echelle spectrograph, i.e., via incident and emergent angle, slit distance, slit width etc.. Of course, the resolving power of the CCD detector should match the one of the spectrograph, i.e., the pixel size of the detector has to be small enough so that it can register the high resolution (Drechsel et al., 2015).

2.3. Echelle Spectrographs Used

In the following, all Echelle spectrographs used to obtain the spectra to be analyzed in chapters 10 and 11 are listed. While the structure of a typical Echelle spectrograph as described in section 2.2 is represented by CASPEC, modern Echelle spectrographs like FEROS, FOCES, HRS, and UVES are fiber-fed, thus resulting in even higher stability. Table 2.1 summarizes the most important references from which the individual spectrograph descriptions are extracted. Additional references used are also marked within the text.

CASPEC - Cassegrain Echelle Spectrograph

The Cassegrain Echelle Spectrograph, short CASPEC, was one of the three high-resolution spectrographs available at La Silla, Chile, in the 1980s and 1990s. It was used at the f/8.09 Cassegrain focus of the 3.6 m telescope and was the first cross-dispersed high-resolution Echelle spectrograph at La Silla operating from about the atmospheric cut-off at 310 nm to the long-wavelength limit of the CCD detectors (1100 nm). Though, it was not suitable for programs aiming at radial velocity measurements with a higher precision than $\sim$ km s^{-1}. Its maximum resolving power was $R \sim 41,000$ achieved by a ~ 1 arcsec wide slit. But, the feature of CASPEC was the availability of two cross dispersion elements (crossdispersers), one for the blue and one for the red spectral range. With the RED crossdisperser no wavelength changes were allowed within a night and the inter-order separation below 5500 nm was too small because of a relatively small groove density so that it could not be used for observations at shorter wavelengths. Also, a change of the crossdisperser during the same night was not possible. So, if both, the red and the blue ranges, were to be observed during the same night, the BLUE crossdisperser had to be used. The square CCD detector chip used for CASPEC was able to cover 120 nm simultaneously with the BLUE and 240 nm with the RED crossdisperser and

Instrument	References
CASPEC	(Randich & Pasquini, 1996)
FEROS	`https://www.eso.org/sci/facilities/lasilla/instruments/feros.html`
FEROS	`https://www.eso.org/sci/facilities/lasilla/instruments/feros/overview.html`
FOCES	(Pfeiffer et al., 1998)
HRS	`http://www.as.utexas.edu/mcdonald/mcdonald.html`
HRS	`http://www.as.utexas.edu/mcdonald/het/het.html`
HRS	`http://hydra.as.utexas.edu/?a=help&h=11`
UVES	`https://www.eso.org/public/germany/teles-instr/vlt/vlt-instr/uves/`

Table 2.1.: References used for the descriptions of the individual spectrographs in chapter 2.3.

limited the full order overlap to wavelengths longer than 710 nm (Randich & Pasquini, 1996).

FEROS - The Fiber-fed Extended Range Optical Spectrograph

Operating as a state-of-the-art bench-mounted, high-resolution and thermally controlled prism-crossdispersed Echelle spectrograph, the Fiber-fed Extended Range Optical Spectrograph, short FEROS, is permanently mounted at the MPG/ESO-2.20 m telescope at the European Southern Observatory (ESO) in La Silla, Chile. Its high efficiency of $\sim 20\%$ and its high resolution of $R \sim 48,000$ over a total of 39 Echelle orders together with the large wavelength range covering almost the complete optical spectral region from $\sim$ 350 nm to $\sim$ 920 nm in only one exposure, make FEROS one of the best astronomical instruments for a large variety of stellar and extra-galactic spectroscopic observation programs requiring high spectral stability. Also, its mechanical and thermal stability result in a precise wavelength calibration based on daytime calibrations. Therefore, a high productivity in gathering scientific data is ensured. Via an included Object-Calibration mode, precise radial velocity measurements with accuracies of $\sim$ 25 m s^{-1} or better can be guaranteed, too. The instrument is fed by two fibres illuminated via 2.0 arcsec apertures on the sky separated by 2.9 arcmins so that spectra of the object plus either of a sky background region or of one of the two calibration lamps for wavelength calibration as well as flat-fielding can be produced simultaneously. The thinned and back-illuminated EEV 2k x 4k CCD detector with its excellent quantum efficiency of $\sim 98\%$ measured at 450 nm contributes considerably to the instrument's high detection efficiency (Kaufer et al., 1999). The core of the FEROS reduction pipeline is even included in the standard MIDAS (*Munich Image Data Analysis System*) distribution and can thus be used user-friendly to reduce the taken data.

FOCES - A Fibre Optics Cassegrain Echelle Spectrograph

The Fibre Optics Cassegrain Echelle Spectrograph, short FOCES, was designed and built in the mid of the 1990s to be mounted at the Cassegrain focus of either the 2.2 m or the 3.5 m telescope at the Calar Alto Observatory (German-Spanish Astronomical Center) located in the Sierra de Los Filabres to the north of Almería, Spain. It is fed by 100 µm optical fibres and the incident light is collimated by means of two off-axis parabolic mirrors. A small folding mirror placed between the two parabolic mirrors guarantees an efficient way to remove scattered light, too. The resulting Echelle image covers the optical spectral region from 380 nm to 750 nm using 70 spectral orders with full spectral coverage. The instrument's maximum spectral resolution is $R \sim 40,600$ with a 2 pixel resolution element. Here, the cross-dispersion is achieved with a tandem prism mounting, separating the particular diffraction orders before the light beam is finally imaged with an f/3 transmission camera onto a field centered on a 1024 x 1024 thinned Tektronix CCD with 24 µm pixel diameter. FOCES also offers a second fibre carrying the sky background signal in order to correct spectra of extremely faint objects. For this alternative mode, an additional prism for higher cross-dispersion has to be used resulting in a correspondingly reduced spectral range, though (Pfeiffer et al., 1998).

HRS - High-Resolution Fiber-Coupled Spectrograph of the Hobby-Eberly Telescope

The McDonald Observatory located in the Davis Mountains of West Texas, i.e., 450 miles west of its research and administrative home at The University of Texas at Austin, offers a wide range of state-of-the-art astronomical instruments for imaging and spectroscopy in the optical and infrared. Amongst others, a high-resolution Echelle spectrograph (HRS) constructed for the Hobby-Eberly Telescope (HET), momentarily one of the world's five largest telescopes built with a unique objective: to gather a very large amount of light, specifically for spectroscopy, at extremely low cost. The HRS is a single channel spectrograph linked to the corrected prime focus of the HET through its Fiber Instrument Feed. Just like FOCES, HRS is a so-called "white pupil" spectrograph. Here, a 2-mirror collimator system is used. While the first mirror serves as the main collimator located off-axis, the second one is even farther off-axis in order to re-collimate the beam, directing all dispersed rays to the white pupil coinciding with the surface of the cross-dispersing grating, and to compensate for the off-axis aberrations of the main mirror. The instrument uses a mosaic of two R-4 Echelle gratings (with a nominal blaze angle of $\Theta = 76^{\circ}$) and a selection of two cross-dispersing gratings to separate spectral orders. The spectral resolving power ranges from $R \sim 15,000$ over $R \sim 30,000$ and $R \sim 60,000$ up to $R \sim 120,000$ depending on the four available effective slit widths used and an overall wavelength range between 420 nm and 1100 nm is covered. Imaging is carried out by an all-refracting camera onto a mosaic of two thinned and anti-reflection coated 2k x 4k Marconi CCDs with 15 µm pixels arranged along their 4k side leaving a $\sim$72 pixel dead space between them. The HRS was officially commissioned in March 2001 (Tull, 1998).

UVES - The UV-Visual Echelle Spectrograph for the VLT

UVES, the UV-Visual Echelle Spectrograph for the Very Large Telescope (VLT) at Paranal Observatory in the Atacama desert of northern Chile, has been placed at the Nasmyth B focus of Unit Telescope 2 (UT2, Kueyen) in the late 1990s. It is a two-arm versatile cross-dispersed Echelle spectrograph covering a wavelength range of 0.3 µm to 0.5 µm (blue) and 0.42 µm to 1.1 µm (red), with a 2-pixel resolution of up to $R \sim 80,000$ and $R \sim 110,000$, respectively. UVES uses a detector system composed of thin, 2048 x 2048 and 15 µm CCD chips (Dekker et al., 1995). The instrument can also be combined with a second fibre system called FLAMES resulting in a lower resolution of $R \sim 47,000$, but then providing high-resolution spectroscopy for up to eight different objects at the same time through fibres fed through the red arm. Therefore, the main scientific goals of UVES are in particular the spectroscopic properties of faint stars and galaxies in the Universe.

3. Model Spectra

In order to get access to the different parameters describing the condition, the composition and the structure, therefore the physical state of a particular stellar atmosphere, quantitative spectral analysis, i.e., the analysis of observed spectral lines in a stellar spectrum, is the most powerful tool (see also chapter 4 for more details). While the analysis of spectra is based on the calculation of synthetic spectra including model atmospheres and solving the radiative transfer, the various methods to calculate synthetic spectra are provided by the theory of stellar atmospheres. The latter includes the complex description of the interaction of radiation and matter in the stellar plasma. Thus, this chapter shall discuss the most important concepts of radiative transfer, model atmosphere construction, and spectral line formation. It closely follows the descriptions in the textbook published by Gray (2005) as well as the theses of Irrgang (2014) and Schaffenroth (2015).

3.1. Radiative Transfer

The radiative transfer equation, accounting for all changes of the macroscopic radiation field due to absorption and emission processes in the traversed matter of the stellar atmosphere, reads:

$$\mathrm{d}I_\nu = -\kappa_\nu I_\nu \mathrm{d}s + \eta_\nu \mathrm{d}s \; . \tag{3.1}$$

Here, I_ν is the so-called specific intensity, defined as the energy $\mathrm{d}E$ per frequency interval $\mathrm{d}\nu$ traversing through an area $\mathrm{d}A$ in the direction of the solid angle $\mathrm{d}\Omega = \sin\Theta \mathrm{d}\Theta \mathrm{d}\varphi$ within a time interval $\mathrm{d}t$. $\mathrm{d}s$ is a small layer thickness in the direction of solid angle $\mathrm{d}\Omega$ and κ_ν and η_ν are the so-called (macroscopic) absorption and (macroscopic) emission coefficients, respectively. κ_ν is often called opacity whereas η_ν is also known as emissivity (Collins, 1989). Generally said, both, opacity and emission coefficient, are a non-trivial function of variables describing the state of matter, amongst others temperature, occupation number densities as well as elemental abundances. Using the concepts of microscopic physics, both quantities can be determined via:

$$\kappa_\nu = \sum_k \sum_i \sum_j \{ \text{ ind. absorber pop. density } \times \text{ ind. atomic cross-section}(\nu) \ \} \tag{3.2}$$

$$\eta_\nu \propto \sum_k \sum_i \sum_j \{ \text{ ind. emitter pop. density } \times \text{ ind. atomic trans. prob.}(\nu) \ \} \; , \tag{3.3}$$

where both frequency-dependent measures, individual cross-sections and transition probabilities, can only be derived from atomic physics, and the sum includes all different (excited) states

j of all ionization levels i of all participating chemical elements k in the stellar atmosphere. As the dimension of κ_ν is m^{-1}, the so-called mean free path λ, i.e., the mean distance a photon can travel before being absorbed, is defined as $\lambda = \kappa_\nu^{-1}$. Concerning absorption processes in the stellar atmosphere, true absorption (bound-bound, bound-free, and free-free atomic transitions), where the photon is destroyed and the energy is thermalized, and scattering, where the photon is deviated in direction and removed from the solid angle being considered, are distinguished. Whereas only bound-bound transitions are responsible for spectral absorption lines, bound-free and free-free transitions as well as scattering processes are important for the continuum formation.

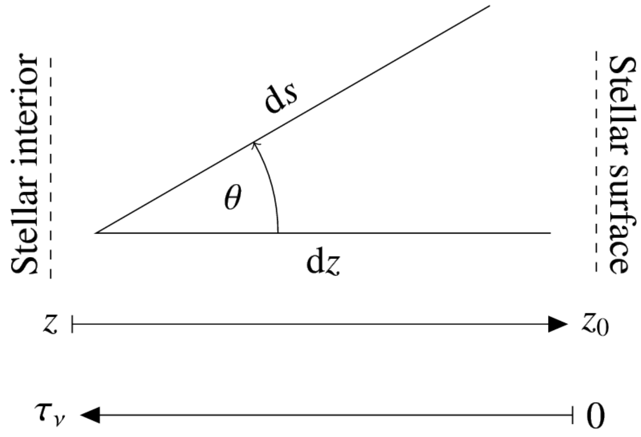

Figure 3.1.1.: The definition of the so-called optical depth in stellar atmospheres using plane-parallel geometry (see section 3.2.1). While the coordinate perpendicular to the plane, i.e., the geometrical depth z, is increasing from inwards to outwards, the optical depth, defined as $\tau_\nu = -\int_0^L \kappa_\nu \mathrm{d}z$ over some path length L, is increasing from outwards to inwards. θ is the angle measured to the normal of the plane and $\mathrm{d}s$ is a small distance measured along the photon's path in its direction of motion. Adopted from Irrgang (2014).

In order to rewrite Eq. (3.1), the unitless frequency-dependent optical depth has to be introduced (see Fig. 3.1.1). It is defined as the product of the frequency-dependent absorption coefficient κ_ν times a small layer thickness $\mathrm{d}z$ over some path length L as $\tau_\nu = -\int_0^L \kappa_\nu \mathrm{d}z$. A medium is optically thick at a particular frequency if $\tau_\nu > 1$ and optically thin if $\tau_\nu < 1$. Also, a distance equal to one optical depth is the thickness of the absorbing gas from which a fraction of 1/e photons can escape. The optical part of a stellar spectrum results from the photosphere which is defined as the surface where its optical depth is $\sim$ 2/3. Because of the frequency dependence of τ_ν, the lower boundary of the photosphere differs for different wavelengths of the absorbed photons, though.

Using the definition of optical depth τ_ν, $\mathrm{d}s$ in Eq. (3.1) can be transformed into $\mathrm{d}s = \mathrm{d}z/\cos\theta = -\mathrm{d}\tau_\nu(\kappa_\nu \cos\theta)^{-1}$. Therefore, the rewritten radiative transfer equation reads:

$$\cos\theta \, \mathrm{d}I_\nu = I_\nu \mathrm{d}\tau_\nu - \frac{\eta_\nu}{\kappa_\nu}\mathrm{d}\tau_\nu \, , \quad (3.4)$$

where the ratio $\frac{\eta_\nu}{\kappa_\nu}$ is defined as the so-called source function S_ν, yielding the form:

$$\cos\theta \, \frac{\mathrm{d}I_\nu}{\mathrm{d}\tau_\nu} = I_\nu - S_\nu \, . \quad (3.5)$$

Hence, the radiative transfer equation transforms into a first-order differential equation with constant coefficients, solvable when the exact form of the source function is known. The formal solution of this differential equation reads:

$$\begin{aligned} I_\nu(\tau_{\nu,1},\cos\theta) &= I_\nu(\tau_{\nu,2},\cos\theta)\exp\left(-\frac{\tau_{\nu,2}-\tau_{\nu,1}}{\cos\theta}\right) \\ &+ \int\limits_{\tau_{\nu,1}}^{\tau_{\nu,2}} S_\nu(t_\nu)\exp\left(-\frac{t_\nu-\tau_{\nu,1}}{\cos\theta}\right)\frac{\mathrm{d}t_\nu}{\cos\theta}\ . \end{aligned} \tag{3.6}$$

This means that radiation along the line at low optical depths $\tau_{\nu,1}$ in direction of positive $\cos\theta$, i.e., from the inner parts of the stellar atmosphere to its outer parts, is composed of the sum of intensities, S_ν, originating at the points t_ν along the line but suffering extinction according to the optical-depth separation $t_\nu - \tau_{\nu,1}$ (second term in Eq. 3.6). Also, any radiation incident at a higher optical depth $\tau_{\nu,2}$, called $I_\nu(\tau_{\nu,2},\cos\theta)$, suffers exponential extinction by a factor of $\exp\left(-\frac{\tau_{\nu,2}-\tau_{\nu,1}}{\cos\theta}\right)$ (first term in Eq. 3.6).
However, in reality the source function S_ν is a complicated one, even being a function of specific intensity I_ν itself because of the interaction between radiation field and matter, influencing both, absorption and emission coefficient. Consequently, the formal solution of the radiative transfer equation, i.e., Eq. (3.6), cannot be used to determine the radiative transfer.

3.2. Model Atmospheres

3.2.1. Basic Assumptions

The stellar atmosphere is the region where the observed optical spectrum results from. In order to simplify the stellar structure equations, often several assumptions are made. These are presented below:

- **Plane-parallel geometry**: Since the thickness of the stellar atmosphere is usually small compared to the radius of the star, the curvature of the star is negligible on length scales of interactions taking place in the atmosphere.
- **Homogeneity**: The stellar atmosphere is said to be homogeneous in each layer except in the normal direction, i.e., there are no variations perpendicular to its normal. This means that for example magnetic fields, spots, granules, etc. are neglected and that one single coordinate is sufficient to give the location within the atmosphere.
- **Stationarity**: Time-dependent effects like, for instance, pulsations are neglected meaning that the stellar atmosphere is stationary.
- **Hydrostatic equilibrium**: Since no relative motion of the atmospheric layers in the normal direction is considered in a stationary atmosphere, hydrostatic equilibrium holds,

meaning that the pressure gradient $\frac{\mathrm{d}P(r)}{\mathrm{d}r}$ is time independent and fulfills the following relation:

$$\frac{\mathrm{d}P(r)}{\mathrm{d}r} = -\frac{GM(r)\rho(r)}{r^2} \approx -\frac{GM\rho(r)}{R^2} =: -g\rho(r)\ . \tag{3.7}$$

Here, G is the gravitation constant, r is the radial distance to the star center, $\rho(r)$ is the density at distance r, and $M(r)$ describes the total mass within a sphere with radius r. The used approximation is valid since the stellar atmosphere thickness is small compared to the radius R of the star, and the mass of the stellar atmosphere is negligible compared to the total mass M of the star. Therefore, the surface gravity g is linked to atmospheric pressure and density stratification, thus being one of the most important parameters characterizing stellar atmospheres.
The pressure P consists of two components. Namely, P_{Plasma}, i.e., the pressure caused by electrons and ions in the stellar plasma itself, and $P_{\text{Radiation}}$, the pressure caused by radiation.

- **Radiative equilibrium**: Not only that a static atmosphere implies hydrostatic equilibrium, stationarity is also responsible for energy conservation at each point. Hence, the net energy flux is constant with depth, since the energy source of the star lies far below the atmosphere on the one hand, and on the other hand no energy enters the atmosphere from the outside. The total net flux is given by the Stefan-Boltzmann law $F = \sigma T_{\text{eff}}^4$ (see also section 3.3), linking the constant flux to another important parameter describing the state of a stellar atmosphere. Namely to T_{eff}, the effective temperature of the star.

- **Constant elemental abundances/Chemical homogeneity**: The atomic abundances are specified and constant throughout the whole stellar atmosphere.

- **Charge conservation**: The whole charge is conserved, meaning that:

  $$\sum_k \sum_i n_{ik} Z_{ik} - n_e = 0 \tag{3.8}$$

  is fulfilled. The sum includes all different ionization levels i of all different elements k in the stellar atmosphere. Here, Z_{ik} is the charge associated with ionization state i belonging to the particular element k (i is zero for neutral atoms, unity for single-ionized atoms, etc.), n_{ik} is the corresponding ion density, and n_e is the electron density in the stellar plasma.

Based on these assumptions, the atmospheric structure depends only on the input parameters effective temperature, T_{eff}, and surface gravity, g. The corresponding structure equations read:

$$\begin{aligned}\frac{\mathrm{d}P_{\text{Plamsa}}(r)}{\mathrm{d}r} &= -g\rho(r) - \frac{\mathrm{d}P_{\text{Radiation}}}{\mathrm{d}r} = -\rho(r)\left(g - \frac{1}{c\rho(r)}\int_0^\infty \kappa_\nu \int_0^{2\pi}\int_0^{\pi} I_\nu \cos\theta \sin\Theta \mathrm{d}\Theta \mathrm{d}\varphi \mathrm{d}\nu\right)\\ &=: -\rho(r)(g - g_{\text{Radiation}})\end{aligned} \tag{3.9}$$

$$\int_0^\infty \int_0^{2\pi} \int_0^\pi I_\nu \cos\theta \sin\Theta \mathrm{d}\Theta \mathrm{d}\varphi \mathrm{d}\nu =: F = \sigma T_{\text{eff}}^4 \tag{3.10}$$

$$\cos\theta \, \frac{\mathrm{d}I_\nu}{\mathrm{d}\tau_\nu} = I_\nu - S_\nu \, , \tag{3.11}$$

where c is the vacuum speed of light and σ is Stefan-Boltzmann's constant. While Eq. (3.9) results from hydrostatic equilibrium, Eq. (3.10) is based on radiative equilibrium. Eq. (3.11) is again the radiative transfer equation.

Typically, an iteration process is used to find the parameters that describe the model atmosphere. For this, detailed knowledge of the radiative transfer through the atmosphere has to be ensured. Given the input parameters effective temperature T_{eff} and g, a trial atmosphere is chosen as a starting point (gray approximation). This trial atmosphere does not fulfill all of the structure Eqs. (3.9), (3.10), and (3.11) at first, but provides hints of what has to be changed in order to guarantee this. For instance, the temperature profile can be changed, resulting in a different guess for density or pressure, respectively. This can then be transferred into a new photon flux resulting in a new temperature stratification. Once the trial functions for all physical quantities are updated, the whole procedure starts anew, stopping when a certain convergence criterion is fulfilled. The final parameters can be used to set up the model atmosphere and to compute a synthetic model spectrum afterwards.

3.2.2. Local Versus Non-Local Thermodynamic Equilibrium

Besides the sophisticated knowledge of the atomic structure concerning energy levels, statistical weights and transition probabilities of the particular atmospheric chemical species, which is provided by so-called model atoms, the statistical properties of the stellar plasma, i.e., opacity and emissivity have to be known in order to get access to the source function and therefore to the radiation field via the radiative transfer. As described in chapter 3.1, both variables depend on the occupation number densities of all atomic levels of all species of participating chemical elements. Level populations can be calculated in local thermodynamic equilibrium (LTE) from Saha-Boltzmann statistics. Departures from LTE, i.e., non-LTE (NLTE) effects, can be determined by the statistical equilibrium equation which is derived from the requirement of stationarity. The velocity distribution for all particles is set by thermodynamic equilibrium (TE).

Thermodynamic Equilibrium (TE)

A system is said to be in thermodynamic equilibrium if the particle velocity distributions as well as the distributions of atoms over excitation and ionization levels can only be described by the absolute temperature T and the total particle number density of the individual element

x, N_x, or the electron density n_e. In the following, the different implications derived from TE are listed:

- **Maxwellian velocity distribution**: All particles follow a velocity distribution of the form:
$$p(v)\mathrm{d}v = \left(\frac{m}{2\pi k_B T}\right)^{3/2} \exp\left(-\frac{mv^2}{2k_B T}\right) 4\pi v^2 \mathrm{d}v \tag{3.12}$$
with particle mass m, particle velocity v, and Boltzmann's constant k_B.

- **Boltzmann excitation formula**: The energy-level population numbers are derived from the formula:
$$\frac{n_{\mathsf{up}}}{n_{\mathsf{low}}} = \frac{g_{\mathsf{up}}}{g_{\mathsf{low}}} \exp\left(-\frac{E_{\mathsf{up}} - E_{\mathsf{low}}}{k_B T}\right) \tag{3.13}$$
with occupation number density n_{up}, statistical weight g_{up}, and energy E_{up} of the upper level with respect to the ground state of the atom/ion. n_{low}, g_{low}, and E_{low} correspond to the lower energy level.

- **Saha ionization equation**: The number densities of different ionization stages of a single element are given by the following equation:
$$\frac{N_I}{N_{I+1}} = \frac{n_e}{2} \frac{U_I}{U_{I+1}} \left(\frac{h^2}{2\pi m_e k_B}\right)^{3/2} T^{-3/2} \exp\left(\frac{\chi_I}{k_B T}\right) \tag{3.14}$$
with total number density N_I of the ionization stage I, Planck constant h, electron mass m_e, ionization potential χ_I, and so-called partition function $U_I = \sum_{j=0}^{j_{\mathsf{max}}} g_j \exp\left(-E_j/k_B T\right)$ of the particular ion. N_{I+1} and U_{I+1} correspond to ionization stage $I+1$. g_j is the statistical weight of the jth excitation level with respect to the ground state of the ion. In combination with charge conservation, i.e., Eq. (3.8), Eqs. (3.13) and (3.14) determine all occupation number densities n_i and N_I.

- **Specific intensity**: The specific intensity I_ν is described by the Planck function B_ν:
$$I_\nu = B_\nu = \frac{2h\nu^3}{c^2} \frac{1}{e^{h\nu/k_B T} - 1} \tag{3.15}$$
with c the vacuum velocity of light and ν the particular frequency.

- **Photon number density**: The photon number density N_ν can be determined by:
$$N_\nu = \frac{B_\nu}{ch\nu} \,. \tag{3.16}$$

However, because of stellar radiation and the dependence of gravitational force, pressure, and temperature on the local position within the star, the assumption of TE cannot be applied to the whole stellar atmosphere at once.

Local Thermodynamic Equilibrium (LTE)

Although TE does not hold globally in stellar atmospheres, its thermodynamic relations can be applied locally. Thus, each atmospheric layer in a plane-parallel geometry can be described only by its local temperature T and its electron density n_e. This concept is called local thermodynamic equilibrium (LTE). In principle, the local source function can then be derived by using Eqs. (3.12), (3.13) and (3.14) together with the information of atomic structure in model atoms. However, LTE is only valid if interactions between photons and particles remain local, i.e., take place in atmospheric layers of almost the same temperature. This is certainly the case in the interior of stars. But for stellar atmospheres, this is not universally valid, since on the one hand, lower particle densities can result in larger mean free paths of particles and photons than the typical distance between two layers of different local temperatures. On the other hand, the photon flux might be high enough so that a non-negligible fraction of photons can leave one atmospheric temperature zone, even interacting with matter of a different one. Departures from LTE in stellar atmospheres therefore increase with higher effective temperatures, implying a high photon flux (see Eq. 3.10 for details), and lower surface gravities, resulting in lower particle densities. For the analyzed B-type stars, typical mean free paths of particles are small enough so that LTE is conserved. The effective temperatures of these stars are already high enough to cause deviations from LTE, though. This results in different occupation numbers than the ones derived from LTE and is summarized by so-called non-local thermodynamic equilibrium (NLTE) effects.

Non-Local Thermodynamic Equilibrium (NLTE)

Typically, in non-local thermodynamic equilibrium (NLTE) the velocities of all particles remain Maxwellian distributed, applying the same local temperature T as for LTE, but the occupation numbers cannot be derived from Eqs. (3.13) and (3.14), respectively. That is why a more general ansatz of stationarity has to be used, introducing the so-called statistical equilibrium or rate equations, which can be expressed as departure coefficients from LTE, restoring the latter one for high particle densities and low photon fluxes. The rate equations for a single atomic level i of one individual chemical element in a certain ionization stage read:

$$n_i \sum_{j \neq i} (R_{ij} + C_{ij}) = \sum_{j \neq i} n_j (R_{ji} + C_{ji}) \ . \tag{3.17}$$

While n_i and n_j describe the occupation number densities of levels i and j, R_{ij} and C_{ij} are the radiative (including bound-bound and bound-free processes) and collisional rates for atomic transitions from level i to level j. R_{ji} and C_{ji} are defined similarly. In consequence, statistical equilibrium means that the depopulation rate (left-hand side of Eq. 3.17) of each state i is equal to its population rate (right-hand side of Eq. 3.17), meaning that stationarity of level population is guaranteed. Usually, radiative and collisional rates depend on the radiation field, on the particle velocity distribution, and on the particular atomic cross-sections.

The set of rate equations for a certain chemical species in the stellar atmosphere has to be solved simultaneously for all excitation levels of the corresponding model atom/ion. In order to do so, the total particle number conservation equation for the different elements, i.e., $\sum_i^I \sum_j^J n_{ij} = N_{\text{total}}$, with the summation extending over all possible excitation levels j of all possible ionization states i of an individual species, has to be used additionally. Thus, the calculation of the occupation number densities and in this way of the source function, can only be performed numerically by solving the complex, non-linear coupled equation system made up of rate equations and total particle number conservation equation.

3.2.3. Hybrid LTE/NLTE approach

As already indicated in the previous section, the computation of synthetic model spectra in NLTE is an extremely time-consuming numerical task. Typically, the determination of atmospheric parameters (see section 4) is done via a grid of model spectra in a multidimensional parameter space (effective temperature, surface gravity, elemental abundances, etc.). Since the analyzed B-type stars show high effective temperatures so that NLTE effects occur, but densities are relatively high because of high surface gravities, it can safely be assumed that departures from LTE have a negligibly small effect on the temperature-density stratification. This allows to use the so-called hybrid LTE/NLTE approach, which also shortens computation time enormously. Within this approach, it is assumed that NLTE effects are only important for the calculation of level population densities. Therefore, the stellar structure equations can be solved in LTE. The resulting LTE model atmosphere is kept fixed while the radiative transfer equation as well as the rate equations are being solved simultaneously. Moreover, the rate equations for the occupation number densities of the individual metals are solved separately, using LTE population number densities for the other "background" metals. This approximation is valid as long as NLTE effects of individual metals on the radiation field are small. As has been shown by Nieva & Przybilla (2007) and Przybilla et al. (2011), the calculated synthetic model spectra are fully consistent with self-consistent NLTE calculations for B-type stars.
The calculation of synthetic model spectra with the hybrid LTE/NLTE approach, as used in chapter 11, makes use of three generic codes. These are:

1. **ATLAS12**: In order to allow the calculation of the LTE atmospheric structure, ATLAS12, developed by Kurucz (1996), is used. This code assumes plane-parallel geometry, chemical homogeneity, and hydrostatic, radiative, and LTE.

2. **DETAIL**: In order to obtain the occupation number densities, the source function, and hence the radiation field in NLTE, the rate equations as well as the radiative transfer equation have to be solved simultaneously. This is performed within DETAIL (Giddings (1981); Butler & Giddings (1985), extended and updated), using a relatively coarse frequency grid and approximated line broadening profiles. In this respect, the resulting model spectra do not represent the actual shape of spectral lines.

3. **SURFACE**: After the coarse radiation field has been calculated within DETAIL, SURFACE (Giddings (1981); Butler & Giddings (1985), extended and updated) computes its

formal solution (see Eq. 3.6 for details), precisely determining the final radiation field by using a much finer frequency grid and more detailed line broadening profiles.

3.3. Spectral Line Formation

A spectral line results from the discrete transition from one atomic state to the other. Given that the associated photon wavelength of one of these atomic transitions can be determined by calculating the difference between the upper and lower atomic level, and because of the uniqueness of the atomic structure and the possible corresponding transitions for each element, spectral lines contain a great deal of information about the chemical species in the stellar atmosphere. However, such a quantitative spectroscopic analysis requires detailed and sophisticated knowledge of different aspects, such as the already mentioned number density of atoms which can absorb radiation at each frequency in a spectral line, the absorption profile, i.e., the wavelength distribution of the particular line's opacity, and the dependence of this profile on the temperature as well as on the density of the plasma in the stellar atmosphere. A simple qualitative model explaining the spectral line formation in a stellar atmosphere shall be presented in the following.

The radiation emitted from gas in the stellar atmosphere is a strong function of temperature. At first approximation, this radiation can be described by a black body, resulting in a temperature dependence to the power of four according to Stefan-Boltzmann law $L \sim T^4$ (see also Eq. 5.1 for details). The corresponding specific intensity emitted by such a black body is well described by Planck's radiation law of Eq. (3.15). Thus, hot matter shines brighter on the one hand, i.e., has a higher intensity than cool matter. On the other hand, temperature and therefore specific intensity decrease in a stellar atmosphere from inwards to outwards. Since the atmospheric matter is less transparent, i.e., its opacity is higher at the wavelength of a certain spectral line λ_0 than for the continuum, the cooler and outer atmospheric matter is responsible for the formation of the line core/center. The neighbored spectral line wings and the continuum result from the hotter matter at deeper atmospheric layers, i.e., larger optical depths, with high flux.

Usually, the so-called equivalent width is measured in order to characterize the strength of an absorption line. It reads:

$$W_\lambda = \int\limits_0^\infty \frac{F_c - F_\lambda}{F_c} \mathrm{d}\lambda \ , \tag{3.18}$$

where F_c is the continuum flux and F_λ the flux in the line. It is customary to write integrals of this type as ranging from 0 to ∞ largely for convenience (Collins, 1989). What is meant is that the integral should cover those wavelengths for which the integrand significantly differs from zero (see also Eq. 5.6 of chapter 5.3). The procedure of calculating W_λ strongly depends on the shape of the line profile, though. Also, the interpretation on the basis of the equivalent width only can be misleading since different shapes may exhibit same equivalent widths. Hence, it is necessary to provide reliable modeling of the detailed line profile. In order to do so, the dependence of spectral line shape on atomic properties of the chemical element and on the state of the surrounding plasma have to be fully understood. In the following, all effects and parameters, affecting the shape as well as the strength of spectral lines, are briefly introduced.

3.3.1. Microscopic Line Broadening

Microscopic line broadening mainly affects the frequency dependence of the bound-bound emission or absorption coefficients, consequently influencing the radiative transfer in stellar atmospheres. In this way, it is indispensable for the exact photon distribution as well as for the number of absorbed and re-emitted photons, i.e. the shape and the strength of spectral lines.

Natural or Radiation Broadening

The basic quantum mechanical approach of natural or radiation broadening involves the Heisenberg uncertainty principle. If an atom is in a certain excited state, then the length of time Δt that it can remain in that state (lifetime) is related to the uncertainty of the energy ΔE of that state by $\Delta E \Delta t \geq \hbar$. For instance, if the lifetime Δt of a particular state is small, the uncertainty of the energy level ΔE is large meaning that a wide range of frequencies can be involved in the transition into or out of that state. In consequence, any line resulting from such a transition will be unusually broad (Collins, 1989). Only ground levels are stable and a typical value for the lifetime of excited states is of the order of 10^{-8} s. The corresponding power spectrum of the energy absorbed or emitted can be derived from a classical damped oscillator. It is a Lorentzian profile and reads:

$$I_{\text{natural}}(\nu) = \frac{\gamma_{\text{rad}}/4\pi^2}{(\nu - \nu_0)^2 + (\gamma_{\text{rad}}/4\pi)^2} \,, \tag{3.19}$$

where ν_0 is the central frequency which can be calculated via the usual energy difference between the upper and lower level $E_0 = h\nu_0$. γ_{rad} is the so-called damping constant or full width at half maximum (FWHM) of the profile. It can either be measured experimentally or obtained theoretically from quantum mechanical calculations of transition probabilities. For a transition taking place between two excited states, which can be labeled u and l, it is derived from the sum of all possible radiative decays of both levels:

$$\gamma_{\text{rad}} = \sum_{i<u} A_{ui} + \sum_{i<l} A_{li} = \frac{1}{\tau_{\text{up}}} + \frac{1}{\tau_{\text{low}}} \,. \tag{3.20}$$

Here, A_{ui} and A_{li} are the so-called Einstein probability coefficients for spontaneous emission for the upper and lower level, respectively. The sum of all possible radiative decays of both levels can be rewritten in terms of the reciprocal mean lifetimes of the upper and lower level $1/\tau_{\text{up}}$ and $1/\tau_{\text{low}}$, respectively (Collins, 1989).

n	Type	Lines affected	Perturber
2	Linear Stark	Hydrogen	Protons, electrons
4	Quadratic Stark	Most lines, especially in hot stars	Ions, electrons
6	Van der Waals	Most lines, especially in cool stars	Neutral hydrogen

Table 3.1.: Types of pressure broadening according to Gray (2005).

Pressure Broadening

Pressure broadening results from the collisional Coulomb interaction between the atoms/ions absorbing the light and other particles in the stellar plasma. The other particles can be electrons, ions, or neutral atoms of the same element as the absorbers or of a different type. In principle, the effect of pressure broadening increases with increasing pressure since then the particles are closer and the Coulomb force becomes stronger. The atomic levels of the transition of interest are disturbed such that their energy is altered. Typically, the upper energy level is more strongly altered than the lower one and the distortion is a function of the separation, R, between the absorber and the perturbing particle. The change of energy for one energy level ΔW induced by the collision as a function of R is often approximated by a power law of the form:

$$\Delta W = \text{constant}/R^n \ , \tag{3.21}$$

where n depends on the type of interaction. This energy change can directly be converted to a change in frequency in the observed spectrum by subtracting Eq. (3.21) for the lower level from Eq. (3.21) for the upper level, yielding:

$$\Delta \nu = C_n/R^n \ . \tag{3.22}$$

The interaction constant C_n has to be measured or calculated for each of the considered transitions and types of interactions. Table 3.1 gives a summary of the types of interactions related to pressure broadening in stellar atmospheres. While the relevant interactions in the case of hot O and B-type stars with a large number of charged particles (mainly ions, protons and electrons) in their stellar atmospheres are the linear and quadratic Stark effect, van der Waals forces, mainly resulting from collisions with neutral hydrogen, dominate in cool stars.

It has to be pointed out that the net effect due to perturbers along a straight line through the stellar photosphere results not only in pressure broadening, but also in line shifts and asymmetries. This mostly depends on the shape of energy level curves as a function of separation R as well as on the total distribution of all encounter separations. However, line asymmetries and shifts due to collisions with absorber particles have been studied very little in stellar spectra so far.

In the context of this work, it is sufficient to concentrate on pressure broadening only and to mention that for moderate stellar plasma densities short-term perturbations dominate its effect. According to Gray (2005), the corresponding power spectrum $I_{\text{pressure}}(\nu)$ can be derived as a Lorentzian profile of the form of Eq. (3.19).

Thermal Doppler Broadening

Each atom in a stellar atmosphere has a component of velocity v along the line of sight to the star due to its thermal motion. In consequence, the rest-frame wavelength, i.e., frequency ν_0 of a photon, absorbed or emitted by an atom, is shifted to some frequency ν due to the well-known Doppler effect:

$$\frac{\nu_0 - \nu}{\nu} = \frac{v}{c} \Rightarrow \nu = \frac{\nu_0}{v/c + 1}\,. \tag{3.23}$$

Here, c is the vacuum velocity of light. Since $v \ll c$, a simple Taylor expansion of Eq. (3.23) leads to the following approximated expression for the line of sight velocity:

$$v \approx \frac{\nu_0 - \nu}{\nu_0} c\,. \tag{3.24}$$

The isotropic thermal velocity distribution $\frac{\mathrm{d}N(v)}{N_\text{total}}$ is related to the Maxwell-Boltzmann statistics and becomes manifest in a Gaussian curve reading:

$$\frac{\mathrm{d}N(v)}{N_\text{total}} = \frac{1}{\sqrt{\pi} v_0} \exp\left(-\frac{v^2}{v_0^2}\right), \tag{3.25}$$

where the variance v_0 is related to the temperature by $v_0^2 = 2k_BT/m$. Here, m is the mass of the atom and k_B is Boltzmann's constant.
Using Eq. (3.24) and Eq. (3.25) in combination with the condition $|I_\text{thermal}(\nu)\mathrm{d}\nu| = |\frac{\mathrm{d}N(v)}{N_\text{total}}\mathrm{d}v|$, the thermal Doppler power spectrum can be derived:

$$\begin{aligned} I_\text{thermal}(\nu) &= \frac{\mathrm{d}N(v)}{N_\text{total}} \left|\frac{\mathrm{d}v}{\mathrm{d}\nu}\right| \approx \frac{c}{\sqrt{\pi} v_0 \nu_0} \exp\left(-\frac{(\nu_0 - \nu)^2 c^2}{v_0^2 \nu_0^2}\right) \\ &=: \frac{1}{\sqrt{\pi}\Delta\nu_\text{thermal}} \exp\left(-\frac{(\nu_0 - \nu)^2}{\Delta\nu_\text{thermal}^2}\right). \end{aligned} \tag{3.26}$$

Therefore, it is a Gaussian distribution parametrized by the thermal Doppler width $\Delta\nu_\text{thermal} := v_0\nu_0/c$, which depends on the local temperature T.

Non-Thermal Doppler Broadening or Microturbulence

The so-called microturbulence has to be postulated so that hydrostatic model spectra match observations. Microturbulence is motivated by small-scale mass motions caused by material whose characteristic dimensions are well below the usual photon mean free path in atmospheric layers, thus exhibiting an additional small-scale non-thermal velocity component. This results in small Doppler shifts analogous to the one arising from thermal motions and the microturbulent power spectrum is therefore identical to Eq. (3.26), in which the variance v_0 simply has to be replaced by the so-called microturbulent dispersion parameter ξ ($\Delta\nu_{\text{non-thermal}} := \xi\nu_0/c$):

$$I_{\text{non-thermal}}(\nu) := \frac{1}{\sqrt{\pi}\Delta\nu_{\text{non-thermal}}} \exp\left(-\frac{(\nu_0-\nu)^2}{\Delta\nu^2_{\text{non-thermal}}}\right) . \tag{3.27}$$

The exact physical origin of microturbulence is still unknown. However, in the case of hot O and B-type stars microturbulent motion might be linked to a possible sub-surface iron convection zone (Cantiello et al., 2009).

Summary of Microscopic Broadening Effects

The four microscopic broadening effects that have been discussed before, take place simultaneously. All of them are uncorrelated, though, meaning that the total line profile (total power spectrum) can be derived by a simple multiple convolution of the individual line profiles:

$$\begin{aligned} I_{\text{total}}(\nu) &= I_{\text{natural}}(\nu) \ast I_{\text{pressure}}(\nu) \ast I_{\text{thermal}}(\nu) \ast I_{\text{non-thermal}}(\nu) \\ &= I_{\text{Lorentz}}(\nu) \ast I_{\text{Gauss}}(\nu) \equiv I_{\text{Voigt}}(\nu) . \end{aligned} \tag{3.28}$$

Here, it was used that convolutions are associative and commutative. The second equality sign comes along with the fact that the convolution of two Lorentzian or Gaussian functions stays a Lorentzian or Gaussian function. The convolution of a Lorentzian and a Gaussian distribution results in the so-called Voigt function. Depending on the considered frequency interval, the shape of this function can either be similar to a Gaussian or a Lorentzian profile. For instance, the line cores of the Balmer lines resulting from neutral hydrogen are heavily influenced by thermal Doppler broadening, shaping this part of the line profile Gaussian, while the relatively broad wings exhibit the shape of a Lorentzian due to pressure broadening.

3.3.2. Macroscopic Line Broadening

While microscopic broadening is responsible for the strength as well as the shape of spectral lines as seen in the previous chapter, macroscopic broadening just redistributes the photons. Thus, it is irrelevant for the line strength, i.e., for the equivalent width, and influences the line shape only.

Rotational Broadening and Macroturbulence

Rotational broadening results from the fact that stars may possibly rotate. Typical values of measured rotation velocities of stars range from a few $\mathrm{km\,s^{-1}}$ (the detection limit) up to several hundred $\mathrm{km\,s^{-1}}$ for the more massive stars on the main sequence. However, when speaking of rotation velocity measurements, only the projection of the rotation velocity on the line-of-sight direction $v_{\text{rot,obs}} = v_{\text{eq}} \sin i \equiv v \sin i$ can be derived. Here, $v_{\text{eq}} \equiv v$ is the equatorial rotation velocity. In any case, the projected rotation velocity macroscopically shifts light coming from different parts of the visible stellar disk via the Doppler effect. To determine the broadening effects coming along with this, and therefore the rotation profile, the emitted and geometrically weighted fluxes from the different parts of the projected stellar disk all have to be summed up, since observed fluxes are typically integrated ones. It can be shown that it is sufficient to convolve the non-rotating flux profile with the rotation profile $I_{\text{rotation}}(\nu)$, though. This is valid as long as the intrinsic line profile, i.e., the ratio of intensity at any point in the spectrum to the continuum intensity, has the same shape over the disk of the star. As shown in Gray (2005), the rotation profile (power spectrum) reads:

$$I_{\text{rotation}}(\nu) = \frac{2(1-\epsilon)\sqrt{1-\left(\frac{\lambda-\lambda_0}{\Delta\lambda_L}\right)^2} + \frac{1}{2}\pi\epsilon\left(1-\left(\frac{\lambda-\lambda_0}{\Delta\lambda_L}\right)^2\right)}{\pi\Delta\lambda_L(1-\epsilon/3)} , \tag{3.29}$$

where $\Delta\lambda_L = \lambda_0 v \sin i/c$ is the maximum shift, corresponding to the disk points on the limb at the equator and ϵ is the so-called linear limb-darkening coefficient. Limb darkening describes the fact that the limb of a stellar disk appears less bright than its center. This effect can be easily understood using the definition of the visible edge of a star, which is defined by means of an optical depth of unity. When the observer looks near the edge of a star, he cannot see to the same optical depth as if he looked at the center since the line of sight must travel at an oblique angle through the stellar gas when looking near the limb, i.e., the distance from the center of the stellar disk at which the observer sees the optical depth of unity increases towards the limb. Because of the atmospheric temperature decrease from inwards to outwards, light emerging from the limb therefore results from cooler outer layers. Consequently, the limb exhibits a lower intensity than the one resulting from the center of the stellar disk.
For simplicity, limb darkening is often approximated by a linear function:

$$I(\theta) = I_0 \cdot (1 - \epsilon + \epsilon \cos\theta) , \tag{3.30}$$

where ϵ is again the linear limb-darkening coefficient. This law sufficiently describes the decrease in the continuum intensity when going from the center of the stellar disk ($\theta = 0°$) to the limb ($\theta = 90°$).
However, turbulent large-scale mass motions, whose dimensions (cells) are much larger compared to the mean free path of photons in the stellar atmosphere, can also induce an additional Doppler shift very similar to the previously discussed rotational broadening. This is referred to as so-called macroturbulence ζ. In the context of this work, it is sufficient to say that each of these "macrocells" emits a separate spectrum that is Doppler shifted with the cell's specific velocity. While for hot massive stars, these turbulent cells can physically be interpreted as the collective effect of stellar pulsations, macroturbulence is mostly driven by convection in cold stars.
Generally, all considered macroscopic line broadening effects, i.e., stellar rotation together with the effects of limb darkening as well as macroturbulence, all have to be taken account simultaneously. In order to derive the final joint macroscopic broadening power spectrum

$I_{\text{macroscopic}}(\nu)$ with which the model spectrum has to be convolved, the integration of the emitted and geometrically weighted flux over the whole projected stellar disk has to be performed numerically.

Instrumental Profile

Due to the finite spectral resolving power of the used spectrograph and CCD detector, spectral lines are additionally blurred. In order to take this effect into account, the synthetic model flux has to be convoluted with the corresponding instrumental profile which is Gaussian. The corresponding profile width can be determined by fitting a Gaussian curve to the observed emission lines of the reference lamp that is used for wavelength calibration. Since these emission lines do not show any intrinsic broadening because of the low temperature of the lamp, their measured width is caused by instrumental smearing only.

4. Quantitative Spectral Analysis

Quantitative spectral analysis allows to determine the (atmospheric) parameters (effective temperature, T_{eff}, surface gravity, $\log{(g)}$, hydrogen and helium abundance, $\log{(y)}$, projected rotation velocity $v \sin i$ and radial velocity v_{rad} as well as microturbulence ξ and macroturbulence ζ) and the individual metal abundances of stars. However, T_{eff}, $\log{(g)}$, $\log{(y)}$ as well as the hydrogen abundance are degenerated, meaning that these parameters cannot be determined separately, but have to be derived simultaneously from fitting the observed spectrum with a grid of synthetic spectra, which will be discussed in a more detailed way in chapters 10 and 11. This degeneracy also holds for ξ and ζ, which are not relevant of the stars in question, though. In order to understand the influence of spectroscopic parameters on synthetic model spectra as used for the analysis part of this thesis, the characteristic spectral line features, from which these parameters are primarily constrained, have to be explained. Fig. 4.5.1 summarizes the effects of parameter variations on strategic spectral lines which shall be presented in the following.

4.1. Effective Temperature

The effective temperature, T_{eff}, which is a measure for the emitted flux (see Eq. 3.10 for details), is one of the key parameters describing the atmospheric structure of a star. This is because temperature stratification is linked to T_{eff} via flux conservation. Consequently, the temperature of any photospheric layer rises or falls when increasing or decreasing T_{eff}. As the excitation and ionization level of chemical elements in a certain atmospheric layer depend on the local temperature, the shape of absorption lines is sensitive to T_{eff}. However, the strength of a spectral line increases quantitatively with T_{eff} as long as the level population of the lower state of the particular atomic transition increases. After having reached a maximum at a certain temperature which increases with the level of excitation and ionization, this level population starts to decrease again, though, since hotter temperatures result in more and more atoms, belonging to energetically higher excitation and ionization stages. In the case of hydrogen Balmer lines, for instance, the temperature value corresponding to the maximum level population of the first excited state lies near 10 000 K, being equivalent to stars of spectral class A0. T_{eff} is well determined by measuring both, depth and width, of spectral lines belonging to chemical elements that show at least two different ionization stages. While lines corresponding to lower ionization levels weaken with higher temperatures, the ones of higher ionized stages strengthen (see the silicon absorption line formation in Fig. 4.5.1). Therefore, the "real" effective temperature of a star can be derived from the best fit for both of them (ionization equilibrium). An additional indicator for T_{eff} is the width of lines showing strong

thermal Doppler broadening, which is the case for most metal lines (see Fig. 4.5.1).
As the analyzed B-type stars in this thesis are not hot enough to show He II absorption lines in their spectra, the cores and wings of the strong hydrogen Balmer lines are used to determine their effective temperature. The already discussed correlation between temperature and level population, i.e., line strength, and the fact that the line cores are mostly thermal Doppler broadened, makes them a good indicator for the particular stellar effective temperature. In addition, since thermal Doppler broadening is the dominant microscopic broadening effect for most metal lines, T_{eff} can be further specified if these lines are taken into account as well. Certainly, metals with varying degree of ionization constrain T_{eff}, too (Irrgang, 2014).

4.2. Surface Gravity

Just as the effective temperature, the surface gravity, often scaled logarithmically and denoted in cgs units via $\log{(g(\text{cm}\,\text{s}^{-2}))}$, affects all spectral lines, since it is closely linked to atmospheric pressure and density stratification through hydrostatic equilibrium (see Eqs. 3.7 and 3.9 for details). Generally, an increase in $\log{(g)}$ results in a denser stellar plasma, thus increasing the probability of electron captures by free ions, which therefore decreases the ionization level of the whole plasma (see Eq. 3.14 for the dependence of Saha's equation on electron density n_e). Hence, as in the case of T_{eff}, it is useful to investigate spectral lines of chemical elements with at least two different ionization stages in order to constrain $\log{(g)}$ effectively (Irrgang, 2014).
As already mentioned, for the analyzed B-type stars no He II absorption lines can be detected in their spectra, though. It is again the hydrogen Balmer lines that are primarily used to derive $\log{(g)}$ instead. Here, the focus is on the wings of the lines showing strong pressure broadening due to the linear and quadratic Stark effect (see section 3.3.1). However, the Balmer wings are sensitive to effective temperature variations, too. That is why in this case Balmer lines cannot be analyzed alone in order to determine both, T_{eff} and $\log{(g)}$, simultaneously. Increasing T_{eff} in hot stars reduces the Balmer line strength on the one hand, resulting in narrower wings, but on the other hand this effect could be compensated by stronger pressure broadening caused by higher surface gravities (see the hydrogen Balmer line formation in Fig. 4.5.1). As for the determination of T_{eff}, other chemical elements showing different ionization stages should be used to further constrain $\log{(g)}$ (Irrgang, 2014).

4.3. Helium Abundance

Helium usually is the second most abundant element right after hydrogen and, therefore, its abundance, denoted as $\log{(y)}$, effects the temperature-density stratification of the particular stellar atmosphere, while the effect of all metals is often considered collectively as metallicity (Irrgang, 2014).

4.4. Radial Velocity

The radial velocity v_{rad}, producing a Doppler shift of the spectrum due to the relative motion between the observed target and the Earth, can be measured with respect to the barycenter, i.e., the center of the whole solar system. It can be derived using the Doppler formula:

$$\frac{\lambda - \lambda_0}{\lambda_0} = \frac{v}{c} = \frac{v_{\text{rad}} + v_{\text{bary}}}{c} \ , \tag{4.1}$$

where c is the vacuum speed of light, v the relative motion between the target and the Earth, λ the observed wavelength, λ_0 the rest-frame wavelength, and v_{bary} is a season-dependent component caused by Earth's rotation and its motion around the barycenter. If the target coordinates, the location of the telescope, and the time of observation are known, this season-dependent parameter can be precisely determined and, hence, corrected. However, this can only be done in combination with v_{rad}, since according to Eq. (4.1):

$$\lambda_0 = \frac{\lambda}{1 + v/c} = \frac{\lambda}{1 + (v_{\text{rad}} + v_{\text{bary}})/c} \ . \tag{4.2}$$

Nevertheless, the barycentric corrections are typically applied in a first step. v_{rad} can then be determined afterwards. This is done by calculating the barycentric corrected wavelength λ_{corr} via:

$$\lambda_{\text{corr}} = \frac{\lambda}{1 + v_{\text{bary}}/c} \ . \tag{4.3}$$

After that, the radial velocity v_{rad} can be simply determined via:

$$v_{\text{rad}} = \frac{\lambda_{\text{corr}} - \lambda_0}{\lambda_0} c \ . \tag{4.4}$$

The error introduced by these two subsequent corrections is negligible as shown by Irrgang (2014).

4.5. Projected Rotation Velocity

This macroscopic broadening parameter, which has already been discussed in section 3.3.2, describes the blurring of spectral lines and can be well determined by investigating the profiles of intrinsically narrow lines, i.e., those resulting from metals (Schaffenroth, 2015). This is because of the effect of atomic mass m on the thermal Doppler width $\Delta\nu_{\text{thermal}} \sim 1/\sqrt{m}$ (see Eq. 3.26 for details). Hence, lines belonging to heavier chemical elements are narrower, i.e. broadened less strongly by thermal Doppler broadening.

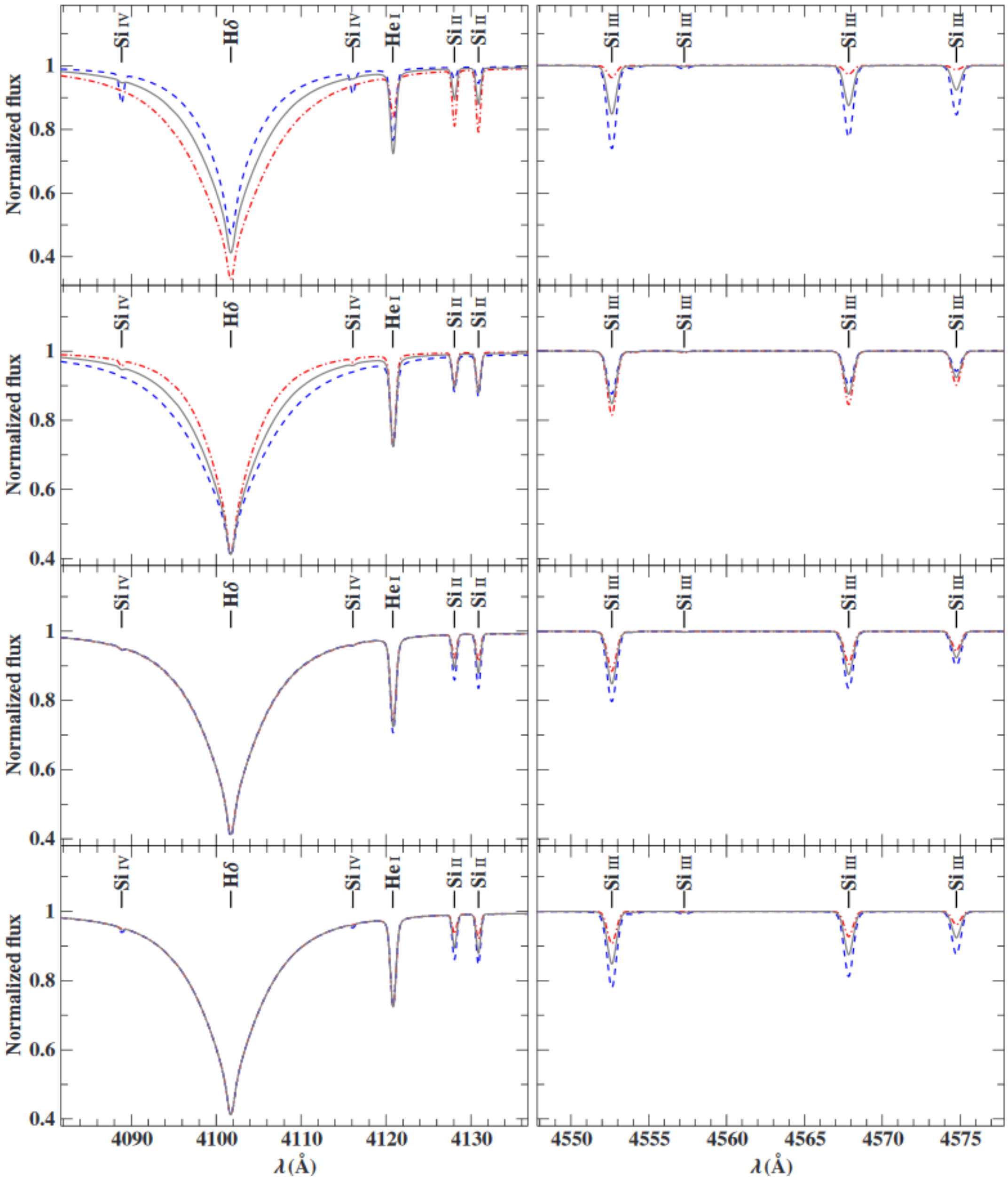

Figure 4.5.1.: Effects of effective temperature T_{eff}, surface gravity $\log(g)$, microturbulence ξ, and silicon abundance $\log(n(\text{Si}))$ variations on hydrogen, helium, and silicon spectral line shapes in a model spectrum. The original reference model ($T_{\text{eff}} = 20\,000$ K, $\log(g) = 4.0$ dex, $\xi = 4\,\text{km}\,\text{s}^{-1}$, $\log(n(\text{Si})) = -4.5$ dex, and $\log(n(\text{He})) = -1.15$ dex) is shown as a gray line in all eight panels. The blue dashed line represents the new model after having increased one of the parameters, whereas the red dashed-dotted line displays the new model after having decreased the exact same parameter. The order of parameter variation from row to row is: Effective temperature ($\Delta T_{\text{eff}} = \pm 5000$ K), surface gravity ($\Delta\log(g) = \pm 0.4$ dex), microturbulence ($\Delta\xi = \pm 4\,\text{km}\,\text{s}^{-1}$), and silicon abundance ($\Delta\log(n(\text{Si})) = \pm 0.6$ dex). Adopted from Irrgang (2014).

4.6. Metal Abundances

The higher the atmospheric elemental abundances of the individual metals, i.e., the higher the number density $n(X)$, where $X \in \{$C, N, O, Ne, Mg, Al, Si, S, Ar, Fe$\}$, the larger the number density of absorbers and the larger the absorption coefficient, i.e., opacity. All elemental abundances enter the continuum opacity and, thus, influence the atmospheric structure as well as individual line profiles. As the metal abundances, i.e. those of elements with larger atomic masses than hydrogen and helium, are usually orders of magnitude lower than those of hydrogen and helium in B-type stars, they can be treated as trace elements, meaning that the continuum flux is mostly independent of and insensitive to changes in their abundances. Their effect is summarized by the so-called metallicity, taking into account both, mean atomic weight as well as the number of free electrons originating from all present metals in the stellar plasma (Irrgang, 2014). In order to determine the metal abundances, the strength of the individual spectral lines can be investigated, though. This is possible since the latter increases with the equivalent width (see Eq. 3.18), and therefore with the number of absorbing atoms. The exact correlation between line strength and equivalent width is called curve of growth and actually turns out to be non-linear (see for instance Gray (2005) for more information).

Besides the already discussed spectroscopic parameters, microturbulence (see section 3.3.1) and macroturbulence (see section 3.3.2) generally can also affect the shape of spectral lines. An example for the effect of microturbulence variations is shown in Fig. 4.5.1. However, for the later analysis of $^{3}\mathrm{He}$ B-type stars presented in chapters 10 and 11, macroturbulence is set to zero and microturbulence is not treated at all, because previous analyses on B-type stars did not show evidence for non-zero micro- and macroturbulences, respectively.

While for the LTE analysis in chapter 10 only effective temperature, surface gravity, radial and projected rotation velocity as well as helium abundance are determined by means of synthetic model spectra, for the hybrid LTE/NLTE approach in chapter 11 also metal abundances are derived. In the latter case, the focus will be on the distinction between $^{3}\mathrm{He}$ and $^{4}\mathrm{He}$ and the determination of their individual elemental abundances in the stellar atmospheres of the analyzed $^{3}\mathrm{He}$ B-type stars, though.

5. Hot Subluminous Stars

This section is largely based on Heber (2009, 2016). Other references are marked at the relevant passages within the text.

5.1. Atmospheric Properties

The discovery of the first hot subdwarf star dates back to the 1950s and was achieved by exploiting the data of the Humason & Zwicky photometric survey of the North Galactic Pole region from 1947. The number of such known objects remained comparatively small over the next 30 years, though. It was only with the Palomar-Green survey of the northern Galactic hemisphere that the number of these stars, also known as subluminous blue stars, strongly increased. Today, after the successful execution of different other photometric and objective prism surveys as well as high quality optical surveys such as the Sloan Digital Sky Survey (SDSS), the catalogue of hot subdwarf stars has increased to more than 5000 stars in total (Geier et al., 2016).

Hot subdwarf stars have very little in common with their cooler traditional counterparts. Representing several stages in the very late evolution of low-mass stars ($\sim 0.5\,\mathrm{M}_\odot$ with radii of about 0.1-0.2 $\mathrm{R}_\odot$), these objects have evolved far beyond the main sequence locating them between the white-dwarf (WD) and main sequence in the HRD (see Fig. 5.1.1). These descendants of red giant (RG) stars, that almost completely lost their hydrogen-rich envelope, mostly consist of helium fusing to carbon and oxygen within their core. According to the extension of the Harvard Spectral Classification System (Drilling et al., 2013), hot subdwarf stars can be divided into two categories: B-type (sdB) and O-type (sdO) subdwarfs. Whereas sdBs lie at the blue end of the horizontal branch (HB) with effective temperatures between $\sim$ 25 000 K and $\sim$ 35 000 K, sdOs with $T_\mathrm{eff} > 37\,000\,\mathrm{K}$ show a large diversity including post red-giant branch, post-HB, and post-asymptotic giant branch stars. Even a couple of central stars of planetary nebulae are sometimes incorporated into the spectral class of sdOs if exhibiting absorption lines only. However at apparent magnitudes brighter than 18 magnitudes, subdwarf B-type stars were found to outnumber all other types of faint blue objects, even the WDs, resulting in an all in all sdB to sdO frequency of 3 to 1.

Typically, the mass of the remaining hydrogen is less than $0.01\,\mathrm{M}_\odot$ for sdBs, thus certainly too little to guarantee further hydrogen-burning. Hence, sdBs evolve directly to the white-dwarf cooling sequence without resting on the asymptotic giant branch (AGB). The small hydrogen abundance within their outer envelope is sufficient for subluminous stars to produce more intense absorption lines than in B-type main-sequence stars, though. Additionally, the spectra of subdwarf B and O stars can be shaped by He I and/or He II lines, whereby only sdOs display

He II, 4686 Å, and sometimes even more He II lines. For the latter ones, the Balmer series may even occasionally be absent. Whereas sdB stars spectroscopically form a homogeneous class and largely contribute to the number of hot stars in old star systems, globular clusters and elliptic galaxies, a large variety of spectra is observed amongst sdO stars spanning two orders of magnitude and, therefore, can be subdivided historically into "luminous" and "compact" ones.

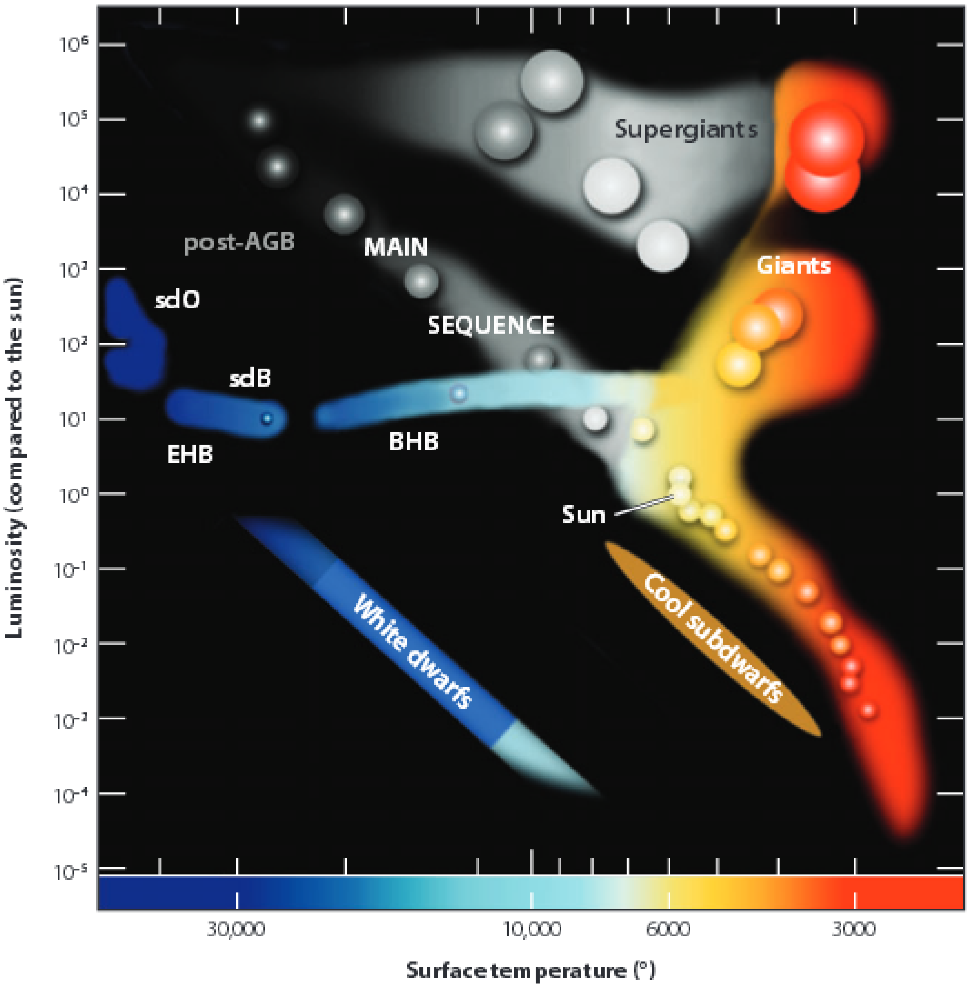

Figure 5.1.1.: Sketch of a Hertzsprung-Russell diagram highlighting the position of the extreme horizontal branch (EHB) populated by hot subdwarf (sdB and sdO) stars located to the left and below the hot end of the main sequence but above the white dwarf sequence. The EHB is separated from the blue horizontal branch (BHB) as well. The traditional cool subdwarfs lie below the lower main sequence. Adopted from Heber (2009).

Depending on the strength of the helium lines, hot subdwarf stars can generally be divided into the following subcategories (Moehler et al., 1990):

- **sdBs**: These stars have strong hydrogen Balmer series and are neutral He weak-lined.

- **He-sdOs**: The Balmer series is only weakly or not even present, but the spectra display strong He I and He II absorption lines.

- **sdOs**: Characteristic for these stars is the presence of strong hydrogen and He II absorption lines in combination with only weak or even not observable neutral helium.

- **sdOBs**: This category describes sdB-like spectra with weak He II. Although the temperature range (between ∼ 30 000 K and ∼ 45 000 K) of these stars exceeds the one of normal sdBs, they are nowadays often subsumed under the sdB class.

- **He-sdBs**: This class of hot subluminous stars exhibits spectra consisting of strong He I lines and a dominant Balmer series. However, He-sdB stars are rare.

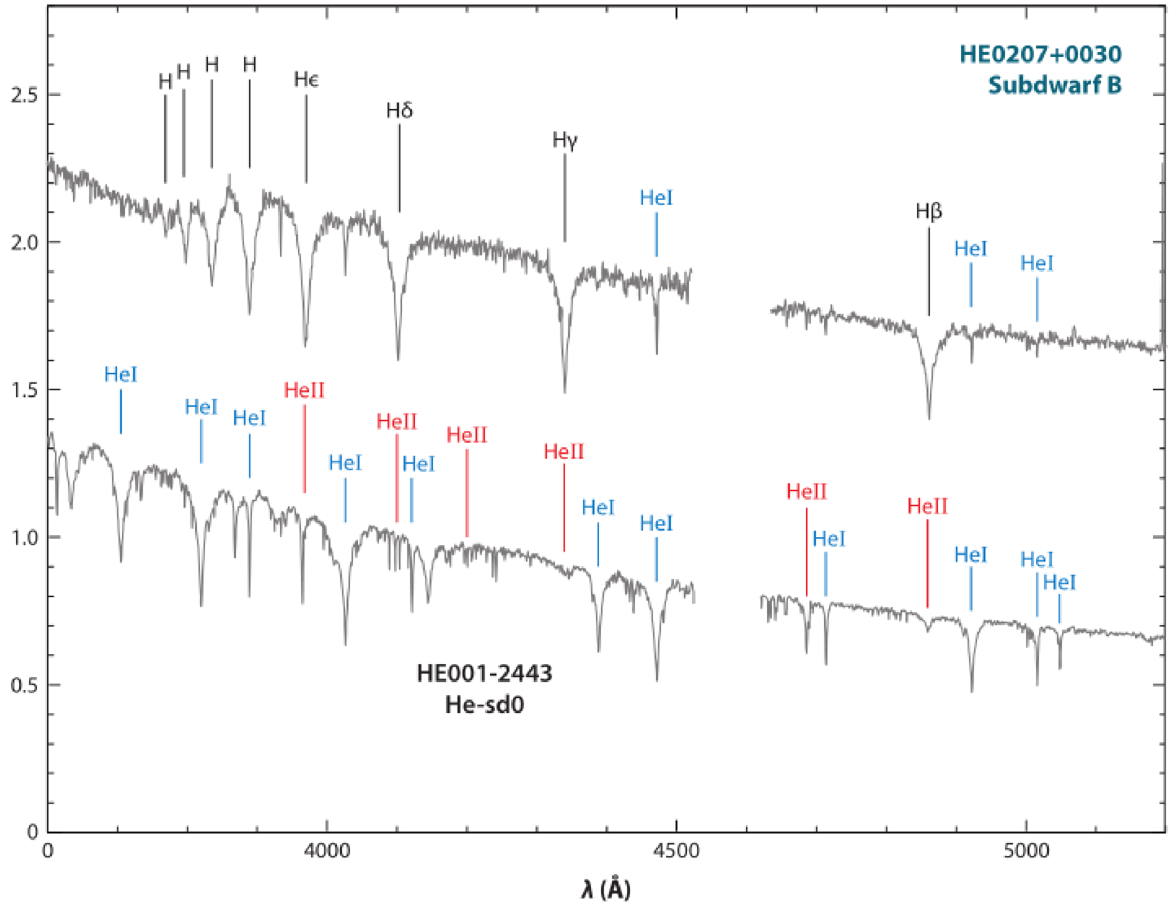

Figure 5.1.2.: Spectra of typical sdB and He-sdO stars displaying important hydrogen and helium absorption lines. Whereas helium lines are weak in sdB stars, the Balmer series is absent and additionally blended with He II Pickering lines in (He-)sdOs. Note that both spectra are not absolutely flux calibrated and shifted to each other. Adopted from Heber (2009).

Consequently, spectra of hot subdwarf stars can be quite different, but one trend has to be pointed out: Spectra of most sdBs are helium-weak and in most of the cases sdOs display quite strong helium lines. This is emphasized by Fig. 5.1.2 showing the comparison of the extremely different intensity profiles of two hot subluminous star spectra, an sdB and a He-sdO, respectively.

Other important characteristics of hot subluminous stars apart from their effective temperatures are gravity, and the helium abundance, usually simply defined as the logarithm of the ratio of helium to hydrogen number density in the stellar atmosphere $\log(y) = \log\left[\frac{N(\mathsf{He})}{N(\mathsf{H})}\right]$. Another way of defining $\log(y)$ is taking the logarithm of the ratio of helium number density to the number density of all the elements in the stellar atmosphere.

Concerning gravity $\log(g)$, the distribution of subdwarf B, subdwarf OB and subdwarf O stars is mostly homogenous within a certain regime. While most sdBs have $\log(g)$ values between 5.0 dex and 5.7 dex, sdOs exhibit values between 5.5 dex and 5.9 dex (Heber et al., 1986). For the group of sdOBs a regime of $5.0\,\mathrm{dex} \leq \log(g) \leq 6.3\,\mathrm{dex}$ has been found. The upper panel of Fig. 5.1.3 shows the distribution of hot subdwarf stars in the T_{eff}-$\log(g)$ plane based on the latest results from major hot subluminous star surveys like the ESO Supernova Ia Progenitor Survey (ESO/SPY), the *GALEX* sample, the Hamburg quasar survey (HQS) sample as well as the PG and EC star surveys. In fact, most of the analyzed hot subdwarf stars lie within typical effective temperatures of ~ 25 000 K and ~ 37 000 K having $5.2\,\mathrm{dex} \leq \log(g) \leq 6.0\,\mathrm{dex}$. Also, a trend is clearly visible: With increasing effective temperature, gravity also increases for most of the stars. This is due to the link of luminosity L and mass M of a star. Since these quantities are given by

$$L = 4\pi R^2 \sigma T_{\mathrm{eff}}^4 \quad \text{and} \tag{5.1}$$

$$M = \frac{gR^2}{G}\,, \tag{5.2}$$

this results in $R^2 = \frac{GM}{g} = \frac{L}{4\pi\sigma T_{\mathrm{eff}}^4}$ and therefore:

$$g \sim T_{\mathrm{eff}}^4\,. \tag{5.3}$$

However, the helium abundance $\log(y)$ for hot subdwarfs strongly depends on the spectral class of the star. General $\log(y)$ values for subdwarf B stars lie between -3 dex and ~-1.6 dex, whereas sdOBs show high fluctuations ranging from ~-3.1 dex to ~-1.2 dex (Heber et al., 1986). Subdwarf O stars exhibit even higher values, though. For these stars, the highest ever measured helium abundance exceeds $\log(y) = 3\,\mathrm{dex}$ and has been found by exploiting data from the *GALEX* sample. For sdB stars, Edelmann et al. (2003) found a linear correlation between effective temperature T_{eff} and helium abundance $\log(y)$. The larger T_{eff}, the larger the helium content $\log(y)$ in the stellar atmosphere. In addition, it was possible to subdivide the hot subluminous B stars into two groups. As can be seen in Fig. 5.1.4, the first group (upper helium sequence containing around 5/6 of the analyzed stars) has much higher helium abundances at the same temperatures than the second group (lower helium sequence containing around 1/6 of the analyzed stars). This behavior can also be seen in the lower

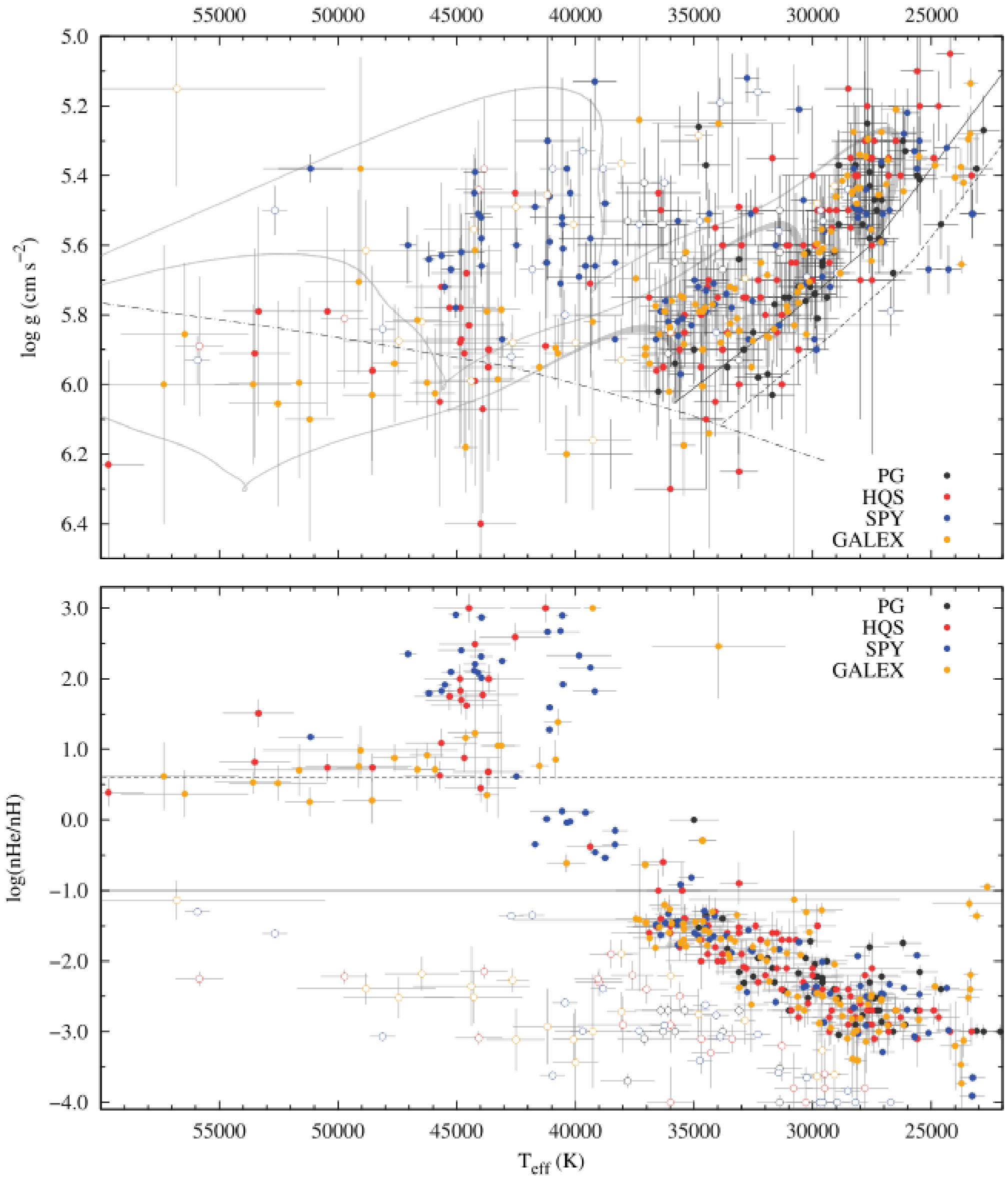

Figure 5.1.3.: *Upper Panel*: Distribution of hot subdwarf stars in the T_{eff}-$\log(g)$ plane. *Lower Panel*: Distribution of hot subdwarf stars in the helium abundances vs. T_{eff} plane. Different colors mark different samples: ESO/SPY sample (blue), *GALEX* sample (yellow), HQS sample (red) and the sample drawn from the PG and EC surveys (black). He-poor and He-rich stars are represented by filled and open circles, respectively. The location of the zero age extreme horizontal branch (ZAEHB) for two different masses ($\sim 0.45\,\mathrm{M}_\odot$, dotted, and $\sim 0.5\,\mathrm{M}_\odot$, full drawn), the helium main sequence (dashed-dotted line) and evolutionary tracks for three hydrogen envelope masses ($\sim 0.000\,\mathrm{M}_\odot$, $\sim 0.001\,\mathrm{M}_\odot$, and $\sim 0.005\,\mathrm{M}_\odot$ in dark gray lines, from bottom to top) with linewidths proportional to evolutionary timescales are also shown in the T_{eff}-$\log(g)$ diagram. The solar helium abundance and one-tenth of it are also shown as a dotted and full drawn horizontal line in the helium abundances vs. T_{eff} diagram, respectively. Adopted from Heber (2016).

panel of Fig. 5.1.3. Edelmann et al. (2003) fitted two linear regressions describing each of the groups which read:

$$\log\left[\frac{N(\mathrm{He})}{N(\mathrm{H})}\right] = -3.53\,\mathrm{dex} + 1.35\cdot\left(\frac{T_{\mathrm{eff}}}{10^4\mathrm{K}} - 2.00\right)\mathrm{dex}\ \text{for the bulk of sdB stars and} \tag{5.4}$$

$$\log\left[\frac{N(\mathrm{He})}{N(\mathrm{H})}\right] = -4.79\,\mathrm{dex} + 1.26\cdot\left(\frac{T_{\mathrm{eff}}}{10^4\mathrm{K}} - 2.00\right)\mathrm{dex}\ \text{for the second group.} \tag{5.5}$$

Over the years, different suggestions have been made in order to explain this behaviour of

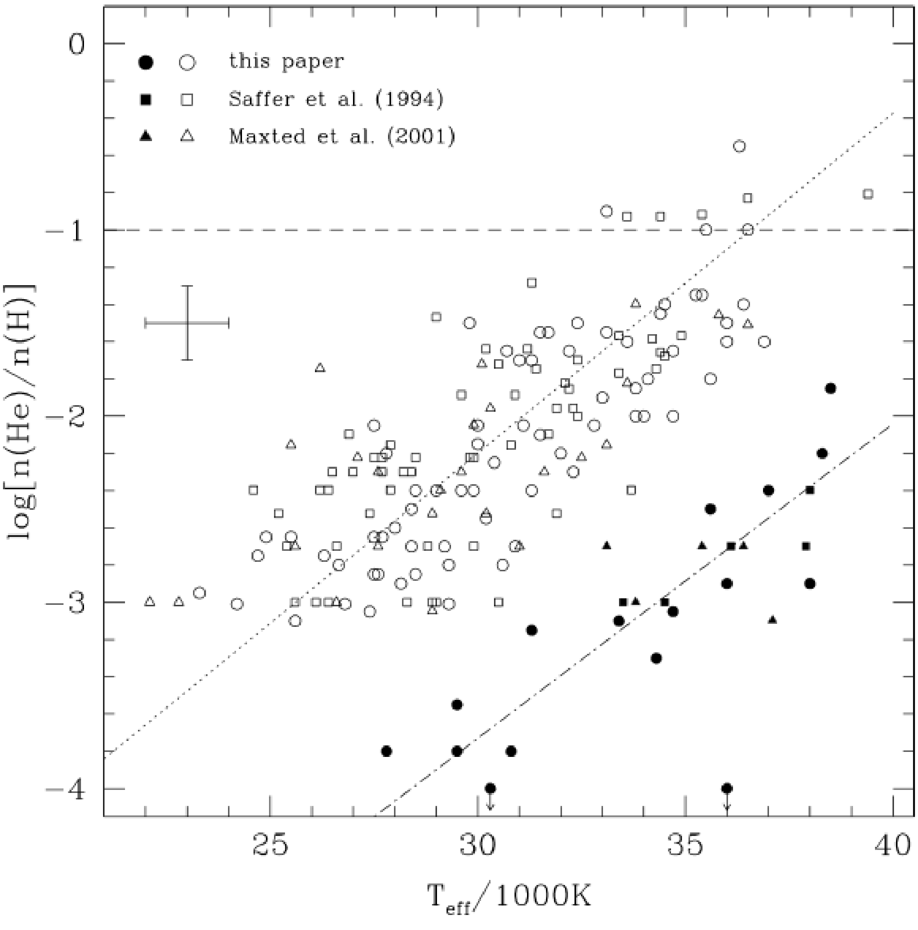

Figure 5.1.4.: Helium abundance vs. effective temperature diagram for three different samples of subdwarf B stars including the results of Saffer et al. (1994), Maxted et al. (2001) and Edelmann et al. (2003). The dotted line indicates the linear regression of Eq. (5.4) for the majority of the subdwarf B stars (marked with open symbols) and the dashed-dotted line displays the linear regression of Eq. (5.5) for the peculiar subdwarf B stars (marked with filled symbols). Additionally, the dashed horizontal line represents the solar helium abundance. Adopted from Edelmann et al. (2003).

subdwarf B stars. For instance, Edelmann et al. (2003) argued that, due to tidal effects, sdBs residing in short-period binaries might exhibit higher helium abundances than long-period systems or single stars. However, Geier et al. (2013a) could disprove this hypothesis. Also, diffusion models by Michaud et al. (2011) predicted neither the observed correlation with temperature nor the two helium sequences. Hence, no reasonable explanation has been found yet.

5.2. Chemical Composition of Subdwarf B Stars

Since the spectra of hydrogen-rich subdwarfs differ significantly from those of hydrogen-poor ones and since most of the subluminous B stars are hydrogen-rich, only hydrogen-rich sdBs shall be discussed in the following. Besides hydrogen and helium, a typical sdB star spectrum shows also prominent metal lines in the optical, resulting notably from carbon, nitrogen, magnesium, silicon, sulfur, and to a lesser extent from iron. For the vast majority of subluminous B stars this anomalous chemical composition is most likely due to atmospheric diffusion. Early analyses have now been extended to more than 100 stars and to elemental abundances of up to 24 different ions per star (Geier, 2013). But in order to do this analysis in a most efficient way, Geier (2013) used a semi-automatic analysis pipeline to fit the synthetic spectra computed from local thermodynamic equilibrium (LTE) models to a standard set of optical spectral lines. Some similarities have been found, although for several elements only upper limits could be derived and the analysis is also dominated by relatively large star-to-star variations (see Fig. 5.2.1).

While oxygen is depleted on average by 1-2 dex compared to the solar abundance value, carbon and nitrogen show very different distributions. The nitrogen abundance is slightly subsolar throughout the entire effective temperature range showing less scatter than for oxygen. But the abundance of carbon varies by orders of magnitude from star to star ranging from strongly subsolar to slightly supersolar.

The magnesium abundance being subsolar by about one order of magnitude on average and the solar iron abundance display little scatter just like nitrogen. However, it is noticeable that the intermediate mass elements just like silicon, aluminum and sulfur are overall depleted, silicon also showing a large star-to-star scatter. All the heavier elements ranging from krypton to cobalt are enriched, whereas peculiar elements like titanium and vanadium are found in at least half or one third of the analyzed sample being strongly enhanced by $+2$ dex (Ti) and $+3$ dex (V), respectively. Also, scandium and chromium are detected in just a few stars but if so, being strongly enriched. Generally, all elements beyond Ar (iron excluded) are enriched. The strength of enhancement varies from star to star but also increases with increasing effective temperature to as much as a factor of 1000.

Spectral analyses of UV spectra are available for a few stars only. These studies overall confirm the findings from optical analyses, also adding heavier elements like Ni, Cu, Zn, Ga, Ge, Sn, and Pb. They extend the information on elements that only have upper limits from optical analyses, too (see Fig. 5.2.2).

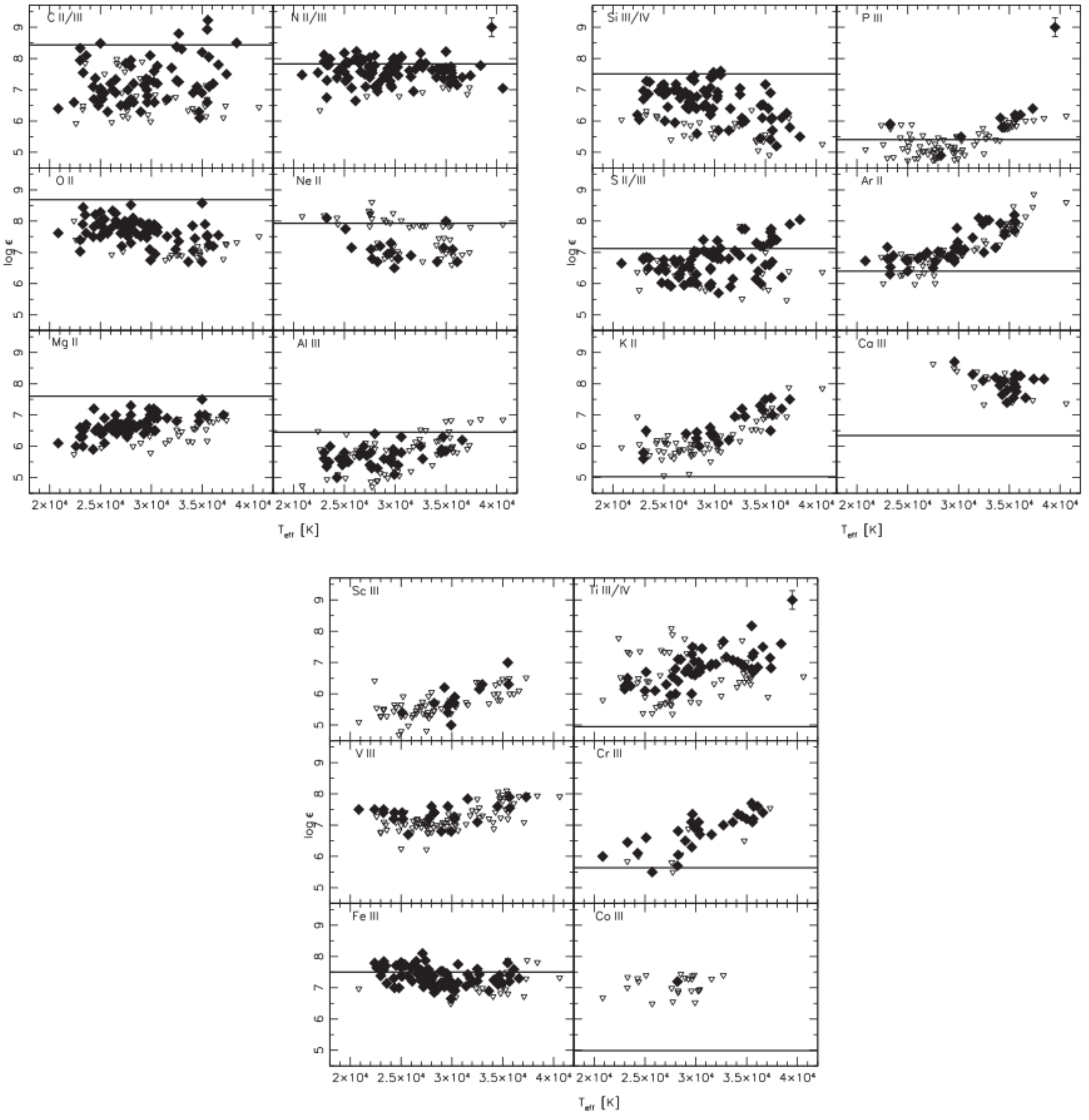

Figure 5.2.1.: Elemental abundances of sdB stars as a function of effective temperature based on LTE models only. Filled diamonds mark measured abundances whereas open triangles mark only upper limits. The solid horizontal lines mark solar abundances and typical error bars are given in the upper right corner. Abundance values are given in $\log \epsilon$. In order to derive negative logarithmic values for the elemental abundances as for instance for the helium abundance $\log(y)$, one has to subtract -12.00 from the particular $\log \epsilon$ value (Asplund et al., 2009). Adopted from Heber (2016).

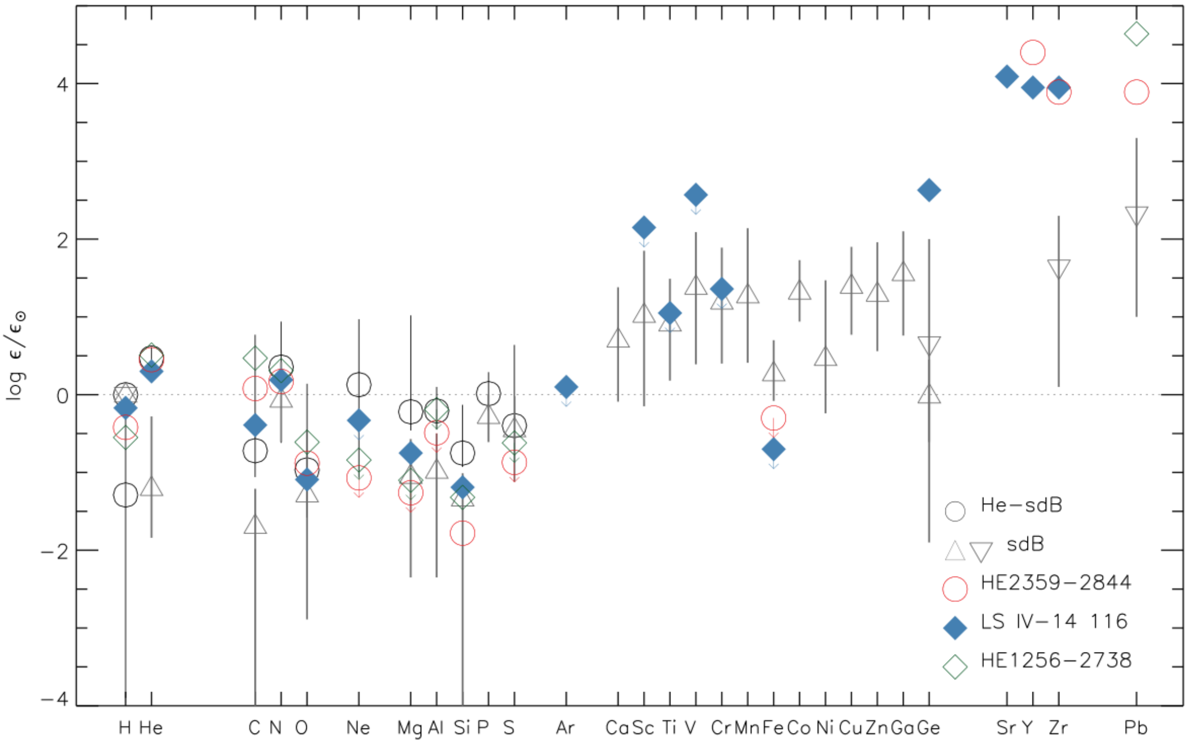

Figure 5.2.2.: Mean elemental abundances and ranges for helium-rich subdwarfs and normal subdwarfs relative to solar values. Also, surface abundances of the zirconium star LS IV-14 116 and the lead stars HE 2359-2844 and HE 1256-2738 are shown. Extracted from Heber (2016); original version Naslim et al. (2013).

5.3. Diffusion Theory

Pure *gravitational settling* is caused by the gravitational force $\sim mg$ acting on a particular chemical element, where m is the mass of the corresponding atom/ion and g is the surface gravity of the star. This means that right after a star has been born, the heavier chemical elements sink out of the stellar atmosphere and only the lightest elements remain. This explains the observation of hydrogen dominated spectra in the case of white dwarfs (WD) in a simple way.

It is assumed that the abundance anomalies of sdB stars discussed in section 5.2 are also caused by atomic diffusion processes in the stellar atmosphere. The most simplistic model acts on the assumption that the particular elemental abundances can be derived from a balance between *gravitational settling* caused by gravity and *radiative levitation* caused by the radiation pressure, since the latter depends on the elemental abundance. For instance in the case of bound-bound (b-b) transitions only, the radiative acceleration g_{ikm} due to a single b-b transition of A_i, i.e., an ion i of atomic species A, from level k to level m, can be obtained by:

$$g_{ikm} = \frac{1}{m_{A_i} c} \int_0^\infty \frac{N_{ik}}{N_i} \sigma_{ikm} F_\nu \mathrm{d}\nu \; . \tag{5.6}$$

Here, $F_\nu \mathrm{d}\nu$ is the net outward radiative energy flux in the frequency range $\mathrm{d}\nu$, the ratio $\frac{N_{ik}}{N_i}$ describes the fraction of A_i in state k, σ_{ikm} is the absorption cross-section for the considered b-b transition, c is the vacuum light velocity, and m_{A_i} the mass of the ion. Remember that the product $N_{ik}\sigma_{ikm}$ is defined as the so-called absorption coefficient κ_{ikm} for the considered transition process. Thus, the higher the elemental abundance of a certain ion, the higher the absorption coefficient, and therefore the radiative acceleration causing higher radiation pressure. This is valid as long as the corresponding absorption line does not saturate. If so, the net outward radiative energy flux F_ν is proportional to κ_{ikm}^{-1}, resulting in $N_{ik}\sigma_{ikm}F_\nu = \text{const.}$. Hence, the integrand in Eq. (5.6) reads $\sim \frac{1}{N_i}$ only, limiting the radiation pressure since the integral extends formally from 0 to ∞, but the integrand vanishes rapidly outside a narrow frequency range determined by the saturated line profile. In a simple picture without using any formulas, saturation means a lack of photons compared to the absorber material, i.e., more absorbers are available than photons can be absorbed. While the line core of the considered absorption line is and remains saturated at any case at some point $(\tau_\nu > 1)$, desaturation may occur in the line wings $(\tau_\nu < 1)$. If so, only the line wings strongly contribute to the integral in Eq. (5.6), also limiting the radiation pressure. The limitation of the radiative acceleration due to saturation effects is important for setting up an equilibrium state between gravitational settling and radiative levitation on timescales that are short compared to the evolutionary time of a subdwarf B star (Michaud et al., 2015).

In the following, the interplay of gravity g and radiative acceleration expressed as g_{rad} shall be demonstrated assuming a simple scenario starting with non-saturated lines.

At first, assume an element whose initial abundance is high enough that the radiative acceleration dominates the gravitational settling in the stellar atmosphere. In the case of an sdB star, this could be for example nitrogen (N) with solar abundance. As long as g_{rad} is larger than g, nitrogen is streaming upwards. But since g_{rad} for nitrogen ions also decreases with decreasing nitrogen abundance, a balance between radiation pressure and gravitational settling will be set up after a certain time interval. The atmospheric abundance of nitrogen has then increased above its initial solar value.

However, by assuming an element whose initial atmospheric abundance results in a radiation force lower than the gravitational one, the element will settle. Nickel (Ni) with solar abundance is a good example in the case of sdB stars. Due to the increase of the atmospheric nickel abundance, g_{rad} for nickel ions also increases until a balance between gravity and radiative acceleration has been set up again. Here in the final equilibrium state, the atmospheric nickel abundance is smaller than its initial solar value.

A peculiarity takes place if the limited upper value of the radiation pressure g_{rad} for an element is lower than gravity. Then the element keeps on settling. For instance, this is the case for helium and metals in a white dwarf's atmosphere since it is almost completely composed of

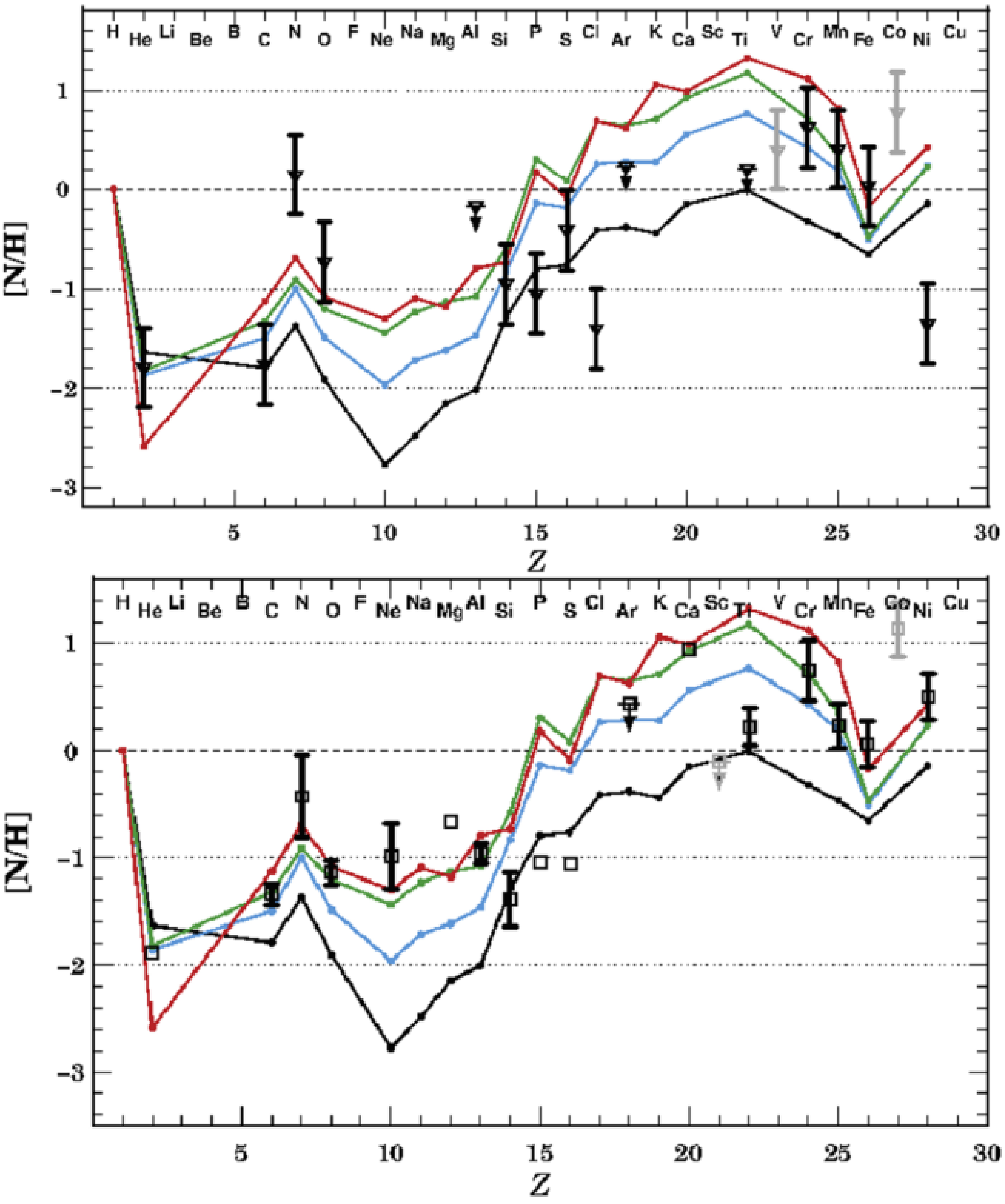

Figure 5.3.1.: Comparison of the observed abundance pattern of the two normal sdB stars PG 0101+039 (top panel) and Feige 48 (bottom panel) with predicted curves calculated by turbulent diffusion models of Michaud et al. (2011) after 25 million years for models with different original metallicities Z_0 (black: $Z_0 = 0.0001$, cyan: $Z_0 = 0.001$, green: $Z_0 = 0.004$ and red: $Z_0 = 0.02$). Cobalt has not been included in the model due to a lack of atomic data (gray symbol). Extracted from Heber (2016); original version Michaud et al. (2011).

hydrogen. The floating of hydrogen and the concomitant settling of helium and metals were essential to understand the surface chemical composition of these stars (Michaud et al., 2015). It is evident that the white dwarf model does not hold for hot subdwarf sdB stars, though, because of the abundance anomalies shown earlier in section 5.2.

However, when applying the simplistic diffusion scenario from above to helium atoms and ions in sdB star atmospheres, the element should be depleted to very low abundances, on timescales much shorter than the evolutionary one. This is because the radiative support for helium is rather small due to a lack of lines in the appropriate spectral range (UV), where the radiation flux is highest (see the dependence of g_{rad} on the net outward radiative energy flux and absorption coefficient in Eq. 5.6 for details). In fact, the equilibrium helium abundance in sdBs is even predicted to be lower by two orders of magnitude than the average observed helium abundance. Usually, at such low abundances no absorption lines should be observable at all in any optical spectrum of an sdB star. Also, radiative acceleration for irons having plenty of UV lines, may be so large that the equilibrium abundance ends up super-solar which is not seen for all metals (see Fig. 5.2.2).

In order to slow down the diffusion process and support the helium atoms and ions against gravitational settling in the stellar atmosphere of an sdB star, additional processes were considered. For instance, Fontaine & Chayer (1997) and Unglaub & Bues (2001) suggested a radiatively driven stellar wind. This model may only explain the observed helium abundance if the mass loss rate is of the order $10^{-13} - 10^{-14}\,\mathrm{M}_{\odot}$ /yr. However, on the other hand Unglaub (2008) showed that the atmospheric densities in sdB stars are so low that metals cannot share their momentum with the lighter elements like hydrogen and helium through collisions. Hence, the stellar wind just fractionates and becomes metallic.

Weak turbulent mixing of the outer $10^{-6}\,\mathrm{M}_{\odot}$ could in principle also explain the observed helium abundances for sdB stars. Michaud et al. (2011) used a turbulence model to derive detailed diffusion calculations for metals in hot subluminous stars amongst others. Their results reproduce moderately well the surface abundances of typical sdB stars (see Fig. 5.3.1), although diffusion calculations for several elements have not been possible yet because of missing atomic data. But the real problem with the turbulence model still remains since it is not supported by any physical model.

Last but not least without going into great detail, different pulsation models have been suggested to match the observed helium abundances. Most likely, the major percentage of pulsating hot sdB stars can be explained by an opacity bump created by iron-group elements. This needs a sufficiently high radiative levitation in subphotospheric layers since mass loss weakens the opacity bump, therefore stopping pulsations. Hu et al. (2011) showed that the mass-loss rates required to explain the observed helium abundances with pulsations are not consistent with observed sdB star pulsations, though.

All in all, there has not been found any reasonable explanation for the high helium abundances as well as for the diversity of abundances of heavier elements in hot subluminous B stars yet.

5.4. Formation and Evolution of Hot Subdwarf Stars

5.4.1. Close Binary Evolution

Since most of the sdB stars can be found in close binary systems, this implies a formation via binary-interactions. Around 50% of all binary sdBs are formed by a red giant (RG) progenitor star which loses its hydrogen envelope just before reaching the tip of the red giant branch (RGB) due to strong mass transfer onto the companion star (Podsiadlowski et al., 2008). However, in order to guarantee mass transfer in a binary system, the system has to be half-separated, i.e., one of the two stars has to fill its Roche lobe.

How an sdB binary is actually formed during Roche-lobe overflow (RLOF) strongly depends on the initial mass ratio $q = \frac{m_p}{m_s}$ of both stars, though. In the case of $q < 1.2 - 1.5$ (see the left panel of Fig. 5.4.1), i.e., the primary mass m_p hardly differs from that of the secondary m_s, two mass transfer phases take place. First, consider a binary system consisting of two main-sequence stars with an orbital period of $P \lesssim 1$ yr so that both stars can interact. Due to the correlation of mass and luminosity, the slightly more massive star will evolve faster, thus reaching the red giant phase earlier. If the red giant star fills its Roche lobe at a certain time before reaching the tip of the RGB and before the helium flash sets in, its expansion rate is not excessively high and the hydrogen mass transfer from the red giant's atmosphere is dynamically stable resulting in a stable RLOF, not least because the companion has not reached the RGB yet. Hence, the companion slowly accretes the matter. Since the accreted gas molecules have a certain angular momentum with respect to the secondary star and undergo the effects of the so-called Coriolis force within the new gravitational potential, either an accretion disk is formed or the gas is directly accreted onto the companion's surface. This depends on the size of the accretor. The successors of this evolution are on the one hand a helium white dwarf (WD) and on the other hand a more massive main-sequence star as a companion. Therefore, the mass ratio has shifted and now reads: $Q = \frac{1}{q} = \frac{m_s}{m_p} > 1.2 - 1.5$.

If the companion core runs out of hydrogen fuel, the star will become a red giant star, too. In consequence, after some time this red giant will also fill its Roche lobe and because of the strong disparity concerning the mass ratio, the WD cannot accrete all the transferred matter at once, hence starting to fill and ultimately overfill its own Roche lobe. This leads to the formation of a common envelope (CE) surrounding both orbiting stars (immersed binary system). This common envelope gets heavily deformed by the gravitationally and centrifugally acting forces. Also, due to friction with the envelope, both components lose orbital energy and angular momentum such that they begin to spiral towards each other. At some point, this spiral-in phase ends since enough orbital energy has been released to eject the common envelope. During the post-common-envelope phase, a much closer binary with an orbital period typically between 0.1 and 10 days is formed, consisting of the core of a giant star, i.e., the new hot subdwarf star with masses between 0.40 and 0.49 $\mathrm{M}_\odot$, and the secondary, a helium white dwarf (Podsiadlowski et al., 2008).

The mass transfer rate is sufficiently high such that the main-sequence companion star will not be able to accrete all the matter, resulting in an unstable RLOF after the more massive main-sequence star has evolved to the RGB, if larger initial mass ratios $q > 1.2 - 1.5$ of the

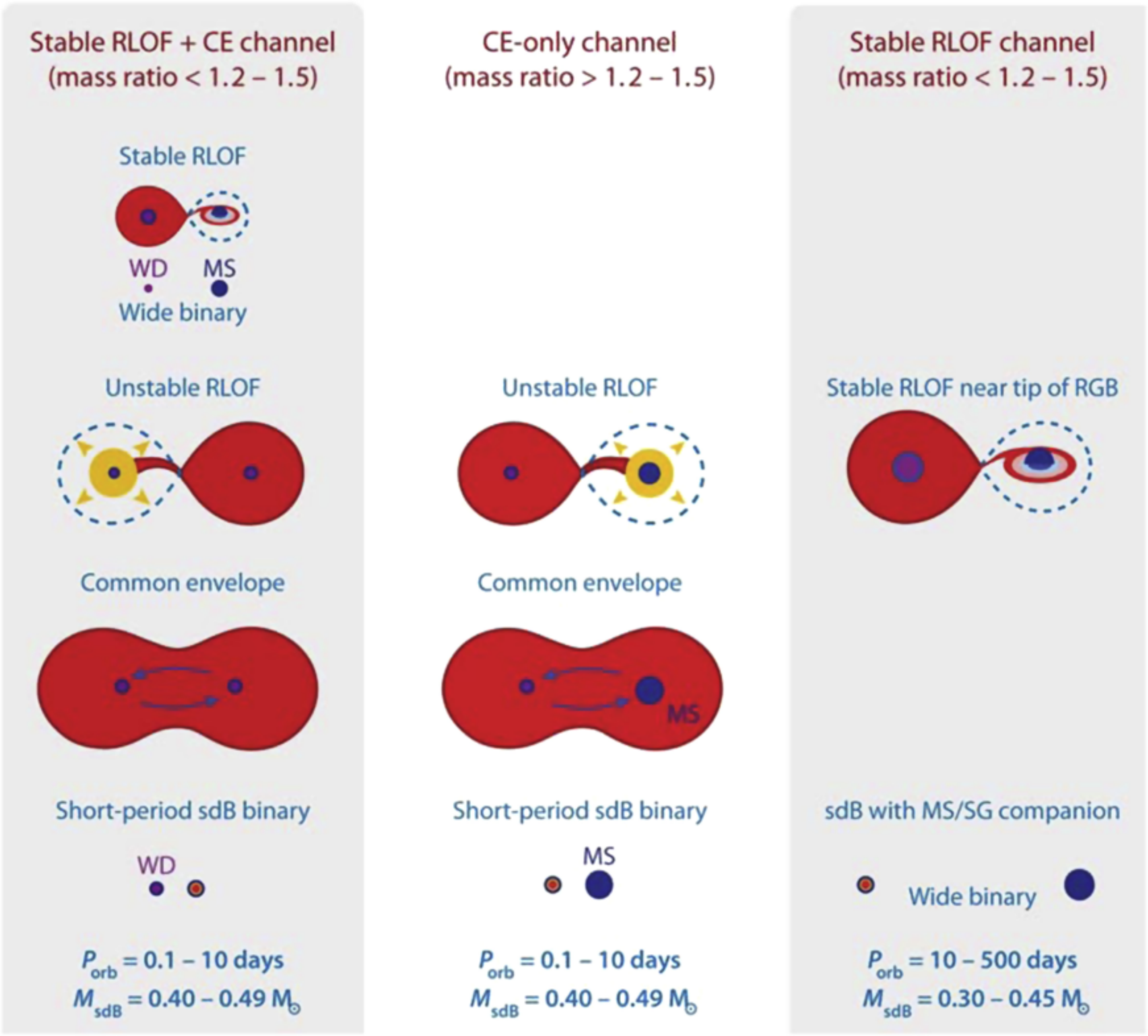

Figure 5.4.1.: Formation channels of sdB stars in close binaries showing the evolution of the system proceeding from top to bottom. *Left Panel*: Small initial mass ratios ($q < 1.2 - 1.5$) lead to two phases of mass transfer. First, mass is transferred via stable Roche-lobe overflow (RLOF), but then followed by an unstable one leading to the ejection of the common envelope (CE). The resulting binary consisting of an sdB star and a white dwarf (WD) has a short-period orbit of around 0.1 and 10 days and the sdB has masses between 0.40 and 0.49 $\mathrm{M}_\odot$. *Middle Panel*: Larger initial mass ratios ($q > 1.2 - 1.5$) directly lead to an unstable RLOF such that the common envelope is ejected. Here, a short-period binary is formed including an sdB star with around the same mass as produced in the $q < 1.2 - 1.5$ channel, and mostly a main-sequence star (MS), i.e., a non-degenerate star. *Left Panel*: In the case of low initial mass ratios ($q < 1.2 - 1.5$), the sdB star may form in the first stable RLOF, then resulting in a wide, long-period sdB binary with a non-degenerate companion (main-sequence or subgiant star). Extracted from Heber (2016); original version Podsiadlowski et al. (2008).

original $P \lesssim 1\,\mathrm{yr}$ binary prevail, though (see the middle panel of Fig. 5.4.1). Consequently, the formed accretion disk further expands beyond the edge of the companion potential well forming a common envelope around both stars (immersed binary system). After the envelope ejection at the end of the spiral-in phase, i.e., during the post-common-envelope phase, a close binary with an orbital period as resulting from the $q < 1.2 - 1.5$ channel is formed including an $0.40 - 0.49\,\mathrm{M}_{\odot}$ sdB star and mostly a main-sequence star (MS) companion, i.e., a non-degenerate star (Podsiadlowski et al., 2008).

In the best-fit model of Han et al. (2003) the birthrate of binary systems consisting of a subdwarf B star and a main-sequence star is $\sim 0.7 \cdot 10^{-2}$ /yr, whereas it is $\sim 0.4 \cdot 10^{-2}$ /yr for sdB stars with white-dwarf companions (Podsiadlowski et al., 2008).

However, if the sdB progenitor star fills its Roche lobe near the tip of the RGB and during the helium flash, a slow and stable Roche-lobe overflow may still occur in the case of low initial mass ratios $q < 1.2 - 1.5$ (see the right panel of Fig. 5.4.1). This is possible since for such low mass ratios the amount of hydrogen in the giant star's envelope has already decreased sufficiently during the RGB phase such that it can slowly be accreted onto the companion. In this channel, the red giant loses its entire envelope to become an $0.30 - 0.49\,\mathrm{M}_{\odot}$ sdB star in a long-period (in the range of $10 - 500$ days) binary with a main-sequence or subgiant component (Han et al., 2003). The period distribution found of such sdB+MS systems lies between values of 700 to 1300 days, though. This is why new binary population synthesis calculations based on Han's models have been reinvestigated recently by Chen et al. (2013), including atmospheric RLOF and a more challenging treatment of the angular momentum losses during the formation of these systems. The new models predict periods up to 1200 days and mostly agree with observed values.

5.4.2. Helium White Dwarf Mergers

The formation and evolution of subdwarf B stars via the common envelope and Roche-lobe overflow channels mentioned above do not explain the occurrence of single isolated sdB stars. However, the merger of two helium white dwarfs producing a single sdB star has already been suggested in 1984 (Webbink, 1984).

In this scenario it is assumed that both stars closely orbit each other with periods of less than $\sim$8 hours before losing energy and angular momentum through gravitational wave emission such that the orbit decreases. At a certain time when the gravitationally and centrifugally acting forces get strong enough to fill the Roche-lobe of one of the components, a half-separated system is formed and stable RLOF sets in. Since the mass-radius relation for white dwarfs reads $R \propto M^{-\frac{1}{3}}$, the less massive WD firstly fills its Roche-lobe transferring mass onto the more massive one. The more mass has been transferred, the larger the radius of the less massive WD gets, therefore strongly intensifying the merging scenario. Fig. 5.4.2 shows the three possible WD merging scenarios (Zhang & Jeffery, 2012).

In the slow merger model (see the left panel of Fig. 5.4.2) the entire mass of the less massive WD is transferred forming a cold disk around the more massive one in a few minutes. During the next several million years, the material remains cold and can be accreted slowly onto the primary surface.

In the fast merger model (see the middle panel of Fig. 5.4.2) no accretion disk forms, though. But the entire mass of the less massive WD directly falls onto the primary's surface forming a hot corona within a few minutes since the material is strongly heated to temperatures of $\sim 10^8$ K and therefore expands.

The right panel of Fig. 5.4.2 displays the so-called composite merger model. This model combines both, slow and fast merging, in which one part of the disrupted companion (30%−50% of its mass) forms a hot corona, whereas the remaining mass fraction forms a cold accretion disk.

In all three models the more massive white dwarf ignites helium at a certain critical mass and will become a single sdB star. The theoretical birthrate of sdB stars in the WD merger scenario lies around $0.8 - 1.6 \cdot 10^{-2}$ /yr and is comparable to that resulting from the common envelope channels. However, the predicted mass distribution of the resulting sdB stars for the merger channel is quite broad with a range from $0.40 - 0.65\,\mathrm{M}_\odot$ and is at odds with the narrow mass distribution of sdB stars determined from asteroseismic analysis (Podsiadlowski et al., 2008).

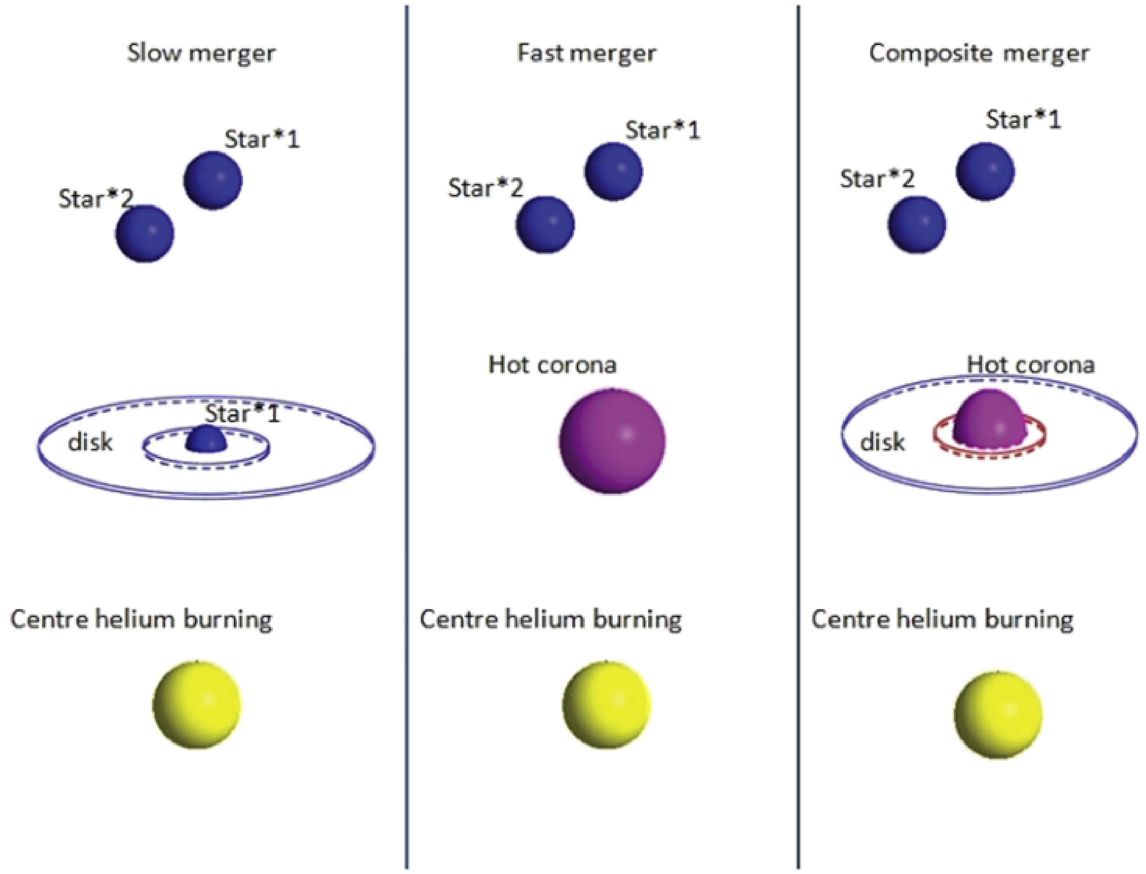

Figure 5.4.2.: Schematic of three possible ways for the merger of two helium white dwarfs. Extracted from Heber (2016); original version Zhang & Jeffery (2012).

5.4.3. Other Formation Scenarios

Besides the already discussed scenarios in which a hot subdwarf B star can be formed, other processes are also conceivable. For instance, Politano et al. (2008) suggest a merger of a low mass star or a brown dwarf with a red-giant core. Here, theoretical predictions for the resulting sdB masses give values of $0.47 - 0.54\,\mathrm{M}_{\odot}$. Clausen & Wade (2011) assume that the merger of a helium white dwarf with a low-mass, hydrogen-burning star could in principle create a star with a helium core and a thick hydrogen envelope which might evolve into an sdB star in a few billion years. Furthermore, models exist in which an sdB star is created by a single progenitor only. But for this purpose the star has to lose a high mass fraction during its evolution on the red giant branch. Potentially, this could either be realized by strong rotation effects or by strong star winds created at the time of the helium flash (Podsiadlowski et al., 2008).

6. The ^{3}He Anomaly in B-Type Stars

Besides the already presented abundance anomalies in section 5.2, the ^{3}He isotopic line shift for subdwarf B stars was first reported by Heber (1987). However, this isotopic shift had also been observed before among blue horizontal branch (BHB) stars (Hartoog, 1979) and chemically peculiar B-type main-sequence stars (Sargent & Jugaku, 1961; Hartoog & Cowley, 1979; Heber, 2016).

The identification of ^{3}He is made by accurately measuring the small isotopic shifts of the He I lines in the visible from high resolution spectra. The isotopic shifts with respect to the ^{4}He isotope vary from line to line. This is illustrated by table 6.1 in which the expected isotopic shifts for pure ^{3}He derived by Fred et al. (1951) are shown. Whereas some lines like ^{3}He I, 5875 Å are shifted only slightly (0.04 Å) towards redder wavelengths, the shifts of ^{3}He I, 4922 Å and ^{3}He I, 6678 Å are sufficiently large (0.33 Å and 0.50 Å, respectively) to be measurable. The very small isotopic shift of ^{3}He I, 5875 Å makes it useful as a check for other effects (amongst others, pressure shifts due to the so-called Stark effect, occurring in electric fields or shifts due to the presence of magnetic fields) which might shift the He I positions relative to lines of other elements. For some stars, especially in the case of Hg-Mn stars, ^{3}He I, 5015 Å and ^{3}He I, 4922 Å are often in complex regions and so badly blended that they cannot be measured. Besides the large expected isotopic shift, ^{3}He I, 6678 Å has two other advantages for measurement. On the one hand, the line is a singlet and therefore the line profile is expected to be symmetric. On the other hand, it typically falls in a relatively uncrowded region of the spectrum, thus not blended by other lines. It tends to be very weak in many helium-deficient stars, though. In order to measure the position of the ^{3}He I, 6678 Å line accurately, a high signal-to-noise ratio (SNR) is desirable. In general, the radial velocity of the star has also to be well determined before the wavelengths of the observed helium lines can be interpreted. Usually, helium lines should be avoided to determine the radial velocity when aiming at ^{3}He (Hartoog & Cowley, 1979; Heber, 2016).

The observed helium lines are blends of lines resulting from ^{3}He and ^{4}He isotopes. Consequently, the larger the observed line shifts, the higher the ^{3}He/^{4}He ratio (Heber, 2016).

6.1. ^{3}He B-Type Main-Sequence Stars

The prototype for the existence of ^{3}He in a B-type main-sequence star is 3 Centauri A. Sargent & Jugaku (1961) found the wavelengths of some of the He I lines (notably ^{3}He I, 6678 Å) to be a few tenths of an angstrom (up to 0.39 Å) greater than would be expected from other lines of He I and lines of other elements. There was a good correlation between

Line [Å]	$\Delta\lambda$ [Å]
3819	+0.08
3867	+0.08
4026	+0.08
4121	+0.07
4388	+0.28
4472	+0.07
4713	+0.07
4922	+0.33
5015	+0.21
5875	+0.04
6678	+0.50

Table 6.1.: Expected isotopic shifts $\Delta\lambda$ for pure $^{3}\mathrm{He}$. Positive values for $\Delta\lambda$ indicate red shifted He I lines due to the occurrence of $^{3}\mathrm{He}$ referred to Fred et al. (1951).

the observed shifts and the isotopic shifts for pure $^{3}\mathrm{He}$ determined by Fred et al. (1951) since amongst others, line broadening due to the Stark effect could be excluded by comparing the displacements in 3 Centauri A with those measured in other B-type main-sequence stars. Using the simple approximation that the observed displacements are linear proportional to the fractional $^{3}\mathrm{He}$ abundances expressed by the ratio $^{3}\mathrm{He}/(^{3}\mathrm{He}+^{4}\mathrm{He})$, Sargent & Jugaku (1961) derived $^{3}\mathrm{He}/(^{3}\mathrm{He}+^{4}\mathrm{He})=0.84 \pm 0.10$. Therefore, they concluded that the $^{3}\mathrm{He}/^{4}\mathrm{He}$ ratio has to lie between 3:1 and 16:1 which is abnormally large compared to the solar photospheric $^{3}\mathrm{He}/^{4}\mathrm{He}$ ratio estimated to be around 10^{-4} (Michaud et al., 2015; Sargent & Jugaku, 1961). In the following years, a spectroscopic search for B-type main-sequence stars with enhanced $^{3}\mathrm{He}$ abundances resulted in the discovery of several new definite or probable $^{3}\mathrm{He}$ stars (see table 6.2). The found $^{3}\mathrm{He}$ stars have total helium abundances being 5 to 20 times lower than normal B-type main-sequence stars, but exhibit $^{3}\mathrm{He}/^{4}\mathrm{He}$ values ranging from 0.35 to 2.7. These values were estimated by computing a large number of λ6678 profiles for various $^{3}\mathrm{He}$ and $^{4}\mathrm{He}$ abundances using very simple assumptions. For instance, the continuum was assumed to be formed in pure absorption, but both, coherent isotropic scattering and pure absorption, were included in the line opacity. Also, the level populations in $^{3}\mathrm{He}$ and $^{4}\mathrm{He}$ were assumed to be the same and both, radiative transfer and statistical equilibrium equations, were not solved simultaneously (more on radiative transfer and statistical equilibrium in chapter 3). However, considering the approximate nature of the calculations, the agreement with the observed spectra was relatively good (Hartoog & Cowley, 1979).

Remarkably, it was found that the $^{3}\mathrm{He}$ stars occupy a narrow strip in the T_{eff}-$\log(g)$ plane between the He-rich B stars (with effective temperatures up to ~32 000 K) and a group of He-weak B stars which show no evidence for $^{3}\mathrm{He}$ (with effective temperatures down to ~13 000 K). The $^{3}\mathrm{He}$ B-type stars lie between effective temperatures of ~18 000 K and ~21 000 K (see also table 6.3). The fractional $^{3}\mathrm{He}$ content tends to increase with increasing effective temperature among the $^{3}\mathrm{He}$ stars, too (Hartoog & Cowley, 1979).

Object	$n(^3\mathrm{He})/[\mathrm{n}(^3\mathrm{He})+n(^4\mathrm{He})]$	$n(^3\mathrm{He})/n(^4\mathrm{He})$	Comments
3 Cen A	0.71	2.5	Definite ^{3}He star
α Scl	0.44	0.79	Definite ^{3}He star
ι Ori B	0.73	2.7	Definite ^{3}He star
HR 1951	0.48	0.92	Definite ^{3}He star
HR 2306	0.71	2.5	Definite ^{3}He star
HR 7129	0.61	1.6	Definite ^{3}He star
HR 7467	0.56	1.3	Definite ^{3}He star
HD 191980	0.66	1.9	Definite ^{3}He star
33 Gem	0.34	0.52	Probable ^{3}He star
40 Gem	0.32	0.47	Probable ^{3}He star
HR 5998	0.44	0.79	Probable ^{3}He star
κ Cnc	$\leq$ 0.26	$\leq$ 0.35	Possible ^{3}He star

Table 6.2.: Definite and probable B-type main-sequence stars which have been reported to (possibly) show ^{3}He. The fractional ^{3}He contents and the $n(^3\mathrm{He})/n(^4\mathrm{He})$ ratios are extracted from Hartoog & Cowley (1979). The HgMn star κ Cnc has later been confirmed as a definite ^{3}He star by Dobrichev et al. (1989) and Zakharova & Ryabchikova (1996) concluding on a value of the $n(^3\mathrm{He})/n(^4\mathrm{He})$ ratio of 0.35.

Object	T_{eff} [K]	$\log(g)$ [dex]	$\log(y)$ [dex]	Reference
3 Cen A	17500	3.80	-1.70	(Pintado et al., 1998)
α Scl	17379	3.60	-	(Schmitt, 1972)
ι Ori B	18000-19000	4.0	-	(Conti & Loonen, 1970)
HR 1951	-	-	-	-
HR 2306	-	-	-	-
HR 7129	-	-	-	-
HR 7467	-	-	-	-
HD 191980	-	-	-	-
33 Gem	14375	3.90	-1.96	(Pintado et al., 1998)
40 Gem	-	-	-	-
HR 5998	-	-	-	-
κ Cnc	13125	3.59	-2.26	(Pintado et al., 1998)

Table 6.3.: Atmospheric parameters of the definite and probable B-type main-sequence stars which have been reported to (possibly) show ^{3}He. The values are extracted from the given references. However, for most of the listed stars no parameters could be found in literature.

These results then have been discussed in the context of the diffusion theory for He-weak and He-rich B-type stars, greatly strengthening the link between both. Michaud (1970) showed that the radiation pressure was not sufficient to support helium, thus tending to sink out of the atmosphere in B-type stars with stable atmospheres. This would explain the He-weak B-type main-sequence stars as well as the general helium deficiency of the peculiar $^3\mathrm{He}$ B-type stars. Later, it was suggested by Osmer & Peterson (1974) that at higher effective temperatures radiation pressure could indeed facilitate helium (presumably $^4\mathrm{He}$) to stream upwards, therefore explaining He-rich stars. They also came up with the idea that at slightly lower effective temperatures $^3\mathrm{He}$ but not $^4\mathrm{He}$ would be radiatively driven resulting in a $^4\mathrm{He}$-deficient, $^3\mathrm{He}$-rich star. At still lower temperatures, neither $^3\mathrm{He}$ nor $^4\mathrm{He}$ could be supported producing a star in which both helium isotopes are depleted (Hartoog & Cowley, 1979).

However, in order to explain the observed $^3\mathrm{He}/^4\mathrm{He}$ values and the total helium abundances for $^3\mathrm{He}$ B-type main-sequence stars, it is necessary to bring $^3\mathrm{He}$ to the surface and deplete $^4\mathrm{He}$ from the surface layers at the same time. If the primordial $^3\mathrm{He}/^4\mathrm{He}$ ratio is close to the solar value of 10^{-4}, allowing $^4\mathrm{He}$ but not $^3\mathrm{He}$ to settle gravitationally, would not leave detectable amounts of $^3\mathrm{He}$ on the star surface (Hartoog & Cowley, 1979). Vauclair et al. (1974) carried out computations of the radiative force on both helium isotopes, amongst others showing that $g_{\mathsf{rad}}(^3\mathrm{He}) \sim g_{\mathsf{rad}}(^4\mathrm{He})$ for an arbitrary number of $^3\mathrm{He}$ absorbers because of the strong similarity of both isotopes concerning atomic structure and line spectrum. They also showed that the radiative force on both helium isotopes is never larger than the gravitational one, except at low helium abundances as in 3 Cen A. But even in the latter case, the replacement of $^4\mathrm{He}$ by $^3\mathrm{He}$ was found to be much slower ($\sim 10^8$ yr) than the gravitational settling of helium (Michaud et al., 1979). This certainly disproved the suggestion made by Osmer & Peterson (1974).

According to Vauclair (1975), producing He-rich main-sequence stars should also be possible if diffusion takes place in a radial mass-loss flux (stellar wind). This was the first time the idea came up that such a stellar mass outflow could maybe also explain the observed $^3\mathrm{He}$ B-type stars. In this case the relationship between effective temperature and observed $^3\mathrm{He}/^4\mathrm{He}$ ratios might arise because of a possible correlation of mass-loss flux with effective temperature (Hartoog & Cowley, 1979). This so-called diffusion mass-loss model is still used today in order to differentiate between He-rich, $^3\mathrm{He}$ and He-weak stars on the main sequence and will be discussed in detail in section 7.1.

6.2. $^3\mathrm{He}$ Blue Horizontal Branch Stars

Since blue horizontal branch (BHB) stars in globular clusters and in the halo were found to be He-weak like the peculiar B-type stars with abnormally large $^3\mathrm{He}/^4\mathrm{He}$ ratios, Hartoog (1979) decided to investigate BHB stars for the presence of $^3\mathrm{He}$ as well. Because of its spectroscopic similarity to the $^3\mathrm{He}$ B-type prototype star 3 Centauri A and given the fact that it is one of the brightest of the faint blue stars in the halo, Feige 86 was chosen for the analysis at first (Hartoog, 1979).

Different observing techniques than for any of the peculiar B stars surveyed before had to

Object	$\frac{n(^3\mathrm{He})}{n(^4\mathrm{He})}$	T_eff [K]	$\log(g)$ [dex]	$\log(y)$ [dex]	Reference	Comments
Feige 86	0.7	16400	4.20	-1.82	(Bonifacio et al., 1995)	^{3}He star
PHL 382	>1	18200	4.1	-2.2	(Heber & Langhans, 1986)	^{3}He star
PHL 25	>1	19500	5.0	-2.0	(Heber & Langhans, 1986)	^{3}He star

Table 6.4.: The definite blue horizontal branch stars which have been reported to show ^{3}He. The $n(^3\mathrm{He})/n(^4\mathrm{He})$ ratios are extracted from Hartoog (1979) for Feige 86, and from Heber (1987) for PHL 382 and PHL 25. The atmospheric parameters are extracted from the given references.

be used for this significantly fainter BHB star. In consequence, during his analysis, Hartoog (1979) concentrated on λ 6678 only because of the largest isotopic shift. The spectrum of Feige 86 clearly showed a considerable shift of the λ 6678 position towards the ^{3}He position. Using the same approximated analysis procedure as presented in section 6.1 for the ^{3}He B-type main-sequence stars, a value of 0.7 for the $^3\mathrm{He}/^4\mathrm{He}$ ratio could be derived. Via photometry it was determined that Feige 86 lies in the same narrow strip of the T_eff-$\log(g)$ plane as the peculiar ^{3}He B-type main-sequence stars, although maybe at a slightly higher surface gravity. This greatly strengthened the link between the He-weak blue horizontal branch stars and the ^{3}He main-sequence stars suggesting that similar radiative diffusion processes could have acted in both classes, on the one hand being responsible for the helium deficiency, but on the other hand resulting in a ^{3}He overabundance, too (Hartoog, 1979).
Later, ^{3}He was also found in two other BHB stars (PHL 382 and PHL 25) by Heber (1987). Using the Cassegrain Echelle Spectrograph (CASPEC, see section 2.3), optical spectra were obtained in the wavelength range from 5800 Å to 6750 Å. Therefore, the spectra allowed relatively precise wavelengths of He I, 5875 Å and He I, 6678 Å to be measured. Heber (1987) concluded that for PHL 382 as well as for PHL 25, the position of He I, 6678 Å is shifted towards the expected position of ^{3}He, clearly indicating $^3\mathrm{He}/^4\mathrm{He} > 1$ (Heber, 1987).
Table 6.4 summarizes the results of the $^3\mathrm{He}/^4\mathrm{He}$ ratios for the definite ^{3}He blue horizontal branch stars that have been found yet.
Because of their slightly higher gravities compared to the peculiar B-type main-sequence stars, new models for the diffusion process of ^{3}He in BHB stars had to be developed. Nevertheless, the ^{3}He anomaly in BHB stars has not been fully understood until today, although the theories presented in section 7 perhaps would also match the time scale for atomic diffusion to take place and the lifetime of typical BHB stars, reading typically $\tau_\mathrm{BHB} \sim \tau_\mathrm{MS}$ (4-5 $M_\odot$).

6.3. ^{3}He Subdwarf B Stars from Literature

The first detected hot subluminous B star containing ^{3}He in its stellar atmosphere was SB 290, for which Heber (1987) detected strong line shifts indicating that basically the whole helium content of the atmosphere consists of ^{3}He, giving $^3\mathrm{He}/^4\mathrm{He} > 1$. Edelmann et al. (2001) and

Heber & Edelmann (2004) found another three $^3\mathrm{He}$ enriched sdB stars (Feige 36, BD+48° 2721 and PG 0133+114). BD+48° 2721 and PG 0133+114 showed line shifts of He I, 4922 Å and He I, 6678 Å, whereas He I, 4471 Å and He I, 4713 Å were unshifted. Hence, taking into account the smaller isotopic line shift of the latter two lines, this behaviour of the helium lines was consistent with the isotopic line shifts for $^3\mathrm{He}$ measured by Fred et al. (1951). In the case of Feige 36, line shifts of the He I lines 4471 Å and 6678 Å were observed, too. While the shift of He I 4713 Å could not be detected again because of its small isotopic line shift, He I 5015 Å did not show the displacement expected from experiment. It was assumed that the line profile of He I lines 5015 Å was blended, though (Edelmann et al., 2001). Up to this point, the $^3\mathrm{He}$ anomaly in sdB stars was found to be rare, i.e., it occurred in less than 5% of the program stars (Edelmann et al., 1999).

Geier et al. (2013a) determined the helium abundances and isotopic shifts caused by enrichment of $^3\mathrm{He}$ of 44 sdB stars from high-resolution spectra. 39 bright subdwarf B stars were observed with the FEROS spectrograph ($R = 48,000$, $3750 - 9200$ Å) and five stars were observed with the FOCES spectrograph ($R = 30,000$, $3800 - 7000$ Å). Although high-resolution Echelle spectrographs are widely used in astronomy, data reduction and analysis of Echelle spectra can be difficult (extraction errors, insufficient order merging or normalization, etc.). Especially for sdB stars, Echelle spectroscopy can be rather challenging because of their low brightness and the fact that most of the important lines for their analysis are found in the bluest parts of optical spectra where Echelle spectrographs are often not very sensitive. Therefore in order to have a well suited comparison to the high-resolution Echelle spectra, Geier et al. (2013a) obtained spectra of at least some of the program stars with medium resolution as well. Twelve sdB stars were observed with the ISIS spectrograph ($R \sim 4000$, $3440 - 5270$ Å), nine stars with the grating spectrograph and intensified Rection Photon Counting System of the SAAO ($R \sim 1300$, $3300 - 5600$ Å) and five with the CAFOS spectrograph ($R \sim 1000$, $3500 - 5800$ Å).

In order to derive atmospheric parameters and helium abundances of the whole sample, model spectra were used to fit the hydrogen Balmer and helium lines of the high-resolution spectra. For this determination the SPAS routine developed by H. Hirsch was applied (see section 8.1 for further information on SPAS). The cooler sdBs (24 000 K $< T_{\text{eff}} <$ 30 000 K) have been analyzed using local thermodynamic equilibrium (LTE) models with solar metallicity, hotter sdBs with $T_{\text{eff}} >$ 30 000 K using LTE models with supersolar metallicity (10 times solar). For both cases, only hydrogen and helium and no metals have been synthesized (Geier et al., 2013a).

All in all, Geier et al. (2013a) found 8 $^3\mathrm{He}$ enriched subdwarf B stars analyzing the high-resolution spectra (see Fig. 6.3.1). One of them was BD+48° 2721, which has already been discovered before by Edelmann et al. (2001). Table 6.5 lists the derived atmospheric parameters together with the used instrument, the number of available (co-added) spectra and their signal-to-noise (S/N) ratio for all found $^3\mathrm{He}$ enriched subdwarf B stars. The final parameters were obtained either from high S/N ISIS and CAFOS spectra, if available, or from high-resolution FEROS and FOCES spectra.

Fig. 6.3.2 shows the distribution of the entire sample under study by Geier et al. (2013a) in the $T_{\text{eff}} - \log{(g)}$-diagram, including the found $^3\mathrm{He}$ enriched sdB stars and the three sdBs with isotopic shifts already discussed before. Remarkably, the $^3\mathrm{He}$ sdBs cluster in a small temper-

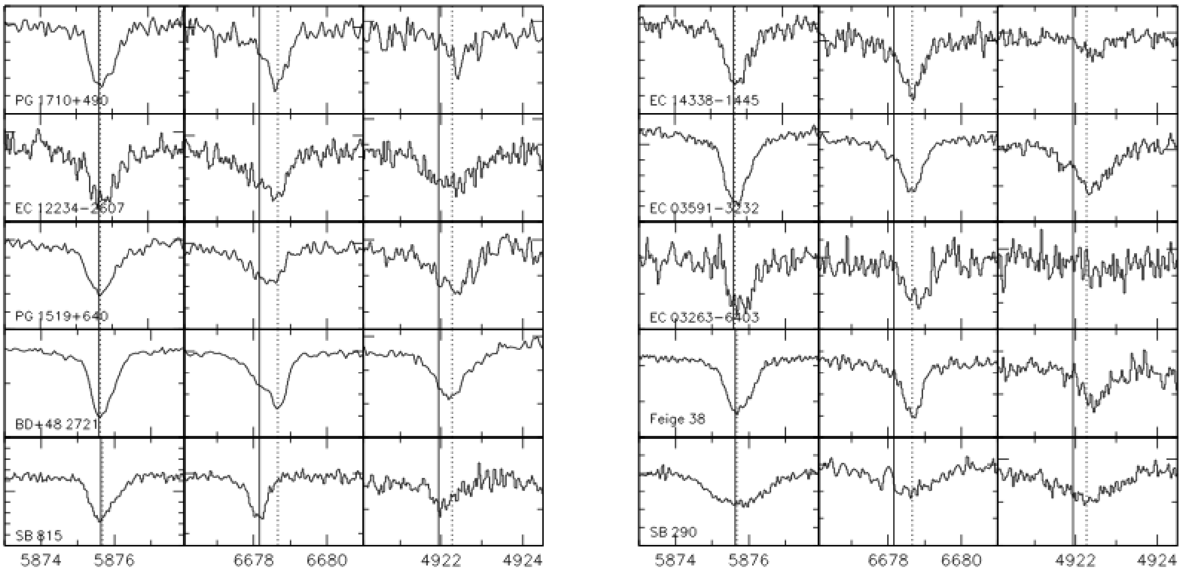

Figure 6.3.1.: Some helium lines of sdB stars. *Left panel*: Subdwarf B stars highly enriched in $^{3}\mathrm{He}$, but also showing a component of $^{4}\mathrm{He}$. For comparison, the helium lines of SB 815 (CD-35° 15910), a star which does not exhibit line shifts due to enrichment of $^{3}\mathrm{He}$, are shown in the lowest panel. *Right Panel*: Subdwarf B stars whose helium lines are entirely shifted to the $^{3}\mathrm{He}$ rest wavelength and where no traces of $^{4}\mathrm{He}$ are visible at all. Here for comparison, the helium lines of SB 290, which is the prototype of sdBs highly enriched in $^{3}\mathrm{He}$, are plotted in the lowest panel. Note that the lines of SB 290 are significantly broadened due to stellar rotation. While the rest wavelengths of $^{4}\mathrm{He}$ are plotted as solid vertical lines in both panels, dotted vertical lines mark the rest wavelengths of the $^{3}\mathrm{He}$ isotope. Adopted from Geier et al. (2013a).

Object	Instrument	no. spec	S/N	T_{eff} [K]	$\log(g)$ [dex]	$\log(y)$ [dex]	Comments
BD+48 2721	FOCES	1	84	24800	5.38	-2.23	$^{3}\mathrm{He}$ star
EC 14338-1445	FEROS	3	37	27700	5.54	-2.82	$^{3}\mathrm{He}$ star
EC 03591-3232	FEROS	2	73	28000	5.55	-2.03	$^{3}\mathrm{He}$ star
EC 12234-2607	FEROS	3	26	28000	5.58	-1.58	$^{3}\mathrm{He}$ star
EC 03263-6403	FEROS	1	17	29300	5.48	-2.51	$^{3}\mathrm{He}$ star
PG 1519+640	ISIS	1	39	30300	5.67	-2.37	$^{3}\mathrm{He}$ star
PG 1710+490	ISIS	1	27	30600	5.66	-2.43	$^{3}\mathrm{He}$ star
Feige 38	ISIS	5	89	30600	5.83	-2.37	$^{3}\mathrm{He}$ star

Table 6.5.: Sample of $^{3}\mathrm{He}$ sdB stars found by Geier et al. (2013a). Listed are the name of the sdB star, the used instrument, the number of available spectra, the signal-to-noise ratio (S/N) together with the derived atmospheric parameters extracted from Geier et al. (2013a).

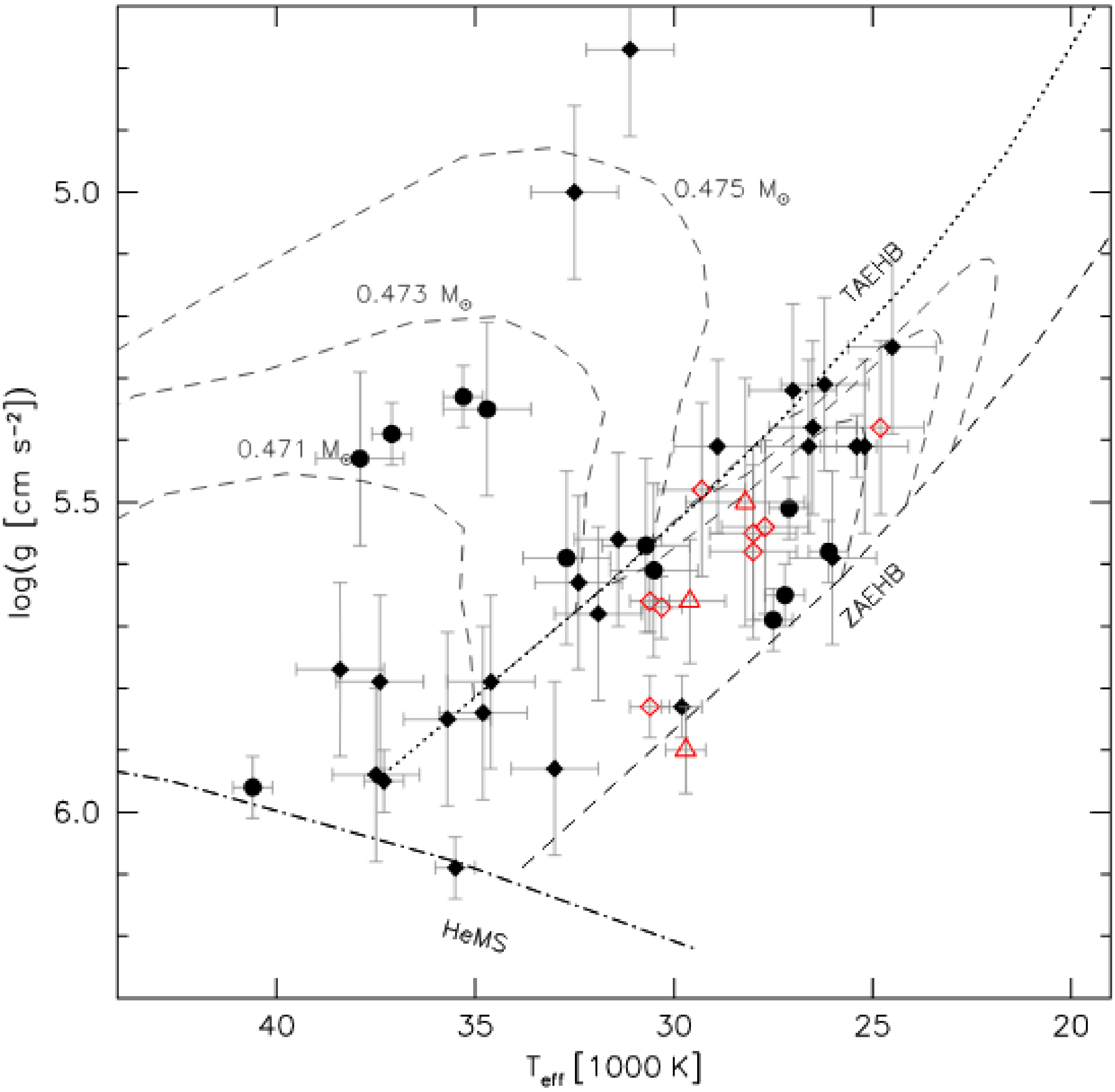

Figure 6.3.2.: $T_{\text{eff}} - \log{(g)}$-diagram for the sample of Geier et al. (2013a). Open symbols mark $^3\mathrm{He}$ enriched sdB stars, filled symbols sdB stars whose atmosphere is dominated by $^4\mathrm{He}$. The triangles mark the three sdBs with enriched $^3\mathrm{He}$ that have already been discussed before (Feige 36, BD+48° 2721 and PG 0133+114). Whereas diamonds highlight objects belonging to the bulk of sdBs (upper helium sequence), circles mark stars belonging to the second group (lower helium sequence). For a definition of both helium sequences see section 5.1. Together with EHB evolutionary tracks for solar metallicity taken from Dorman et al. (1993) labeled with their masses, the helium main sequence (HeMS), the zero-age extreme horizontal branch (ZAEHB) and the terminal-age extreme horizontal branch (TAEHB) are plotted. Adopted from Geier et al. (2013a).

ature strip between $\sim$27 000 K and $\sim$31 000 K very similar to the known ^{3}He main-sequence B-type stars, which also cluster in a narrow range, although at different temperatures (see section 6.1). BD+48° 2721 is the only outlier with $T_\mathrm{eff} = 24\,800$ K. Also, all ^{3}He enriched subdwarf B stars belong to the upper helium sequence. However, this has to be further proved, because maybe the diagnostic helium lines are too weak to measure the isotopic shifts in the case of helium-poor sdBs belonging to the lower helium sequence. But the similarity to the ^{3}He B-type main-sequence stars becomes even more evident when looking at the upper helium sequence only. Here, the helium abundance is scattering around $\log(y) \sim$-2.5 dex for effective temperatures below 31 000 K (see Fig. 5.1.4), but ^{3}He is enriched at around this very temperature. For higher temperatures ($T_\mathrm{eff} > 31\,000$ K) the helium abundance rises. This would argue for a division of the upper helium sequence into "normal" helium sdBs, ^{3}He sdBs and helium-rich ones (Geier et al., 2013a).
In particular, part of the ^{3}He sdB stars exhibit clear displacements of the He I, 6678 Å line, indicating that ^{3}He is the dominant isotope in the stellar atmosphere (see the right-hand panel of Fig. 6.3.1). The other part of the ^{3}He sdB stars shows strong lines of ^{3}He blended with weak components of ^{4}He (see the left-hand panel of Fig. 6.3.1). Since these stars cover the whole ^{3}He effective temperature strip (see for example the positions of BD+48° 2721, EC 12234-2607 and PG 1519+640 in Fig. 6.3.2), there is no correlation between the helium isotopic ratio and effective temperature (Geier et al., 2013a).
As for the ^{3}He enriched B-type main-sequence and BHB stars, the ^{3}He anomaly in hot subluminous B stars is most probably related to diffusion processes in the stellar atmosphere. A promising diffusion model that could possibly explain this anomaly in sdBs will be presented in section 7.2.

6.4. ^{3}He Subdwarf B Stars from the ESO SPY Project

The ESO Supernova Ia Progenitor Survey, short ESO SPY, obtained high-resolution optical spectra of over 1000 white dwarf candidates (Ströer et al., 2005), including 137 previously misclassified hot subdwarf stars (79 hydrogen rich sdBs, 58 sdOs). All observations were obtained at the ESO Very Large Telescope equipped with the UVES spectrograph ($R \sim 90,000$, $3300 - 6650$ Å with gaps at $4500 - 4600$ Å and $5600 - 5700$ Å, see also section 2.3). Hence, the analyzed UVES spectra do not include the helium line with the strongest isotopic shift, He I, 6678 Å. In consequence, concerning the determination of ^{3}He and ^{4}He as well as of the isotopic abundance ratio, the tip of the iceberg cannot be reached for the stars from the ESO SPY project. Nevertheless, several other helium lines are covered, also including He I, 4922 Å, i.e., the line with the second strongest line shift.
Therefore, a sample of 76 additional sdBs in total from the hot subdwarf list of the ESO Supernova Ia Progenitor Survey (Lisker et al., 2005) is investigated within this thesis, too, whereby only stars lying in the ^{3}He sdB effective temperature regime between $\sim$27 000 K and $\sim$31 000 K are spectroscopically analyzed. Four of these candidates can actually be identified as ^{3}He enriched hot subdwarf B stars by means of their derived isotopic abundance ratios (see table 6.6). Their atmospheric parameters and metal abundances are determined in chapter 12

Object	Instrument	Comments
HE 0929-0424	UVES	^{3}He star
HE 1047-0436	UVES	^{3}He star
HE 2156-3927	UVES	^{3}He star
HE 2322-0617	UVES	^{3}He star

Table 6.6.: The four additional ^{3}He sdBs taken from the hot subdwarf list of the ESO Supernova Ia Progenitor Survey (Lisker et al., 2005).

and are listed in tables 12.1, 12.5, and 12.6, respectively.

7. $^3\mathrm{He}$ Diffusion Models for B-Type Stars

7.1. Diffusion Mass-Loss Model for Main-Sequence Stars

In order to explain the occurrence of helium-weak (14 000 K $\lesssim T_{\mathrm{eff}} \lesssim$ 21 000 K), $^3\mathrm{He}$ (18 000 K $\lesssim T_{\mathrm{eff}} \lesssim$ 21 000 K) and helium-rich B-type main-sequence stars (20 000 K $\lesssim T_{\mathrm{eff}} \lesssim$ 25 000 K, but also up to $\sim$ 32 000 K), modeling of their envelopes in the framework of atomic diffusion started already at the beginning of the 1970s. While the helium deficiency in the upper atmospheric layers for B-type main-sequence stars could be easily understood within the model with atomic diffusion (gravitational settling due to the weakness of the radiative acceleration of helium), no reasonable explanation for the existence of $^3\mathrm{He}$ in helium-weak stars, as well as helium overabundances in hotter B stars was found. The smaller atomic mass of the $^3\mathrm{He}$ isotope compared to $^4\mathrm{He}$ results in a slower gravitational settling for $^3\mathrm{He}$, slowly increasing the $^3\mathrm{He}/^4\mathrm{He}$ ratio with time. Vauclair et al. (1974) showed that the time needed to obtain the observed overabundances in $^3\mathrm{He}$ is too long (compared to the stellar lifetime) to explain $^3\mathrm{He}$ B-type main-sequence stars, though. However, as already mentioned at the end of section 6.1, Vauclair (1975) presented a more sophisticated unified model, even giving a satisfying framework for the explanation of the whole group of main-sequence stars with helium anomalies. In this so-called diffusion mass-loss model, the competition between atomic diffusion and stellar mass outflow plays an important role, since the corresponding velocities of both processes can have opposite signs for some elements. This shall be presented in the following by means of the textbook released by Michaud et al. (2015).

- **Helium-weak Stars**: Here, the mass loss is weak enough so that the gravitational settling of helium dominates. Consequently, both helium isotopes are depleted in outer atmospheric layers.
- **$^3\mathrm{He}$ Stars**: In this case, stronger mass loss, i.e., higher wind velocity, leads to the dominance of gravitational settling for $^4\mathrm{He}$, but not for $^3\mathrm{He}$. This is due to the smaller atomic mass and therefore slower settling velocity of $^3\mathrm{He}$. At a given interior radius, helium gets twice ionized (He III) and the collisional coupling through Coulomb forces gets strong enough so that $^3\mathrm{He}$ is dragged towards the exterior. Closer to the surface, helium recombines to He II and since then the settling velocity dominates for $^3\mathrm{He}$, helium cannot leave the star and $^3\mathrm{He}$ accumulates at the surface.
- **He-rich Stars**: For strong mass loss, the wind velocity dominates for both helium isotopes. Hence, all helium ($^3\mathrm{He}$ and $^4\mathrm{He}$) which gets twice ionized at a certain interior radius as in the case of $^3\mathrm{He}$ stars, recombines to He II and accumulates at the surface

since it cannot leave the star. Of course, this provides that the density of the wind is not too high at all. Otherwise, helium is expelled in the interstellar medium together with hydrogen.

All in all, if the wind velocity increases with effective temperature, this unified diffusion mass-loss model explains qualitatively well the whole sequence of helium-weak/^{3}He and helium-rich stars. Abbott (1982) and Babel (1996) showed that there is strong evidence for such a correlation. Stars with peculiar helium abundances therefore lie in an effective temperature regime where the mass-loss rate is mainly depending on the amount of transferred momentum from the radiation field to matter. But, the resulting wind velocities have to be compatible with atomic diffusion, i.e., the wind velocity should be small enough with respect to the diffusion velocity so that elemental separation can take place. This simple model is not generally acceptable as an explanation for helium-rich stars, though, because hydrogen and helium can get coupled and leave the stellar atmosphere, hence causing a problem in order to explain the observed helium overabundances. For instance, this could be the case if strong magnetic fields are present or if the field lines are vertical (Krtička, 2006) as is the case for e.g. σ Orionis E (Groote & Hunger, 1997). However, in order to explain the helium overabundances, Babel (1996) and Hunger et al. (1996) came up with the idea that hydrogen and helium fully decouple from the rest of the stellar wind at relevant effective temperatures of $T_{\text{eff}} \lesssim 20\,000$ K. At these temperatures the density of the wind decreases and the coupling via collisions between the metal ions absorbing the photons and hydrogen and helium becomes weak, resulting in helium and possibly hydrogen decoupling as well. Hence, the stellar wind just fractionates and becomes metallic. The result is a metal-poor, but helium-rich main-sequence star (Hunger & Groote, 1999). In order to suppress turbulent motions resulting from a photosphere, which has helium on top of hydrogen, and might transport matter of original composition to the surface, a strong magnetic field as detected in several helium-rich stars is needed (Przybilla et al., 2016).

7.2. LID - Light Induced Drift

In principle, the diffusion mass-loss model for B-type main-sequence stars presented in the previous section could possibly be applied for the hot subluminous B stars, too. In consequence, the effective temperature dependent sequence of "normal" helium sdBs, ^{3}He enriched sdBs and helium-rich ones (see section 6.3) would then also be related to the increasing stellar wind strength. However, the strength and influence of the wind velocity in subdwarf B stars is hard to model because of their higher effective temperatures. Because of this difficulty and the lack of experience coming along with it, different diffusion models have been investigated. One of them is the so-called light induced drift (LID) which has originally been suggested by Atutov (1986) to be even more efficient at causing abundance anomalies than radiation driven diffusion in B-type main-sequence stars. It is applicable for all B-type stars exhibiting sufficiently strong stellar winds and will be presented in the following, also making use of the textbook published by Michaud et al. (2015).

LID occurs when the radiative flux is asymmetric with respect to the absorption line center, i.e., the stronger this asymmetry the larger the influence of LID. In order to keep the explanation of LID simple, a purely Doppler broadened resonance line of a trace element (see chapter 3.3 for detailed information on spectral line formation) is considered. For the following, the atom is moving outwards with an increasing velocity because of the stellar wind. This results in a blue shifted absorption due to the Doppler effect, i.e., light (flux) from the blue side of the line center in the stellar reference frame is absorbed. If the flux is larger in the red half, this will lead to more excited atoms by absorption on the red side of the profile (when they move towards the star) than on the blue side (when they move away from the star). Since the collisional cross section for momentum exchange between atoms and the hydrogen-dominated main gas strongly depends on the radius of the electrons around the nucleus, the corresponding collision rate is larger for the excited state than for the ground state. For instance, the collision rate for the interaction of excited helium atoms with hydrogen turns out to be about nine times larger than that for the ground state of helium (LeBlanc & Michaud, 1993). In consequence, there will be a larger collision rate, i.e. a smaller mean free path, for atoms moving towards the star. Finally, this imbalance results in an additionally induced drift of the particular element away from the star.

The maximum effect of LID is expected for neutral helium. This is because all lines of the dominant isotope, $^4\mathrm{He}$, cause a frequency anisotropy on the same (blue) side of the lines of the less abundant isotope, $^3\mathrm{He}$ (see table 6.1). This makes LID not only a possible scenario for the understanding of diffusion processes having occurred in $^3\mathrm{He}$ B-type main-sequence stars, but also in $^3\mathrm{He}$ enriched hot subdwarf B stars. In any case, LID leads to an upwards drift of $^3\mathrm{He}$ immediately after the star has been formed as discussed shortly before. For a B-type main-sequence star such as 3 Cen A, starting with normal abundances of the two helium isotopes on the main sequence, this would reduce the time needed for $^3\mathrm{He}$ to replace $^4\mathrm{He}$ in the stellar atmosphere by a factor of $\sim$3-10, compared to the case if LID is neglected and only particle diffusion (gravitational settling) is responsible for the progressive decrease of both, $^3\mathrm{He}$ and $^4\mathrm{He}$, throughout the atmosphere (LeBlanc & Michaud, 1993). Hence, $^3\mathrm{He}$ enrichment can take place within the life time of the star when LID is taken into account. As the total helium abundance ($^3\mathrm{He}$ and $^4\mathrm{He}$) is reduced by LID acting on $^3\mathrm{He}$ and gravitational settling acting on $^4\mathrm{He}$, the relative effect of LID progressively decreases in the particular atmospheric layers, becoming even negligible once the total helium abundance has been reduced to around 10^{-5} of its original value (see bottom right panel of Fig. 7.2.1 and LeBlanc & Michaud (1993) for details). This has to do with the disappearance of the lines causing the flux anisotropy which is the driving force for LID.

LeBlanc & Michaud (1993) implemented LID in their atomic diffusion models showing that it accelerates the separation of $^3\mathrm{He}$ from $^4\mathrm{He}$ in the atmosphere of a main-sequence star with $T_{\mathrm{eff}} = 18\,000\,\mathrm{K}$ and $\log(g) = 4.0\,\mathrm{dex}$. Fig. 7.2.1 shows the comparison of the contributions of LID and radiation driven diffusion to the transport velocity of $^3\mathrm{He}$ due to the He I, 584 Å line as a function of the Rosseland optical depth[1] in the considered atmosphere for different total

---

[1] The Rosseland optical depth is a special characterization for the depth of a particular atmospheric layer. As the normal optical depth, it is unitless and often logarithmically scaled and increases with increasing atmospheric depth.

helium abundances. Focusing on a total helium abundance of $N(\mathrm{He})/N(\mathrm{H}) = 0.01$ (see the upper right panel of Fig. 7.2.1), the effect of LID dominates for 1% ^{3}He over $0 < \log \tau_R < 2.5$ LeBlanc & Michaud (1993). In consequence, at least one case where LID dominates the particle transport in one part of a B-type main-sequence star's stellar atmosphere can be found to explain the observed helium abundance anomalies. For different total helium abundances, the $\log \tau_R$ interval, where LID dominates radiative acceleration, slightly shifts to other atmospheric layers, even disappearing for total helium abundances lower than $N(\mathrm{He})/N(\mathrm{H}) = 10^{-6}$ as can be seen from the different panels of Fig. 7.2.1.

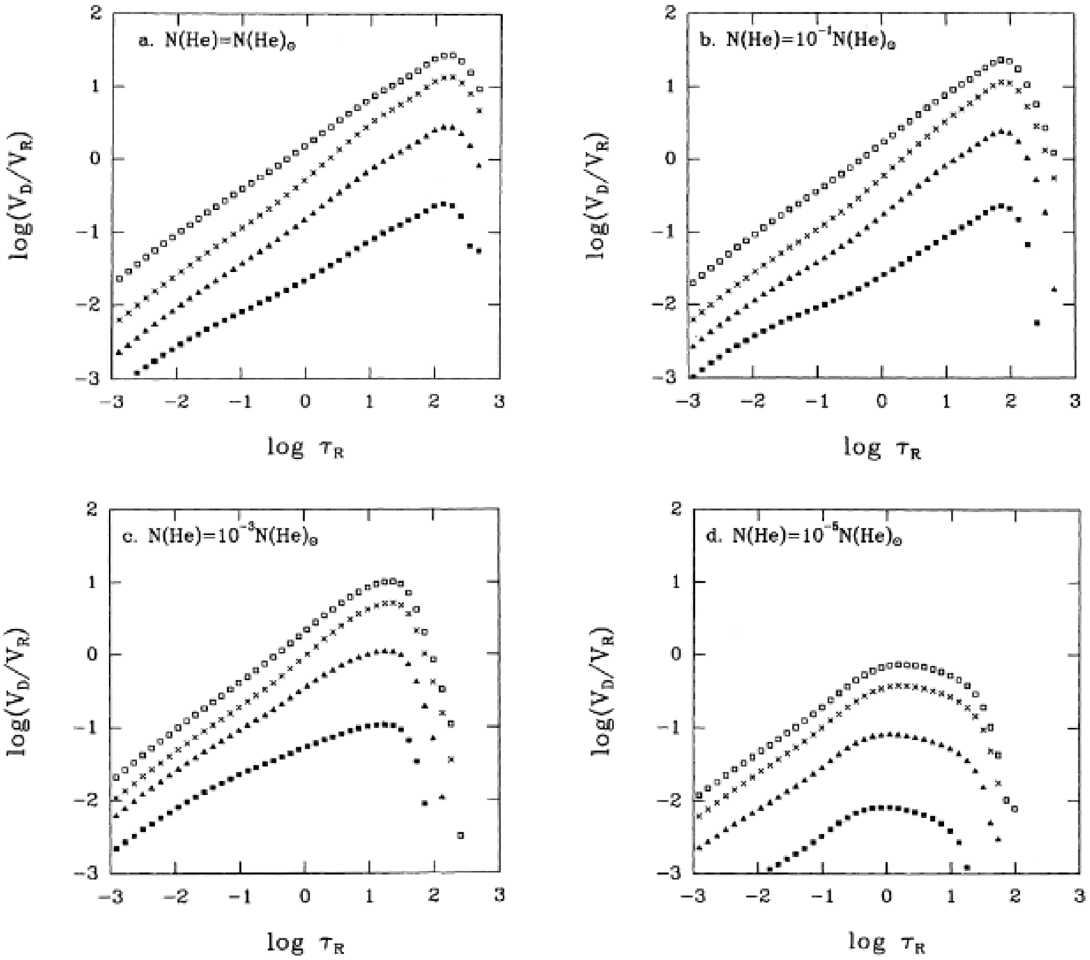

Figure 7.2.1.: Ratio of the LID (V_D) to the radiative acceleration (V_R) contributions to the transport velocity of ^{3}He due to the transition from ground to first excited state, He I, 584 Å, as a function of the Rosseland optical depth ($T_{\mathrm{eff}} = 18\,000$ K, $\log(g) = 4.0$ dex). The various curves correspond to different ^{3}He contents of the total helium abundance: 1% (open squares), 50% (crosses), 90% (triangles), and 99% (filled squares), respectively. The different parts of the figure belong to different total helium abundances which is also indicated on the particular subpanels. Adopted from LeBlanc & Michaud (1993).

Although the effects of LID on atomic diffusion processes including both helium isotopes, $^3\mathrm{He}$ and $^4\mathrm{He}$, in main-sequence stars and/or hot subdwarf B stars cannot be denied at all, detailed time dependent calculations including a more precise evaluation of the LID velocity than currently available, have to be carried out. The interplay of mass loss and gravitational settling may still be the dominant factor leading to the $^3\mathrm{He}$ isotope anomaly in these stars.

8. Analysis Programs

8.1. SPAS - Spectrum Plotting and Analysis Suite

For the LTE spectral analysis presented in chapter 10, the analysis program "Spectrum Plotting and Analysis Suite", short SPAS, is used. SPAS was designed by Heiko Hirsch and is based on FITSB2, which had been developed earlier by Napiwotzki et al. (2004). While FITSB2 had been a great and reliable program, it was not very user-friendly at the same time. Therefore, Hirsch (2009) developed SPAS, providing a graphical user interface for easy and fast access to parameters like spectral resolution, fit ranges, start parameters, etc. (Hirsch, 2009).

SPAS also provides an elaborated quantitative spectral analysis by fitting models of synthetic spectra to the observed spectrum. In this way, the atmospheric parameters, i.e., effective temperature T_{eff}, surface gravity $\log{(g)}$, and total helium abundance $\log{(y)}$ are determined. This is done via the so-called downhill simplex algorithm from Nelder & Mead (1965). A simplex in an N dimensional space is an (N+1)-polyhedron, i.e., a triangle in 2D or a tetrahedron in 3D space. A point in the four-dimensional parameter space, consisting of the three atmospheric coordinates T_{eff}, $\log{(g)}$, and $\log{(y)}$ as well as of the corresponding test function (in this case, the continuous χ^2 probability distribution of Eq. 11.7) value, is called a vertex. Generally, linear interpolation between different parameter values for $\log{(y)}$, then for $\log{(g)}$ and last for T_{eff} within a grid of synthetic model spectra using a simple cubic spline is performed in order to compute all vertices. In short words, the test function is used to determine the goodness of each vertex and replaces the worst one by a new vertex in each iteration by either contracting or expanding the simplex in the multidimensional parameter space. The algorithm stops when either the relative difference of the test functions evaluated at each vertex falls below a certain threshold, or a maximum number of iterations has been performed. The found minimum is not necessarily the global minimum, though (Hirsch, 2009).

If necessary, projected rotation velocity $v_{\text{rot,obs}} = v \sin i$ as well as macroturbulence ζ can be determined, too. However, in the context of this analysis (see chapter 10), it is sufficient to derive $v_{\text{rot,obs}}$ only and to set macroturbulence always to zero. Afterwards, the synthetic spectrum is folded with the instrumental profile (Hirsch, 2009).

Radial velocities of spectra are derived by fitting a combination of Lorentzian, Gaussian and straight line (in order to model the slope of the continuum) function to the line profiles of the selected absorption lines. Here, the particular line core position λ of each used spectral line is calculated and converted into its corresponding radial velocity value via the simple Doppler formula $\frac{\lambda-\lambda_0}{\lambda_0} = \frac{v_{\text{rad}}}{c}$, where λ_0 is the rest-frame wavelength of the considered spectral line (Hirsch, 2009).

Error determination is done by using the so-called bootstrapping method. Here, the data

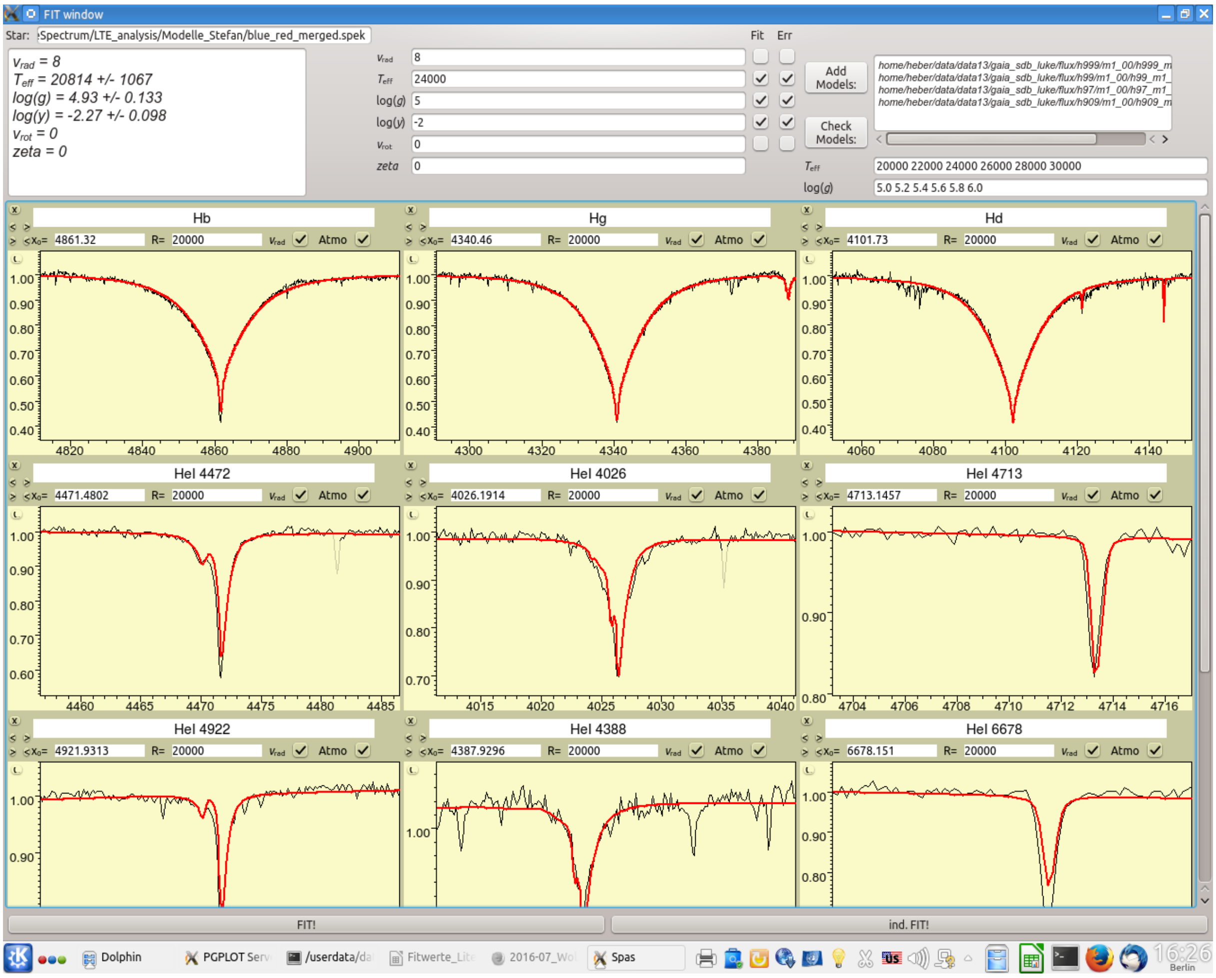
FIT window

Star: :Spectrum/LTE_analysis/Modelle_Stefan/blue_red_merged.spek

v_{rad} = 8
T_{eff} = 20814 +/- 1067
log(g) = 4.93 +/- 0.133
log(y) = -2.27 +/- 0.098
v_{rot} = 0
zeta = 0

		Fit	Err
v_{rad}	8	☐	☐
T_{eff}	24000	☑	☑
log(g)	5	☑	☑
log(y)	-2	☑	☑
v_{rot}	0	☐	☐
zeta	0		

home/heber/data/data13/gaia_sdb_luke/flux/h999/m1_00/h999_m
home/heber/data/data13/gaia_sdb_luke/flux/h99/m1_00/h99_m1_
home/heber/data/data13/gaia_sdb_luke/flux/h97/m1_00/h97_m1_
home/heber/data/data13/gaia_sdb_luke/flux/h909/m1_00/h909_m

T_{eff} 20000 22000 24000 26000 28000 30000
log(g) 5.0 5.2 5.4 5.6 5.8 6.0

Hb: X_0= 4861.32 R= 20000 v_{rad} ☑ Atmo ☑
Hg: X_0= 4340.46 R= 20000 v_{rad} ☑ Atmo ☑
Hd: X_0= 4101.73 R= 20000 v_{rad} ☑ Atmo ☑
HeI 4472: X_0= 4471.4802 R= 20000 v_{rad} ☑ Atmo ☑
HeI 4026: X_0= 4026.1914 R= 20000 v_{rad} ☑ Atmo ☑
HeI 4713: X_0= 4713.1457 R= 20000 v_{rad} ☑ Atmo ☑
HeI 4922: X_0= 4921.9313 R= 20000 v_{rad} ☑ Atmo ☑
HeI 4388: X_0= 4387.9296 R= 20000 v_{rad} ☑ Atmo ☑
HeI 6678: X_0= 6678.151 R= 20000 v_{rad} ☑ Atmo ☑

Figure 8.1.1.: A screenshot of SPAS' fitwindow showing all important features. *Upper Part*: While the binary synthetic model files are entered in the upper right text field in order of increasing (helium) abundance, the effective temperature and surface gravity gridpoints, which shall be used for linear interpolation, are listed below. For each (helium) abundance, a separate binary file is used. The selection of parameters to be fitted together with their start values can be entered in the center. In contrast, the current best fit values are displayed in the left text field. *Lower Part:* Important spectral lines are added or deleted manually and the corresponding fit ranges can also be simply fixed by user interaction. The current best fit is plotted as a red line over the black observed spectrum.

themselves are used to determine parameter errors. This is done by randomly resampling the data with replacement a large number of times and performing a parameter fit for each of the iterations. The standard error of each parameter can then be derived from the standard deviation of the particular parameter bootstrap distribution. Nevertheless, in this way the computed errors are realistically low (Hirsch, 2009).
SPAS is limited to the simultaneous determination of four parameters (T_{eff}, $\log(g)$, $\log(y)$, and projected rotation velocity, $v \sin i$), though. That is why a distinction between $^3\mathrm{He}$ and $^4\mathrm{He}$ is difficult to realize within SPAS. Another important disadvantage of SPAS for the analysis of $^3\mathrm{He}$ stars in general is, that it treats the radial velocity separately. A simultaneous treatment would be useful for these stars (see chapter 11.1 for further information).
Fig. 8.1.1 displays a screenshot of SPAS' fitwindow including all important features.

8.2. ISIS

In order to successfully perform the hybrid LTE/NLTE spectral analysis presented in chapter 11, it is carried out completely within the "Interactive Spectral Interpretation System", short ISIS, which was designed at the Massachusetts Institute of Technology (MIT) by Houck & Denicola (2000) in order to facilitate the interpretation and analysis of high resolution X-ray spectra. ISIS simplifies the investigation significantly since useful functions and tools as well as several minimization algorithms, such as the simplex (see section 8.1) and various gradient methods, are provided. Consequently, ISIS is more flexible, also allowing many-parameter fits. Hence, it overcomes the limitations of SPAS. Usually, the investigated χ^2 landscapes are well behaved so that finding the global minimum is guaranteed after a relatively small number of iteration steps. The strategy used will be discussed in detail throughout chapter 11.3.

9. Observation and Preparation of Data

The analyzed B-type stellar spectra all were obtained by five different Echelle spectrographs introduced in chapter 2.3. Table 9.1 provides a detailed overview of the observed sample and the data. While the analyzed CASPEC spectra ($R \sim 14,000$, 4000-6850 Å) obtained by U. Heber date back to October 1986, the HRS spectra of PHL 25 ($R \sim 60,000$, 3660-9950 Å) were obtained by H. Edelmann in July 2006. The FEROS ($R \sim 40,000$, 3530-9200 Å) as well as the FOCES ($R \sim 40,000$, 3800-7000 Å) data are provided by S. Geier via private communication and the UVES data ($R \sim 90,000$, 3290-6640 Å), taken from the hot subdwarf list of the ESO Supernova Ia Progenitor Survey (Lisker et al., 2005), are again provided by U. Heber. While the FEROS and FOCES spectra have already been reduced before by S. Geier by means of the MIDAS (*Munich Image Data Analysis System*) package and the UVES spectra by Karl (2004), the remaining data still has to be re-investigated in the context of cosmics, dead or hot pixels, insufficient order merging, etc.. Also, issues such as extraction errors, flat fielding, normalization, and reduction artifacts still remain even in the case of sophisticated data reduction. In the following, the principles of order merging, normalization and co-addition of spectra as well as the determination of signal-to-noise ratios (S/N) shall be demonstrated.

9.1. Order Merging

Despite the fact that sophisticated data reduction pipelines are available for Echelle spectrographs, insufficient flat fielding and merging of individual diffraction orders (see chapter 2.2) often still remains. Typically, the whole continuous spectrum is created by merging these individual orders in an appropriate way, i.e., by determining a weighted mean at the edges of neighboring diffraction orders. In the case of the analyzed CASPEC spectra, where the overlapping orders always exhibit the same measured wavelength points, the wavelength difference, i.e., the difference between the last wavelength value of the previous diffraction order and the first wavelength value of the subsequent one, is calculated at first. Then, this determined wavelength difference is halved and the previous diffraction order is simply cut off at the approximate position of the first wavelength value of the subsequent one plus the halved wavelength difference. Fig. 9.1.1 and 9.1.2 display the principle of order merging for two overlapping orders in the single CASPEC spectrum of the $^3\mathrm{He}$ sdB star SB 290 in SPAS.
Order merging only has to be applied manually to the analyzed CASPEC spectra of table 9.1. It has already been applied to all the other spectra before.

Object	Instrument	No. Spec	Resolution	S/N	Comments
HD 4539	CASPEC	1	14,000	241	He-normal comparison sdB star
CD-35 15910	FEROS	2	40,000	56	He-normal comparison sdB star
PHL 25	CASPEC	1	14,000	204	$^{3}\mathrm{He}$ enriched BHB star
PHL 25	HRS	2	60,000	40	$^{3}\mathrm{He}$ enriched BHB star
PHL 382	FEROS	7	40,000	88	$^{3}\mathrm{He}$ enriched BHB star
SB 290	CASPEC	2	14,000	278	$^{3}\mathrm{He}$ sdB star
SB 290	FEROS	2	40,000	68	$^{3}\mathrm{He}$ sdB star
EC 03263-6403	FEROS	2	40,000	23	$^{3}\mathrm{He}$ sdB star
EC 03591-3232	FEROS	2	40,000	65	$^{3}\mathrm{He}$ sdB star
EC 12234-2607	FEROS	4	40,000	28	$^{3}\mathrm{He}$ enriched sdB star
EC 14338-1445	FEROS	3	40,000	38	$^{3}\mathrm{He}$ sdB star
Feige 38	FEROS	5	40,000	69	$^{3}\mathrm{He}$ sdB star
BD+48 2721	FOCES	1	40,000	84	$^{3}\mathrm{He}$ enriched sdB star
PG 1519+640	FOCES	1	40,000	39	$^{3}\mathrm{He}$ enriched sdB star
PG 1710+490	FOCES	1	40,000	27	$^{3}\mathrm{He}$ enriched sdB star
HE 0929-0424	UVES	2	90,000	22	$^{3}\mathrm{He}$ enriched sdB star
HE 1047-0436	UVES	4	90,000	25	$^{3}\mathrm{He}$ enriched sdB star
HE 2156-3927	UVES	3	90,000	29	$^{3}\mathrm{He}$ enriched sdB star
HE 2322-0617	UVES	2	90,000	26	$^{3}\mathrm{He}$ enriched sdB star

Table 9.1.: Target sample and data of the analyzed B-type stars. The four additional $^{3}\mathrm{He}$ sdB stars (HE 0929-0424, HE 1047-0436, HE 2156-3927, and HE 2322-0617) are taken from the hot subdwarf list of the ESO Supernova Ia Progenitor Survey (Lisker et al., 2005) and are only investigated using ISIS in combination with the hybrid LTE/NLTE approach presented throughout chapter 11.3.

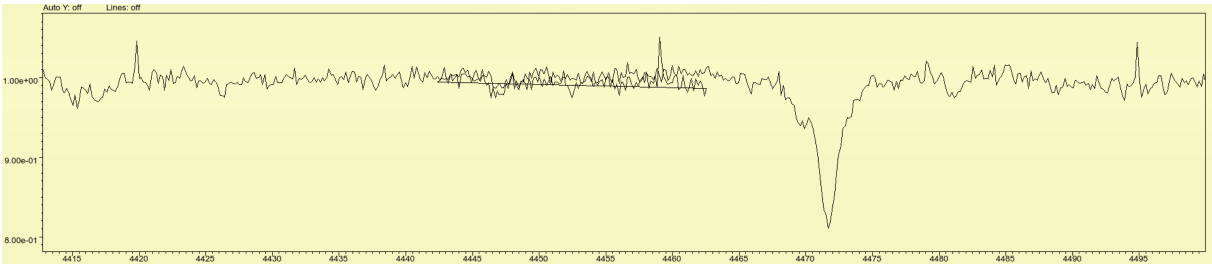

Figure 9.1.1.: Two overlapping diffraction orders in the single CASPEC spectrum of the $^{3}\mathrm{He}$ sdB star SB 290 in SPAS.

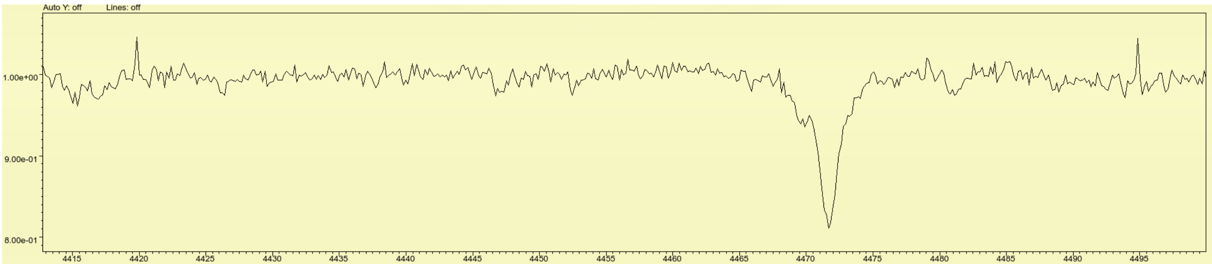

Figure 9.1.2.: Same diffraction orders in the single CASPEC spectrum of the $^{3}\mathrm{He}$ sdB star SB 290 in SPAS as in Fig. 9.1.1, but after applied order merging.

9.2. Normalization

Normalization usually is the last step in the data reduction procedure. The stellar continuum is approximately set to unity (ideally exactly to unity) so that several spectra can be compared. However, this can cause errors since it is not always obvious where to set the continuum. Especially in the case of broad absorption lines like the hydrogen Balmer ones, it is difficult or impossible to judge the curve of the continuum within the far line wings.

The provided CASPEC and FOCES spectra are already normalized. Reconstructing this normalization process is impossible, though. Thus, wrong continuum determination can only be excluded to a certain extent for all of these spectra. FEROS, HRS and UVES spectra are normalized by means of the analysis program SPAS (see section 8.1 for details) for the following analysis. In order to do so, numerous anchor points have to be set where the continuum in the spectrum, which has to be normalized, is assumed. In this way, a so-called spline function is formed describing the approximate stellar continuum. The normalized spectrum can be determined by dividing the original spectrum by the spline function. This procedure is demonstrated in Fig. 9.2.1 and 9.2.2. Nevertheless, the continuum is mostly set by eye and hence, this normalization procedure is prone to errors, too.

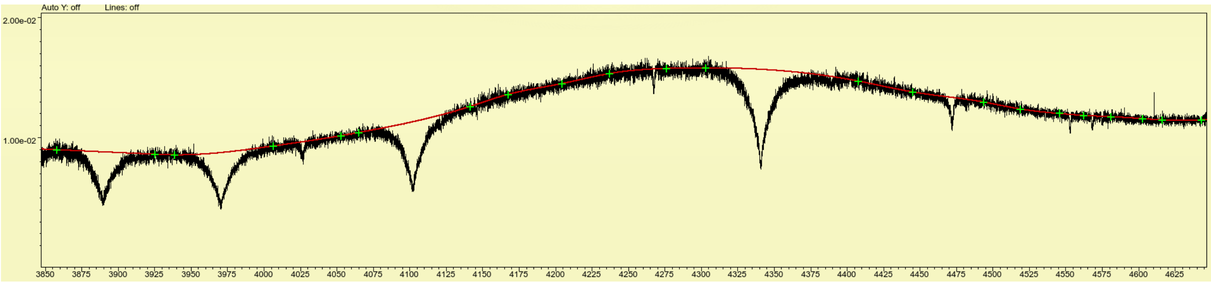

Figure 9.2.1.: Section of a single and not normalized FEROS spectrum of the $^{3}\mathrm{He}$ sdB star SB 290 in SPAS. The continuum is assumed to follow the red spline function which is defined by setting numerous green anchor points by eye.

Figure 9.2.2.: Same section of a single but normalized FEROS spectrum of the $^3\mathrm{He}$ sdB star SB 290 in SPAS as in Fig. 9.2.1. The normalized spectrum is derived by dividing the original spectrum by the red spline function in Fig. 9.2.1.

9.3. Co-Addition

After order merging and normalization have been successfully performed, the single spectra of all sample stars are co-added after correction for the radial velocity in order to achieve higher signal-to-noise ratios (S/N). The signal-to-noise ratio (see table 9.1) is typically defined as the ratio of mean signal to standard deviation considered over some continuum spectral range. A co-added spectrum consists of an addition of all single spectra, whereby the individual signal-to-noise ratios and thereby also the individual exposure times are taken into account. In consequence, the co-added spectrum has a significantly higher S/N, allowing a detailed line identification. The comparison between a single and a co-added spectrum is shown in Fig. 9.3.1 and 9.3.2.

In order to conduct co-addition, the single spectra have to be radial-velocity (RV)-corrected at first. RV are determined via SPAS as described in chapter 8.1. Since it is not ensured that all of the spectra are barycentric corrected, the derived RV values are not barycentric corrected RV, but a combination of the season-dependent component caused by Earth's rotation and its motion around the barycenter (v_{bary}), and the actual RV v_{rad} (see also section 4.4 for details). In the case of the two He-normal comparison stars HD 4539 and CD-35° 15910, all available helium absorption lines in the spectrum can be used to determine RV. As can be seen in table 9.2, these lines originate from neutral helium (He I). Much broader lines, in particular the hydrogen Balmer ones, are not well suited for RV measurements and therefore are excluded. In the case of $^3\mathrm{He}$ (enriched) stars, RV can only be approximately determined via $^3\mathrm{He}$ I, 5875 Å because of its only slight isotopic shift of 0.04 Å. All other helium lines exhibit much stronger shifts due to $^3\mathrm{He}$ enrichment (see also table 6.1) and cannot be used to accurately measure exact RV because a $^3\mathrm{He}$ model atom for the LTE analysis is missing. By including other absorption lines, in particular those from metals, a more precise RV measurement is guaranteed. An extremely precise RV measurement is not only important for illustrating the isotopic shift due to $^3\mathrm{He}$ enrichment, but also for an accurate measurement of the particular $^4\mathrm{He}/^3\mathrm{He}$ ratio (see chapter 11.1.3 for further information). This is ensured in the hybrid LTE/NLTE analysis performed in ISIS which will be discussed in chapter 11.3. However, in order to properly co-add the single spectra, the number of helium lines used is sufficient. Also, for RV measurements in SPAS an old rest-frame wavelength for the He I, 5875 Å line has been

Table 9.2.: Neutral helium absorption lines used for the RV determination. Whereas for the two He-normal comparison stars HD 4539 and CD-35° 15910 in principle all listed lines can be used, if visible, in the case of $^3\mathrm{He}$ (enriched) stars, He I, 5875 Å is the only suitable line to accurately measure RV. All other helium lines exhibit much stronger shifts due to $^3\mathrm{He}$ enrichment (see also table 6.1).

Object	Instrument	He I 4026.1914 Å	He I 4387.9296 Å	He I 4471.4802 Å	He I 4713.1457 Å	He I 4921.9313 Å	He I 5015.6783 Å	He I 5047.7380 Å	He I 5875.7500 Å [a]	He I 6678.1510 Å
HD 4539	CASPEC	1	1	1	1	1	0	0	1	1
CD-35 15910	FEROS	1	0	1	1	1	1	0	1	1
PHL 25	CASPEC	0	0	0	0	0	0	0	1	0
PHL 25	HRS	0	0	0	0	0	0	0	1	0
PHL 382	FEROS	0	0	0	0	0	0	0	1	0
SB 290	CASPEC	0	0	0	0	0	0	0	1	0
SB 290	FEROS	0	0	0	0	0	0	0	1	0
EC 03263-6403	FEROS	0	0	0	0	0	0	0	1	0
EC 03591-3232	FEROS	0	0	0	0	0	0	0	1	0
EC 12234-2607	FEROS	0	0	0	0	0	0	0	1	0
EC 14338-1445	FEROS	0	0	0	0	0	0	0	1	0
Feige 38	FEROS	0	0	0	0	0	0	0	1	0
BD+48 2721	FOCES	0	0	0	0	0	0	0	1	0
PG 1519+640	FOCES	0	0	0	0	0	0	0	1	0
PG 1710+490	FOCES	0	0	0	0	0	0	0	1	0
HE 0929-0424	UVES	0	0	0	0	0	0	0	1	0
HE 1047-0436	UVES	0	0	0	0	0	0	0	1	0
HE 2156-3927	UVES	0	0	0	0	0	0	0	1	0
HE 2322-0617	UVES	0	0	0	0	0	0	0	1	0

Notes:

[a] Note the old value of 5875.7500 Å compared to the actual one derived from NIST which is 5875.6210 Å. Therefore, an old rest-frame wavelength is used for the LTE analysis.

0: Line not used for RV measurement

1: Line used for RV measurement

used. Instead of the actual rest-frame wavelength of 5875.621 Å, for instance accessible by means of the spectral data base of the *"**N**ational **I**nstitute of **S**tandards and **T**echnology"*, short NIST[2], an old value of 5875.750 Å has been used. All in all, the $^3\mathrm{He}$ model atom used for the hybrid LTE/NLTE analysis and the accurate modeling of the corresponding $^3\mathrm{He}$ line components going along with it, generally ensure that even more accurate RV values can be derived, too. Hence, the RV-corrected spectra shown in appendix B.1 and derived from the hybrid LTE/NLTE analysis are certainly reliable.

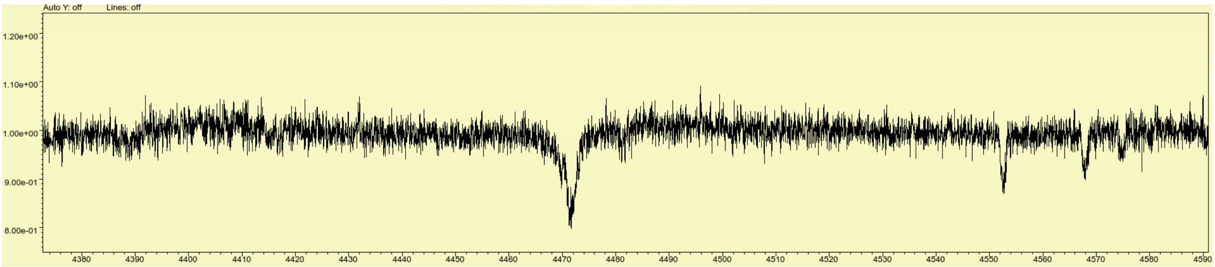

Figure 9.3.1.: Section of a single and normalized FEROS spectrum of the $^3\mathrm{He}$ sdB star SB 290 in SPAS. Line identification is difficult because of the spectrum's low signal-to-noise ratio (S/N).

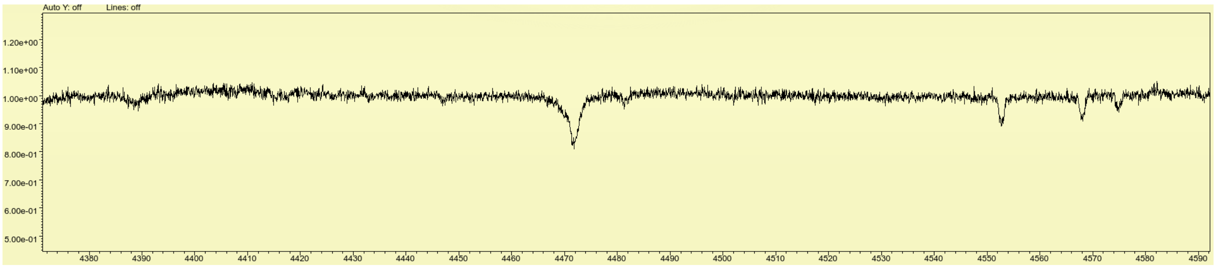

Figure 9.3.2.: Section of a co-added and normalized FEROS spectrum of the $^3\mathrm{He}$ sdB star SB 290 in SPAS. Compared to Fig. 9.3.1, line identification is easier because of the spectrum's higher signal-to-noise ratio (S/N) after co-addition of the two available single spectra. Note that the lines of SB 290 are significantly broadened due to stellar rotation.

9.4. Line Identification

Besides the already mentioned helium absorption lines listed in table 9.2, hydrogen Balmer as well as various metal lines are individually identified in all analyzed spectra. This is done by means of the spectral data base of the *"**N**ational **I**nstitute of **S**tandards and **T**echnology"*,

---

[2] `http://physics.nist.gov/PhysRefData/ASD/lines_form.html`

Ion	Wavelength [Å]	Ion	Wavelength [Å]	Ion	Wavelength [Å]	Ion	Wavelength [Å]
H I	6562.790	N II	3994.997	Si II	4128.070	S III	4364.682
H I	4861.350	N II	4035.080	Si II	4130.890	S III	4677.615
H I	4340.472	N II	4041.310	Si III	4574.757	Ar II	4426.001
H I	4101.734	N II	4043.530	Si III	4716.654	Ar II	4609.567
H I	3970.075	N II	4630.539	Si III	4813.333	Ar II	4735.906
He I	4026.191	N II	4643.086	Si III	4819.712	Ar II	4806.021
He I	4387.930	N III	4640.640	Si III	4828.951	Ar II	4879.863
He I	4471.480	O II	4185.440	Si III	4829.030	Fe III	4137.764
He I	4713.146	O II	4189.788	Si III	4829.111	Fe III	4139.350
He I	4921.931	O II	4317.139	Si III	5739.734	Fe III	4164.731
He I	5015.678	O II	4319.630	Si IV	4088.862	Fe III	4164.916
He I	5047.738	O II	4590.972	Si IV	4116.104	Fe III	4166.840
He I	5875.621	O II	4596.175	Si IV	4654.312	Fe III	4222.271
He I	6678.151	O II	4650.838	S II	4815.552	Fe III	4371.337
C II	4267.261	O II	4661.632	S II	5212.267	Fe III	4419.596
C II	5145.165	Ne I	6402.247	S II	5212.620	Fe III	5302.602
C II	5889.780	Mg II	4481.126	S II	5320.723	Kr II	4088.337
C II	6578.050	Mg II	4481.325	S II	5345.712	Kr II	4355.477
C II	6582.880	Al III	4479.890	S II	5346.084	Kr II	4658.876
C III	4647.418	Al III	4512.570	S II	5432.797	Kr II	4739.001
C III	4650.246	Al III	4529.190	S III	4253.589	Cl II	4785.364
C III	4651.473	Al III	5696.603	S III	4284.979	Cl II	4794.550
C III	5695.920	Al III	5722.728	S III	4361.476	Cl II	4810.060

Table 9.3.: Standard line list displaying example (metal) absorption lines. The abundances of exotic elements such as chlorine and krypton cannot be measured because of a lack of appropriate model atoms (see text for further information). For a full list of analyzed lines see appendix B.1.

short NIST, as well as of the book *Atomic Transition Probabilities Volume I, Hydrogen Through Neon - A Critical Data Compilation* of the *U.S. Department of Commerce* (Connor et al., 1966). While the hydrogen Balmer lines ($H_\alpha = 6565$ Å, $H_\beta = 4863$ Å, $H_\gamma = 4342$ Å, $H_\delta = 4103$ Å, and $H_\epsilon = 3970$ Å) are visible in all analyzed spectra, the individual metal line strengths differ from star to star. A shortened list of analyzed lines is presented in table 9.3. Also, appendix B.1 displays the spectral fits of all analyzed star spectra and therefore provides deep insights into all (metal) lines found for each individual star. Besides hydrogen and helium, nearly all of the stars contain carbon, nitrogen, oxygen, sulfur, and silicon. Whereas carbon, nitrogen and sulfur occur either in singly or doubly ionized states, oxygen is found as O II only and silicon exhibits singly (Si II, in particular in the cooler BHB stars PHL 25 and PHL 382), doubly (Si III) and triply (Si IV) ionized states. In addition, magnesium (Mg II) and aluminum (Al III) as well as iron (Fe III) can be found, whereby especially the latter one is not detected in all of the

spectra. Moreover, the stellar atmosphere of some analyzed stars contains noble gases such as argon (Ar II) and neon (Ne I), too. The atmosphere of the $^3\mathrm{He}$ enriched BHB star PHL 382 is also found to be slightly enriched by another noble gas, namely krypton (Kr II, see Fig. 9.4.1). The spectra of PHL 25, another $^3\mathrm{He}$ enriched BHB star, also include chlorine (Cl II, see Fig. 9.4.2). The corresponding metal abundances are determined in combination with the hybrid LTE/NLTE approach (see chapter 12.4 and tables 12.5 and 12.6). The abundances of exotic elements such as chlorine and krypton cannot be determined because of a lack of appropriate model atoms, though.
Interstellar lines such as Ca II, 3933.66 Å, Ca II, 3968.47 Å, Na I, 5889.95 Å and Na I, 5895.92 Å, resulting from the interaction between emitted starlight and the interstellar medium between observer and object, are extracted from fitting, if visible. The same holds for telluric lines originating from the interaction between starlight and Earth's atmosphere components, mainly water ($\mathrm{H_2O}$) in the red and near-infrared and ozone in the UV range. Since the spectra at hand do not range to lower wavelengths than $\sim$ 3500 Å, the contamination by telluric lines results from $\mathrm{H_2O}$ only and roughly starts at 5000 Å becoming even more present at larger wavelengths (see also appendix B.1 for further details).

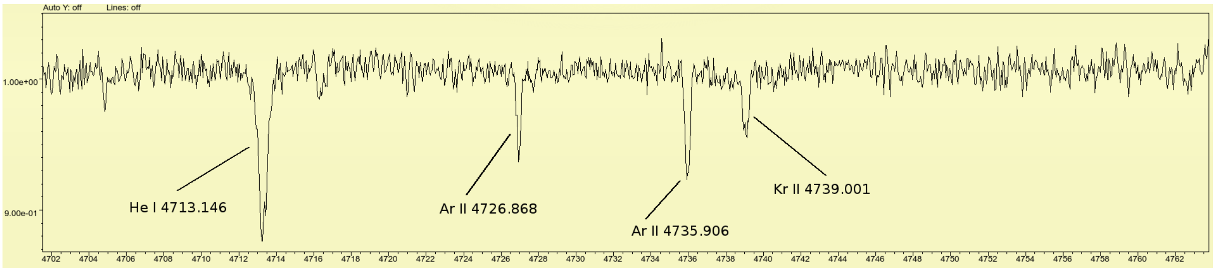

Figure 9.4.1.: Section of the co-added FEROS spectrum of the $^3\mathrm{He}$ enriched BHB star PHL 382 showing the exotic metal krypton. Besides the displayed Kr II, 4739.001 Å line, all listed krypton lines of table 9.3 can also be detected in the spectrum.

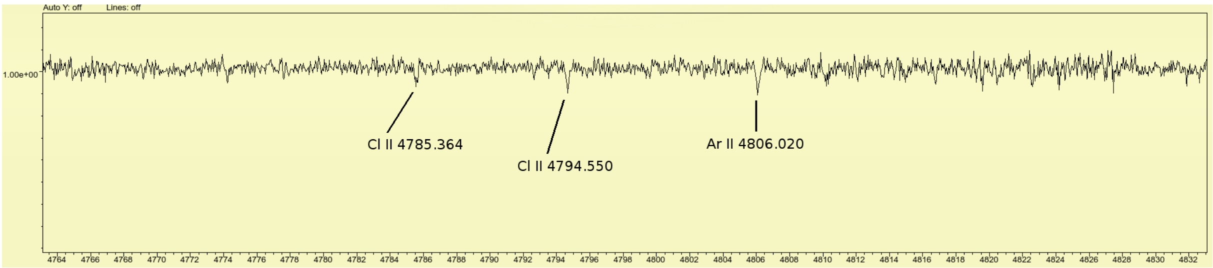

Figure 9.4.2.: Section of the co-added HRS spectrum of the $^3\mathrm{He}$ enriched BHB star PHL 25 showing the exotic metal chlorine. Besides the displayed Cl II, 4785.364 Å and Cl II, 4794.550 Å lines, the third listed chlorine line of table 9.3, Cl II, 4810.060 Å, can also be weakly detected in the spectrum. However, it is not separately marked in this figure because of its weakness.

10. LTE Analysis in SPAS

The analysis performed in local thermodynamic equilibrium (LTE) within the "Spectrum Plotting and Analysis Suite", short SPAS (see chapter 8.1), and its results are presented in this chapter. Hereafter, this analysis is denoted as LTE analysis.

The already prepared spectra (see the previous chapter 9 for details on data preparation) listed in table 9.1 are now analyzed in LTE in terms of atmospheric parameters, i.e., effective temperature, T_{eff} (see section 4.1), surface gravity, $\log(g)$ (see section 4.2), and atmospheric helium abundance, $\log(y)$ (see section 4.6). In addition to the measured radial velocity discussed in section 9.3 of the previous chapter, the projected rotation velocity, $v_{\text{rot,obs}} = v \sin i$ (see sections 3.3.2 and 4.5), is also determined. As already mentioned in section 4, microturbulence and macroturbulence in principle can also affect the shape of spectral lines, but are neglected in the context of the following analysis. Therefore, macroturbulence ζ is set to zero and microturbulence ξ is not treated at all. Metal abundances are not derived, too. This will be topic in chapter 11.3, however, when the hybrid LTE/NLTE approach in combination with ISIS is used.

In principle, the synthetic spectra already used by S. Geier for the analysis of $^3\mathrm{He}$ (enriched) subdwarf B stars presented in section 6.3 are used for this LTE analysis as well. These models are provided by U. Heber, whereby model atmospheres were computed assuming plane-parallel geometry, chemical homogeneity, and hydrostatic, radiative, and LTE (see section 3.2 for details). The grid used is based on solar metallicity and consists of model spectra with 0.01%, 0.1%, 1%, 3% and 9.1% helium abundance, respectively. Only hydrogen and helium lines are synthesized.

In total, the analyzed LTE sample consists of 13 B-type stars, including two He-normal comparison sdB stars (HD 4539 and CD-35° 15910), two $^3\mathrm{He}$ BHB stars (PHL 25 and PHL 382), and nine $^3\mathrm{He}$ (enriched) sdB stars (see table 9.1). The four additional $^3\mathrm{He}$ sdB stars (HE 0929-0424, HE 1047-0436, HE 2156-3927, and HE 2322-0617), also listed in table 9.1, are taken from the hot subdwarf list of the ESO Supernova Ia Progenitor Survey (Lisker et al., 2005) and are not investigated here using the LTE approach (see section 6.4). But they will be included in the sample for the hybrid LTE/NLTE approach performed in ISIS and presented throughout chapter 11.3. Since different spectrographs (see section 2.3) were used to obtain the spectra to be analyzed, it is important to know their correct resolving powers (listed in table 9.1) in order to perform a reliable analysis.

All available helium and hydrogen absorption lines that can be analyzed for each spectrum are included for the analysis. In principle, they consist of the standard lines shown in table 9.3, but also including the higher transition lines belonging to the hydrogen Balmer series, H8-H12, if convenient. All lines to be analyzed are added manually to SPAS' fitwindow and the corresponding fit ranges are also adjusted (see section 8.1). Generally, the first hydrogen

Balmer line, $H_\alpha = 6565\,\text{Å}$, is excluded for all stars because of strong non-LTE effects going along with it which cannot be modeled properly in LTE (see left panel of Fig. 10.0.1). Also, as a convenient $^3\mathrm{He}$ model atom is not included for the produced LTE model spectra as well, all helium lines showing strong isotopic line shifts due to $^3\mathrm{He}$ enrichment are excluded from the LTE analysis (see right panel of Fig. 10.0.1). Since the degree of $^3\mathrm{He}$ enrichment differs from star to star, the excluded helium lines also vary. Last but not least, SPAS automatically defines the continuum in cases where it has obviously not been set properly at the end of data reduction. Direct normalization is avoided by matching model and observed spectrum and both ends of the selected spectral range for each individual line. For some stars, however, see for instance the line fits in the FOCES spectrum of the $^3\mathrm{He}$ enriched sdB star BD+48° 2721 displayed in Fig. 10.0.2, parts of the hydrogen Balmer wings even have to be excluded from fitting because of wrong normalization at the end of data reduction. Appendix A.1 summarizes the analyzed hydrogen and helium absorption lines for each individual spectrum. All of the previously discussed adjustments have been made.

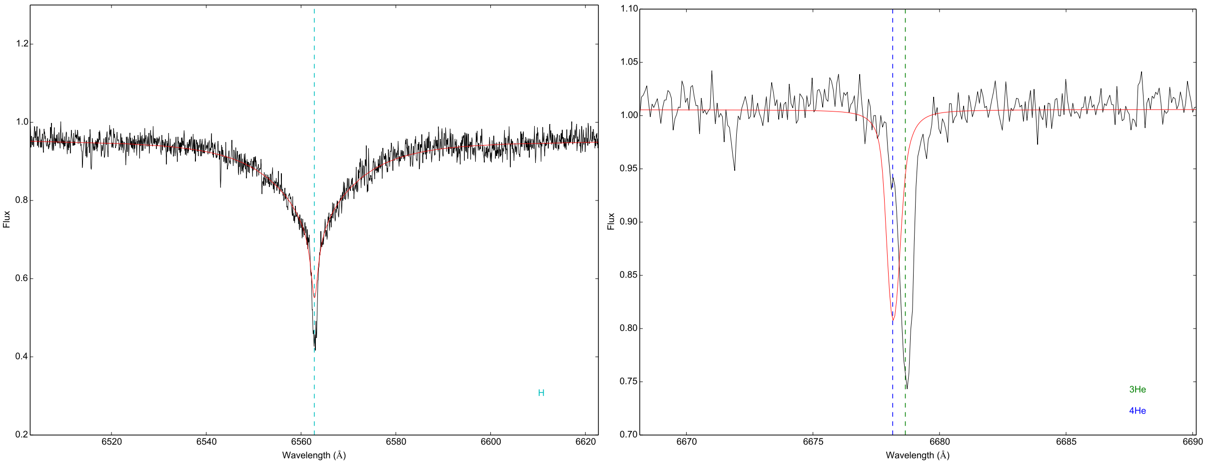

Figure 10.0.1.: *Left panel*: Comparison between best fit model spectrum (red line) and co-added star spectrum (black line) for the non-LTE affected hydrogen Balmer line $H_\alpha = 6565\,\text{Å}$ in the case of the He-normal comparison star CD-35° 15910 used for the LTE analysis via SPAS. *Right panel*: Comparison between best fit model spectrum (red line) and co-added star spectrum (black line) for He I, 6678 Å in the case of the $^3\mathrm{He}$ sdB star Feige 38 used for the LTE analysis via SPAS. The particular positions of the rest-frame wavelengths of hydrogen (cyan), $^4\mathrm{He}$ (blue) and $^3\mathrm{He}$ (green) are marked by dashed lines. Obviously, in both cases the star spectrum cannot be reproduced. That is why H_α (strongly affected by NLTE) and helium absorption lines showing strong isotopic shifts due to $^3\mathrm{He}$ enrichment like He I, 6678 Å are generally extracted from LTE fitting (see text and appendix A.1).

Sorted by the spectrograph used, the comparison between best fit model spectrum (red line) and stellar spectrum (black line) for the hydrogen and helium lines used for the LTE analysis via SPAS of the different sample stars are also shown in appendix A.1. The particular positions of the rest-frame wavelengths of hydrogen (cyan), $^4\mathrm{He}$ (blue) and $^3\mathrm{He}$ (green) are marked by dashed lines. Best fit model spectrum and the resulting best fit values for the atmospheric parameters T_{eff}, $\log(g)$, as well as for the helium abundance, $\log(y)$, are determined by the downhill simplex algorithm implemented in SPAS and already presented in section 8.1. The determined values are shown in table 10.1 together with the derived projection rotation velocities. Besides these parameters, radial velocities (not barycentric corrected) for each single spectrum are listed, too. Co-added spectra have been RV-corrected. Error determination for all parameters is done by using SPAS' bootstrapping method which has also been discussed before in section 8.1.

As can be seen from table 10.1, SB 290 and PHL 25 are the only two stars where rotation velocities different from zero are needed to properly reproduce the observed spectral line shapes. This is in good agreement with the fact that most hot sudbwarf B stars are known to be slow rotators (Heber, 2016). Especially in the case of SB 290, the derived values are consistent with literature. Geier et al. (2013b) measured values between $v \sin i = 48 \pm 2$ and $v \sin i = 58 \pm 1$, depending on whether metal lines only or a combination of hydrogen Balmer and helium absorption lines are used to determine the projected rotation velocity of SB 290. In the case of PHL 25, however, no significant projected rotation velocity values have been observed so far. This will be further investigated in chapter 12.3.3 when metal lines are included using the hybrid LTE/NLTE approach, though. Only then, a reliable projected rotation velocity can be determined.

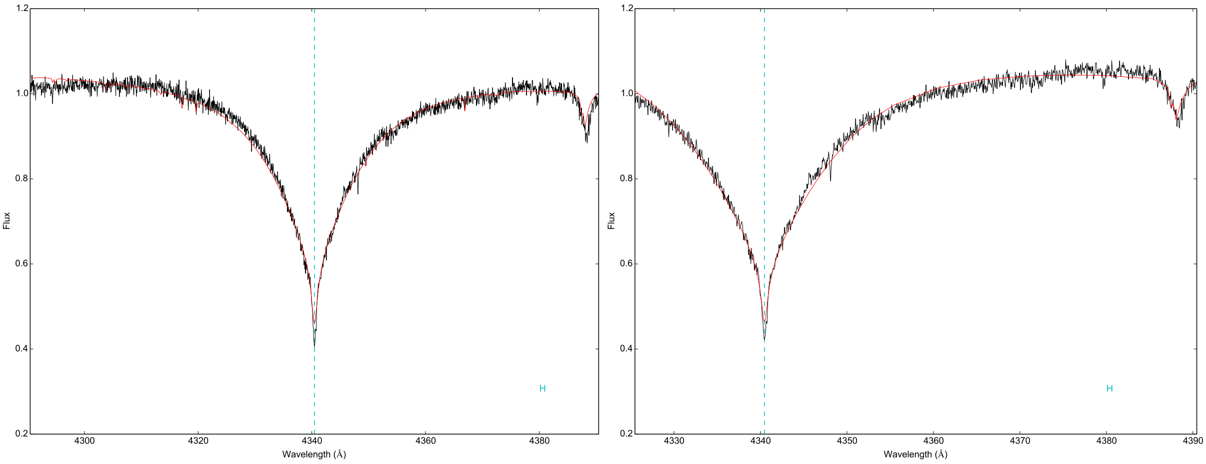

Figure 10.0.2.: *Left Panel*: Unmodified $H_\gamma = 4342$ Å line in the FOCES spectrum of the $^3\mathrm{He}$ enriched sdB star BD+48° 2721. Obviously, the asymmetry of the H_γ line is an artifact of the normalization procedure. *Right Panel*: $H_\gamma = 4342$ Å line in the FOCES spectrum of the $^3\mathrm{He}$ enriched sdB star BD+48° 2721 used for the LTE analysis via SPAS. Part of the left line wing is excluded from fitting because of wrong continuum setting during normalization.

Fig. 10.0.3 displays the T_{eff}-$\log(g)$ diagram derived from the LTE analysis via SPAS. Each data point with error bars represents one of the analyzed stars of table 10.1. While all $^3\mathrm{He}$ stars are marked with blue dots, both He-normal comparison stars, HD 4539 and CD-35°

15910, are represented in green. For the stars, where two (co-added) spectra are available, the measured parameter values are averaged. This is the case for SB 290 and PHL 25 (see table 10.1), where propagated errors are derived according to Gaussian error propagation afterwards. Overall, the derived effective temperatures and surface gravities of the analyzed hot subdwarf B stars match the typical trend seen in the upper panel of Fig. 5.1.3, clearly placing them on the extreme horizontal branch.

The two dots at the cool end of the sequence in Fig. 10.0.3 represent the $^3\mathrm{He}$ enriched BHB stars PHL 25 and PHL 382. The derived values for PHL 382, $T_{\text{eff}} = 16,500 \pm 700$ K and $\log{(g)} = 3.77 \pm 0.06$, match the values determined by Kilkenny & van Wyk (1990) reading $T_{\text{eff}} = 18,000 \pm 1,000$ K and $\log{(g)} = 3.75 \pm 0.25$. The averaged values of effective temperature and surface gravity for PHL 25 ($T_{\text{eff}} = 18,550 \pm 400$ K, $\log{(g)} = 4.64 \pm 0.05$) differ from

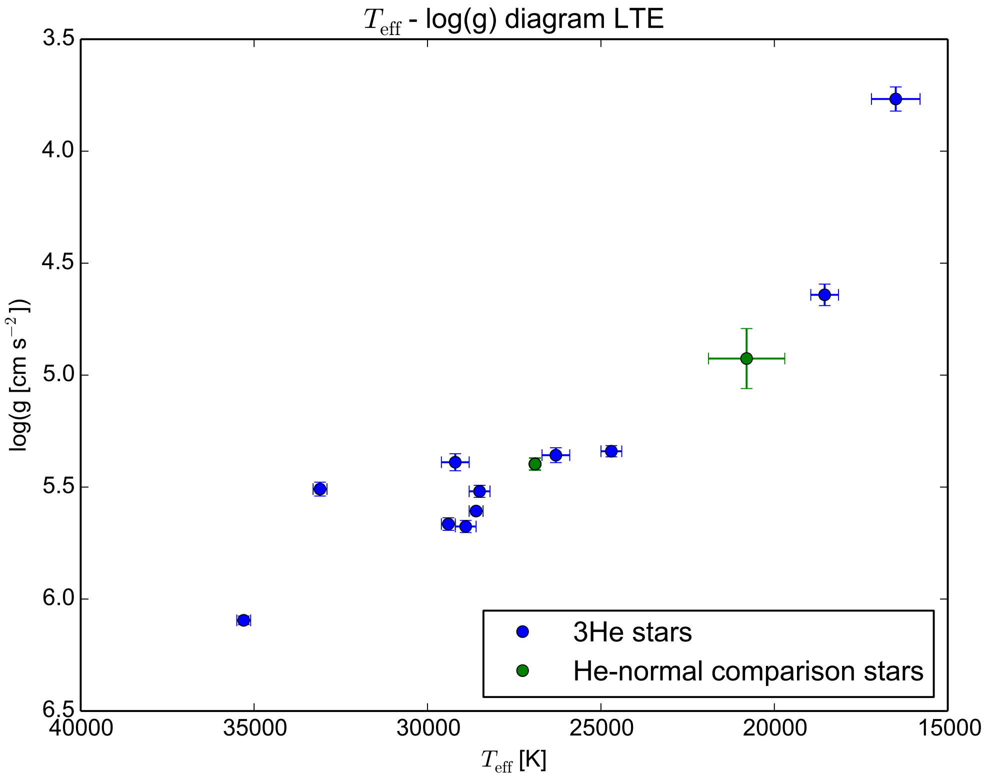

Figure 10.0.3.: T_{eff}-$\log{(g)}$ diagram derived from the LTE analysis via SPAS. $^3\mathrm{He}$ stars are marked with blue dots. Both He-normal comparison stars, HD 4539 and CD-35° 15910, are represented in green. While the two dots at the cool end of the sequence represent the $^3\mathrm{He}$ enriched BHB stars PHL 25 and PHL 382, the two dots at the hot end correspond to the $^3\mathrm{He}$ enriched sdB stars PG 1519+640 and PG 1710+490. Concerning the latter ones, the derived temperatures are too high for typical sdB stars. A possible explanation for this discrepancy could be bad normalization of the FOCES spectra (see text for more details), in particular of the hydrogen Balmer lines.

$T_{\text{eff}} = 19,500$ K and $\log(g) = 5.0$ derived by Heber & Langhans (1986). However, because of the higher spectral resolving power of the analyzed HRS spectra and since no error bars were determined by Heber & Langhans (1986), the results seem to be consistent.

As can be also seen from Fig. 10.0.3, two stars lie within a hotter temperature regime. For these two sdBs, PG 1519+640 and PG 1710+490, values of $T_{\text{eff}} = 30\,300$ K and $\log(g) = 5.67$, and $T_{\text{eff}} = 30\,600$ K and $\log(g) = 5.66$, respectively, can be found in the literature (Geier et al., 2013a). Therefore, especially the derived temperature values listed in table 10.1 are most likely not reliable, not least because the singly ionized helium line, He II, 4686 Å, is predicted by atmospheric models to be visible at these high temperatures, giving an upper limit for T_{eff}, which reads $T_{\text{eff}} \lesssim 31\,000$ K. However, He II, 4686 Å is not visible in the analyzed FOCES spectra. Since both parameters, T_{eff} and $\log(g)$, amongst others are predominantly constrained by the hydrogen Balmer line series (see chapter 4 for details), the measurement of such high effective temperatures and a wrong surface gravity (for PG 1519+640) could be due to bad normalization of the corresponding lines. Though, this is hard to reconstruct, in particular since all FOCES spectra have already been normalized before being provided. Furthermore, Geier et al. (2013a) did not use the FOCES spectra which are investigated in this thesis, but additionally available high signal-to-noise (S/N) ISIS spectra in order to determine T_{eff} and $\log(g)$. Hence, deviations from the results of Geier et al. (2013a) may be expected.

All other ^3He (enriched) sdB stars cluster in a small temperature strip between $\sim$ 26 000 K and 30 000 K, BD+48° 2721 being the only exception with $T_{\text{eff}} = 24,700 \pm 300$ K. This is overall in good agreement with the results of Geier et al. (2013a) who measured a narrow strip between $\sim$ 27 000 K and $\sim$ 31 000 K for these stars (see chapter 6.3). The derived surface gravities for these stars also match the ones determined by Geier et al. (2013a), keeping in mind that they used high S/N ISIS spectra, if available, in order to derive T_{eff} and $\log(g)$.

In addition, the values for T_{eff} and $\log(g)$ of the He-normal comparison star CD-35° 15910 do not show any discrepancy to literature. For this star, Geier et al. (2013a) measured $T_{\text{eff}} = 27\,000$ K and $\log(g) = 5.32$ compared to the results shown in table 10.1, reading $T_{\text{eff}} = 26,900 \pm 100$ K and $\log(g) = 5.40 \pm 0.03$. In contrast, the parameters determined for HD 4539 ($T_{\text{eff}} = 20,800 \pm 1,100$ K, $\log(g) = 4.93 \pm 0.14$), a well-studied sdB star, differ from those estimated by Heber & Langhans (1986) ($T_{\text{eff}} = 24,800$ K, $\log(g) = 5.4$), Baschek et al. (1972) ($T_{\text{eff}} = 25,000 \pm 2,000$ K, $\log(g) = 5.4 \pm 0.2$), and Saffer et al. (1994) ($T_{\text{eff}} = 27,000$ K, $\log(g) = 5.46$), respectively. This could be due to the lower spectral resolving power of the analyzed CASPEC spectrum, although Heber & Langhans (1986) also used CASPEC spectra for their analysis.

The determined helium abundances, $\log(y)$, of the ^3He (enriched) sdB stars match the literature values determined by Geier et al. (2013a), too, again keeping in mind that they used high S/N ISIS spectra, if available, though. Also, the derived helium abundances for both ^3He enriched BHB stars, PHL 382 ($\log(y) = -2.30 \pm 0.12$) and PHL 25 ($\log(y) = -2.05 \pm 0.04$), are consistent with the values from Heber & Langhans (1986), reading $\log(y) \sim -2.20$ and $\log(y) = -2.00$, respectively. The measured helium abundance for PHL 25 is an average using the helium abundances derived from the co-added HRS as well as from the single CASPEC spectrum given in table 10.1. Concerning both He-normal comparison stars, HD 4539 and CD-35° 15910, the derived helium abundances reproduce literature values of $\log(y) \sim -2.30$

determined by Saffer et al. (1994) and $\log{(y)} \sim -2.32$ determined by Heber & Langhans (1986), respectively, in the case of HD 4539, and $\log{(y)} = -2.90$ determined by Geier et al. (2013a) in the case of CD-35° 15910.

All in all, it has to be highlighted that especially effective temperatures, T_{eff}, but also surface gravities, $\log{(g)}$, of the analyzed stars derived from the hybrid LTE/NLTE approach discussed in the next chapter will slightly differ from the ones determined in LTE. In particular, this is the case because the line cores of the first two absorption lines belonging to the hydrogen Balmer line series, H_{α} (excluded from fitting in LTE) and H_{β}, are influenced by NLTE effects. A better modeling of these line cores definitely helps to derive more reliable atmospheric parameters, in particular T_{eff}. However, at this point it should be pointed out that a self-consistent comparison of atmospheric parameters (T_{eff}, $\log{(g)}$) derived from both, LTE and hybrid LTE/NLTE, presented in this thesis is not readily possible since the analyzed hydrogen Balmer lines may not be the same. Thus, a systematic error which is mainly due to a lack of proper modeling of higher transition lines, i.e., H8-H12 in the case of the hybrid LTE/NLTE approach is introduced. This error will not be further investigated in the further course of this thesis, though.

It also has to be pointed out that the determined helium abundances listed in table 10.1 are derived by neglecting absorption lines showing strong isotopic shifts due to $^{3}\mathrm{He}$ enrichment. This is why, for instance, He I, 6678 Å is generally excluded from fitting. Therefore, the measured helium abundances can only be reliable to a certain extent and need further investigation by means of a convenient $^{3}\mathrm{He}$ model atom. Such a $^{3}\mathrm{He}$ model atom has been developed by Maza et al. (2014) and will be used for the hybrid LTE/NLTE approach presented in the next chapter.

Table 10.1.: Atmospheric parameters, helium abundances as well as radial (not barycentric corrected) and projected rotation velocities of the analyzed $^3\mathrm{He}$ and two He-normal comparison B-type stars (HD 4539, CD-35° 15910) determined by the LTE analysis performed in SPAS. Co-added spectra have been RV-corrected. SB 290 and PHL 25 are the only two stars where projected rotation velocities different from zero are measured. All standard errors are determined via the bootstrapping method implemented in SPAS and described in section 8.1.

Star	Instrument	T_{eff} [K]	$\log\left(g(\mathrm{cm\,s^{-2}})\right)$ [dex]	v_{rad} [$\mathrm{km\,s^{-1}}$]	$v\sin(i)$ [$\mathrm{km\,s^{-1}}$]	$\log(y) = \log[n(\mathrm{He})/n(\mathrm{H})]$ [dex]
HD 4539	CASPEC	$20,800 \pm 1,100$	4.93 ± 0.14	7.8 ± 2.7	0.0 [a]	-2.27 ± 0.10
CD-35 15910	FEROS co-added	$26,900 \pm 100$	5.40 ± 0.03	RV-corr.	0.0 [a]	-2.94 ± 0.03
PHL 25	CASPEC	$17,800 \pm 600$	4.55 ± 0.10	102.7 ± 8.9	35.3 ± 6.9	-1.97 ± 0.06
PHL 25	HRS co-added	$19,300 \pm 300$	4.74 ± 0.03	RV-corr.	41.2 ± 3.0	-2.12 ± 0.04
PHL 382	FEROS co-added	$16,500 \pm 700$	3.77 ± 0.06	RV-corr.	0.0 [a]	-2.30 ± 0.12
SB 290	CASPEC co-added	$26,900 \pm 600$	5.46 ± 0.07	RV-corr.	47.4 ± 2.6	-2.60 ± 0.04
SB 290	FEROS co-added	$25,700 \pm 200$	5.25 ± 0.03	RV-corr.	62.5 ± 1.6	-2.48 ± 0.02
EC 03263-6403	FEROS co-added	$29,200 \pm 400$	5.39 ± 0.04	RV-corr.	0.0 [a]	-2.55 ± 0.04
EC 03591-3232	FEROS co-added	$28,600 \pm 200$	5.61 ± 0.02	RV-corr.	0.0 [a]	-2.12 ± 0.06
EC 12234-2607	FEROS co-added	$29,400 \pm 200$	5.67 ± 0.03	RV-corr.	0.0 [a]	-1.52 ± 0.03
EC 14338-1445	FEROS co-added	$28,500 \pm 300$	5.52 ± 0.03	RV-corr.	0.0 [a]	-2.85 ± 0.04
Feige 38	FEROS co-added	$28,900 \pm 300$	5.68 ± 0.03	RV-corr.	0.0 [a]	-2.66 ± 0.06
BD+48 2721	FOCES	$24,700 \pm 300$	5.34 ± 0.03	-1.5 ± 0.3	0.0 [a]	-2.18 ± 0.02
PG 1519+640	FOCES	$35,300 \pm 200$	6.10 ± 0.02	-2.4 ± 0.4	0.0 [a]	-2.00 ± 0.02
PG 1710+490	FOCES	$33,100 \pm 200$	5.51 ± 0.04	-0.7 ± 0.6	0.0 [a]	-2.27 ± 0.04

Note:

[a] Fixed value

11. Hybrid LTE/NLTE Analysis-Technique

In this chapter the hybrid LTE/NLTE approach based on ATLAS12, DETAIL, and SURFACE (see chapter 3.2.3 for details) is applied to the same set of spectra as in chapter 10 in order to redetermine atmospheric parameters. This approach has only been applied to subdwarf B stars before by Przybilla et al. (2005) and Latour et al. (2016). It has not been applied to any BHB star yet.

The main objective will be the distinction between $^{3}\mathrm{He}$ and $^{4}\mathrm{He}$ and the determination of their individual elemental abundances in the stellar atmospheres of the analyzed $^{3}\mathrm{He}$ B-type stars. Additionally, $^{4}\mathrm{He}/^{3}\mathrm{He}$ ratios also will be determined. Last but not least, metal abundances for C, N, O, Ne, Mg, Al, Si, S, Ar, and Fe will be derived, too, since the availability of the corresponding model atoms is ensured. All model atoms, including the lately developed $^{3}\mathrm{He}$ one by Maza et al. (2014), are provided by María-Fernanda Nieva and Norbert Przybilla from the *Institute for Astro- and Particle Physics, University of Innsbruck, Austria* and are used to calculate non-LTE occupation number densities within DETAIL and the emergent flux spectrum with SURFACE. Not only hydrogen and helium as for the LTE analysis, but also metal lines are synthesized. Again, macroturbulence ζ and microturbulence ξ are set to zero.

LTE model atmospheres computed with ATLAS12 are based on the mean metallicity for hot sdB stars. That means, metal abundances similar to that in Fig. 5.2.2 are used for atmospheric structure computations. The actual individual mean metal abundances for sdBs used for this analysis at hand are given in table 11.1 as base-10 logarithmic particle densities relative to the density of all particles.

Throughout the analysis presented in this chapter, both helium isotopes, $^{3}\mathrm{He}$ and $^{4}\mathrm{He}$, are treated simultaneously in order to facilitate NLTE calculations and to account for the overlap of lines and continua. The determination of the particular (atmospheric) parameters is done via a grid of model spectra in a 5-dimensional parameter space (effective temperature, T_{eff}, surface gravity, $\log(g)$, isotopic helium abundance for $^{3}\mathrm{He}$ and $^{4}\mathrm{He}$ as well as one of the individual metal abundances, $\log(n(\mathrm{X})) := \log\left[\frac{N(\mathrm{X})}{N(\text{all elements})}\right]$, where $X \in \{$C, N, O, Ne, Mg, Al, Si, S, Ar, Fe$\}$, and $n(\mathrm{X})$ is the ratio of the number density corresponding to element X to the number density of all the elements in the stellar atmosphere). That means, for each metal under consideration, a multi-dimensional mesh spanned by T_{eff} (step size: 1000 K), $\log(g)$ (step size: 0.2 dex), and isotopic helium abundances (step size: 0.2 dex) is calculated. Arbitrary parameter combinations within this mesh are approximated by linear interpolation between the calculated synthetic spectra. Each of the normalized spectra, containing spectral lines of hydrogen, helium, and the individual element under investigation, is divided by a model for same T_{eff}, $\log(g)$, and isotopic helium abundances, which only contains synthesized hydrogen and helium lines. A combined normalized spectra of the individual elements, taking into account all of the primary parameters, can be derived by multiplying the resulting

Table 11.1.: Individual mean metal abundances for hot subdwarf B stars used for the calculation of NLTE occupation number densities within DETAIL and SURFACE given as base-10 logarithmic particle densities relative to the density of all particles (Naslim et al., 2013). The values are similar to that displayed in Fig. 5.2.2. Solar abundances taken as a basis come from Asplund et al. (2009).

Sp.	Ab.	Tim. sol.	Sp.	Ab.	Tim. sol.	Sp.	Ab.	Tim. sol.	Sp.	Ab.	Tim. sol.	Sp.	Ab.	Tim. sol.
Li	-10.99	1	V	-7.11	10	Tc	-20.30	-	Eu	-11.52	1	Bi	-11.39	-
Be	-10.66	1	Cr	-5.40	10	Ru	-10.28	1.02	Gd	-10.99	0.95	Po	-20.30	-
B	-9.34	1	Mn	-5.61	10	Rh	-10.98	1.41	Tb	-11.72	1.05	At	-20.30	-
C	-4.84	0.06	Fe	-4.54	1	Pd	-10.39	1.20	Dy	-10.91	1.07	Rn	-20.30	-
N	-4.44	0.59	Co	-6.05	10	Ag	-10.84	1.82	Ho	-11.57	0.97	Fr	-20.30	-
O	-4.34	0.10	Ni	-4.82	10	Cd	-10.33	-	Er	-11.12	1	Ra	-20.30	-
F	-7.62	0.72	Cu	-6.85	10	In	-11.28	0.91	Tm	-11.92	1.05	Ac	-20.30	-
Ne	-5.04	0.12	Zn	-6.48	10	Sn	-8.00	100	Yb	-11.12	1.20	Th	-11.95	1.17
Na	-5.80	1	Ga	-8.00	10	Sb	-11.03	-	Lu	-11.95	0.98	Pa	-20.30	-
Mg	-5.24	0.16	Ge	-7.39	10	Te	-9.86	-	Hf	-11.33	0.72	U	-12.02	1
Al	-6.34	0.18	As	-9.74	-	I	-10.49	-	Ta	-12.16	-	Np	-20.30	-
Si	-5.54	0.10	Se	-8.70	-	Xe	-9.80	1	W	-11.19	1	Pu	-20.30	-
P	-6.63	1	Br	-9.50	-	Cs	-10.96	-	Re	-11.78	-	Am	-20.30	-
S	-5.54	0.24	Kr	-8.79	1	Ba	-9.86	1	Os	-10.64	1	Cm	-20.30	-
Cl	-6.81	0.54	Rb	-9.52	1	La	-10.94	1	Ir	-10.72	0.87	Bk	-20.30	-
Ar	-5.64	1	Sr	-7.17	100	Ce	-10.46	1	Pt	-10.42	-	Cf	-20.30	-
K	-7.01	1	Y	-7.83	100	Pr	-11.28	1.10	Au	-11.24	0.76	Es	-20.30	-
Ca	-5.70	1	Zr	-7.46	100	Nd	-10.62	1	Hg	-10.87	-			
Sc	-7.89	10	Nb	-10.63	0.89	Pm	-20.30	-	Tl	-11.27	0.74			
Ti	-6.09	10	Mo	-10.10	1.15	Sm	-11.08	1	Pb	-8.29	100			

"corrected" spectra with each other and with the hydrogen-helium model (Irrgang et al., 2014).

11.1. Pre-Analysis in SPAS

In order to achieve this thesis' main objective, i.e., the distinction between $^3\mathrm{He}$ and $^4\mathrm{He}$ and the determination of their individual elemental abundances in the stellar atmospheres of the analyzed $^3\mathrm{He}$ B-type stars, in total more than four parameters have to be fitted at once. Besides effective temperature, T_{eff}, surface gravity, $\log(g)$, and projected rotation velocity, $v \sin i$, a separation of the total helium abundance, $\log(y)$, into $^3\mathrm{He}$ and $^4\mathrm{He}$ isotopic abundances is necessary. Since SPAS is limited to four fit parameters only, namely T_{eff}, $\log(g)$, $\log(y)$, and $v \sin i$ (see section 8.1), this routine has to be modified. In the following, three different approaches on how to realize this will be presented. Each ansatz still has its own problems which will be discussed, too. Thus, SPAS turned out to be not well-suited and therefore is replaced by an ISIS procedure for the accurate determination of both isotopic helium abundances as will be described in section 11.3.

11.1.1. Variable Isotopic Helium Abundance and Fixed Abundance Ratio

The idea behind the first approach is the approximate determination of $^4\mathrm{He}/^3\mathrm{He}$ using the position of He I, 6678 Å, i.e., the helium absorption line with the strongest isotopic line shift. For this purpose, grids of synthetic model spectra for varying effective temperatures and surface gravities, but fixed $^4\mathrm{He}/^3\mathrm{He}$ abundance ratios, for instance 1/1, 1/2, 1/4, 1/8, 1/10, etc., are created, whereby the $^4\mathrm{He}$ isotopic helium abundance is always set to 1/1, 1/2, 1/4, 1/8, 1/10, etc. of the variable $^3\mathrm{He}$ abundance fitted as parameter $\log(y)$ within SPAS. Both, T_{eff} and $\log(g)$, are chosen such that both cover the individual temperature and gravity range for each star determined in LTE (see table 10.1). Thereby, all suitable hydrogen absorption lines in combination with He I, 6678 Å are implemented in SPAS' fitting routine. Secondly, the determined $\log(y)$ value in SPAS, i.e., the determined $^3\mathrm{He}$ abundance, is used to generate a new model grid exhibiting variable T_{eff} and $\log(g)$ as well as variable $^4\mathrm{He}/^3\mathrm{He}$ abundance ratio as a new fit parameter $\log(y)$ within SPAS. Here, the $^4\mathrm{He}/^3\mathrm{He}$ grid points should refine the roughly determined $^4\mathrm{He}/^3\mathrm{He}$ isotopic ratio derived in step one. Again, all suitable hydrogen absorption lines in combination with He I, 6678 Å are implemented in the fitting routine. Last but not least, the optimized $^3\mathrm{He}$ abundance is determined after generating a refined model grid using the precisely determined $^4\mathrm{He}/^3\mathrm{He}$ ratio of step two and a small T_{eff} and $\log(g)$ regime and fitting it to data, this time including all suitable hydrogen and helium absorption lines. Hence, an accurate measurement of T_{eff} and $\log(g)$ as well as of $^4\mathrm{He}/^3\mathrm{He}$ and $^3\mathrm{He}$ is guaranteed. The $^4\mathrm{He}$ isotopic abundance can be determined afterwards using $^4\mathrm{He}/^3\mathrm{He}$ and $^3\mathrm{He}$, whereby a linear scale is used in the following formulas:

$$R := {}^4\mathrm{He}/{}^3\mathrm{He} \tag{11.1}$$

$$^4\mathrm{He} = R \cdot {}^3\mathrm{He}\ . \tag{11.2}$$

Yet in practice it appears that the precisely determined $^4\mathrm{He}/^3\mathrm{He}$ isotopic ratio in step two is often significantly smaller than the roughly determined one of step one when using the fixed $^3\mathrm{He}$ abundance. The fitting routine implemented in SPAS achieves a better fit (see Fig. 11.1.1), i.e., finds a new minimum (see section 8.1 for details on the fitting algorithm used in SPAS), when reducing $^4\mathrm{He}/^3\mathrm{He}$ for fixed $^3\mathrm{He}$ abundance. This is due to the fact that the He I, 6678 Å line is weakened since the total helium abundance is reduced. However, a smaller $^4\mathrm{He}/^3\mathrm{He}$ abundance ratio then also results in a wrong isotopic shift towards the $^3\mathrm{He}$ position (see Fig. 11.1.1). Consequently, an accurate distinction between $^3\mathrm{He}$ and $^4\mathrm{He}$ as well as the correct determination of $^4\mathrm{He}/^3\mathrm{He}$ is not possible using this approach.

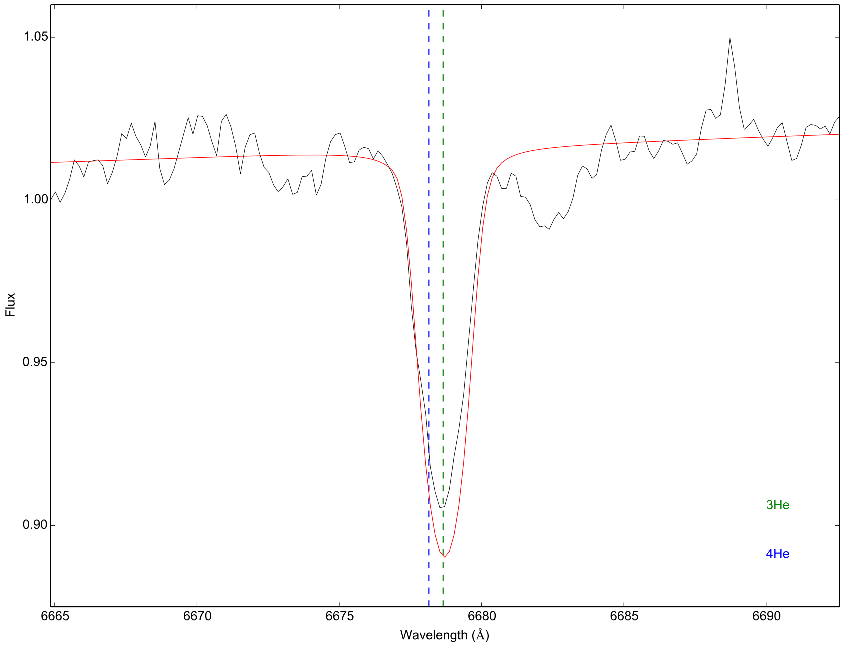

Figure 11.1.1.: Best fit for He I, 6678 Å in the co-added CASPEC spectrum of the $^3\mathrm{He}$ sdB star SB 290 for determined fixed $^3\mathrm{He}$ abundance and variable $^4\mathrm{He}/^3\mathrm{He}$ isotopic ratio after step two of the approach described in section 11.1.1. By reducing $^4\mathrm{He}/^3\mathrm{He}$ for fixed $^3\mathrm{He}$ abundance, the best fit not only weakens He I, 6678 Å, but also slightly shifts the line towards the $^3\mathrm{He}$ position. An accurate distinction between $^3\mathrm{He}$ and $^4\mathrm{He}$ as well as the correct determination of the isotopic ratio $^4\mathrm{He}/^3\mathrm{He}$ therefore is not possible.

11.1.2. Fixed Total Helium Abundance and Variable Abundance Ratio

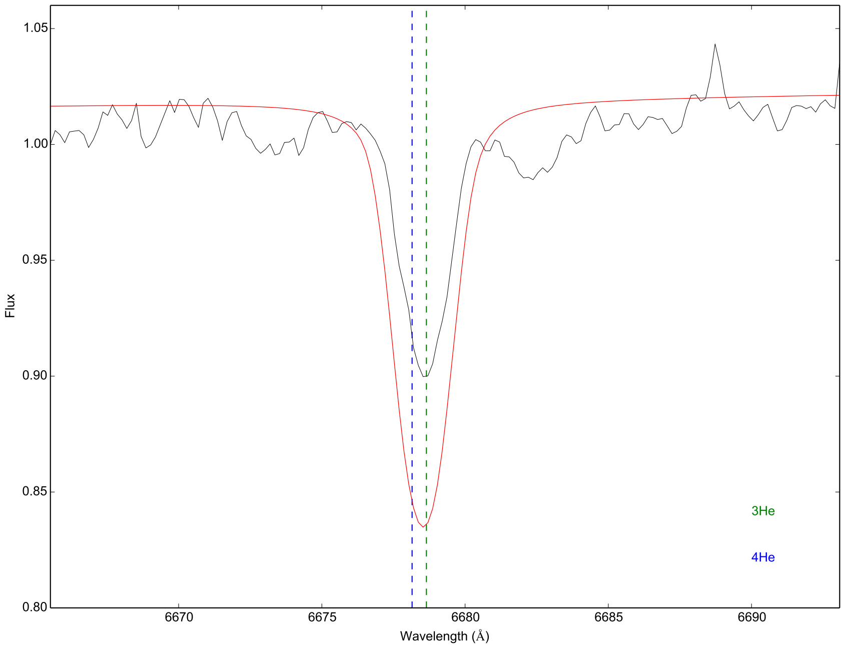

Figure 11.1.2.: Best fit for He I, 6678 Å in the co-added CASPEC spectrum of the $^3\mathrm{He}$ sdB star SB 290 for fixed total helium abundance and variable $^4\mathrm{He}/^3\mathrm{He}$ isotopic ratio as described in section 11.1.2. The variable abundance ratio results in a desired line shift, but the equivalent width (see Eq. 3.18) also changes in spite of the fixed total helium abundance. An accurate measurement of $^3\mathrm{He}$ and $^4\mathrm{He}$ in combination with a correct determination of the isotopic ratio $^4\mathrm{He}/^3\mathrm{He}$ therefore is not possible.

One of the problems of the approach presented in section 11.1.1 is the reduction of the total helium abundance in step two. In this way, SPAS achieves a better fit for the He I, 6678 Å line at the expense of a wrong isotopic shift towards the $^3\mathrm{He}$ position.

In principle, this should be solvable by using model grids exhibiting fixed total helium abundances on the one hand, but also variable abundance ratios corresponding to SPAS' fit parameter $\log{(y)}$ in combination with varying effective temperatures and surface gravities on the other hand. Both, T_{eff} and $\log{(g)}$, are again chosen such that both cover the individual temperature and gravity range for each star determined in LTE (see table 10.1). Also, the chosen fixed total helium abundances lie within the regime derived from LTE. All used model grids for individually fixed total helium abundance, hereafter denoted as He, should be fine enough. This also applies to the abundance-ratio plane so that $^4\mathrm{He}/^3\mathrm{He}$ can be precisely determined. This can be achieved by iteratively refining the initially created coarse model grids. All suitable hydrogen and helium absorption lines are included in SPAS' fitting routine in order to determine the best fit parameters for T_{eff}, $\log{(g)}$, and $^4\mathrm{He}/^3\mathrm{He}$.

The individual isotopic abundances of $^{3}\mathrm{He}$ and $^{4}\mathrm{He}$ can be derived afterwards by using the following correlations based on a linear scale:

$$^{3}\mathrm{He} + {}^{4}\mathrm{He} = \text{He} \quad \text{(Total helium abundance)} \tag{11.3}$$

$$R := {}^{4}\mathrm{He}/{}^{3}\mathrm{He} \quad \text{(Abundance ratio definition).} \tag{11.4}$$

This results in

$$^{3}\mathrm{He} = \frac{\text{He}}{R+1} \tag{11.5}$$

and

$$^{4}\mathrm{He} = \frac{R \cdot \text{He}}{R+1} \tag{11.6}$$

for both helium isotopic abundances.

However, in practice the picture again is different. On the one hand, the varying abundance ratio results in a desired shift of the He I, 6678 Å line. On the other hand, the equivalent width (see Eq. 3.18) of He I, 6678 Å, in particular its depth and width, also changes in spite of the fixed total helium abundance, though (see Fig. 11.1.2). In consequence, the abundance ratio $^{4}\mathrm{He}/^{3}\mathrm{He}$ not only influences the line shift, but also to a certain extent the line shape. Therefore, it is extremely difficult to determine $^{3}\mathrm{He}$ and $^{4}\mathrm{He}$ in combination with the correct abundance ratio using this approach. Hence, the only solution remaining in order to do the analysis within SPAS should make use of a variable total helium abundance as well as of a variable abundance ratio.

11.1.3. Variable Total Helium Abundance and Variable Abundance Ratio

As has been seen in the previous sections, an accurate hybrid LTE/NLTE SPAS analysis, including a correct determination of $^{3}\mathrm{He}$ and $^{4}\mathrm{He}$ as well as of $^{4}\mathrm{He}/^{3}\mathrm{He}$ could only be possible if the total helium abundance is incorporated as a variable fit parameter, too.

Again, this is done iteratively. Since this time not only a variable abundance ratio but also a varying total helium abundance is used, a second fit parameter in SPAS has to be fixed, though. This is in contrast to the two presented approaches from above. In this case, surface gravity, $\log(g)$, is fixed and its used value for each individual star results from the LTE results (see table 10.1). To summarize, a model grid consisting of varying total helium abundance and abundance ratio corresponding to SPAS' fit parameter $\log(y)$ and $\log(g)$, respectively, in combination with variable effective temperature but fixed surface gravity is generated at first. Here, T_{eff} and total helium abundance both cover the individual temperature and $\log(y)$ range for each star determined in LTE (see table 10.1). Second, if necessary, the projected rotation velocity, $v \sin i$, is fitted in SPAS, whereby only He I, 6678 Å is selected. This value then is fixed while adjusting the total helium abundance ($\log(y)$ fit parameter in SPAS) manually until the fit matches the line's equivalent width. Thereby, the line shape is more important than the line core position. Finally, T_{eff}, total helium abundance, and abundance ratio ($\log(g)$

fit parameter in SPAS) as well as $v \sin i$, if necessary, are fitted simultaneously. Now, it should be paid attention to the actual position of He I, 6678 Å and thus $^{4}\mathrm{He}/^{3}\mathrm{He}$ only, as all other fitted parameters are certainly wrongly determined using this single He I, 6678 Å line fit.
After having determined the abundance ratio $^{4}\mathrm{He}/^{3}\mathrm{He}$, another model grid is created. It exhibits variable total helium abundance ($\log(y)$ fit parameter in SPAS), varying effective temperature, T_{eff}, and surface gravity, $\log(g)$, but constant abundance ratio, $^{4}\mathrm{He}/^{3}\mathrm{He}$, namely the one derived via the presented procedure from above. The correct fit parameter values for T_{eff}, $\log(g)$, and total helium abundance, $\log(y)$, as well as $v \sin i$, if necessary, can then be determined by implementing all suitable hydrogen and helium absorption lines in SPAS' fitting routine. The individual isotopic abundances of $^{3}\mathrm{He}$ and $^{4}\mathrm{He}$ can be derived afterwards by using Eqs. (11.5) and (11.6).

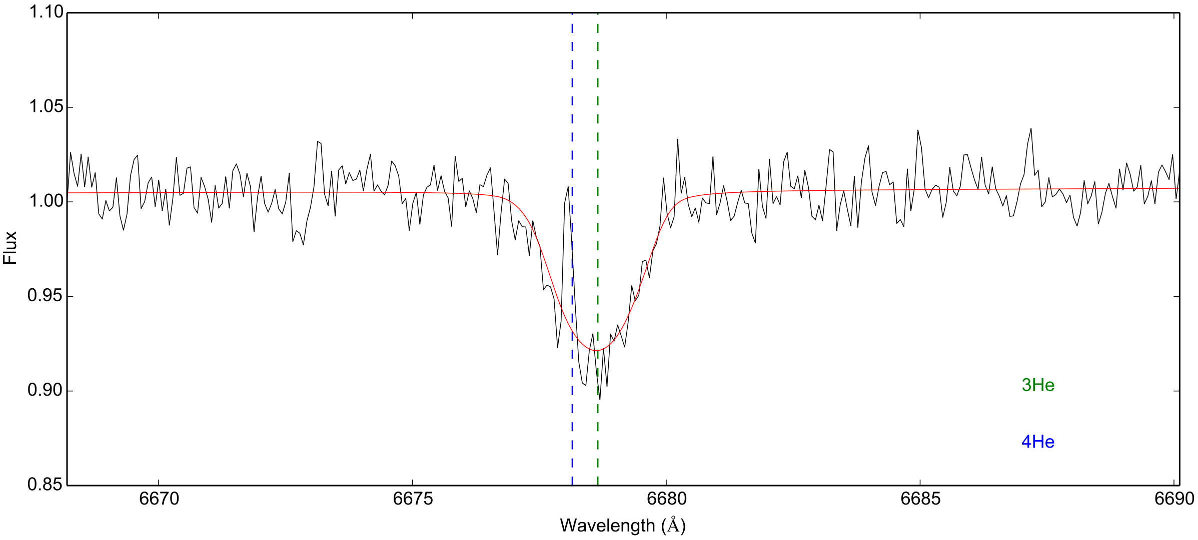

Figure 11.1.3.: Best fit for He I, 6678 Å in the co-added FEROS spectrum of the $^{3}\mathrm{He}$ sdB star SB 290 for variable total helium abundance and variable $^{4}\mathrm{He}/^{3}\mathrm{He}$ isotopic ratio as described in section 11.1.3. The spectrum has been RV-corrected applying the old rest-frame wavelength for the He I, 5875 Å line used for the LTE analysis (see section 9.3 for further information). All in all, the line can be reproduced, giving $v \sin i \sim 52$ km s^{-1}, $T_{\text{eff}} \sim 32,400$ K, total helium abundance ~ -2.80, and $^{4}\mathrm{He}/^{3}\mathrm{He} \sim 0.09$ for fixed surface gravity $\log(g) \sim 5.25$. The latter value comes from LTE as described in the text (to this, see also table 10.1).

This time, it becomes evident that an additional accurate radial velocity measurement is indispensable, though. This has already been mentioned in section 9.3 and shall be discussed in detail now. As has already been pointed out, an old rest-frame wavelength for the He I, 5875 Å line was used for RV measurements in SPAS (see table 9.2), namely 5875.750 Å. In order to demonstrate the significant effect of radial velocity on the derived abundance ratio, $^{4}\mathrm{He}/^{3}\mathrm{He}$, a comparison between a single He I, 6678 Å line fit as described earlier in this chapter using the actual rest-frame wavelength of 5875.621 Å derived from NIST and a second one using the old value of 5875.750 Å is performed by means of the co-added FEROS spectrum of the $^3\mathrm{He}$ sdB star SB 290 (see Fig. 11.1.3 and 11.1.4). The wavelength difference only results in a radial velocity shift of about 6.6 km s^{-1} which can be determined via Eq. (4.1). However, this small shift results in a surprisingly large change in $^4\mathrm{He}/^3\mathrm{He}$ of ~ 0.3, while leaving all other fit parameters more or less unchanged (compare the line fit of Fig. 11.1.4 to that of Fig. 11.1.3). This clearly indicates that the approach presented in this section is also not well-suited for the accurate measurement of $^3\mathrm{He}$ and $^4\mathrm{He}$ in combination with a correct determination of the isotopic ratio $^4\mathrm{He}/^3\mathrm{He}$. Before analyzing $^3\mathrm{He}$ and $^4\mathrm{He}$ in order to derive the correct $^4\mathrm{He}/^3\mathrm{He}$ isotopic ratio, v_{rad} has to be accurately determined. As already mentioned in section 9.3, this can be realized by including other absorption lines, in particular those resulting from metals. This is ensured in the analysis performed within ISIS (see section 8.2), whose procedure will be discussed in chapter 11.3.

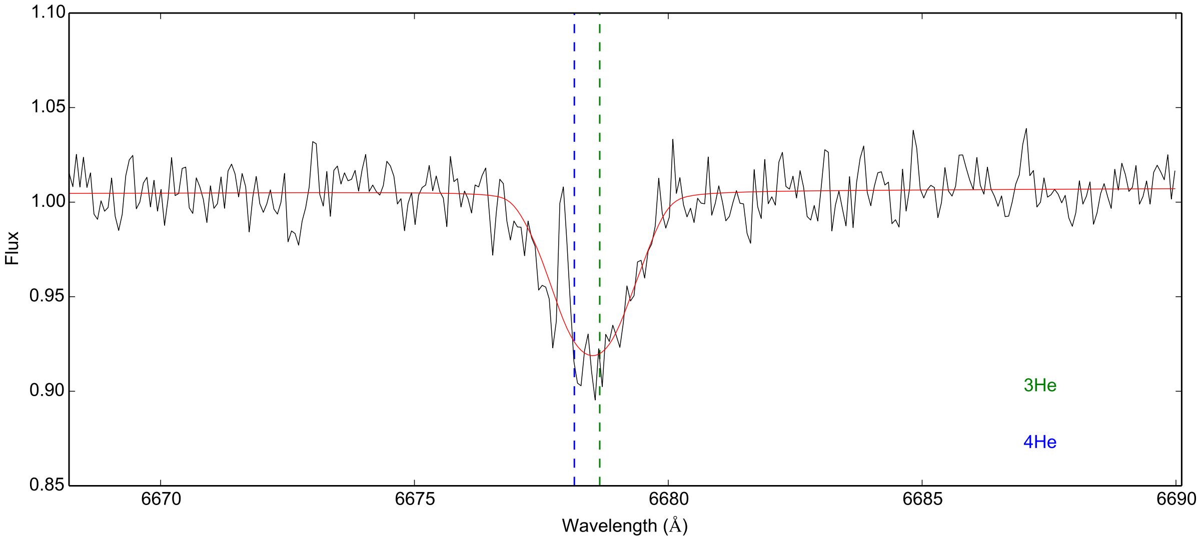

Figure 11.1.4.: Best fit for He I, 6678 Å in the co-added FEROS spectrum of the $^3\mathrm{He}$ sdB star SB 290 for variable total helium abundance and variable $^4\mathrm{He}/^3\mathrm{He}$ isotopic ratio as described in section 11.1.3. Thereby, a radial velocity of 6 km s^{-1} resulting from the difference between old and actual rest-frame wavelength for the He I, 5875 Å line is applied to the fit (see text for details). All in all, the line can be reproduced, this time giving $v \sin i \sim 49$ km s^{-1}, $T_{\mathrm{eff}} \sim 32,700$ K, total helium abundance ~ -2.85, and $^4\mathrm{He}/^3\mathrm{He} \sim 0.41$ for fixed surface gravity $\log(g) \sim 5.25$. The latter value comes from LTE as described in the text (to this, see also table 10.1). Surprising is the strong influence of v_{rad} on $^4\mathrm{He}/^3\mathrm{He}$. A difference of around 6 km s^{-1} results in a change in $^4\mathrm{He}/^3\mathrm{He}$ of ~ 0.3 (compare this figure to Fig. 11.1.3), clearly showing that the approach presented in section 11.1.3 is also not well-suited for the accurate measurement of $^3\mathrm{He}$ and $^4\mathrm{He}$ in combination with a correct determination of the isotopic ratio $^4\mathrm{He}/^3\mathrm{He}$.

11.2. The $^3\mathrm{He}$ Model Atom and its Influence on Spectral Line Formation

The $^3\mathrm{He}$ I model atom used for this hybrid LTE/NLTE analysis was developed by Maza et al. (2014) in order to perform a non-LTE spectral analysis of the $^3\mathrm{He}$ and $^4\mathrm{He}$ isotopes in the B-type main-sequence prototype HgMn star κ Cancri (see also κ Cnc in table 6.2). It was constructed in analogy to that of $^4\mathrm{He}$ by Przybilla (2005), whereby isotopic line shifts as measured by Fred et al. (1951) are taken into account (see table 6.1). Although set up as individual model atoms, $^3\mathrm{He}$ and $^4\mathrm{He}$ have to be treated simultaneously when solving the statistical equilibrium equations and the radiative transfer in DETAIL and SURFACE because all relevant lines are overlapping.

Fig. 11.2.1 displays synthetic model spectra showing He I, 4922 Å, He I, 5875 Å, and He I, 6678 Å for fixed effective temperature $T_{\mathrm{eff}} = 28\,000\,\mathrm{K}$, fixed surface gravity $\log(g) = 5.60$, but three different combinations of $^3\mathrm{He}$ and $^4\mathrm{He}$ abundances. T_{eff} and $\log(g)$ are chosen to lie within the typical hot subdwarf B regime. As can be seen from the top right panel of Fig. 11.2.1, the influence of both isotopes mainly manifests in the line strength of He I, 5875 Å and not in a measurable isotopic shift. This is in good agreement with the fact that He I, 5875 Å is used as a reference line (see chapter 6). However, in the case of He I, 6678 Å (bottom panel of Fig. 11.2.1) the isotopic ratio strongly influences the line shape. Here, the isotopic shift is clearly visible. Whereas no $^3\mathrm{He}$ component is visible if $^4\mathrm{He}/^3\mathrm{He} = 100$ (black curve), both components are identifiable if $^4\mathrm{He}/^3\mathrm{He} = 1$ (red curve). But the $^4\mathrm{He}$ component disappears for $^4\mathrm{He}/^3\mathrm{He} = 0.01$ (green curve). Concerning He I, 4922 Å, different isotopic ratios produce line shifts, too, but to a smaller extent compared to He I, 6678 Å (see top left panel of Fig. 11.2.1). This is to be expected since the pure line shift due to $^3\mathrm{He}$ enrichment only reads $\Delta\lambda = +0.33\,\text{Å}$ for He I, 4922 Å compared to $\Delta\lambda = +0.50\,\text{Å}$ for He I, 6678 Å (see table 6.1). Certainly, different combinations of $^3\mathrm{He}$ and $^4\mathrm{He}$ abundances also influence the line strengths of He I, 4922 Å and He I, 6678 Å, respectively.

11.3. Final Analysis in ISIS

As chapter 11.1 showed, SPAS has to be replaced in order to perform a reliable and meaningful analysis distinguishing between both helium isotopes, $^3\mathrm{He}$ and $^4\mathrm{He}$. It is extremely important to know the exact radial velocity v_{rad} of the individual stellar spectrum, since it strongly influences the measured abundance ratio $^4\mathrm{He}/^3\mathrm{He}$. A precise radial velocity determination can be realized by including other absorption lines besides the helium ones of table 9.2, in particular those resulting from metals. Hence, the whole hybrid LTE/NLTE spectral analysis is carried out completely within the "Interactive Spectral Interpretation System", short ISIS, which has already been briefly introduced in section 8.2.

Whereas SPAS fits a combination of Lorentzian and Gaussian function to the line profiles of preselected absorption lines, ISIS makes use of the whole spectrum at once, including all synthesized metal lines. In this way, the entire wavelength scale of the model spectrum can be

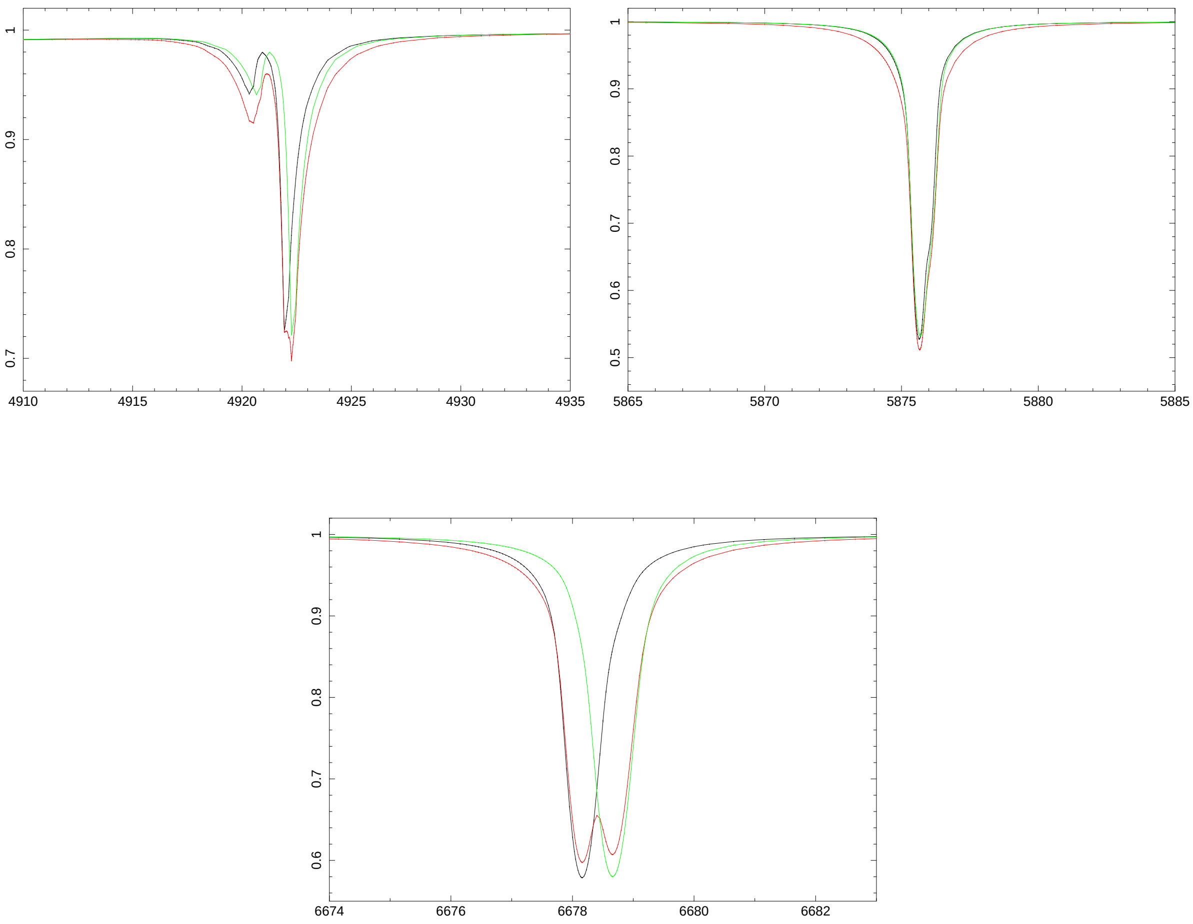

Figure 11.2.1.: *Top Left Panel*: Synthetic model spectra showing He I, 4922 Å for fixed effective temperature $T_{\text{eff}} = 28\,000$ K, fixed surface gravity $\log{(g)} = 5.60$, but three different combinations of $^3\mathrm{He}$ and $^4\mathrm{He}$ abundances. *Top Right Panel*: Same as left hand panel but for He I, 5875 Å. *Bottom Panel*: Same as above but for He I, 6678 Å. The corresponding helium isotopic abundances are $\log{(n(^3\mathrm{He}))} = -4.00$ and $\log{(n(^4\mathrm{He}))} = -2.00$ (black curve), $\log{(n(^3\mathrm{He}))} = -2.00$ and $\log{(n(^4\mathrm{He}))} = -2.00$ (red curve), and $\log{(n(^3\mathrm{He}))} = -2.00$ and $\log{(n(^4\mathrm{He}))} = -4.00$ (green curve), respectively. $^3\mathrm{He}$ introduces a visible isotopic line shift in the case of He I, 6678 Å and He I, 4922 Å, but not for He I, 5875 Å (see table 6.1) as predicted by Fred et al. (1951).

shifted and adjusted to the real spectrum according to Eq. (4.1), resulting in a more accurately determined value for v_{rad} than measurable using SPAS (Irrgang et al., 2014). Since the $^3\mathrm{He}$ isotopic shifts shall be illustrated, the individual spectra are again radial-velocity corrected, resulting in v_{rad} values of around zero. Furthermore, stellar rotation, $v \sin i$, is treated as described in section 3.3.2 (Irrgang et al., 2014).

It has to be pointed out that the list of synthesized metal lines is not complete, though. For instance, several O II lines are missing in the model atom for high temperatures. Together with other spectral regions exhibiting features being not properly included in the used synthetic models, these lines are overall excluded from fitting. Such features can be, for instance, the shape of absorption lines that cannot be fitted properly, in particular in the case of stars showing strong helium stratification like PHL 25 (see chapter 12.3 for further information on the evidence of helium stratification in some of the analyzed $^3\mathrm{He}$ (enriched) B-type stars), cosmics, normalization problems, interstellar or telluric lines, hot pixels, reduction artifacts, noise or non-overlapping diffraction orders at the end of the individual spectrum. Generally, light colors mark regions excluded from fitting in the helium line fits of Fig. 12.2.1 to 12.2.11, of Fig. 12.3.1 to 12.3.8, and of Fig. 12.3.10 to 12.3.12, as well as in the fitted spectra listed in appendix B.1.

In total, the analyzed sample now consists of 17 B-type stars, including the two $^3\mathrm{He}$ BHB stars (PHL 25 and PHL 382), and 15 sdB stars (13 definite $^3\mathrm{He}$ sdBs and two He-normal sdBs, HD 4539 and CD-35° 15910). Four $^3\mathrm{He}$ sdBs are taken from the hot subdwarf list of the ESO Supernova Ia Progenitor Survey (Lisker et al., 2005), being the only ones of this sample lying in the $^3\mathrm{He}$ sdB effective temperature regime between $\sim 27\,000$ K and $\sim 31\,000$ K and showing $^3\mathrm{He}$ enrichment (see section 6.4).

As already mentioned in the beginning of chapter 11, the determination of the particular (atmospheric) parameters is done via a grid of model spectra in a 5-dimensional parameter space (effective temperature T_{eff}, surface gravity $\log(g)$, isotopic helium abundance for $^3\mathrm{He}$ and $^4\mathrm{He}$ as well as one of the individual metal abundances, $\log(n(\mathrm{X})) := \log[\frac{N(\mathrm{X})}{N(\text{all elements})}]$, where $X \in \{$C, N, O, Ne, Mg, Al, Si, S, Ar, Fe$\}$). Within ISIS, T_{eff}, $\log(g)$ and both isotopic helium abundances have to be fitted simultaneously because of their degeneracy (see chapter 4 for details). Metal abundances are fitted successively afterwards. Since ISIS was designed to significantly facilitate the interpretation and analysis of X-ray spectra by means of useful functions and tools as well as several minimization algorithms, it is more flexible than SPAS. All of the implemented algorithms (non-gradient ones like *simplex* (see section 8.1) and *powell*, and gradient methods like *mpfit*, etc.) are based on a typical χ^2 minimization, being only feasible if the statistical uncertainties of the individually measured values are Gaussian distributed. Thereby, the so-called χ^2 is a measure for the goodness of fit, reading:

$$\chi^2 := \sum_{i=1}^{n} \frac{(y_i - y(x_i))^2}{\sigma_i^2} \ . \tag{11.7}$$

While y_i and σ_i describe the measured values (observed flux) and their corresponding errors (uncertainty in the observed flux), respectively, $y(x_i)$ are the individual fit functional values (model flux) at all data points (pixels) i, which have not been excluded from fitting. While a larger weight is given to lines with more data points, lines with less information are weighted less heavily. It can be shown (Press et al., 1986) that a maximum goodness of fit is accomplished for a minimization of χ^2. The number of degrees of freedom (DOF) is given by the difference between the number of measurement points n and the number of fit parameters k (DOF $=$ $n-k$). The so-called reduced χ^2, denoted as χ^2_{red}, can be calculated via:

$$\chi^2_{\text{red}} := \frac{\chi^2}{\text{DOF}} \tag{11.8}$$

and should lie near unity for the best fit (Press et al., 1986). This should be kept in mind as a "best fit signature" when performing the following analysis. $\chi^2_{\text{red}} < 1$ means that uncertainties are overestimated. Generally, the χ^2 landscape of all investigated problems is well-behaved and the global minimum is found after a relatively small number of steps (Irrgang et al., 2014).
After having determined accurate radial velocities for all spectra to be analyzed, the whole analysis is performed iteratively. At first, model grids are generated, including hydrogen and helium, but no metals, in order to synthesize all helium and hydrogen Balmer absorption lines. Higher Balmer transitions, i.e., H8-H12, cannot be synthesized reliably because of deficits of the line-broadening tables in the relevant wavelength regimes, though. The size of the individually generated grids is more or less given by the LTE values for effective temperatures, T_{eff}, surface gravities, $\log{(g)}$, and helium abundances, $\log{(y)}$ (see table 10.1). Effective temperatures range about 4000-5000 K around the individual stellar effective temperatures derived from the LTE analyses and have a step size of 1000 K. $\log{(g)}$ values range about 0.4 dex (with a step size of 0.2 dex) around the ones derived from LTE. The particular abundance intervals of both helium isotopes, ^3He and ^4He, also vary around the $\log{(y)}$ values derived from LTE. Nevertheless, large (about 1 dex) and fine (0.2 dex steps) are chosen in order to guarantee a correct determination of the individual isotopic abundances. Later, these intervals are narrowed when metals are included and a reasonable fit has been found. As only hydrogen Balmer and helium absorption lines should be reproduced as good as possible during this first iteration step, all metal lines are excluded from fitting to ensure a χ^2_{red} as low as possible. In particular, the He I, 6678 Å line core position should match the actual one since it is crucial for the correct determination of the individual abundance ratio $^4\text{He}/^3\text{He}$.
In order to determine the individual metal abundances, the mean metal abundances for hot subdwarf B stars are used as starting points and in the model atmosphere grid (see Fig. 5.2.2 and table 11.1). Typically, an analysis including four iteration steps is used. First, coarse model grids are generated, more or less exhibiting the same T_{eff} and $\log{(g)}$ regimes as used for the hydrogen and helium only grids. However, since ^3He and ^4He can be measured quite reasonably in most cases before including any metals, the corresponding abundance intervals are narrowed. At first, the individual metal abundance intervals lie around the corresponding mean abundance values for hot subdwarf B stars by ± 1 dex, setting up a very coarse grid, but extremely efficient to get a first estimate in which direction the fitting algorithm runs. The following iterations then use the same intervals for T_{eff}, $\log{(g)}$, ^3He and ^4He as before. Only metal abundances are adjusted. For instance, during the second iteration step, individual metal abundances are adjusted, if the fit ran towards one of the original interval edges. This is checked for all elements under investigation. The third iteration has not to be used in all

cases, but in those where the fit still ran towards one of the grid boundaries for one of the metals to be investigated after iteration step two. Last but not least, the final grid uses the size of the adjusted metal abundance intervals, although refining all of them. For this purpose, a narrow step size of 0.2 dex is used.

After having set up the final grid for each individual star, the best fit is found by a sequence of different fitting algorithms. First, *simplex* is used to find the global minimum of the χ^2 landscape. Then, *powell* is used to verify this global minimum. Eventually, *mpfit* checks the local landscape near the found global minimum. The aim is to achieve a reduced χ^2 of $\chi^2_{\text{red}} = 1$ for all performed fits. In most cases, $\chi^2_{\text{red}} \sim 1.1 - 3.0$ is achieved, whereby better fits are accomplished for higher spectral resolving powers (UVES, HRS, FEROS and FOCES) and high S/N. The analysis of CASPEC spectra mainly results in worse χ^2_{red} values. For all fits, the residuals are artificially constrained between values of $+2$ and -2, though. Additionally, strong deviations between best fit model spectrum and stellar spectrum are weighted less heavily - to be more precise - they are equally weighted. The residuals are artificially set to -1 and $+1$ in these regions, respectively. Consequently, the plotted residuals in the spectra of appendix B.1 cannot be simply used to determine poorly fitted spectral ranges or lines. However, by using these artificially set residuals, $\chi^2_{\text{red}} \approx 1$ is ensured for all analyzed spectra, in particular for the CASPEC ones, too.

Errors are also determined for all derived values via Monte Carlo simulations. All of them are given as 1σ ($\approx$ 68%) statistical confidence intervals throughout chapter 12.

12. Results of the Hybrid LTE/NLTE Analysis in ISIS

Before discussing the actual hybrid LTE/NLTE results derived from ISIS, it should be pointed out again that a self-consistent comparison of atmospheric parameters (T_{eff}, $\log(g)$) derived from both, LTE and hybrid LTE/NLTE, presented in this thesis is not readily possible since the set of analyzed hydrogen Balmer and helium absorption lines may be different. Thus, a systematic error which is mainly due to a lack of proper modeling of higher Balmer transition lines, i.e., H8-H12 in the case of the hybrid LTE/NLTE approach is introduced.

12.1. Effective Temperatures and Surface Gravities

Fig. 12.1.1 displays the T_{eff}-$\log(g)$ diagram derived from the hybrid LTE/NLTE analysis performed in ISIS. As in Fig. 10.0.3, each data point characterizes one of the analyzed stars of table 12.1. Again, if two (co-added) spectra are available, the individually measured parameter values are averaged and propagated errors are derived according to Gaussian error propagation afterwards. This is done for SB 290 and PHL 25 (see table 12.1). The color coding highlights stars showing (strong) helium stratification, which will be topic in section 12.3. Both He-normal comparison stars, HD 4539 and CD-35° 15910, are marked with green dots. As in the case of LTE, all derived effective temperatures and surface gravities of the analyzed hot subdwarf B stars match the extreme horizontal branch, i.e., the typical trend seen in the upper panel of Fig. 5.1.3. It should be also noted that the given 1σ errors are overall lower than for the LTE results.
The two dots at the cool end of the sequence displayed in Fig.12.1.1 again represent both $^{3}\mathrm{He}$ enriched BHB stars PHL 25 and PHL 382. As in the case of the LTE analysis, two stars lie within a hotter temperature regime of typical sdOBs (see section 5.1 for details on sdOBs). These represent the sdBs PG 1519+640 and PG 1710+490. Because the first singly ionized helium line, He II, 4686 Å, is predicted to be visible by model spectra at such high effective temperatures, but is not in the analyzed FOCES spectra, the derived temperatures are most likely not reliable for these stars. This has already been discussed in detail in chapter 10.
Nevertheless, all other $^{3}\mathrm{He}$ (enriched) sdB stars cluster in a narrow temperature strip between $\sim$ 26 000 K and 30 000 K, BD+48° 2721 being the only exception with $T_{\mathrm{eff}} = 22,300 \pm 100$ K, i.e., even cooler than in the LTE analysis. The four additionally analyzed $^{3}\mathrm{He}$ enriched sdB stars (HE 0929-0424, HE 1047-0436, HE 2156-3927, and HE 2322-0617) from the hot subdwarf list of the ESO Supernova Ia Progenitor Survey (Lisker et al., 2005) lie in this regime, too. As for the LTE results, this is overall in good agreement with the results of Geier et al. (2013a)

Table 12.1.: Atmospheric parameters and projected rotation velocities for the analyzed $^3\mathrm{He}$ and two He-normal comparison B-type stars (HD 4539, CD-35° 15910) determined via the hybrid LTE/NLTE approach performed in ISIS. All spectra have been RV-corrected. The four stars, whose UVES spectra have been analyzed, were taken from the hot subdwarf list of the ESO Supernova Ia Progenitor Survey (Lisker et al., 2005) and have been identified as $^3\mathrm{He}$ hot subdwarf B-type stars (see also tables 12.2 and 12.3). All statistical errors are given as 1σ (≈ 68%) confidence intervals.

Star	Instrument	T_{eff} [K]	$\log{(g(\text{cm s}^{-2}))}$ [dex]	v_{rad} [km s^{-1}]	$v \sin{(i)}$ [km s^{-1}]
HD 4539	CASPEC	$22,600 \pm 100$	5.24 ± 0.01	RV-corr.	$6.7^{+0.4}_{-0.5}$
CD-35 15910	FEROS co-added	$27,100 \pm 100$	5.35 ± 0.01	RV-corr.	7.1 ± 0.2
PHL 25	CASPEC	$20,800^{+200}_{-100}$	4.90 ± 0.02	RV-corr.	≤ 6.0 [a]
PHL 25	HRS co-added	$19,400^{+100}_{-200}$	4.75 ± 0.02	RV-corr.	$6.3^{+0.5}_{-0.1}$
PHL 382	FEROS co-added	$16,800 \pm 100$	3.85 ± 0.01	RV-corr.	13.3 ± 0.1
SB 290	CASPEC	$26,900 \pm 100$	5.48 ± 0.01	RV-corr.	$52.0^{+0.3}_{-0.2}$
SB 290	FEROS co-added	$26,500 \pm 100$	5.37 ± 0.01	RV-corr.	48.4 ± 0.1
EC 03263-6403	FEROS co-added	$28,800 \pm 200$	$5.19^{+0.02}_{-0.03}$	RV-corr.	$1.0^{+1.2}_{-1.1}$
EC 03591-3232	FEROS co-added	$28,700 \pm 100$	5.55 ± 0.01	RV-corr.	$0.0^{+1.2}_{-0.1}$
EC 12234-2607	FEROS co-added	$28,700 \pm 100$	5.59 ± 0.02	RV-corr.	$1.2^{+1.0}_{-1.3}$
EC 14338-1445	FEROS co-added	$27,900 \pm 100$	5.48 ± 0.02	RV-corr.	2.9 ± 0.6
Feige 38	FEROS co-added	$28,100 \pm 100$	5.53 ± 0.01	RV-corr.	$2.1^{+0.3}_{-0.5}$
BD+48 2721	FOCES	$22,300 \pm 100$	4.99 ± 0.01	RV-corr.	5.6 ± 0.3
PG 1519+640	FOCES	$35,400 \pm 100$	6.14 ± 0.02	RV-corr.	$0.9^{+0.8}_{-0.9}$
PG 1710+490	FOCES	$32,300 \pm 200$	$5.65^{+0.02}_{-0.03}$	RV-corr.	$1.6^{+1.3}_{-1.6}$
HE 0929-0424	UVES co-added	$29,300 \pm 100$	5.62 ± 0.01	RV-corr.	$6.3^{+0.2}_{-0.5}$
HE 1047-0436	UVES co-added	$29,600 \pm 100$	5.67 ± 0.01	RV-corr.	$6.6^{+0.1}_{-0.3}$
HE 2156-3927	UVES co-added	$27,600 \pm 100$	5.58 ± 0.01	RV-corr.	6.2 ± 0.1
HE 2322-0617	UVES co-added	$27,800 \pm 100$	5.43 ± 0.01	RV-corr.	$5.3^{+0.2}_{-0.3}$

Note:

[a] Upper limit

who measured a small strip between ~ 27 000 K and ~ 31 000 K for the $^3\mathrm{He}$ sdB stars (see chapter 6.3).

All in all, the difference in T_{eff} and $\log{(g)}$ between LTE and hybrid LTE/NLTE is ~ 2000 K and ~ 0.3 dex at most, respectively. Such high discrepancies are only measured for BD+48° 2721 and PHL 25, though. All other data points in Fig. 12.1.1 more or less match the particular ones of Fig. 10.0.3. Also, the additional systematic error introduced in the case of the hybrid LTE/NLTE approach, for instance mentioned at the beginning of chapter 12, generally has to be taken into account when comparing both analyses.

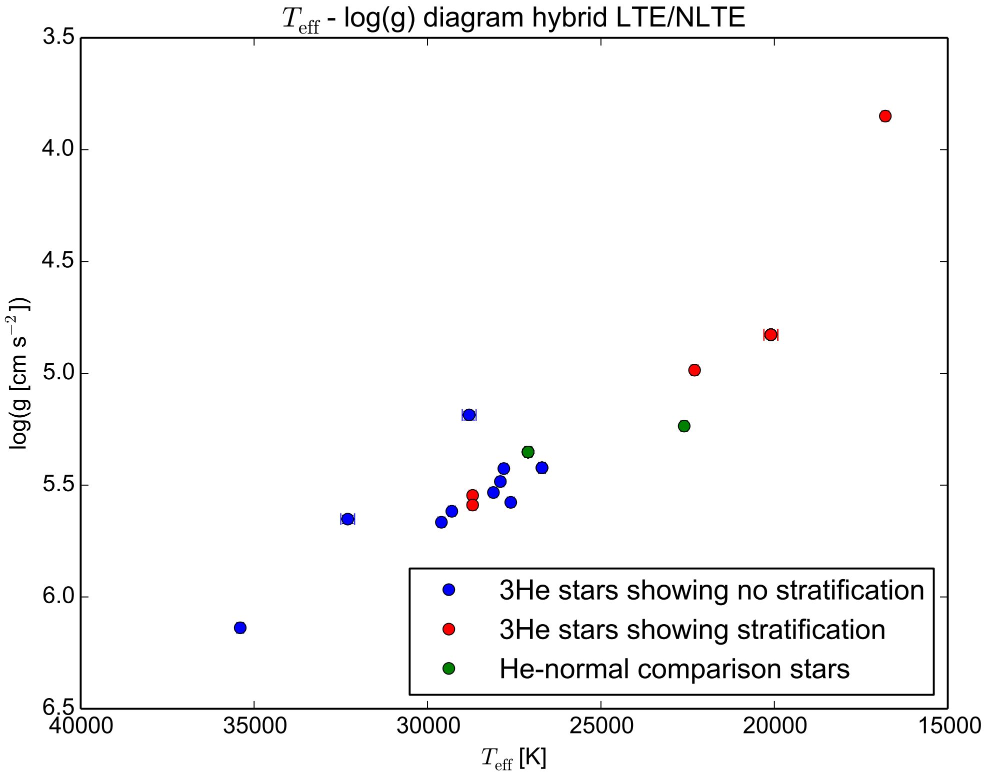

Figure 12.1.1.: T_{eff}-$\log(g)$ diagram derived from the hybrid LTE/NLTE analysis via ISIS. While stars showing no helium stratification are marked with blue dots, stars marked with red dots exhibit (strong) helium stratification (see chapter 12.3 for further information on found stratification effects). The He-normal comparison stars are represented by green dots. As in Fig. 10.0.3, the two dots at the cool end of the sequence represent the ^{3}He enriched BHB stars PHL 25 and PHL 382, whereas the two dots at the hot end correspond to the ^{3}He enriched sdB stars PG 1519+640 and PG 1710+490. Concerning the latter ones, the derived temperatures are too high for typical sdB stars. A possible explanation for this discrepancy could be bad normalization of the FOCES spectra (see chapter 10 and text for more details), in particular of the hydrogen Balmer lines.

12.2. ^{3}He and ^{4}He Helium Abundances

Table 12.3 displays the derived ^{4}He and ^{3}He abundances as well as the determined isotopic abundance ratios, ^{4}He/^{3}He, for all analyzed B-type stars. The corresponding helium line fits can be seen in Fig. 12.2.1 to 12.2.11, in Fig. 12.3.1 to 12.3.8 as well as in Fig. 12.3.10 to 12.3.12. All in all, the hybrid LTE/NLTE approach performed in ISIS gives reasonable results.

Star	$\frac{10^{[^4\mathrm{He}]}}{10^{[^3\mathrm{He}]}}$	Before analysis	After analysis
HD 4539	$\geq 6,000$	He-normal comparison sdB star	He-normal comparison sdB star
CD-35 15910	$\geq 1,200$	He-normal comparison sdB star	He-normal comparison sdB star
PHL 25	–	^{3}He enr. BHB star	^{3}He enr. stratified BHB star
PHL 25	–	^{3}He enr. BHB star	^{3}He enr. stratified BHB star
PHL 382	–	^{3}He enr. BHB star	^{3}He stratified BHB star
SB 290	$0.08^{+0.06}_{-0.05}$	^{3}He sdB star	^{3}He sdB star
SB 290	$0.07^{+0.04}_{-0.05}$	^{3}He sdB star	^{3}He sdB star
EC 03263-6403	0.01 ± 0.01	^{3}He sdB star	^{3}He sdB star
EC 03591-3232	–	^{3}He sdB star	^{3}He stratified sdB star
EC 12234-2607	–	^{3}He enr. sdB star	^{3}He enr. stratified sdB star
EC 14338-1445	0.13 ± 0.04	^{3}He sdB star	^{3}He sdB star
Feige 38	$0.16^{+0.03}_{-0.04}$	^{3}He sdB star	^{3}He sdB star
BD+48 2721	–	^{3}He enr. sdB star	^{3}He enr. stratified sdB star
PG 1519+640	$6.88^{+1.51}_{-1.66}$	^{3}He enr. sdB star	^{3}He enr. sdB star
PG 1710+490	$0.10^{+0.03}_{-0.04}$	^{3}He enr. sdB star	^{3}He sdB star
HE 0929-0424	$2.95^{+0.52}_{-0.59}$	He-normal sdB star	^{3}He enr. sdB star
HE 1047-0436	1.00 ± 0.10	He-normal sdB star	^{3}He enr. sdB star
HE 2156-3927	0.76 ± 0.08	He-normal sdB star	^{3}He enr. sdB star
HE 2322-0617	1.12 ± 0.10	He-normal sdB star	^{3}He enr. sdB star

Table 12.2.: Classification of sample stars before and after the performed hybrid LTE/NLTE analysis in ISIS. For stars showing (strong) helium stratification (marked in red), isotopic abundance ratios are not determined (see table 12.3). Both isotopic helium abundances derived for each star are listed in table 12.3.

Both He-normal comparison hot subdwarf B stars, HD 4539 and CD-35° 15910, exhibit no ^{3}He at all, resulting in a very high isotopic abundance ratio as might be expected. However, in these cases synthetic spectra have been calculated only using an upper limit of -6.00 dex for the ^{3}He abundance, which is, in fact, even subsolar. Using the solar value of $\sim$ -5.11 dex for the ^{3}He abundance would have resulted in less high abundance ratios for both stars, which are more reliable. Nevertheless, both comparison stars can be classified as He-normal stars. All other ^{3}He (enriched) B-type stars show ratios ranging from $\sim$ 0-7. Therefore, the derived abundance ratios match the observed isotopic line shifts.

Depending on the derived isotopic abundance ratio, the individual stars now can be actually classified into ^{3}He, ^{3}He enriched and ^{4}He stars. While the latter ones are characterized by a significantly high abundance ratio ($\gtrsim$ 1000 in this analysis), the natural boundary for the former ones lies around $^4\mathrm{He}/^3\mathrm{He} \sim 0.5$. Table 12.2 summarizes the classification for the sample stars and compares it to the one before the performed hybrid LTE/NLTE analysis. Most ^{3}He stars even exhibit abundance ratios below 0.2, meaning that in fact nearly all atmospheric helium is ^{3}He. Interestingly, two stars can now be additionally classified as ^{3}He B-type stars,

Table 12.3.: Isotopic helium abundances and abundance ratios for the analyzed ^{3}He and two He-normal comparison B-type stars (HD 4539, CD-35° 15910) determined via the hybrid LTE/NLTE approach performed in ISIS. The four stars, whose UVES spectra have been analyzed, were taken from the hot subdwarf list of the ESO Supernova Ia Progenitor Survey (Lisker et al., 2005) and have been identified as ^{3}He hot subdwarf B-type stars. As will be described in chapter 12.3, some of the analyzed stars show atmospheric stratification effects and therefore need more sophisticated synthetic model spectra. While these stars are marked in red, green stars do not show stratification in their spectra. If (strong) helium stratification is not present, all statistical errors are given as 1σ ($\approx$ 68%) confidence intervals. Otherwise, a fit by eye is performed (see note b).

Star	Instrument	$\log n(^4\mathrm{He})$ [dex]	$\log n(^3\mathrm{He})$ [dex]	$\frac{n(^4\mathrm{He})}{n(^3\mathrm{He})}$
HD 4539	CASPEC	-2.22 ± 0.01	≤ -6.00 [a]	$\geq 6,000$
CD-35 15910	FEROS co-added	-2.93 ± 0.01	≤ -6.00 [a]	$\geq 1,200$
PHL 25	CASPEC	-2.69 ± 0.04 [b]	-2.89 ± 0.05 [b]	b
PHL 25	HRS co-added	$-2.88^{+0.05}_{-0.04}$ [b]	-2.71 ± 0.03 [b]	b
PHL 382	FEROS co-added	-3.69 ± 0.08 [b]	-2.38 ± 0.01 [b]	b
SB 290	CASPEC	$-3.74^{+0.29}_{-0.23}$	$-2.63^{+0.03}_{-0.04}$	$0.08^{+0.06}_{-0.05}$
SB 290	FEROS co-added	$-3.71^{+0.18}_{-0.26}$	-2.57 ± 0.02	$0.07^{+0.04}_{-0.05}$
EC 03263-6403	FEROS co-added	$-4.80^{+0.42}_{-0.76}$	$-2.77^{+0.02}_{-0.03}$	0.01 ± 0.01
EC 03591-3232	FEROS co-added	$-3.52^{+0.12}_{-0.14}$ [b]	-2.08 ± 0.01 [b]	b
EC 12234-2607	FEROS co-added	-1.85 ± 0.03 [b]	-2.10 ± 0.04 [b]	b
EC 14338-1445	FEROS co-added	$-3.88^{+0.13}_{-0.11}$	$-2.99^{+0.02}_{-0.04}$	0.13 ± 0.04
Feige 38	FEROS co-added	$-3.55^{+0.07}_{-0.10}$	-2.77 ± 0.02	$0.16^{+0.03}_{-0.04}$
BD+48 2721	FOCES	-2.96 ± 0.03 [b]	-2.38 ± 0.02 [b]	b
PG 1519+640	FOCES	-2.05 ± 0.03	$-2.89^{+0.09}_{-0.10}$	$6.88^{+1.51}_{-1.66}$
PG 1710+490	FOCES	$-3.37^{+0.12}_{-0.16}$	-2.37 ± 0.03	$0.10^{+0.03}_{-0.04}$
HE 0929-0424	UVES co-added	-2.06 ± 0.03	$-2.53^{+0.07}_{-0.08}$	$2.95^{+0.52}_{-0.59}$
HE 1047-0436	UVES co-added	-2.73 ± 0.03	-2.73 ± 0.03	1.00 ± 0.10
HE 2156-3927	UVES co-added	$-2.91^{+0.04}_{-0.03}$	$-2.79^{+0.02}_{-0.03}$	0.76 ± 0.08
HE 2322-0617	UVES co-added	$-2.33^{+0.02}_{-0.03}$	$-2.38^{+0.03}_{-0.02}$	1.12 ± 0.10

Notes:

[a] The solar value of ~ -5.11 dex as an upper limit for the ^{3}He abundance would have resulted in a less high and more reliable abundance ratio (see text). Nevertheless, the particular He-normal comparison stars are identified.

[b] (Strong) helium stratification (see chapter 12.3 for further information).

namely the former $^3\mathrm{He}$ enriched sdB star PG 1710+490 and PHL 382, i.e., one of the two analyzed $^3\mathrm{He}$ enriched BHB stars. In total, four stars from the hot subdwarf list of the ESO Supernova Ia Progenitor Survey, short ESO SPY (Lisker et al., 2005), lying in the $^3\mathrm{He}$ sdB effective temperature regime between ~27 000 K and ~31 000 K, can be identified as $^3\mathrm{He}$ hot subdwarf B-type stars because of their isotopic ratio of ~ 1-3, although the analyzed UVES spectra do not include the helium line with the strongest isotopic shift, He I, 6678 Å (see also Fig. 12.2.8 to 12.2.11). In consequence, concerning the determination of $^3\mathrm{He}$ and $^4\mathrm{He}$ as well as of the isotopic abundance ratio, the tip of the iceberg cannot be reached for the stars from the ESO SPY project. The status of all other analyzed stars remains unchanged.

The two upper panels of Fig. 12.4.1 summarize the determined isotopic helium abundances in a $T_{\mathrm{eff}}-\log n(^3\mathrm{He})$ and $T_{\mathrm{eff}}-\log n(^4\mathrm{He})$ diagram for all stars, respectively. For stars, where two (co-added) spectra are available, measured abundances are averaged. This is the case for SB 290 and PHL 25, where propagated errors are derived according to Gaussian error propagation afterwards. Stars showing helium stratification are again marked with red dots and thus have to be treated with a grain of salt. Both He-normal comparison stars, HD 4539 and CD-35° 15910, are marked with green dots. All determined $^4\mathrm{He}$ abundances lie within the typical sdB regime (see chapter 5.1). For both He-normal comparison sdB stars, a subsolar upper limit for $^3\mathrm{He}$ (-6.00 dex) has been used for the analysis. As has already been discussed before, the solar $^3\mathrm{He}$ abundance of ~ -5.11 dex as an upper limit would have been more reliable. Thus, the used upper limits for these stars are not included in the $T_{\mathrm{eff}} - \log n(^3\mathrm{He})$ diagram of Fig. 12.4.1. Compared to the solar $^3\mathrm{He}$ value, all other determined $^3\mathrm{He}$ abundances are clearly overabundant, whereby a solar photospheric abundance ratio of $\sim 10^4$ and the solar $^4\mathrm{He}$ abundance determined by Asplund et al. (2009) are used. Thereby, the latter one is given as base-10 logarithmic particle density relative to the density of all particles.

The following chapters 12.2.1 to 12.2.3 summarize and discuss the individual helium line fits of both He-normal sdBs, HD 4539 and CD-35° 15910, as well as of the $^3\mathrm{He}$ sdBs showing no helium stratification.

12.2.1. The He-Normal Subdwarf B Stars HD 4539 and CD-35° 15910

Overall, the helium line fits of both He-normal hot subdwarf B stars, HD 4539 and CD-35° 15910, look reasonably well. All suitable $^{4}\mathrm{He}$ absorption lines, including the reference line, He I, 5875 Å, and both helium lines with the strongest possible isotopic line shift, He I, 4922 Å and He I, 6678 Å, are fitted perfectly as can be seen from Fig. 12.2.1 and 12.2.2.

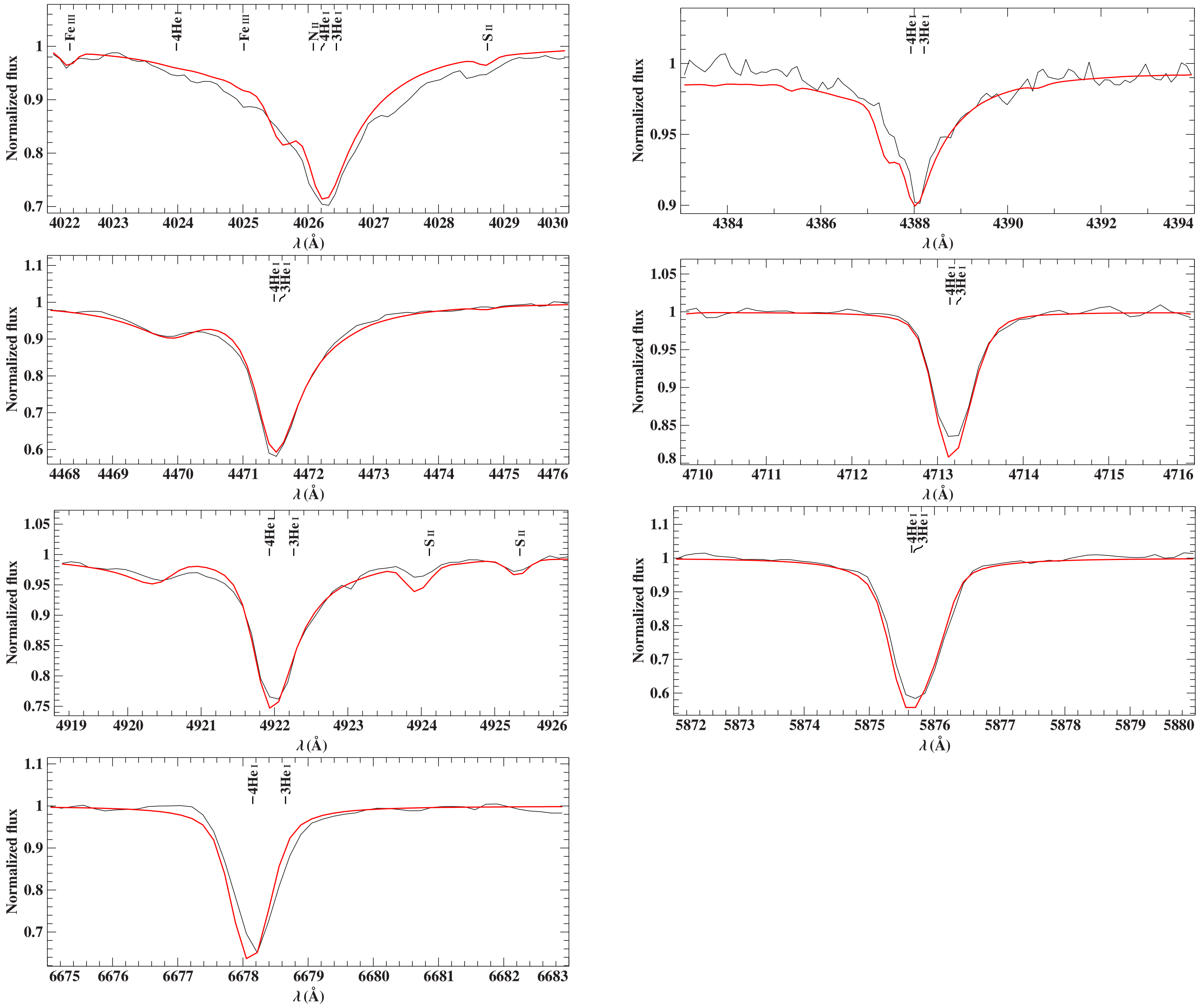

Figure 12.2.1.: Helium lines in the CASPEC spectrum of the He-normal comparison star HD 4539 used for the hybrid LTE/NLTE analysis with ISIS.

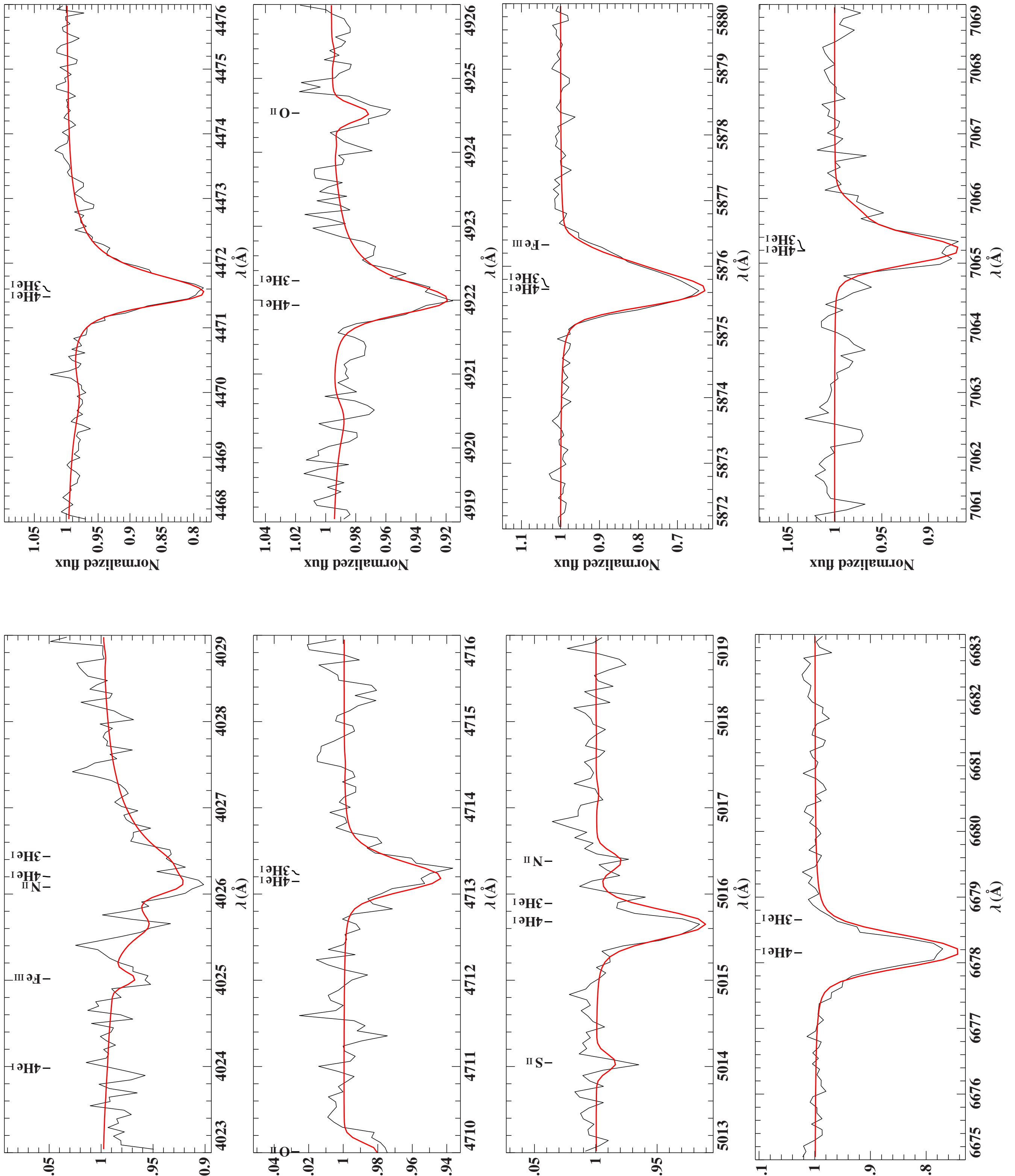

Figure 12.2.2.: Helium lines in the FEROS spectrum of the He-normal comparison star CD-35° 15910 used for the hybrid LTE/NLTE analysis with ISIS.

12.2.2. $^3\mathrm{He}$ Subdwarf B Stars with Known $^3\mathrm{He}$ Anomaly

Fig. 12.2.3 to 12.2.7 display the individual helium line fits of all known $^3\mathrm{He}$ sdB stars showing no stratification effects, i.e., of EC 03263-6403, EC 14338-1445, Feige 38, PG 1710+490, and PG 1519+640. Those with strong helium stratification will be discussed in section 12.3. Whereas all line fits look similarly well as for the He-normal sdBs in the case of EC 03263-6403, EC 14338-1445, Feige 38, and PG 1710+490 (see Fig. 12.2.3 to 12.2.6), in particular He I, 4922 Å and He I, 5875 Å show significant mismatches in the case of PG 1519+640 (see Fig. 12.2.7). However, the effective temperature derived for PG 1519+640 is overestimated as described before in chapters 10 and 12.1 and might therefore be a plausible explanation for the observed mismatches.

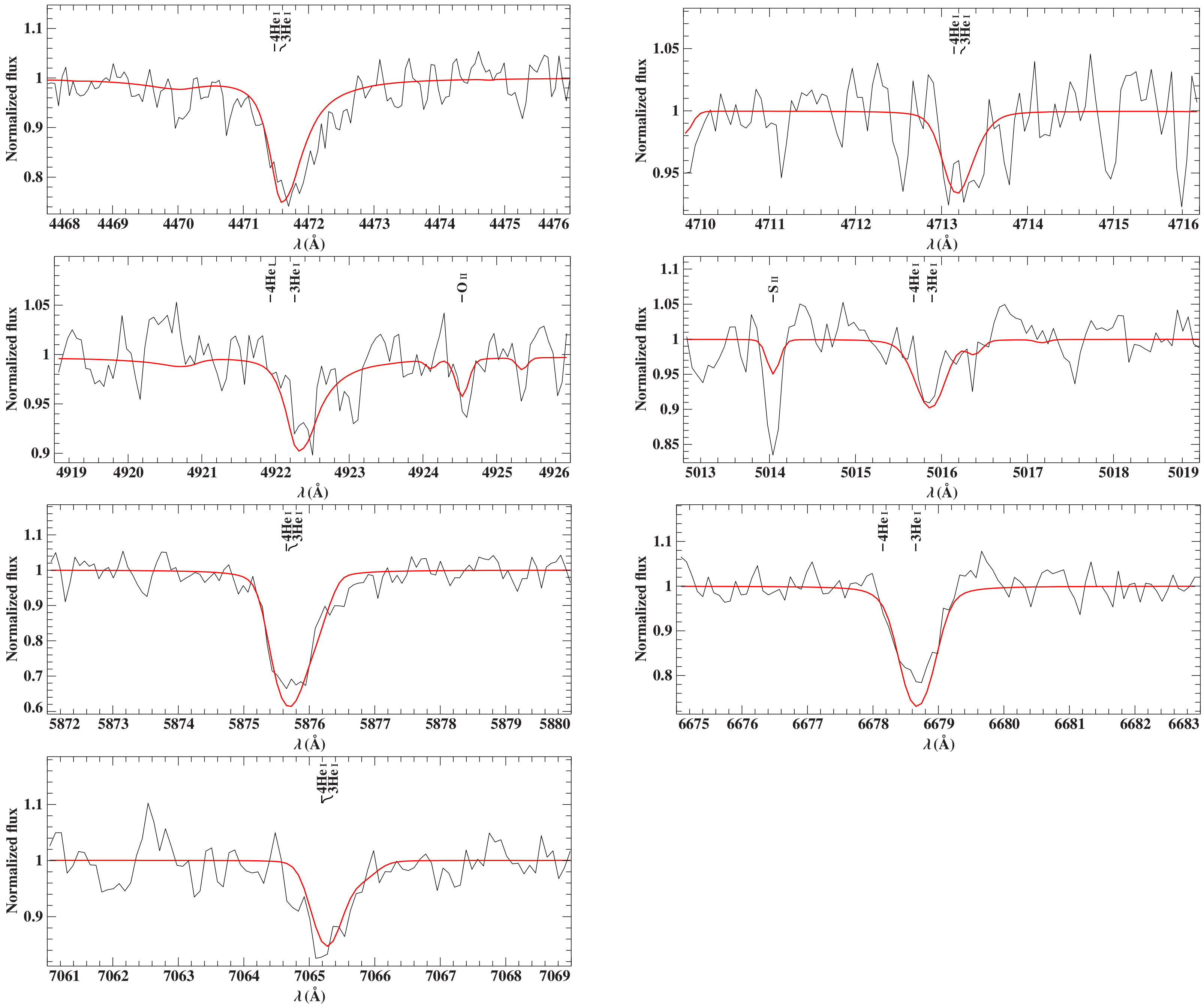

Figure 12.2.3.: Helium lines in the FEROS spectrum of the ^{3}He star EC 03263-6403 used for the hybrid LTE/NLTE analysis with ISIS.

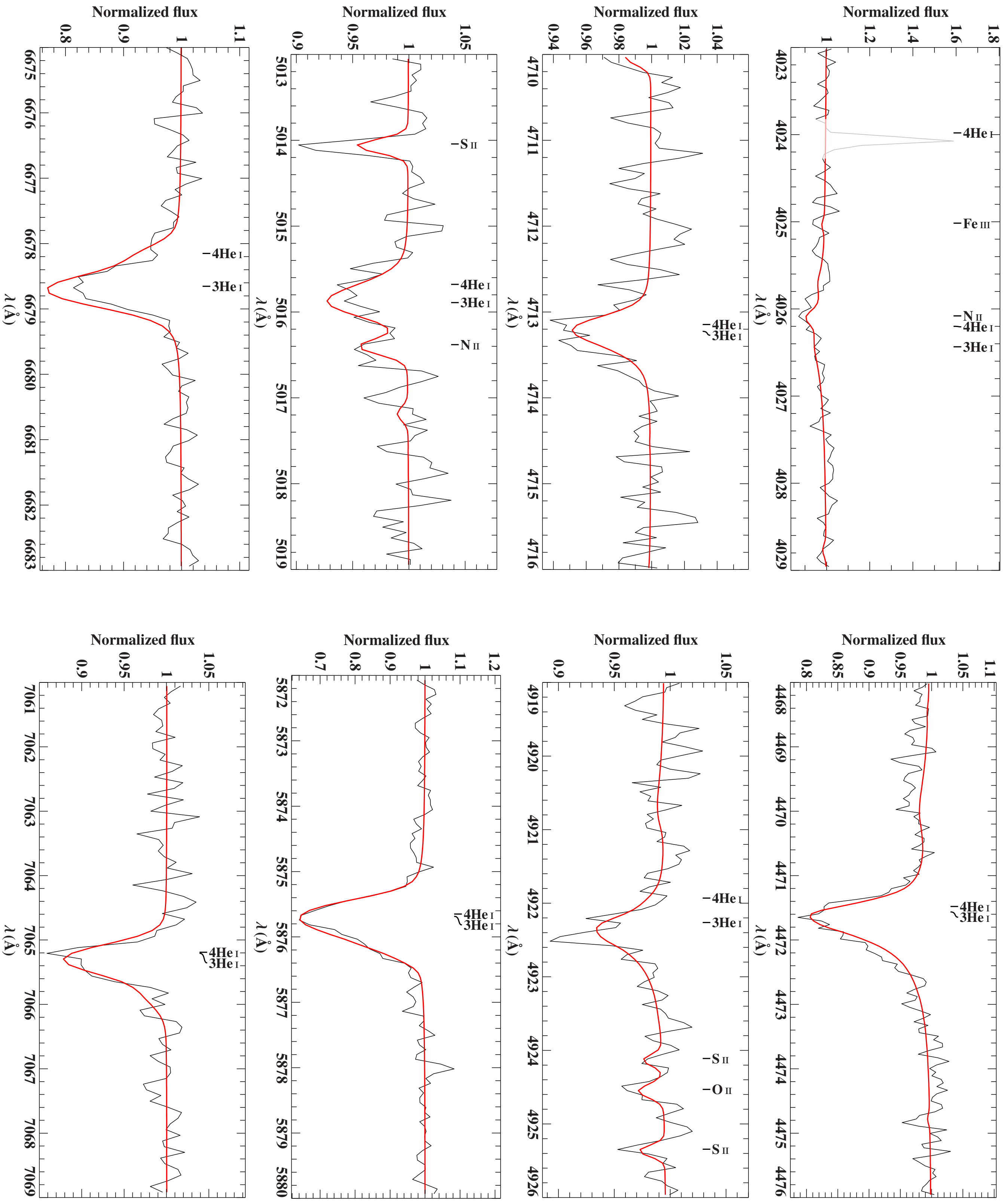

Figure 12.2.4.: Helium lines in the FEROS spectrum of the ^{3}He star EC 14338-1445 used for the hybrid LTE/NLTE analysis with ISIS.

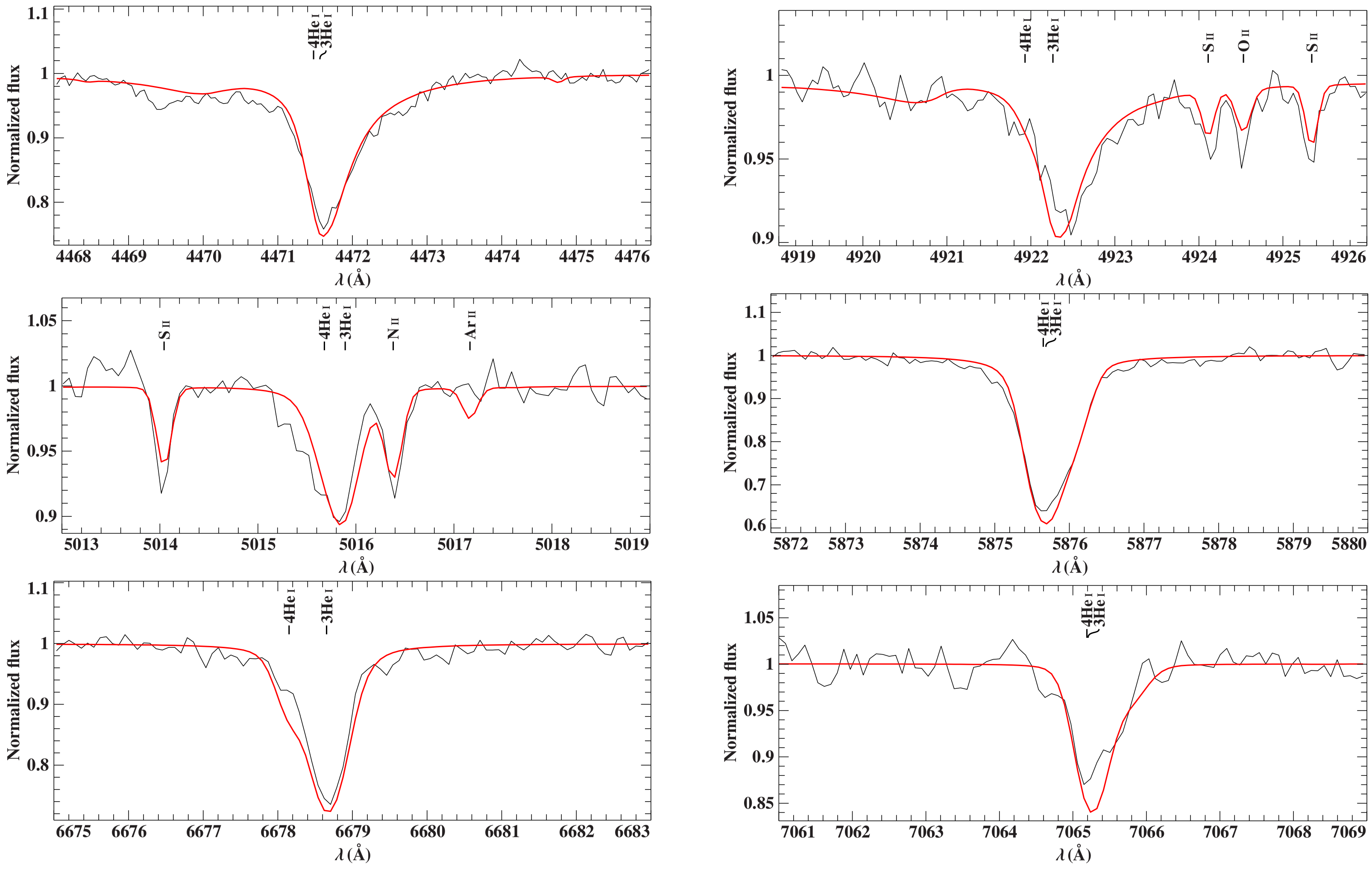

Figure 12.2.5.: Helium lines in the FEROS spectrum of the ^{3}He star Feige 38 used for the hybrid LTE/NLTE analysis with ISIS.

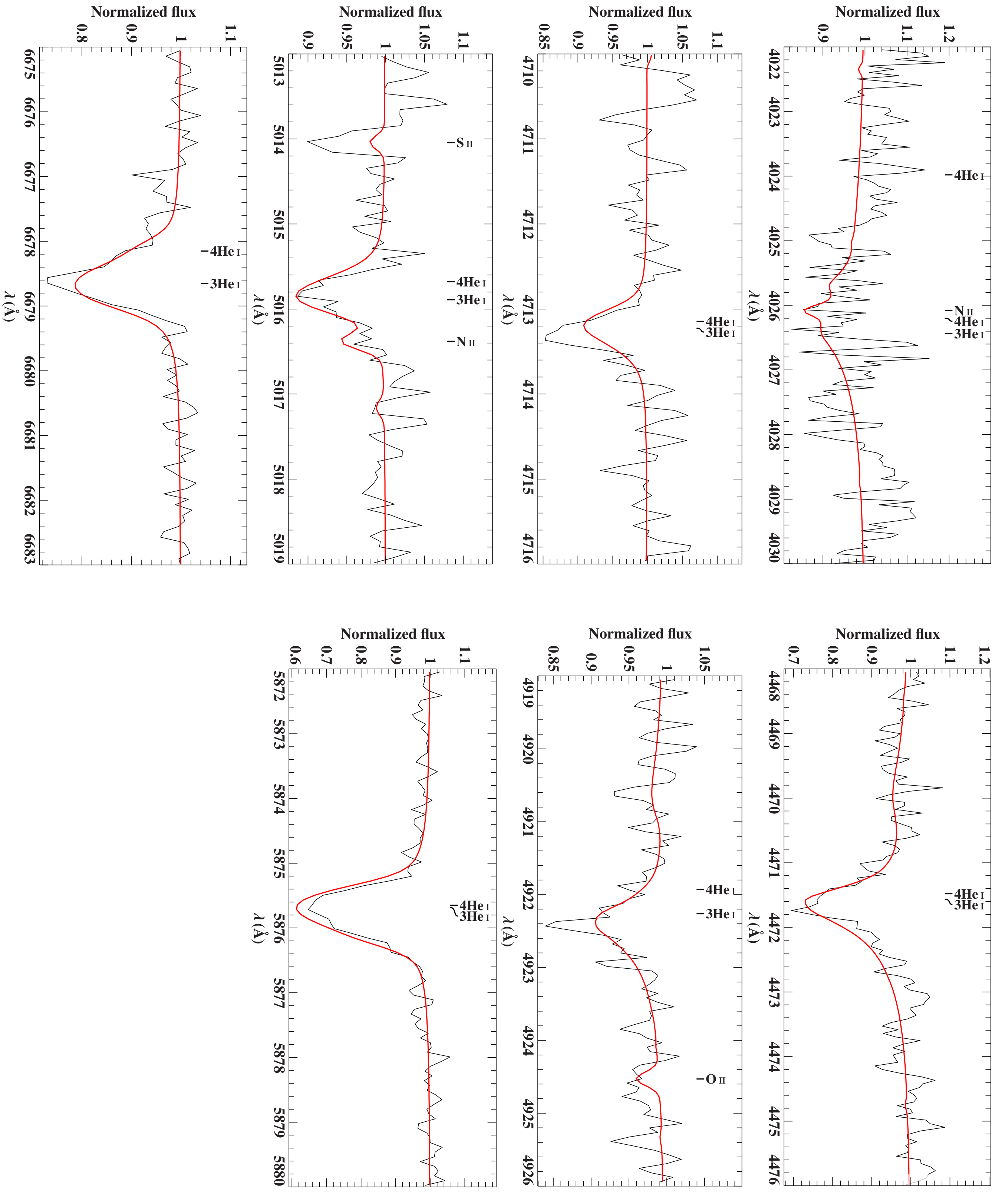

Figure 12.2.6.: Helium lines in the FOCES spectrum of the $^{3}\mathrm{He}$ star PG 1710+490 used for the hybrid LTE/NLTE analysis with ISIS.

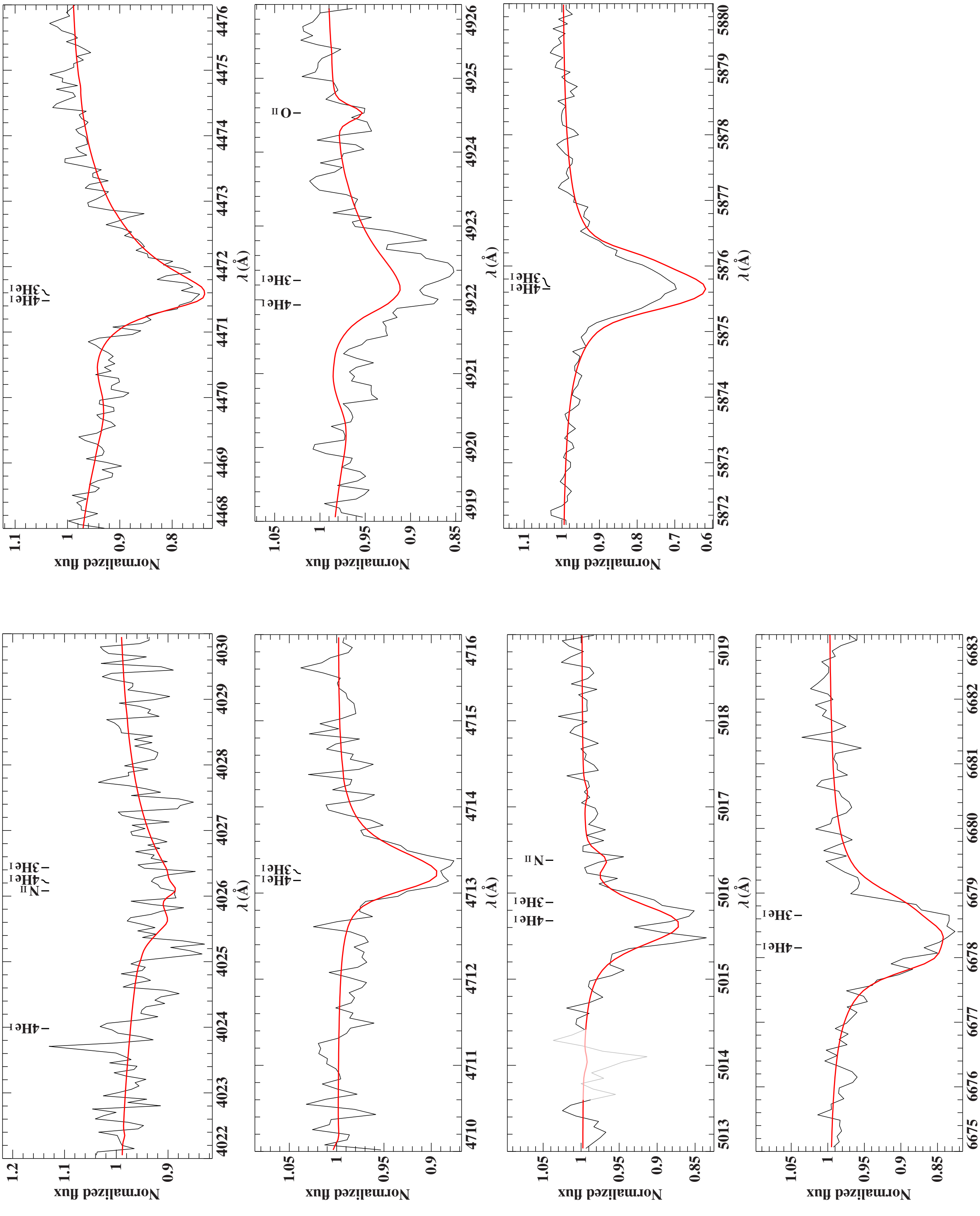

Figure 12.2.7.: Helium lines in the FOCES spectrum of the ^{3}He enriched star PG 1519+640 used for the hybrid LTE/NLTE analysis with ISIS.

12.2.3. Four $^{3}\mathrm{He}$ Subdwarf B Stars from the ESO SPY Project

Fig. 12.2.8 to 12.2.11 display the individual helium line fits of the four newly found $^{3}\mathrm{He}$ sdB stars from the ESO SPY project, i.e., of HE 0929-0424, HE 1047-0436, HE 2156-3927, and HE 2322-0617. Because of the wavelength regime covered by UVES (see sections 2.3 and 6.4), the analyzed spectra do not include the helium line with the strongest isotopic shift, He I, 6678 Å. Therefore, the second most sensitive line, He I, 4922 Å, is the most important indicator in order to spectroscopically study the $^{3}\mathrm{He}$ anomaly in these stars. In general, the analyzed UVES spectra are more noisy than those of the other stars (see also table 9.1). While the line fits look okay in the case of the rather noisy spectrum of HE 0929-0424, the core of the reference line, He I, 5875 Å, is too strong for HE 1047-0436 and HE 2156-3927. All other helium lines are fitted reasonably well for these stars, though. However, the 5875 Å mismatch even increases for HE 2322-0617, which also has slight mismatches in the cores of He I, 4472 Å and He I, 5015 Å.

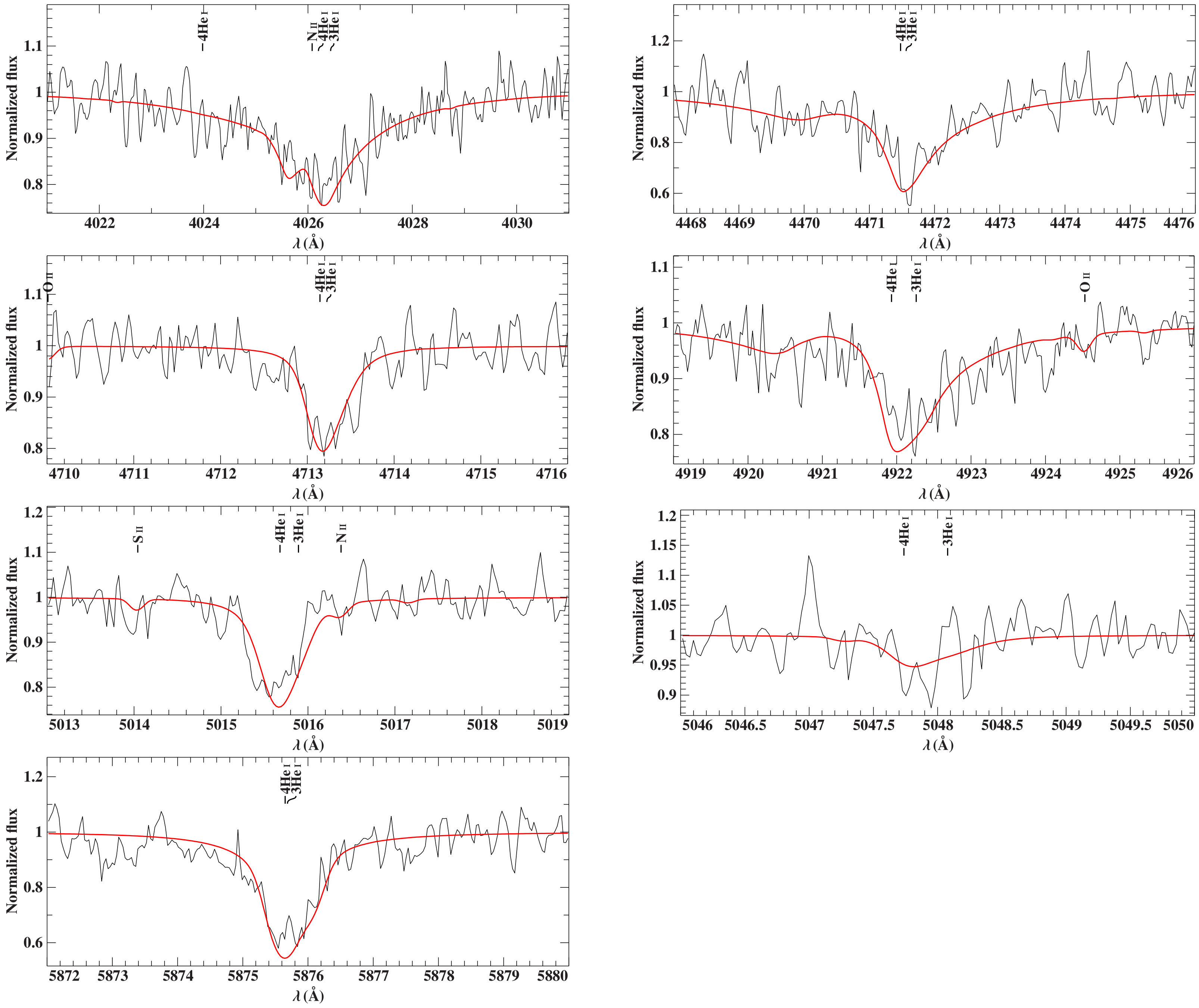

Figure 12.2.8.: Helium lines in the UVES spectrum of the ^{3}He enriched star HE 0929-0424 used for the hybrid LTE/NLTE analysis with ISIS.

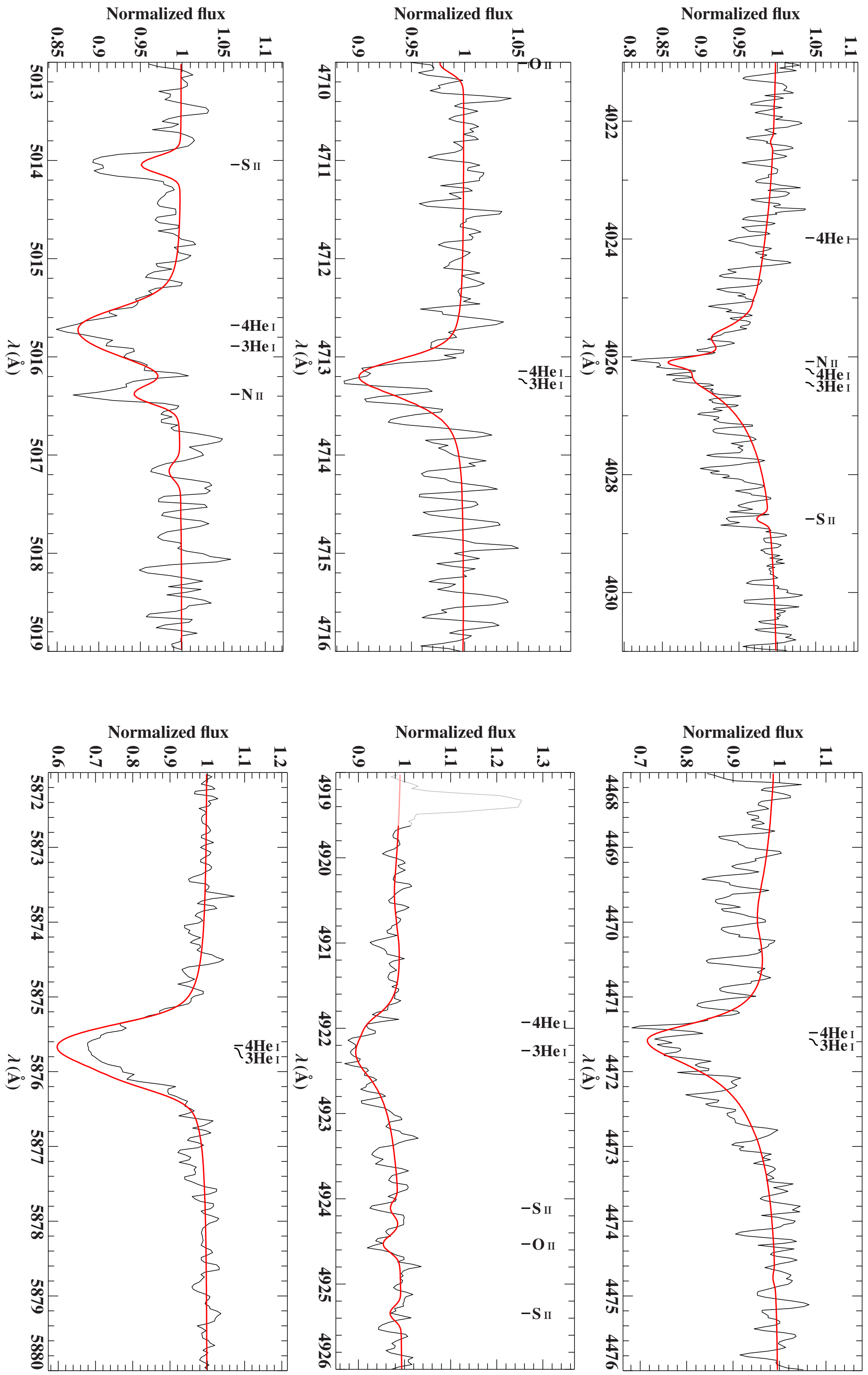

Figure 12.2.9.: Helium lines in the UVES spectrum of the $^{3}\mathrm{He}$ enriched star HE 1047-0436 used for the hybrid LTE/NLTE analysis with ISIS.

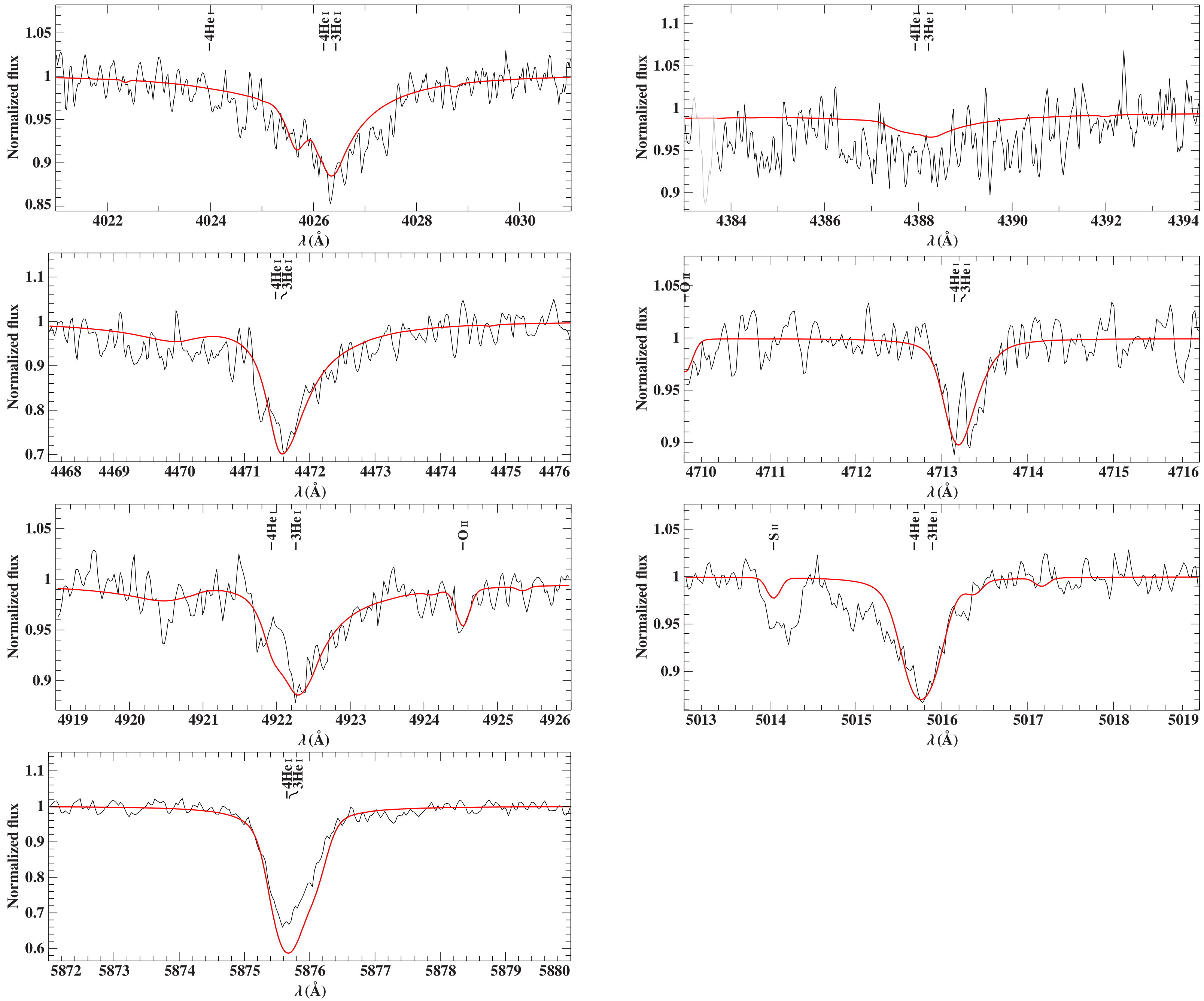

Figure 12.2.10.: Helium lines in the UVES spectrum of the ^{3}He enriched star HE 2156-3927 used for the hybrid LTE/NLTE analysis with ISIS.

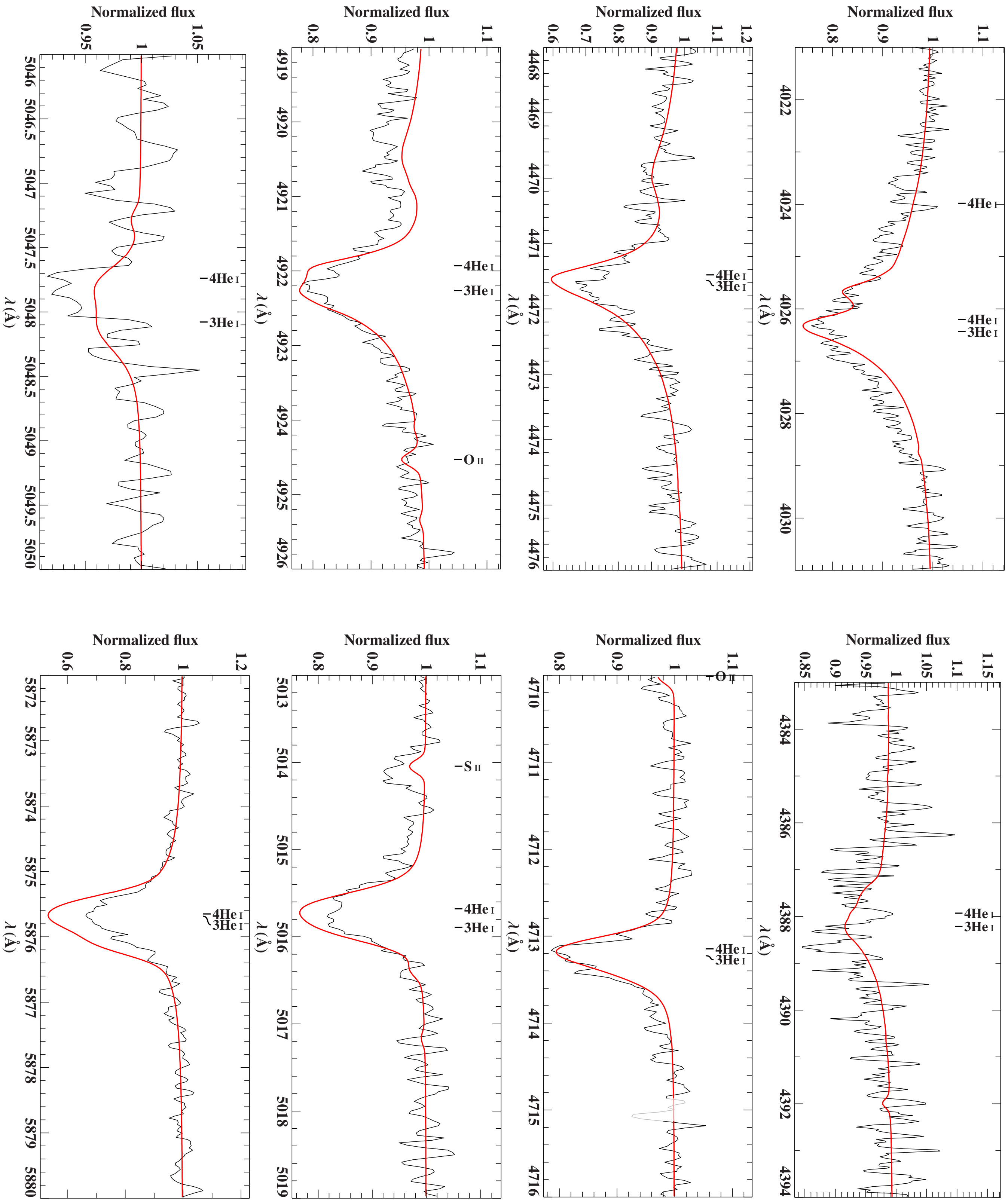

Figure 12.2.11.: Helium lines in the UVES spectrum of the ^{3}He enriched star HE 2322-0617 used for the hybrid LTE/NLTE analysis with ISIS.

12.3. Evidence for Helium Stratification

The observed helium line profiles are matched very well by the hybrid LTE/NLTE analysis for both He-normal comparison stars and many $^{3}\mathrm{He}$ sdBs, as shown in section 12.2. These stars are marked in green in tables 12.2, 12.3, 12.5, and 12.6. The observed mismatches (see chapters 12.2.2 and 12.2.3), as seen in a single (He I, 5875 Å) or in a few lines (He I, 5875 Å together with He I, 4471 Å and He I, 5015 Å) could be due to deficits of model atoms. Most remarkably, however, the helium line profiles cannot be reproduced satisfactorily at all for both analyzed $^{3}\mathrm{He}$ (enriched) BHB stars, PHL 25 and PHL 382, and the $^{3}\mathrm{He}$ (enriched) hot subdwarf B stars EC 03591-3232, EC 12234-2607, and BD+48° 2721 (see Fig. 12.3.1 to 12.3.8). A lack of appropriate model atoms can be ruled out in these cases, though. Therefore, these stars are marked in red in the particular tables 12.2, 12.3, 12.5, and 12.6 as well as in Fig. 12.1.1, 12.4.1, and 12.4.2. It has to be pointed out that in particular the results for both isotopic helium abundances, $^{3}\mathrm{He}$ and $^{4}\mathrm{He}$, as well as the resulting abundance ratios in tables 12.2 and 12.3 are only reliable to a certain extent for the relevant stars because of the insufficient line fitting.

The following chapters 12.3.1 and 12.3.2 summarize and discuss the individual helium line fits of both stratified $^{3}\mathrm{He}$ (enriched) BHB stars, PHL 25 and PHL 382, as well as of the $^{3}\mathrm{He}$ (enriched) sdBs showing helium stratification, i.e., of EC 03591-3232, EC 12234-2607, and BD+48° 2721.

12.3.1. The BHB Stars PHL 25 and PHL 382

Fig. 12.3.1 to 12.3.4 display the individual helium line fits of both $^{3}\mathrm{He}$ (enriched) BHB stars showing strong helium stratification, i.e., of PHL 25 and PHL 382. A significant mismatch of the cores of many He I lines is obvious. Only the weakest He I lines can be fitted half-decently for both stars.

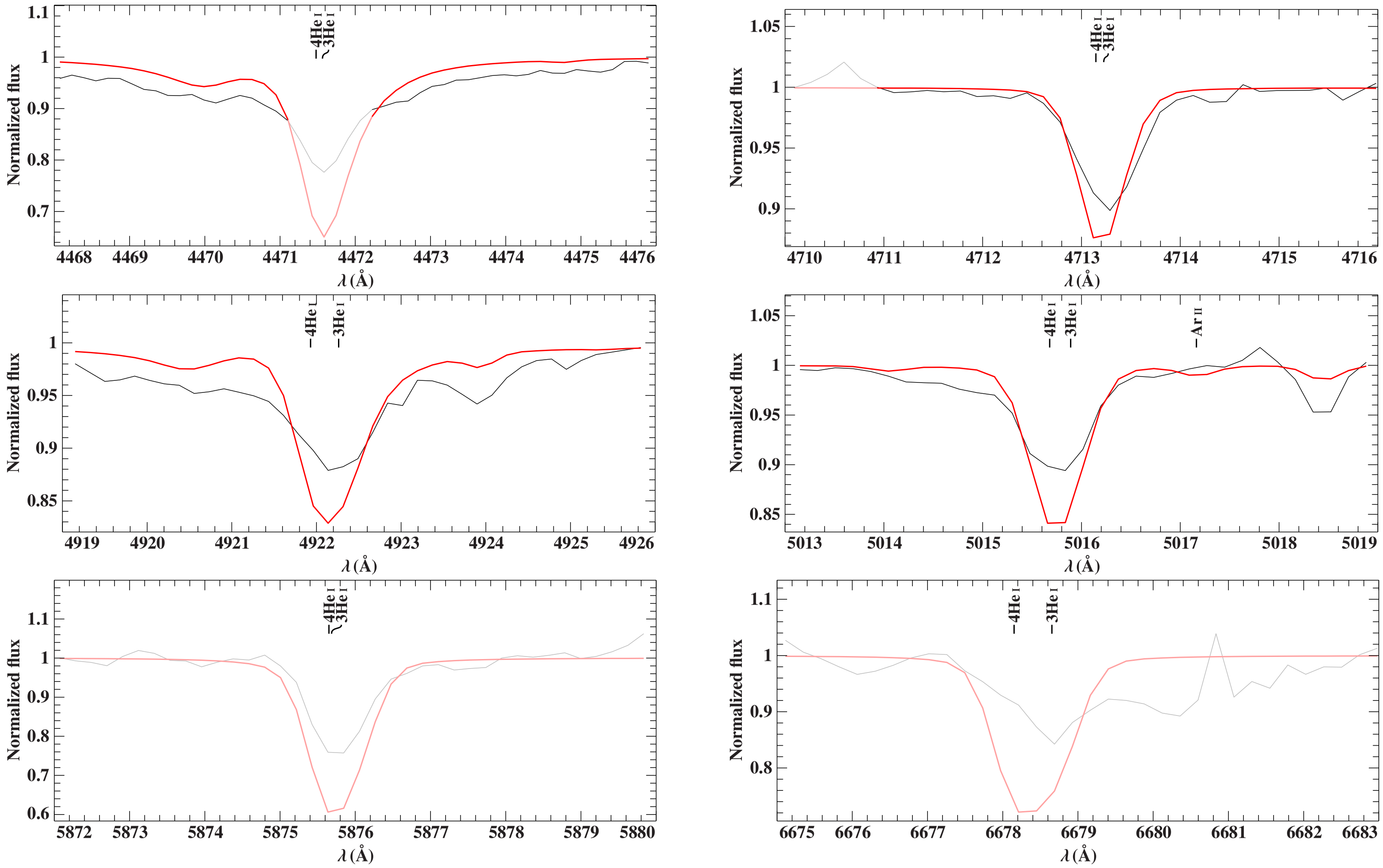

Figure 12.3.1.: Helium lines in the CASPEC spectrum of the $^3\mathrm{He}$ enriched star PHL 25. Note that not all of the shown lines have been used for the hybrid LTE/NLTE analysis with ISIS because of strong stratification effects and fitting problems coming along with it as is obvious from the mismatch of the cores of many He I lines (see chapter 12.3.3 for details). Consequently, light colored regions/helium lines have been excluded from fitting.

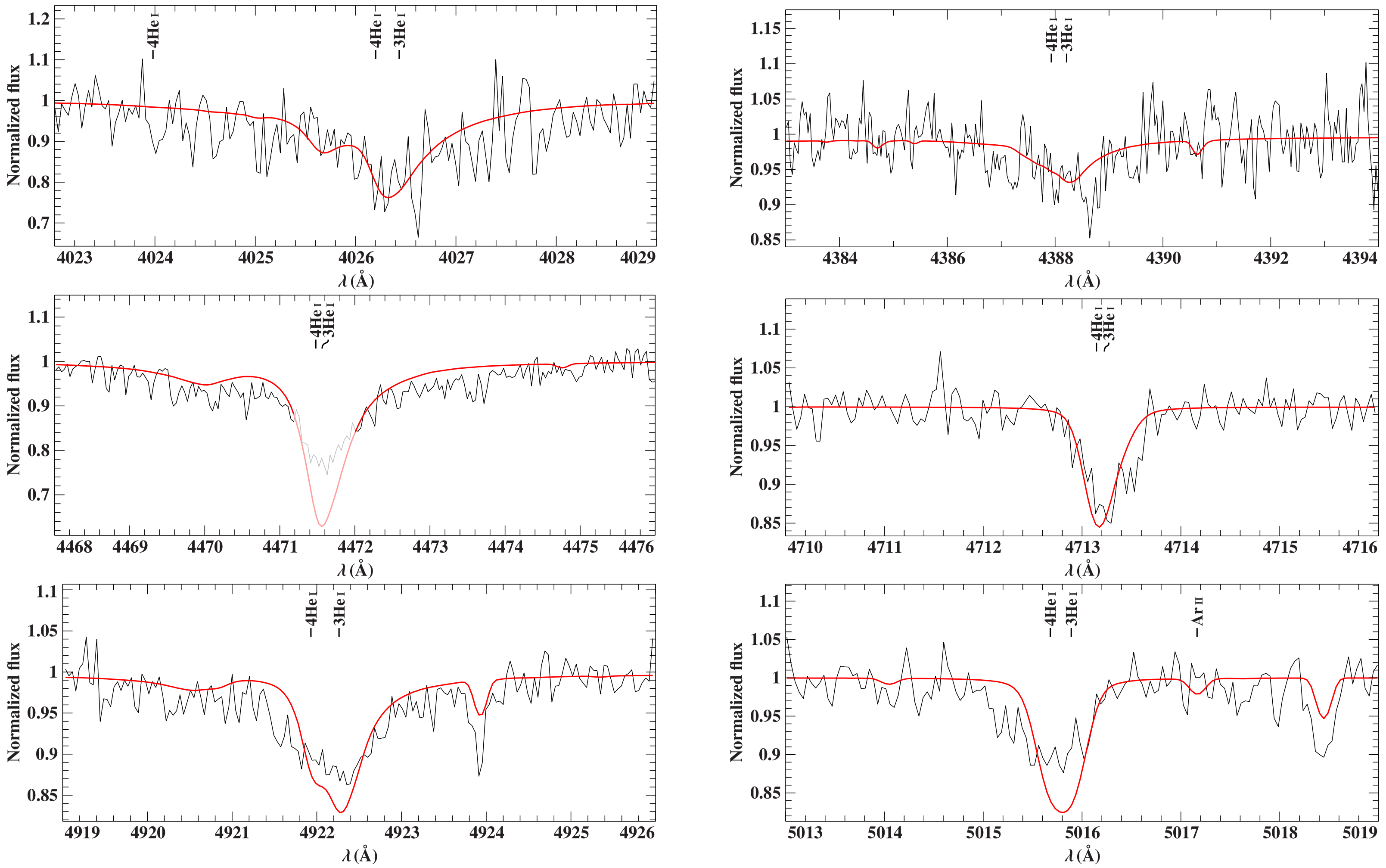

Figure 12.3.2.: Helium lines in the HRS spectrum of the $^3\mathrm{He}$ enriched star PHL 25 - Part 1. Note that not all of the shown lines have been used for the hybrid LTE/NLTE analysis with ISIS because of strong stratification effects and fitting problems coming along with it as is obvious from the mismatch of the cores of many He I lines (see chapter 12.3.3 for details). Consequently, light colored regions/helium lines have been excluded from fitting.

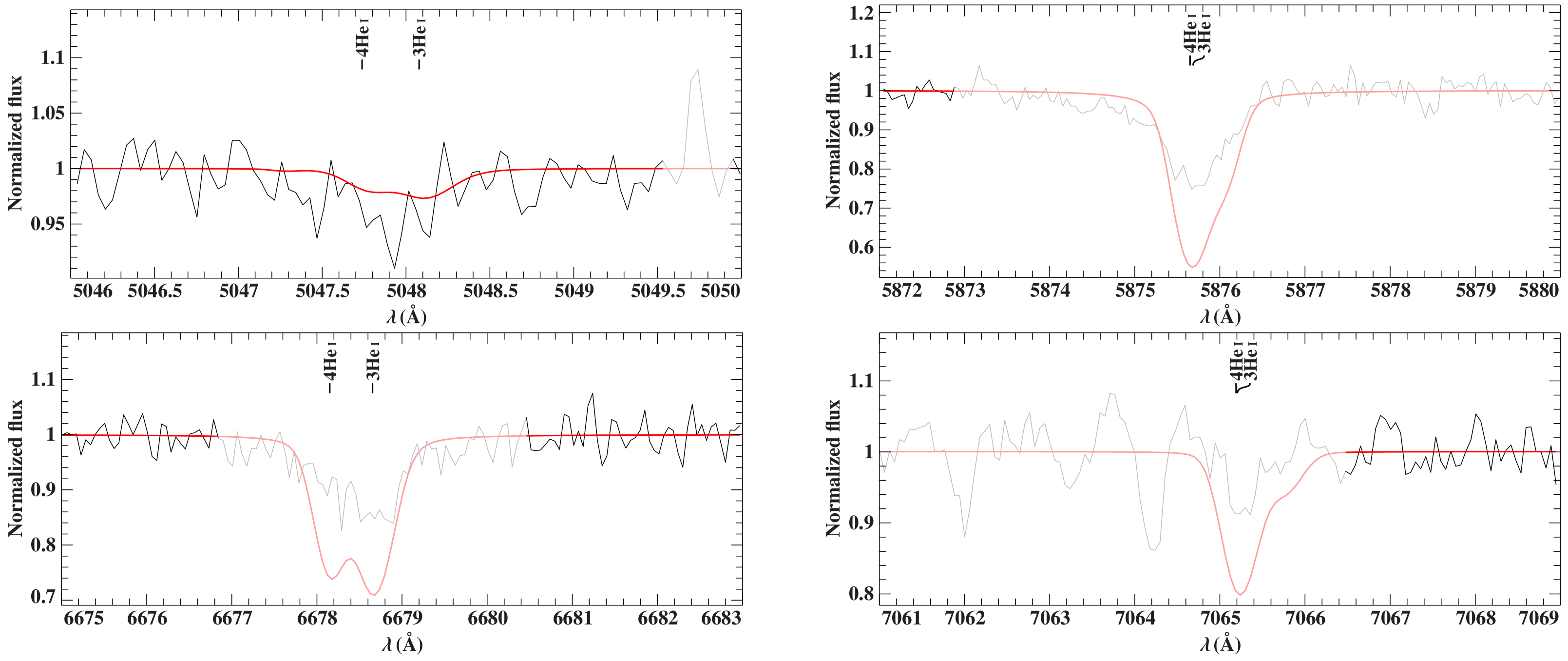

Figure 12.3.3.: Helium lines in the HRS spectrum of the $^3\mathrm{He}$ enriched star PHL 25 - Part 2. Note that not all of the shown lines have been used for the hybrid LTE/NLTE analysis with ISIS because of strong stratification effects and fitting problems coming along with it as is obvious from the mismatch of the cores of many He I lines (see chapter 12.3.3 for details). Consequently, light colored regions/helium lines have been excluded from fitting.

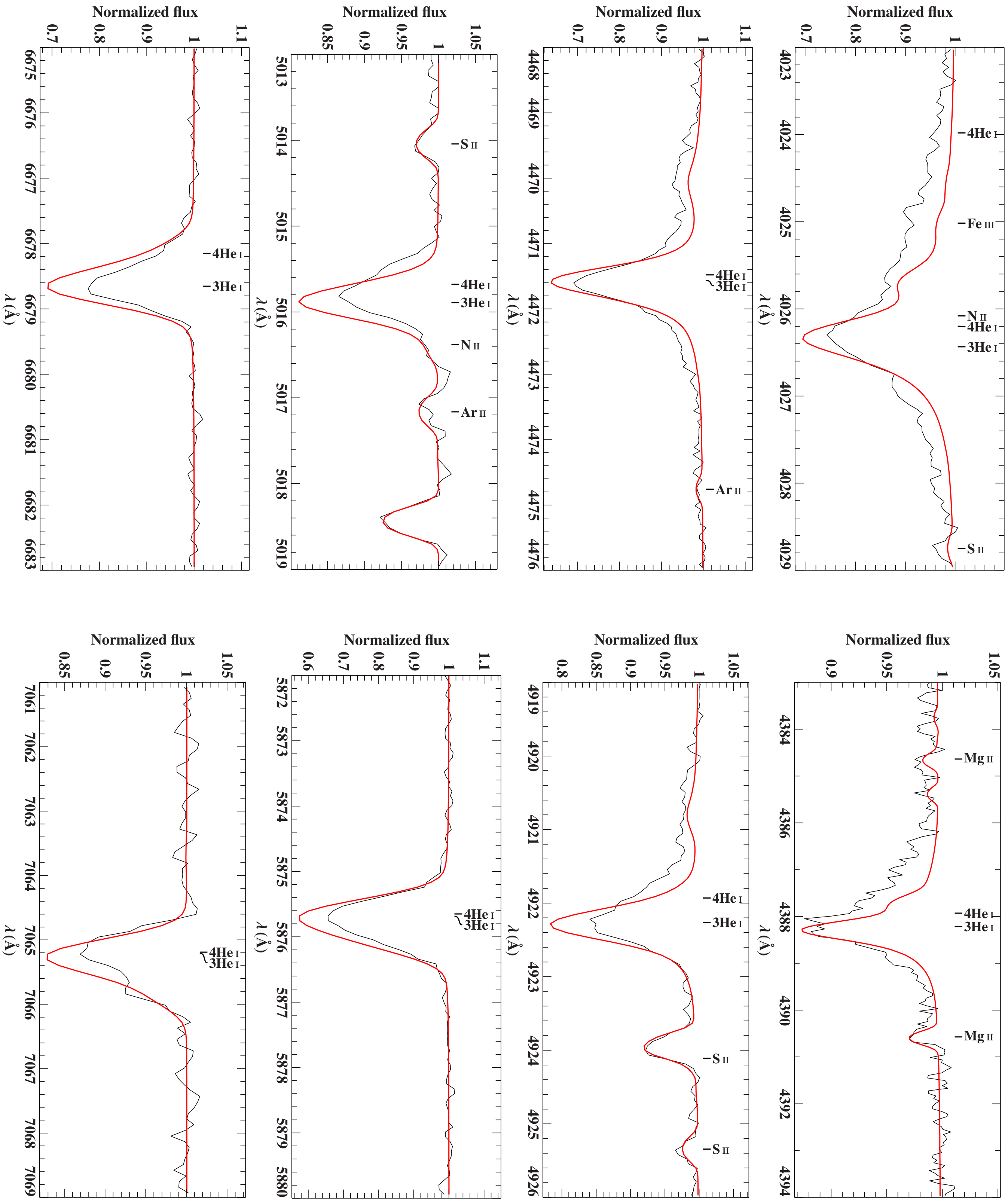

Figure 12.3.4.: Helium lines in the FEROS spectrum of the ^{3}He star PHL 382 used for the hybrid LTE/NLTE analysis with ISIS. The star shows strong helium stratification as is obvious from the mismatch of the cores of many He I lines (see chapter 12.3.3 for details).

12.3.2. The $^3\mathrm{He}$ Subdwarf B Stars EC 03591-3232, EC 12234-2607 and BD+48° 2721

Fig. 12.3.5 to 12.3.8 display the individual helium line fits of the $^3\mathrm{He}$ (enriched) sdB stars showing strong helium stratification, i.e., of EC 03591-3232, EC 12234-2607, and BD+48° 2721. As for both analyzed $^3\mathrm{He}$ BHB stars, PHL 25 and PHL 382, a significant mismatch of the cores of many He I lines is obvious. Only the weakest He I lines can be fitted half-decently for these stars.

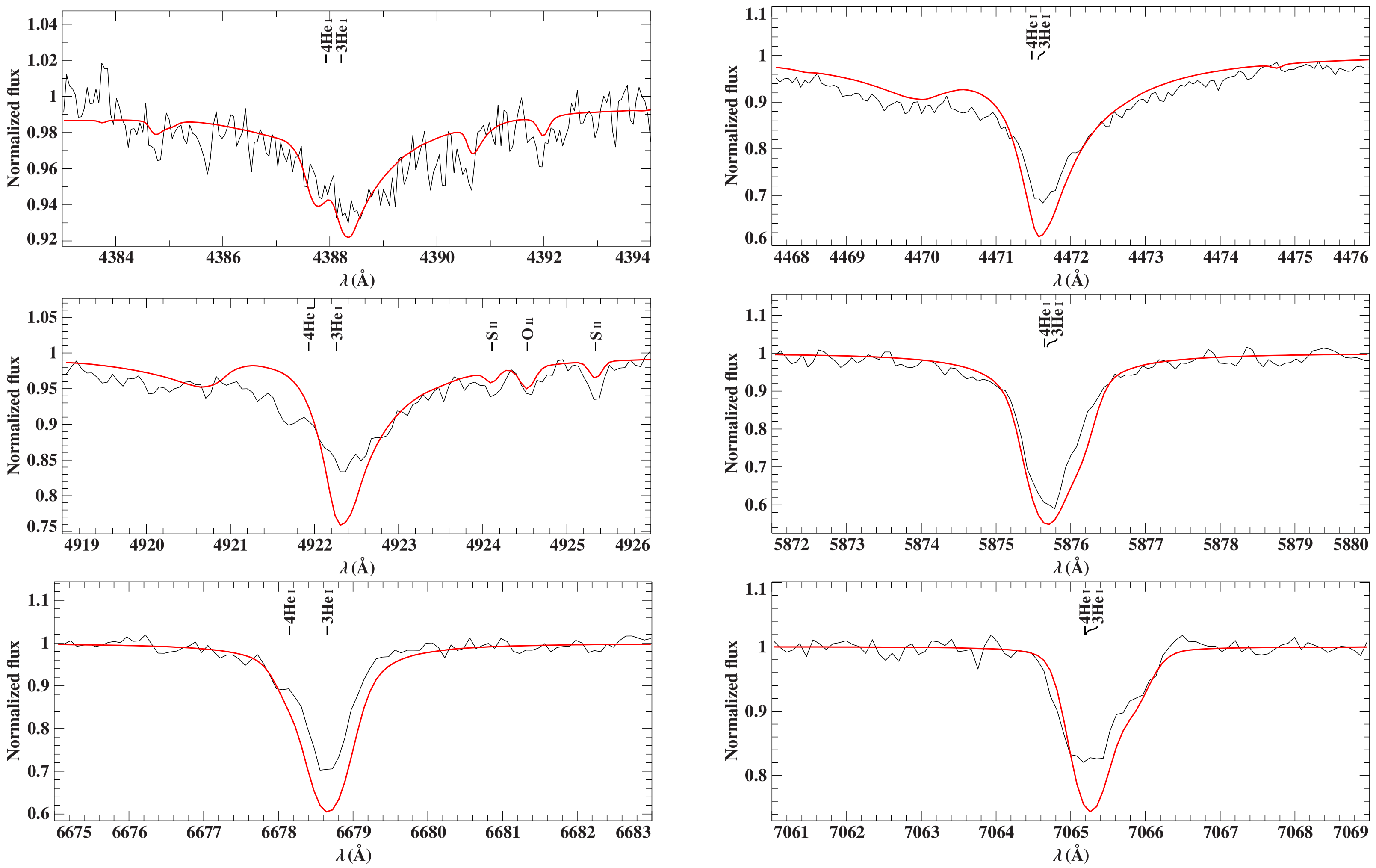

Figure 12.3.5.: Helium lines in the FEROS spectrum of the $^{3}\mathrm{He}$ star EC 03591-3232 used for the hybrid LTE/NLTE analysis with ISIS. The star shows helium stratification as is obvious from the mismatch of the cores of several strong He I lines (see chapter 12.3.3 for details).

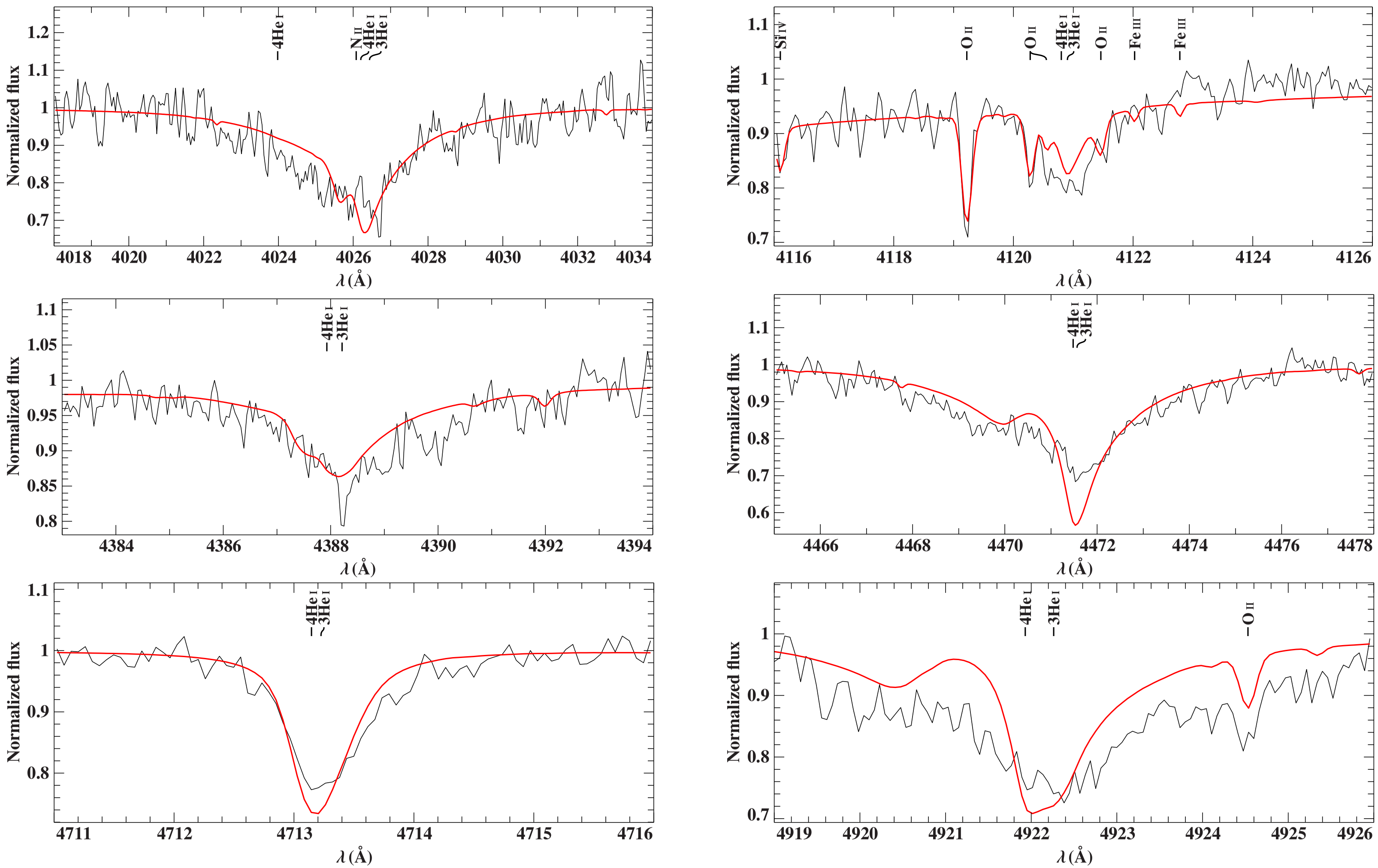

Figure 12.3.6.: Helium lines in the FEROS spectrum of the $^{3}\mathrm{He}$ enriched star EC 12234-2607 used for the hybrid LTE/NLTE analysis with ISIS - Part 1. The star shows strong helium stratification as is obvious from the mismatch of the cores of many He I lines (see chapter 12.3.3 for details).

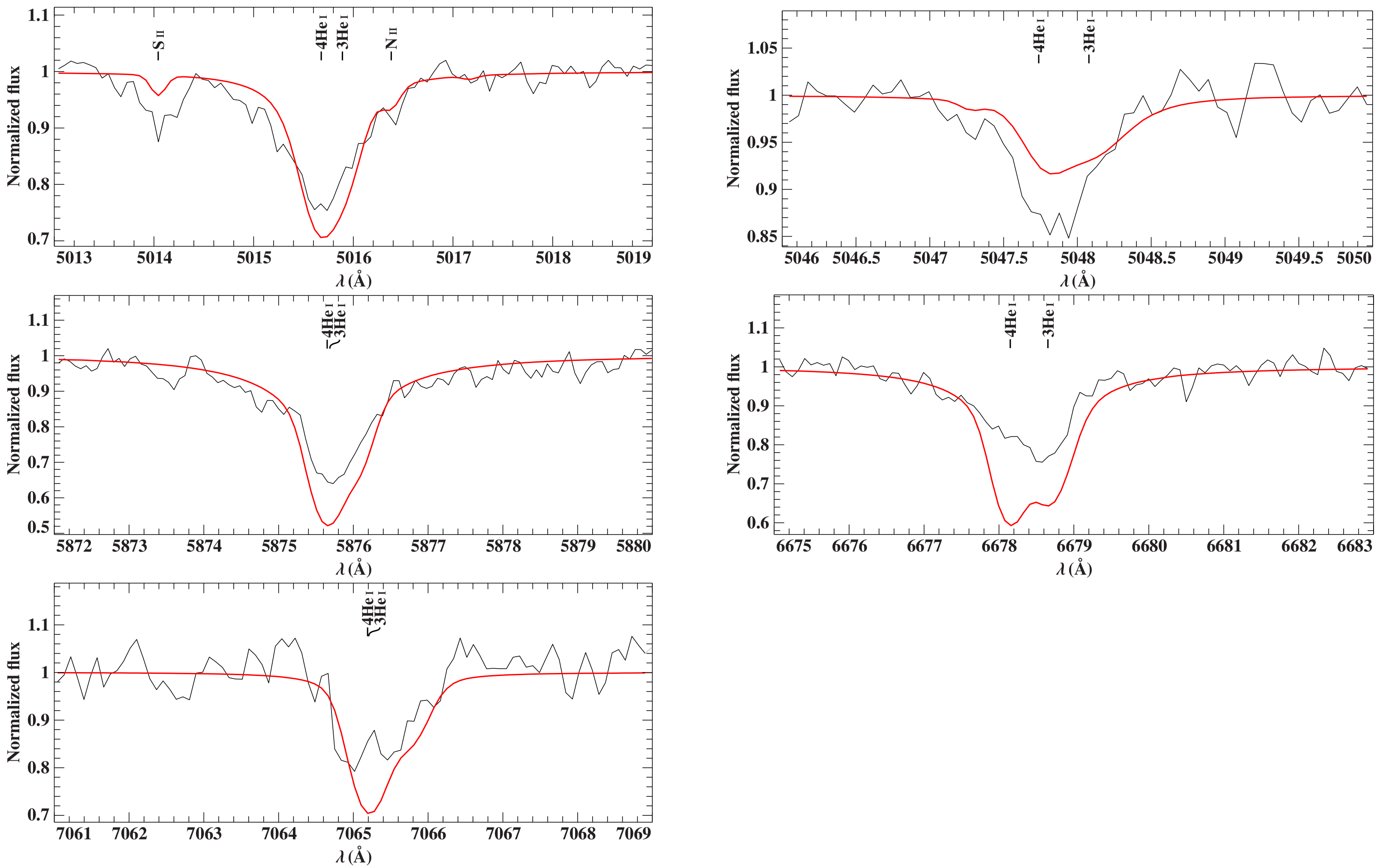

Figure 12.3.7.: Helium lines in the FEROS spectrum of the $^3\mathrm{He}$ enriched star EC 12234-2607 used for the hybrid LTE/NLTE analysis with ISIS - Part 2. The star shows strong helium stratification as is obvious from the mismatch of the cores of many He I lines (see chapter 12.3.3 for details).

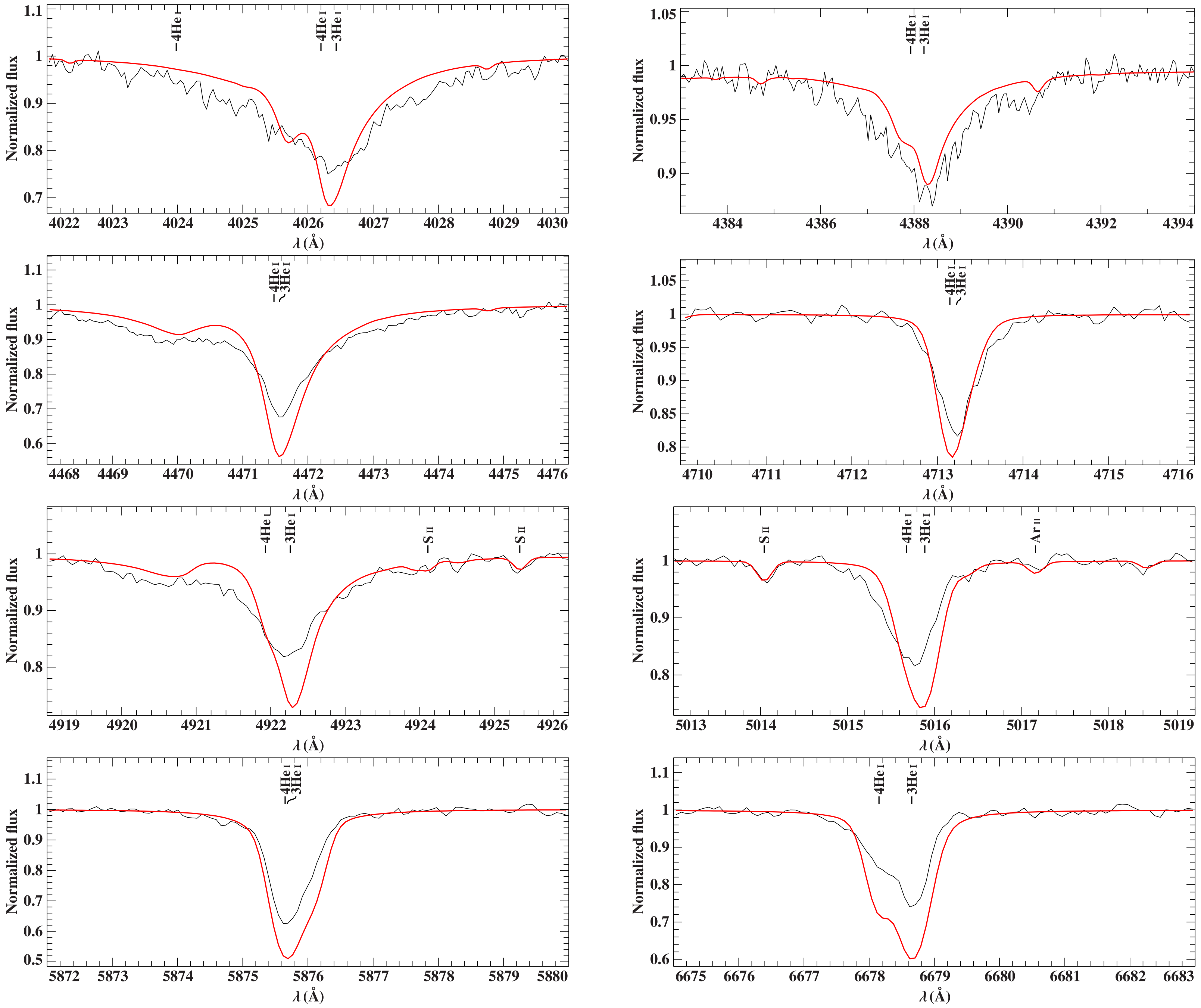

Figure 12.3.8.: Helium lines in the FOCES spectrum of the $^{3}\mathrm{He}$ enriched star BD+48° 2721 used for the hybrid LTE/NLTE analysis with ISIS. The star shows strong helium stratification as is obvious from the mismatch of the cores of many He I lines (see chapter 12.3.3 for details).

12.3.3. Explaining the Line Profile Anomalies

The question remains why the investigated helium line profiles cannot be properly reproduced in the cases of PHL 25, PHL 382, EC 03591-3232, EC 12234-2607, and BD+48° 2721. A whole set of He I profiles for a large variety of helium abundances has been calculated, but none of them is able to simultaneously match both the wings and the core of the analyzed absorption lines of the relevant stars. In particular, the strongest among the diffuse He I lines, at λ4026 Å and λ4472 Å, exhibit shallow cores in combination with unusually broad wings, being a clear sign that the element is not homogeneously distributed throughout the stellar atmosphere, but instead shows a vertical abundance stratification. This has been reported for only a few $^3\mathrm{He}$ (enriched) B-type stars so far, including the main-sequence prototype HgMn star κ Cancri (Maza et al., 2014) and Feige 86 (see chapter 6.2), a BHB star (Bonifacio et al., 1995). In fact, Bonifacio et al. (1995) calculated He I profiles for a large variety of helium abundances, too, but were also not able to obtain a shape which could simultaneously match both the wings and the core of the analyzed absorption lines in the spectrum of Feige 86. Stratification has also been found in other chemically peculiar stars by Dworetsky (2004) and Castelli & Hubrig (2007), but not in any hot subdwarf B star yet. Another trend can be derived from Fig. 12.3.1 to 12.3.8, too. The further out in the stellar atmosphere the particular helium absorption line is formed, i.e., the stronger the individual absorption line (see chapter 3.3 for further information on spectral line formation), the worse the line core can be reproduced by synthetic model spectra. This particularly applies to λ4472 Å, λ4922 Å, λ5016 Å, λ5875 Å, λ6678 Å as well as to λ7065 Å and indicates that the helium abundance is higher in deeper layers of the atmospheres (where the line wings form) than in the outer layers (where the line cores form). Hence, for instance not all of the shown helium lines in Fig. 12.3.1 to 12.3.3, belonging to the $^3\mathrm{He}$ enriched BHB star PHL 25, are used in order to derive isotopic helium abundances. Especially, the best fit for He I, 6678 Å here would result in a wrong isotopic abundance ratio.

The projected rotation velocity of $v \sin i \lesssim 6.3\,\mathrm{km\,s^{-1}}$ (see table 12.1) determined for PHL 25 is at odds with the former one derived from LTE ($v \sin i \sim 38\,\mathrm{km\,s^{-1}}$). However, due to the fact that using the whole stellar spectrum with all included metal lines, as done within the hybrid LTE/NLTE analysis, typically results in a much more meaningful projected rotation velocity measurement, a significant rotation velocity can indeed be excluded for PHL 25. Therefore, the LTE values, making use of hydrogen Balmer and helium absorption lines only, are most likely wrongly determined. Such high values for $v \sin i$ cannot reproduce the observed metal lines at all. The $v \sin i$ values wrongly derived from LTE could be explained by helium stratification as well, since helium lines appear broader in the case of stratified atmospheres. Therefore, a high projected rotation velocity is needed to reproduce the relevant helium lines. Metal lines are unaffected by stratification and, thus, give the correct projected rotation velocity value. Hence, PHL 25 does not rotate.

However, no suitable synthetic model spectra including vertical atmospheric stratification can be calculated by the ATLAS, DETAIL, and SURFACE versions used for the hybrid LTE/NLTE analysis at hand. The easiest way to model vertical atmospheric abundance stratification is to make use of a smooth step function (Farthmann et al., 1994), i.e. setting the helium

Star - Fitted line	Instrument	$\log n(^3\mathrm{He})$ [dex]	$\log n(^4\mathrm{He})$ [dex]	$\frac{n(^4\mathrm{He})}{n(^3\mathrm{He})}$
PHL 25 - He I, 6678 Å core	CASPEC	$-3.30^{+0.10}_{-0.20}$	$-4.00^{+0.40}_{-0.50}$	$0.20^{+0.19}_{-0.20}$
PHL 25 - He I, 4922 Å core	CASPEC	$-2.90^{+0.10}_{-0.10}$	$-3.10^{+0.10}_{-0.20}$	$0.63^{+0.21}_{-0.33}$
PHL 25 - He I, 4922 Å wings	CASPEC	$-2.00^{+0.30}_{-0.40}$	$-2.30^{+0.30}_{-0.60}$	$0.50^{+0.49}_{-0.50}$
PHL 25 - He I, 6678 Å core	HRS co-added	$-3.50^{+0.03}_{-0.10}$	$-3.90^{+0.20}_{-0.10}$	$0.40^{+0.19}_{-0.13}$
PHL 25 - He I, 4922 Å core	HRS co-added	$-3.00^{+0.10}_{-0.10}$	$-3.00^{+0.10}_{-0.10}$	1.00 ± 0.33
PHL 25 - He I, 4922 Å wings	HRS co-added	$-2.60^{+0.20}_{-0.60}$	$-2.30^{+0.20}_{-0.30}$	$2.00^{+1.30}_{-2.00}$
PHL 382 - He I, 6678 Å core	FEROS co-added	$-2.80^{+0.10}_{-0.10}$	$-3.80^{+0.20}_{-0.30}$	$0.10^{+0.06}_{-0.08}$
PHL 382 - He I, 4922 Å core	FEROS co-added	$-2.70^{+0.10}_{-0.20}$	$-3.20^{+0.20}_{-0.40}$	$0.32^{+0.17}_{-0.32}$
PHL 382 - He I, 4922 Å wings	FEROS co-added	$-2.70^{+0.30}_{-0.20}$	$-2.00^{+0.30}_{-0.50}$	$5.01^{+4.90}_{-5.01}$
EC 03591-3232 - He I, 6678 Å core	FEROS co-added	$-2.60^{+0.10}_{-0.10}$	$-3.60^{+0.30}_{-0.40}$	$0.10^{+0.08}_{-0.10}$
EC 03591-3232 - He I, 4922 Å core	FEROS co-added	$-2.40^{+0.10}_{-0.10}$	$-3.40^{+0.40}_{-1.20}$	0.10 ± 0.10
EC 03591-3232 - He I, 4922 Å wings	FEROS co-added	$-2.10^{+0.20}_{-0.40}$	$-2.40^{+0.40}_{-0.30}$	$0.50^{+0.52}_{-0.50}$
EC 12234-2607 - He I, 6678 Å core	FEROS co-added	$-2.80^{+0.10}_{-0.20}$	$-3.20^{+0.20}_{-0.20}$	$0.40^{+0.21}_{-0.26}$
EC 12234-2607 - He I, 4922 Å core	FEROS co-added	$-2.10^{+0.20}_{-0.20}$	$-2.20^{+0.20}_{-0.40}$	$0.79^{+0.52}_{-0.79}$
EC 12234-2607 - He I, 4922 Å wings	FEROS co-added	$-1.70^{+0.30}_{-0.50}$	$-1.60^{+0.20}_{-0.30}$	$1.26^{+1.05}_{-1.26}$
BD+48 2721 - He I, 6678 Å core	FOCES	$-3.10^{+0.10}_{-0.20}$	$-3.60^{+0.10}_{-0.20}$	$0.32^{+0.11}_{-0.21}$
BD+48 2721 - He I, 4922 Å core	FOCES	$-2.80^{+0.10}_{-0.20}$	$-2.80^{+0.10}_{-0.20}$	$1.00^{+0.33}_{-0.66}$
BD+48 2721 - He I, 4922 Å wings	FOCES	$-2.50^{+0.30}_{-0.80}$	$-2.20^{+0.20}_{-0.40}$	$2.00^{+1.66}_{-2.00}$

Table 12.4.: Results of the individually performed fits by eye for all analyzed stars showing helium stratification. The line forming atmospheric depth increases when going from He I, 6678 Å to the wings of He I, 4922 Å (see text for further information).

abundance in the outer atmospheric layers to a lower level than further in. By implementing such a step function into the ATLAS code, being responsible for the modeled atmospheric structure, line cores which are formed in the outer cooler atmospheric layers are weakened. At the same time, line wings which are formed in the hotter inner layers are strengthened. This could improve the fit results.

In the following, a similar approach to that of the two-component fit presented by Maza et al. (2014) shall be performed in order to verify vertical helium stratification and in order to estimate the limits of both helium isotopic abundances, $^3\mathrm{He}$ and $^4\mathrm{He}$, in parts of the outer and inner stellar atmospheres, respectively. These limits might be assessable by looking at the different line forming atmospheric depths. While the core of the strongest helium line, He I, 6678 Å, is formed further out than the line core of He I, 4922 Å, the wings of the latter one are formed even further inside the stellar atmosphere. Thus, three fits by eye are performed individually for the relevant stars, making use of the determined best fit values for effective temperature, surface gravity, projected rotation and radial velocity. The focus of the first two is on the line core of both helium absorption lines. A third fit by eye is performed in order to reproduce the line wings of He I, 4922 Å as well as possible. If a (linear) correlation between atmospheric depth and isotopic helium abundances can be derived, this would verify the stratification hypothesis. However, all derived values depend on the author's personal view and therefore are not engraved in stone. Errors for $^{3}\mathrm{He}$ and $^{4}\mathrm{He}$ are also determined by eye and obviously have to be treated with extreme caution as well. Gaussian error propagation is used to determine errors for the resulting isotopic abundance ratios. Table 12.4 summarizes all results of the individually performed fits by eye for all analyzed stars showing helium stratification and Fig. 12.3.9 displays example best fits for the investigated helium lines in the HRS spectrum of PHL 25. These line fits are representative of all performed fits by eye, resulting in the listed values of table 12.4.

From table 12.4, two results have to be pointed out. First, the line core position of He I, 6678 Å is best-suited for the correct determination of the particular isotopic abundance ratio, $^{4}\mathrm{He}/^{3}\mathrm{He}$, as can be seen from the individually determined errors. Especially, $^{4}\mathrm{He}/^{3}\mathrm{He}$ cannot be constrained by properly fitting the line wings of He I, 4922 Å only. That is why a well-determined single line fit of He I, 6678 Å is a first good indicator for the actually predominant abundance ratio, but certainly not for the individual isotopic helium abundances.

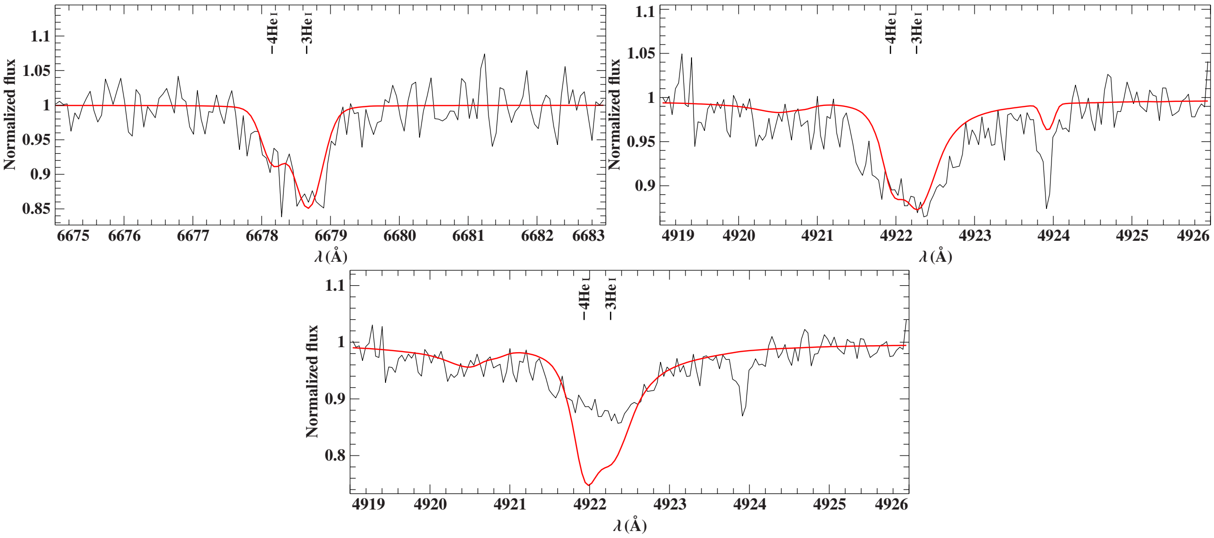

Figure 12.3.9.: Best fit by eye for the analyzed lines of table 12.4 in the HRS spectrum of PHL 25. *Top Left Panel*: He I, 6678 Å. *Top Right Panel*: Line core of He I, 4922 Å. *Bottom Panel*: Line wings of He I, 4922 Å.

Second, the isotopic helium abundances overall increase when going from outer (He I, 6678 Å) to inner (line core and line wings of He I, 4922 Å) in the stellar atmosphere of the analyzed stars. The $^{3}\mathrm{He}$ abundance increase ranges from 0.10 dex for PHL 382 up to 1.30 dex for PHL 25. The change of $^{4}\mathrm{He}$ is even more significant, though, ranging from 1.20 dex for EC 03591-3232 up to 1.80 dex for PHL 382. This is a clear indication for the inhomogeneous distribution of helium in the atmosphere, i.e., for vertical stratification. A linear correlation between line forming atmospheric depth and (isotopic) helium abundances therefore is possible.

A determination of the formation depth from the atmospheric models would be required to trace the stratification.

12.3.4. The rotating $^3\mathrm{He}$ Subdwarf B Star SB 290

As can be seen from table 12.1, SB 290 is the only sdB star exhibiting projected rotation velocity values significantly different from zero. This is in good agreement with the fact that most hot sudbwarf B stars are known to be slow rotators (Heber, 2016). The measured value for SB 290 of about 50 $\mathrm{km\,s^{-1}}$ is consistent with literature (Geier et al., 2013b) and the result from the LTE analysis (see table 10.1), too.
Fig 12.3.10 to 12.3.12 display the individual helium line fits of SB 290. Significant mismatches of the cores of the strongest He I lines are obvious, although less strong than for the stratified stars PHL 25, PHL 382, EC 03591-3232, EC 12234-2607, and BD+48° 2721. Hence, vertical helium stratification is possible for SB 290, too. Because of the star's high rotation velocity and the line broadening coming along with it, however, larger problems in fitting due to stratification, as seen for the other stratified stars, might be hidden.

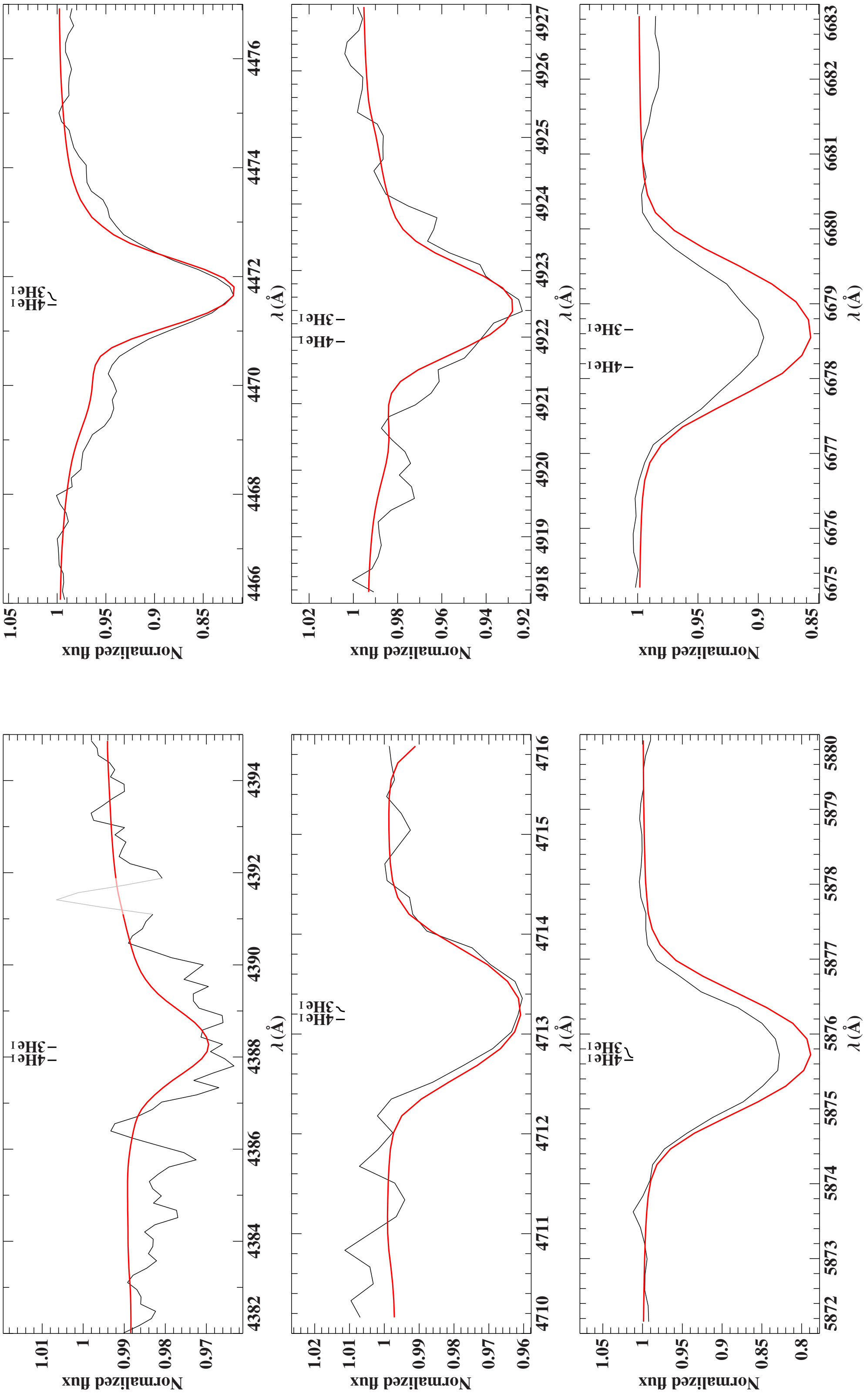

Figure 12.3.10.: Helium lines in the CASPEC spectrum of the $^{3}\mathrm{He}$ star SB 290 used for the hybrid LTE/NLTE analysis with ISIS. The star is rotating, but has significant mismatches in the strongest He I lines, too. Rotational broadening could therefore hide problems in fitting coming along with possible helium stratification (see chapter 12.3.4 for details).

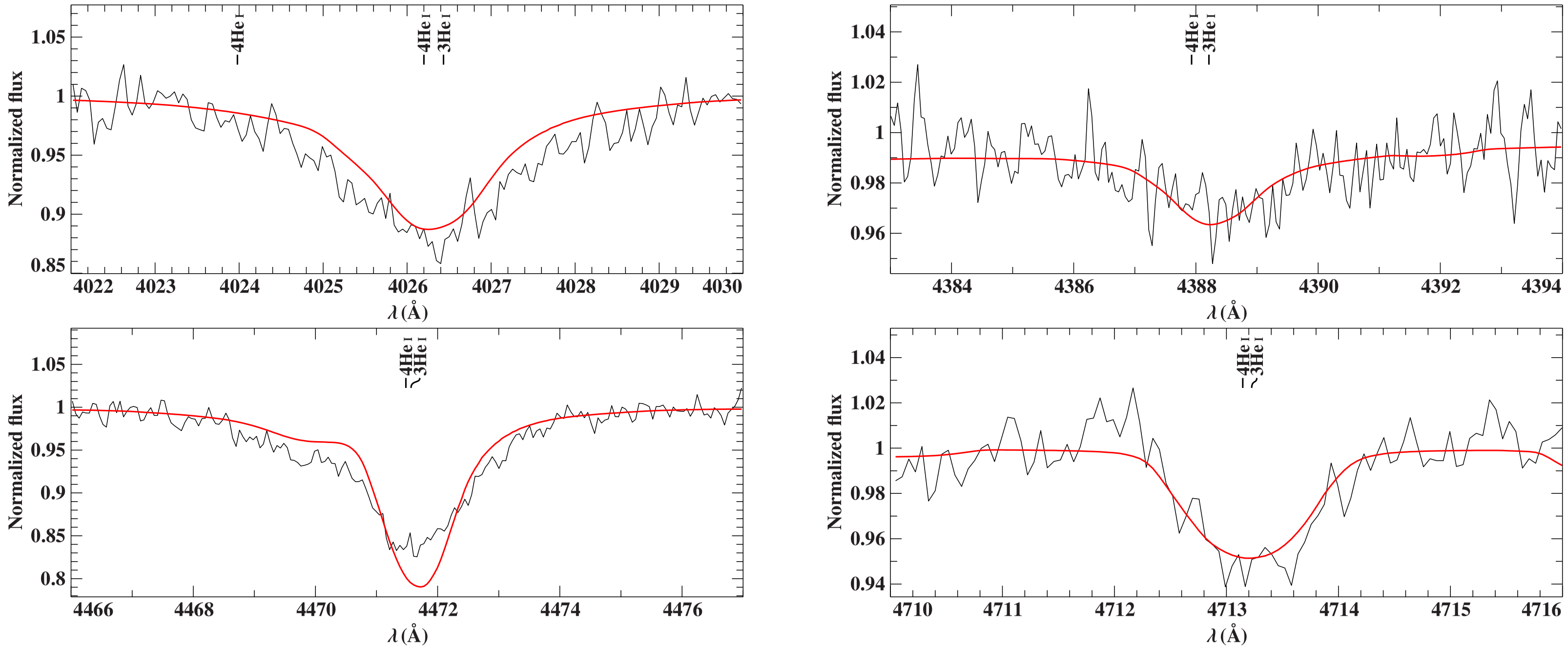

Figure 12.3.11.: Helium lines in the FEROS spectrum of the $^3\mathrm{He}$ star SB 290 used for the hybrid LTE/NLTE analysis with ISIS - Part 1. The star is rotating, but has significant mismatches in the strongest He I lines, too. Rotational broadening could therefore hide problems in fitting coming along with possible helium stratification (see chapter 12.3.4 for details).

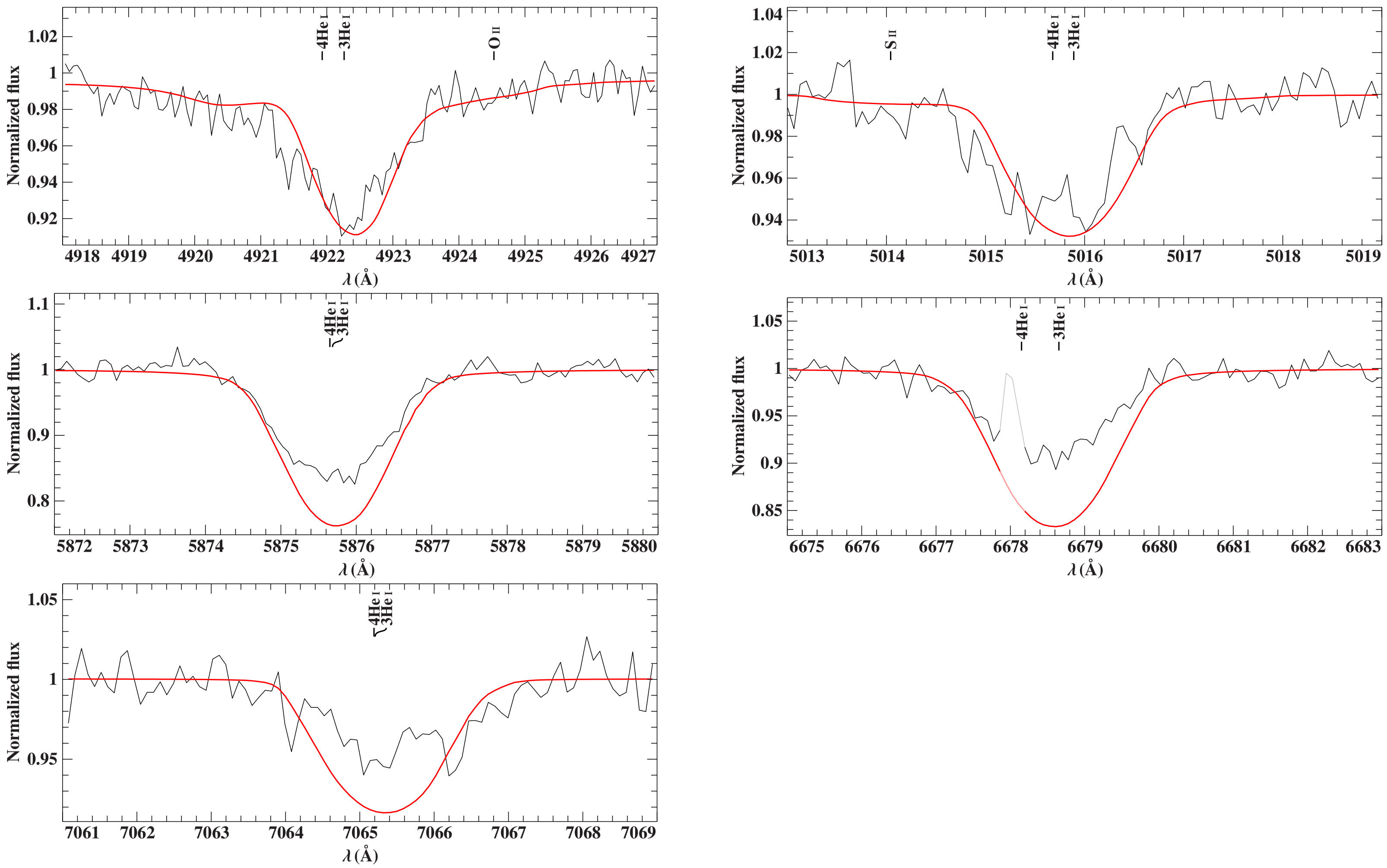

Figure 12.3.12.: Helium lines in the FEROS spectrum of the $^3\mathrm{He}$ star SB 290 used for the hybrid LTE/NLTE analysis with ISIS - Part 2. The star is rotating, but has significant mismatches in the strongest He I lines, too. Rotational broadening could therefore hide problems in fitting coming along with possible helium stratification (see chapter 12.3.4 for details).

12.4. Metal Abundances

Tables 12.5 and 12.6 as well as Fig. 12.4.1 and 12.4.2 summarize the derived isotopic helium and metal abundances. Solar abundances (Asplund et al., 2009) are marked by solid horizontal lines and are given as base-10 logarithmic particle densities relative to the density of all particles in both figures. The same applies to the mean metal abundances for hot subdwarf B stars (see table 11.1 and Fig. 5.2.2) from Naslim et al. (2013), which are marked by dashed lines. The mean sdB abundance for argon (Ar) and iron (Fe) is solar. Whereas dots mark measured abundances, triangles mark upper limits only in all subpanels of Fig. 12.4.1 and 12.4.2. Stars showing no helium stratification are characterized by blue and stratified stars are represented by red dots. Both He-normal comparison stars, HD 4539 and CD-35° 15910, are marked in green. Error bars are also given according to tables 12.5 and 12.6. For stars, where two (co-added) spectra are available, measured abundances are averaged and the highest abundance is chosen if only upper limits were derived for both spectra. Since the isotopic helium abundances have already been discussed in chapter 12.2, hereafter only the derived metal abundances will be interpreted. The metal abundances for all analyzed elements, $\log\left(n(\mathsf{X})\right) := \log\left[\frac{N(\mathsf{X})}{N(\mathsf{all\ elements})}\right]$, where $X \in \{$C, N, O, Ne, Mg, Al, Si, S, Ar, Fe$\}$, and $n(\mathsf{X})$ is the ratio of the number density corresponding to element X to the number density of all the elements in the stellar atmosphere, result from the hybrid LTE/NLTE metal line fits, being accessible in appendix B.1. Table 9.3 only gives a short overview about some of the analyzed lines.

Hereafter, metal abundances, which have been derived for stars from different kinds of spectra, shall be compared. While the discrepancies between the abundances derived from the CASPEC and FEROS spectra are large for silicon ($\sim$ 0.30 dex) and sulfur ($\sim$ 0.25 dex), and smaller for carbon ($\sim$ 0.15 dex) in the case of SB 290, only silicon ($\sim$ 0.30 dex) is discrepant for PHL 25, when comparing CASPEC and HRS spectra (see tables 12.5 and 12.6). Thus, simply taking the mean value of these abundances, as described above, might be an additional source of error.

In the following, the derived metal abundances on the one hand shall be compared to hot subdwarf B-type literature values (see Fig. 5.2.1) given by the LTE analysis of Geier (2013) and, on the other hand, to sdB mean metal abundances (see table 11.1 and Fig. 5.2.2) from Naslim et al. (2013).

- **Carbon**: Similar to what has been found by Geier (2013), the observed carbon sdB abundances derived from C II/III lines scatter from $\sim$ -2.40 dex to $\sim$ -0.30 dex subsolar (solar abundance: -3.61 dex). No analyzed sdB stars show supersolar C abundances and no trend with effective temperature is visible at all. Most of the $^3\mathrm{He}$ (enriched) sdBs have slightly higher abundances (about $+0.80$ dex) than the mean sdB abundance for C (-4.84 dex) from Naslim et al. (2013). The stars therefore belong to the carbon-rich sdBs.

- **Nitrogen**: The N II/III abundances (solar abundance: -4.21 dex), also not showing any trend with temperature, range from $\sim$ -0.65 dex subsolar to $\sim$ $+0.60$ dex supersolar for the analyzed sdBs. This is consistent with the abundances determined by Geier (2013). Most of the derived N abundances for the $^3\mathrm{He}$ (enriched) sdBs are located around the mean sdB abundance for N (-4.44 dex) from Naslim et al. (2013). Some of them scatter from about -0.40 dex to about +0.85 dex, though.

- **Oxygen**: The observed oxygen abundances (solar abundance: -3.35 dex) derived from O II lines range from $\sim$ -1.30 dex to $\sim$ -0.35 dex subsolar for the analyzed sdBs, thus falling within the region of Geier (2013). However, an average abundance shift of -0.50 dex at an effective temperature of $\sim$ 30 000 K with respect to the cooler stars in the sample, as measured by Geier (2013), cannot be confirmed. A reason for this might be the smaller sample size compared to Geier (2013). All in all, the derived O abundances for all $^{3}\mathrm{He}$ (enriched) sdBs match the mean sdB abundance (-4.34 dex) from Naslim et al. (2013).
- **Neon**: The neon abundance is determined by a single line only, namely Ne I, 6402.247 Å (see table 9.3 and appendix B.1). No Ne II lines could be investigated in any of the analyzed spectra. Hence, often only upper limits can be derived for the Ne I abundance (solar abundance: -4.11 dex), scattering from $\sim$ -2.90 dex to $\sim$ -0.10 dex subsolar for the analyzed sdBs. The lower boundary is significantly lower than the one measured by Geier (2013). Geier (2013) determined Ne II abundances only, though. Most of the derived Ne abundances for the $^{3}\mathrm{He}$ (enriched) sdBs also lie below the mean sdB abundance of -5.04 dex from Naslim et al. (2013).
- **Magnesium**: In contrast to the results of Geier (2013), no clear trend with temperature can be seen in the magnesium abundance (solar abundance: -4.44 dex) for the analyzed sdBs. The Mg II abundance, ranging from $\sim$ -2.20 dex to $\sim$ -0.10 dex subsolar, scatters more than in the sample of Geier (2013). This might indicate that magnesium is more strongly influenced by NLTE. Nevertheless, most of the observed Mg abundances for the $^{3}\mathrm{He}$ (enriched) sdBs lie in the regime of the mean sdB abundance of -5.24 dex from Naslim et al. (2013).
- **Aluminum**: Geier (2013) measured a slight trend for the Al III abundance in sdB stars, which is confirmed here. It slightly increases with effective temperature ranging from $\sim$ -2.40 dex subsolar to about solar (solar abundance: -5.59 dex). Most of the observed abundances for all $^{3}\mathrm{He}$ (enriched) sdBs scatter from $\sim$ -0.75 dex to $\sim$ +0.80 dex around the mean sdB abundance (-6.34 dex) from Naslim et al. (2013).
- **Silicon**: The observed abundances from Si III/IV (solar abundance: -4.53 dex) for all analyzed sdBs show a large scatter similar to what has been measured by Geier (2013). Silicon scatters from $\sim$ -2.10 dex subsolar to $\sim$ +0.20 dex supersolar, not showing any trend in the analyzed temperature regime. Most of the analyzed $^{3}\mathrm{He}$ (enriched) sdBs have higher Si abundances (up to $\sim$ +1.20 dex) compared to the mean abundance (-5.54 dex) from Naslim et al. (2013). The stars therefore belong to the silicon-rich sdBs.
- **Sulfur**: The sulfur abundance derived from S II/III (solar abundance: -4.92 dex) exhibits a large scatter between $\sim$ -0.90 dex subsolar and $\sim$ +0.50 dex supersolar for the analyzed sdBs. Therefore, it scatters less strongly than measured by Geier (2013). Most of the analyzed $^{3}\mathrm{He}$ (enriched) sdBs lie well above (up to $\sim$ +1.15 dex) the mean sdB

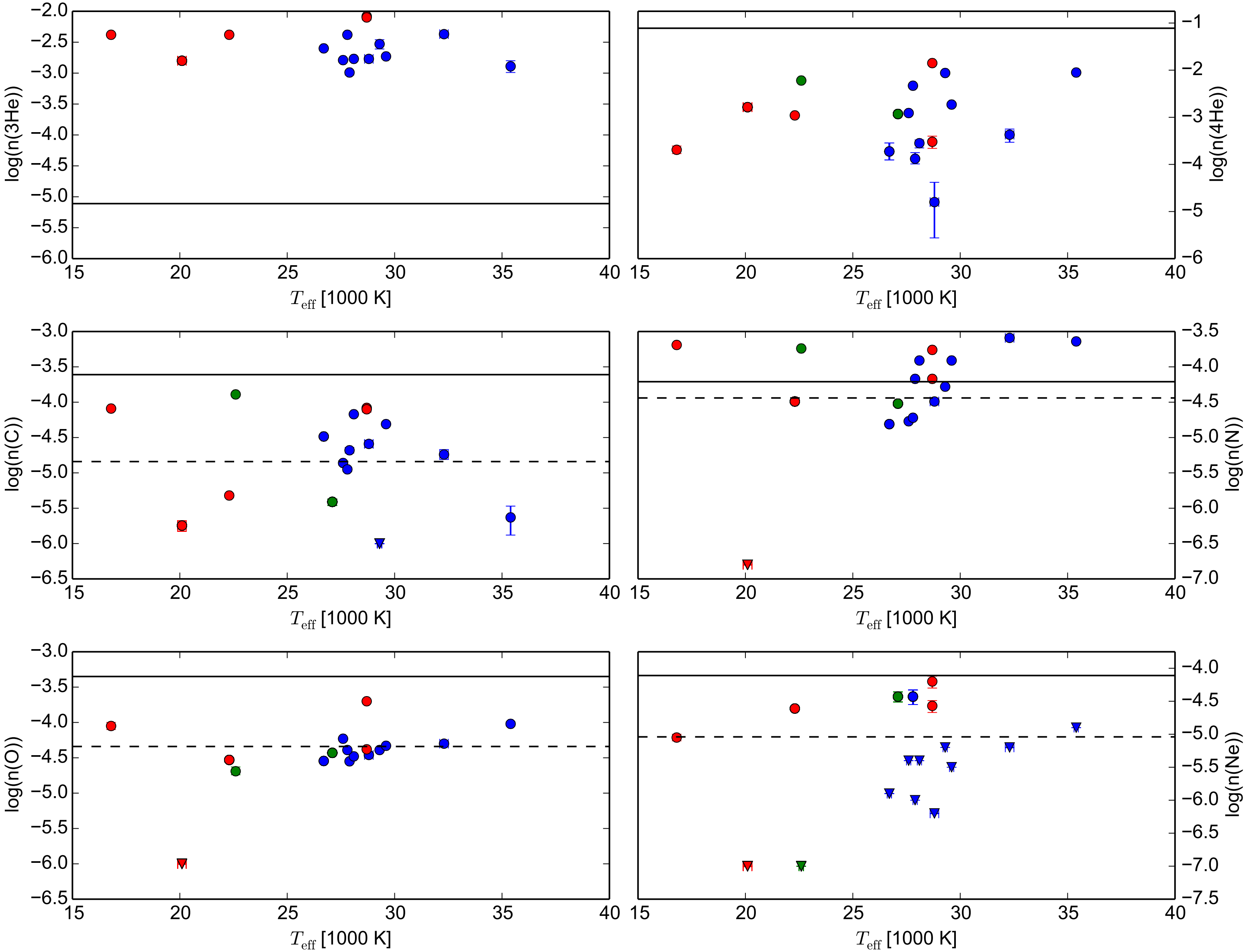

Figure 12.4.1.: Elemental abundances from $^3\mathrm{He}$ to neon plotted against effective temperature according to tables 12.1, 12.3, and 12.5. Stars showing helium stratification (see chapter 12.3) are characterized in red and their determined $^3\mathrm{He}$ and $^4\mathrm{He}$ values hence have to be treated with caution. While blue dots represent non-stratified $^3\mathrm{He}$ stars, both He-normal comparison stars, HD 4539 and CD-35° 15910, are marked in green. Dots mark measured abundances, whereas triangles mark upper limits. Error bars are also given according to the relevant tables. The solid horizontal lines mark solar abundances according to Asplund et al. (2009) and are given as base-10 logarithmic particle densities relative to the density of all particles. The same applies to the mean metal abundances for sdBs (see Naslim et al. (2013), Fig. 5.2.2, and table 11.1), which are marked by dashed lines.

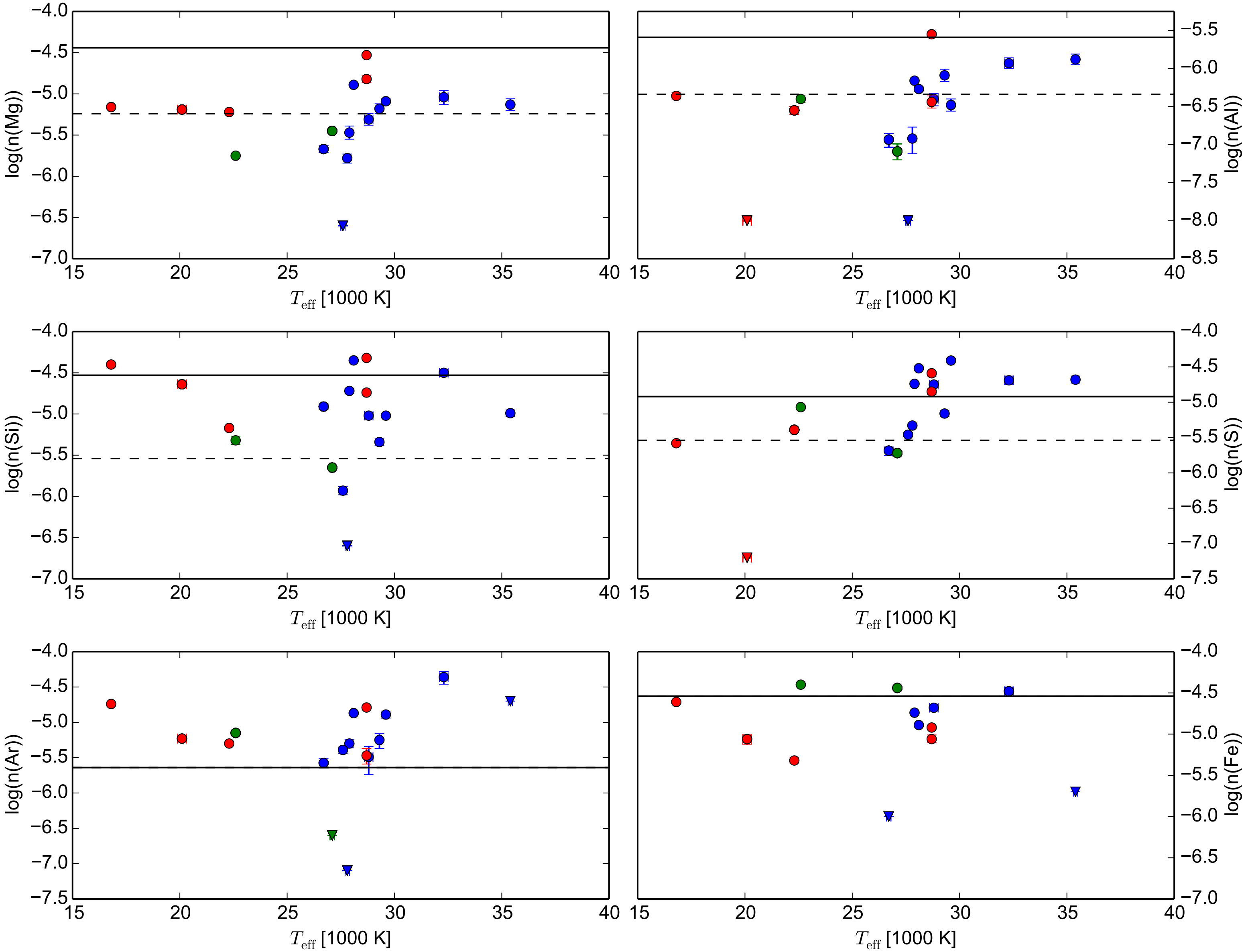

Figure 12.4.2.: Elemental abundances from magnesium to iron plotted against effective temperature according to tables 12.1, 12.5, and 12.6. Stars showing helium stratification (see chapter 12.3) are characterized in red and their determined $^3\mathrm{He}$ and $^4\mathrm{He}$ values hence have to be treated with caution. While blue dots represent non-stratified $^3\mathrm{He}$ stars, both He-normal comparison stars, HD 4539 and CD-35° 15910, are marked in green. Dots mark measured abundances, whereas triangles mark upper limits. Error bars are also given according to the relevant tables. The solid horizontal lines mark solar abundances according to Asplund et al. (2009) and are given as base-10 logarithmic particle densities relative to the density of all particles. The same applies to the mean metal abundances for sdBs (see Naslim et al. (2013), Fig. 5.2.2, and table 11.1), which are marked by dashed lines. The mean sdB abundance is solar for argon and iron.

abundance (-5.54 dex) from Naslim et al. (2013), though. The stars hence belong to the sulfur-rich sdBs.

- **Argon**: In principle, the Ar II abundance (solar abundance: -5.64 dex) increase with effective temperature, as found by Geier (2013) for hot subdwarf B stars, is confirmed, although a larger sample is needed in order to clarify the issue. Two sdB stars, CD-35° 15910 and HE 2322-0617, fall out of the series with measured upper limits of -6.60 dex and -7.10 dex, respectively. Overall, the observed argon abundance strongly scatters between ∼ -1.50 dex subsolar and ∼ +1.30 dex supersolar, if CD-35° 15910 and HE 2322-0617 are included. If not, between solar and ∼ +1.30 dex supersolar, being rather similar to what has been found by Geier (2013). As for silicon and sulfur, most of the observed argon abundances of the analyzed $^3\mathrm{He}$ (enriched) sdBs lie above the mean sdB abundance from Naslim et al. (2013), which is solar (-5.64 dex). The stars thus belong to the argon-rich sdBs.
- **Iron**: Both, the solar and the mean sdB abundance for iron from Naslim et al. (2013) lie at -4.54 dex. For the analyzed sdB stars, the hybrid LTE/NLTE approach results in iron abundance values between ∼ -1.50 dex subsolar for SB 290 and ∼ +0.15 dex supersolar for HD 4539. The lowest abundances are given by upper limits only, though, since no iron lines are measured in the relevant stars. Excluding these stars (SB 290 and PG 1519+640), the Fe III abundance stays more or less constant between ∼ -0.80 dex subsolar and ∼ +0.15 dex supersolar, i.e., similar to what has been found by Geier (2013), where a constant abundance with temperature ranging from -0.70 dex subsolar to +0.50 dex supersolar has been derived.
  However, Fe abundances could not be derived for the newly found $^3\mathrm{He}$ sdBs from the hot subdwarf list of the ESO Supernova Ia Progenitor Survey (Lisker et al., 2005), i.e., for HE 0929-0424, HE 1047-0436, HE 2156-3927, and HE 2322-0617 (see table 12.6). For these stars, simulations, in which the S/N is modeled, are required in order to determine reliable upper limits. None of the relevant stars is incorporated in the subpanel of Fig. 12.4.2, showing the Fe abundances of all analyzed stars.
- **BHB stars**: Whereas the $^3\mathrm{He}$ enriched BHB star PHL 382 shows the same abundance pattern as the analyzed hot subdwarf B stars, PHL 25 has a puzzling one. While no nitrogen, oxygen, neon, aluminum, and sulfur are detectable, leading to strongly subsolar upper limits of their abundances (N by ∼ -2.60 dex, O by ∼ -2.70 dex, Ne by ∼ -2.90 dex, Al by ∼ -2.40 dex, and S by ∼ -2.30 dex), the measured carbon, magnesium, silicon, argon, and iron abundances, however, match the abundance pattern of the analyzed sdBs reasonably well.

Table 12.5.: Elemental abundances for the analyzed $^3\mathrm{He}$ and two He-normal comparison B-type stars (HD 4539, CD-35° 15910) determined via the hybrid LTE/NLTE approach performed in ISIS - Part 1. The four stars, whose UVES spectra have been analyzed, were taken from the hot subdwarf list of the ESO Supernova Ia Progenitor Survey (Lisker et al., 2005) and have been identified as $^3\mathrm{He}$ enriched hot subdwarf B-type stars. All statistical errors are given as 1σ ($\approx$ 68%) confidence intervals. Solar abundances according to Asplund et al. (2009) are also listed as base-10 logarithmic particle densities relative to the density of all particles.

Star	Instrument	$\log n$(C) [dex]	$\log n$(N) [dex]	$\log n$(O) [dex]	$\log n$(Ne) [dex]	$\log n$(Mg) [dex]
HD 4539	CASPEC	-3.89 ± 0.02	$-3.74^{+0.02}_{-0.01}$	$-4.69^{+0.06}_{-0.05}$	≤ -7.00 [a]	-5.75 ± 0.02
CD-35 15910	FEROS co-added	$-5.41^{+0.04}_{-0.05}$	-4.52 ± 0.01	-4.43 ± 0.02	$-4.43^{+0.07}_{-0.08}$	-5.45 ± 0.03
PHL 25	CASPEC	$-5.82^{+0.05}_{-0.06}$	≤ -6.80 [a]	≤ -7.00 [a]	≤ -7.00 [a]	-5.13 ± 0.04
PHL 25	HRS co-added	$-5.67^{+0.11}_{-0.13}$	≤ -6.80 [a]	≤ -6.00 [a]	≤ -7.00 [a]	$-5.25^{+0.03}_{-0.04}$
PHL 382	FEROS co-added	-4.09 ± 0.02	-3.69 ± 0.02	-4.05 ± 0.05	-5.05 ± 0.05	-5.16 ± 0.02
SB 290	CASPEC co-added	-4.42 ± 0.03	-4.85 ± 0.03	$-4.59^{+0.02}_{-0.03}$	≤ -6.50 [a]	-5.63 ± 0.04
SB 290	FEROS co-added	$-4.55^{+0.02}_{-0.03}$	-4.77 ± 0.02	-4.50 ± 0.02	≤ -5.90 [a]	-5.71 ± 0.05
EC 03263-6403	FEROS co-added	-4.59 ± 0.05	-4.49 ± 0.03	-4.46 ± 0.03	≤ -6.20 [a]	-5.31 ± 0.07
EC 03591-3232	FEROS co-added	-4.08 ± 0.02	-3.76 ± 0.01	-4.38 ± 0.01	$-4.57^{+0.08}_{-0.10}$	-4.53 ± 0.02
EC 12234-2607	FEROS co-added	-4.10 ± 0.04	-4.17 ± 0.02	-3.70 ± 0.02	$-4.20^{+0.08}_{-0.10}$	-4.82 ± 0.04
EC 14338-1445	FEROS co-added	-4.68 ± 0.04	-4.17 ± 0.01	-4.55 ± 0.02	≤ -6.00 [a]	-5.47 ± 0.08
Feige 38	FEROS co-added	-4.17 ± 0.02	-3.91 ± 0.01	-4.48 ± 0.01	≤ -5.40 [a]	-4.89 ± 0.02
BD+48 2721	FOCES	-5.32 ± 0.03	-4.49 ± 0.02	-4.53 ± 0.03	-4.61 ± 0.03	-5.22 ± 0.02
PG 1519+640	FOCES	$-5.63^{+0.16}_{-0.25}$	-3.64 ± 0.02	-4.02 ± 0.03	≤ -4.90 [a]	-5.13 ± 0.07
PG 1710+490	FOCES	-4.74 ± 0.07	$-3.59^{+0.02}_{-0.03}$	$-4.30^{+0.03}_{-0.04}$	≤ -5.20 [a]	$-5.04^{+0.08}_{-0.09}$
HE 0929-0424	UVES co-added	≤ -6.00 [a]	-4.28 ± 0.02	-4.39 ± 0.02	≤ -5.20 [a]	-5.18 ± 0.06
HE 1047-0436	UVES co-added	$-4.31^{+0.03}_{-0.02}$	-3.91 ± 0.01	-4.33 ± 0.02	≤ -5.50 [a]	-5.09 ± 0.03
HE 2156-3927	UVES co-added	-4.86 ± 0.03	-4.77 ± 0.01	-4.23 ± 0.01	≤ -5.40 [a]	≤ -6.60 [a]
HE 2322-0617	UVES co-added	-4.95 ± 0.03	-4.72 ± 0.02	-4.39 ± 0.01	$-4.43^{+0.10}_{-0.12}$	$-5.78^{+0.05}_{-0.06}$
Solar Abundance		-3.61	-4.21	-3.35	-4.11	-4.44

Note:
[a] Upper limit

Table 12.6.: Elemental abundances for the analyzed ^{3}He and two He-normal comparison B-type stars (HD 4539, CD-35° 15910) determined via the hybrid LTE/NLTE approach performed in ISIS - Part 2. The stars, whose UVES spectra have been analyzed, were taken from the hot subdwarf list of the ESO Supernova Ia Progenitor Survey (Lisker et al., 2005) and have been identified as ^{3}He enriched hot subdwarf B-type stars. All statistical errors are given as 1σ ($\approx$ 68%) confidence intervals. Solar abundances according to Asplund et al. (2009) are also listed as base-10 logarithmic particle densities relative to the density of all particles.

Star	Instrument	$\log n$(Al) [dex]	$\log n$(Si) [dex]	$\log n$(S) [dex]	$\log n$(Ar) [dex]	$\log n$(Fe) [dex]
HD 4539	CASPEC	$-6.40^{+0.04}_{-0.05}$	-5.32 ± 0.05	-5.07 ± 0.03	-5.15 ± 0.02	-4.40 ± 0.02
CD-35 15910	FEROS co-added	$-7.09^{+0.10}_{-0.11}$	-5.65 ± 0.02	-5.72 ± 0.04	≤ -6.60 [a]	-4.44 ± 0.01
PHL 25	CASPEC	≤ -8.00 [a]	$-4.80^{+0.03}_{-0.04}$	≤ -8.00 [a]	-5.28 ± 0.03	$-5.16^{+0.08}_{-0.11}$
PHL 25	HRS co-added	≤ -8.00 [a]	$-4.48^{+0.05}_{-0.04}$	≤ -7.20 [a]	-5.18 ± 0.03	$-4.96^{+0.06}_{-0.07}$
PHL 382	FEROS co-added	-6.36 ± 0.04	$-4.40^{+0.02}_{-0.03}$	-5.58 ± 0.02	-4.74 ± 0.02	-4.61 ± 0.02
SB 290	CASPEC co-added	-6.90 ± 0.10	-4.74 ± 0.03	$-5.80^{+0.07}_{-0.11}$	$-5.62^{+0.08}_{-0.11}$	≤ -6.40 [a]
SB 290	FEROS co-added	$-6.97^{+0.10}_{-0.15}$	-5.08 ± 0.03	$-5.57^{+0.05}_{-0.06}$	-5.53 ± 0.07	≤ -6.00 [a]
EC 03263-6403	FEROS co-added	$-6.40^{+0.07}_{-0.09}$	-5.02 ± 0.04	-4.75 ± 0.04	$-5.49^{+0.15}_{-0.25}$	-4.68 ± 0.04
EC 03591-3232	FEROS co-added	-5.55 ± 0.02	-4.32 ± 0.02	$-4.59^{+0.02}_{-0.04}$	-4.79 ± 0.02	-4.92 ± 0.02
EC 12234-2607	FEROS co-added	-6.44 ± 0.08	-4.74 ± 0.03	-4.85 ± 0.04	$-5.47^{+0.10}_{-0.12}$	$-5.06^{+0.05}_{-0.04}$
EC 14338-1445	FEROS co-added	-6.16 ± 0.03	-4.72 ± 0.03	-4.74 ± 0.03	-5.30 ± 0.06	-4.74 ± 0.02
Feige 38	FEROS co-added	-6.27 ± 0.03	-4.35 ± 0.01	-4.52 ± 0.01	-4.87 ± 0.02	-4.89 ± 0.02
BD+48 2721	FOCES	-6.55 ± 0.05	$-5.17^{+0.02}_{-0.03}$	-5.39 ± 0.02	-5.30 ± 0.02	$-5.32^{+0.04}_{-0.03}$
PG 1519+640	FOCES	-5.88 ± 0.07	-4.99 ± 0.04	-4.68 ± 0.05	≤ -4.70 [a]	≤ -5.70 [a]
PG 1710+490	FOCES	-5.93 ± 0.07	-4.50 ± 0.04	-4.69 ± 0.06	$-4.36^{+0.08}_{-0.10}$	$-4.48^{+0.05}_{-0.06}$
HE 0929-0424	UVES co-added	-6.09 ± 0.08	-5.34 ± 0.04	-5.16 ± 0.04	$-5.25^{+0.09}_{-0.12}$	b
HE 1047-0436	UVES co-added	-6.48 ± 0.08	-5.02 ± 0.02	$-4.41^{+0.03}_{-0.02}$	-4.89 ± 0.05	b
HE 2156-3927	UVES co-added	≤ -8.00 [a]	-5.93 ± 0.05	-5.46 ± 0.03	$-5.39^{+0.04}_{-0.05}$	b
HE 2322-0617	UVES co-added	$-6.92^{+0.15}_{-0.20}$	≤ -6.60 [a]	$-5.33^{+0.03}_{-0.02}$	≤ -7.10 [a]	b
Solar Abundance		-5.59	-4.53	-4.92	-5.64	-4.54

Note:

[a] Upper limit

[b] An upper limit could not be derived (see chapter 12.4 for details).

13. Summary and Outlook

In the recent past, $^3\mathrm{He}$ isotope enrichment in helium-weak B-type main-sequence (14 000 K $\lesssim T_{\text{eff}} \lesssim$ 21 000 K) as well as in blue horizontal branch (BHB) and hot subdwarf B stars (27 000 K $\lesssim T_{\text{eff}} \lesssim$ 31 000 K) has been discovered. Atomic diffusion processes occurring in the atmosphere of these stars lead to the observed abundance anomalies. However, normal diffusion processes driven by gravitational settling take too long and therefore are inadequate to explain the observed $^3\mathrm{He}$ stars. That is why other diffusion theory models like the presented diffusion mass-loss model for main-sequence stars and the light induced drift (LID) had to be developed. Empirical information on the photospheric $^3\mathrm{He}/^4\mathrm{He}$ abundance ratios are required to constrain these theoretical concepts, though.
That is why this thesis' main goal was the distinction between $^3\mathrm{He}$ and $^4\mathrm{He}$ and the determination of their individual elemental abundances in the atmospheres of a sample of 17 B-type stars, consisting of two $^3\mathrm{He}$ BHB, and 15 subdwarf B stars (13 $^3\mathrm{He}$ sdBs and two He-normal sdBs) in order to spectroscopically study the $^3\mathrm{He}$ anomaly. The total analyzed sdB sample included the eight $^3\mathrm{He}$ sdB stars found by Geier et al. (2013a), the rotating sdB star SB 290 as well as the four newly discovered $^3\mathrm{He}$ enriched sdB stars, HE 0929-0424, HE 1047-0436, HE 2156-3927, and HE 2322-0617, taken from the hot subdwarf list of the ESO Supernova Ia Progenitor Survey (Lisker et al., 2005). For the latter ones, the isotopic line shift of the strongest helium line, He I, 6678 Å, could not be measured, though, since the analyzed UVES spectra do not cover it. Overall, high-resolution spectra obtained by five different Echelle spectrographs, including CASPEC, FEROS, FOCES, HRS, and UVES, were used in order to perform the quantitative spectroscopic analyses in the framework of this thesis.
At first, a quantitative spectral analysis in LTE was performed with SPAS in order to estimate atmospheric parameters (effective temperature, T_{eff}, surface gravity, $\log(g)$, helium abundance, $\log(y)$, projected rotation velocity, $v \sin i$, as well as radial velocity, v_{rad}). As SPAS is limited to four fit parameters only, it is not well-suited for the accurate determination of both isotopic helium abundances at once, though. Hence, and because of the fact that a well-determined radial velocity is needed, SPAS' fitting routine had to be replaced by ISIS in the framework of the hybrid LTE/NLTE approach (Irrgang et al., 2014), which was performed in the second part of this thesis. Synthetic model spectra were calculated using the three generic codes ATLAS12, DETAIL, and SURFACE in order to further investigate the results derived from LTE. This approach has only been applied to subdwarf B stars before by Przybilla et al. (2005) and Latour et al. (2016). It has not been applied to any BHB star yet. The main focus was on the $^3\mathrm{He}$ anomaly, but also metal abundances for C, N, O, Ne, Mg, Al, Si, S, Ar, and Fe were derived iteratively. LTE model atmospheres computed within ATLAS12 are based on the mean metallicity for hot sdB stars and all model atoms used, including a lately developed $^3\mathrm{He}$ one, were used to calculate non-LTE occupation number densities within

DETAIL and SURFACE. The whole hybrid LTE/NLTE spectroscopic analysis was carried out completely within ISIS, which significantly facilitated the investigations as useful functions and tools as well as several different minimization algorithms could be used. Since ISIS also makes use of the whole spectrum, all synthesized metal lines were included to accurately determine radial velocities and correct for them.
Hereafter, the main results of the hybrid LTE/NLTE analysis are summarized in four sections.

Effective Temperatures and Surface Gravities

The effective temperatures and surface gravities of all analyzed hot subdwarf B stars derived from the hybrid LTE/NLTE analysis match the extreme horizontal branch, even resulting in lower 1σ errors than for LTE. Excessively high effective temperatures ($T_{\text{eff}} > 32\,000$ K) for PG 1519+640 and PG1710+490 are measured in hybrid LTE/NLTE, too, although He II, 4686 Å is not seen at all in the relevant FOCES spectra. This strengthens the hypothesis of poorly normalized spectra and results in an upper limit of $T_{\text{eff}} \lesssim 31\,000$ K for both stars. Similar to LTE results, BD+48° 2721 ($T_{\text{eff}} = 22,300 \pm 100$ K) is the sole exception to the clustering of all ^3He sdB stars in a narrow temperature strip between $\sim 26\,000$ K and $30\,000$ K, i.e., also very similar to the results of Geier et al. (2013a). Even the four newly found ^3He enriched sdB stars (HE 0929-0424, HE 1047-0436, HE 2156-3927, and HE 2322-0617) lie in this regime.

Isotopic Abundance Ratios

The distinction between ^3He and ^4He and the determination of the individual isotopic abundances as well as of the corresponding abundance ratios, $^4\text{He}/^3\text{He}$, all in all give reasonable results. Both He-normal comparison stars, HD 4539 and CD-35° 15910, do not show any ^3He at all, resulting in an extremely large abundance ratio of $^4\text{He}/^3\text{He}$ as expected. All other investigated ^3He B-type stars show ratios ranging from $\sim$ 0-7, being consistent with the observed isotopic line shifts. A new classification scheme based on the derived abundance ratio is proposed. Therefore, a natural boundary of $^4\text{He}/^3\text{He} \sim 0.5$ (number ratio) is set dividing the ^3He (with $^4\text{He}/^3\text{He} < 0.5$) from ^3He enriched (with $^4\text{He}/^3\text{He} > 0.5$) B-type stars. He-normal comparison stars, however, are characterized by a significantly high abundance ratio ($\gtrsim 1000$ in this analysis for HD 4539 and CD-35° 15910). The detection limit for ^3He enriched B-type stars has not been determined, though. All in all, seven ^3He B-type stars (PHL 382, SB 290, EC 03263-6403, EC 03591-3232, EC 14338-1445, Feige 38, and PG 1710+490) and eight ^3He enriched B-type stars (PHL 25, EC 12234-2607, BD+48 2721, PG 1519+640, HE 0929-0424, HE 1047-0436, HE 2156-3927, and HE 2322-0617) have been found. HE 0929-0424, HE 1047-0436, HE 2156-3927, and HE 2322-0617 are identified as ^3He hot subdwarf B-type stars because of their isotopic ratio of $\sim$ 1-3, although the analyzed UVES spectra do not include the helium line with the strongest isotopic shift, He I, 6678 Å. Consequently, concerning the determination of $^3\mathrm{He}$ and $^4\mathrm{He}$ as well as of the isotopic abundance ratio, the tip of the iceberg cannot be reached for the stars from the ESO Supernova Ia Progenitor Survey.

Evidence for Helium Stratification

For some stars the investigated helium line profiles cannot be properly reproduced. These stars show evidence for helium stratification, in particular both analyzed BHB stars, PHL 25 and PHL 382, but also three sdB stars (EC 03591-3232, EC 12234-2607, and BD+48° 2721). It is the first time that helium stratification has been observed in any sdB star. The strongest among the diffuse He I lines, at λ4026 Å and λ4472 Å, exhibit shallow cores in combination with unusually broad wings, being a clear sign that the element is not homogeneously distributed throughout the stellar atmosphere, but instead shows a vertical abundance stratification, meaning that the (isotopic) helium abundances are low in outer layers, but high in deeper ones. This is very similar to what has been reported on the main-sequence prototype HgMn star κ Cancri by Maza et al. (2014) and on the BHB star Feige 86 by Bonifacio et al. (1995), respectively. Moreover, the stratification hypothesis is supported by another observation. The further out the particular helium absorption line core is formed in the stellar atmosphere, the worse it can be reproduced by synthetic model spectra, too, particularly applying to λ4472 Å, λ4922 Å, λ5016 Å, λ5875 Å, λ6678 Å as well as to λ7065 Å. By implementing a smooth step function as shown by Farthmann et al. (1994), setting the helium abundance in the outer atmospheric layers to a lower level than further in, into the ATLAS code, being responsible for the modeled atmospheric structure, line cores which are produced in the outer cooler atmospheric layers are weakened. At the same time, line wings which are produced in the hotter inner layers are strengthened. Hence, this would account for stratification. In order estimate the limits of both helium isotopic abundances in the outer and inner stellar atmosphere of the relevant stars, a step in (isotopic) helium abundance was assumed. Therefore, three fits by eye were performed individually, including the line core of both helium absorption lines with the strongest isotopic line shift, He I, 6678 Å and He I, 4922 Å. The third fit by eye was performed in order to reproduce the line wings of He I, 4922 Å. The isotopic helium abundances overall increase when going from outer (He I, 6678 Å) to inner (line core and line wings of He I, 4922 Å) atmospheric layers. While the $^3\mathrm{He}$ abundance increase is 1.30 dex at most, the change of $^4\mathrm{He}$ in the analyzed stars is even more significant, reading 1.80 dex at most. A linear correlation between line forming atmospheric depth and (isotopic) helium abundances therefore might be possible.

The hybrid LTE/NLTE analysis also shows that SB 290 is the only star having a projected rotation velocity significantly different from zero ($\sim$ 50 km s^{-1}) which is consistent with the finding of Geier et al. (2013b) and the fact that most sdBs are known to be slow rotators. Significant mismatches of the cores of the strongest He I lines are obvious for SB 290, too, although less strong than for the other stratified stars. Thus, vertical helium stratification might also be possible for SB 290. Because of the star's high rotation velocity and the line broadening coming along with it, however, larger problems in fitting due to stratification, as seen for the other stratified stars, might be hidden. The determined projected rotation velocity value for PHL 25 ($v \sin i \lesssim 6.3\,\mathrm{km\,s^{-1}}$) is at odds with the former one derived from LTE ($v \sin i \sim 38\,\mathrm{km\,s^{-1}}$). However, high rotations for PHL 25 can be excluded because they cannot reproduce the observed metal lines at all. The $v \sin i$ values wrongly derived from LTE could be explained by helium stratification as well, since helium lines appear broader in the case of stratified atmospheres. Therefore, a high projected rotation velocity is needed to reproduce the relevant helium lines. Metal lines are unaffected by stratification and, thus, give the correct projected rotation velocity value. Hence, PHL 25 does not rotate.

Metal Abundance Pattern of $^3\mathrm{He}$ Stars

The derived $^3\mathrm{He}$ sdB metal abundances all in all match the ones measured by Geier (2013). Only small deviations occur. Carbon, nitrogen, and oxygen show similar results compared to Geier (2013). The derived neon abundance is hardly comparable to the one of Geier (2013) since only a single Ne I line but no Ne II lines could be analyzed. While magnesium does not show any clear trend with temperature, aluminum does as measured by Geier (2013). Silicon exhibits no clear trend in the analyzed temperature regime, but scatters similarly strong compared to Geier (2013). Sulfur and argon strongly scatter, although the former one not as much as measured by Geier (2013). In principle, argon increases with effective temperature as found by Geier (2013), although a larger sample is needed in order to clarify the issue. Last, the iron abundance more or less stays constant for all temperatures, if stars showing upper limits only are excluded. This is in good agreement with Geier (2013), too.

When comparing the observed $^3\mathrm{He}$ sdB metal abundances to mean sdB abundances from Naslim et al. (2013), this results in high abundances for carbon, silicon, sulfur, and argon for most of the analyzed $^3\mathrm{He}$ sdBs. Hence, the $^3\mathrm{He}$ hot sudbwarf B stars belong to the group of carbon-, silicon-, sulfur-, and argon-rich sdBs. Whereas the observed neon abundance is actually lower than the mean one for sdBs (only a single Ne I line has been investigated, though), all other elemental abundances, i.e., nitrogen, oxygen, magnesium, aluminum, and iron only scatter slightly around their respective mean sdB value for most $^3\mathrm{He}$ sdBs.

Concerning the metal abundances of both analyzed $^3\mathrm{He}$ enriched BHB stars, PHL 382 shows the same abundance pattern as the analyzed hot subdwarf B stars and PHL 25 has much lower nitrogen, oxygen, neon, aluminum, and sulfur abundances. These derived abundances for PHL 25 are upper limits only, though. The measured carbon, magnesium, silicon, argon, and iron abundances for PHL 25, however, match the abundance patterns of the analyzed sdBs reasonably well.

Outlook

This thesis' results have shown that quantitative spectral analyses of $^3\mathrm{He}$ (enriched) B-type stars are an interesting but at the same time difficult task. Nevertheless, they are indispensable in order to constrain current diffusion theory models. The detection of helium stratification in some of the analyzed $^3\mathrm{He}$ stars makes the understanding of the atmospheric structure and of diffusion processes in the stellar atmospheres of these stars even more complicated, though. Today, only a few tens of B-type stars are classified as $^3\mathrm{He}$ (enriched) stars and for some of them excellent high-resolution spectra are available. The hybrid LTE/NLTE approach presented in this thesis would allow to perform a sophisticated quantitative analysis on them. This would allow to compare the properties of $^3\mathrm{He}$ stars among BHB, main-sequence and sdB stars and would gain insights into helium stratification, if detectable.

A quantitative spectral analysis of the stratification profile can be carried out by implementing a smooth step function into the ATLAS code, which sets the helium abundance in the outer atmospheric layers to a lower level than further in. By doing so, deeper insights on the atmospheric structure and on diffusion processes occurring in the stellar atmospheres of the relevant stratified $^3\mathrm{He}$ B-type stars are ensured.

On the observational side, infrared spectra would be most useful because the He I line at 10 830 Å is known to show the largest isotopic line shift ($\sim$ 1.32 Å), i.e., more than twice as large as measured for He I 6678 Å ($\sim$ 0.50 Å). This wavelength range now becomes accessible, e.g., by the CARMENES spectrograph at the Calar Alto 3.5 m telescope.

A. LTE Analysis

A.1. Hydrogen and Helium Line Fits

Sorted by the spectral type, the comparison between best fit model spectrum (red line) and stellar spectrum (black line) for the hydrogen and helium lines used for the LTE analysis via SPAS (see chapter 10) of the different sample stars are shown in the following. Generally, $H_\alpha = 6565\,\text{Å}$ is excluded for all stars because of strong non-LTE effects going along with it which cannot be modeled properly in LTE. Also, all helium lines showing strong isotopic line shifts due to $^3\mathrm{He}$ enrichment are not used for the LTE analysis. Since the degree of $^3\mathrm{He}$ enrichment differs from star to star, the excluded helium lines also vary. Last but not least, the continuum is defined manually within SPAS in cases where it has obviously not been set properly at the end of data reduction. Frequently, this is the case for hydrogen Balmer lines (see chapter 9.2 for details). For some stars, see for instance the line fits of BD+48° 2721 in Fig. A.1.28 and A.1.29, parts of the hydrogen Balmer wings even have to be excluded from fitting because of wrong normalization. In total, the analyzed sample consists of 13 B-type stars, including two He-normal sdB comparison stars (HD 4539 and CD-35° 15910), two $^3\mathrm{He}$ BHB stars (PHL 25 and PHL 382), and nine $^3\mathrm{He}$ sdB stars. In order to illustrate the $^3\mathrm{He}$ isotopic shifts, all spectra have been radial-velocity (RV)-corrected. The particular positions of the rest-frame wavelengths of hydrogen (cyan), $^4\mathrm{He}$ (blue) and $^3\mathrm{He}$ (green) are marked by dashed lines. The grid used is based on solar metallicity and consists of model spectra with 0.01%, 0.1%, 1%, 3% and 9.1% helium abundance, respectively (see chapter 10 for details). Only hydrogen and helium lines are synthesized. Macroturbulence ζ is set to zero and microturbulence ξ is not treated at all for the LTE analysis in SPAS.

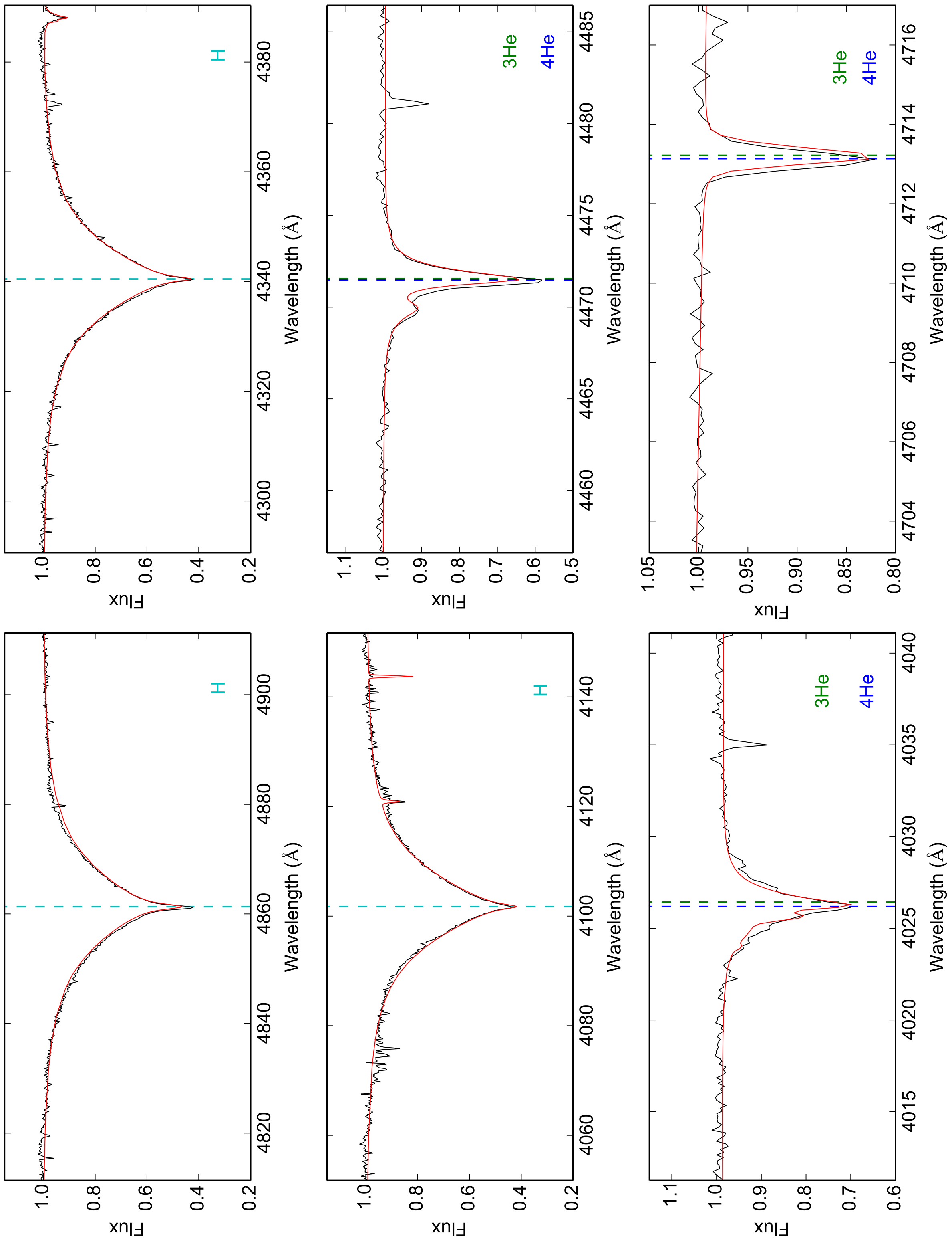

Figure A.1.1.: Hydrogen and helium lines in the CASPEC spectrum of the He-normal comparison star HD 4539 used for the LTE analysis with SPAS - Part 1.

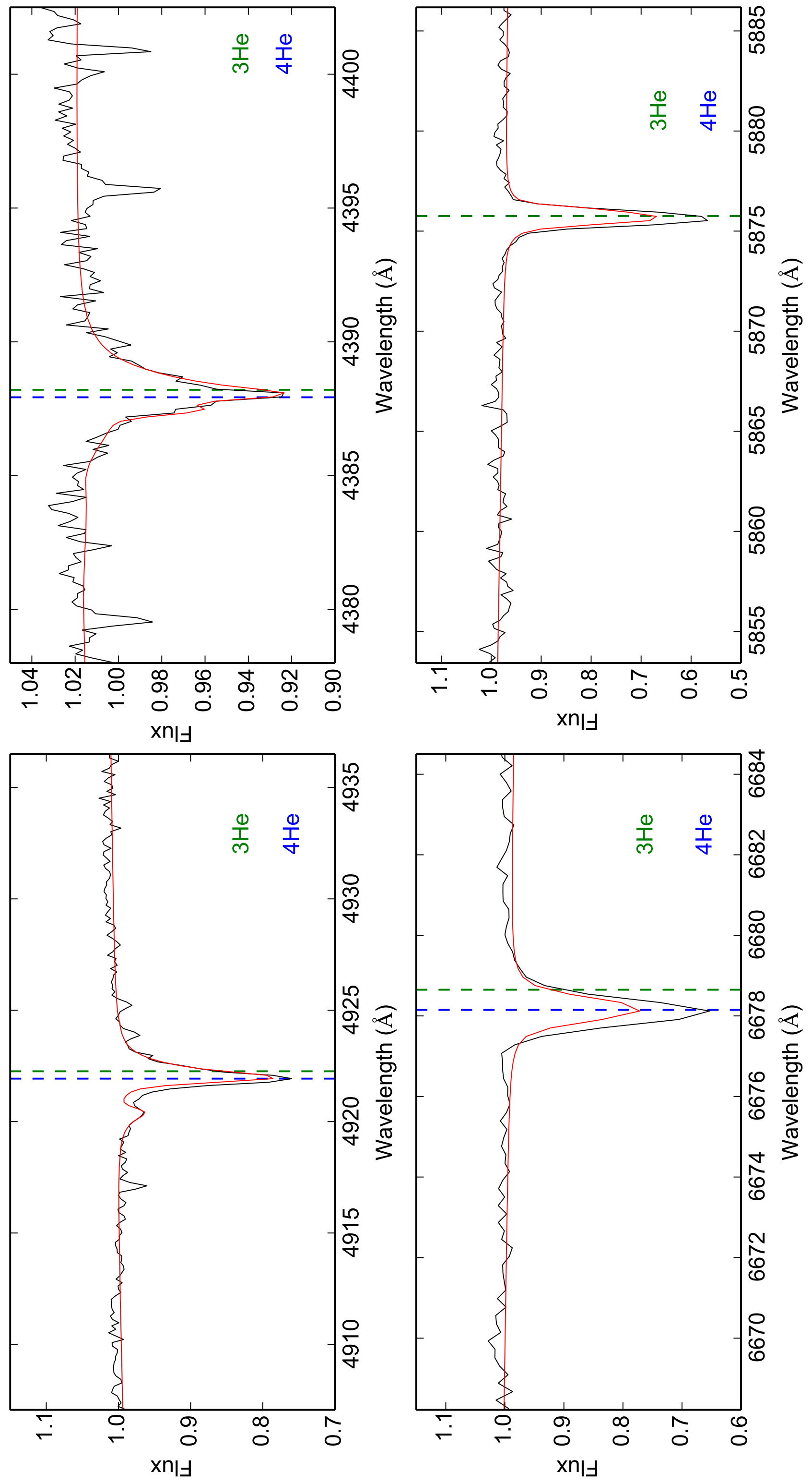

Figure A.1.2.: Hydrogen and helium lines in the CASPEC spectrum of the He-normal comparison star HD 4539 used for the LTE analysis with SPAS - Part 2.

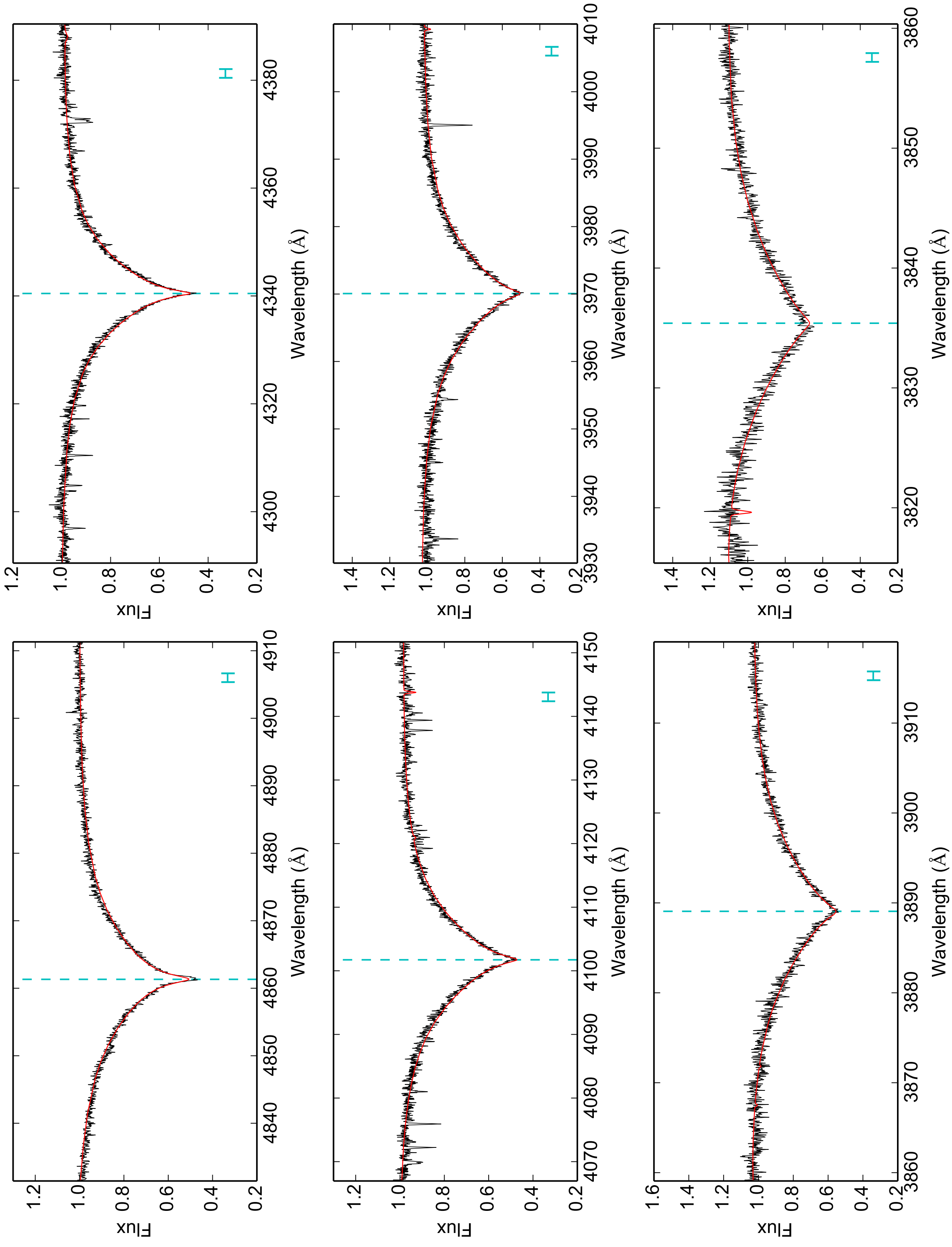

Figure A.1.3.: Hydrogen and helium lines in the co-added FEROS spectrum of the He-normal comparison star CD-35° 15910 used for the LTE analysis with SPAS - Part 1.

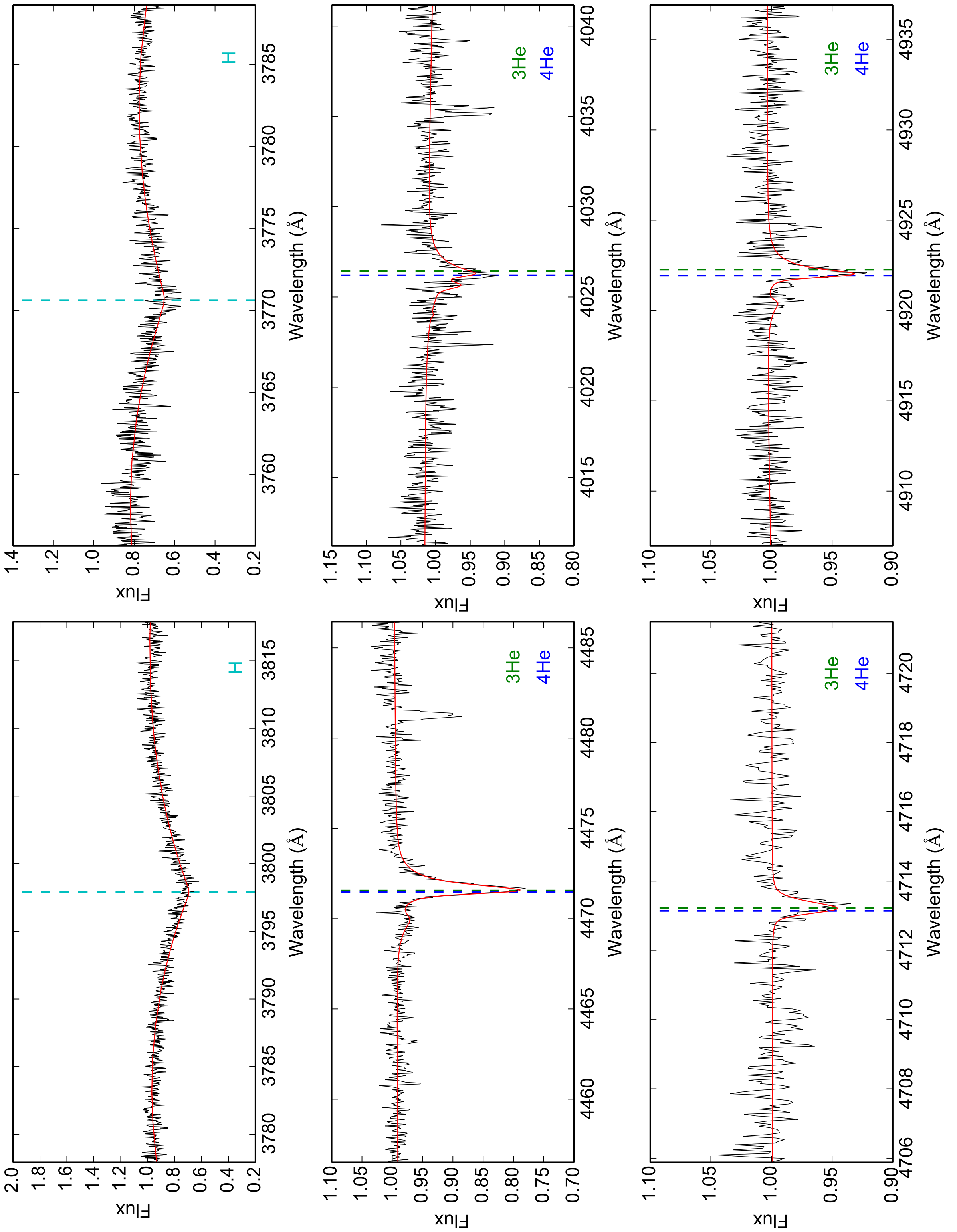

Figure A.1.4.: Hydrogen and helium lines in the co-added FEROS spectrum of the He-normal comparison star CD-35° 15910 used for the LTE analysis with SPAS - Part 2.

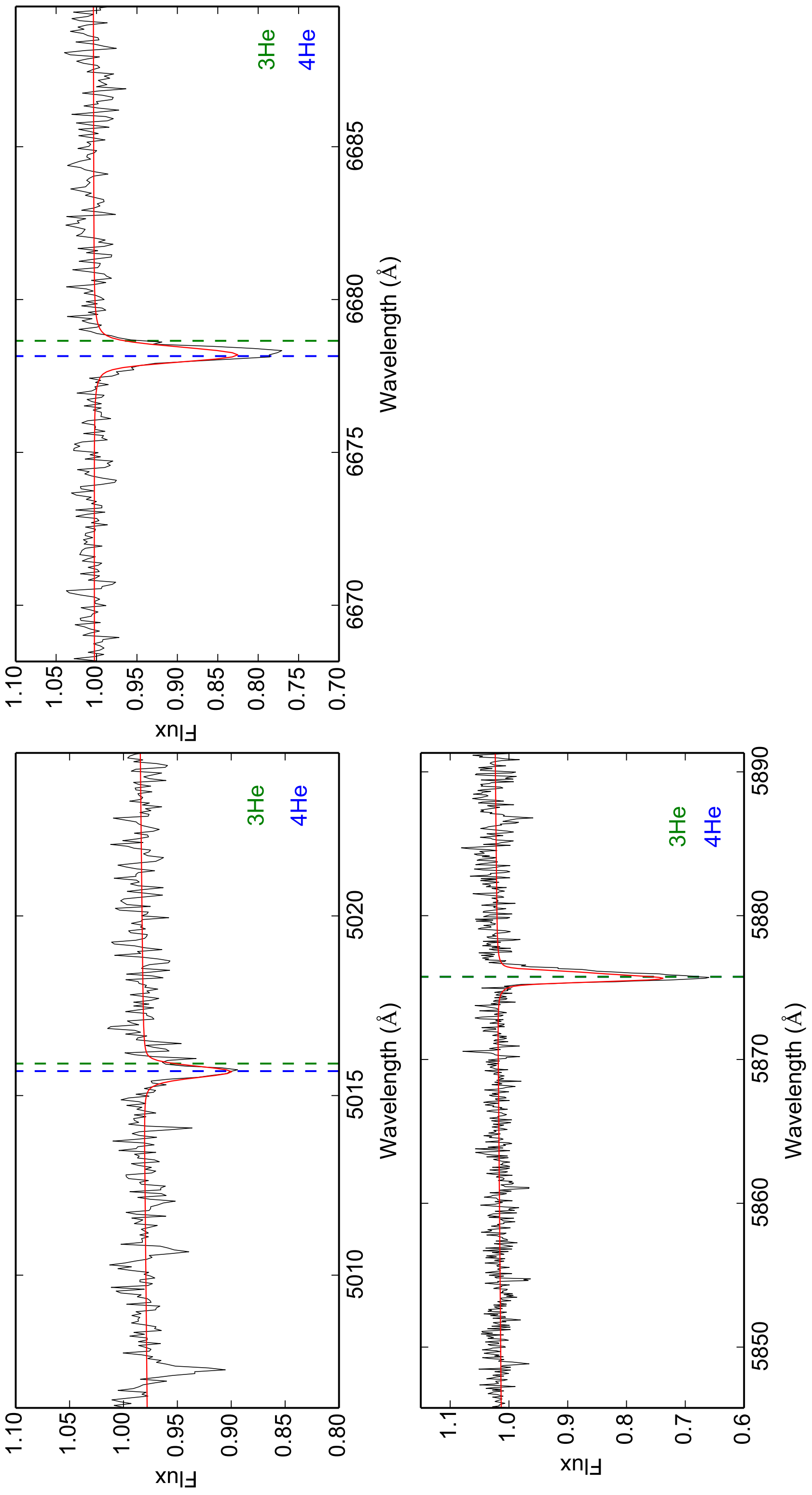

Figure A.1.5.: Hydrogen and helium lines in the co-added FEROS spectrum of the He-normal comparison star CD-35° 15910 used for the LTE analysis with SPAS - Part 3.

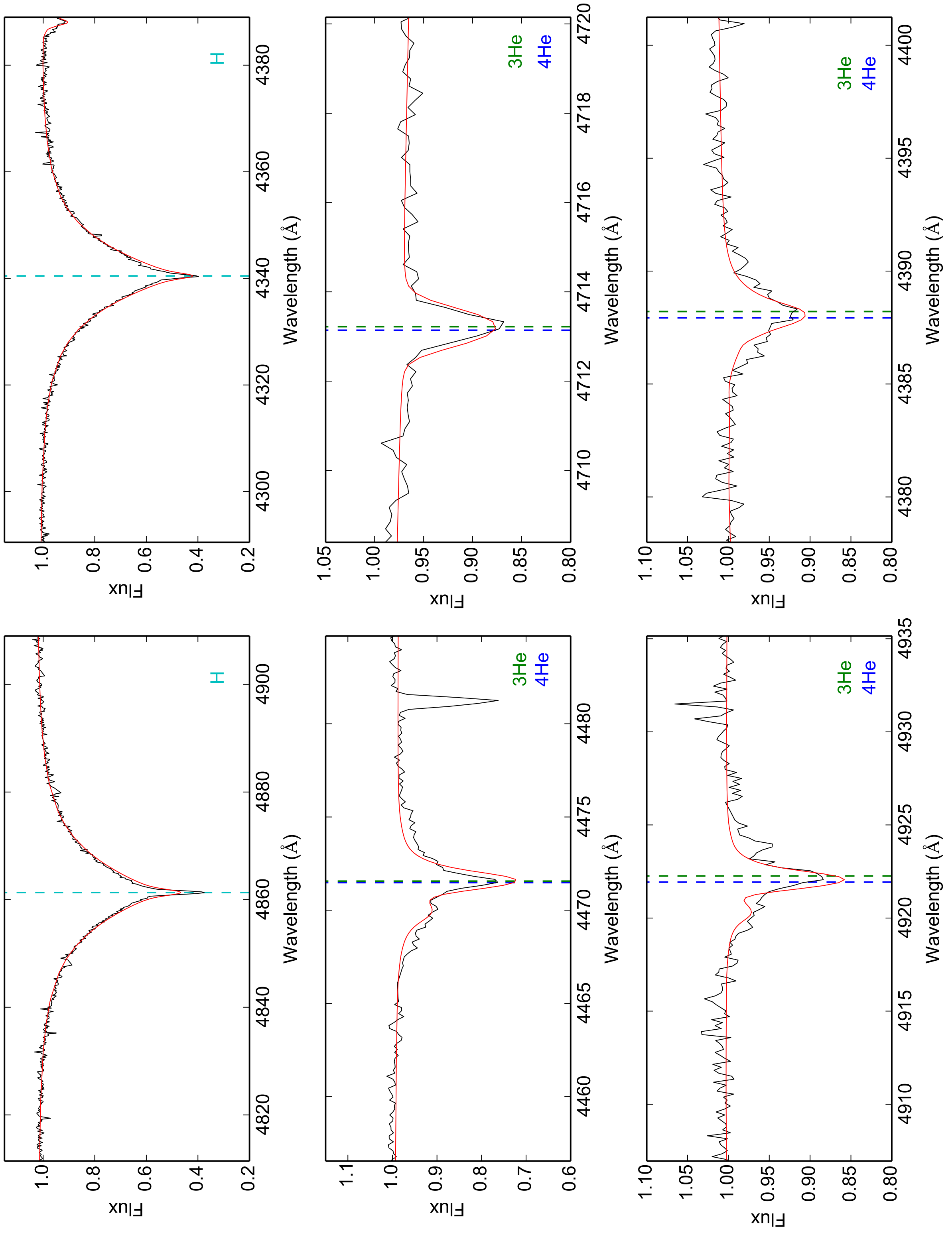

Figure A.1.6.: Hydrogen and helium lines in the CASPEC spectrum of the $^{3}\mathrm{He}$ enriched star PHL 25 used for the LTE analysis with SPAS - Part 1.

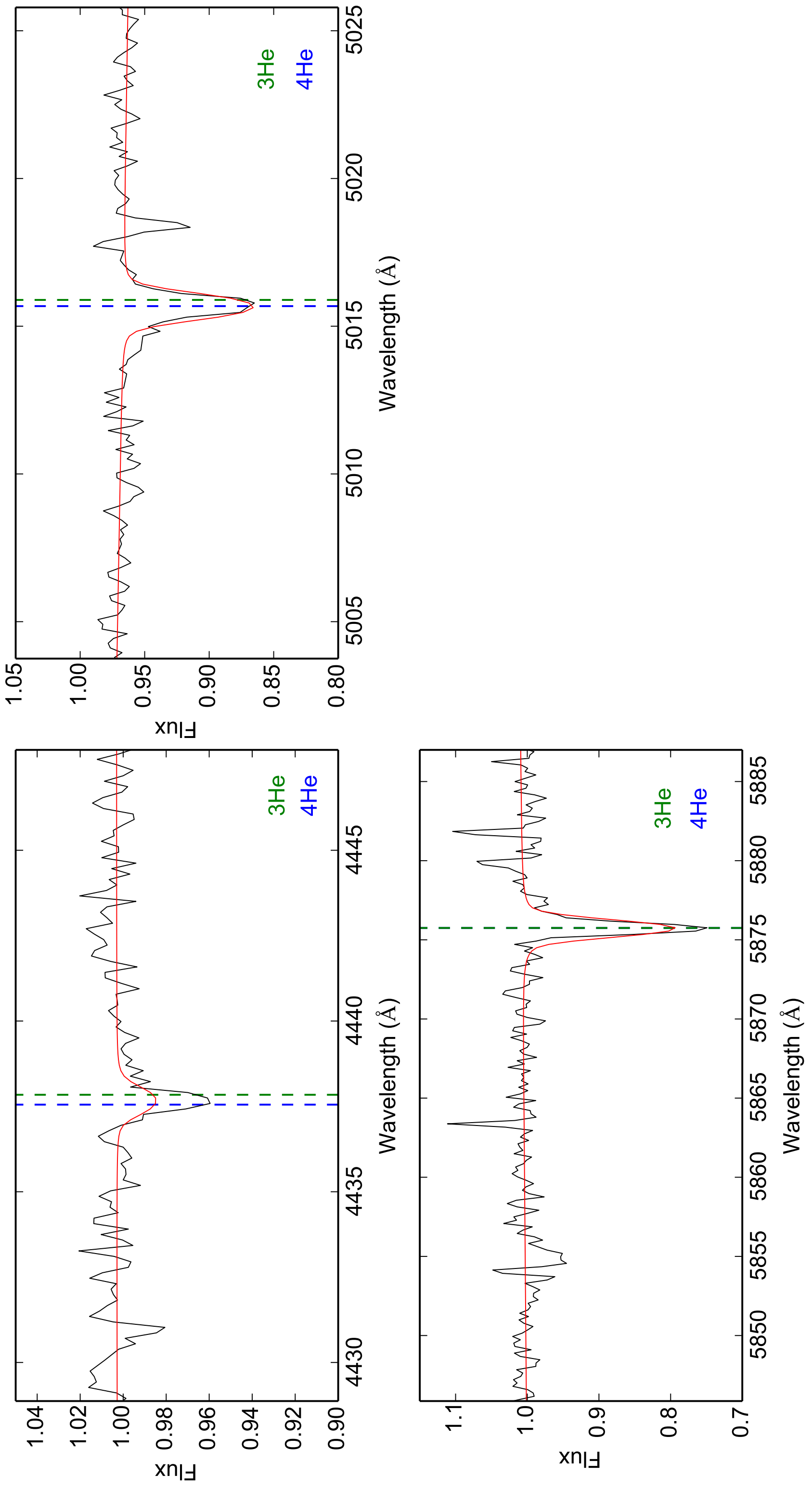

Figure A.1.7.: Hydrogen and helium lines in the CASPEC spectrum of the $^3\mathrm{He}$ enriched star PHL 25 used for the LTE analysis with SPAS - Part 2.

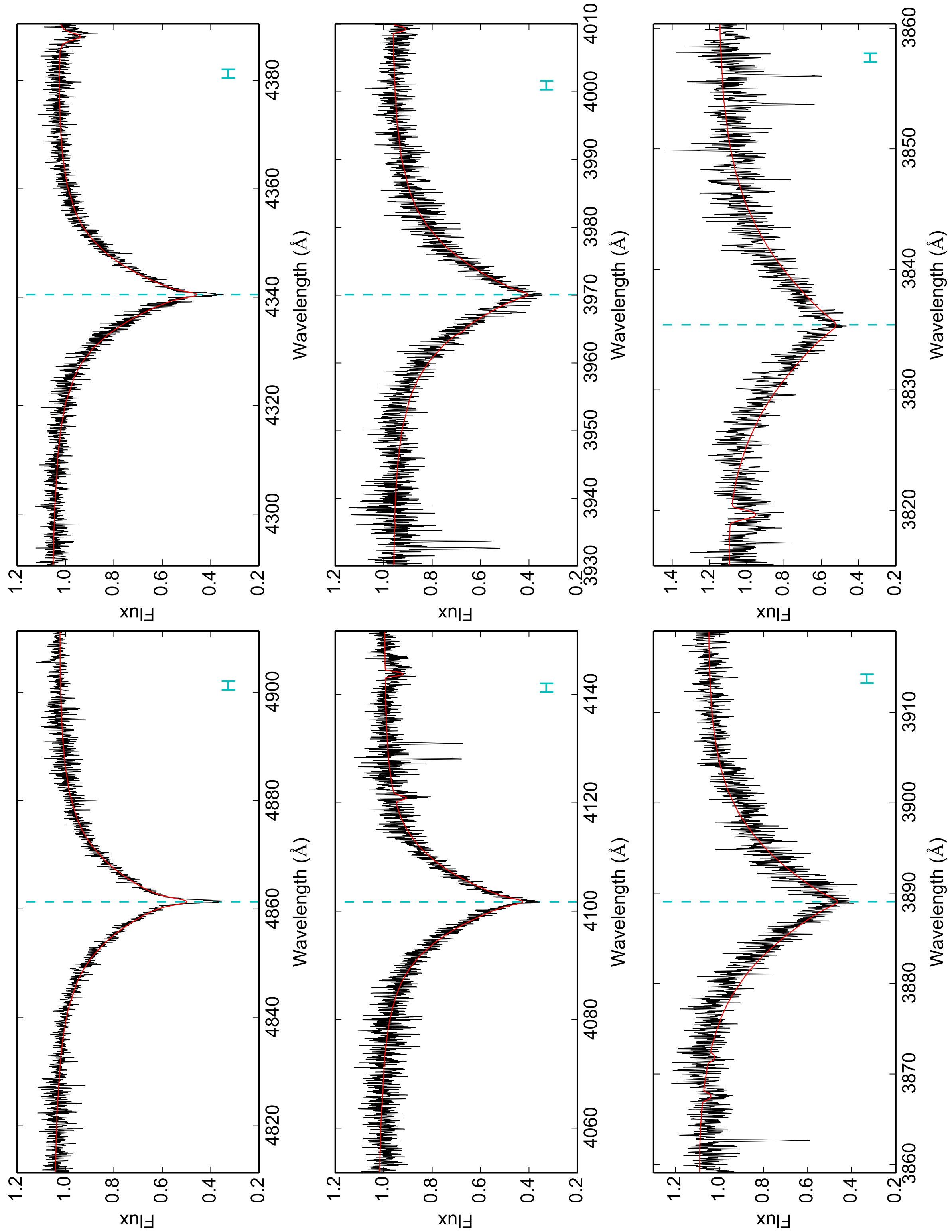

Figure A.1.8.: Hydrogen and helium lines in the co-added HRS spectrum of the $^{3}\mathrm{He}$ enriched star PHL 25 used for the LTE analysis with SPAS - Part 1.

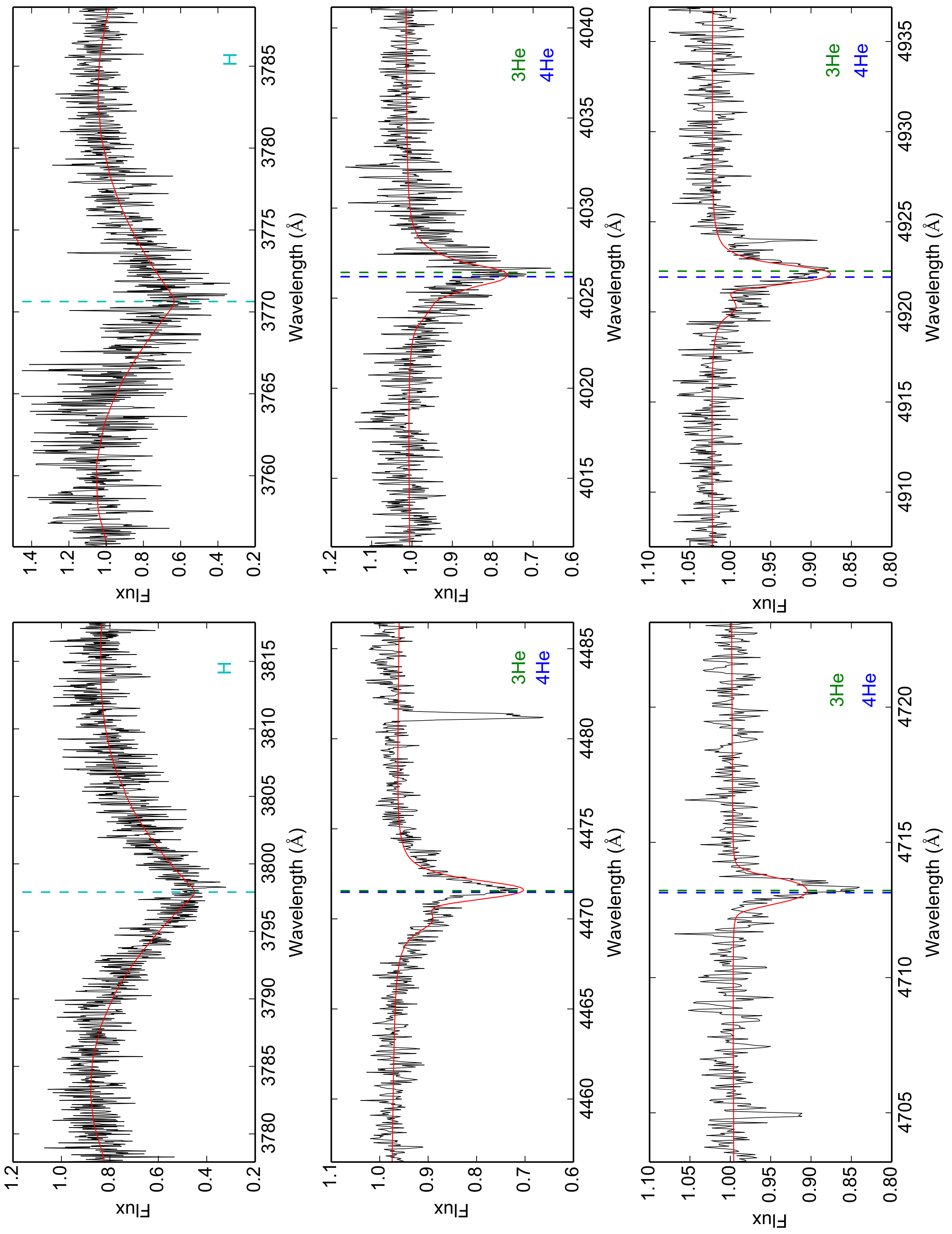

Figure A.1.9.: Hydrogen and helium lines in the co-added HRS spectrum of the ${}^{3}\mathrm{He}$ enriched star PHL 25 used for the LTE analysis with SPAS - Part 2.

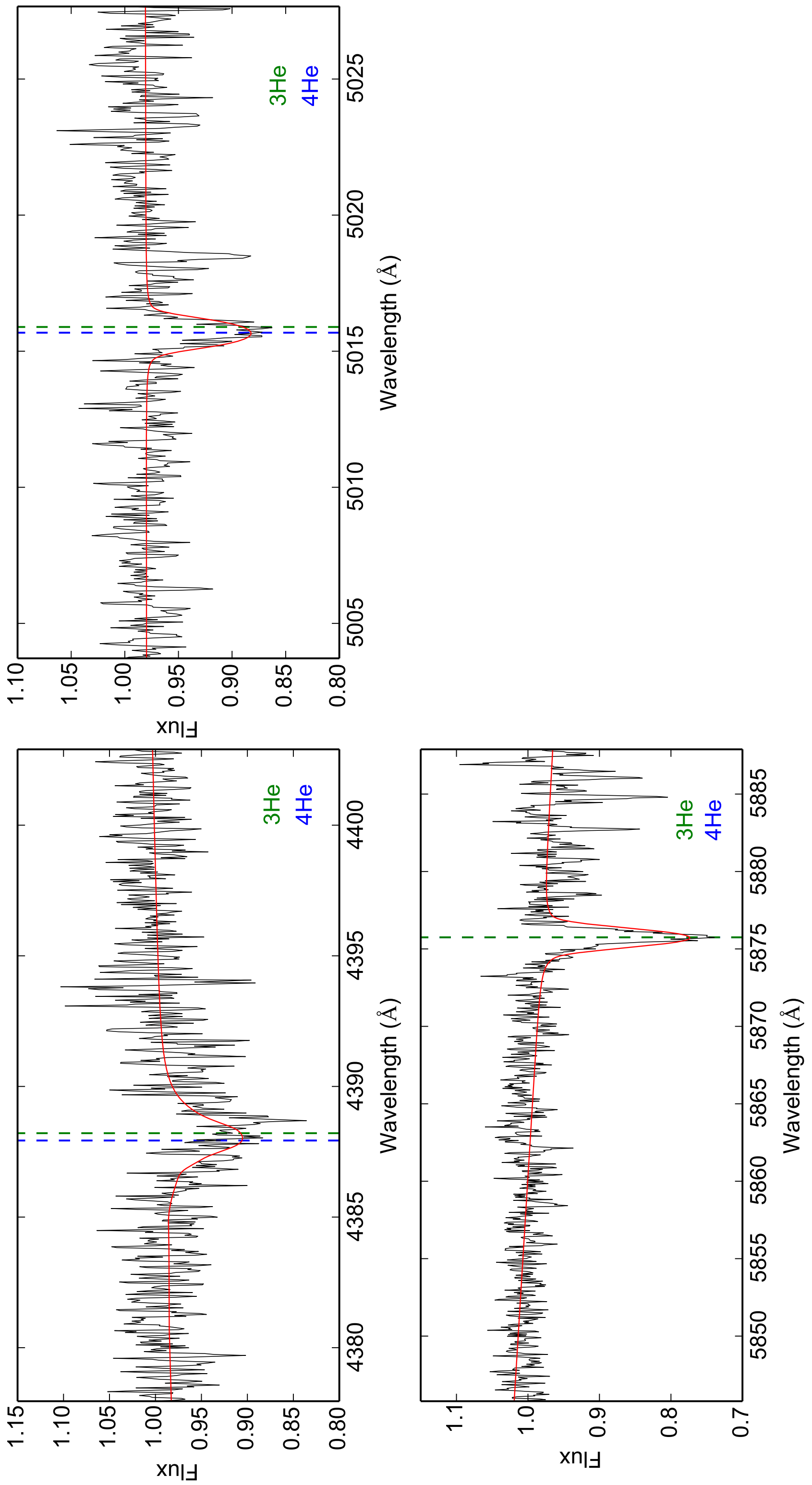

Figure A.1.10.: Hydrogen and helium lines in the co-added HRS spectrum of the $^{3}\mathrm{He}$ enriched star PHL 25 used for the LTE analysis with SPAS - Part 3.

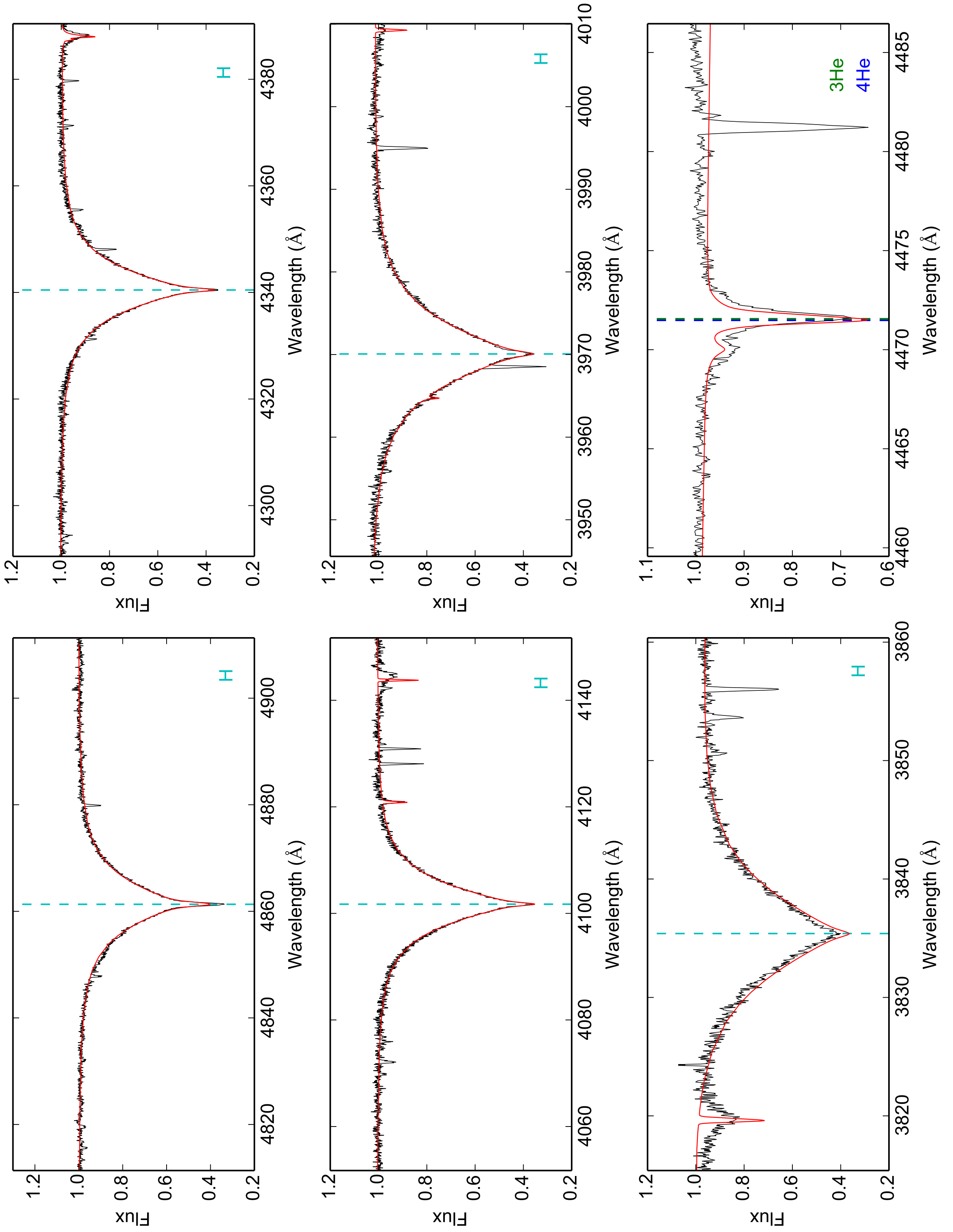

Figure A.1.11.: Hydrogen and helium lines in the co-added FEROS spectrum of the $^{3}\mathrm{He}$ enriched star PHL 382 used for the LTE analysis with SPAS - Part 1.

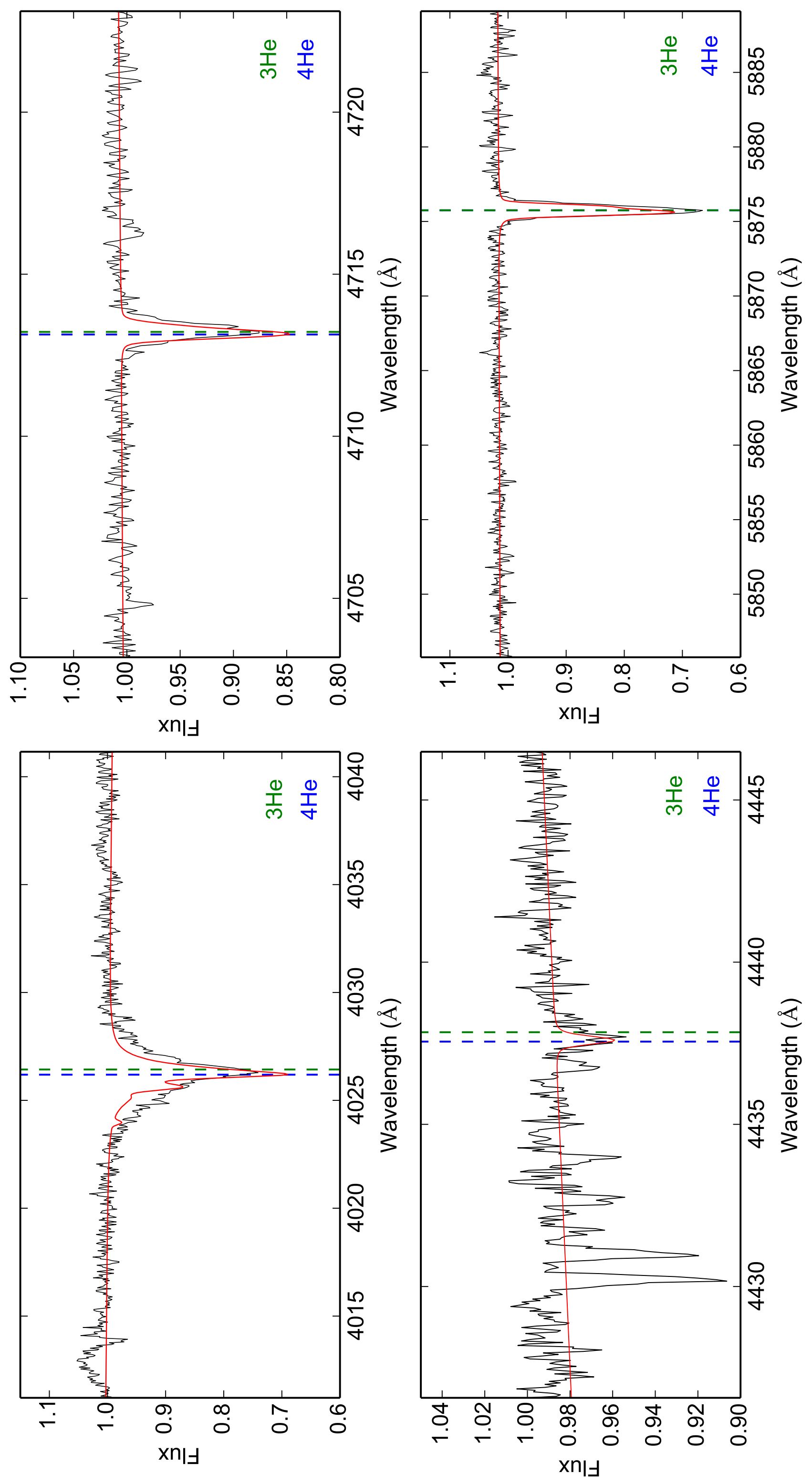

Figure A.1.12.: Hydrogen and helium lines in the co-added FEROS spectrum of the $^{3}\mathrm{He}$ enriched star PHL 382 used for the LTE analysis with SPAS - Part 2.

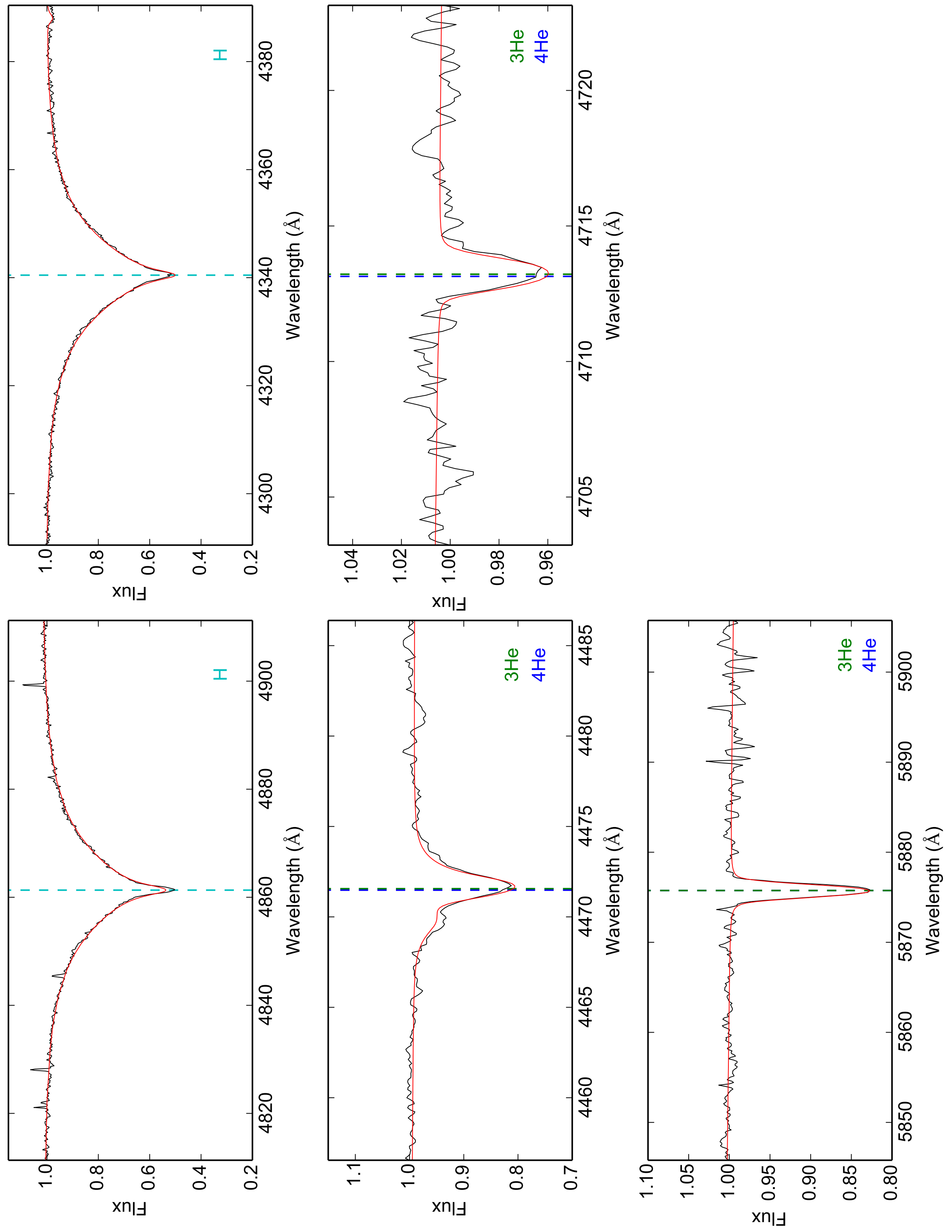

Figure A.1.13.: Hydrogen and helium lines in the co-added CASPEC spectrum of the $^{3}\mathrm{He}$ star SB 290 used for the LTE analysis with SPAS.

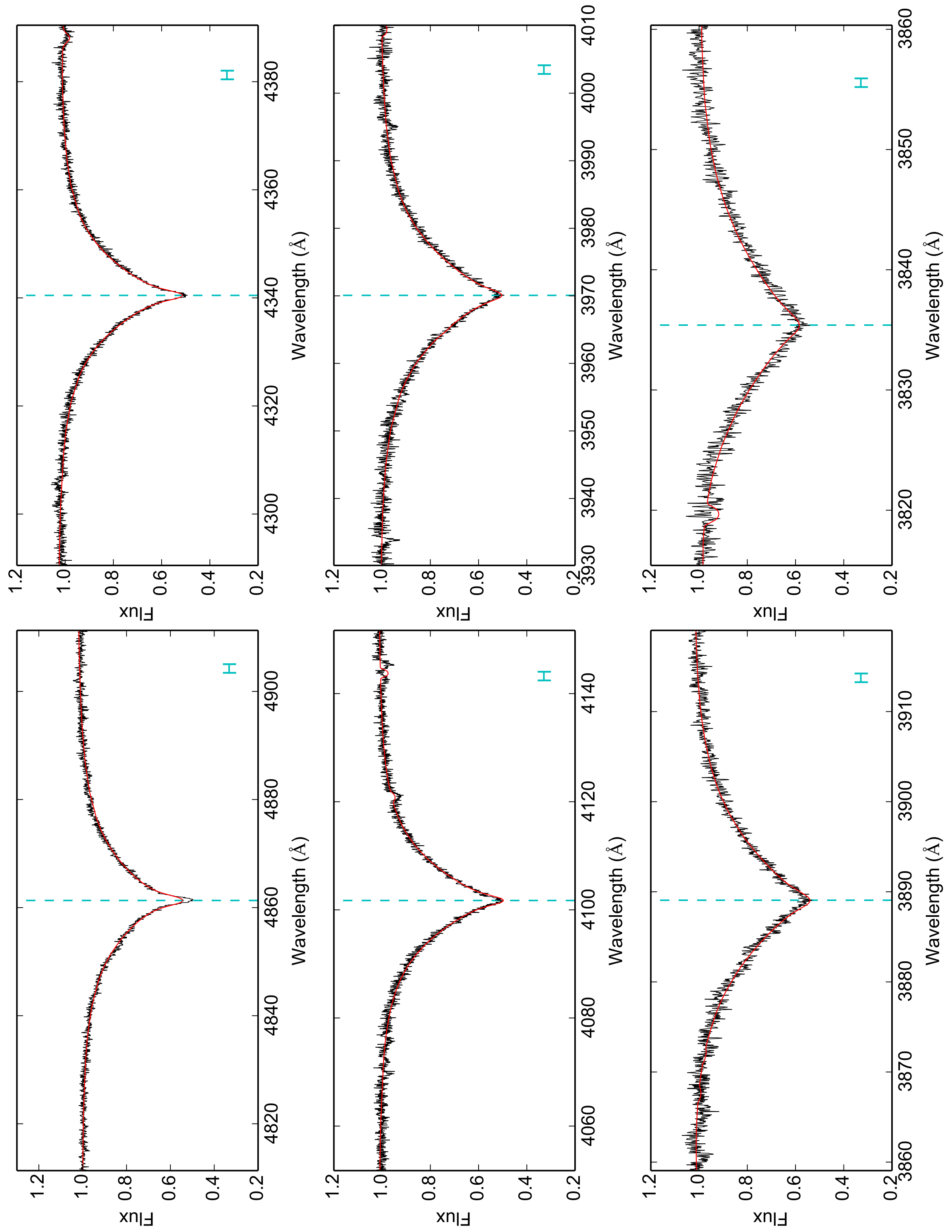

Figure A.1.14.: Hydrogen and helium lines in the co-added FEROS spectrum of the $^{3}\mathrm{He}$ star SB 290 used for the LTE analysis with SPAS - Part 1.

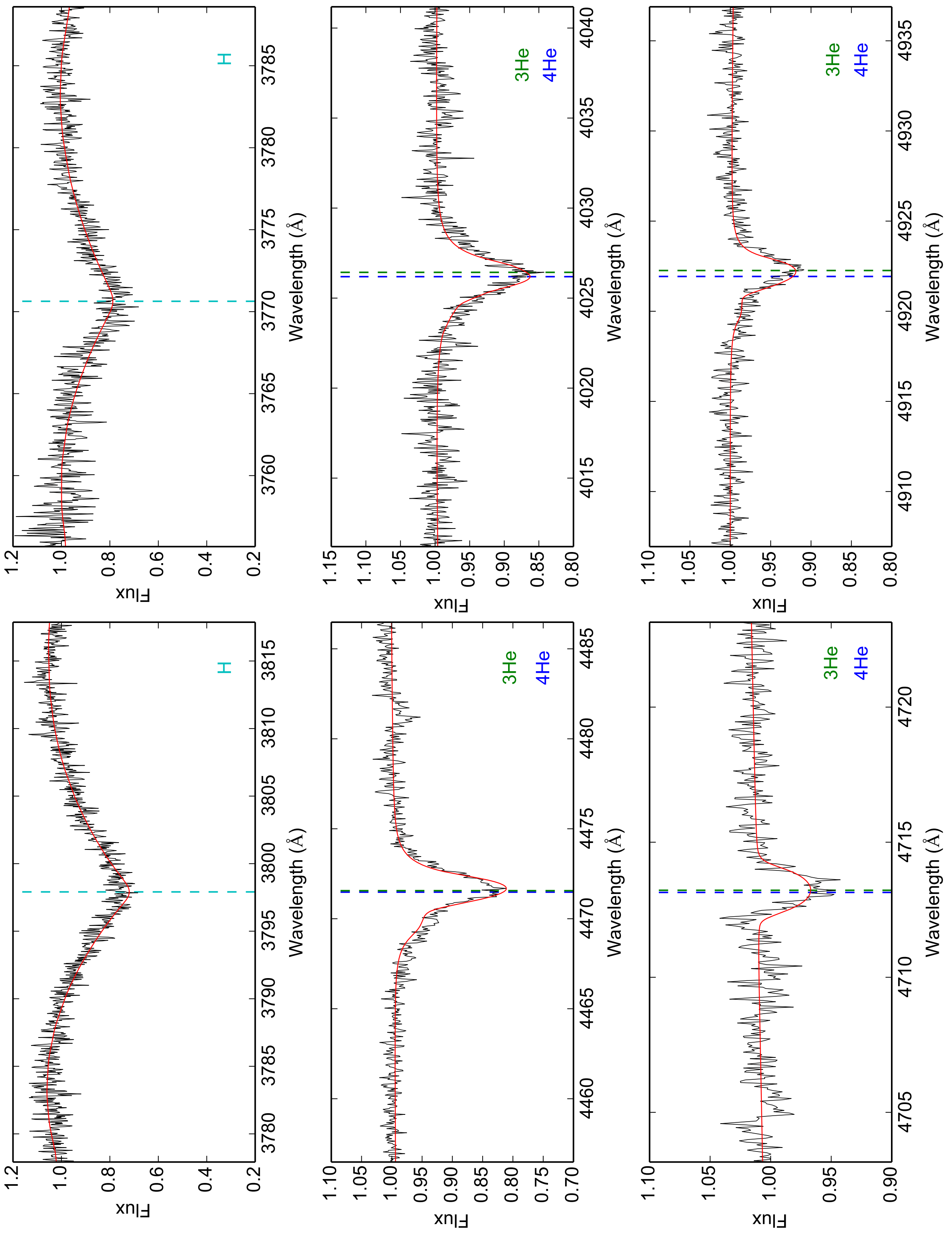

Figure A.1.15.: Hydrogen and helium lines in the co-added FEROS spectrum of the $^3\mathrm{He}$ star SB 290 used for the LTE analysis with SPAS - Part 2.

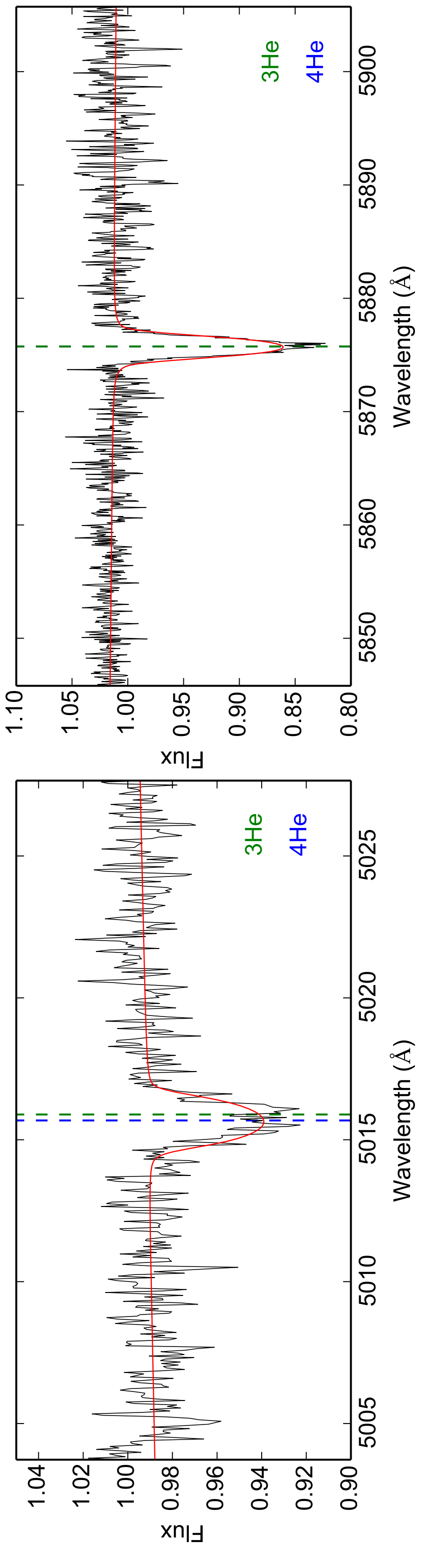

Figure A.1.16.: Hydrogen and helium lines in the co-added FEROS spectrum of the $^{3}\mathrm{He}$ star SB 290 used for the LTE analysis with SPAS - Part 3.

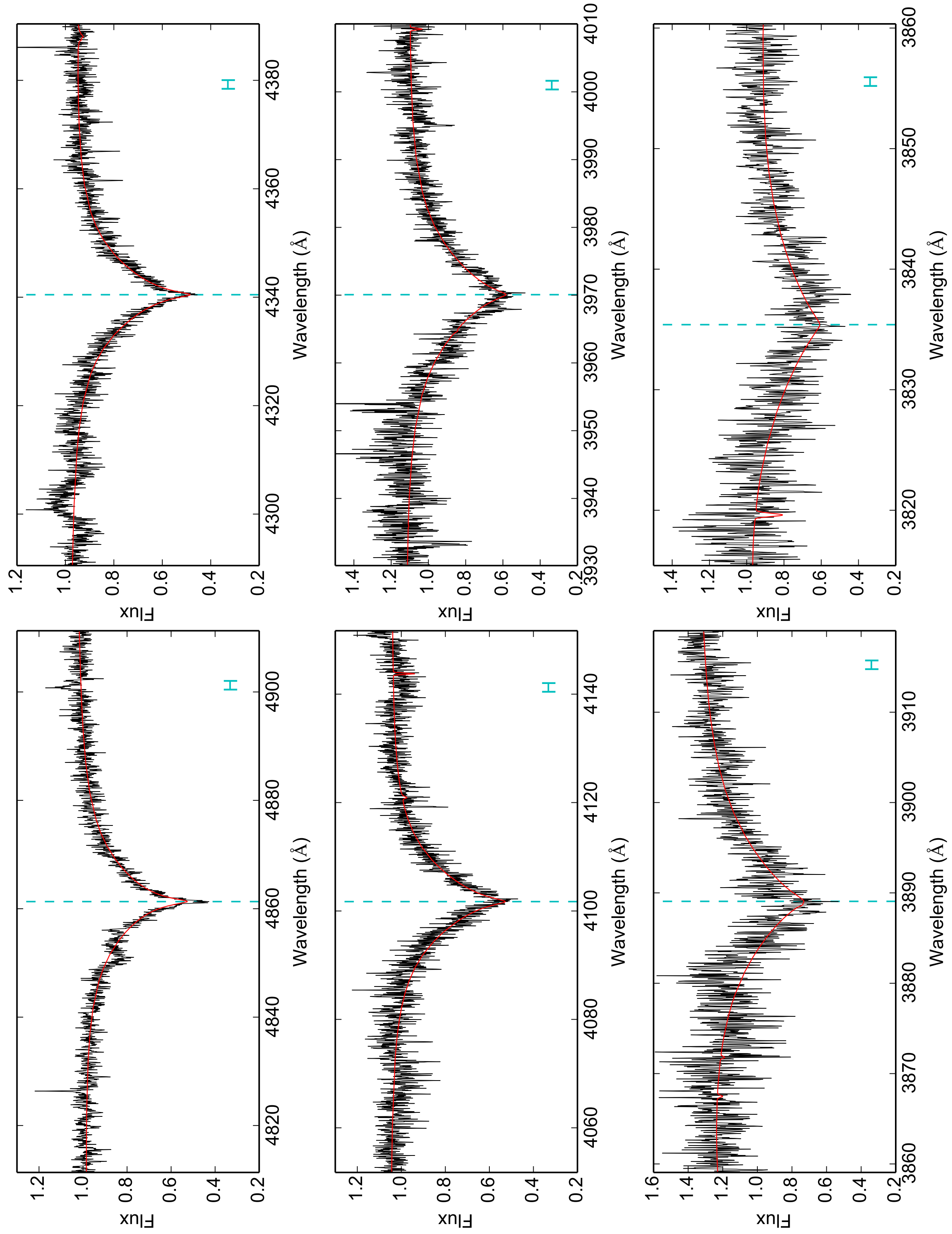

Figure A.1.17.: Hydrogen and helium lines in the co-added FEROS spectrum of the $^3\mathrm{He}$ star EC 03263-6403 used for the LTE analysis with SPAS - Part 1.

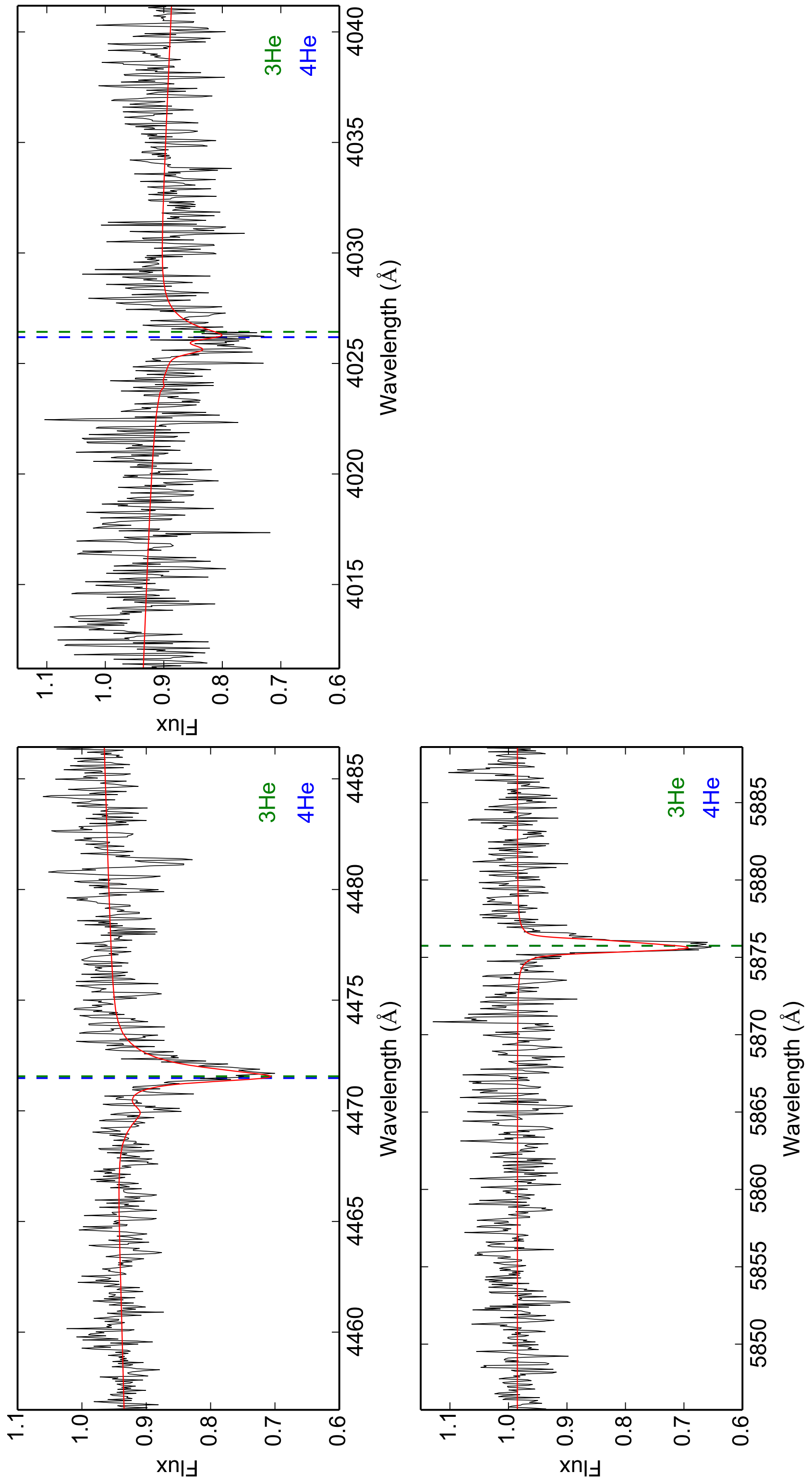

Figure A.1.18.: Hydrogen and helium lines in the co-added FEROS spectrum of the $^{3}\mathrm{He}$ star EC 03263-6403 used for the LTE analysis with SPAS - Part 2.

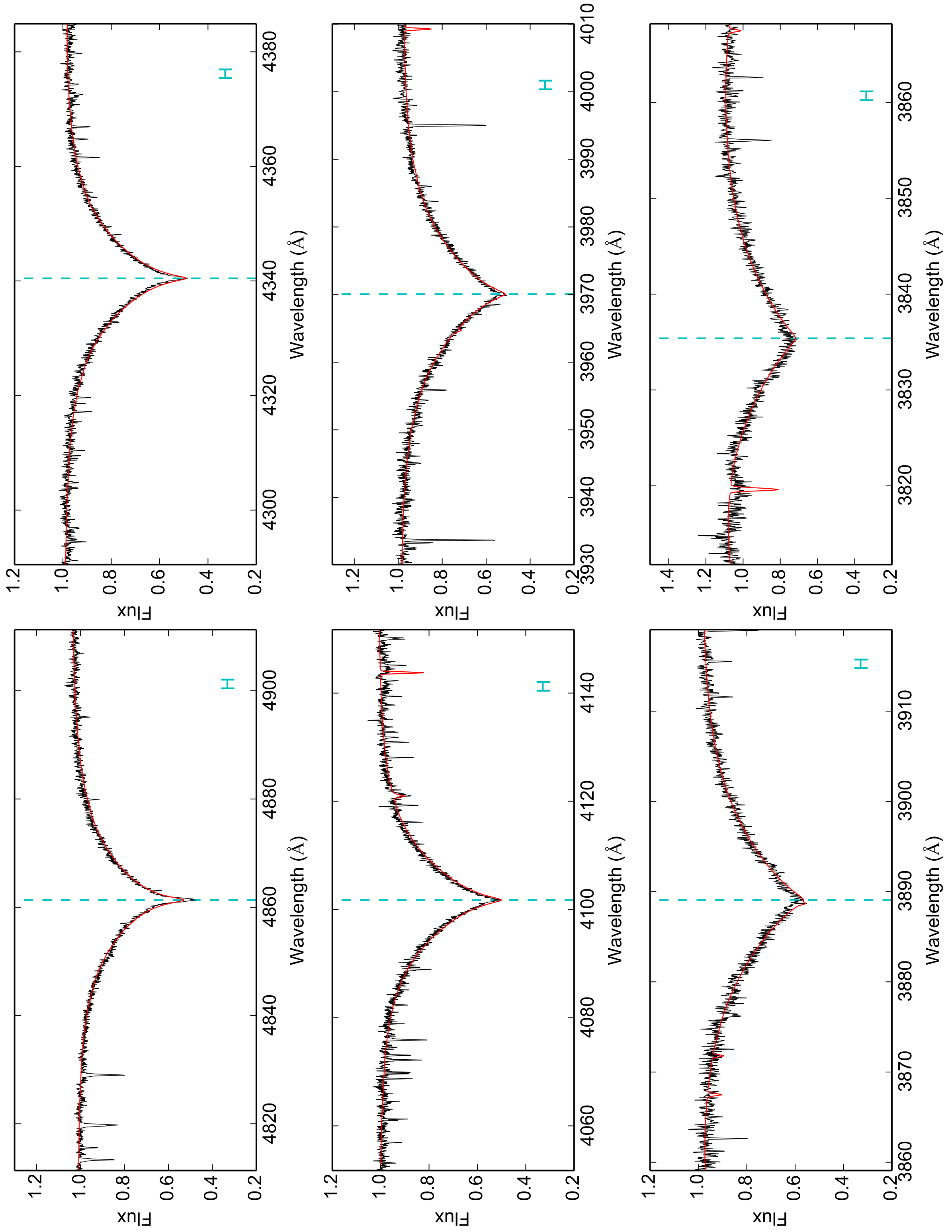

Figure A.1.19.: Hydrogen and helium lines in the co-added FEROS spectrum of the $^{3}\mathrm{He}$ star EC 03591-3232 used for the LTE analysis with SPAS - Part 1.

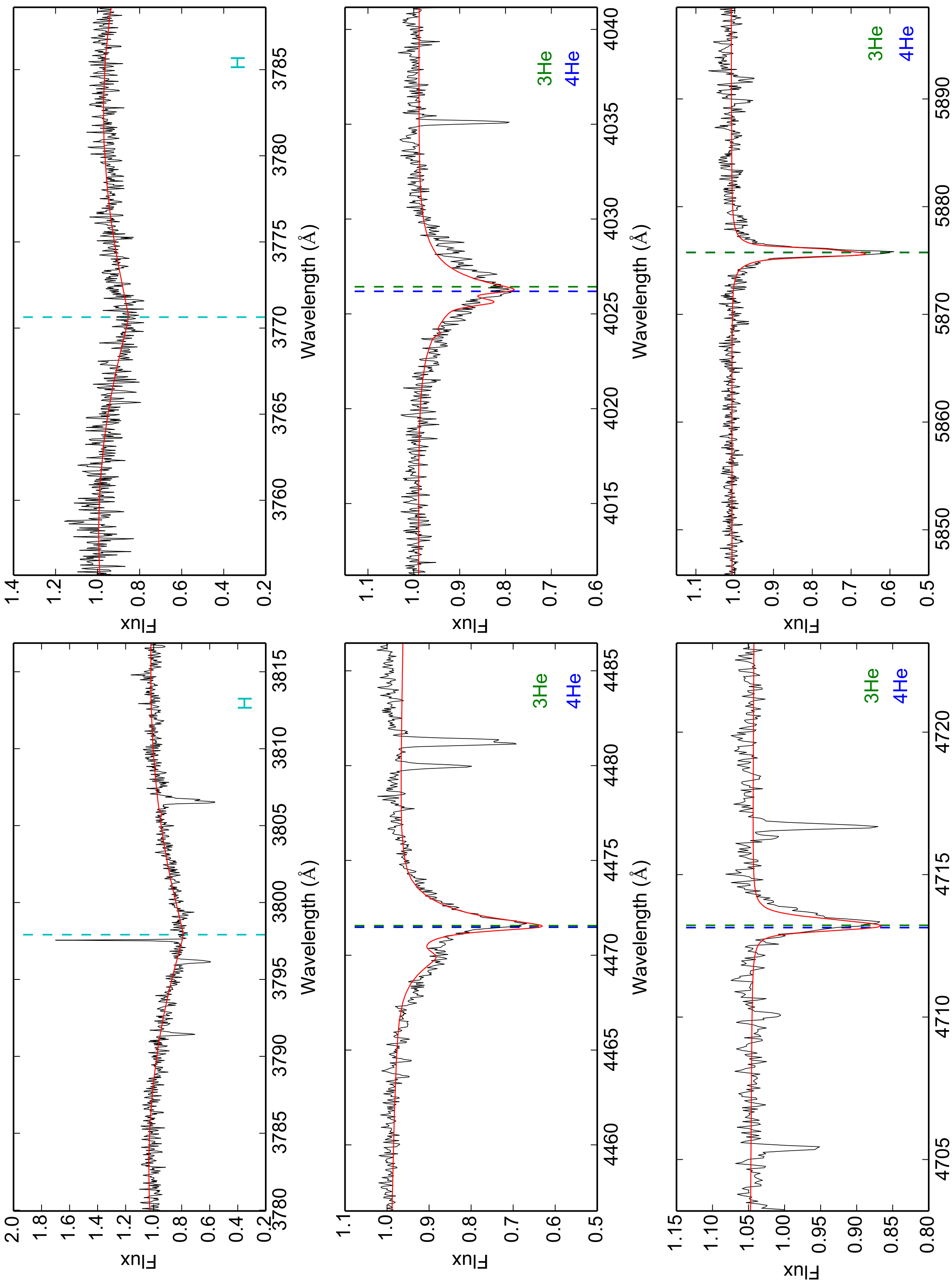

Figure A.1.20.: Hydrogen and helium lines in the co-added FEROS spectrum of the $^3\mathrm{He}$ star EC 03591-3232 used for the LTE analysis with SPAS - Part 2.

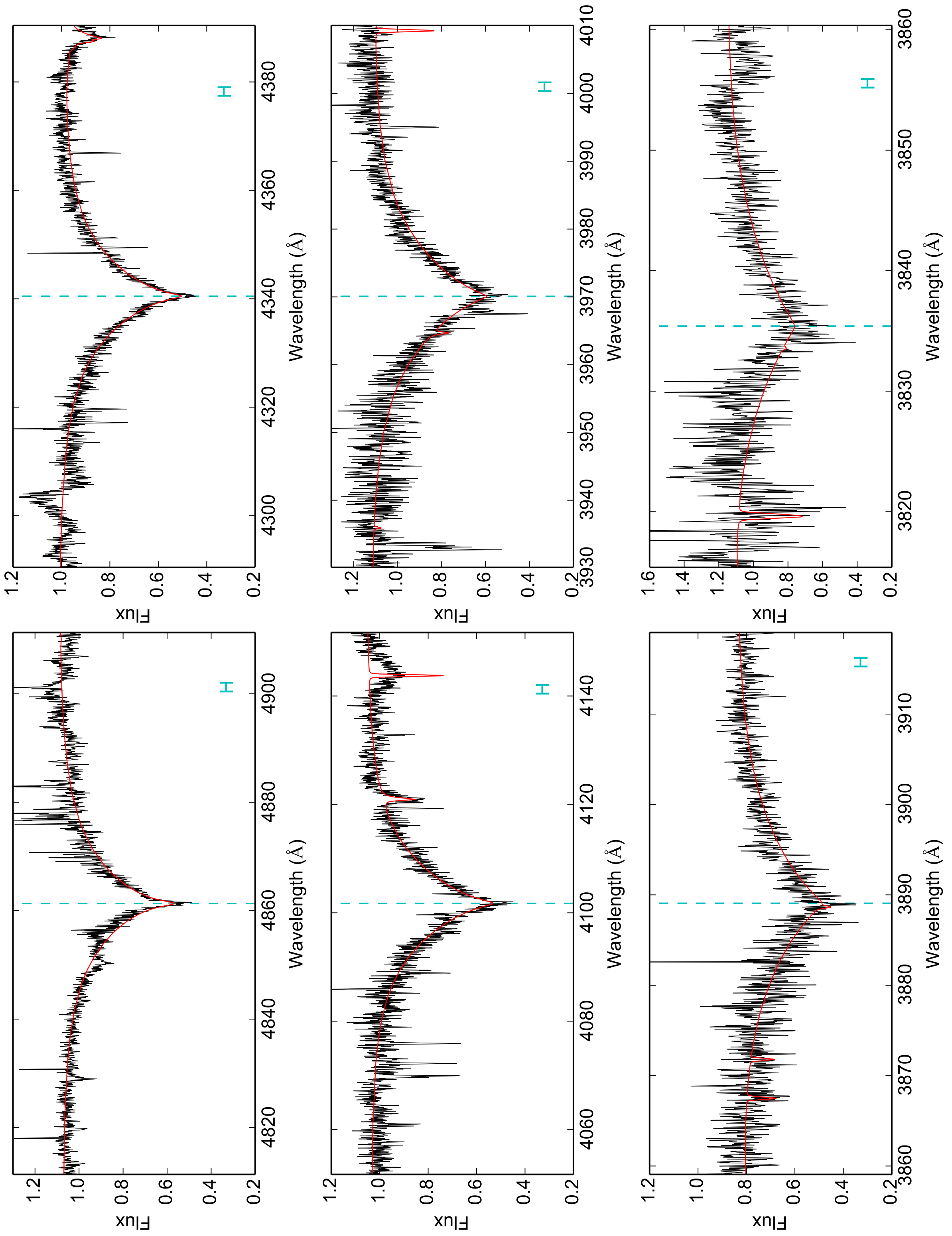

Figure A.1.21.: Hydrogen and helium lines in the co-added FEROS spectrum of the $^3\mathrm{He}$ enriched star EC 12234-2607 used for the LTE analysis with SPAS - Part 1.

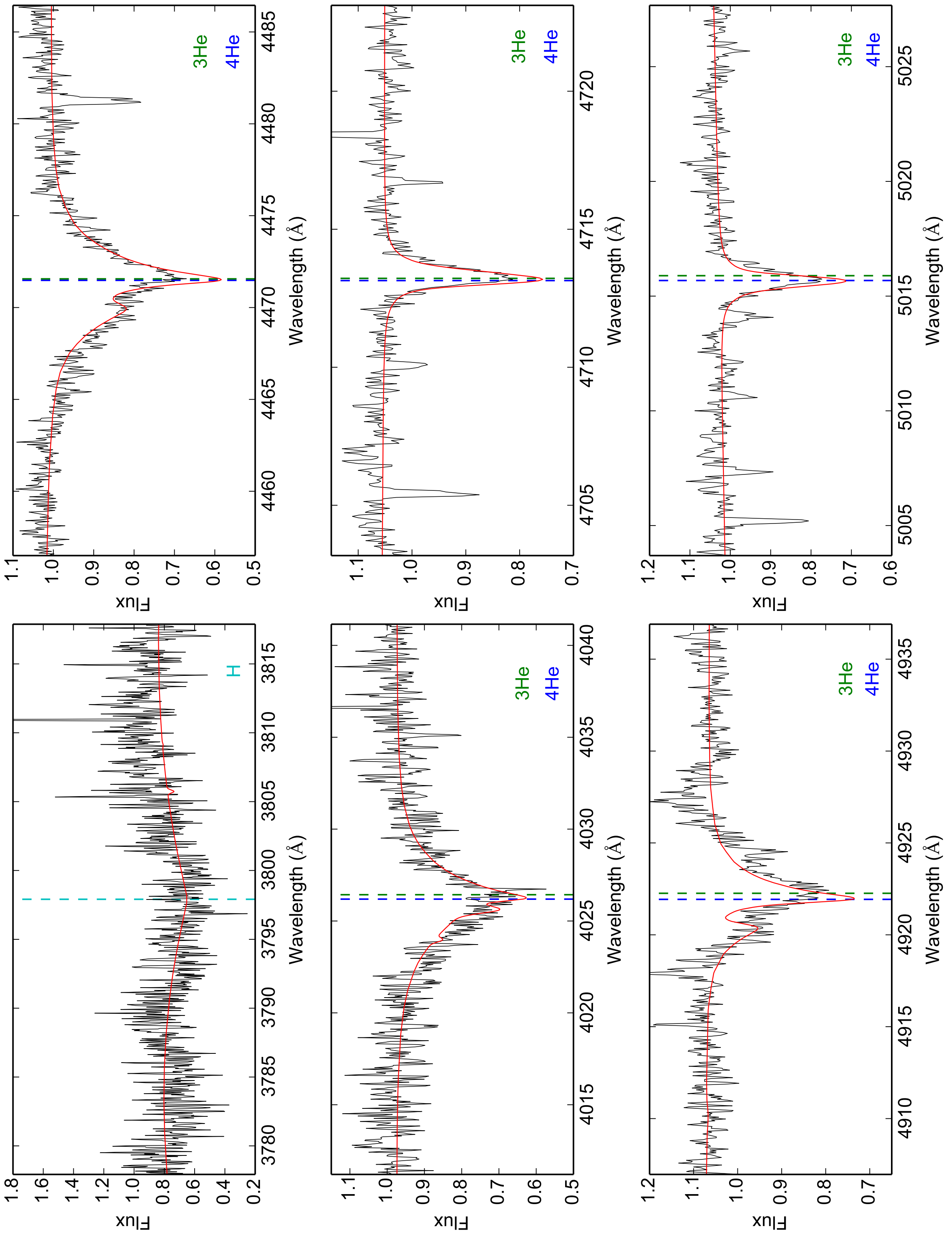

Figure A.1.22.: Hydrogen and helium lines in the co-added FEROS spectrum of the $^{3}\mathrm{He}$ enriched star EC 12234-2607 used for the LTE analysis with SPAS - Part 2.

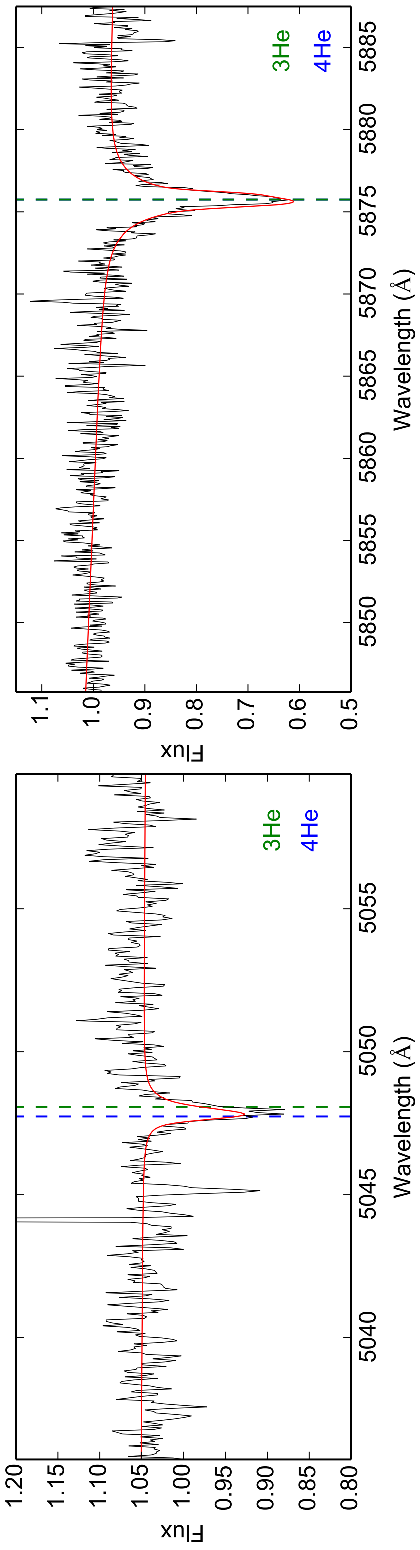

Figure A.1.23.: Hydrogen and helium lines in the co-added FEROS spectrum of the $^{3}\mathrm{He}$ enriched star EC 12234-2607 used for the LTE analysis with SPAS - Part 3.

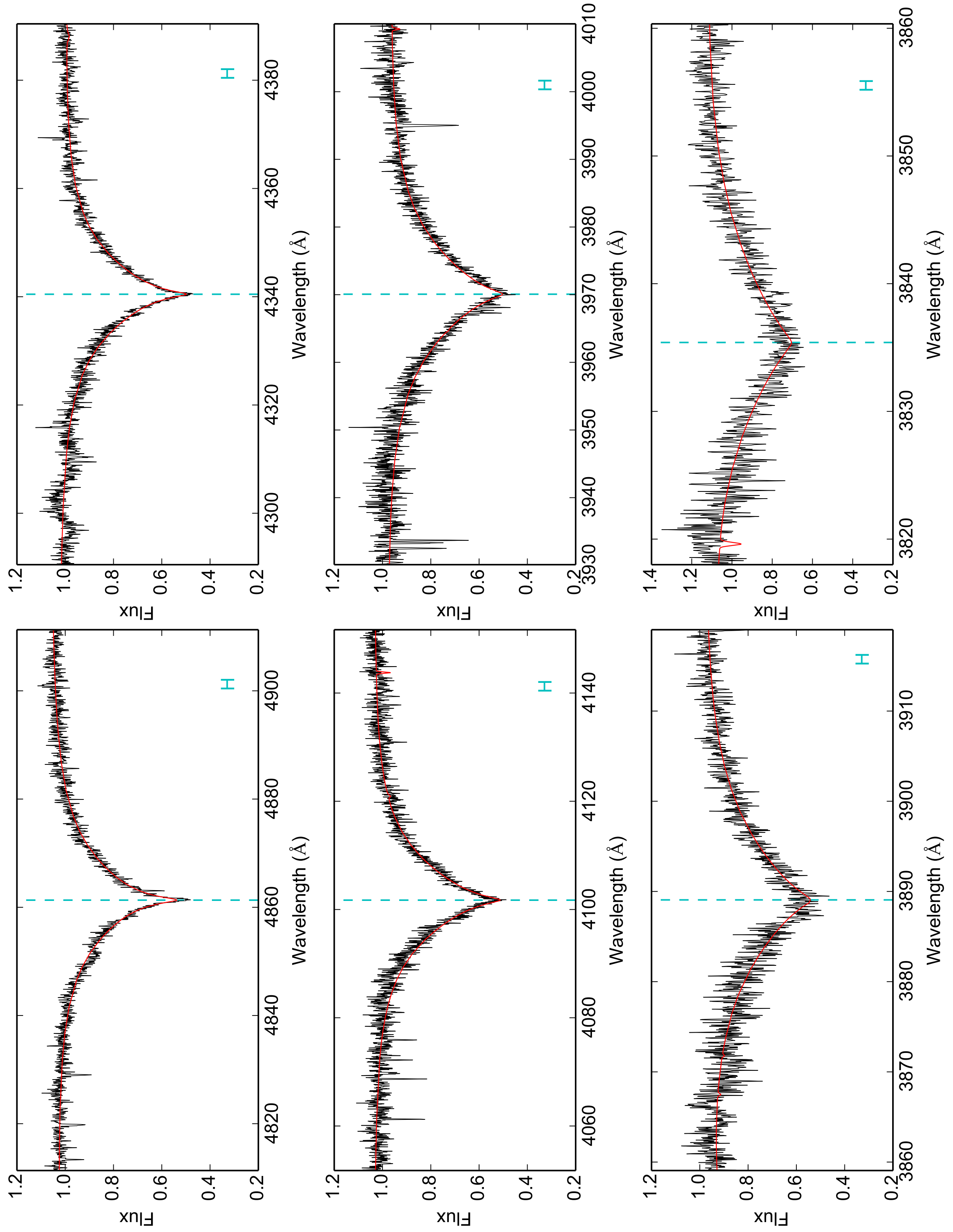

Figure A.1.24.: Hydrogen and helium lines in the co-added FEROS spectrum of the $^{3}\mathrm{He}$ star EC 14338-1445 used for the LTE analysis with SPAS - Part 1.

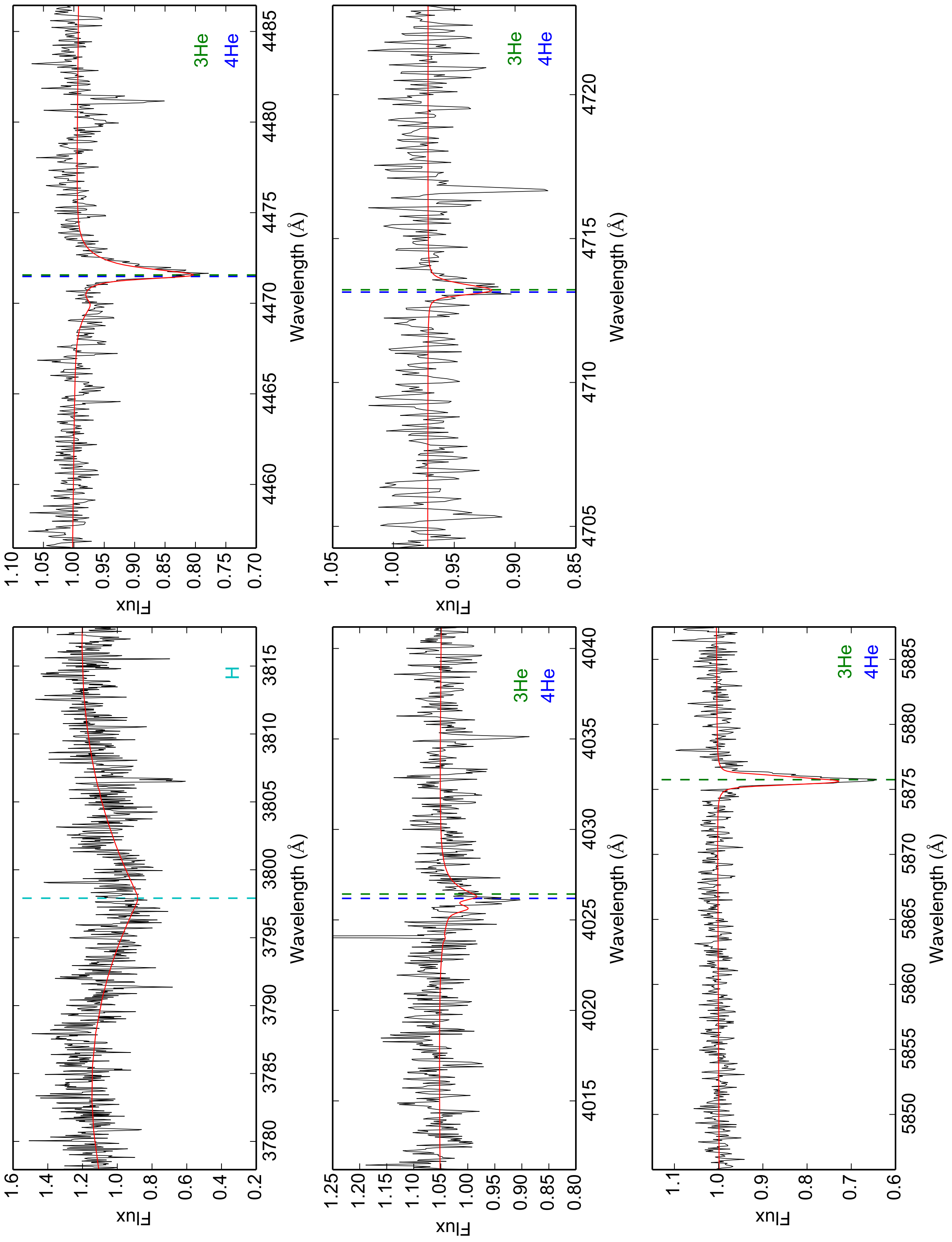

Figure A.1.25.: Hydrogen and helium lines in the co-added FEROS spectrum of the $^{3}\mathrm{He}$ star EC 14338-1445 used for the LTE analysis with SPAS - Part 2.

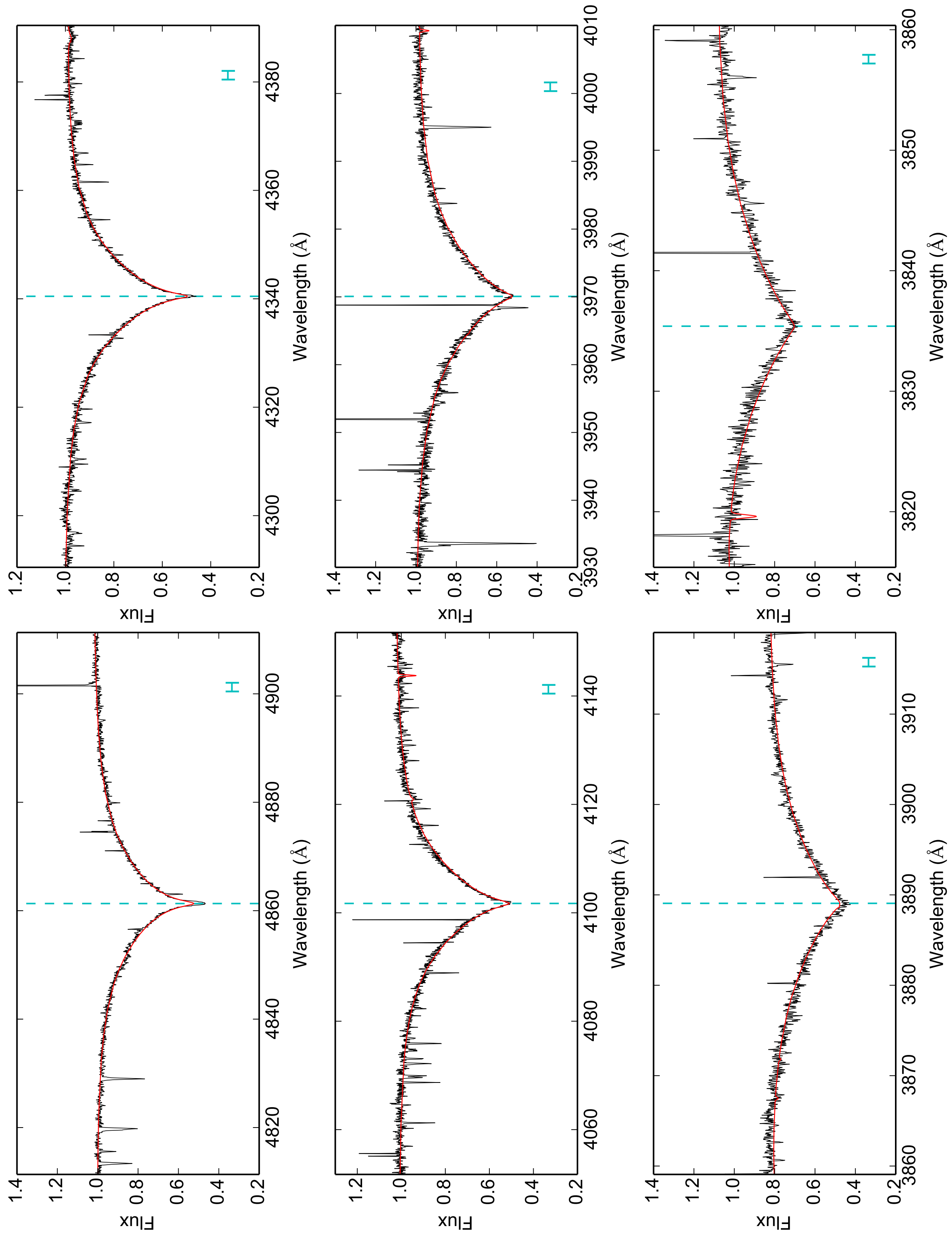

Figure A.1.26.: Hydrogen and helium lines in the co-added FEROS spectrum of the $^{3}\mathrm{He}$ star Feige 38 used for the LTE analysis with SPAS - Part 1.

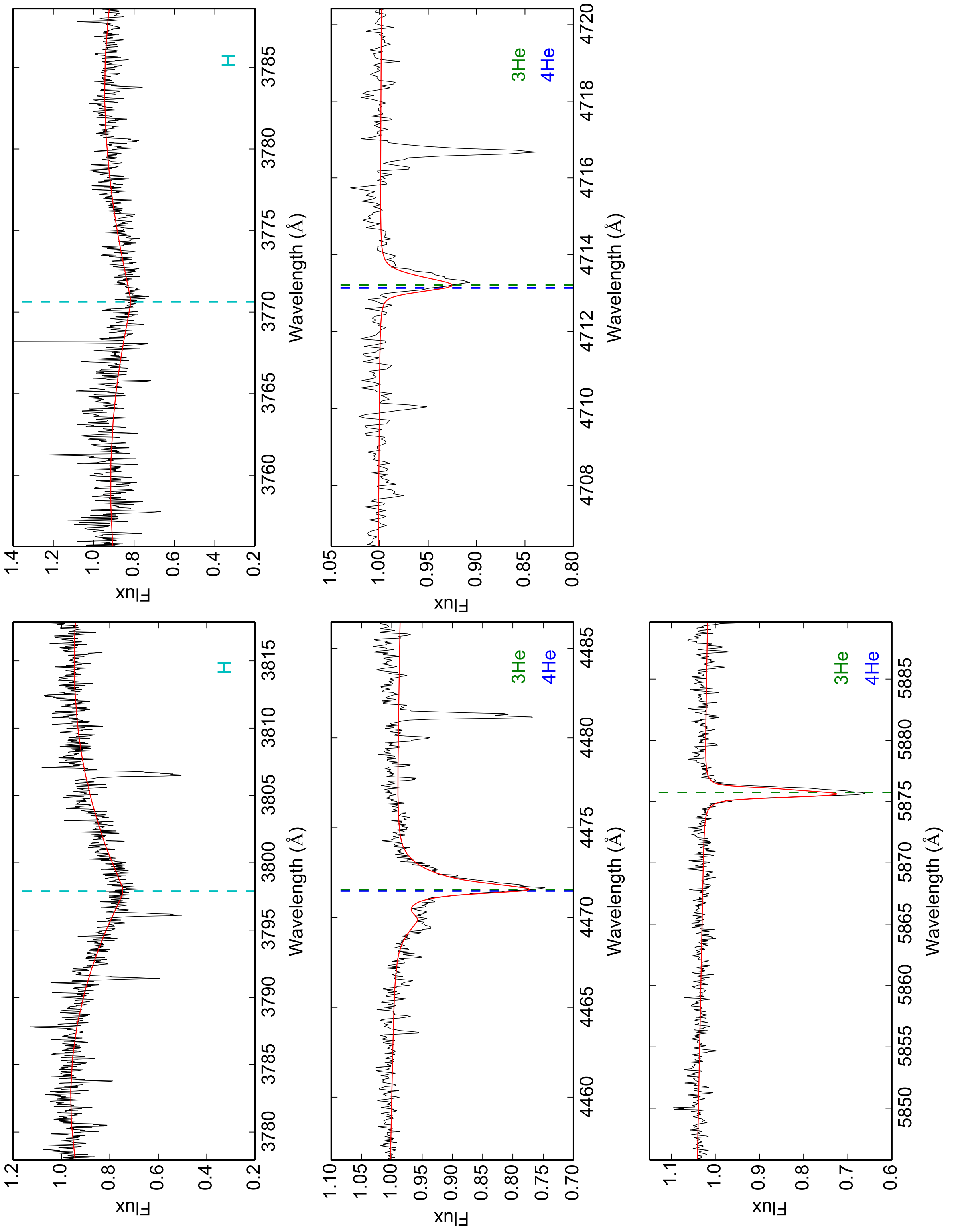

Figure A.1.27.: Hydrogen and helium lines in the co-added FEROS spectrum of the $^{3}\mathrm{He}$ star Feige 38 used for the LTE analysis with SPAS - Part 2.

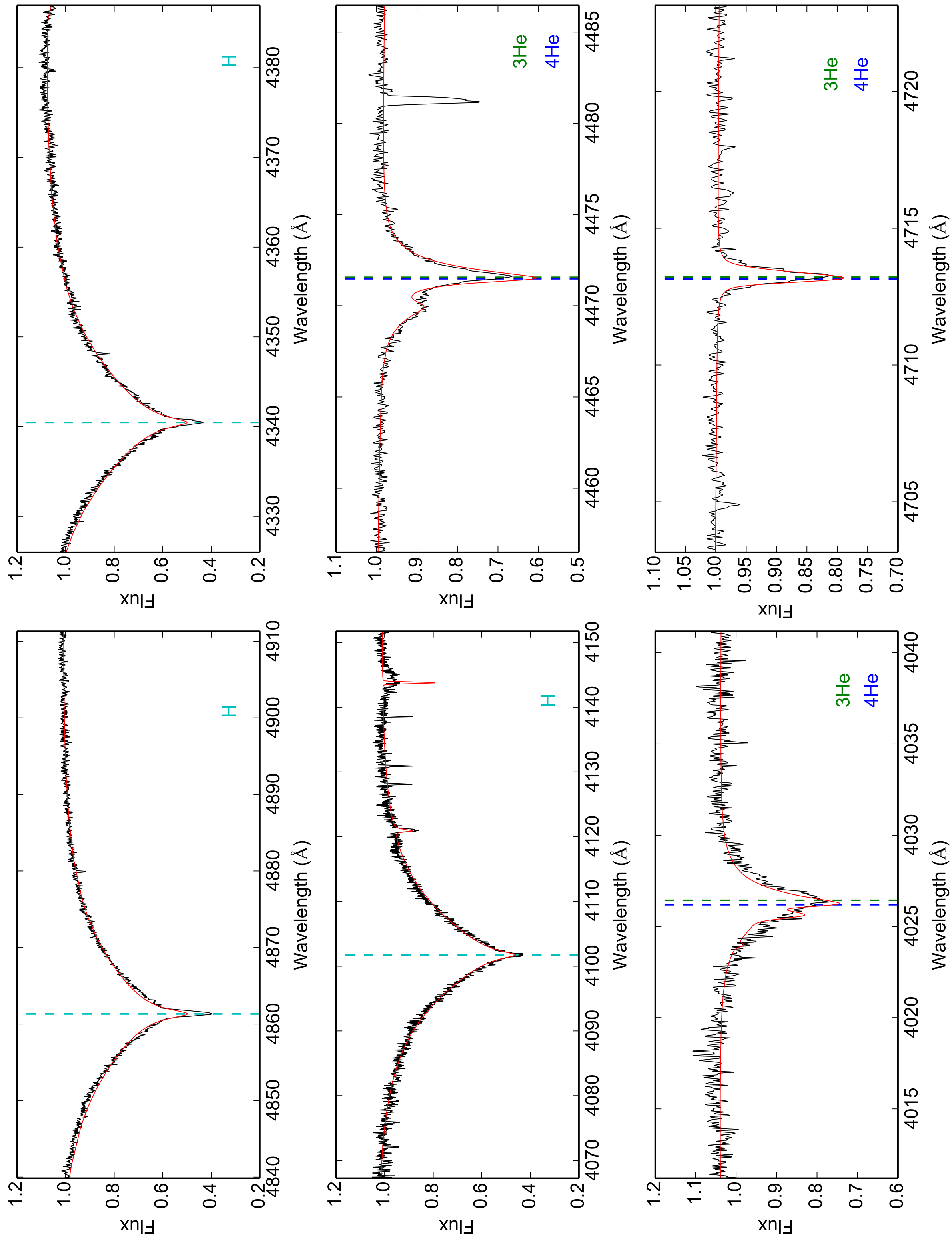

Figure A.1.28.: Hydrogen and helium lines in the FOCES spectrum of the $^{3}\mathrm{He}$ enriched star BD+48° 2721 used for the LTE analysis with SPAS - Part 1.

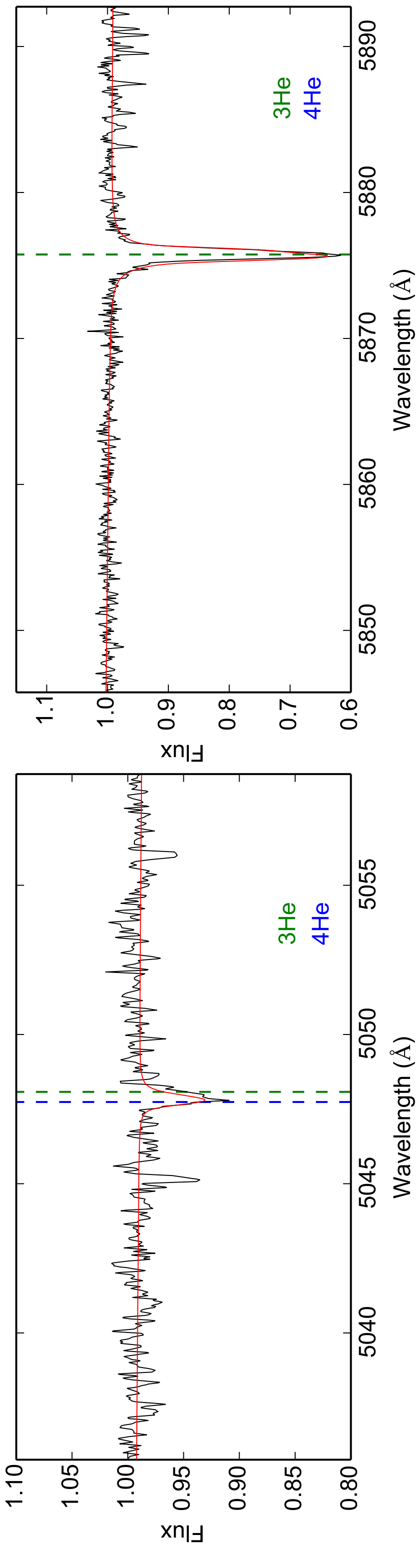

Figure A.1.29.: Hydrogen and helium lines in the FOCES spectrum of the $^3\mathrm{He}$ enriched star BD+48° 2721 used for the LTE analysis with SPAS - Part 2.

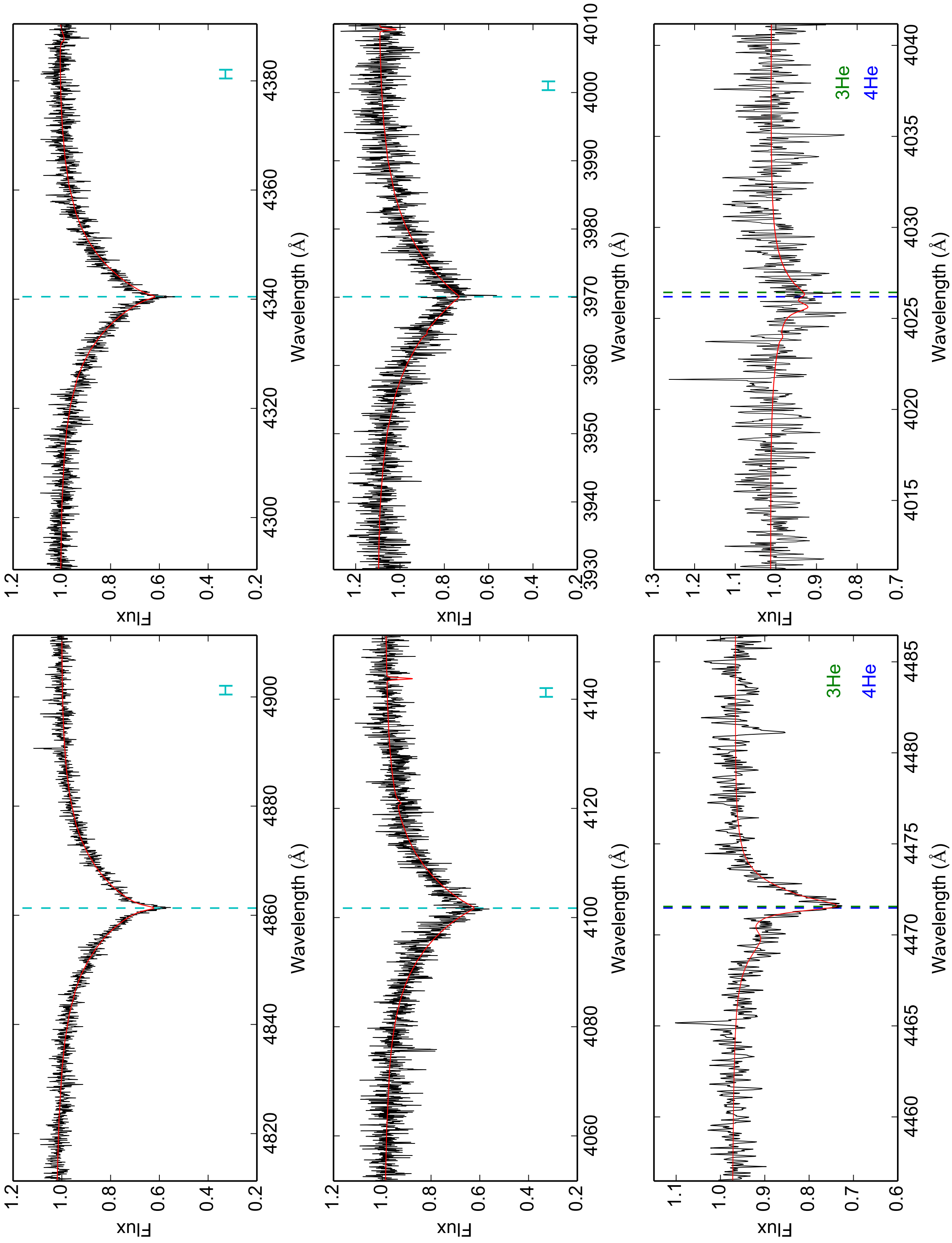

Figure A.1.30.: Hydrogen and helium lines in the FOCES spectrum of the $^{3}\mathrm{He}$ enriched star PG 1519+640 used for the LTE analysis with SPAS - Part 1.

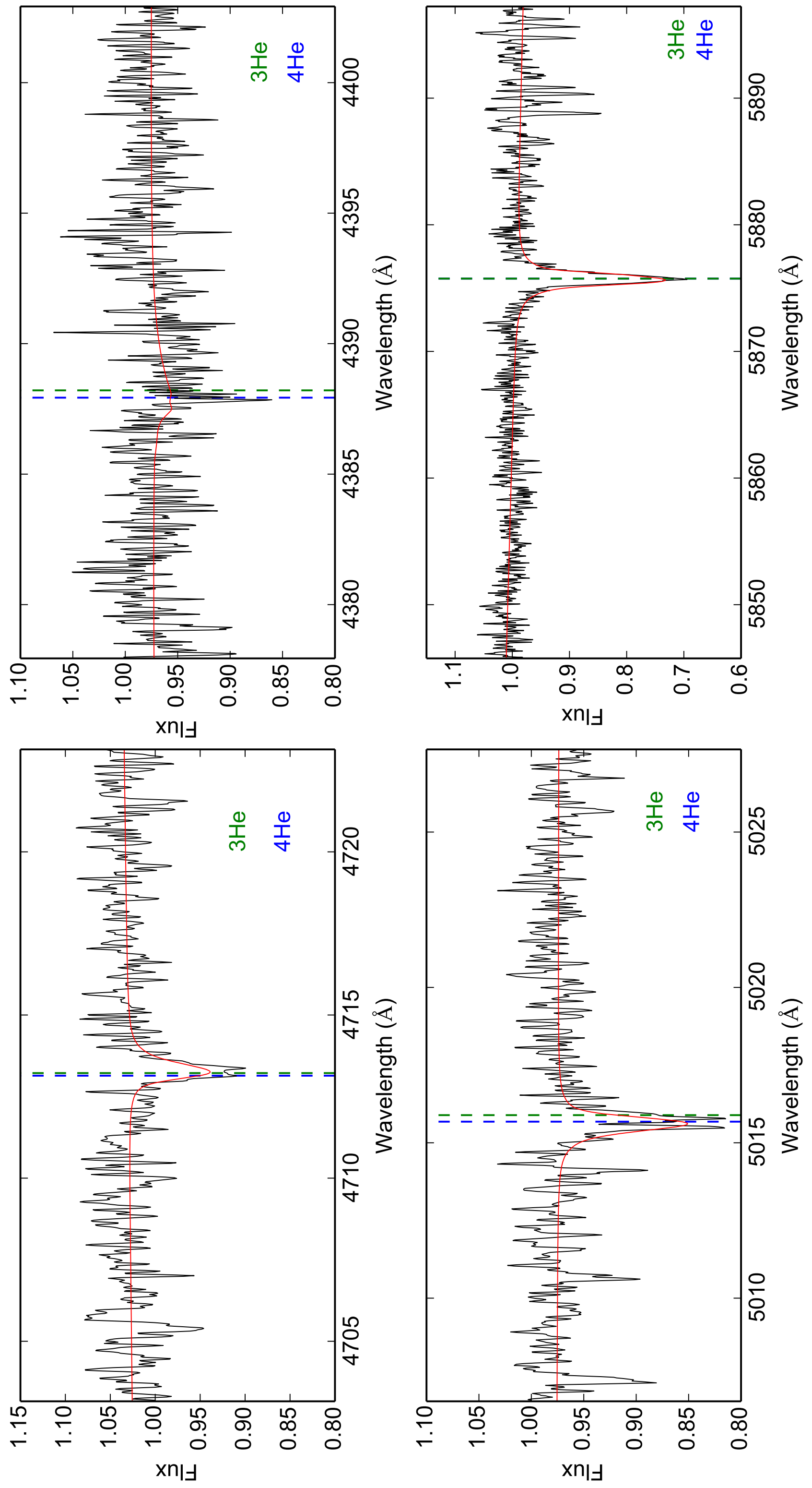

Figure A.1.31.: Hydrogen and helium lines in the FOCES spectrum of the $^{3}\mathrm{He}$ enriched star PG 1519+640 used for the LTE analysis with SPAS - Part 2.

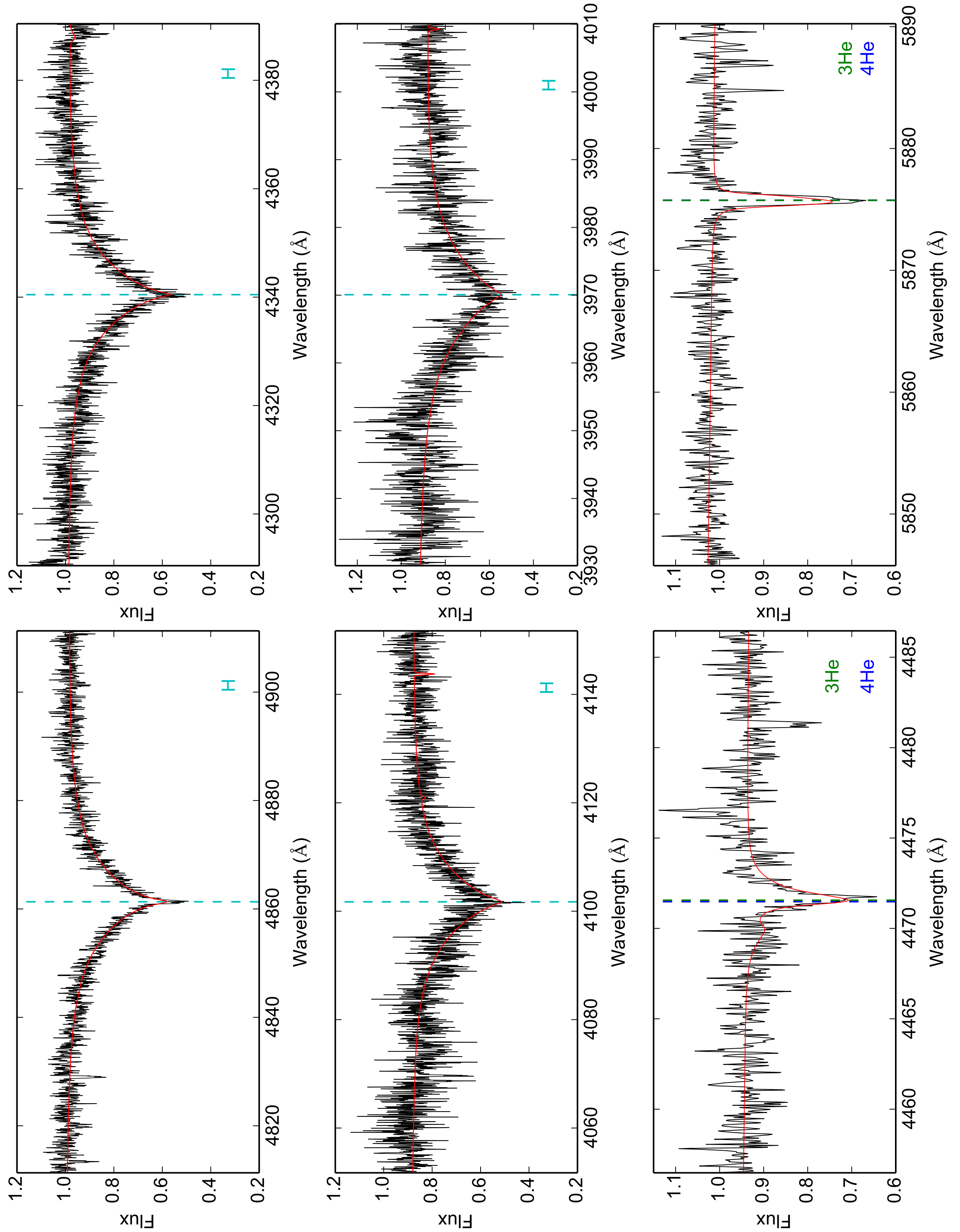

Figure A.1.32.: Hydrogen and helium lines in the FOCES spectrum of the $^{3}\mathrm{He}$ enriched star PG 1710+490 used for the LTE analysis with SPAS.

B. Hybrid LTE/NLTE Analysis

B.1. Full Spectral Synthesis

Sorted by the spectral type, the comparison between best fit model spectrum (red line) and stellar spectrum (black line) for the hybrid LTE/NLTE analysis via ISIS (see chapter 11.3) of the different sample stars are shown in the following. In total, the analyzed sample consists of 17 B-type stars, including the two $^3\mathrm{He}$ BHB stars (PHL 25 and PHL 382), and 15 sdB stars (13 $^3\mathrm{He}$ sdBs and two He-normal comparison stars, HD 4539 and CD-35° 15910). Four $^3\mathrm{He}$ sdBs were taken from the hot subdwarf list of the ESO Supernova Ia Progenitor Survey (Lisker et al., 2005). In order to illustrate the $^3\mathrm{He}$ isotopic shifts, all spectra have been radial-velocity (RV)-corrected. The calculated model atmospheres are always based on the mean metallicity for sdBs (see Fig. 5.2.2 and table 11.1) from Naslim et al. (2013). Therefore, in addition to hydrogen and helium, metal lines are also synthesized. Macroturbulence ζ is set to zero and microturbulence ξ is not treated at all for the hybrid LTE/NLTE analysis in ISIS (see chapter 11 for details). Only the strongest spectral lines which have been used for the analysis are labeled, but the list of modeled lines is not complete. For instance, several O II lines are missing in the model atom for high temperatures. Light colors mark spectral regions, which have been excluded from fitting because of the presence of features being not properly included in the synthetic models used. These features can be the shape of absorption lines that cannot be fitted properly, in particular in the case of stars showing strong helium stratification like PHL 25 (see chapter 12.3 for further information), cosmics, normalization problems, interstellar, telluric or missing model lines, hot pixels, reduction artifacts, noise or non-overlapping diffraction orders at the end of the individual spectrum. The residuals, denoted as χ, are overall artificially constrained between values of $+2$ and -2. Additionally, strong deviations between best fit model spectrum and star spectrum are weighted less heavily - to be more precise - they are equally weighted. The residuals are artificially set to -1 and $+1$ in these regions, respectively. Consequently, the plotted residuals cannot be used to simply determine the badly fitted spectral ranges or lines. However, by using these artificially set residuals, a reduced χ^2 of $\chi^2_{\text{red}} \approx 1$ is ensured. For the sake of clarity, regions that have been excluded from fitting exhibit residuals with $\chi <$ -2 and $\chi > +2$, too.

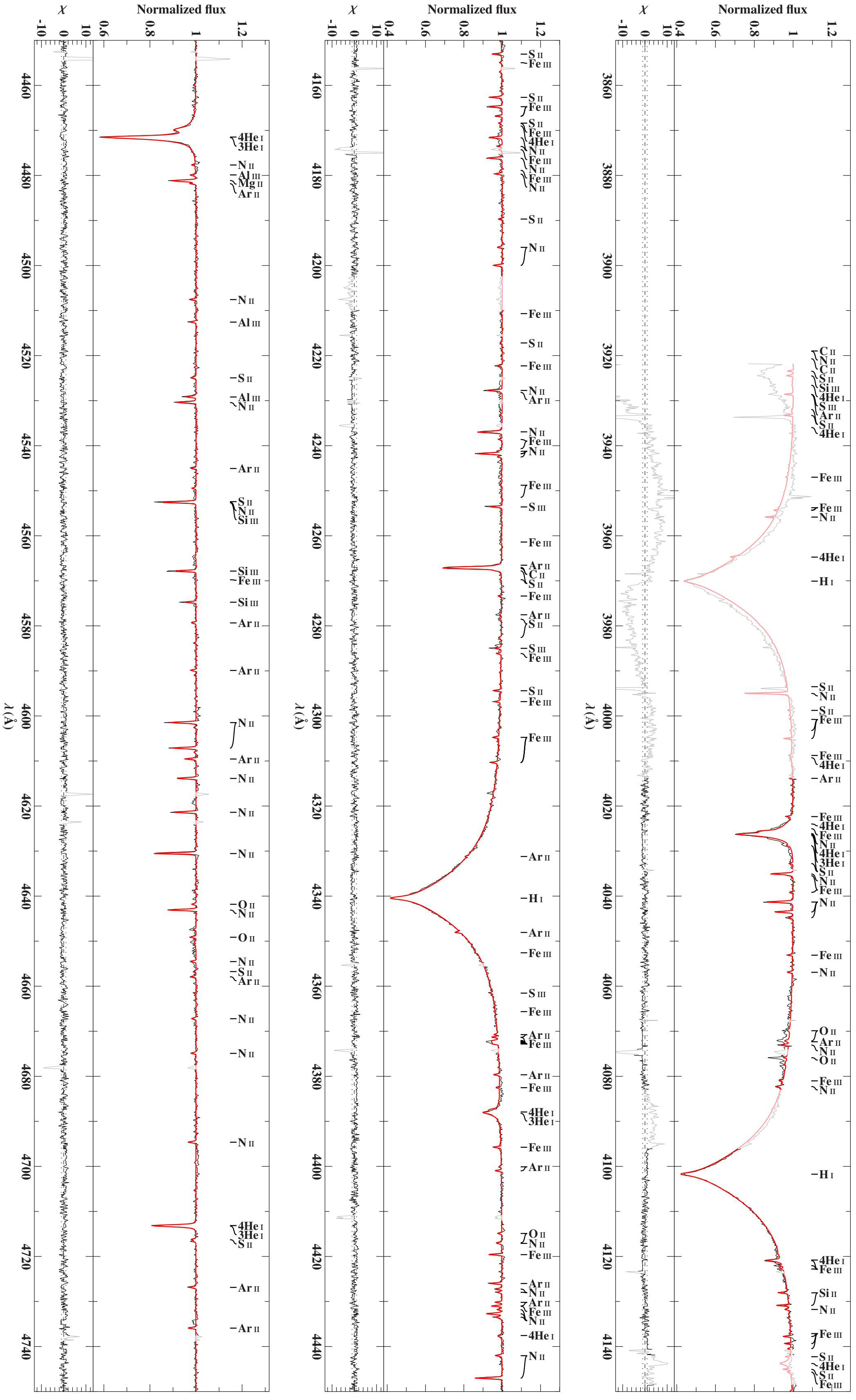

Figure B.1.1.: Fitted CASPEC spectrum of the He-normal comparison star HD 4539 using the hybrid LTE/NLTE analysis with ISIS - Part 1.

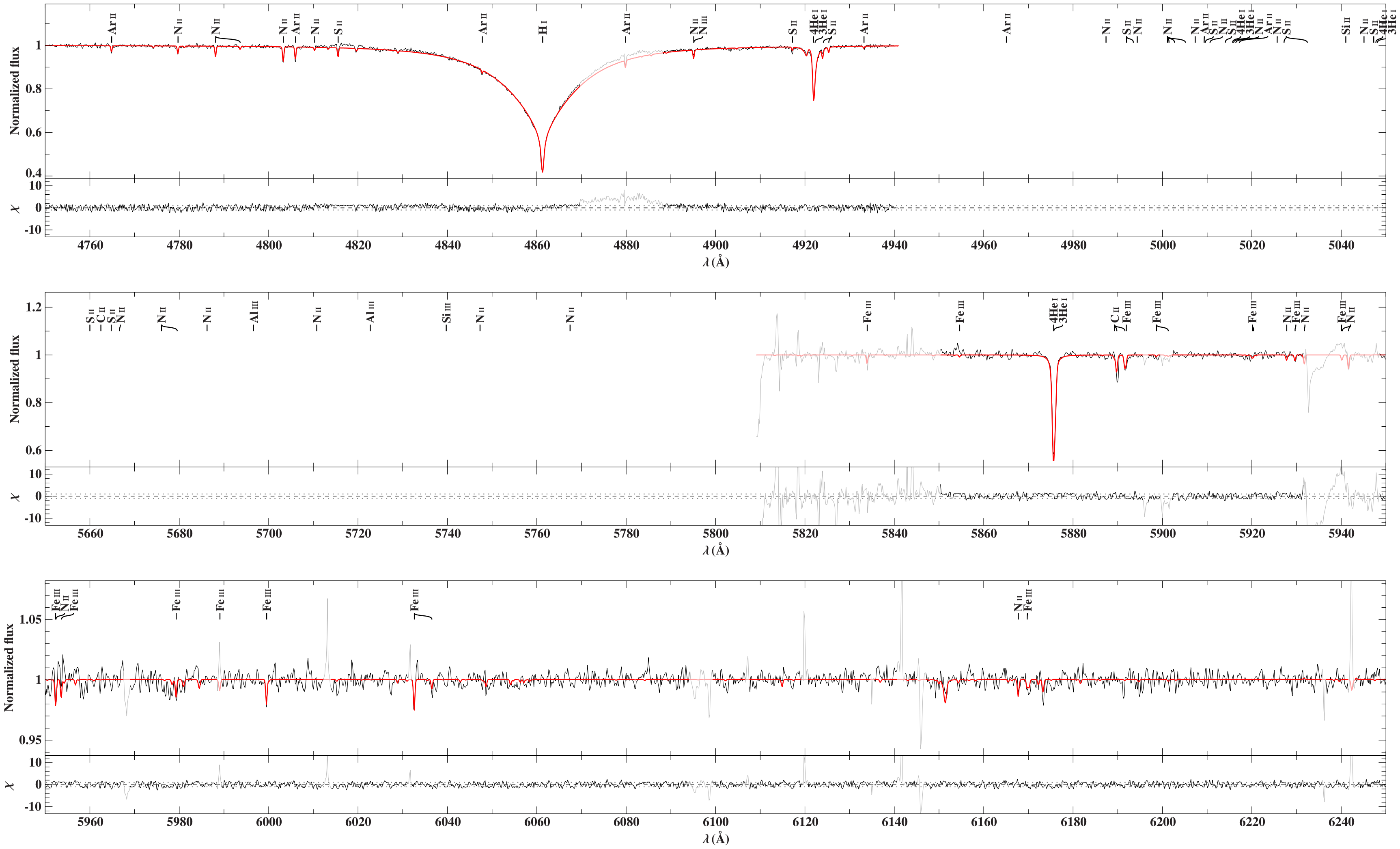

Figure B.1.2.: Fitted CASPEC spectrum of the He-normal comparison star HD 4539 using the hybrid LTE/NLTE analysis with ISIS - Part 2.

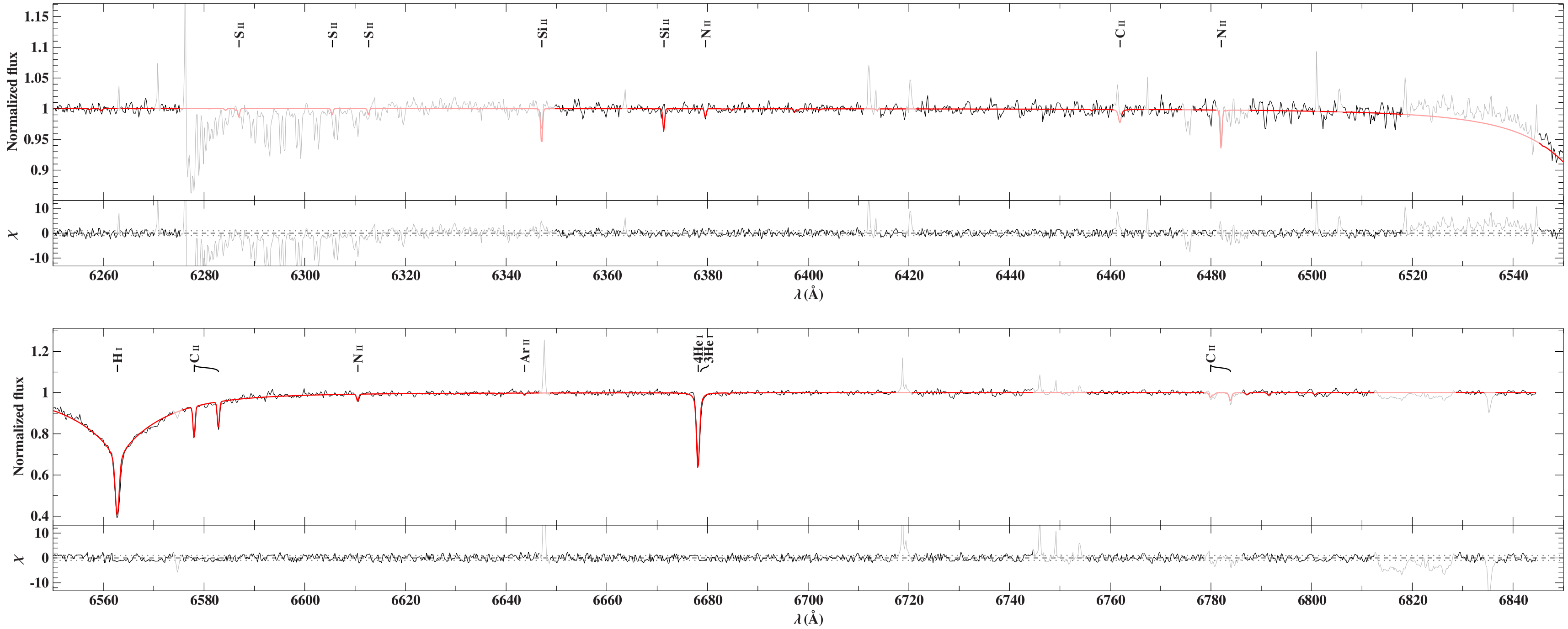

Figure B.1.3.: Fitted CASPEC spectrum of the He-normal comparison star HD 4539 using the hybrid LTE/NLTE analysis with ISIS - Part 3.

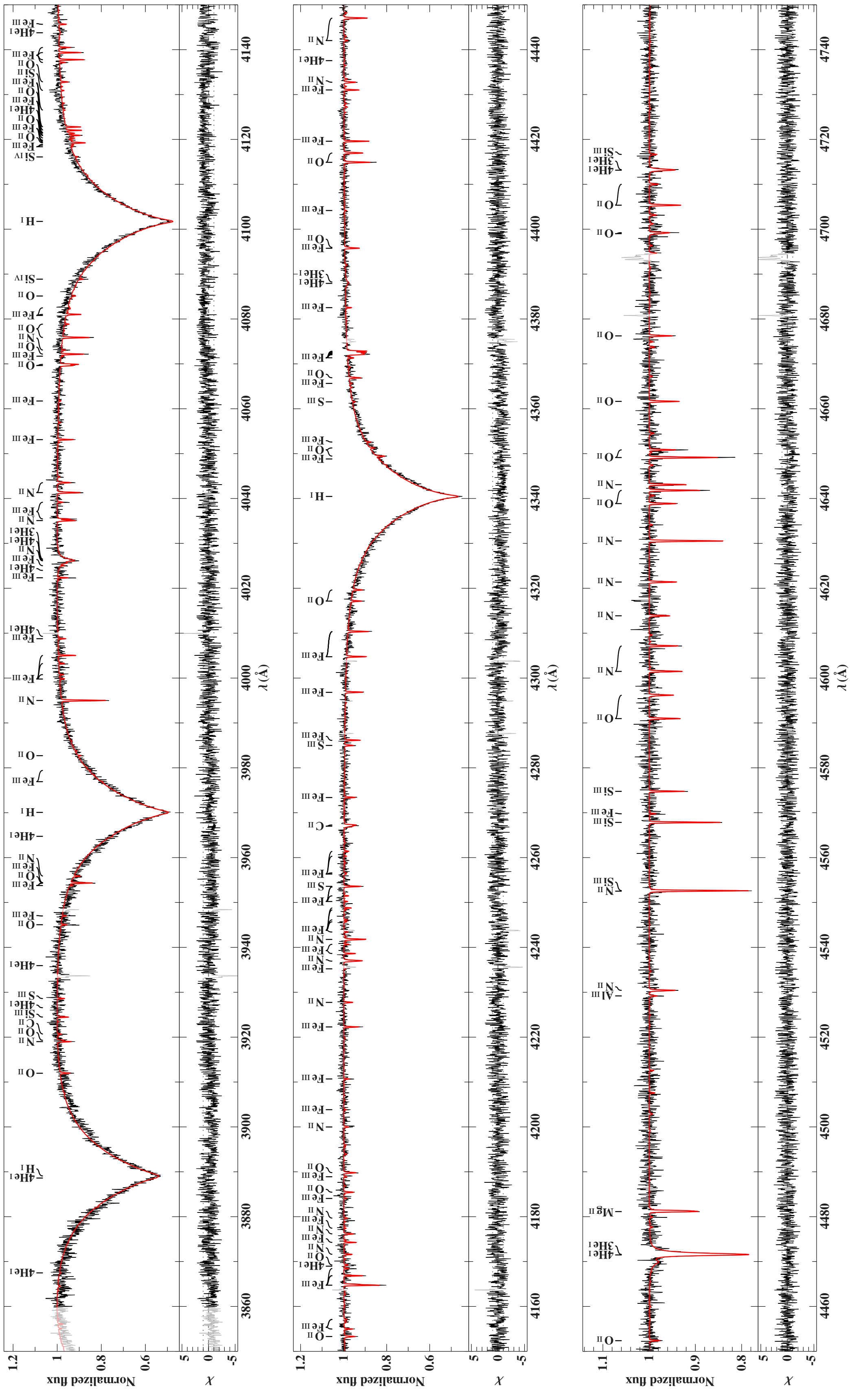

Figure B.1.4.: Fitted FEROS spectrum of the He-normal comparison star CD-35° 15910 using the hybrid LTE/NLTE analysis with ISIS - Part 1.

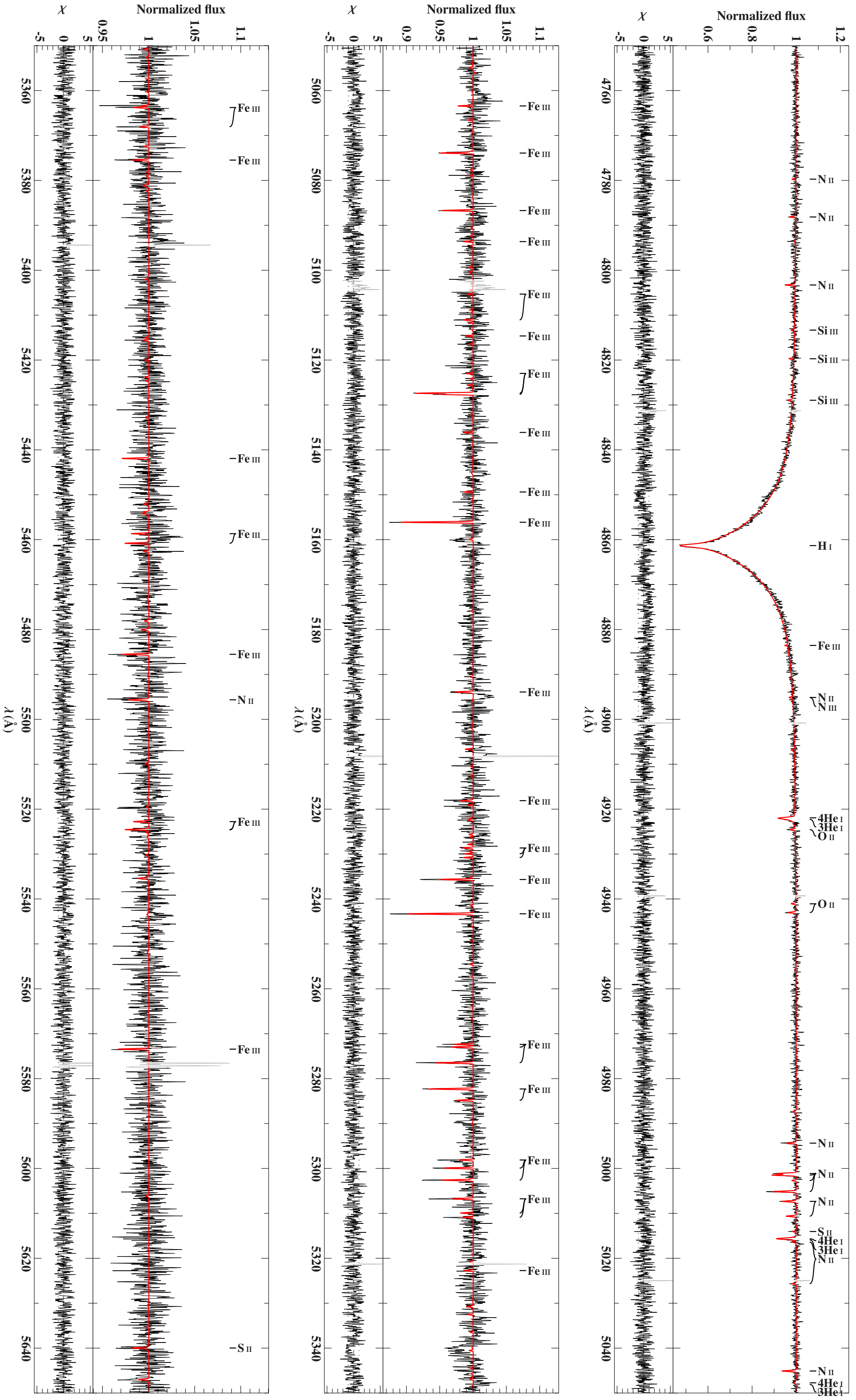

Figure B.1.5.: Fitted FEROS spectrum of the He-normal comparison star CD-35° 15910 using the hybrid LTE/NLTE analysis with ISIS - Part 2.

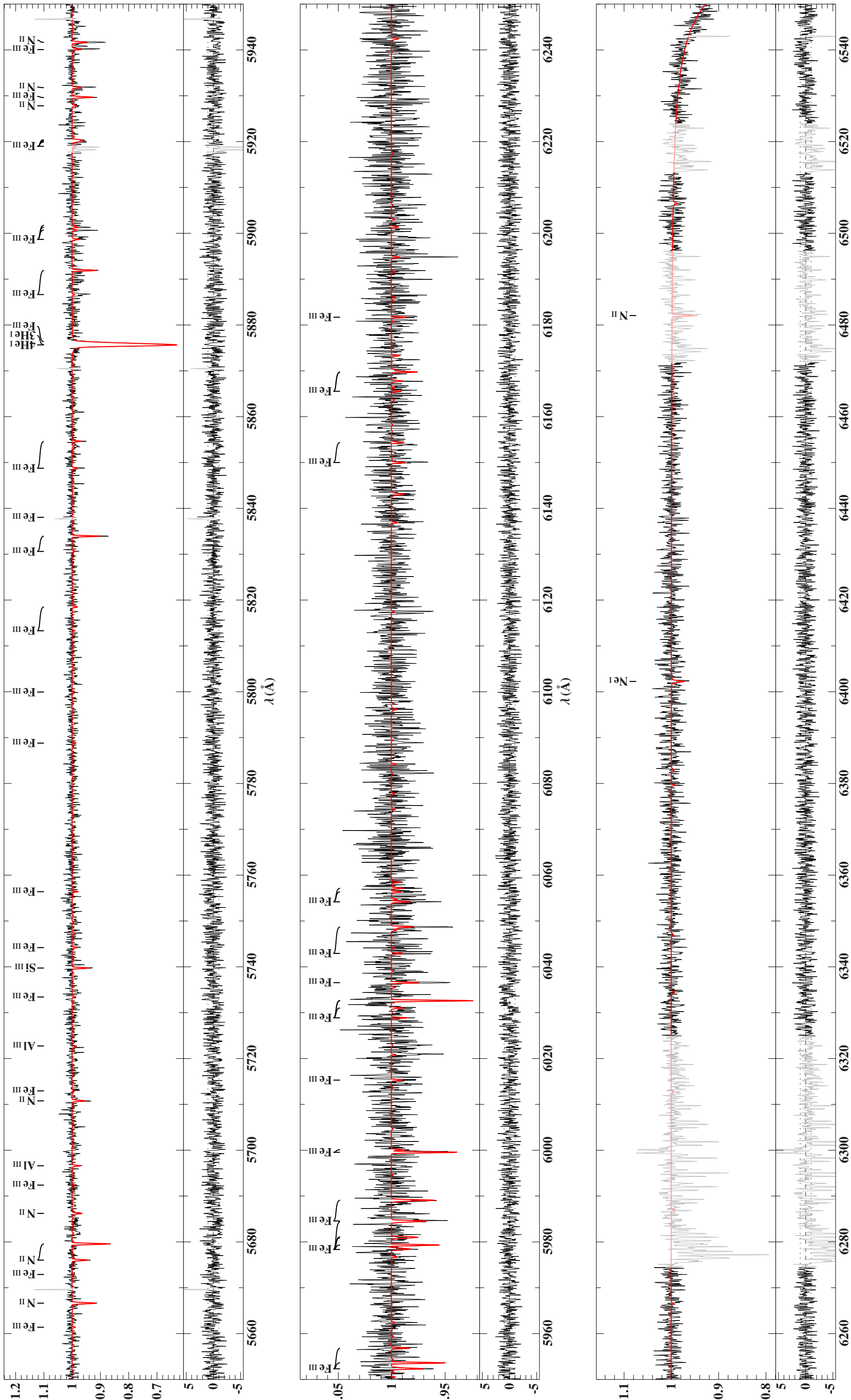

Figure B.1.6.: Fitted FEROS spectrum of the He-normal comparison star CD-35° 15910 using the hybrid LTE/NLTE analysis with ISIS - Part 3.

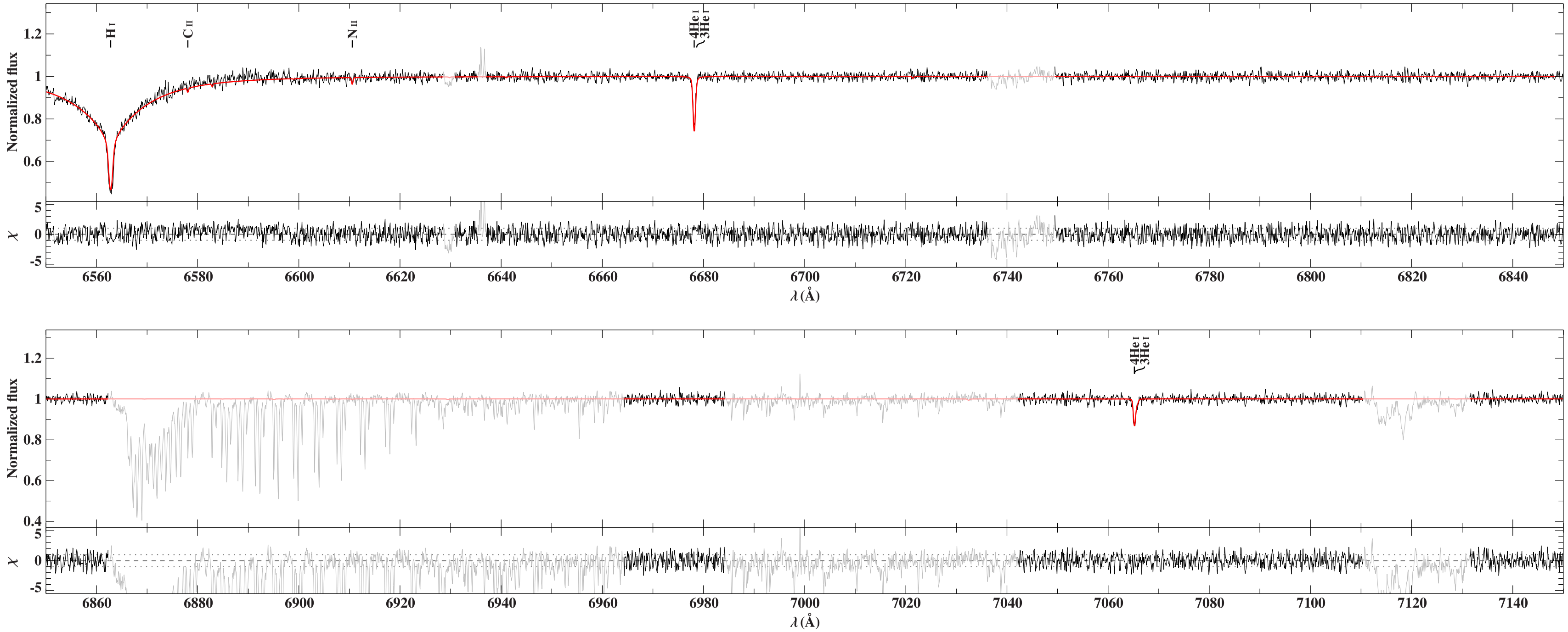

Figure B.1.7.: Fitted FEROS spectrum of the He-normal comparison star CD-35° 15910 using the hybrid LTE/NLTE analysis with ISIS - Part 4.

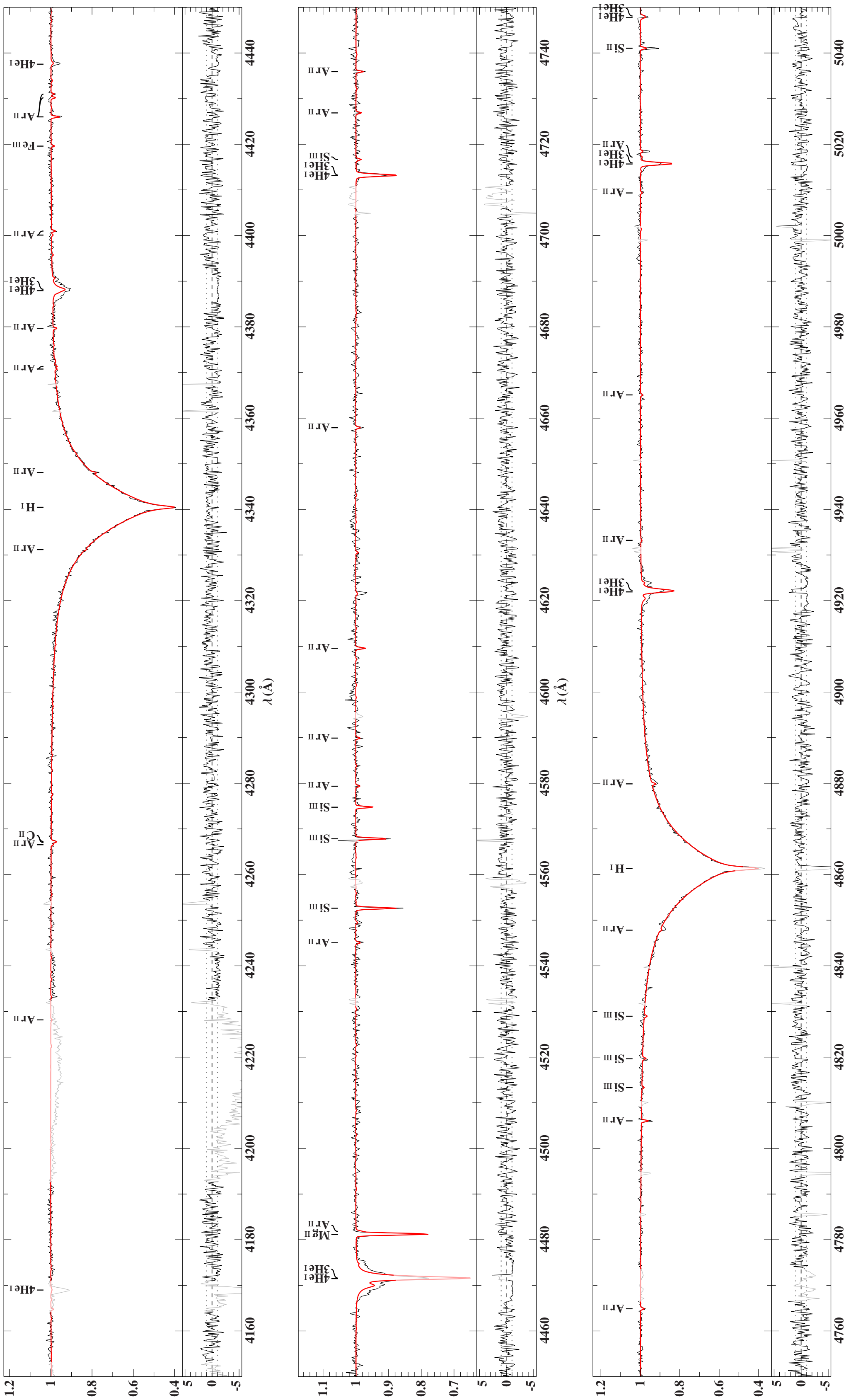

Figure B.1.8.: Fitted CASPEC spectrum of the ^{3}He enriched star PHL 25 using the hybrid LTE/NLTE analysis with ISIS - Part 1.

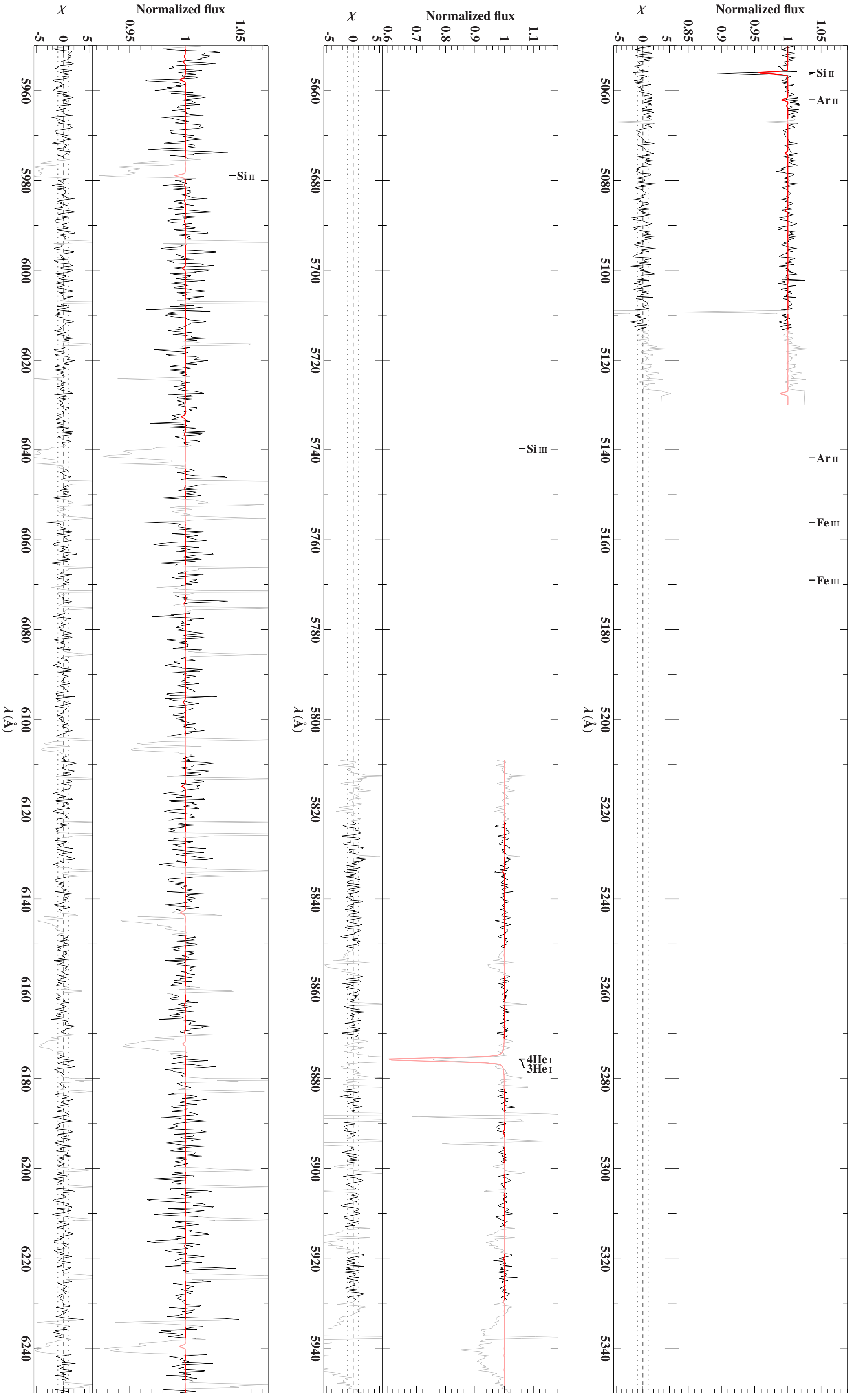

Figure B.1.9.: Fitted CASPEC spectrum of the $^{3}\mathrm{He}$ enriched star PHL 25 using the hybrid LTE/NLTE analysis with ISIS - Part 2.

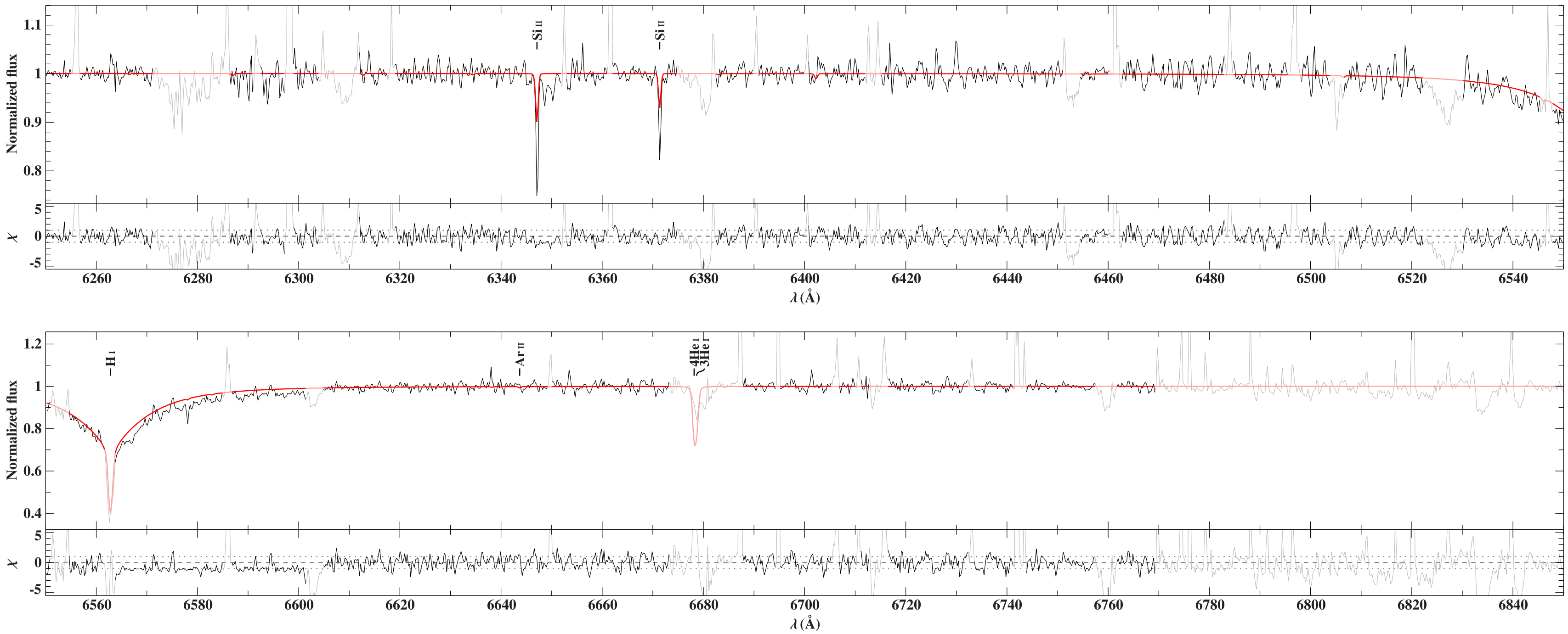

Figure B.1.10.: Fitted CASPEC spectrum of the $^{3}\mathrm{He}$ enriched star PHL 25 using the hybrid LTE/NLTE analysis with ISIS - Part 3.

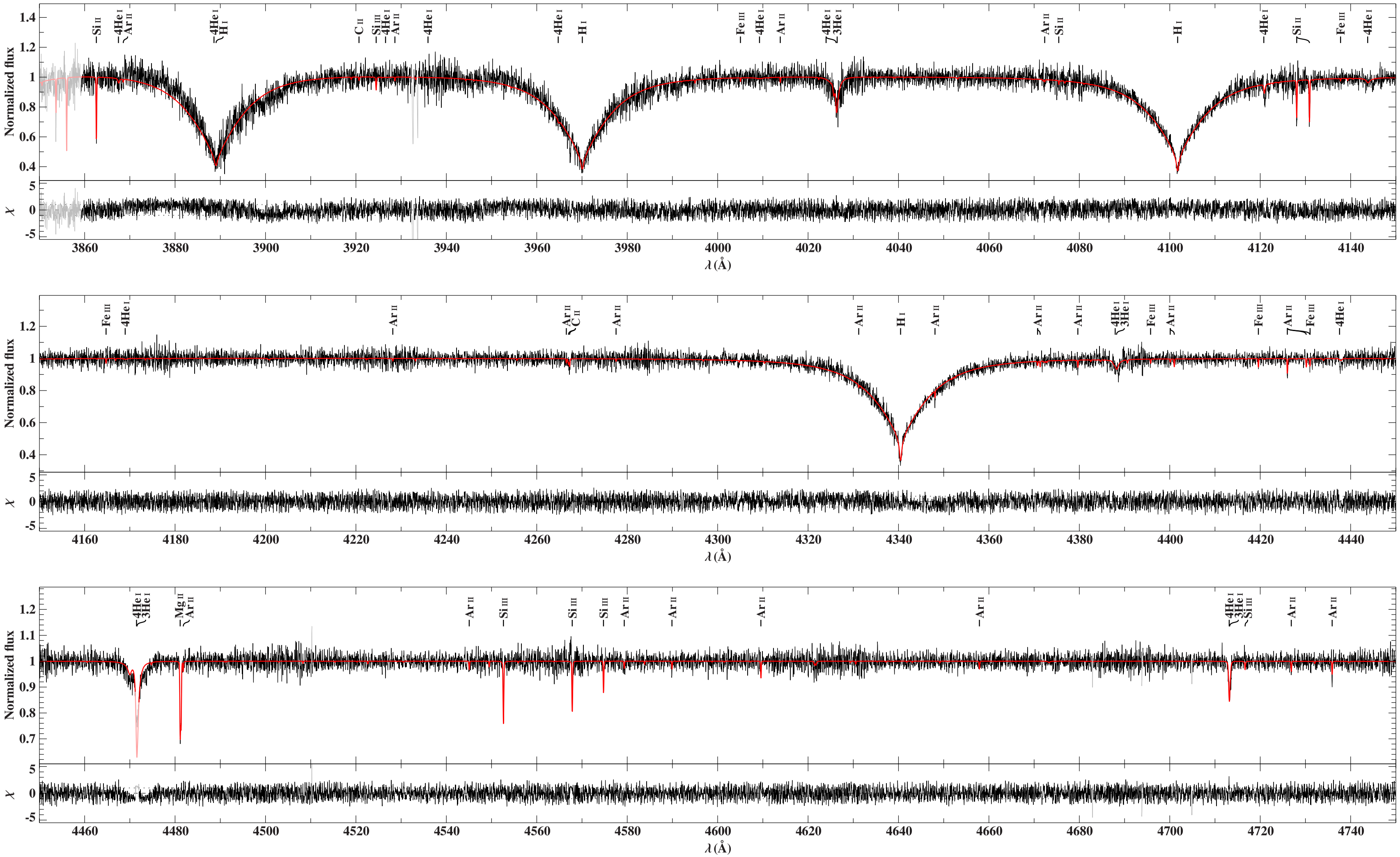

Figure B.1.11.: Fitted HRS spectrum of the $^{3}\mathrm{He}$ enriched star PHL 25 using the hybrid LTE/NLTE analysis with ISIS - Part 1.

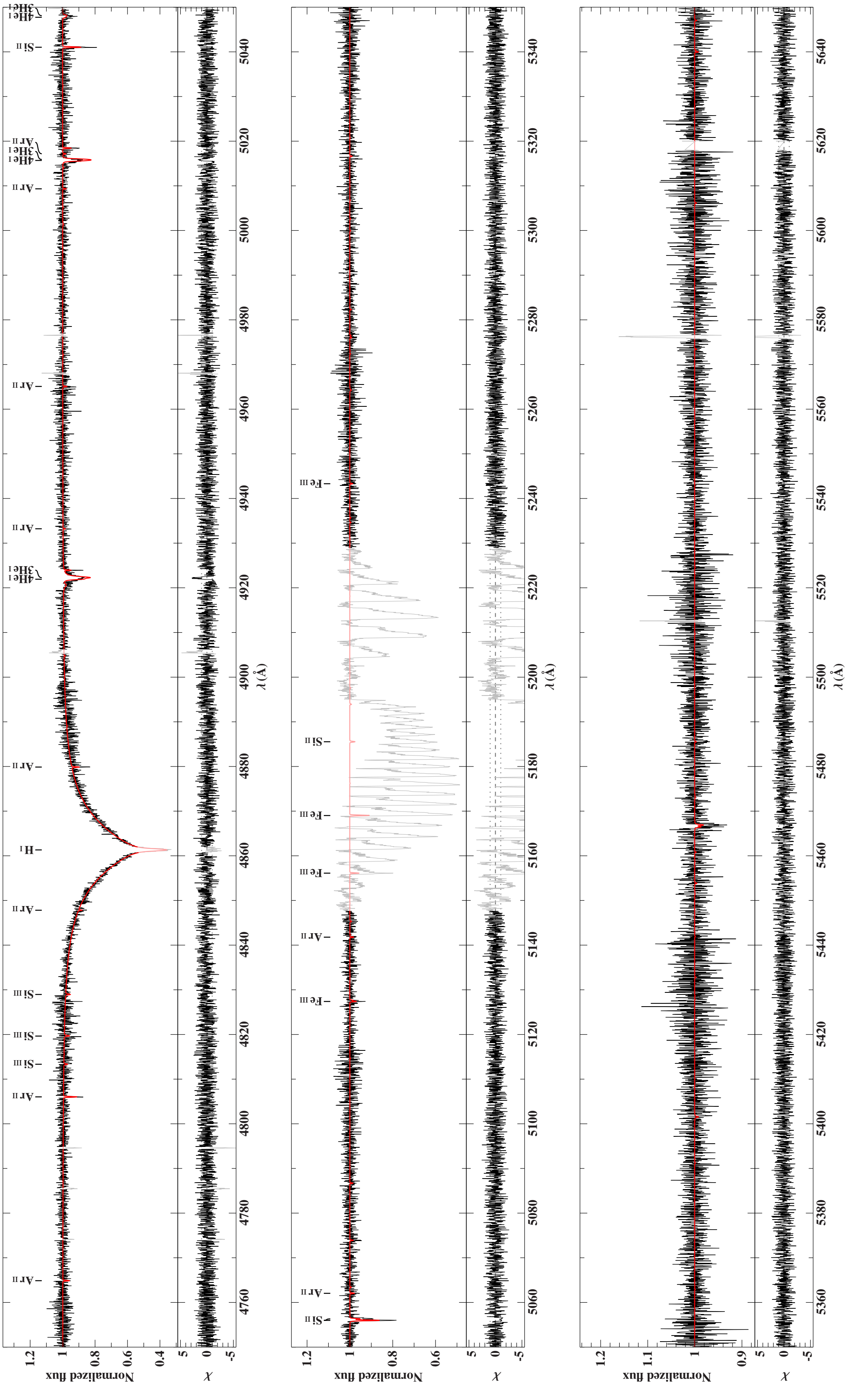

Figure B.1.12.: Fitted HRS spectrum of the $^3\mathrm{He}$ enriched star PHL 25 using the hybrid LTE/NLTE analysis with ISIS - Part 2.

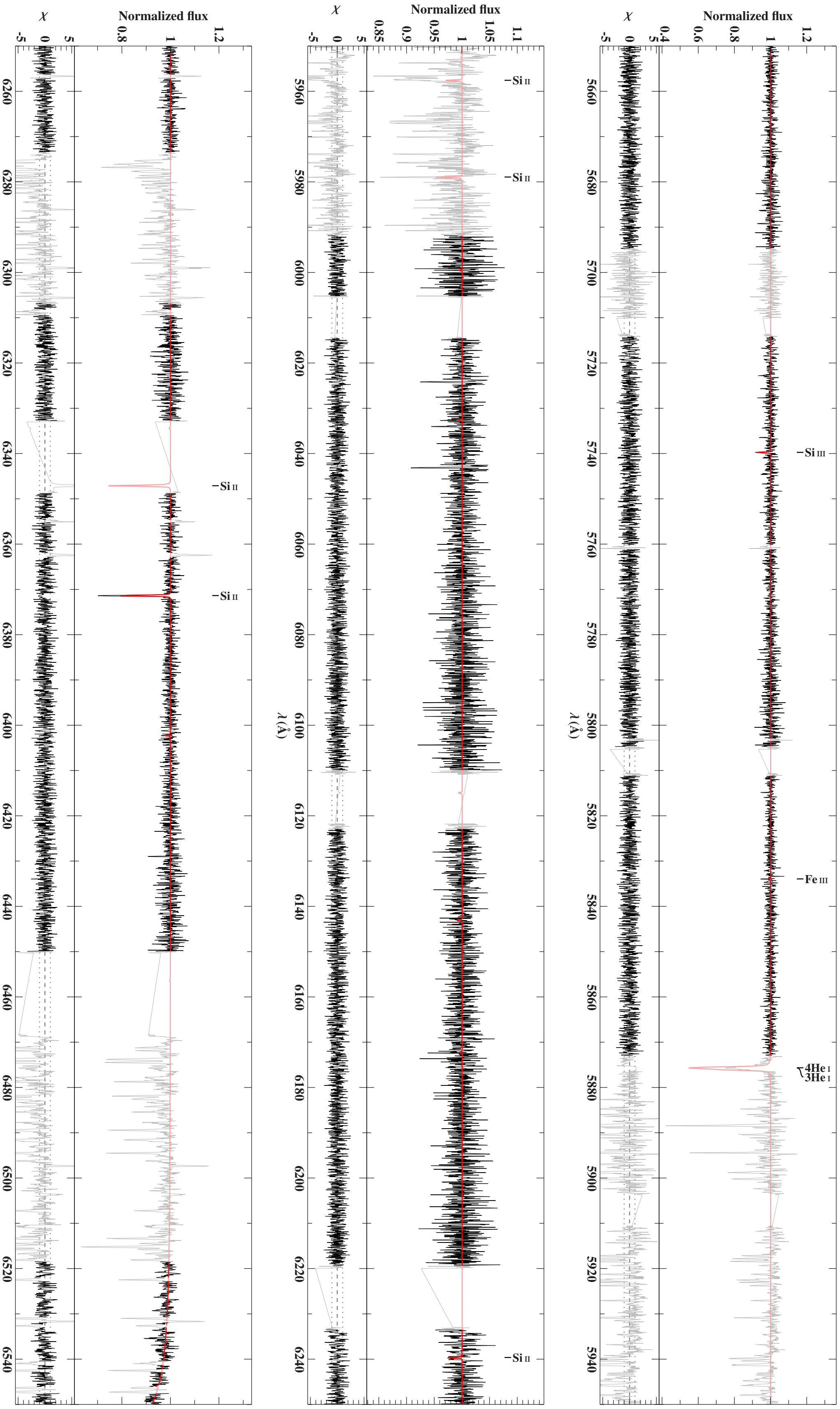

Figure B.1.13.: Fitted HRS spectrum of the $^3\mathrm{He}$ enriched star PHL 25 using the hybrid LTE/NLTE analysis with ISIS - Part 3.

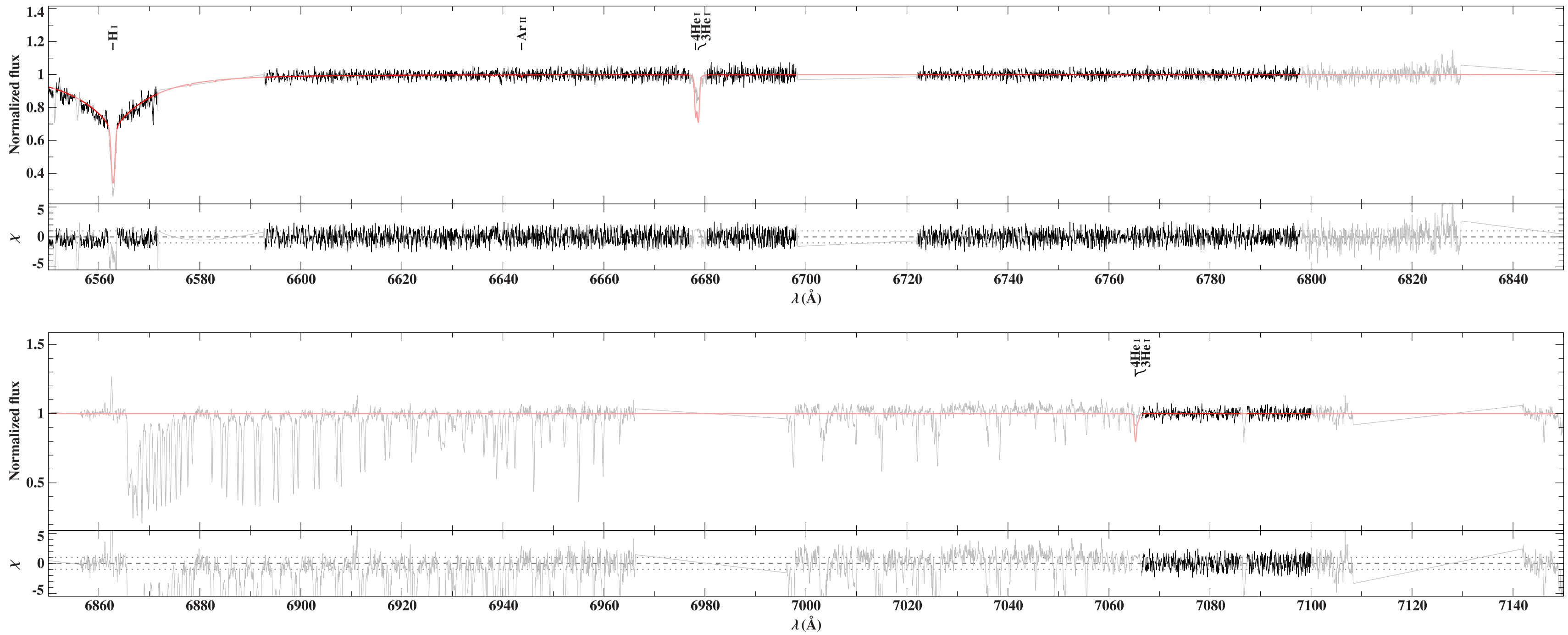

Figure B.1.14.: Fitted HRS spectrum of the $^3\mathrm{He}$ enriched star PHL 25 using the hybrid LTE/NLTE analysis with ISIS - Part 4.

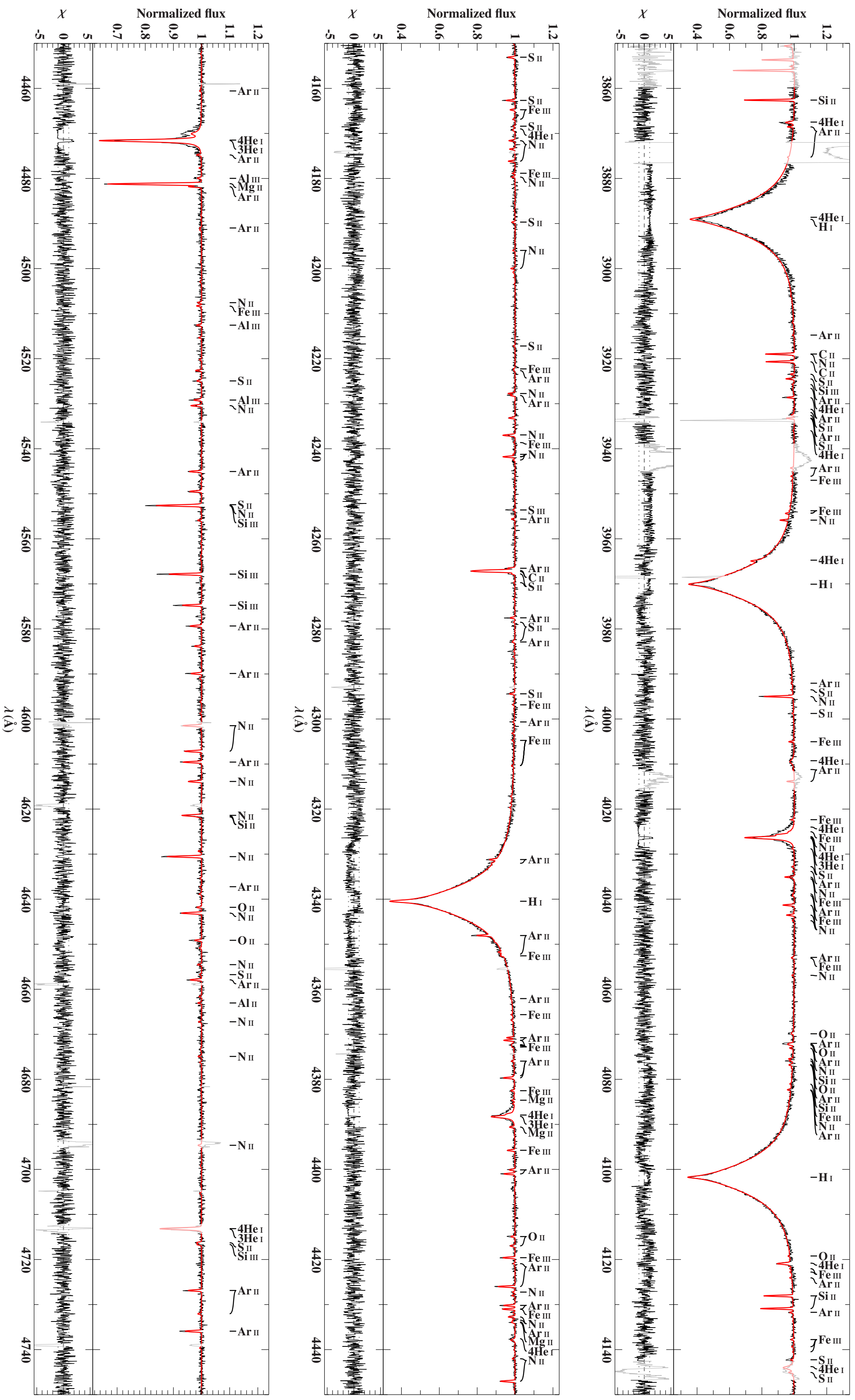

Figure B.1.15.: Fitted FEROS spectrum of the ^{3}He star PHL 382 using the hybrid LTE/NLTE analysis with ISIS - Part 1.

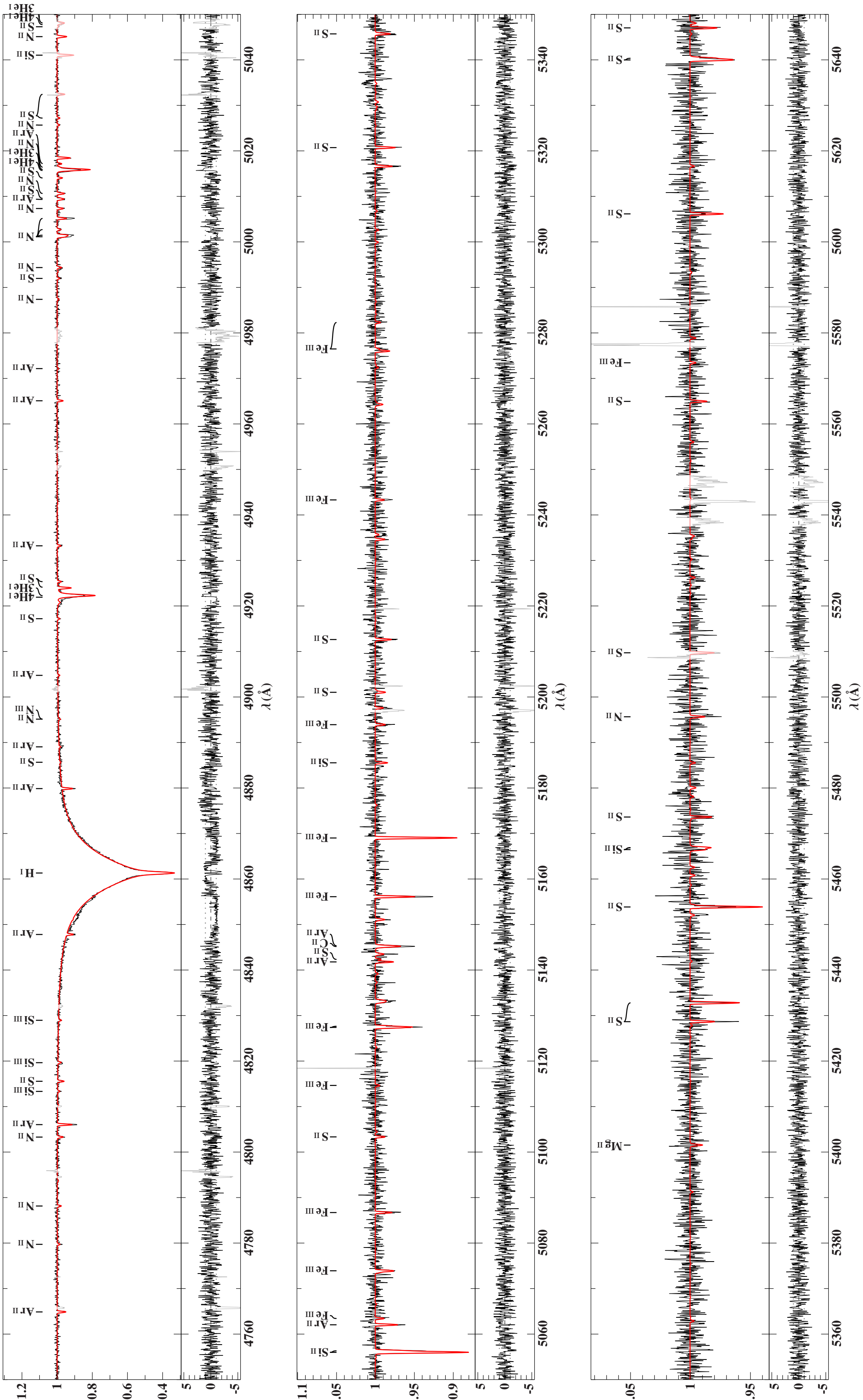

Figure B.1.16.: Fitted FEROS spectrum of the ^{3}He star PHL 382 using the hybrid LTE/NLTE analysis with ISIS - Part 2.

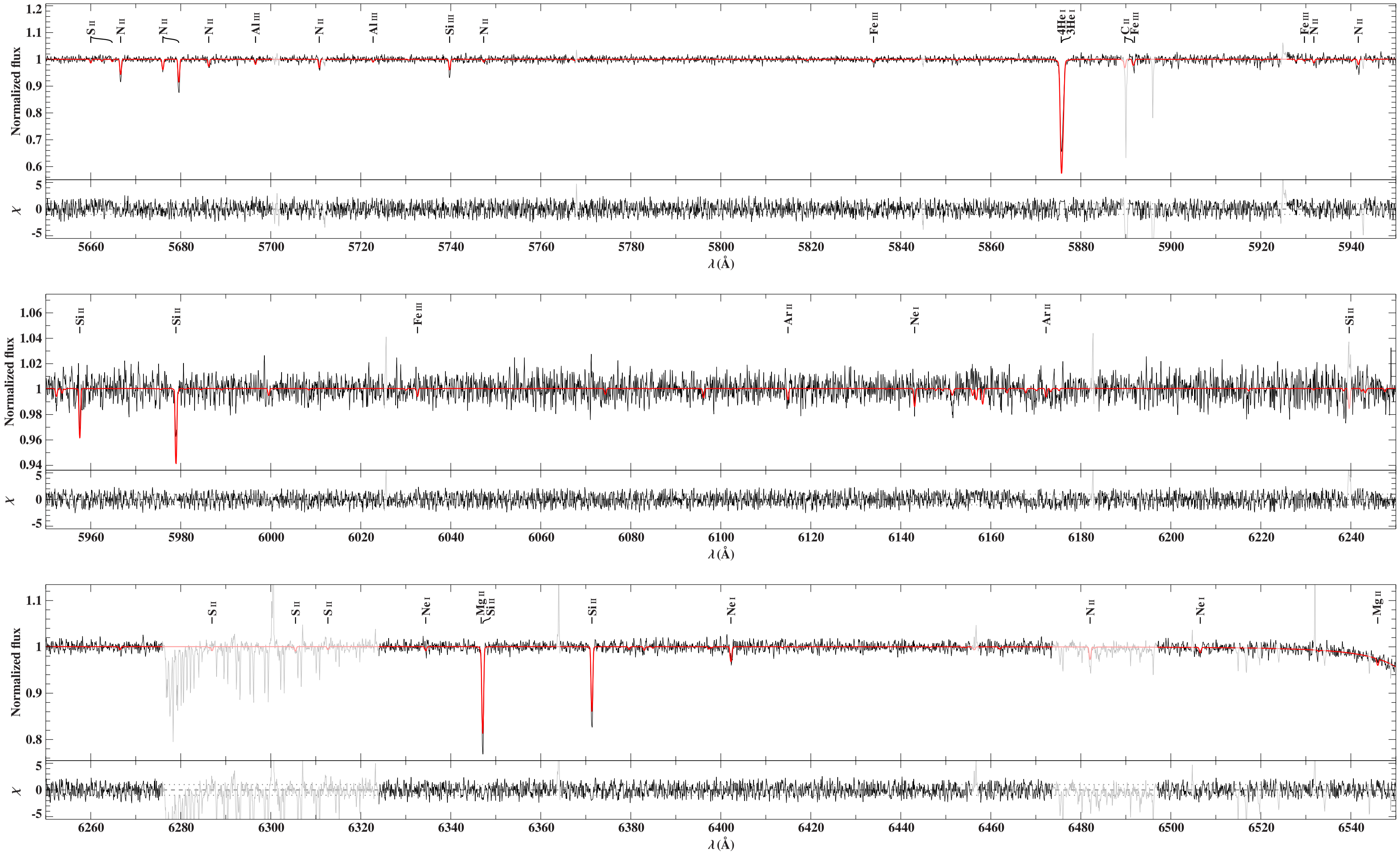

Figure B.1.17.: Fitted FEROS spectrum of the $^{3}\mathrm{He}$ star PHL 382 using the hybrid LTE/NLTE analysis with ISIS - Part 3.

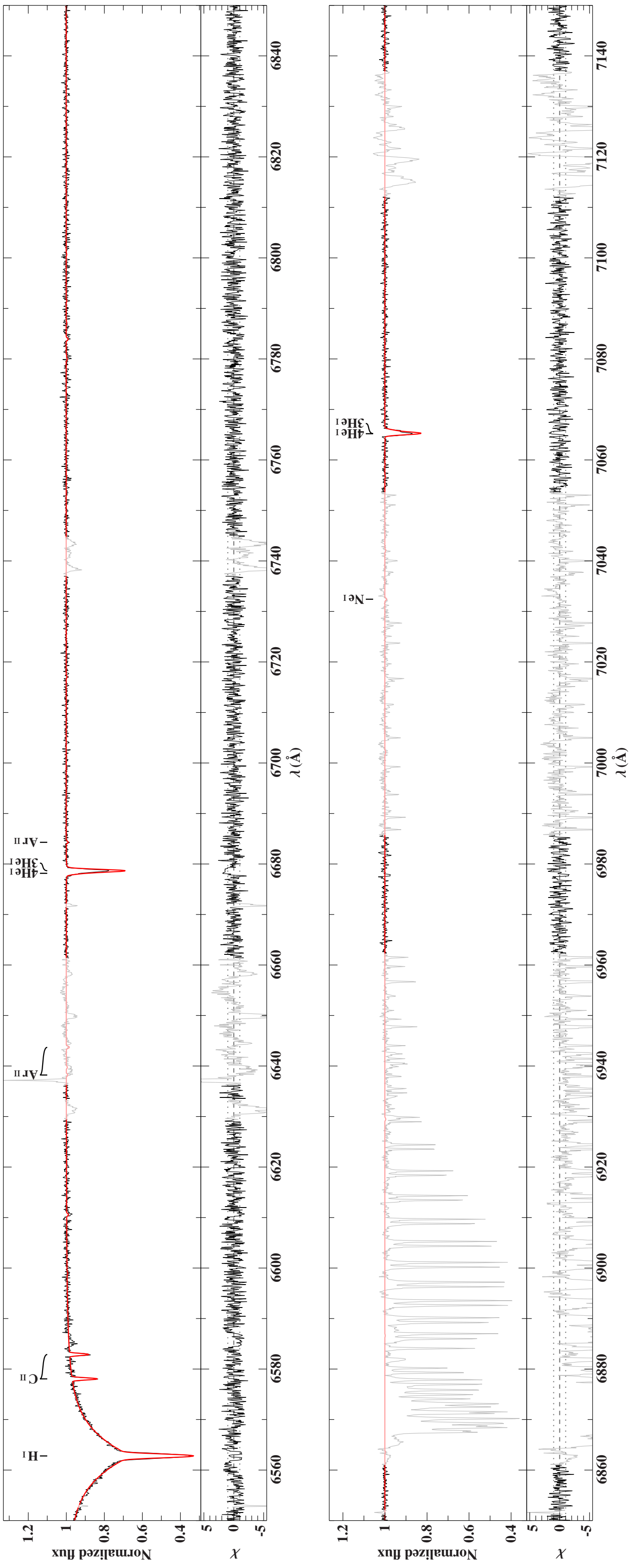

Figure B.1.18.: Fitted FEROS spectrum of the ^{3}He star PHL 382 using the hybrid LTE/NLTE analysis with ISIS - Part 4.

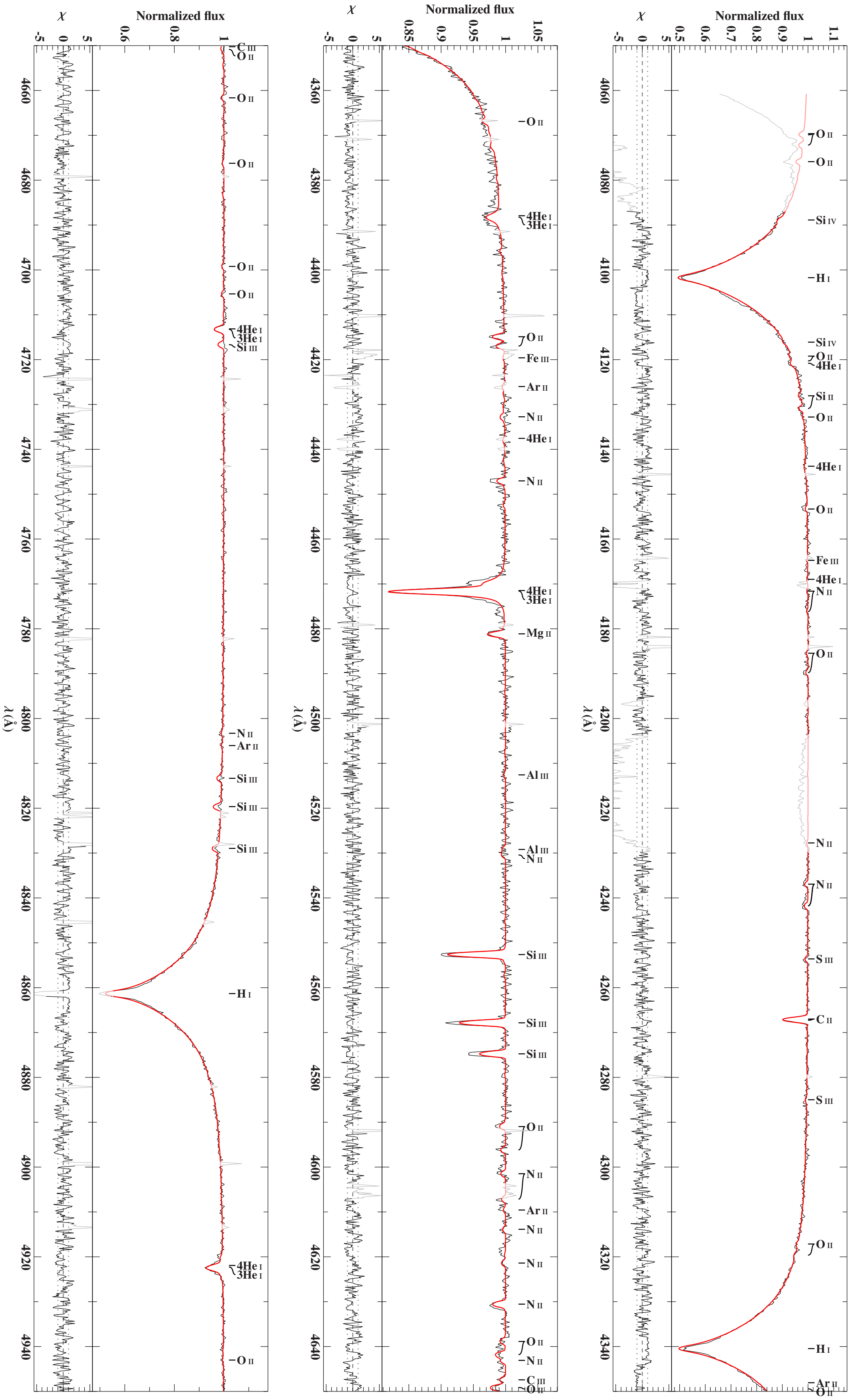

Figure B.1.19.: Fitted CASPEC spectrum of the ^{3}He star SB 290 using the hybrid LTE/NLTE analysis with ISIS - Part 1.

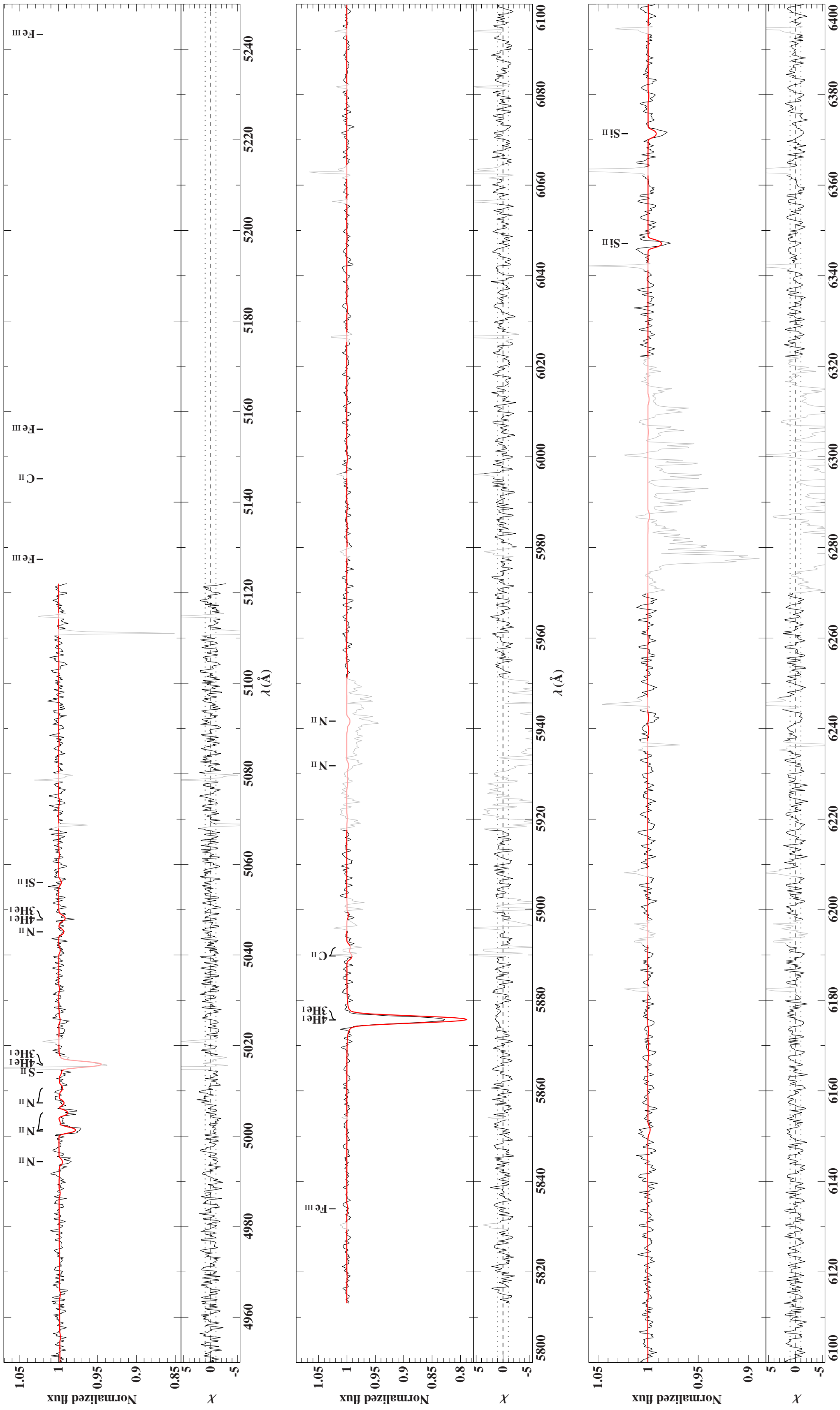

Figure B.1.20.: Fitted CASPEC spectrum of the ^{3}He star SB 290 using the hybrid LTE/NLTE analysis with ISIS - Part 2.

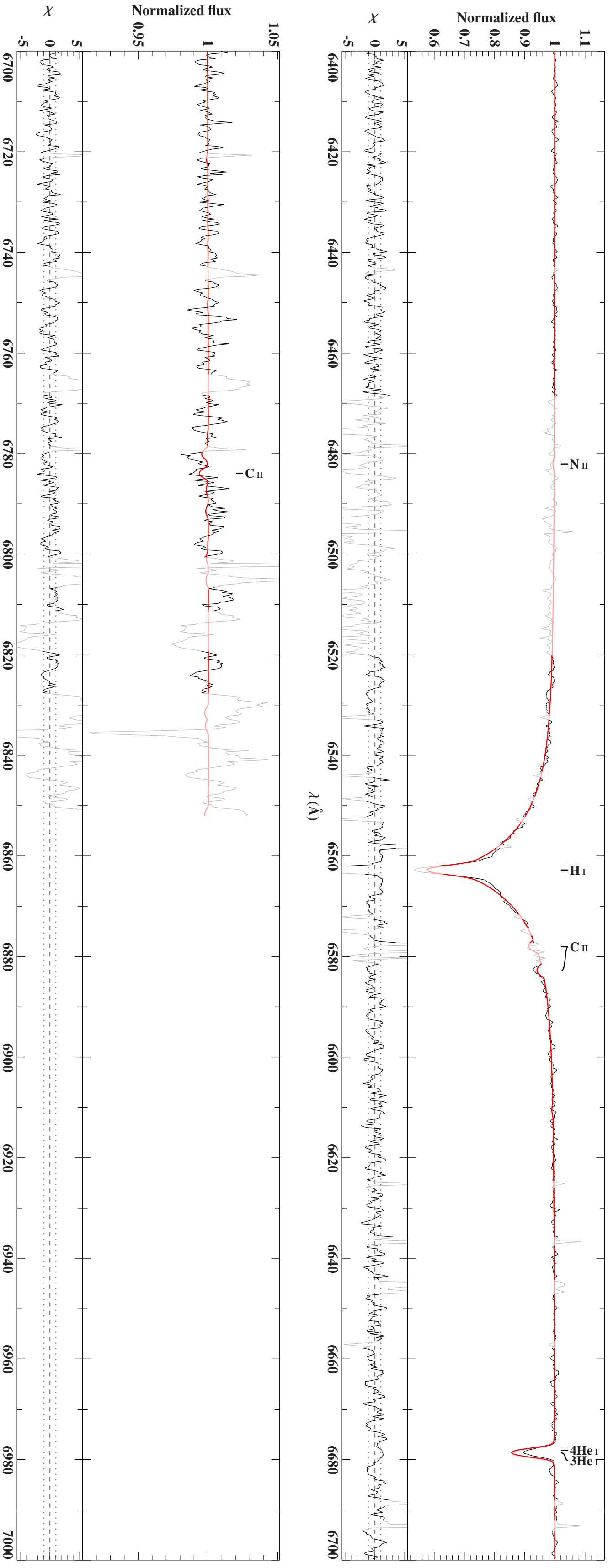

Figure B.1.21.: Fitted CASPEC spectrum of the ^{3}He star SB 290 using the hybrid LTE/NLTE analysis with ISIS - Part 3.

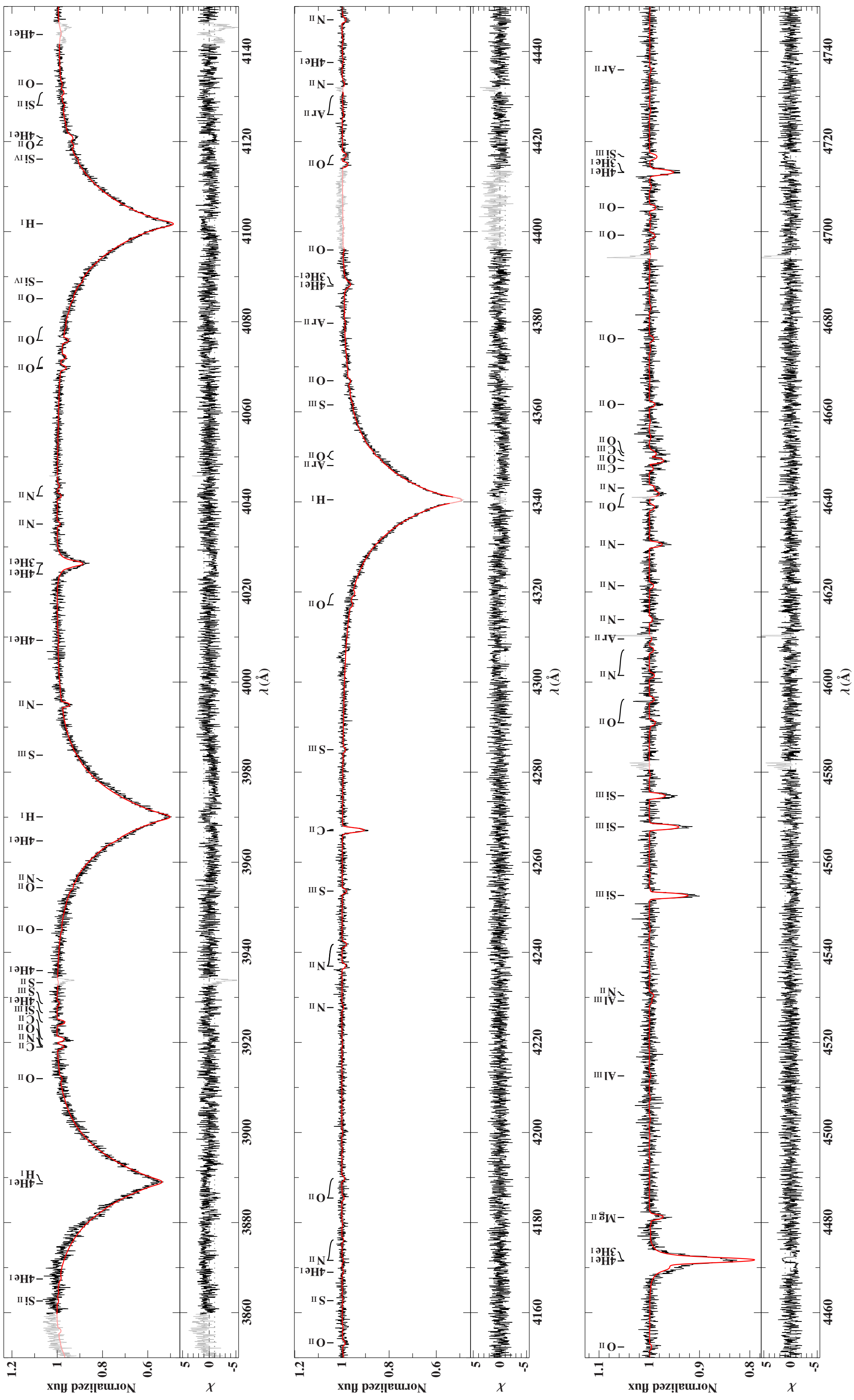

Figure B.1.22.: Fitted FEROS spectrum of the $^3\mathrm{He}$ star SB 290 using the hybrid LTE/NLTE analysis with ISIS - Part 1.

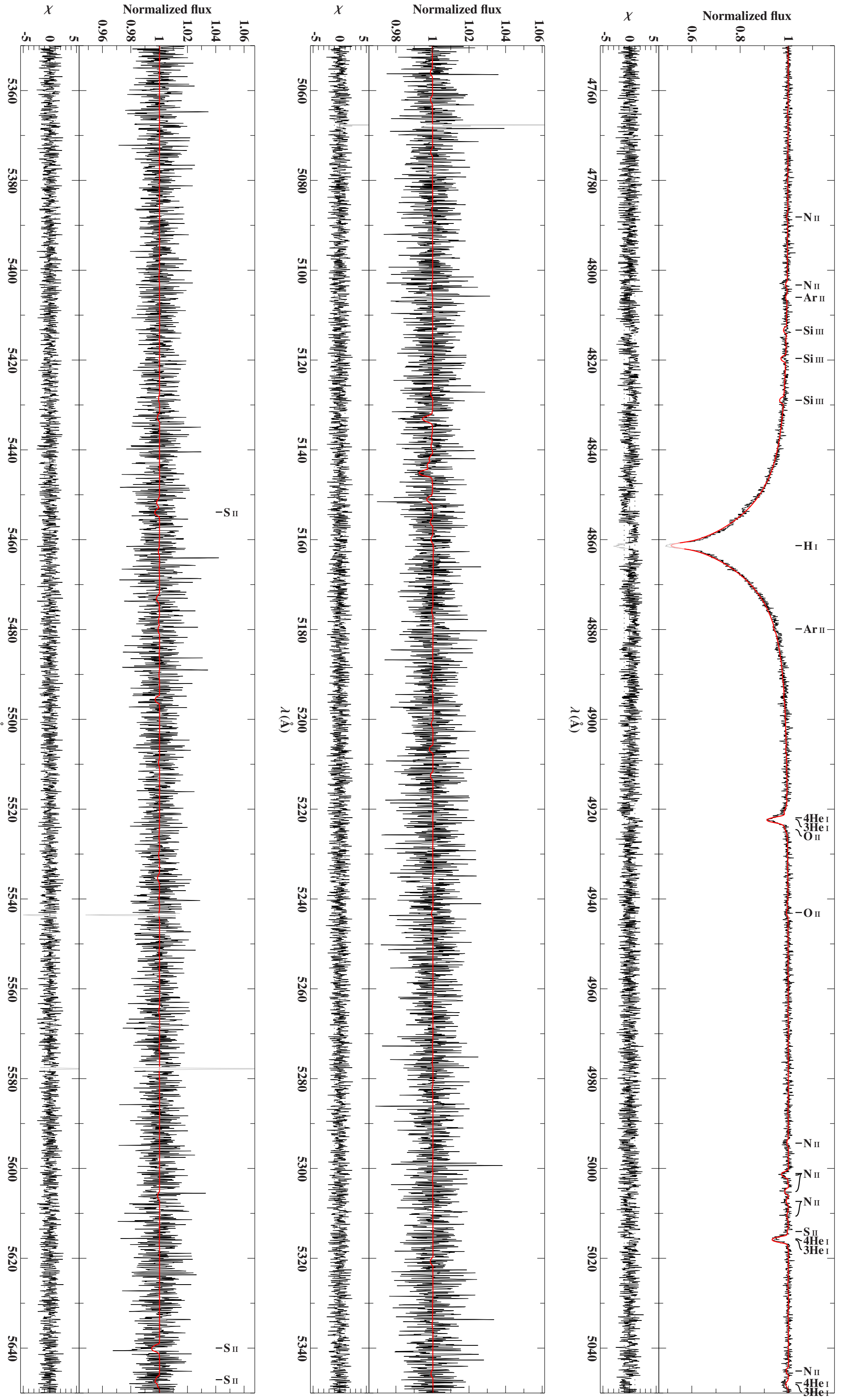

Figure B.1.23.: Fitted FEROS spectrum of the ^{3}He star SB 290 using the hybrid LTE/NLTE analysis with ISIS - Part 2.

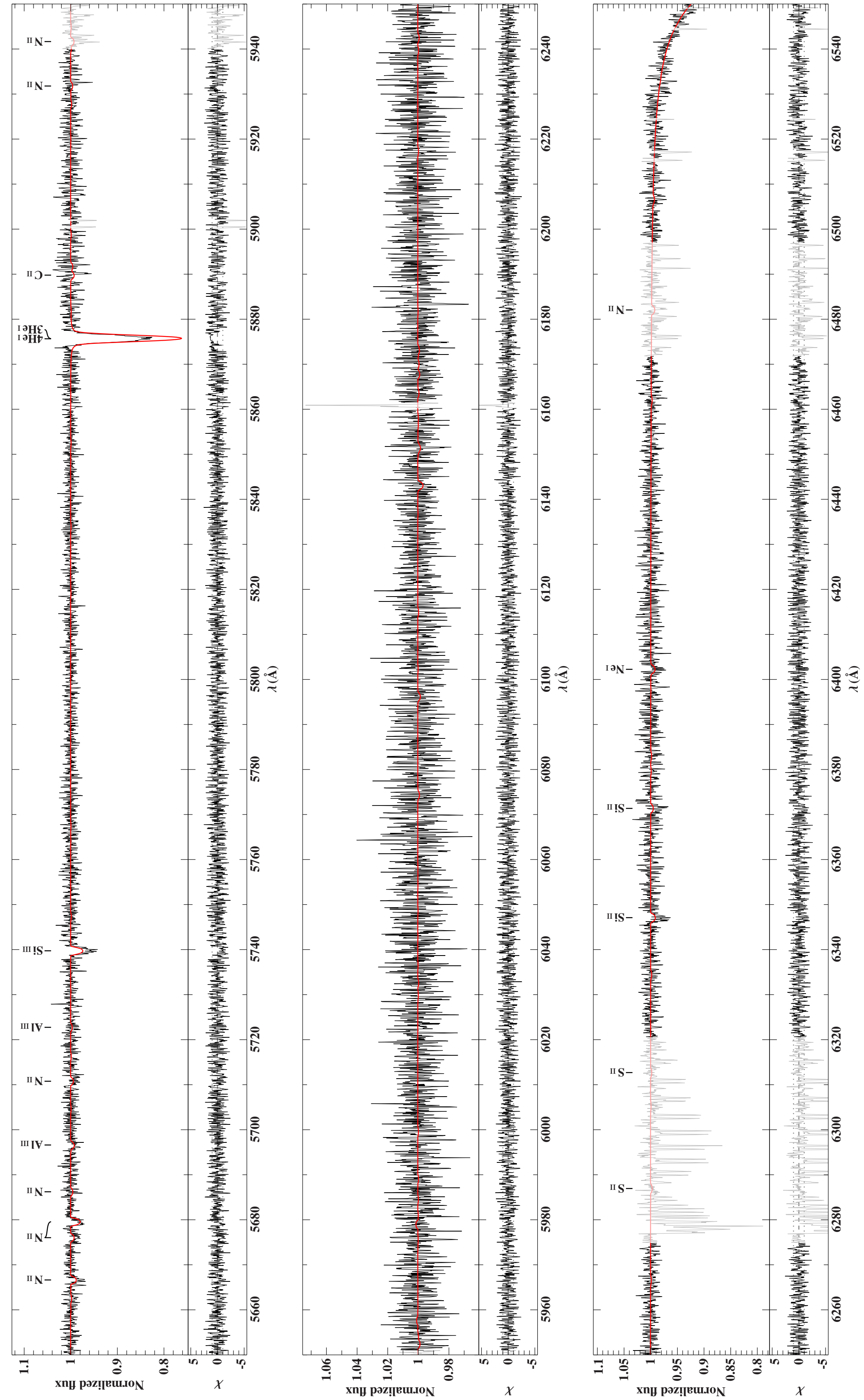

Figure B.1.24.: Fitted FEROS spectrum of the ^{3}He star SB 290 using the hybrid LTE/NLTE analysis with ISIS - Part 3.

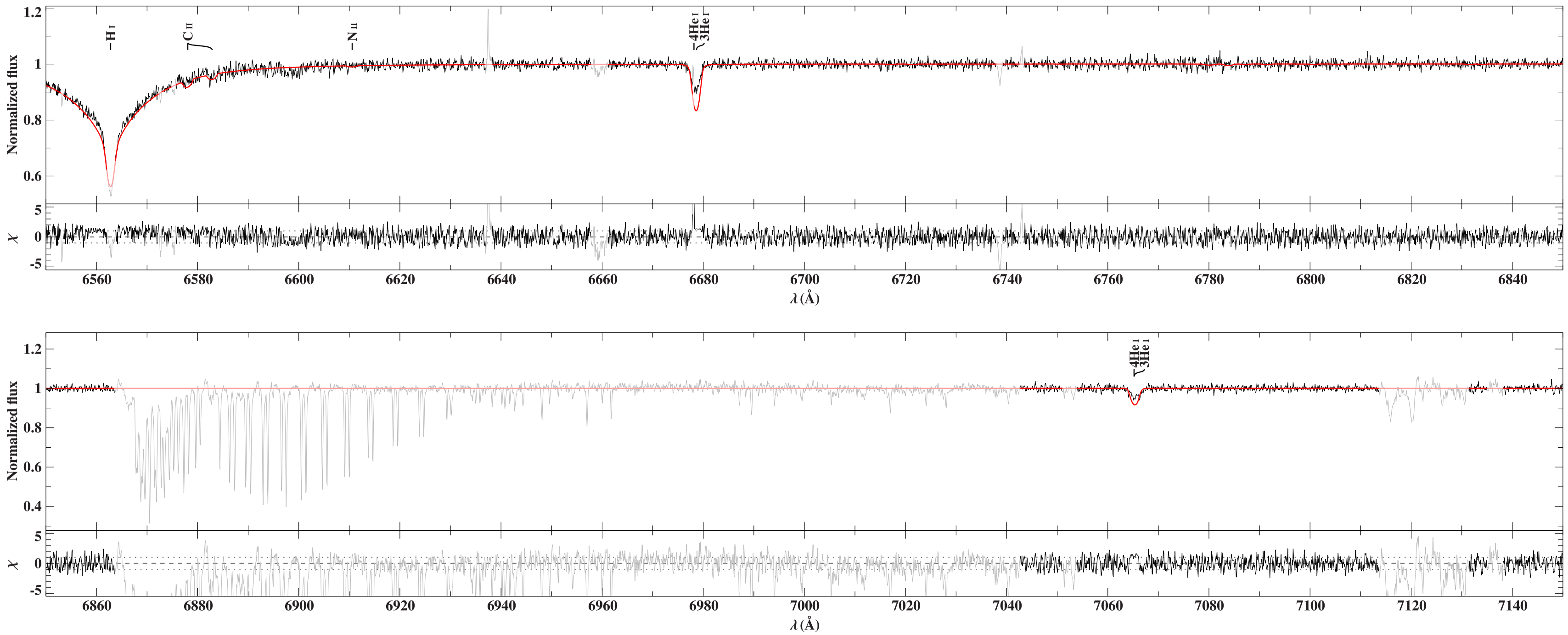

Figure B.1.25.: Fitted FEROS spectrum of the $^3\mathrm{He}$ star SB 290 using the hybrid LTE/NLTE analysis with ISIS - Part 4.

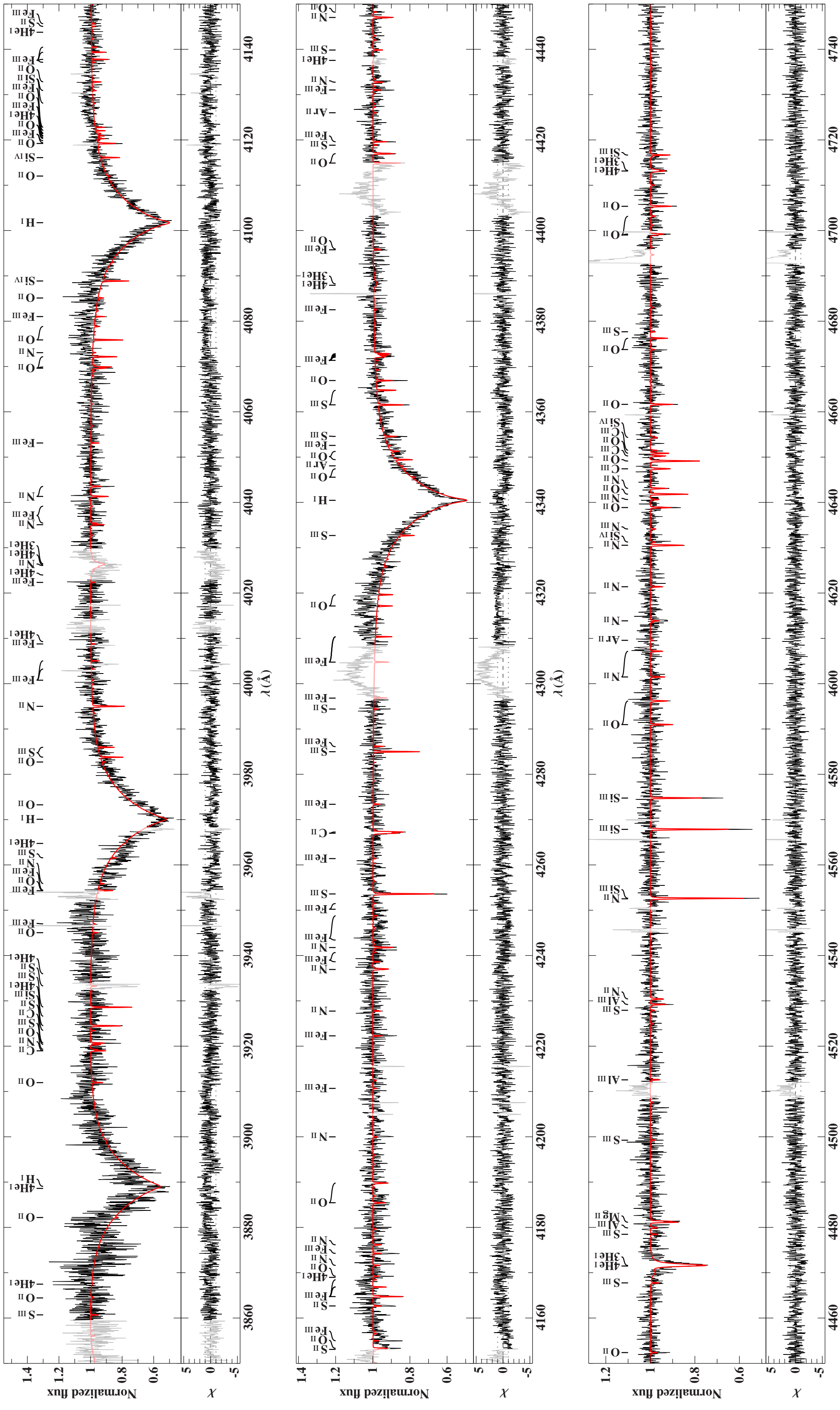

Figure B.1.26.: Fitted FEROS spectrum of the ^{3}He star EC 03263-6403 using the hybrid LTE/NLTE analysis with ISIS - Part 1.

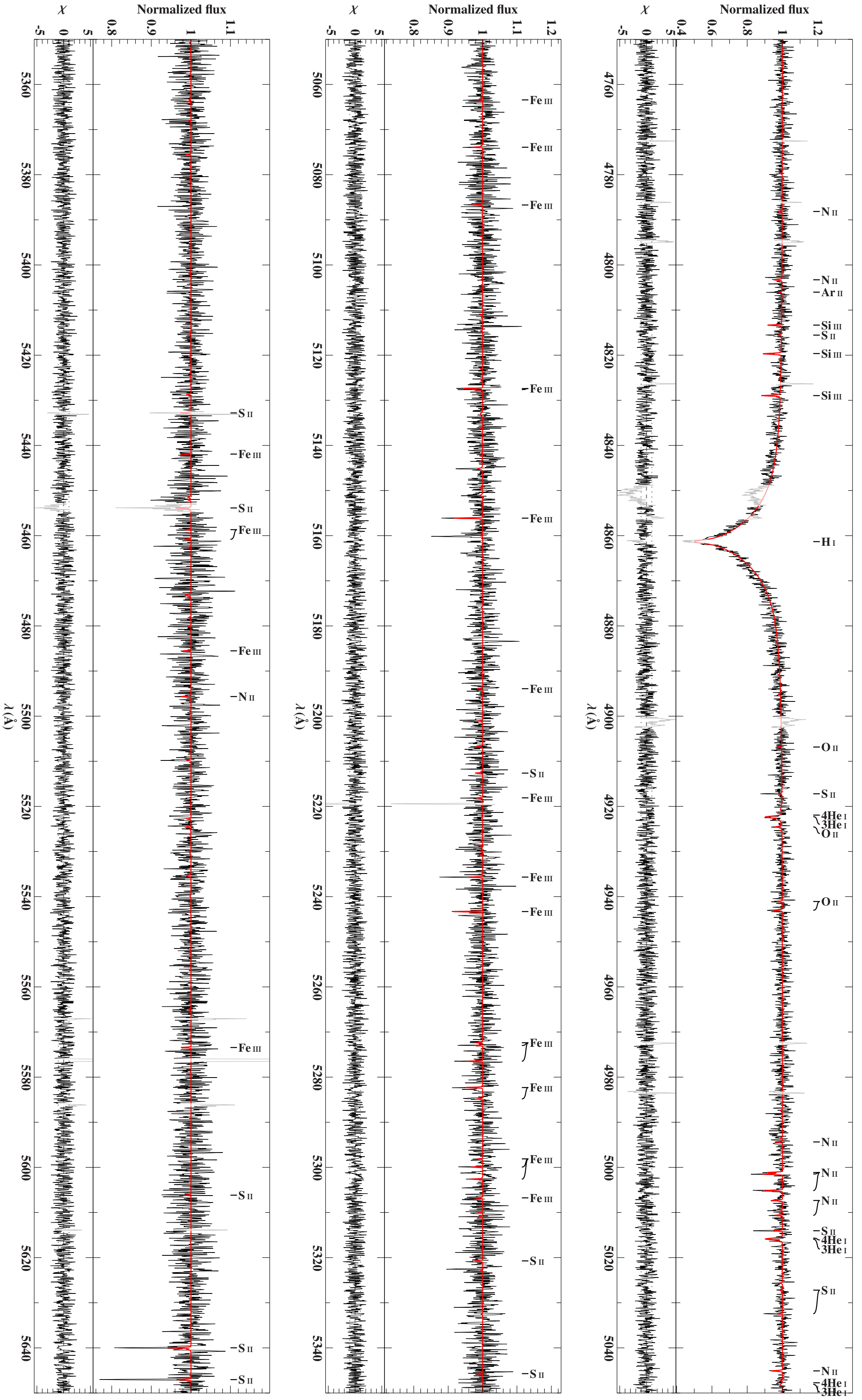

Figure B.1.27.: Fitted FEROS spectrum of the ^{3}He star EC 03263-6403 using the hybrid LTE/NLTE analysis with ISIS - Part 2.

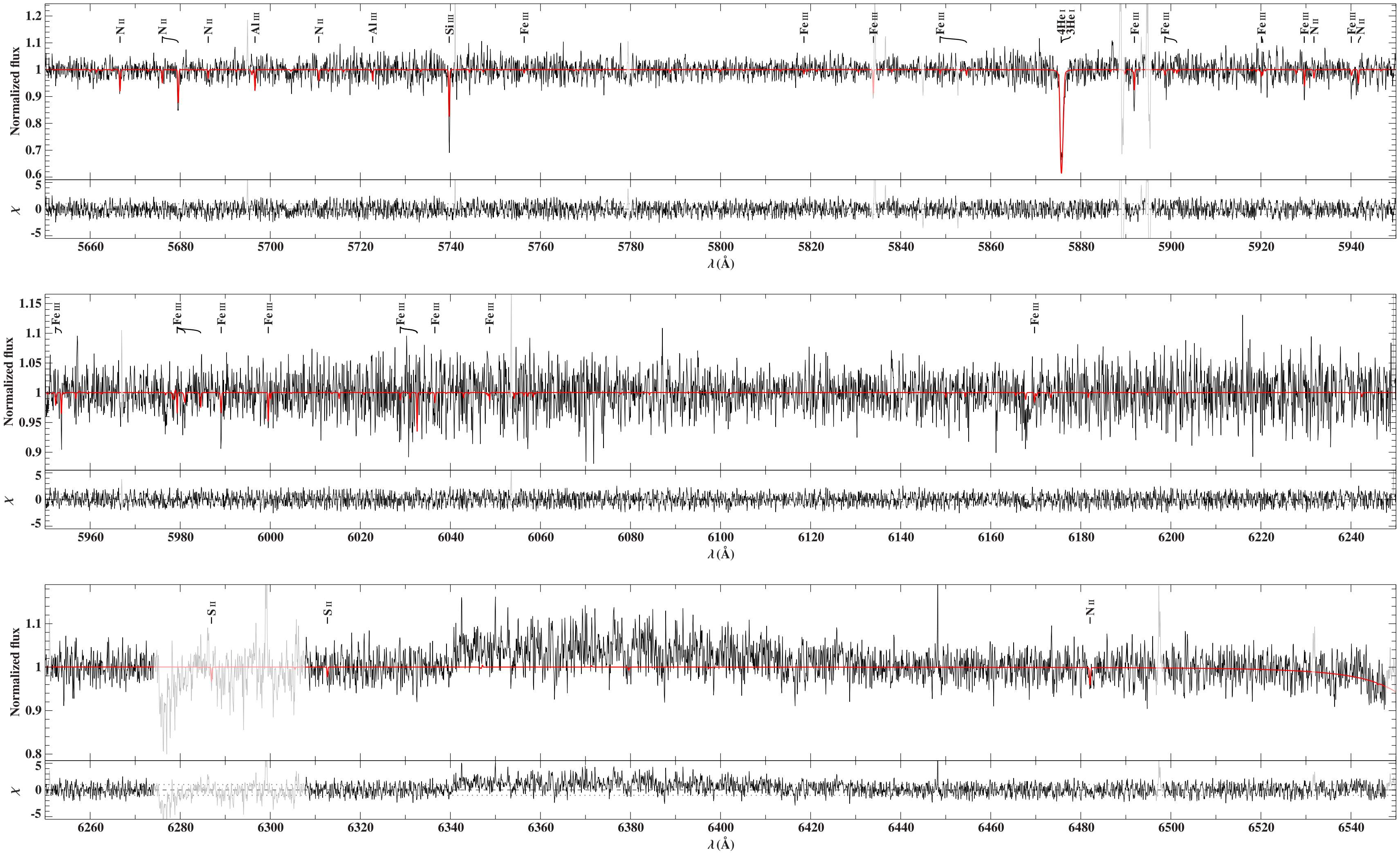

Figure B.1.28.: Fitted FEROS spectrum of the $^{3}\mathrm{He}$ star EC 03263-6403 using the hybrid LTE/NLTE analysis with ISIS - Part 3.

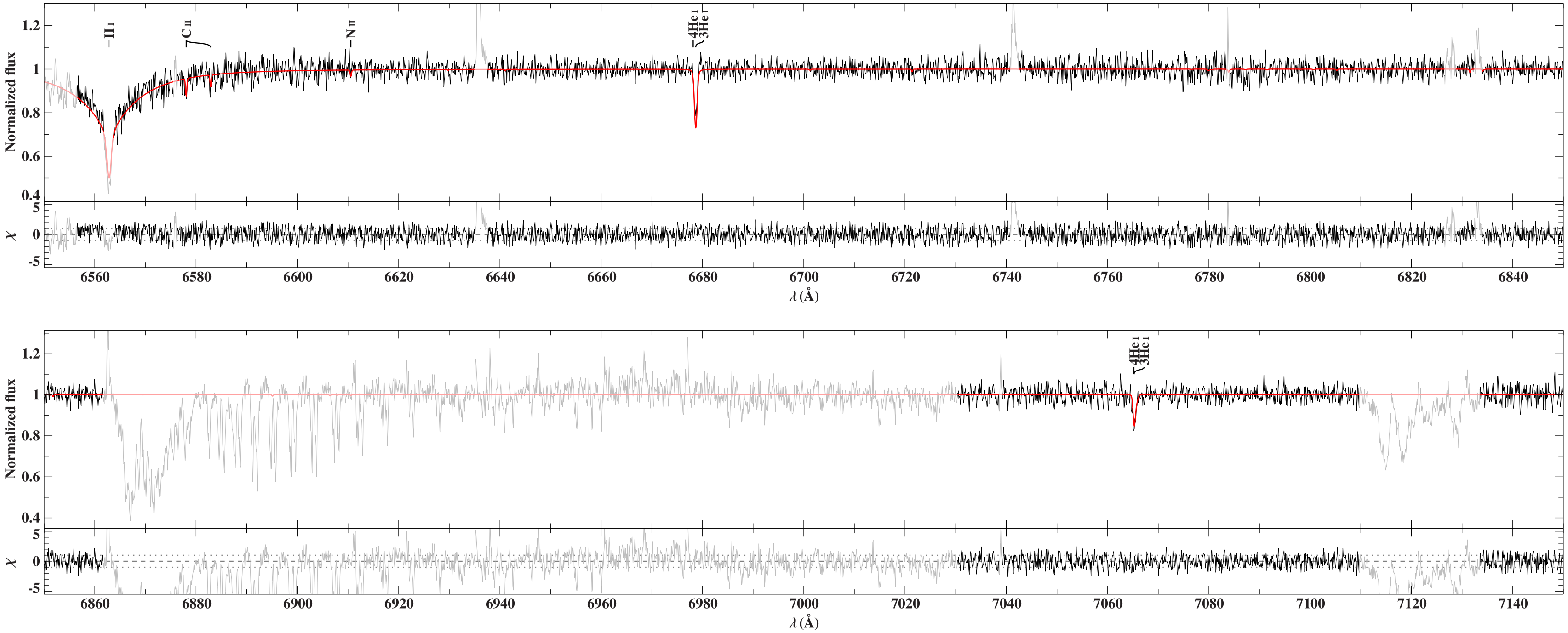

Figure B.1.29.: Fitted FEROS spectrum of the $^{3}\mathrm{He}$ star EC 03263-6403 using the hybrid LTE/NLTE analysis with ISIS - Part 4.

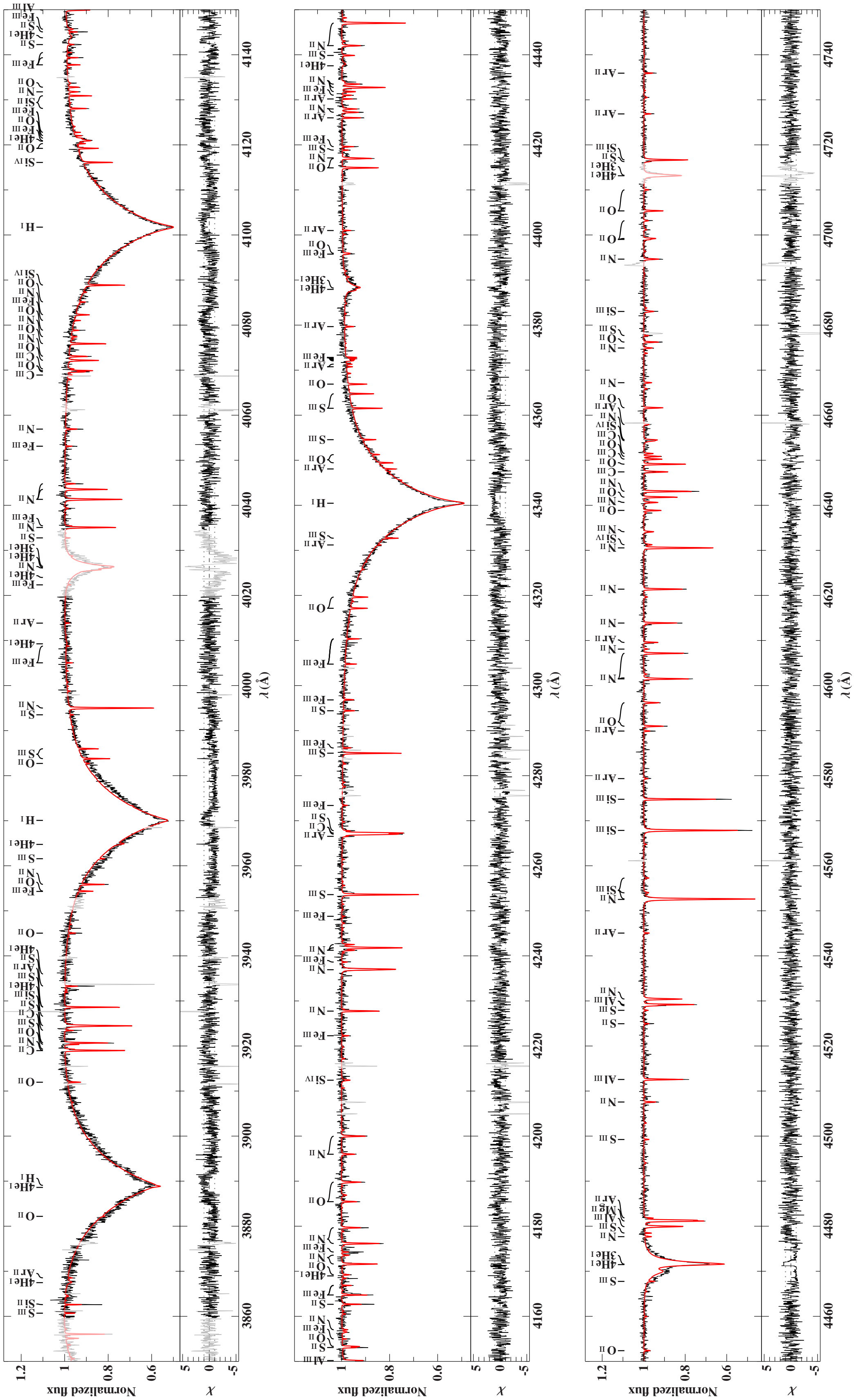

Figure B.1.30.: Fitted FEROS spectrum of the ^{3}He star EC 03591-3232 using the hybrid LTE/NLTE analysis with ISIS - Part 1.

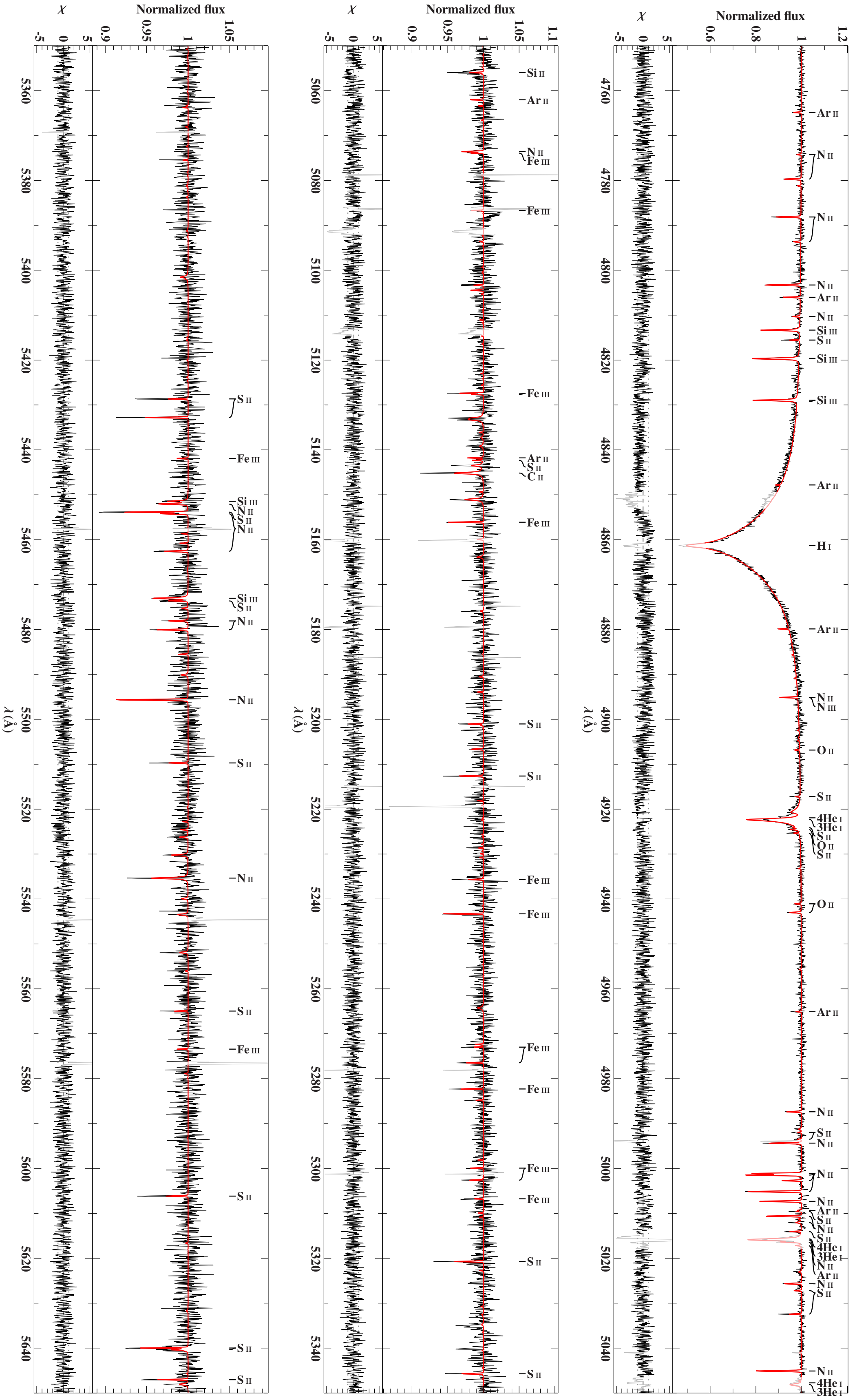

Figure B.1.31.: Fitted FEROS spectrum of the ^{3}He star EC 03591-3232 using the hybrid LTE/NLTE analysis with ISIS - Part 2.

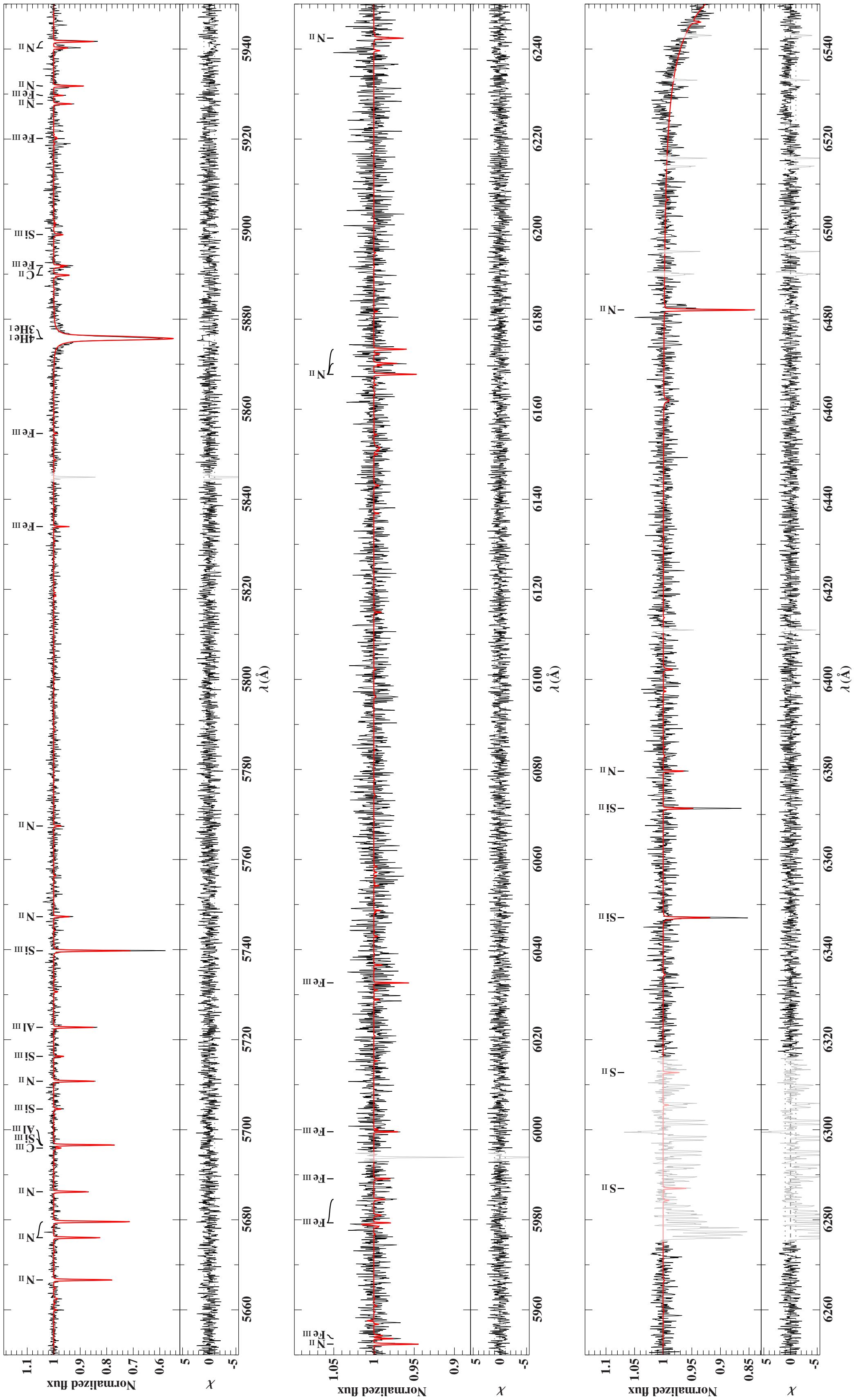

Figure B.1.32.: Fitted FEROS spectrum of the ^{3}He star EC 03591-3232 using the hybrid LTE/NLTE analysis with ISIS - Part 3.

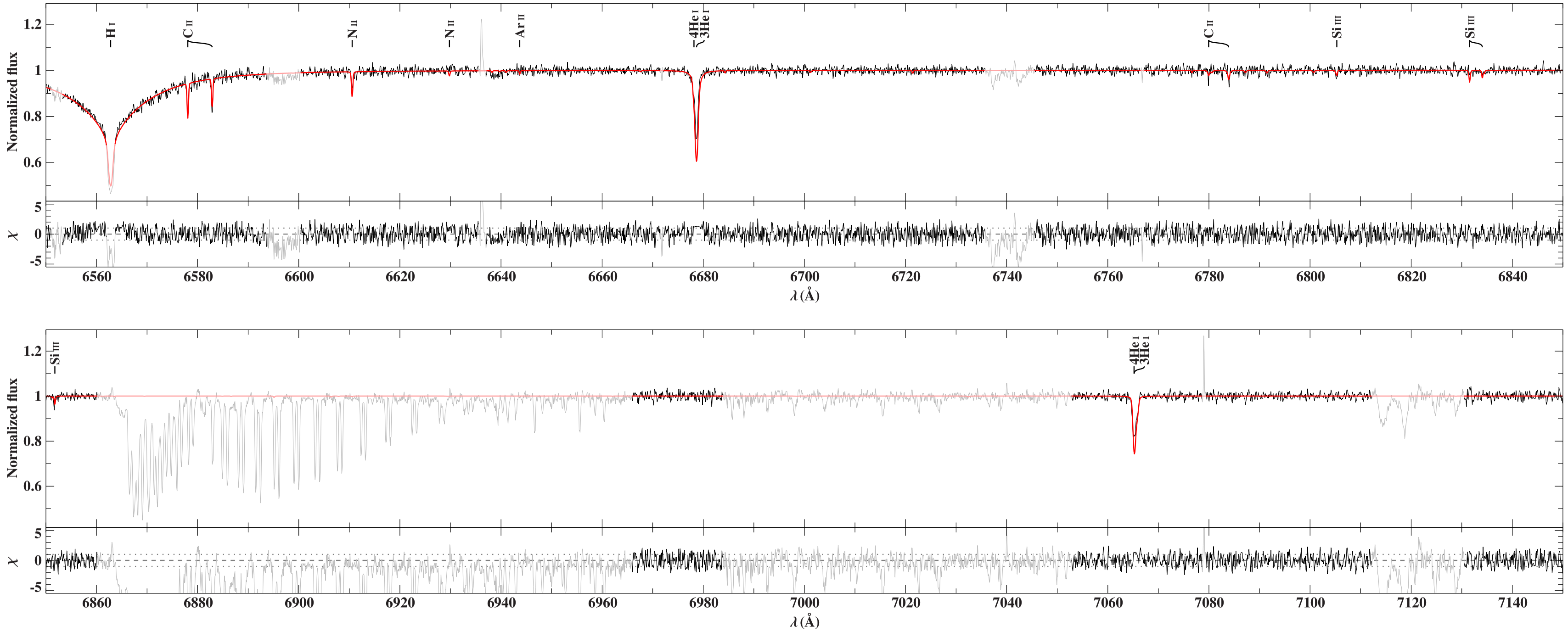

Figure B.1.33.: Fitted FEROS spectrum of the $^{3}\mathrm{He}$ star EC 03591-3232 using the hybrid LTE/NLTE analysis with ISIS - Part 4.

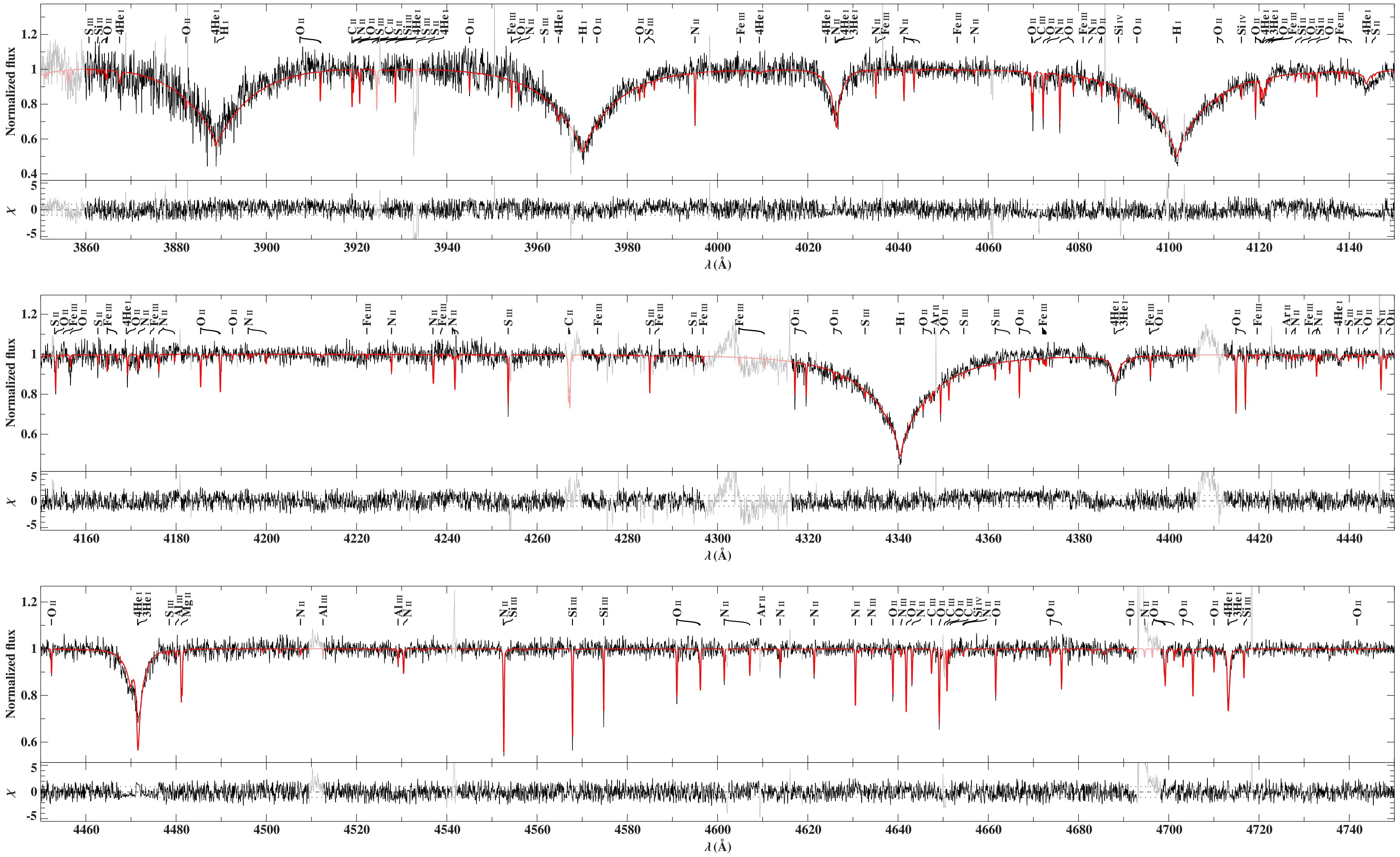

Figure B.1.34.: Fitted FEROS spectrum of the $^{3}\mathrm{He}$ enriched star EC 12234-2607 using the hybrid LTE/NLTE analysis with ISIS - Part 1.

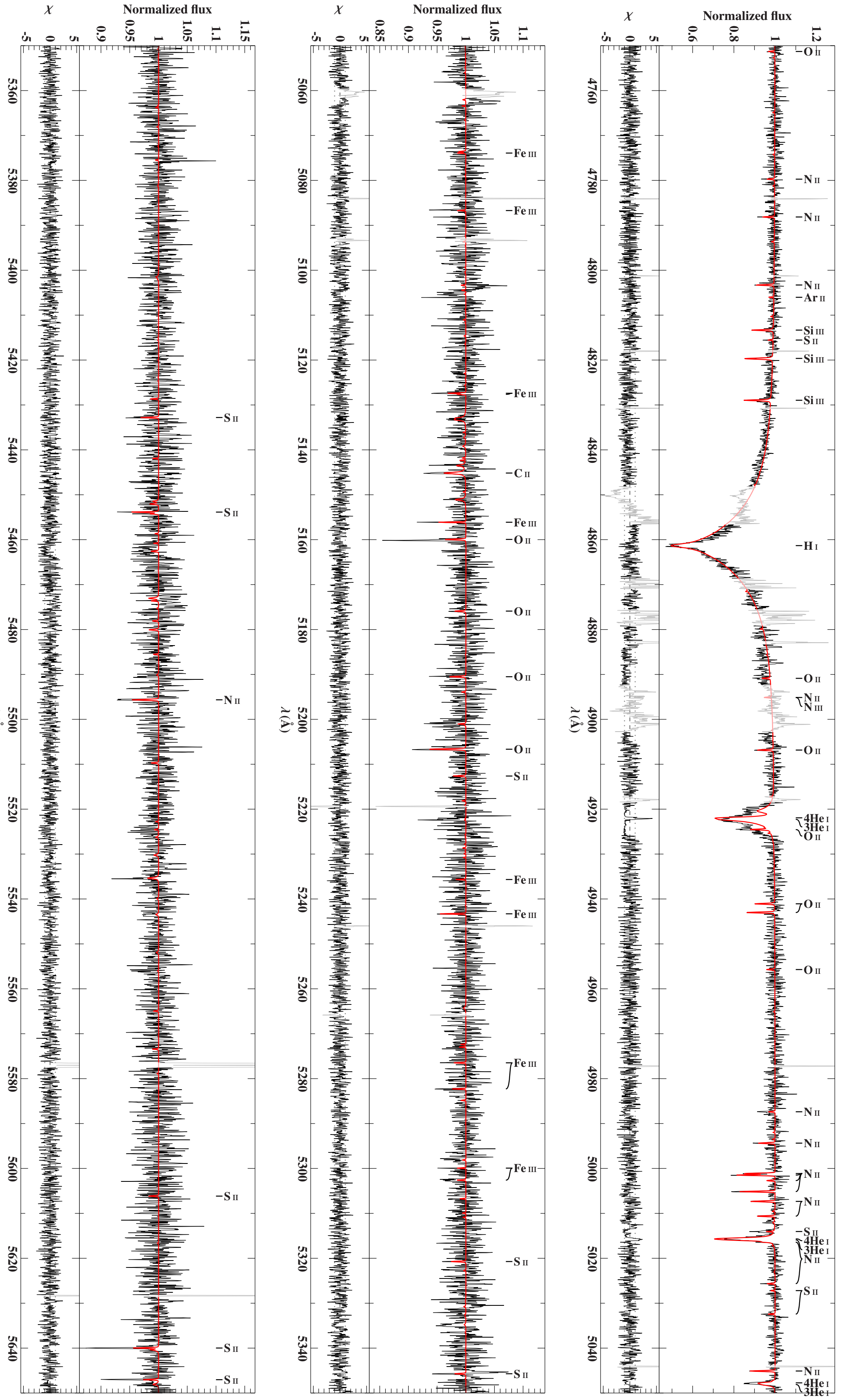

Figure B.1.35.: Fitted FEROS spectrum of the ^{3}He enriched star EC 12234-2607 using the hybrid LTE/NLTE analysis with ISIS - Part 2.

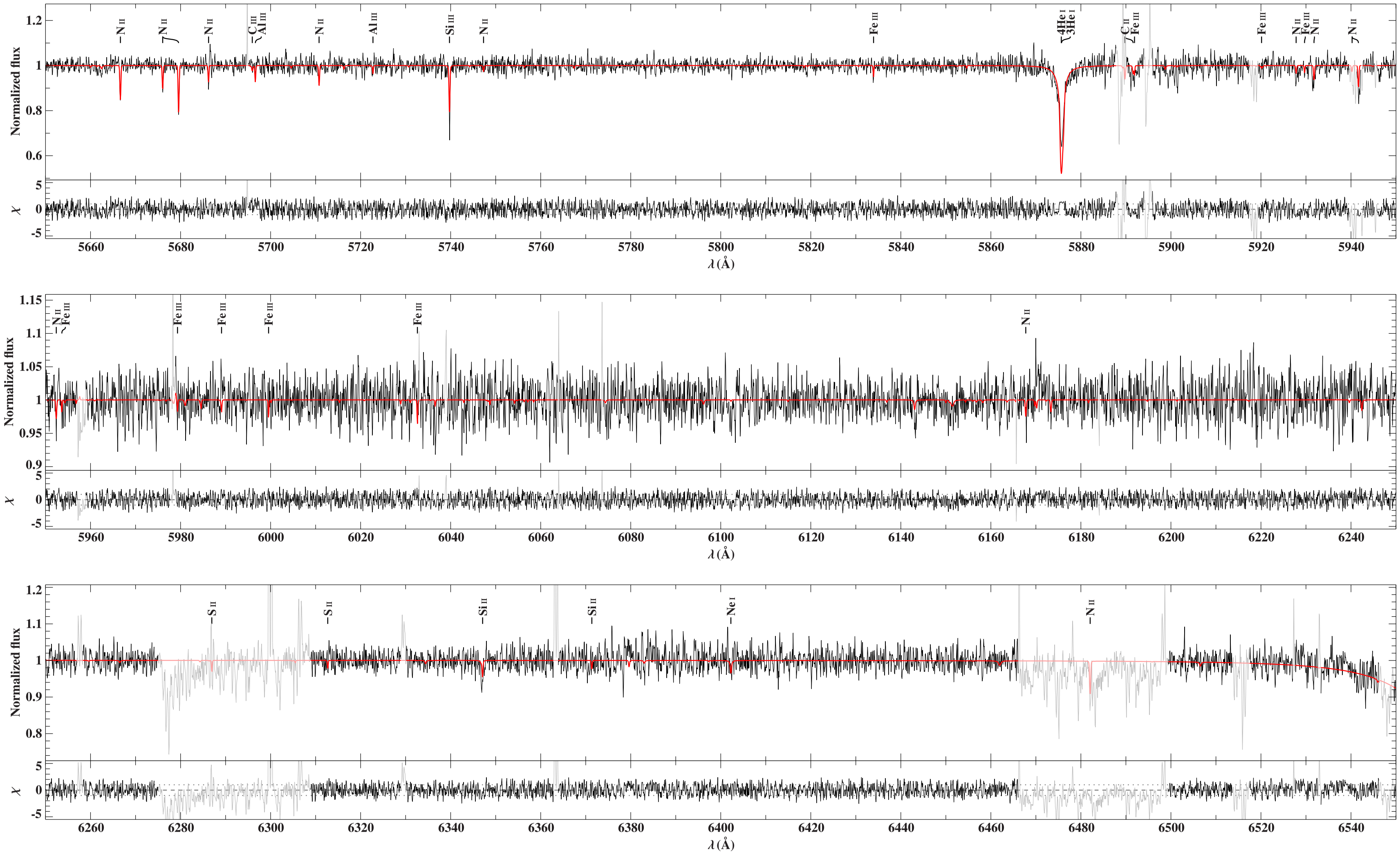

Figure B.1.36.: Fitted FEROS spectrum of the $^{3}\mathrm{He}$ enriched star EC 12234-2607 using the hybrid LTE/NLTE analysis with ISIS - Part 3.

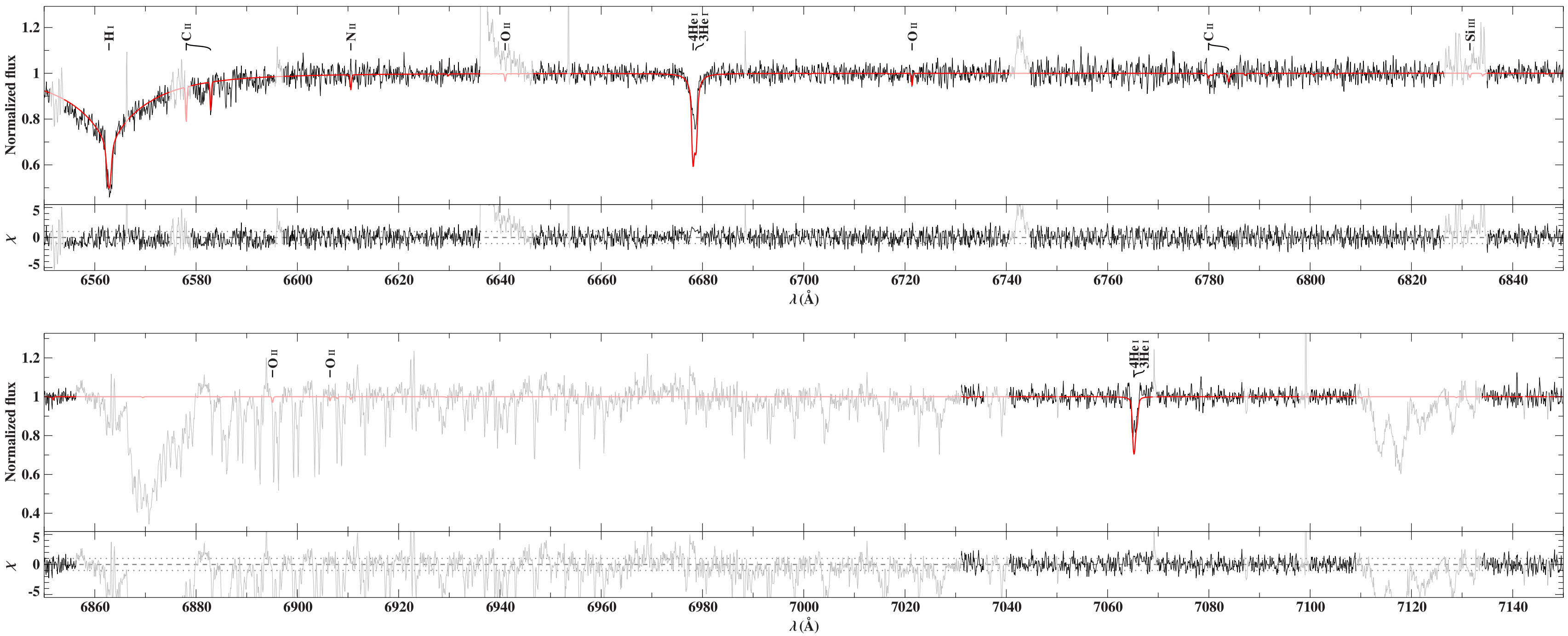

Figure B.1.37.: Fitted FEROS spectrum of the $^3\mathrm{He}$ enriched star EC 12234-2607 using the hybrid LTE/NLTE analysis with ISIS - Part 4.

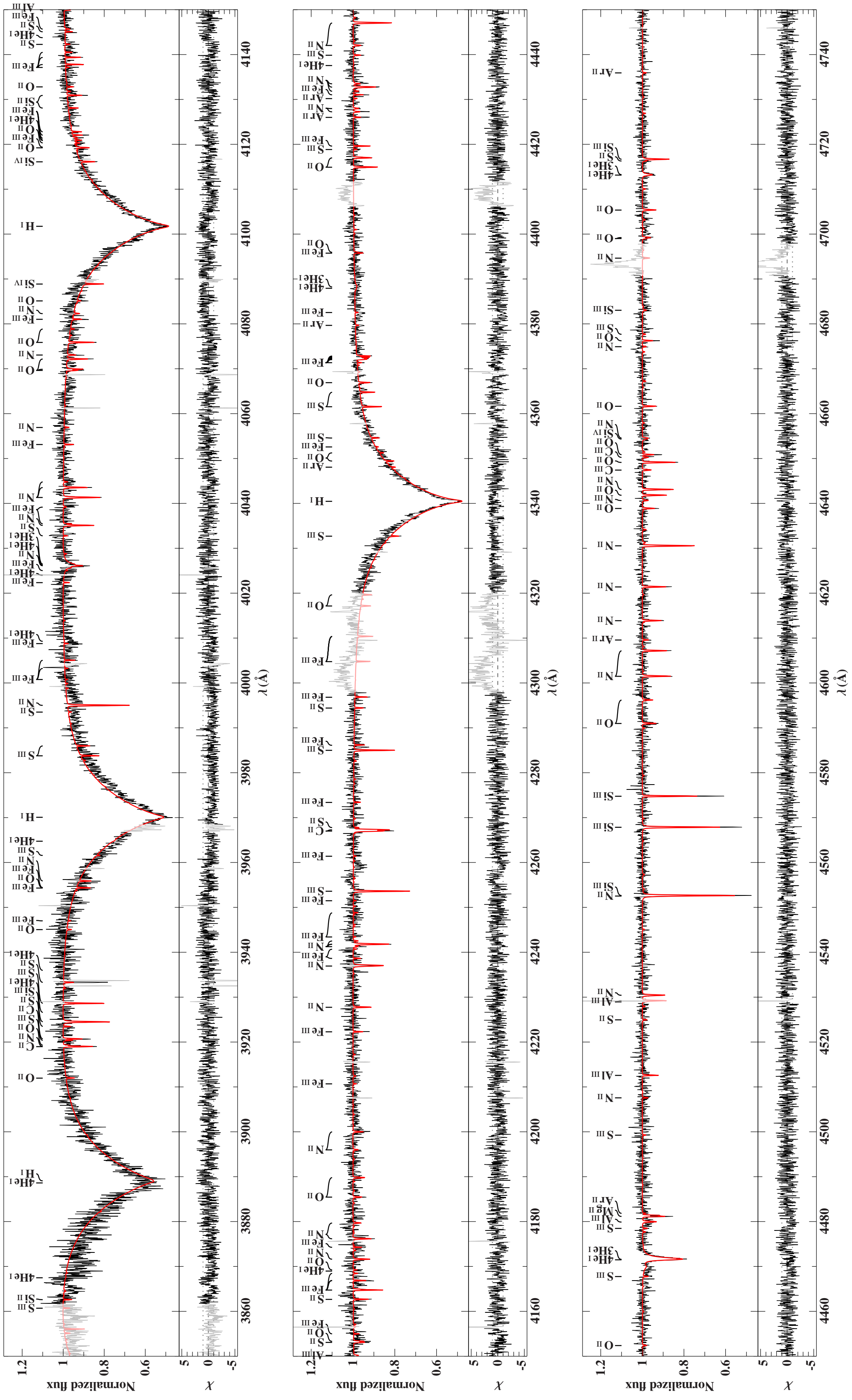

Figure B.1.38.: Fitted FEROS spectrum of the ^{3}He star EC 14338-1445 using the hybrid LTE/NLTE analysis with ISIS - Part 1.

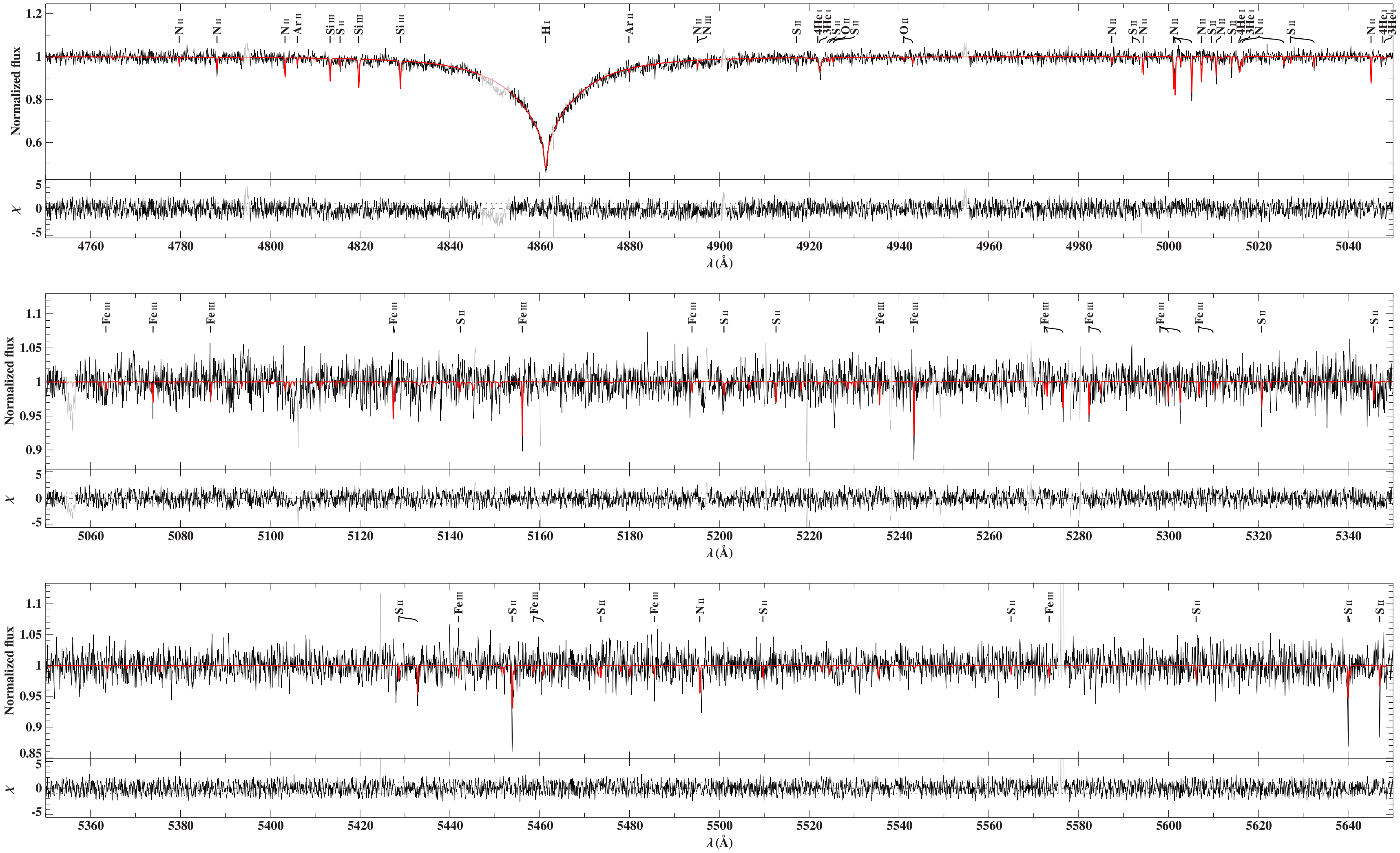

Figure B.1.39.: Fitted FEROS spectrum of the $^3\mathrm{He}$ star EC 14338-1445 using the hybrid LTE/NLTE analysis with ISIS - Part 2.

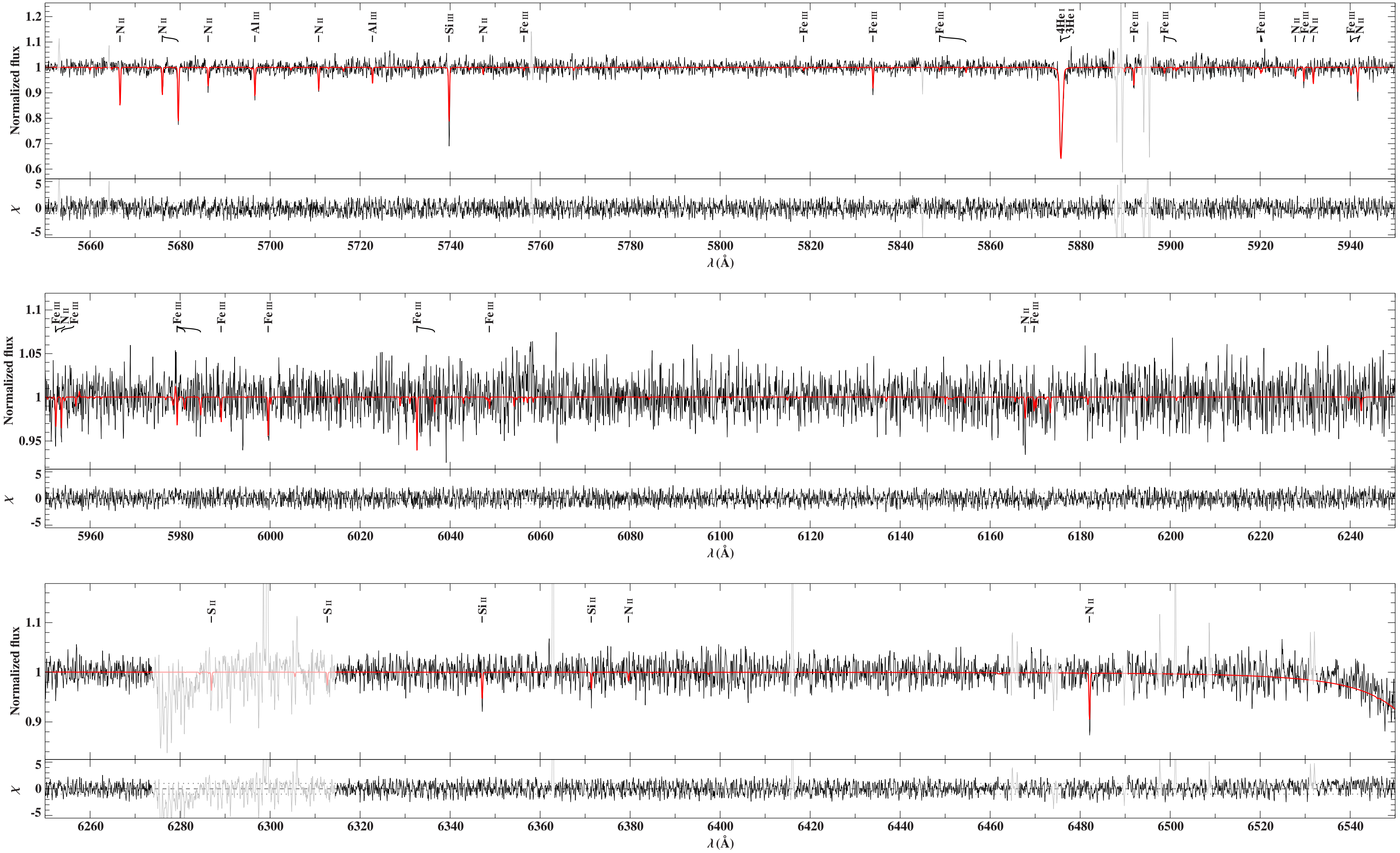

Figure B.1.40.: Fitted FEROS spectrum of the $^{3}\mathrm{He}$ star EC 14338-1445 using the hybrid LTE/NLTE analysis with ISIS - Part 3.

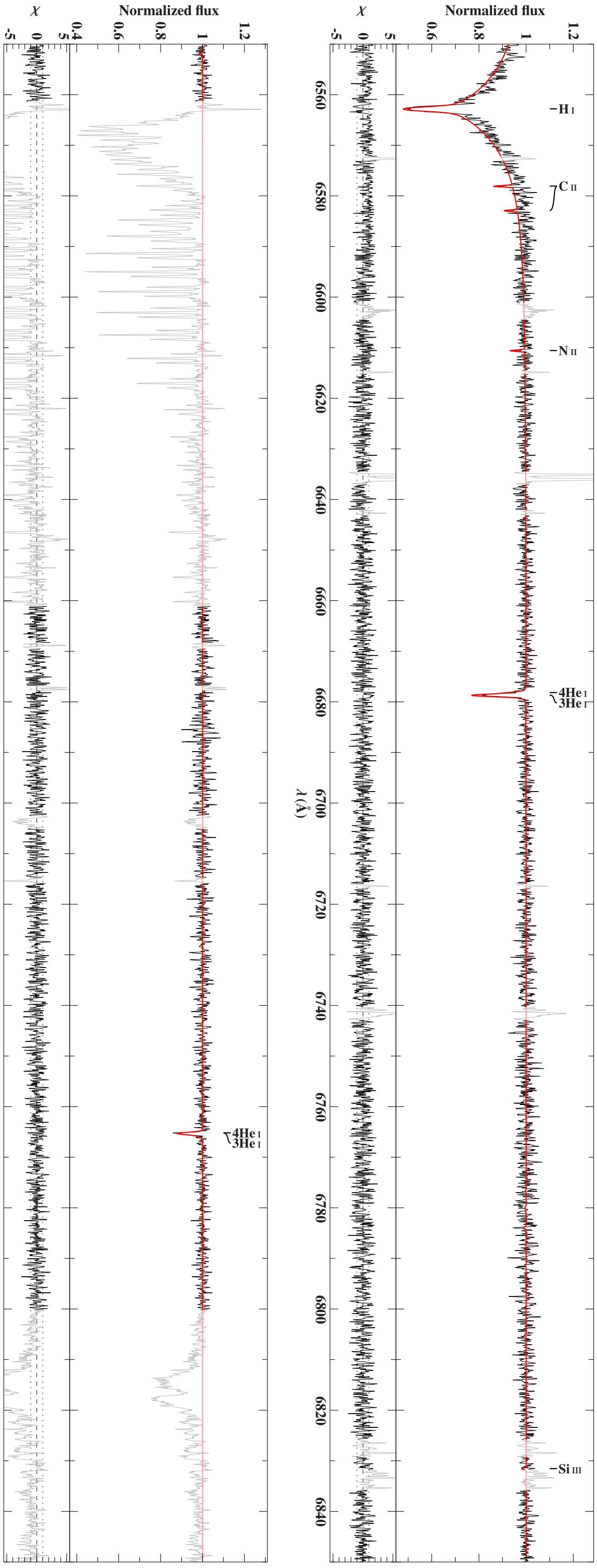

Figure B.1.41.: Fitted FEROS spectrum of the ^{3}He star EC 14338-1445 using the hybrid LTE/NLTE analysis with ISIS - Part 4.

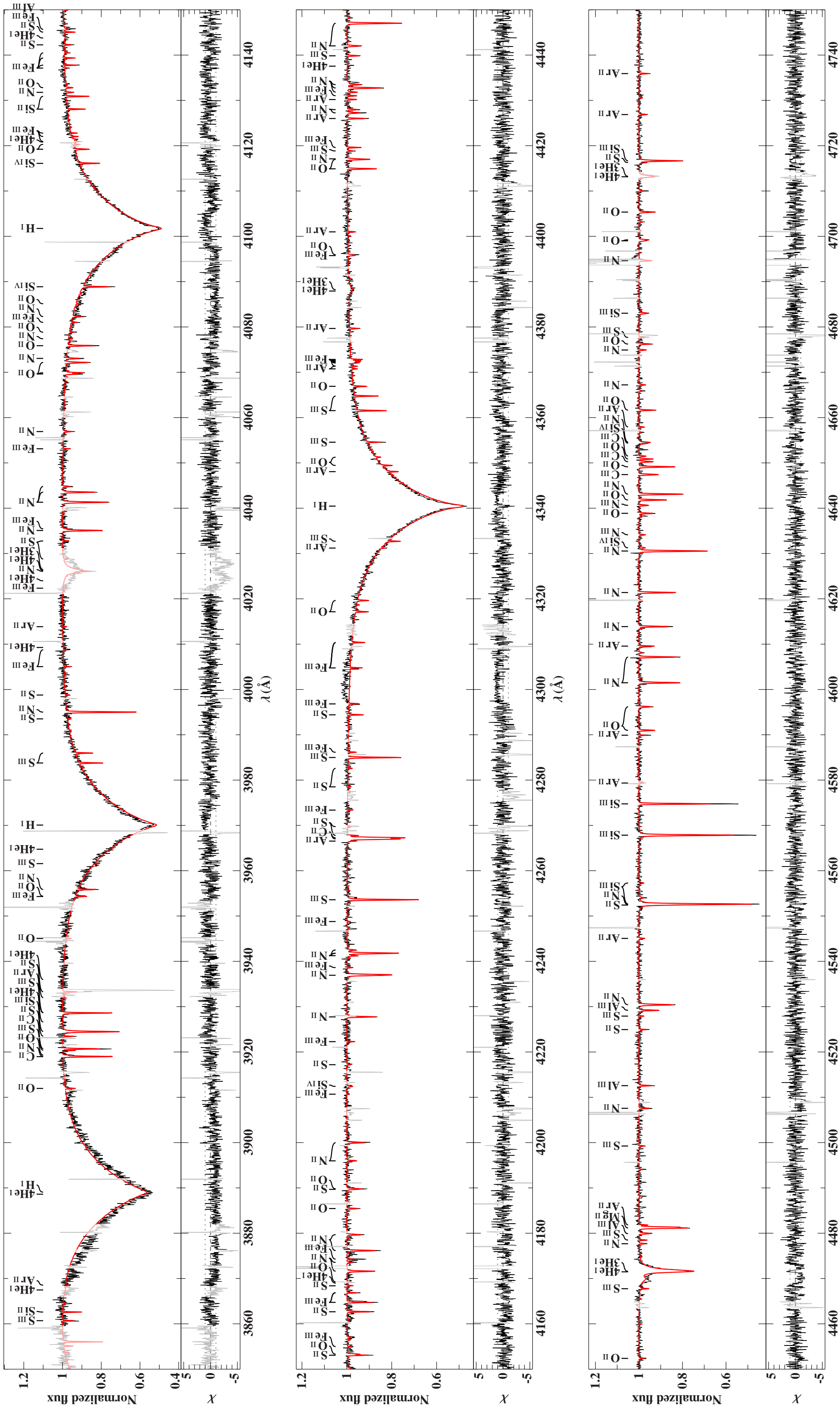

Figure B.1.42.: Fitted FEROS spectrum of the ^{3}He star Feige 38 using the hybrid LTE/NLTE analysis with ISIS - Part 1.

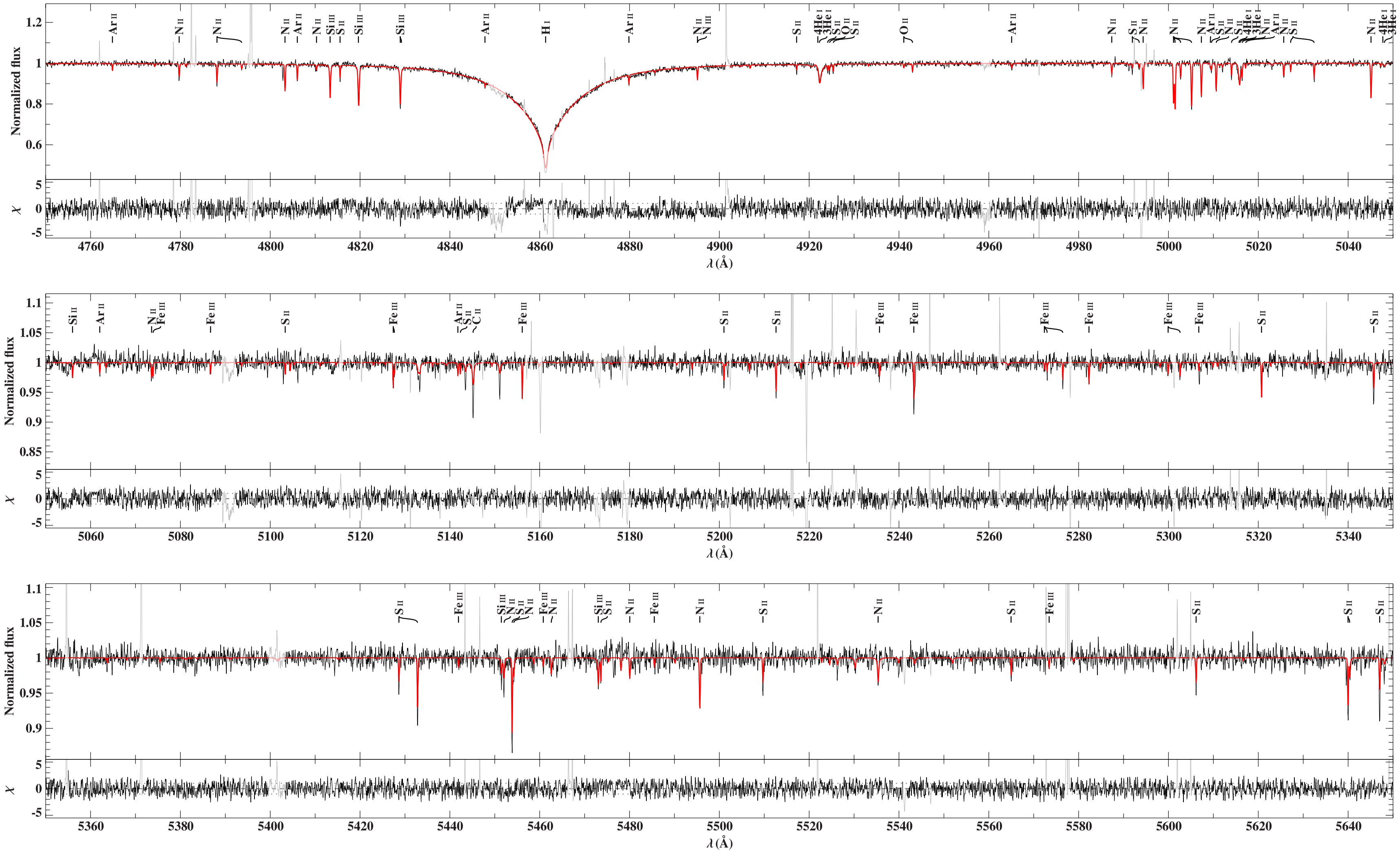

Figure B.1.43.: Fitted FEROS spectrum of the $^3\mathrm{He}$ star Feige 38 using the hybrid LTE/NLTE analysis with ISIS - Part 2.

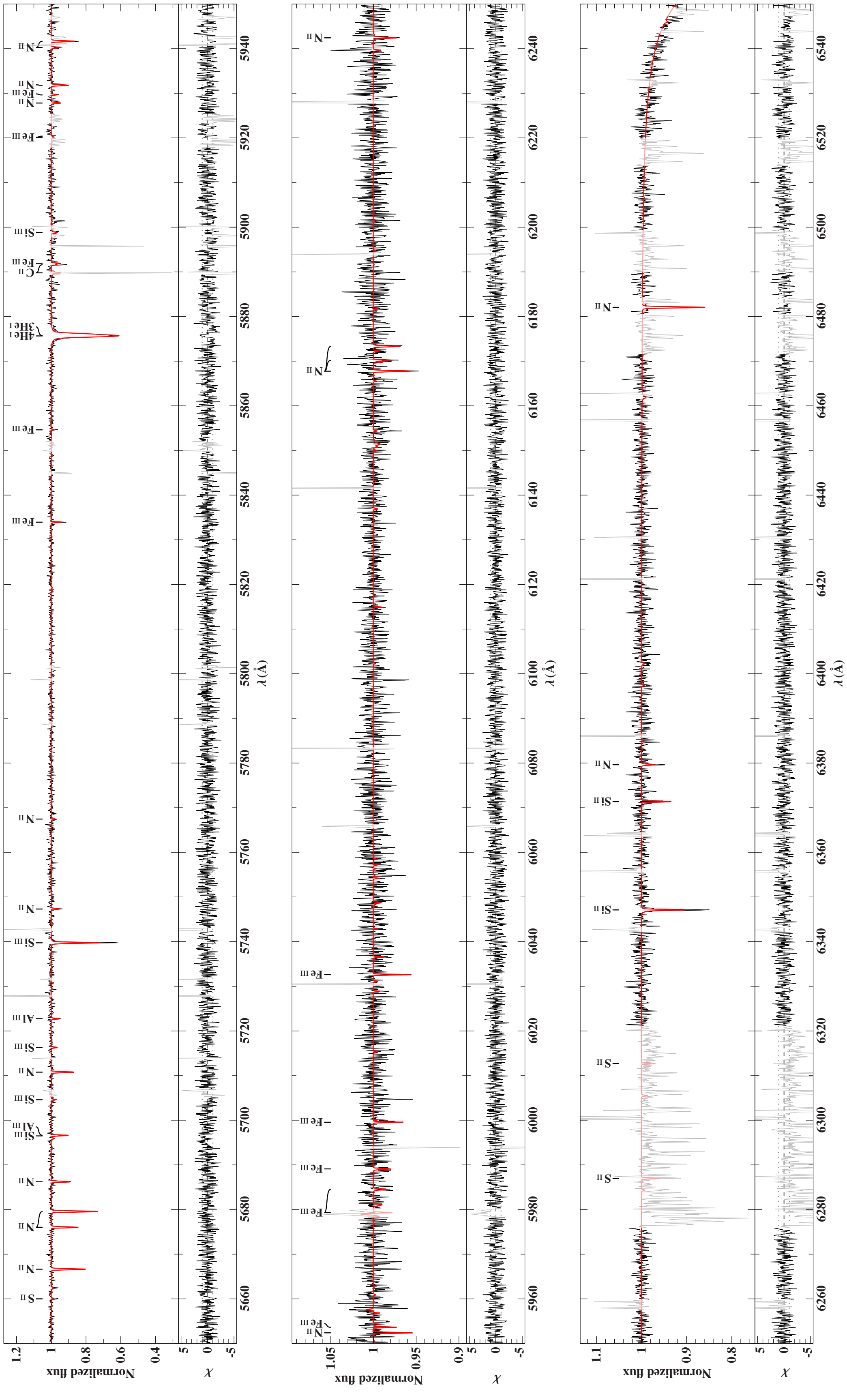

Figure B.1.44.: Fitted FEROS spectrum of the ^{3}He star Feige 38 using the hybrid LTE/NLTE analysis with ISIS - Part 3.

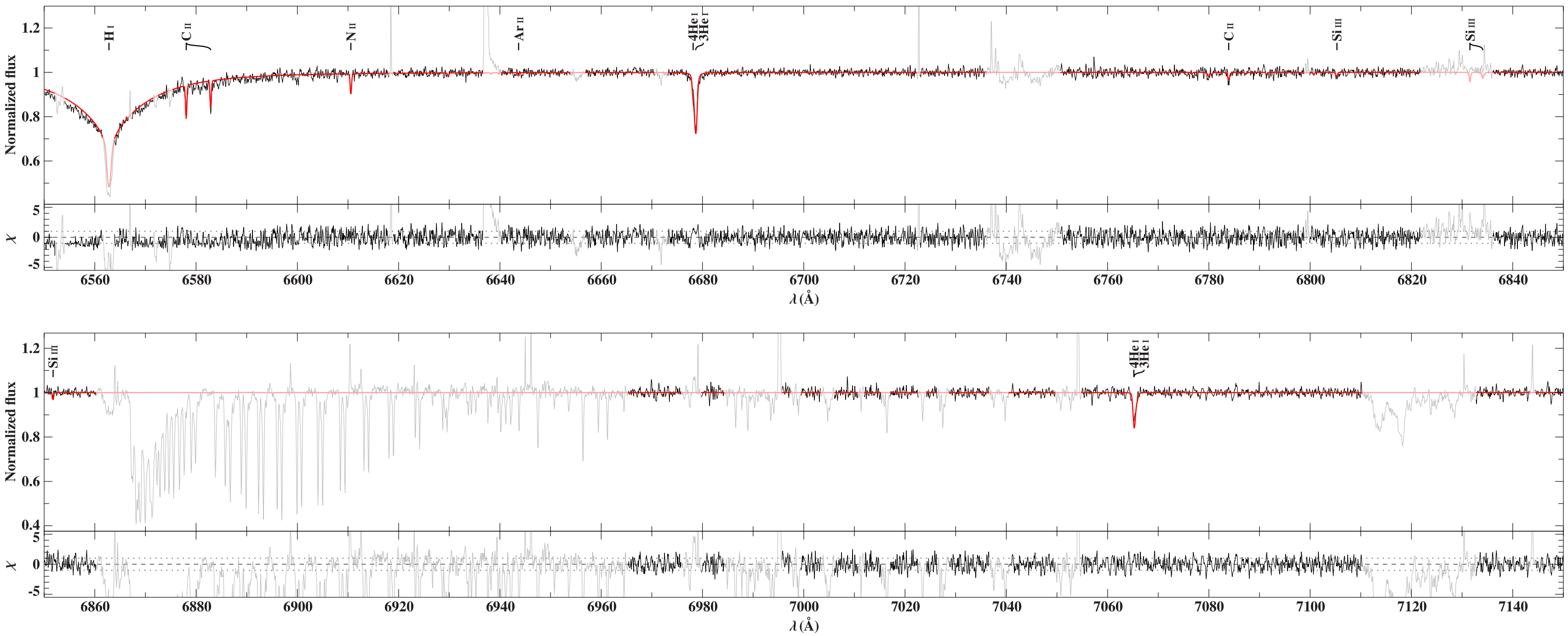

Figure B.1.45.: Fitted FEROS spectrum of the $^{3}\mathrm{He}$ star Feige 38 using the hybrid LTE/NLTE analysis with ISIS - Part 4.

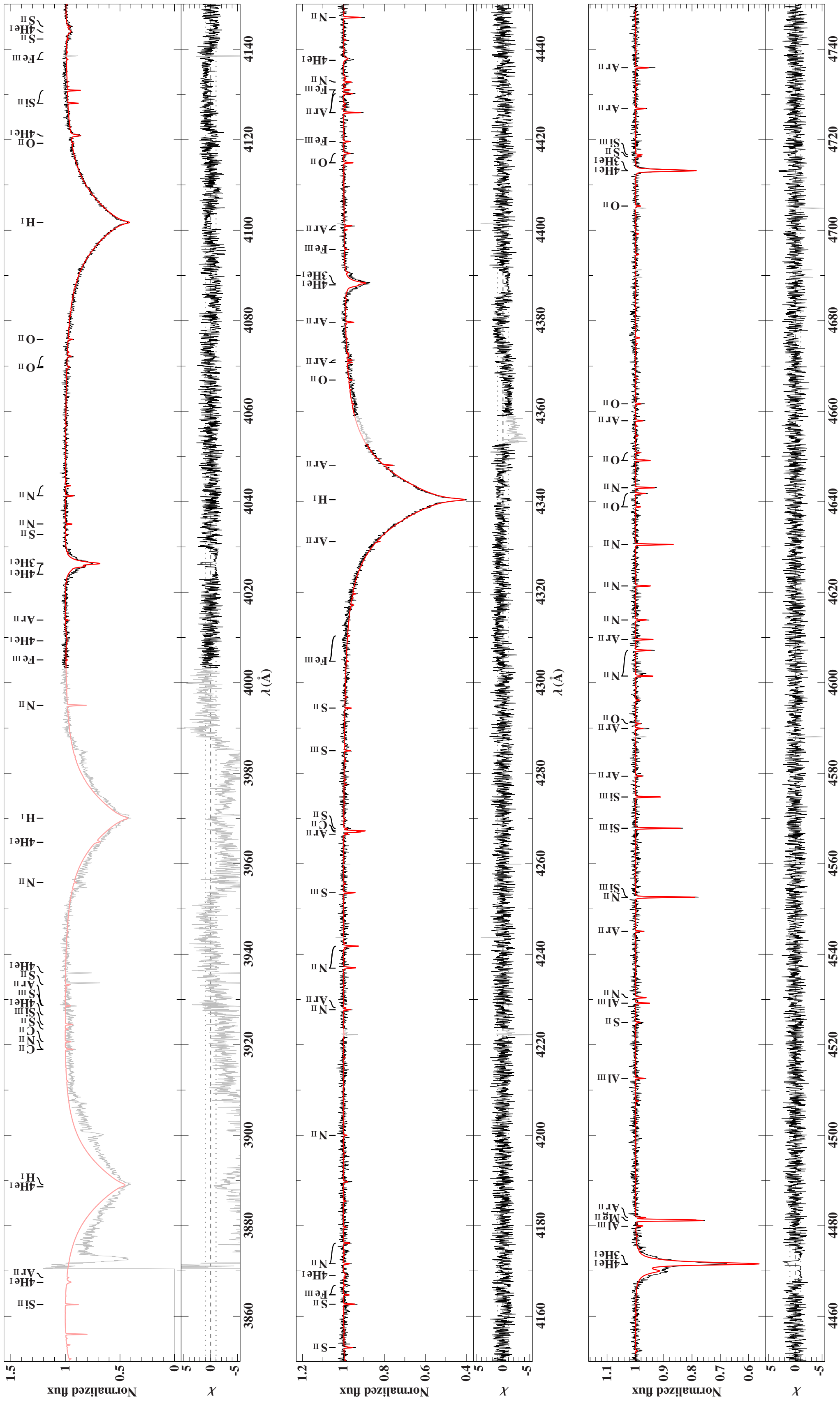

Figure B.1.46.: Fitted FOCES spectrum of the $^3\mathrm{He}$ enriched star BD+48° 2721 using the hybrid LTE/NLTE analysis with ISIS - Part 1.

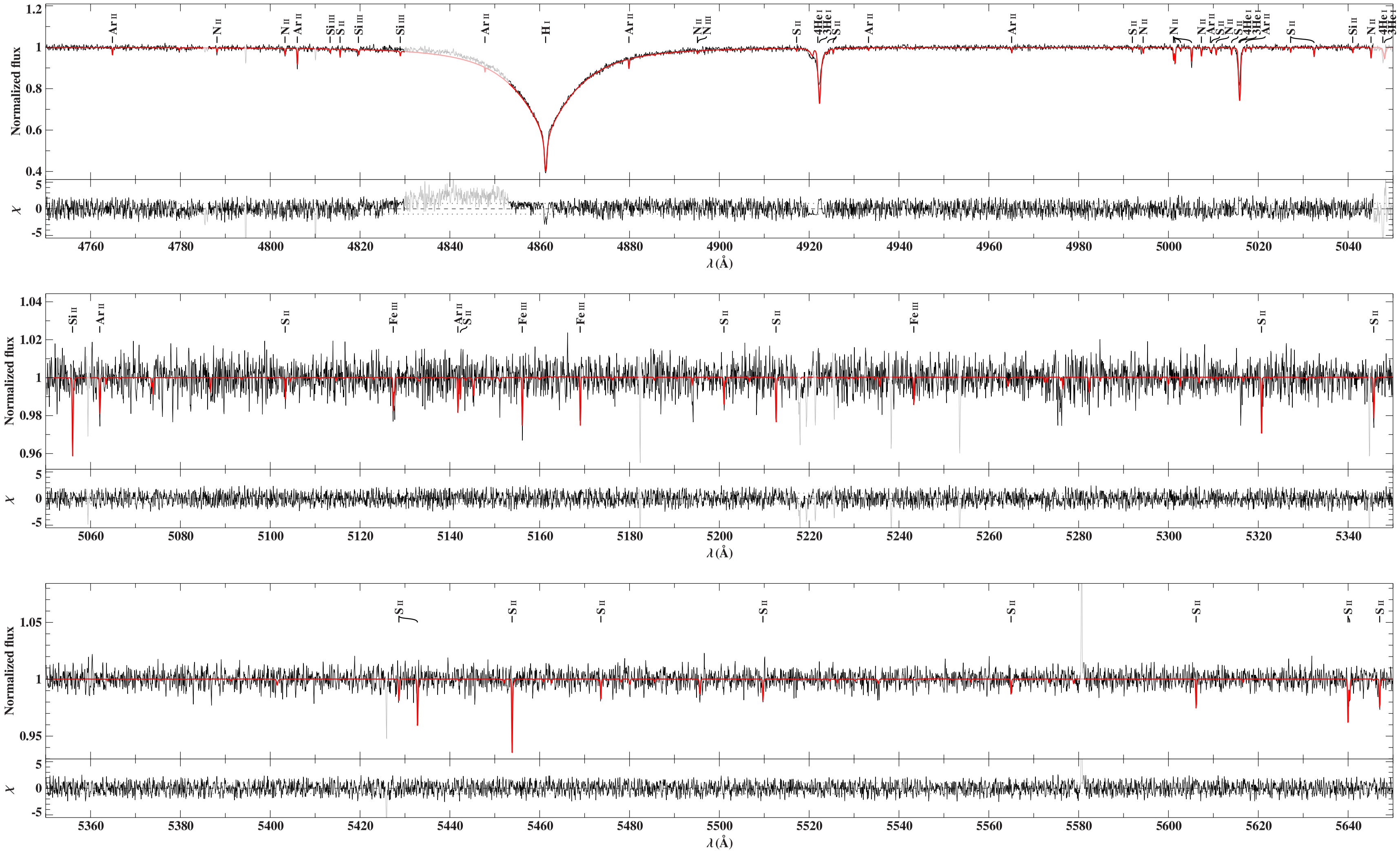

Figure B.1.47.: Fitted FOCES spectrum of the $^3\mathrm{He}$ enriched star BD+48° 2721 using the hybrid LTE/NLTE analysis with ISIS - Part 2.

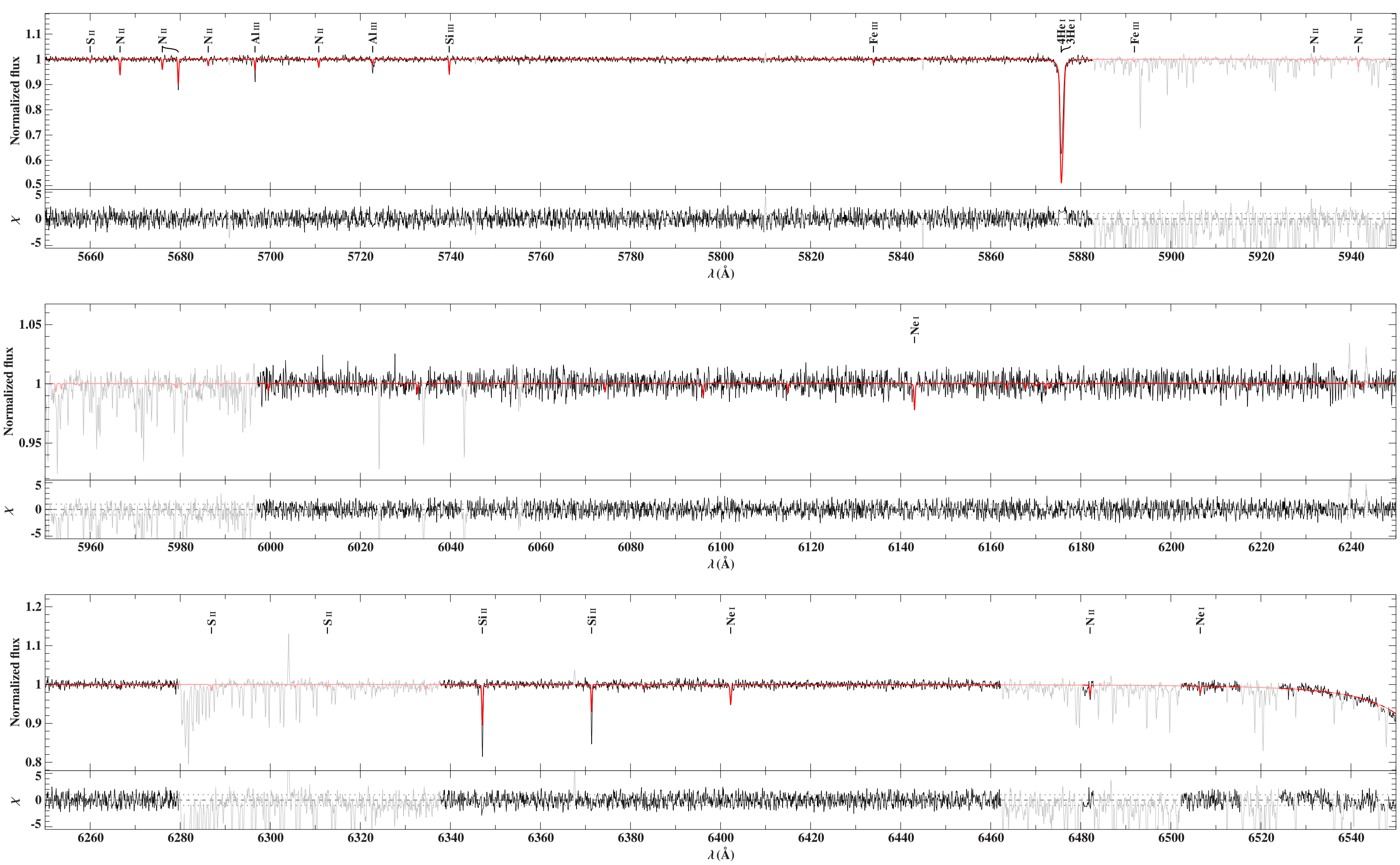

Figure B.1.48.: Fitted FOCES spectrum of the $^{3}\mathrm{He}$ enriched star BD+48° 2721 using the hybrid LTE/NLTE analysis with ISIS - Part 3.

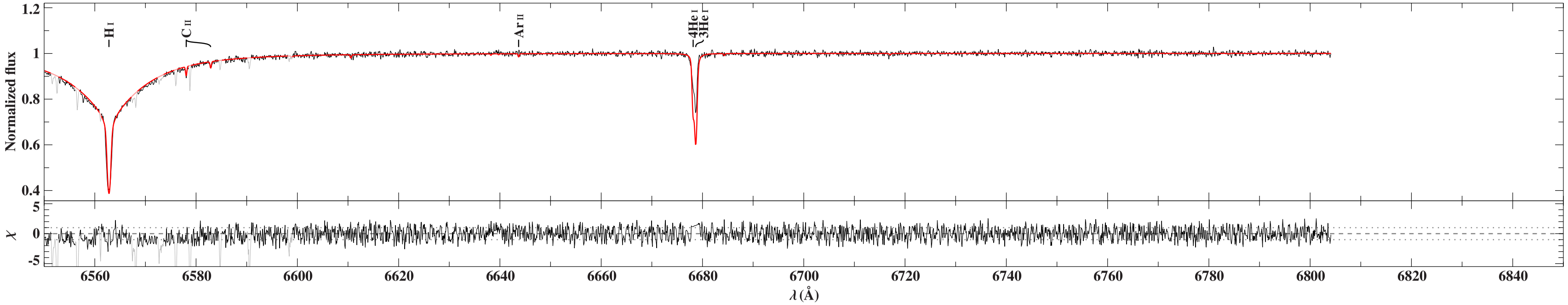

Figure B.1.49.: Fitted FOCES spectrum of the $^{3}\mathrm{He}$ enriched star BD+48° 2721 using the hybrid LTE/NLTE analysis with ISIS - Part 4.

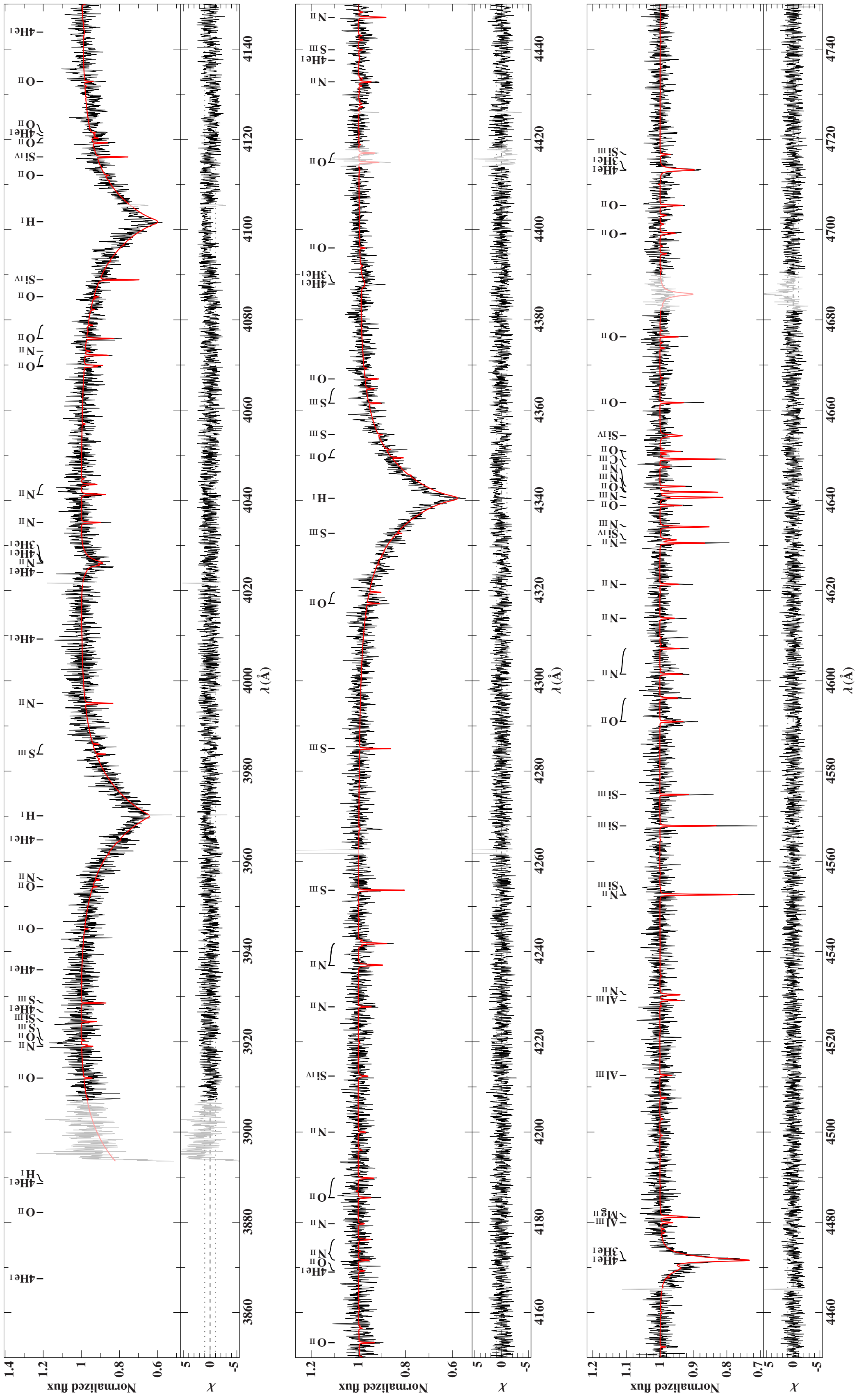

Figure B.1.50.: Fitted FOCES spectrum of the $^3\mathrm{He}$ enriched star PG 1519+640 using the hybrid LTE/NLTE analysis with ISIS - Part 1.

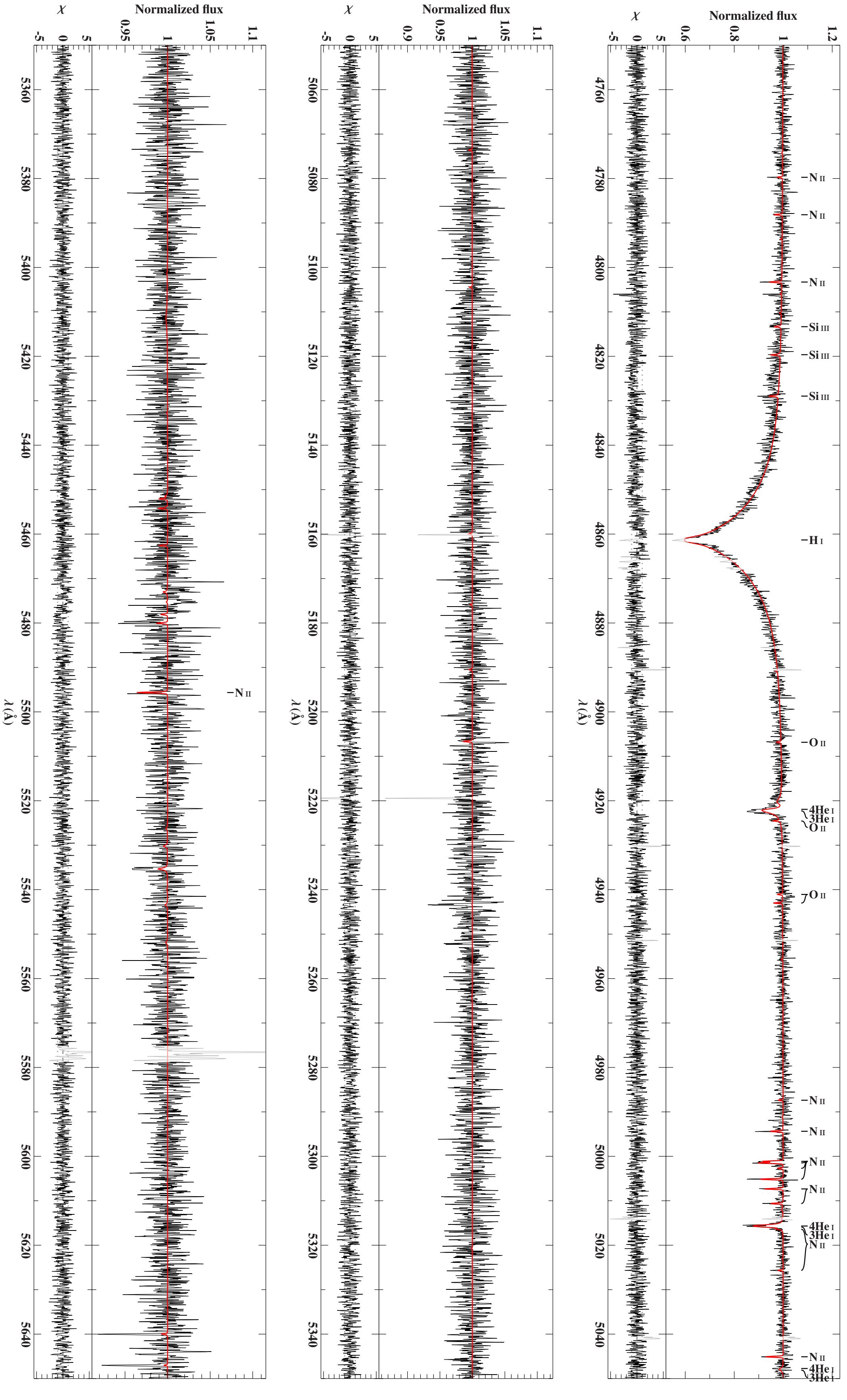

Figure B.1.51.: Fitted FOCES spectrum of the $^{3}\mathrm{He}$ enriched star PG 1519+640 using the hybrid LTE/NLTE analysis with ISIS - Part 2.

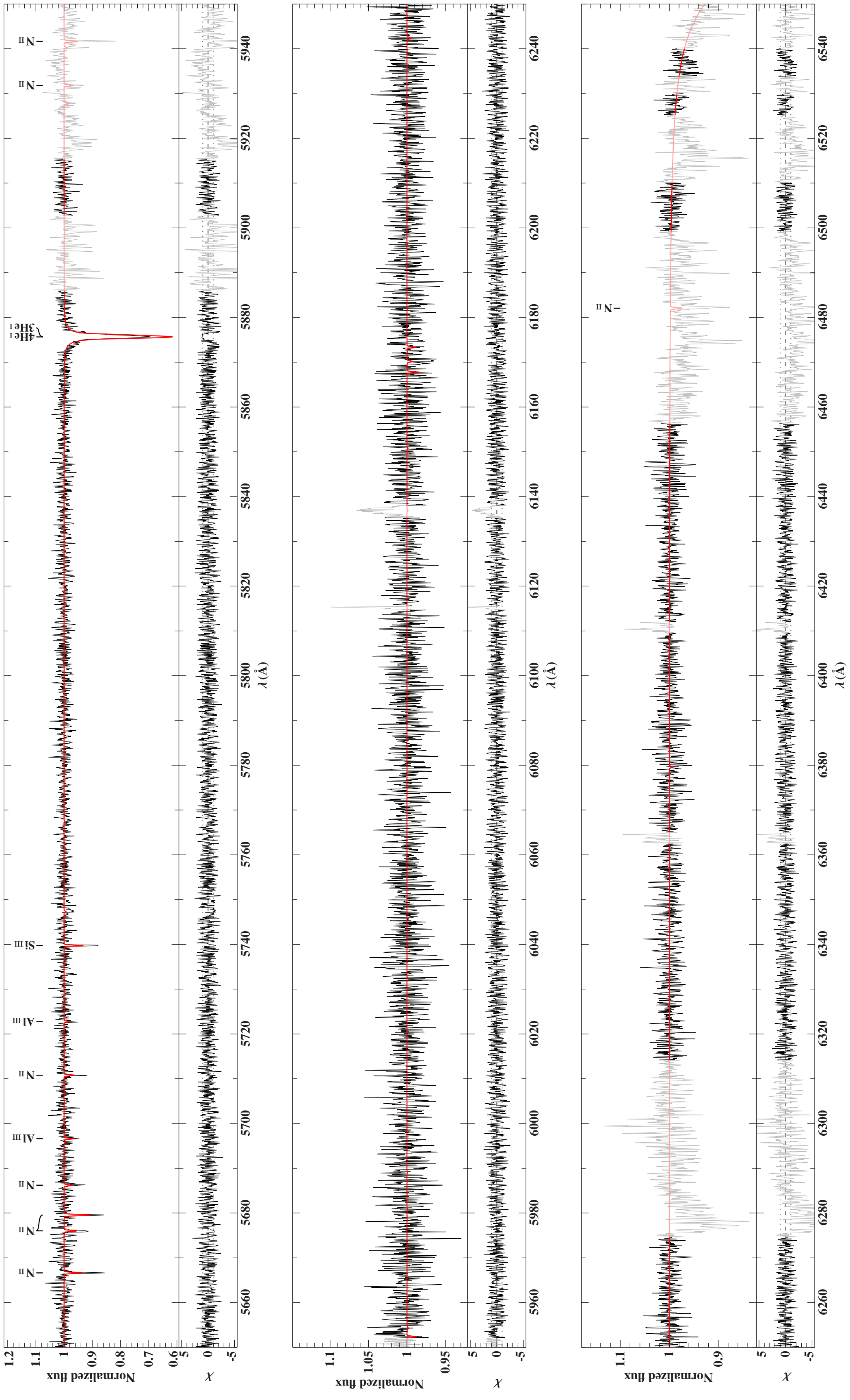

Figure B.1.52.: Fitted FOCES spectrum of the $^{3}\mathrm{He}$ enriched star PG 1519+640 using the hybrid LTE/NLTE analysis with ISIS - Part 3.

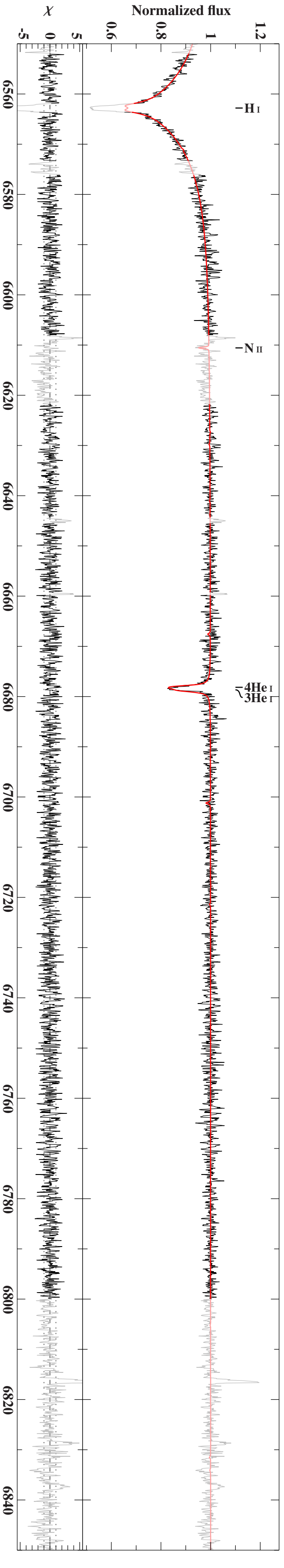

Figure B.1.53.: Fitted FOCES spectrum of the $^{3}\mathrm{He}$ enriched star PG 1519+640 using the hybrid LTE/NLTE analysis with ISIS - Part 4.

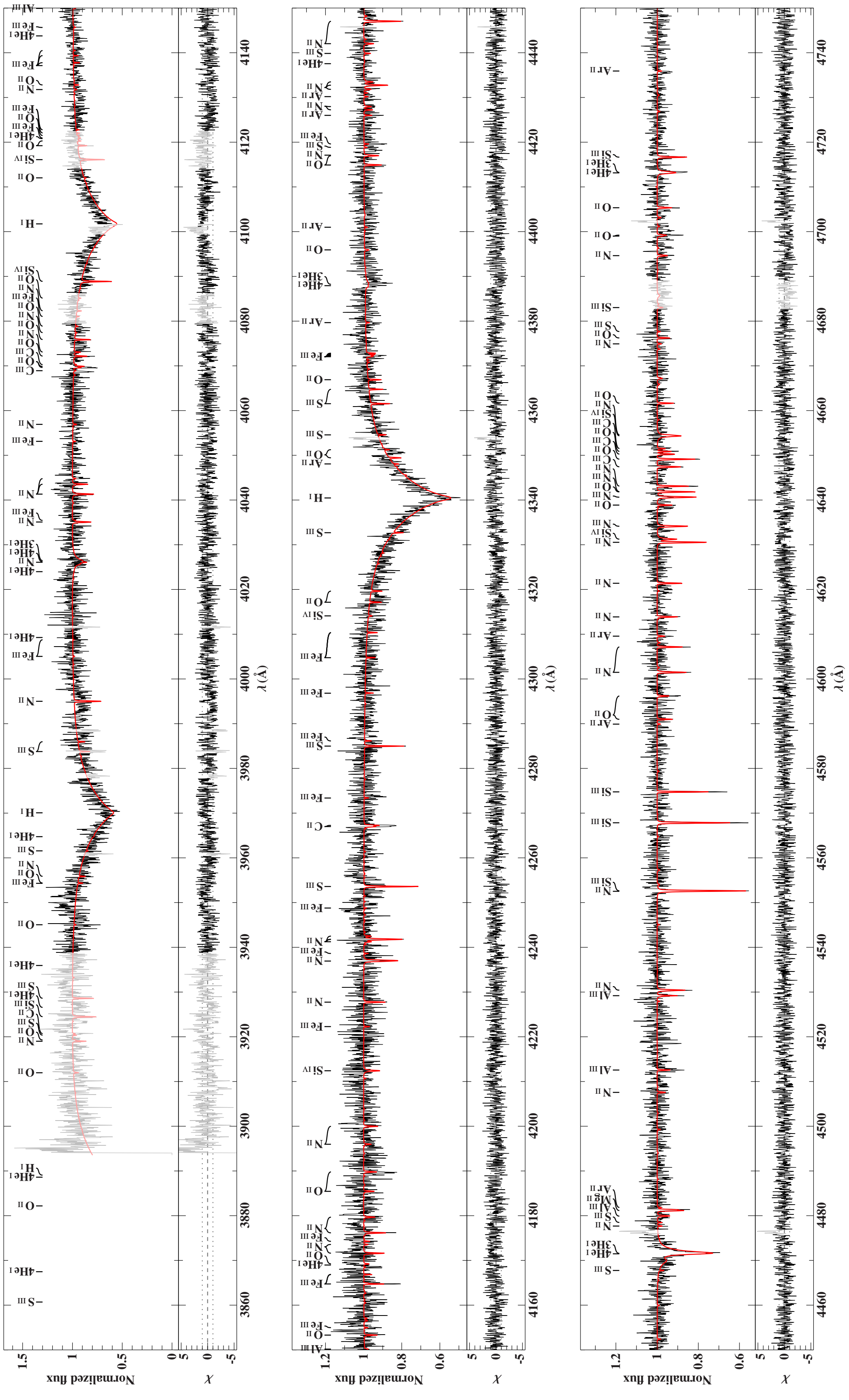

Figure B.1.54.: Fitted FOCES spectrum of the $^{3}\mathrm{He}$ star PG 1710+490 using the hybrid LTE/NLTE analysis with ISIS - Part 1.

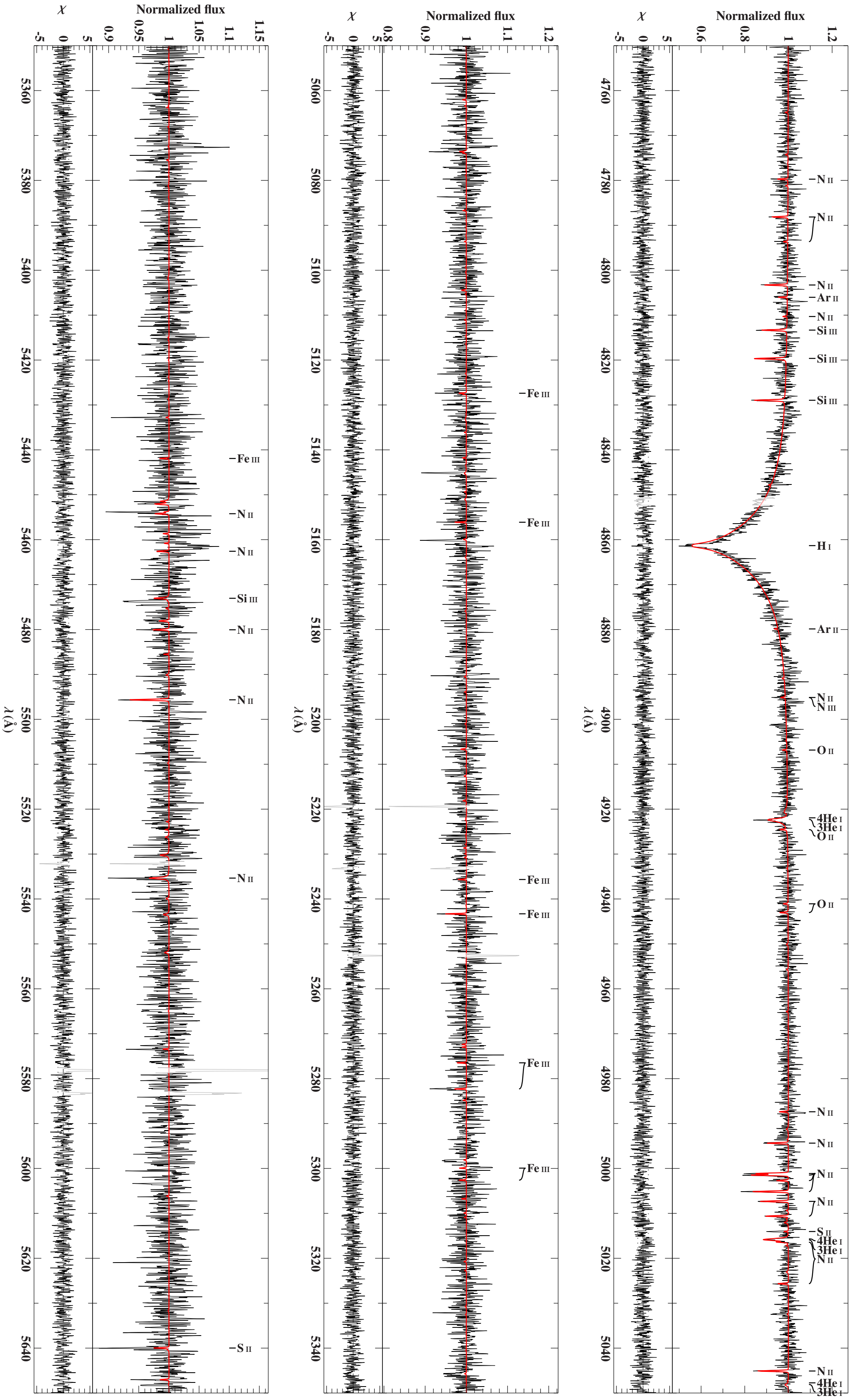

Figure B.1.55.: Fitted FOCES spectrum of the ^{3}He star PG 1710+490 using the hybrid LTE/NLTE analysis with ISIS - Part 2.

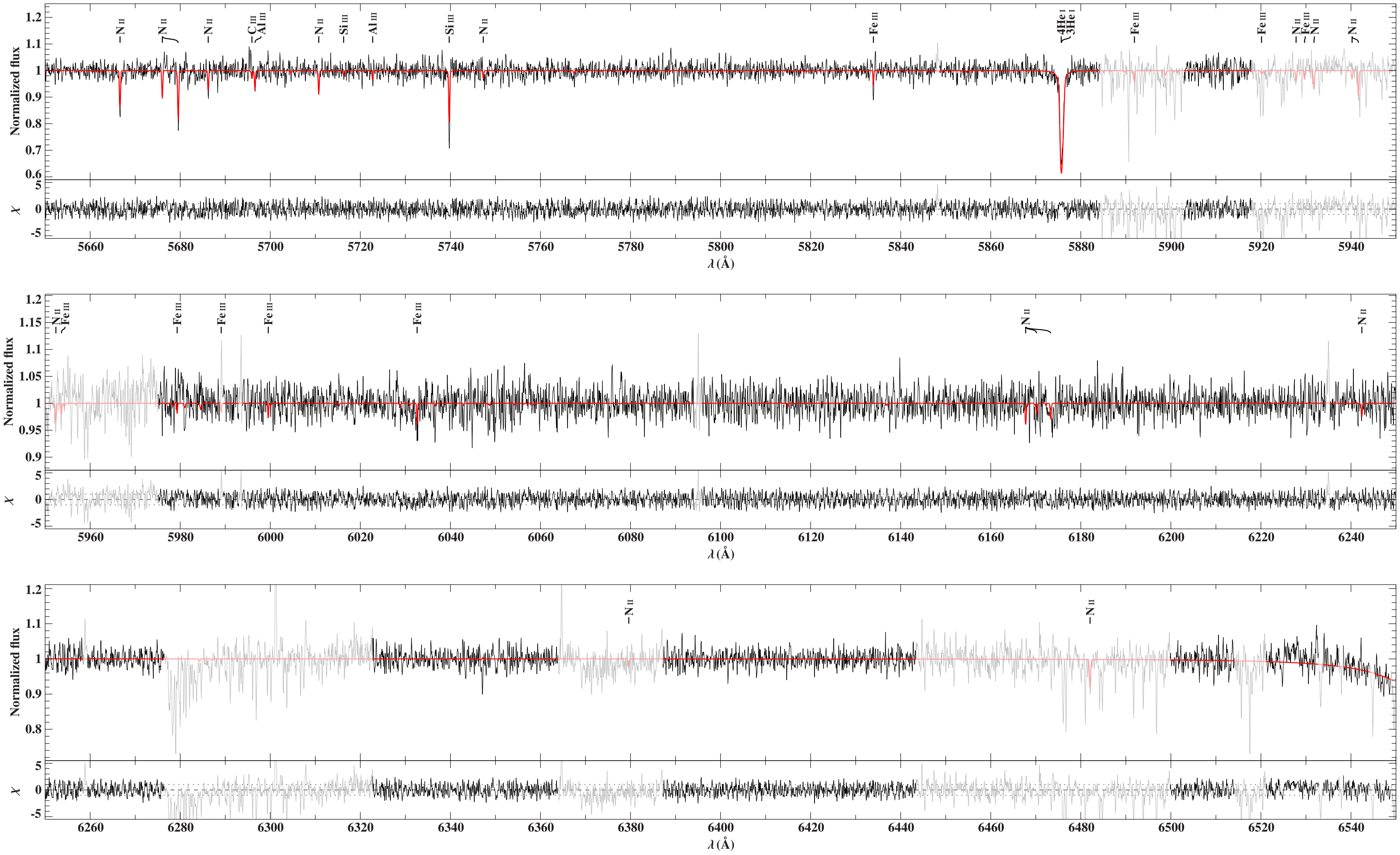

Figure B.1.56.: Fitted FOCES spectrum of the $^{3}\mathrm{He}$ star PG 1710+490 using the hybrid LTE/NLTE analysis with ISIS - Part 3.

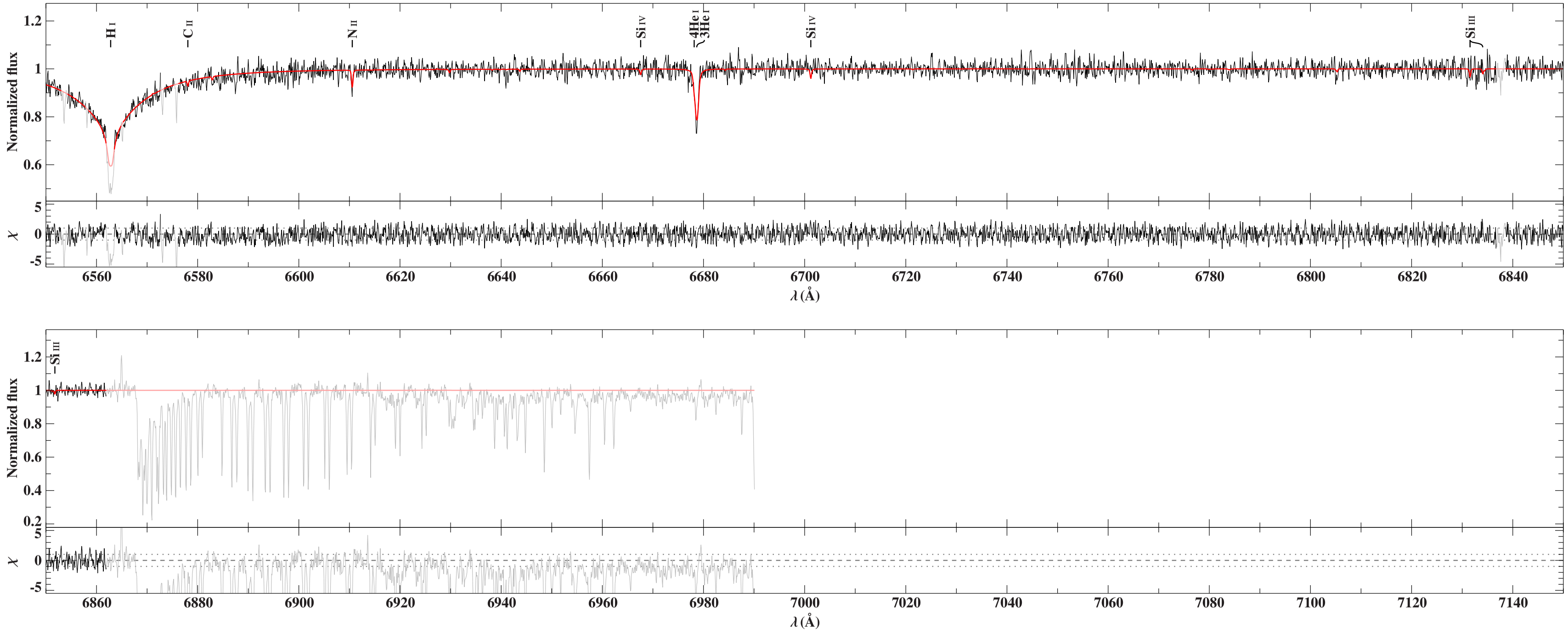

Figure B.1.57.: Fitted FOCES spectrum of the $^{3}\mathrm{He}$ star PG 1710+490 using the hybrid LTE/NLTE analysis with ISIS - Part 4.

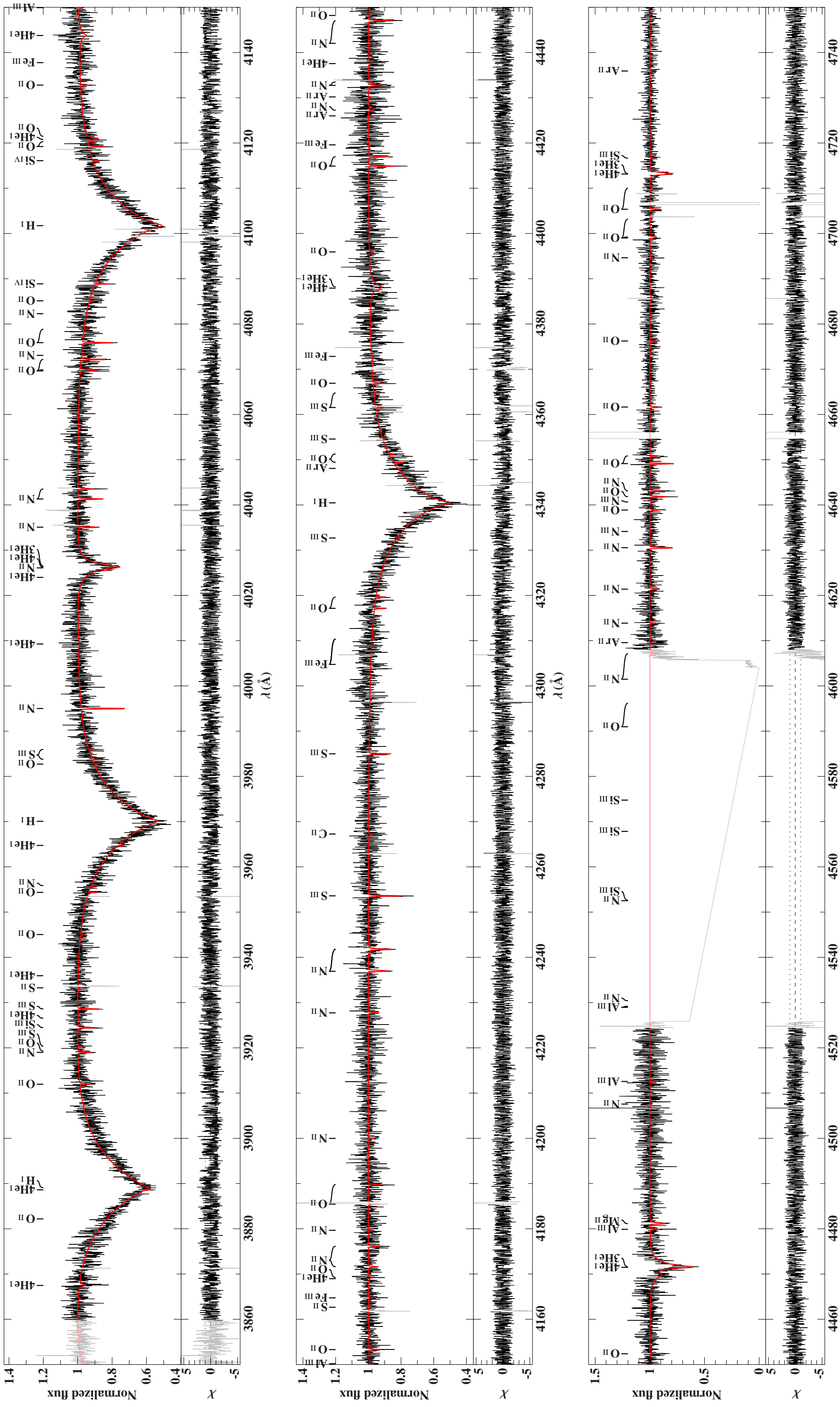

Figure B.1.58.: Fitted UVES spectrum of the $^3\mathrm{He}$ enriched star HE 0929-0424 using the hybrid LTE/NLTE analysis with ISIS - Part 1.

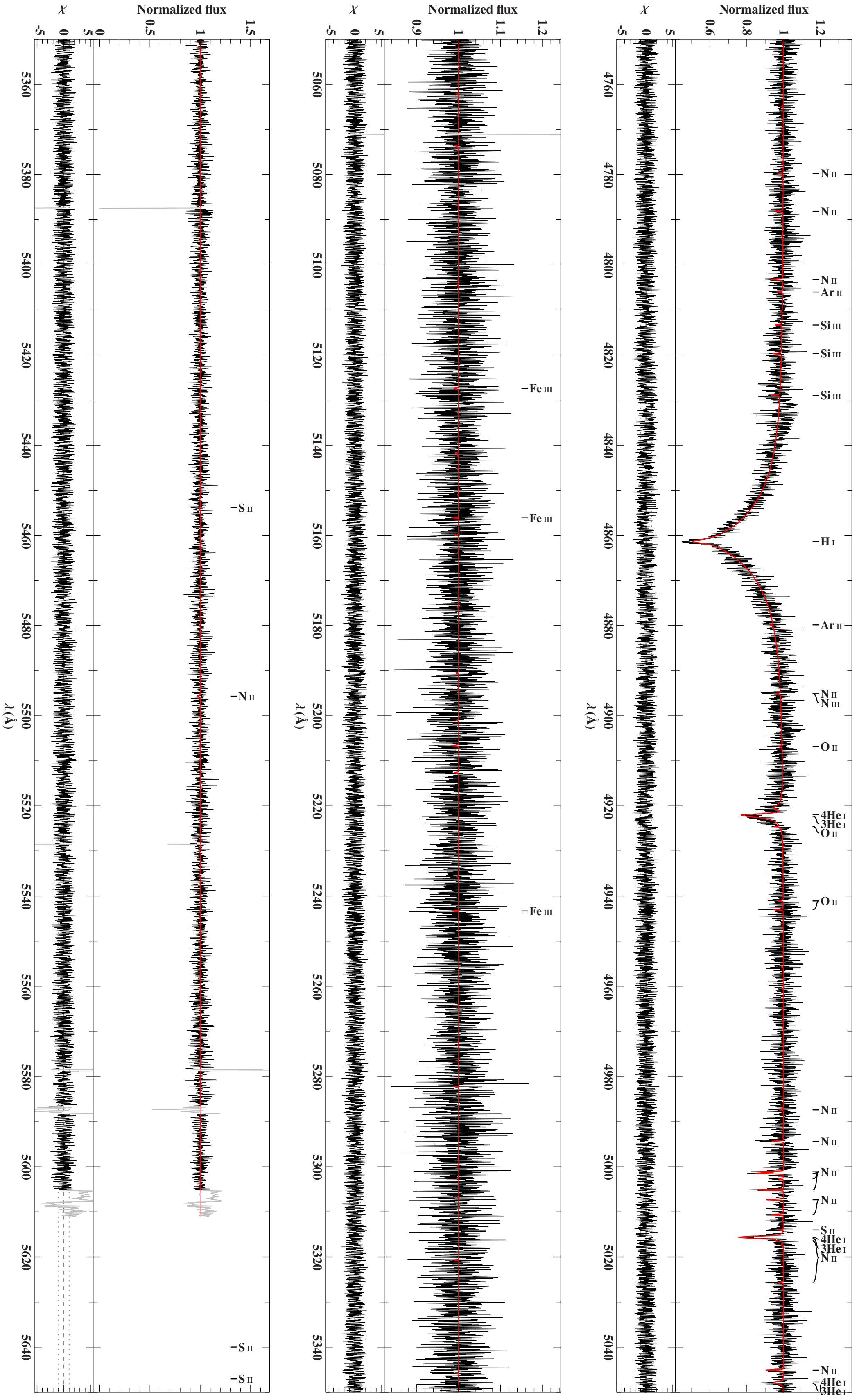

Figure B.1.59.: Fitted UVES spectrum of the ^{3}He enriched star HE 0929-0424 using the hybrid LTE/NLTE analysis with ISIS - Part 2.

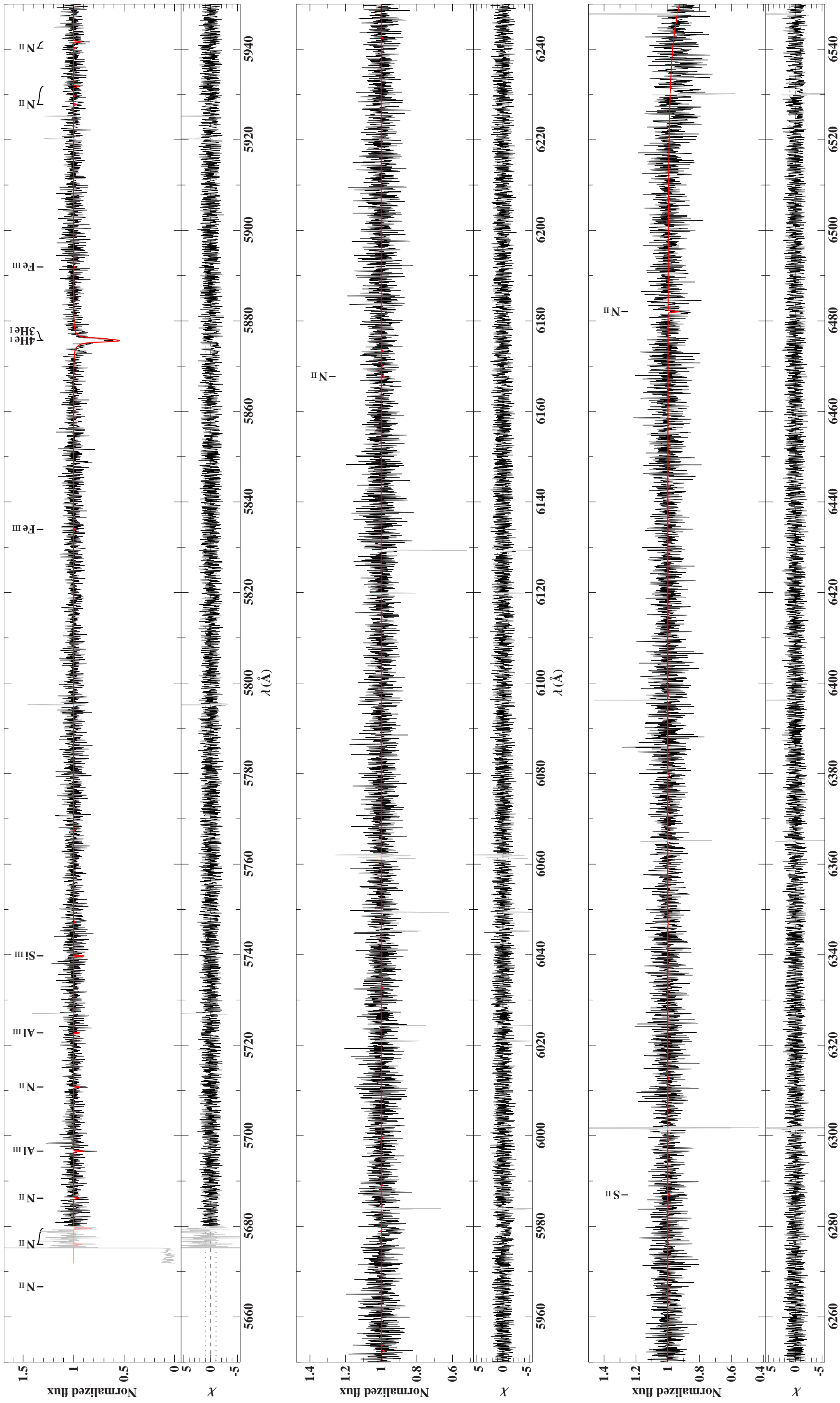

Figure B.1.60.: Fitted UVES spectrum of the $^{3}\mathrm{He}$ enriched star HE 0929-0424 using the hybrid LTE/NLTE analysis with ISIS - Part 3.

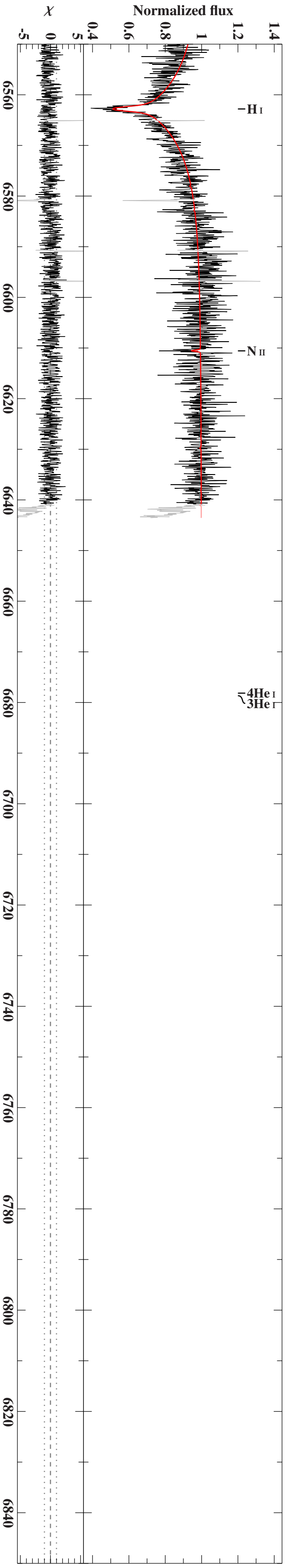

Figure B.1.61.: Fitted UVES spectrum of the $^3\mathrm{He}$ enriched star HE 0929-0424 using the hybrid LTE/NLTE analysis with ISIS - Part 4.

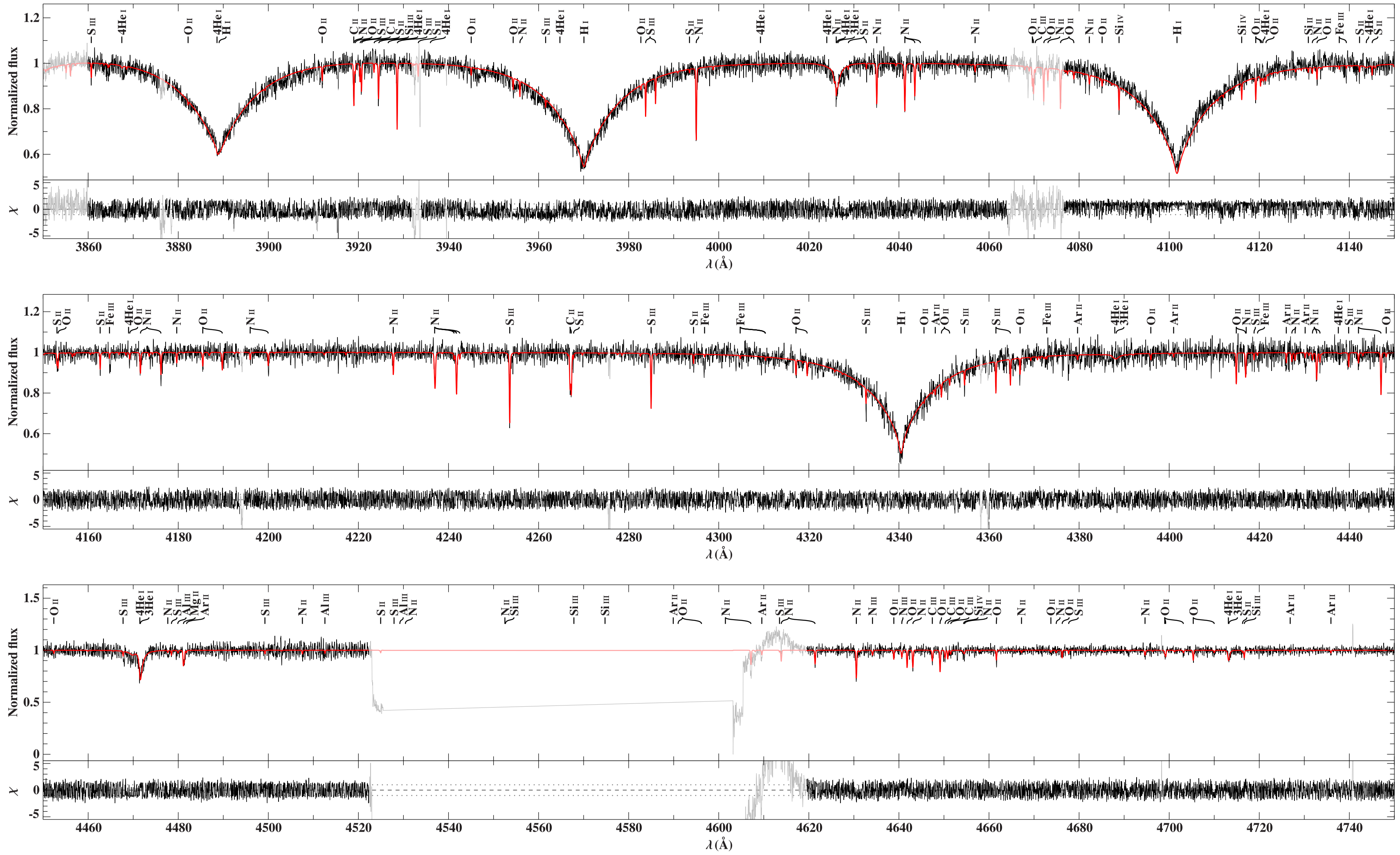

Figure B.1.62.: Fitted UVES spectrum of the $^{3}\mathrm{He}$ enriched star HE 1047-0436 using the hybrid LTE/NLTE analysis with ISIS - Part 1.

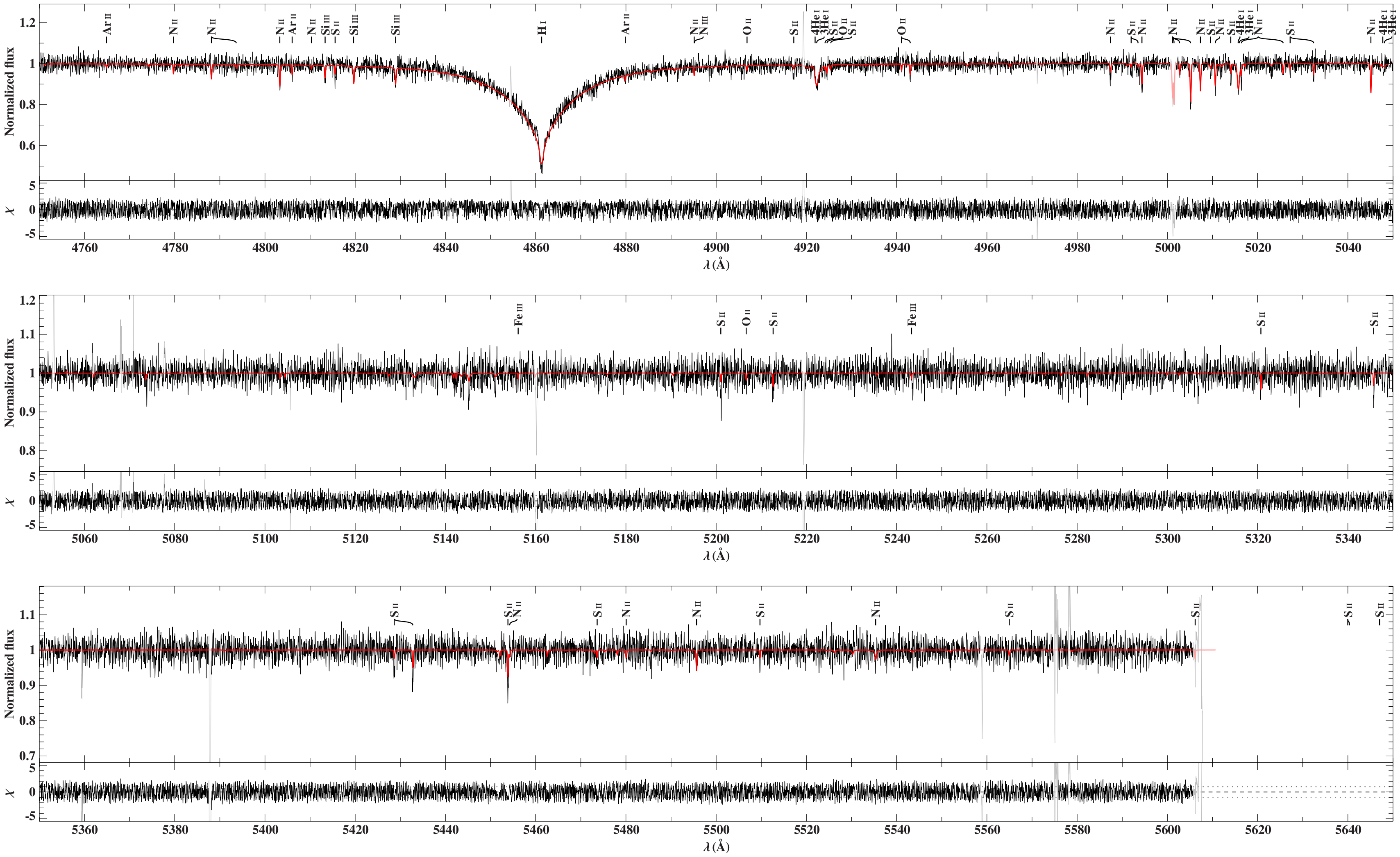

Figure B.1.63.: Fitted UVES spectrum of the ^{3}He enriched star HE 1047-0436 using the hybrid LTE/NLTE analysis with ISIS - Part 2.

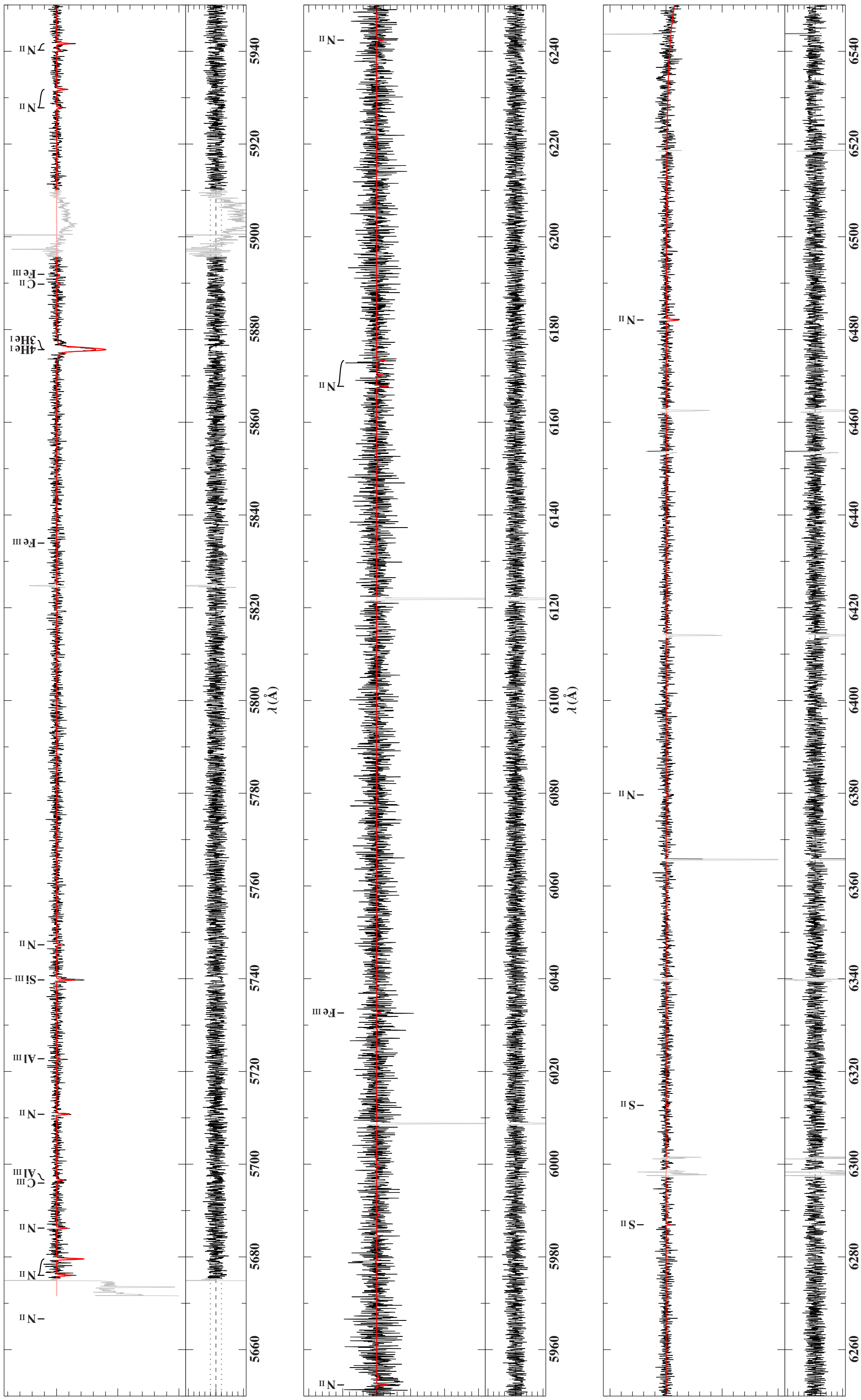

Figure B.1.64.: Fitted UVES spectrum of the $^3\mathrm{He}$ enriched star HE 1047-0436 using the hybrid LTE/NLTE analysis with ISIS - Part 3.

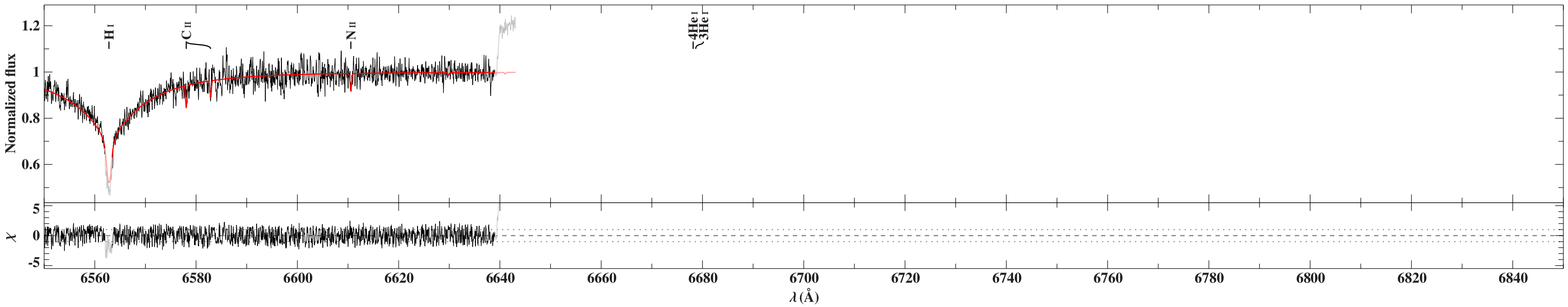

Figure B.1.65.: Fitted UVES spectrum of the $^{3}\mathrm{He}$ enriched star HE 1047-0436 using the hybrid LTE/NLTE analysis with ISIS - Part 4.

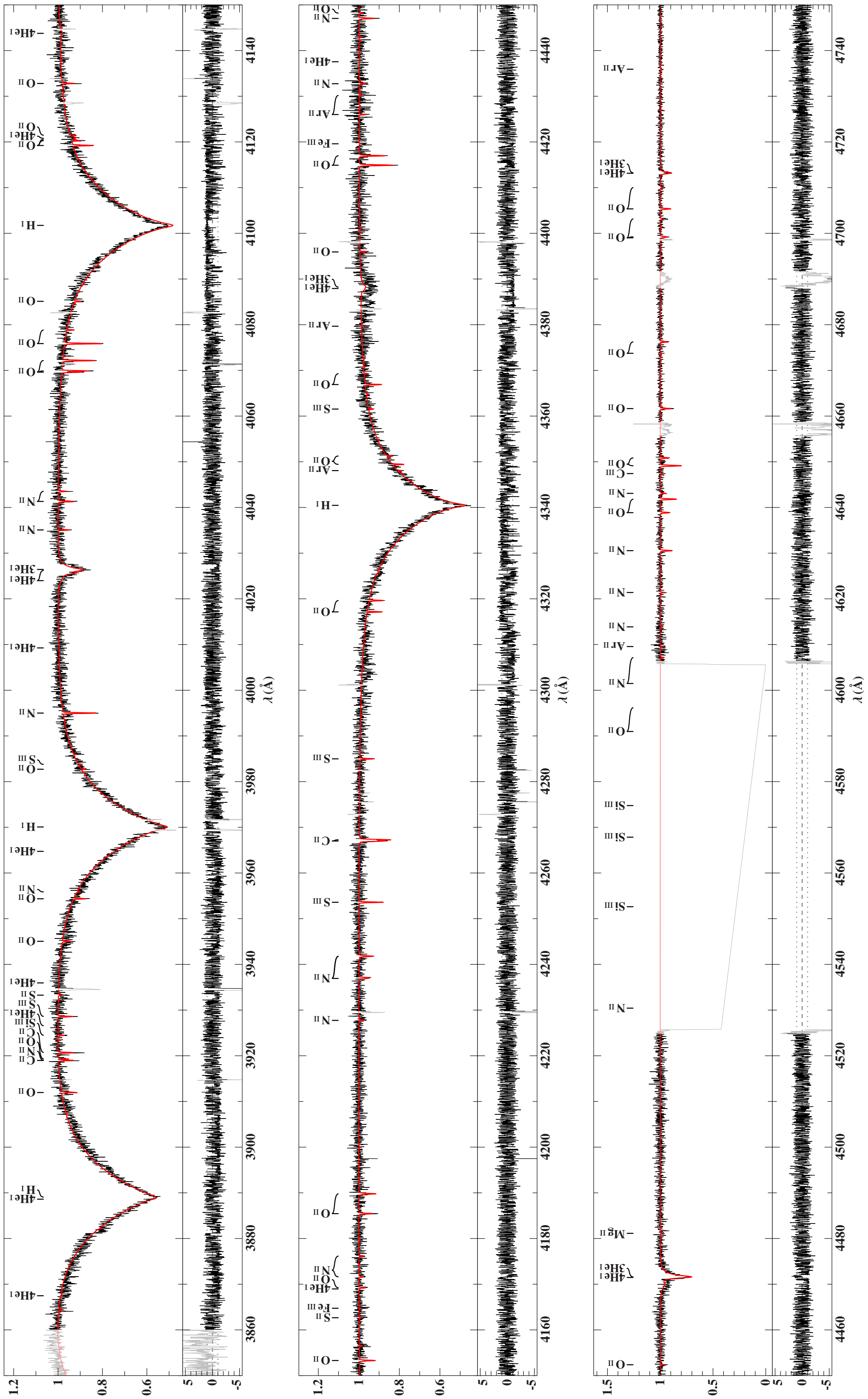

Figure B.1.66.: Fitted UVES spectrum of the $^{3}\mathrm{He}$ enriched star HE 2156-3927 using the hybrid LTE/NLTE analysis with ISIS - Part 1.

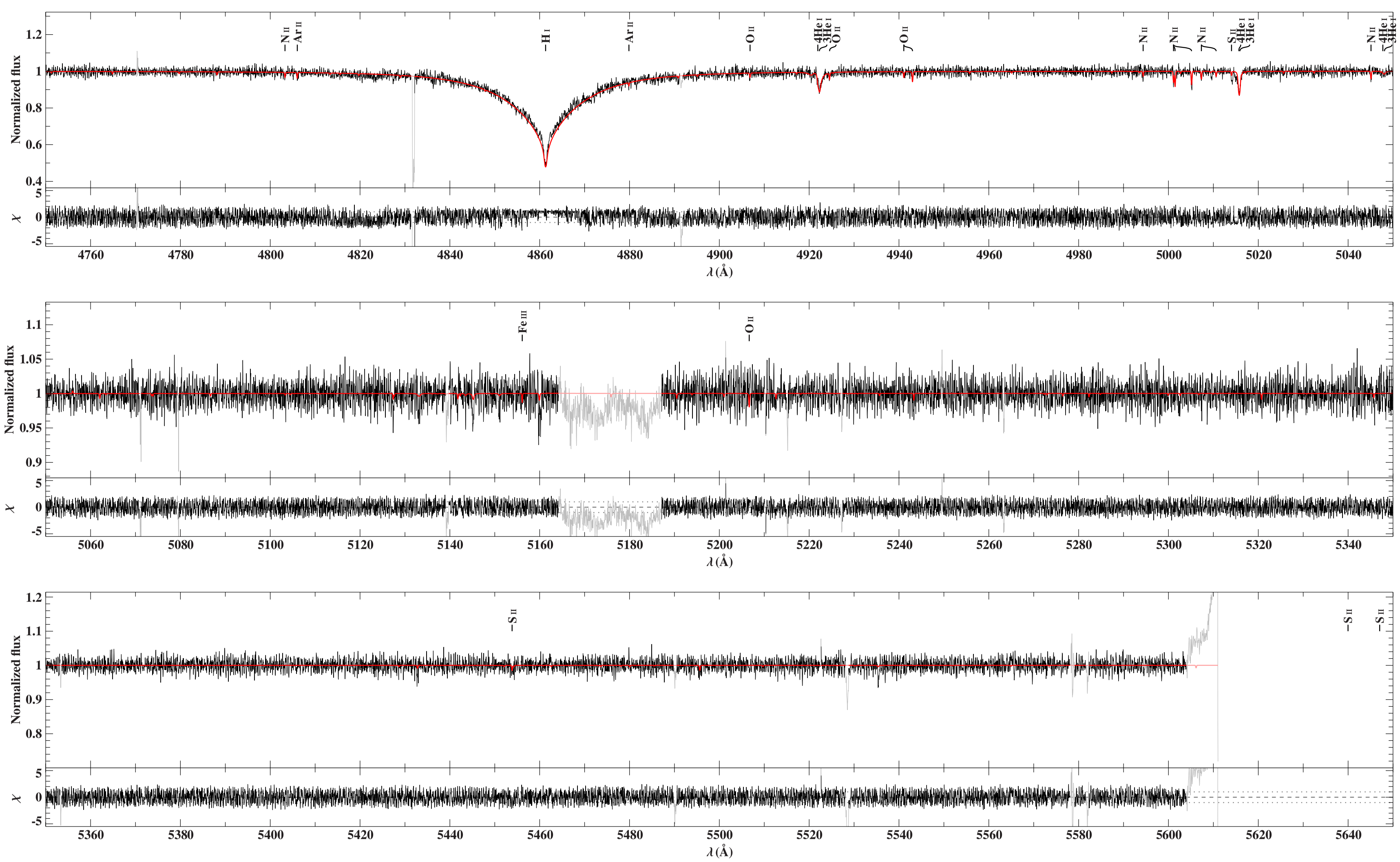

Figure B.1.67.: Fitted UVES spectrum of the $^{3}\mathrm{He}$ enriched star HE 2156-3927 using the hybrid LTE/NLTE analysis with ISIS - Part 2.

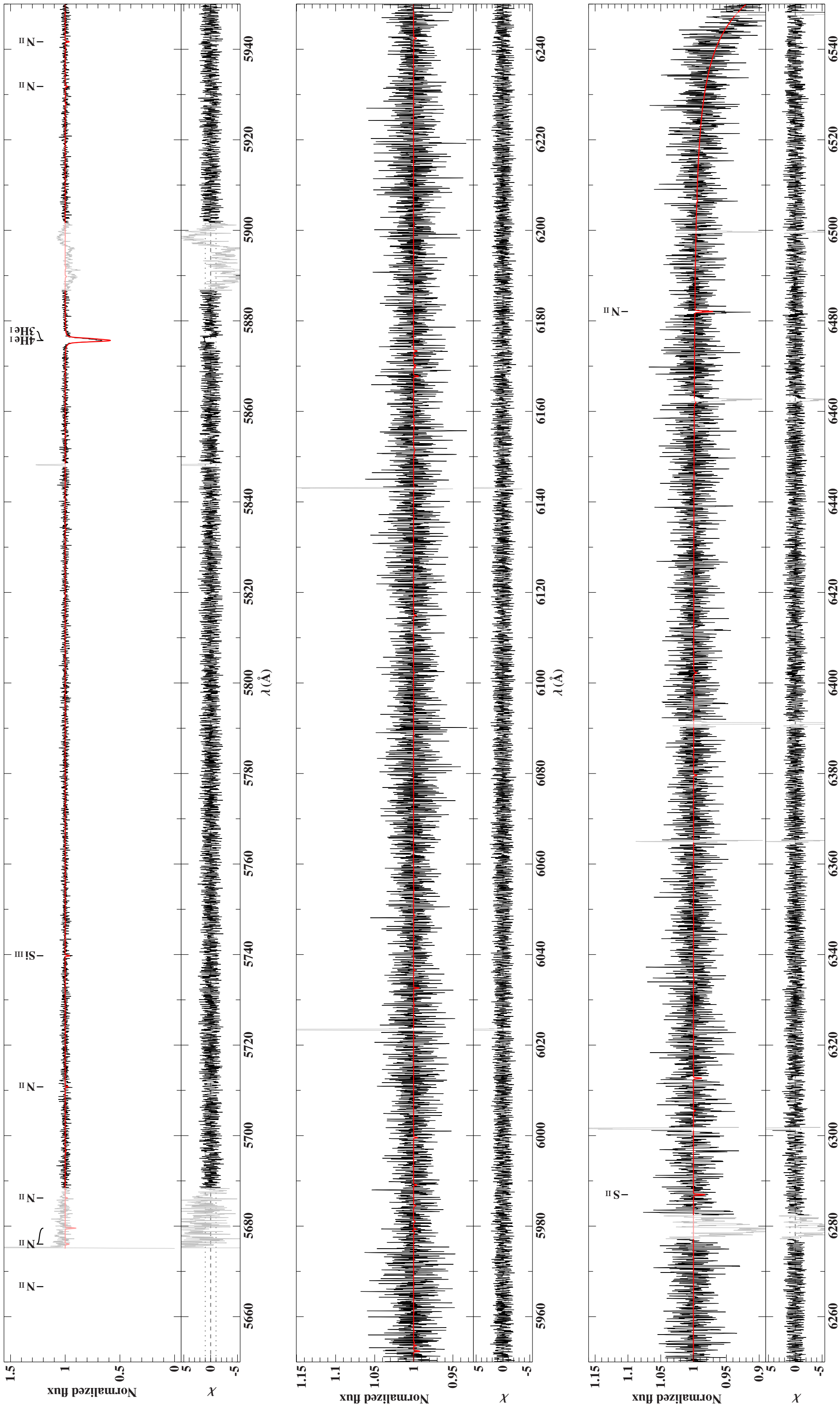

Figure B.1.68.: Fitted UVES spectrum of the $^3\mathrm{He}$ enriched star HE 2156-3927 using the hybrid LTE/NLTE analysis with ISIS - Part 3.

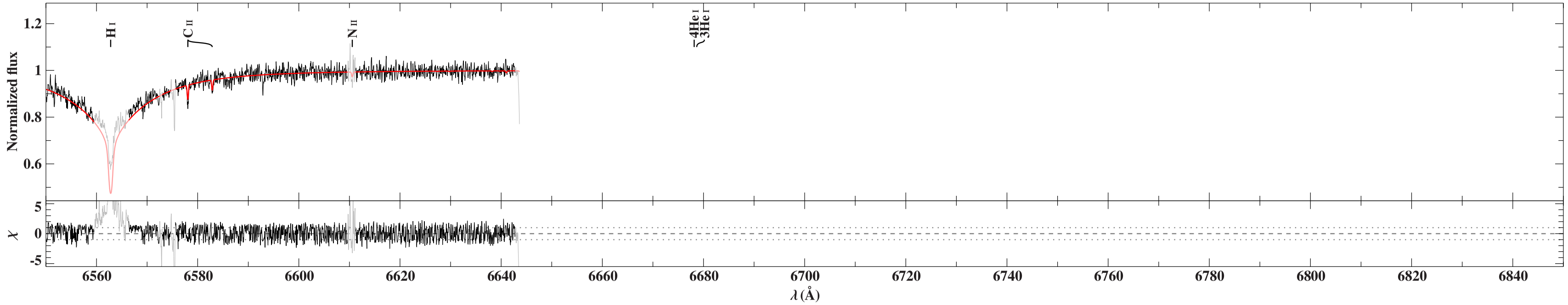

Figure B.1.69.: Fitted UVES spectrum of the $^3\mathrm{He}$ enriched star HE 2156-3927 using the hybrid LTE/NLTE analysis with ISIS - Part 4.

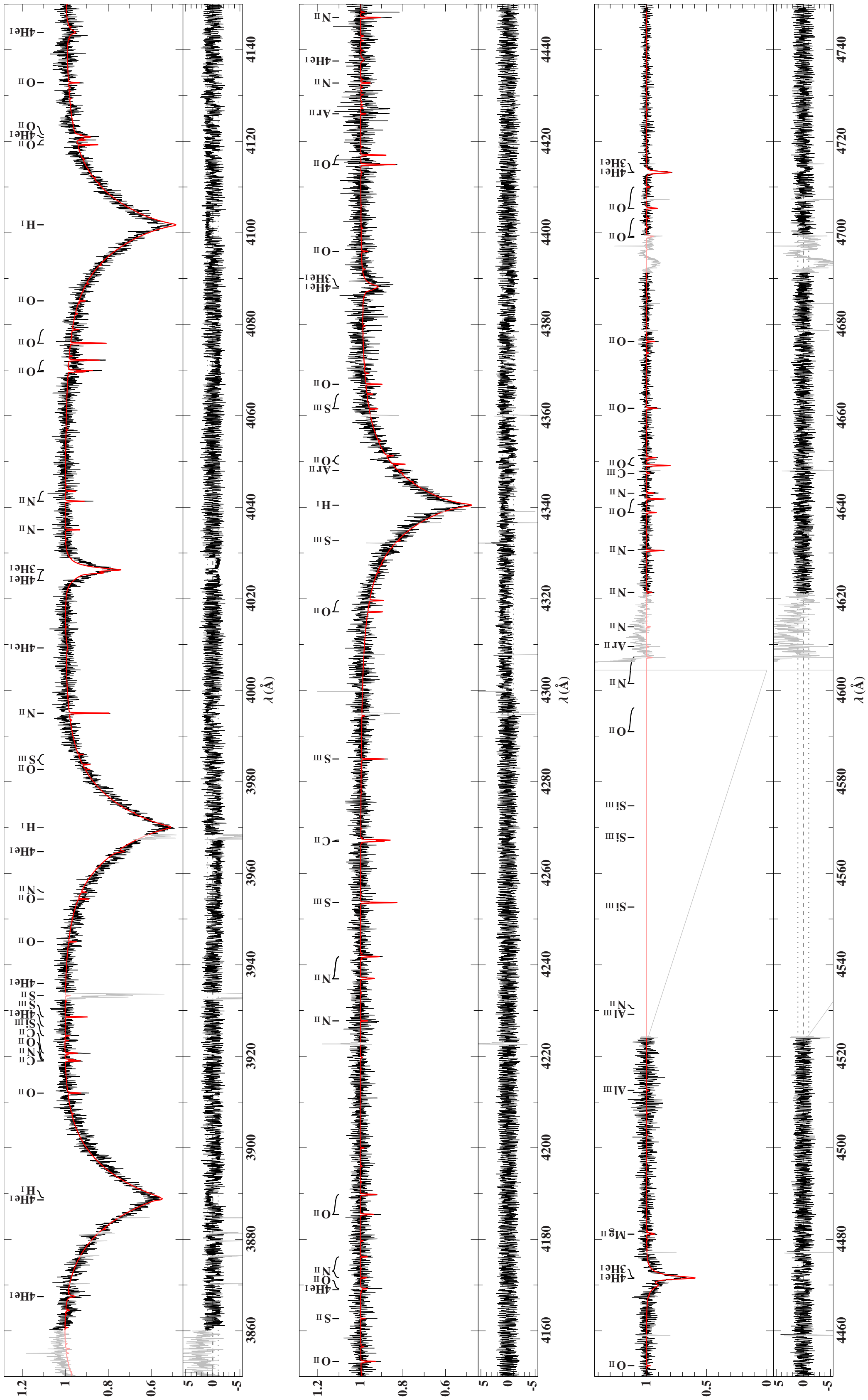

Figure B.1.70.: Fitted UVES spectrum of the ^{3}He enriched star HE 2322-0617 using the hybrid LTE/NLTE analysis with ISIS - Part 1.

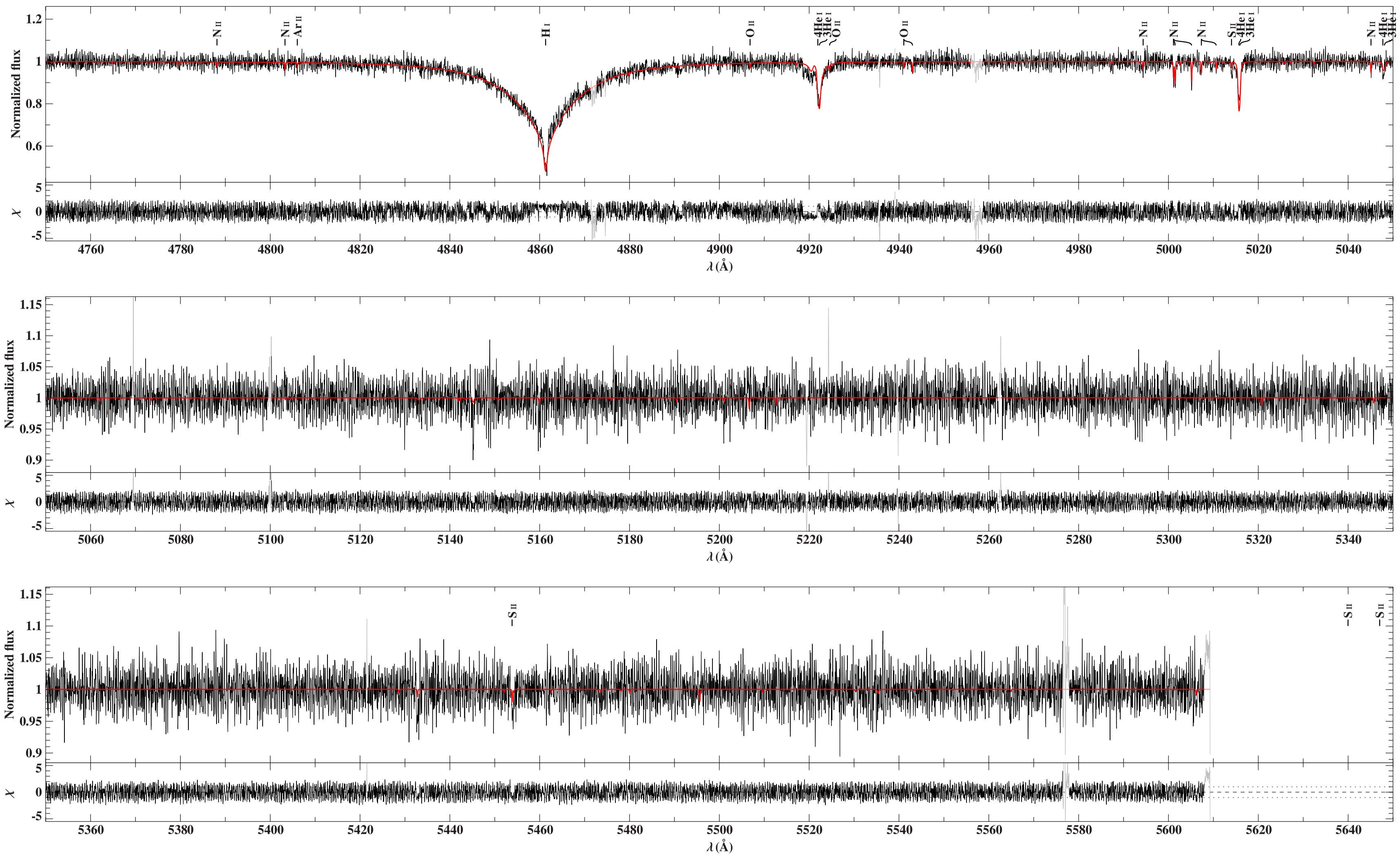

Figure B.1.71.: Fitted UVES spectrum of the $^3\mathrm{He}$ enriched star HE 2322-0617 using the hybrid LTE/NLTE analysis with ISIS - Part 2.

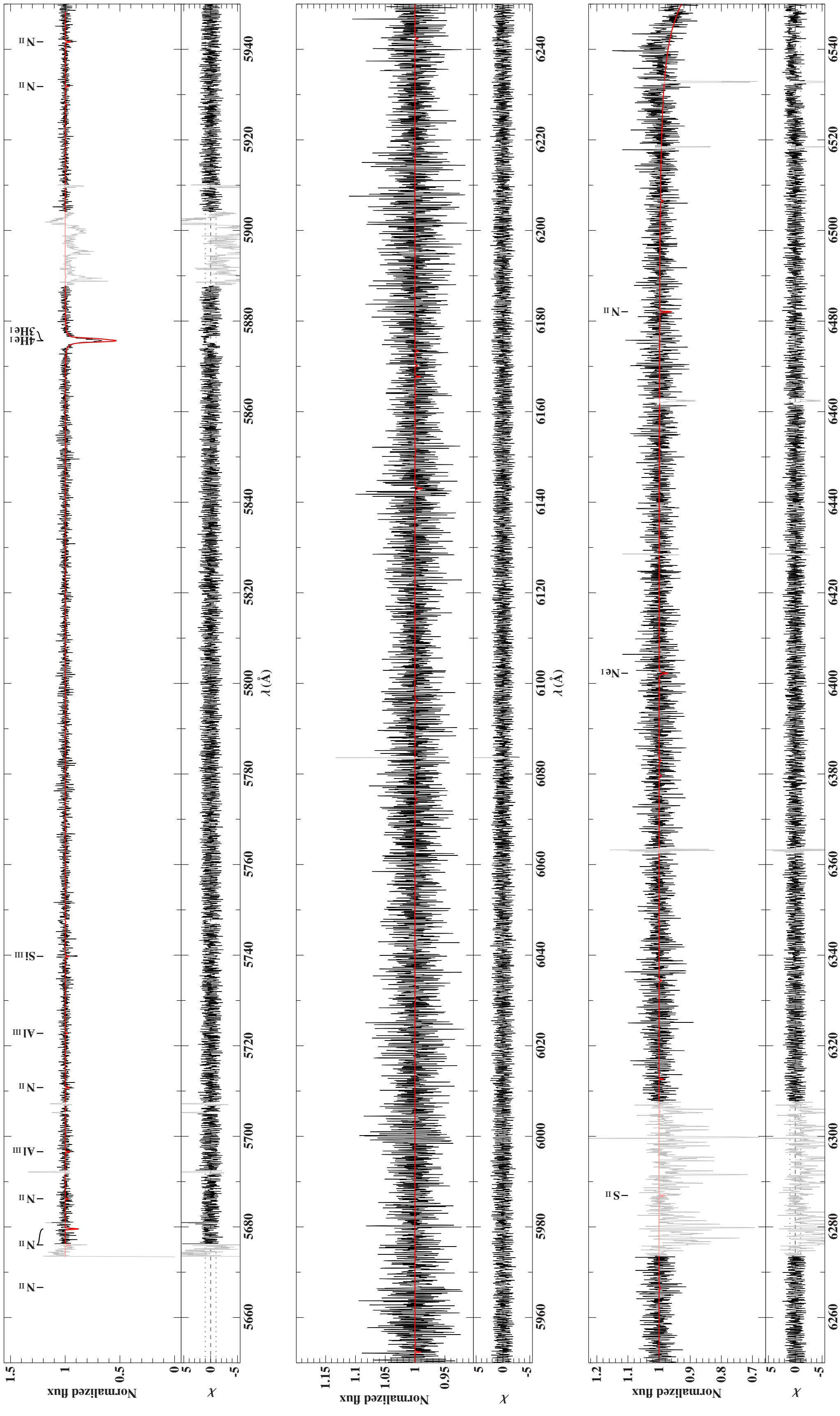

Figure B.1.72.: Fitted UVES spectrum of the $^3\mathrm{He}$ enriched star HE 2322-0617 using the hybrid LTE/NLTE analysis with ISIS - Part 3.

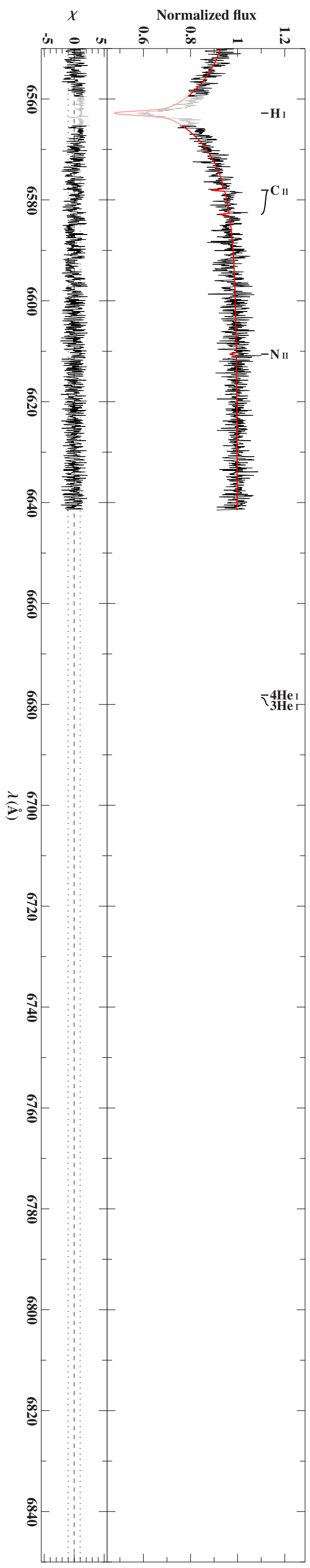

Figure B.1.73.: Fitted UVES spectrum of the $^{3}\mathrm{He}$ enriched star HE 2322-0617 using the hybrid LTE/NLTE analysis with ISIS - Part 4.

Bibliography

Abbott, D. C. 1982, ApJ, 259, 282 [ADS]

Asplund, M. et al. 2009, ARA&A, 47, 481 [ADS]

Atutov, S. N. 1986, Physics Letters A, 119, 121

Babel, J. 1996, A&A, 309, 867 [ADS]

Baschek, B. et al. 1972, ApJ, 173, 611 [ADS]

Bonifacio, P. et al. 1995, A&AS, 110, 441 [ADS]

Butler, K. & Giddings, J. R. 1985, in Newsletter of Analysis of Astronomical Spectra, No. 9, (Univ. London)

Cantiello, M. et al. 2009, A&A, 499, 279 [ADS]

Castelli, F. & Hubrig, S. 2007, A&A, 475, 1041 [ADS]

Chen, X. et al. 2013, MNRAS, 434, 186 [ADS]

Clausen, D. & Wade, R. A. 2011, ApJL, 733, L42 [ADS]

Collins, G. W. 1989, The Fundamentals of Stellar Astrophysics (W. H. Freeman and Company)

Connor, J. T. et al. 1966, Atomic Transition Probabilities Volume I, Hydrogen Through Neon - A Critical Data Compilation (U.S. Department of Commerce, National Bureau of Standards)

Conti, P. S. & Loonen, J. P. 1970, A&A, 8, 197 [ADS]

Dekker, H. et al. 1995, ARI[ADS]

Dobrichev, V. M. et al. 1989, Ap, 30, 53 [ADS]

Dorman, B. et al. 1993, ApJ, 419, 596 [ADS]

Drechsel, H. et al. 2015, Praktikumsanleitung des Astronomischen Praktikums, Friedrich-Alexander-Universität Erlangen-Nürnberg [LINK]

Drilling, J. S. et al. 2013, A&A, 551, id. A31, 12 pp. [ADS]

Dworetsky, M. M. 2004, in The A-Star Puzzle, eds. J. Zverko, J. Ziznovsky, S. J. Adelman, and W. W. Weiss, IAU Symp., 224, 727 [ADS]

Edelmann, H. et al. 1999, 11th European Workshop on White Dwarfs, ASP Conference Series 169, ed. by S.-E. Solheim and E. G. Meistas. Astronomical Society of the Pacific (San Francisco), 546 [ADS]

—. 2001, AN, 322, 401 [ADS]

—. 2003, A&A, 400, 939 [ADS]

Farthmann, M. et al. 1994, A&A, 291, 919 [ADS]

Fontaine, G. & Chayer, P. 1997, in The Third Conf. on Faint Blue Stars, ed. A.G.D. Philip et al. (Schenectady, NY: L. Davis), 169 [ADS]

Fred, M. et al. 1951, Phys. Rev., 82, 406

Geier, S. 2013, A&A, 549, A110 [ADS]

Geier, S. et al. 2013a, A&A, 557, A122 [ADS]

—. 2013b, A&A, 551, id. L4, 5 pp. [ADS]

—. 2016, A&A, arXiv, 11 pages, A&A accepted [ADS]

Giddings, J. R. 1981, PhD thesis, University of London [LINK]

Gray, D. F. 2005, The Observation and Analysis of Stellar Photospheres (Cambridge University Press)

Groote, D. & Hunger, K. 1997, A&A, 319, 250 [ADS]

Han, Z. et al. 2003, MNRAS, 341, 669 [ADS]

Hartoog, M. R. 1979, ApJ, 231, 161 [ADS]

Hartoog, M. R. & Cowley, A. P. 1979, ApJ, 228, 229 [ADS]

Heber, U. 1987, MitAG, 70, 79 [ADS]

—. 2009, ARA&A, 47, 211 [ADS]

—. 2016, ASP, 128 [ADS]

Heber, U. & Edelmann, H. 2004, Ap&SS, 291, 341 [ADS]

Heber, U. & Langhans, G. 1986, in Proc. New insights in astrophysics, ESA SP-263, 279 [ADS]

Heber, U. et al. 1986, A&A, 155, 33 [ADS]

Hirsch, H. 2009, PhD thesis, Friedrich-Alexander-Universität Erlangen-Nürnberg [LINK]

Houck, J. C. & Denicola, L. A. 2000, in Astronomical Data Analysis Software and Systems IX, ed. Manset, N.; Veillet, C.; and Crabtree, D., ASP Conf. Ser., 216, 591 [ADS]

Hu, H. et al. 2011, MNRAS, 418, 195 [ADS]

Hunger, K. & Groote, D. 1999, A&A, 351, 554 [ADS]

Hunger, K. et al. 1996, Hydrogen deficient stars, ASP Conference Series 96, ed. by C. S. Jeffery and U. Heber. Astronomical Society of the Pacific (San Francisco), 179 [ADS]

Irrgang, A. 2014, PhD thesis, Friedrich-Alexander-Universität Erlangen-Nürnberg [LINK]

Irrgang, A. et al. 2014, A&A, 565, A63, 31 pp. [ADS]

Karl, C. 2004, PhD thesis, Friedrich-Alexander-Universität Erlangen-Nürnberg [LINK]

Kaufer, A. et al. 1999, Commissioning FEROS, the New High-resolution Spectrograph at La Silla, `https://www.eso.org/sci/facilities/lasilla/instruments/feros/doc/messenger-no.95.pdf`, [Last called on August 22, 2016]

Kilkenny, D. & van Wyk, F. 1990, MNRAS, 244, 727 [ADS]

Krtička, J. 2006, A&A, 460, 145 [ADS]

Kurucz, R. L. 1996, in Model Atmospheres and Spectrum Synthesis, ed. Adelman, S. J.; Kupka, F.; and Weiss, W. W., 108, 160 [ADS]

Latour, M. et al. 2016, A&A, 585, A115, 17 pp. [ADS]

LeBlanc, F. & Michaud, G. 1993, ApJ, 408, 251 [ADS]

Lisker, T. et al. 2005, A&A, 430, 223 [ADS]

Maxted, P. F. L. et al. 2001, MNRAS, 326, 1391 [ADS]

Maza, N. L. et al. 2014, A&A, 572, id. A112, 7 pp. [ADS]

Michaud, G. 1970, ApJ, 160, 641 [ADS]

Michaud, G., Alecian, G. & Richer, J. 2015, Atomic Diffusion in Stars, Vol. 1 (Springer International Publishing Switzerland)

Michaud, G. et al. 1979, ApJ, 234, 206 [ADS]

—. 2011, A&A, 529, A60 [ADS]

Moehler, S. et al. 1990, A&AS, 86, 53 [ADS]

Napiwotzki, R. et al. 2004, ASP Conf. Ser., 318, 402 [ADS]

Naslim, N. et al. 2013, MNRAS, 434, 1920 [ADS]

Nelder, J. A. & Mead, R. 1965, Computer Journal, 7, 308

Nieva, M. F. & Przybilla, N. 2007, A&A, 467, 295 [ADS]

Osmer, P. S. & Peterson, D. M. 1974, ApJ, 187, 117 [ADS]

Pfeiffer, M. J. et al. 1998, A&A, 130, 381 [ADS]

Pintado, O. I. et al. 1998, A&AS, 129, 563 [ADS]

Podsiadlowski, P. et al. 2008, ASP Conf. Ser., 392, 15 [ADS]

Politano, M. et al. 2008, ApJ, 687, 99 [ADS]

Press, W. H., Flannery, B. P., Teukolsky, S. A. et al. 1986, Numerical Recipes - The Art of Scientific Computing, Vol. 1 (Cambridge University Press)

Przybilla, N. 2005, A&A, 443, 293 [ADS]

Przybilla, N. et al. 2005, A&A, 443, L25 [ADS]

—. 2011, Journal of Physics: Conference Series, 328, 012015 [ADS]

—. 2016, A&A, arXiv, 15 pages,, A&A accepted [ADS]

Randich, S. & Pasquini, L. 1996, CASPEC - Operating Manual

Saffer, R. et al. 1994, ApJ, 432, 351 [ADS]

Sargent, A. W. L. W. & Jugaku, J. 1961, ApJ, 134, 777 [ADS]

Schaffenroth, V. 2015, PhD thesis, Friedrich-Alexander-Universität Erlangen-Nürnberg [LINK]

Schmitt, A. 1972, A&AS, 9, 427 [ADS]

Schneider, D. 2014, Eine Radialgeschwindigkeitsstudie des Röntgen-Doppelsterns BD $+37^\circ$ 442, Friedrich-Alexander-Universität Erlangen-Nürnberg [LINK]

Ströer, A. et al. 2005, 14th European Workshop on White Dwarfs, ASP Conference Series 334, ed. by D. Koester and S. Moehler. Astronomical Society of the Pacific (San Francisco), 309 [ADS]

Tull, R. S. 1998, High-resolution fiber-coupled spectrograph of the Hobby-Eberly Telescope, `http://hydra.as.utexas.edu/imgs/HRS-Tull_SPIE_Vol3355_1998.pdf`, [Last called on August 25, 2016]

Unglaub, K. 2008, A&A, 486, 923 [ADS]

Unglaub, K. & Bues, I. 2001, A&A, 374, 570 [ADS]

Vauclair, S. 1975, A&A, 45, 233 [ADS]

Vauclair, S. et al. 1974, A&A, 31, 381 [ADS]

Webbink, R. F. 1984, ApJ, 277, 355 [ADS]

Zakharova, L. A. & Ryabchikova, T. A. 1996, Astron. Lett., 22, 152 [ADS]

Zhang, X. & Jeffery, C. S. 2012, ASP Conf. Ser., 452, 13 [ADS]

List of Figures

List of Tables

Acknowledgments

At this point, I would really like to thank each and everyone of the people without whom the writing of this thesis certainly would not have been possible at all. Without their technical and not to forget psychological support, I would never have been able to achieve such a great deal.

First of all, I would like to thank Prof. Dr. Ulrich Heber who proposed this extremely interesting topic so early to me. He always had an open ear and was able to help me in matters of difficulties in understanding the theoretical background or in the evaluation of my analysis, respectively.

Whenever I had questions concerning the analysis methods and ISIS scripts used for this thesis, I always could address myself to Dr. Andreas Irrgang right from the beginning. He provided me most of these scripts and assisted and advised me on how to use them properly.

Special thanks also go to Prof. Dr. Norbert Przybilla and Dr. Maria Fernanda Nieva, who provided the developed $^{3}\mathrm{He}$ model atom by Maza et al. (2014). Without this model atom, the analysis performed in the framework of this thesis would not have been possible at all.

Certainly, I have to thank Dr. Dr. Stephan Geier and Dr. Heinz Edelmann, too, who provided me most of the analyzed spectra.

I am also very grateful to both of the administrators, Dr. Ingo Kreykenbohm and Fritz-Walter Schwarm, for maintaining and improving the Remeis computer cluster that has been extensively used for this study. They always had an open ear for my questions on the Remeis Torque and its features.

Actually, the whole stellar astronomy group made life so much easier at the office. My special thanks here go to Dr. Marilyn Latour, Dr. Peter Nemeth and Markus Schindewolf who invested their time to help me to learn Python and to use it for making nice plots. I enjoyed the extremely helpful discussions we had concerning my work. But I am also glad that they provided me detailed insights in their interesting fields of work. In this way, I definitely learned a lot. Together with Maximilian Wolz, Jan Friedmann, Johannes Schaffenroth, Simon Kreuzer, Monika Schork and Laura Federle, I could really laugh a lot and I am therefore thankful for the variety of topics of conversation we had during this hard time.

In addition, I want to highlight my fellow students Jens Holzmeier, Maximilian Düll, Florian Wolz, Philipp Schuster, Mona Pistel and Lisa Seitz. Although working on very different physical topics for their bachelor/master theses, they have been very helpful by just letting me know that I am not the only one having difficulties during the analysis and in completing the thesis. I really appreciate our weekly meetings here and there.

Not only my fellow students but also my former school friends in and around Erlangen always encouraged me to not just stop but continue my physicist career. Andreas Voinea, Dominik Penk, Florian Zmija, Maximilian Pritsching, Christoph Biernoth, David Weiß and Jonas Wilkes

have to be named here. Special thanks to you for your psychological support.
Last but not least, I want to point out my lovely parents Edgar and Veronika Schneider who essentially supported me financially, but also psychologically. I am also extremely thankful that they always believe in me and that I have their full support and confidence at all the things I (want to) do, in particular at becoming a physicist.
All of you, also the ones I forgot to mention by name here, really have helped me during all the setbacks within this stressful time. Thank you very much.

Erklärung

Ich versichere, dass ich meine Masterarbeit ohne Hilfe Dritter und ohne Benutzung anderer als der angegebenen Quellen und Hilfsmittel angefertigt habe und die aus benutzten Quellen wörtlich oder inhaltlich entnommenen Stellen als solche kenntlich gemacht habe. Diese Arbeit hat in gleicher oder ähnlicher Form noch keiner Prüfungsbehörde vorgelegen.

Bamberg, den 6. Februar 2017

David Schneider